Annual reports on NMR Spectroscopy

Volume 72

Annual Reports on

NMR SPECTROSCOPY

VOLUME **72**

This page intentionally left blank

Annual Reports on
NMR SPECTROSCOPY

VOLUME 72

Edited by

GRAHAM A. WEBB
Royal Society of Chemistry
Burlington House
Piccadilly, London, UK

Amsterdam • Boston • Heidelberg • London • New York • Oxford
Paris • San Diego • San Francisco • Singapore • Sydney • Tokyo
Academic Press is an imprint of Elsevier

Academic Press is an imprint of Elsevier
Linacre House, Jordan Hill, Oxford OX2 8DP, UK
32 Jamestown Road, London NW1 7BY, UK
Radarweg 29, PO Box 211, 1000 AE Amsterdam, The Netherlands
30 Corporate Drive, Suite 400, Burlington, MA 01803, USA
525 B Street, Suite 1900, San Diego, CA 92101-4495, USA

First edition 2011

Copyright © 2011 Elsevier Ltd. All rights reserved

No part of this publication may be reproduced, stored in a retrieval system or transmitted in any form or by any means electronic, mechanical, photocopying, recording or otherwise without the prior written permission of the publisher

Permissions may be sought directly from Elsevier's Science & Technology Rights Department in Oxford, UK: phone (+44) (0) 1865 843830; fax (+44) (0) 1865 853333; email: permissions@elsevier.com. Alternatively you can submit your request online by visiting the Elsevier web site at http://elsevier.com/locate/permissions, and selecting *Obtaining permission to use Elsevier material*

Notice
No responsibility is assumed by the publisher for any injury and/or damage to persons or property as a matter of products liability, negligence or otherwise, or from any use or operation of any methods, products, instructions or ideas contained in the material herein. Because of rapid advances in the medical sciences, in particular, independent verification of diagnoses and drug dosages should be made

British Library Cataloguing in Publication Data
A catalogue record for this book is available from the British Library

Library of Congress Cataloging-in-Publication Data
A catalog record for this book is available from the Library of Congress

ISBN: 978-0-12-385857-3
ISSN: 0066-4103

For information on all Academic Press publications
visit our web site at elsevierdirect.com

Printed and bound in Great Britain
11 12 13 10 9 8 7 6 5 4 3 2 1

Working together to grow
libraries in developing countries
www.elsevier.com | www.bookaid.org | www.sabre.org
ELSEVIER BOOK AID International Sabre Foundation

CONTENTS

This page intentionally left blank

CONTRIBUTORS

Shuhui Cai
Department of Physics, Fujian Key Laboratory of Plasma and Magnetic Resonance, State Key Laboratory of Physical Chemistry of Solid Surfaces, Xiamen University, Xiamen, China

Zhong Chen
Department of Physics, Fujian Key Laboratory of Plasma and Magnetic Resonance, State Key Laboratory of Physical Chemistry of Solid Surfaces, Xiamen University, Xiamen, China

Jürgen Finsterbusch
Department of Systems Neuroscience, University Medical Center Hamburg-Eppendorf, Hamburg, Germany

Paul Hodgkinson
Department of Chemistry, Durham University, Durham, United Kingdom

Yuqing Huang
Department of Physics, Fujian Key Laboratory of Plasma and Magnetic Resonance, State Key Laboratory of Physical Chemistry of Solid Surfaces, Xiamen University, Xiamen, China

Yanqin Lin
Department of Physics, Fujian Key Laboratory of Plasma and Magnetic Resonance, State Key Laboratory of Physical Chemistry of Solid Surfaces, Xiamen University, Xiamen, China

Norbert Müller
Institute of Organic Chemistry, Johannes Kepler University Linz, Linz, Austria

William P. Power
Department of Chemistry, University of Waterloo, Waterloo, Ontario, Canada

Judith Schlagnitweit
Institute of Organic Chemistry, Johannes Kepler University Linz, Linz, Austria

Wolfgang Schoefberger
Institute of Inorganic Chemistry, Johannes Kepler University Linz, Linz, Austria

N. Suryaprakash
NMR Research Centre, Indian Institute of Science, Bangalore, India

This page intentionally left blank

PREFACE

Volume 72 of Annual reports on NMR consists of a collection of reviews from a diverse selection of areas of molecular science. The volume commences with an account of 'Recent Developments in HMBC (Heteronuclear Multibond Correlation) Experiments' by W. Schoefberger, J. Schlagnitweit and N. Mueller; N. Suryaprakash covers 'Two Dimensional Higher Quantum Correlation and Resolved Techniques for the Analyses of Complex ^{1}H NMR Spectra of Scalar Coupled Spins'; W.P. Power reports on 'High Resolution Magic Angle Spinning; Enabling Applications of NMR Spectroscopy to Semi-Solid Phases'; 'Accurate Measurement of Small J Couplings' is reported upon by Z. Chen, Y. Huang, Y. Lin and S. Cai; P. Hodgkinson discusses 'High Resolution ^{1}H NMR Spectroscopy of Solids'; finally, J. Finsterbusch provides an account of 'Multiple-Wave-Vector Diffusion-Weighted NMR'.

It is a pleasure for me to express my gratitude to all of these reporters for their interesting and comprehensive accounts.

G. A. Webb
Royal Society of Chemistry
Burlington House
Piccadilly, London, UK

This page intentionally left blank

CHAPTER 1

Recent Developments in Heteronuclear Multiple-Bond Correlation Experiments

Wolfgang Schoefberger,* Judith Schlagnitweit,† and **Norbert Müller†,1**

Contents

* Institute of Inorganic Chemistry, Johannes Kepler University Linz, Linz, Austria
† Institute of Organic Chemistry, Johannes Kepler University Linz, Linz, Austria
[1] Corresponding author.

Annual Reports on NMR Spectroscopy, Volume 72
ISSN 0066-4103, DOI: 10.1016/B978-0-12-385857-3.00001-3

© 2011 Elsevier Ltd.
All rights reserved.

Abstract Today, structure elucidation of complex organic molecules relies heavily on the application of proton-detected heteronuclear NMR techniques. Among these techniques, the HMBC experiment is one of the most useful 2D NMR methods. Carbon–proton HMBC experiments allow the assignment of structural fragments through correlations between protons and carbons separated by more than one bond, usually two or three bonds via small $^{1}H–^{13}C$ couplings, usually $^{2}J_{CH}$ and $^{3}J_{CH}$, but also over longer bond chains, $^{n>3}J_{CH}$, especially in conjugated systems. In the decade preceding this review, several significant extensions to the basic HMBC experiment have been made. The main directions of developments were widening the range of accessible long-range *J*-coupling constants, improving sensitivity, refining resolution, suppressing one-bond correlations and accurately determining long-range coupling constants. In addition, increasing the efficiency of multi-dimensional NMR techniques, an important contemporary trend in NMR, has also had its impact on HMBC, with multiplex approaches and parallel acquisition techniques emerging. Structure elucidation and signal assignment of proton-deficient molecules like condensed aromatics has benefited most substantially from the new possibilities for a detailed analysis of long-range correlations. In this review, we summarize the basic variants of HMBC and discuss recent developments related to the technique, focusing on developments of new pulse sequences and processing protocols.

Key Words: NMR, Heteronuclear coupling, Long-range heteronuclear shift correlation, HMBC, D-HMBC, 3D-HMBC, 3D-*J*-HMBC, CT-HMBC, ACCORD-HMBC, IMPEACH-HMBC, BIRD-HMBC, CIGAR-HMBC, IMPACT-HMBC, COSY–HMBC, TS-HMBC, Γ-HMBC, HMSC, Clean HMBC, Multiplicity editing, Ultrafast HMBC, Cartesian product operators, Covariance processing.

1. INTRODUCTION

Over 2000 scientific papers mentioning the HMBC (heteronuclear multiple-bond correlation) experiment in the title or keywords have been published between the year 2000 and the time of writing this review, according to the Scopus database. A rough analysis of the respective journals' scopes shows that ca. 80% of these articles are not NMR-centric, that is, not focused on method development in NMR. These numbers evidence that HMBC and derivative experiments are considered crucial by researchers in diverse fields of application. Notably, more than a third of these articles appeared in journals dedicated to natural products research, emphasizing that HMBC is an indispensable tool for structure elucidation of organic natural products, in which isotopic labelling usually is not a viable alternative assignment strategy. HMBC-type experiments are not widely used in mainstream protein NMR, where isotopic labelling is relatively easy, and highly specialized correlation methods exploiting the well-defined narrow ranges of heteronuclear one- and two-bond coupling constants prevail. In this review, we focus on methodological advances and will mention some application examples, which are necessarily not fully representative of the method's scope. The application examples selected are almost exclusively carbon–hydrogen correlation experiments, which are, in practice, the most important application areas in organic and biological chemistry. ^{15}N long-range correlation experiments have been reviewed in this series previously.[1]

The HMBC experiment, which is based on multiple-quantum experiments proposed by L. Müller[2] and improved by Bax and Summers,[3] has developed through many incarnations into one of the most versatile and indispensable NMR tools for elucidating structures of organic molecules, in particular, complex natural products. Normally used as a 2D technique, it is crucial for establishing long-range correlations (i.e. over two or more bonds) between protons and heteronuclei, especially for non-protonated nuclei such as condensed aromatic ring systems. The basic HMBC experiment has a few drawbacks that have prompted the development of a variety of new pulse sequences. Some of the more recent of these will be discussed in this review. Previous progress in HMBC has been summarized in earlier review chapters[4,5] and will not be covered in detail here.

The directions of improvement of HMBC experiments can be categorized as follows (1) extending the limited range of coupling constants, (2) enhancing the relatively low sensitivity, (3) eliminating the influence of homonuclear couplings and (4) using alternative processing methods. These four goals will be discussed in context after a comprehensive summary of the spin dynamics in fundamental HMBC pulse sequences in the next section. When comparing the sensitivity of various pulse sequences, one must bear in mind that through the technological advances in NMR electronics and probes (in particular, cryogenically cooled probes), the sensitivity limit has been pushed by approximately an order of magnitude in the past decade, which makes experiments practically applicable, which were previously just considered 'proofs of concept'.

While focusing on long-range *J*-coupling correlations, it should be borne in mind that cross-correlated relaxation may cause effects, which are similar to scalar spin–spin coupling. Such behaviour has also been observed and exploited in HMBC spectra.[6,7]

2. THEORY

The original HMBC experiment[3] illustrated in Figure 1 is based on heteronuclear MQT experiments[2] and the heteronuclear multiple-quantum coherence (HMQC) experiment.[8]

In all pulse sequence graphics within this review, we use a consistent representation, with the following conventions as follows: Narrow and wide rectangular blocks represent 90° and 180° rf-pulses, respectively. In some sequences, even narrower blocks are used to indicate smaller flip angles (e.g. $\pi/4$-pulses in TANGO elements). Trim pulses and decoupling pulse trains are indicated by hatched blocks. Besides standard delays t_1 (evolution time) and t_2 (acquisition time), all other delays are designated by different variable names, which are defined in the text or the figure caption. Coupling constants J_{AB} without prepended superscript denote one-bond couplings and ${}^nJ_{AB}$ long-range couplings. Gradient pulses are represented by bell shapes. In some experiments, filled and open blocks are used for pulses, where the open blocks denote the pulses, which are phase-cycled for coherence pathway selection. Numbers above or below gradient pulse symbols indicate the relative gradient strengths. The recycle delay t_{rd} will be omitted from further pulse sequence graphs, to save space.

However, different approaches to long-range correlation building on the HSQC pulse sequence,[9] like HSQMBC (heteronuclear single-quantum multiple-bond correlation),[10] are available, as HMQC-based experiments yield, in principle, the same basic correlations as HSQC-derived ones. The differences between the spectra obtained by these experiments pertain to sensitivity and peak shapes and are mostly due to variations in the evolution of homonuclear couplings and relaxation.

To highlight some of the issues associated with the HMBC experiment, we analysed the basic HMBC sequence without low-pass J-filter (shown in Figure 2 applied to a spin system consisting of three protons (I_1–I_3) and one heteronucleus (S, spin 1/2) assuming the following coupling network: I_2–I_1–S_4–I_3; that is, an abundant nucleus I_1 coupled through a long-range coupling to a rare nucleus S and via homonuclear coupling to I_2; in addition, S is coupled to another abundant spin I_3. Product operator calculations using POMA[11,12] show that (neglecting relaxation and strong coupling effects) the I_1–S cross-peak amplitude C obtained from this basic pulse sequence exhibits a complex phase dependence in the indirect dimension, which is very much depending on the homonuclear coupling:

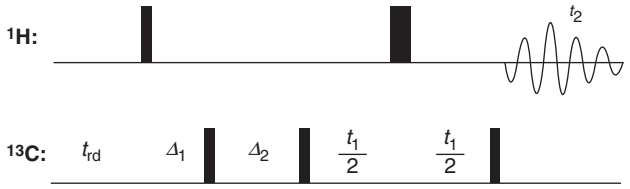

Figure 1 Original HMBC pulse sequence with low-pass *J*-filter by Bax and Summers.[3] With $\Delta_1 = (2\,{}^1J_{IS})^{-1}$, $\Delta_2 = (2\,{}^nJ_{IS})^{-1}$.

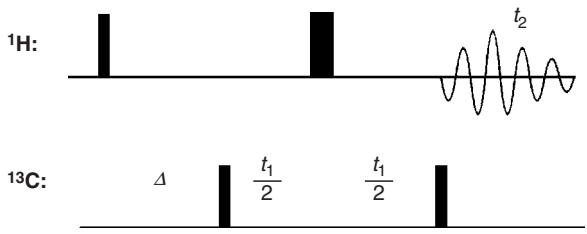

Figure 2 HMBC pulse sequence without LPJF, $\Delta = (2\,{}^{n}J_{\mathrm{IS}})^{-1}$.

$$C(\Delta) = \cos(t_1\Omega_{\mathrm{S}})\sin(\pi\Delta J_{1,\mathrm{S}})[\sin(\pi J_{12}t_1 + \pi\Delta J_{12})(4\sin(\Delta\Omega_1)\mathrm{I}_{1x}\mathrm{I}_{2z}\mathrm{S}_{4z} + 4\cos(\Delta\Omega_1)\mathrm{I}_{1y}\mathrm{I}_{2z}\mathrm{S}_{4z}) + \cos(\pi J_{12}t_1 + \pi\Delta J_{12})(2\cos(\Delta\Omega_1)\mathrm{I}_{1x}\mathrm{S}_{4z} - 2\sin(\Delta\Omega_1)\mathrm{I}_{1y}\mathrm{S}_{4z})]. \tag{1}$$

Even in the case of an ideal match of the delay $\Delta = (2J_{1,\mathrm{S}})^{-1}$, one obtains a rather unwieldy expression

$$C\left(\Delta = (2J_{1,\mathrm{S}})^{-1}\right) = \cos(t_1\Omega_{\mathrm{S}})\left[\sin\left(\frac{\pi J_{12}}{2J_{1,\mathrm{S}}} + \pi J_{12}t_1\right)\left(4\mathrm{I}_{1x}\mathrm{I}_{2z}\mathrm{S}_{4z}\sin\left(\frac{\Omega_1}{2J_{1,\mathrm{S}}}\right) + 4\mathrm{I}_{1y}\mathrm{I}_{2z}\mathrm{S}_{4z}\cos\left(\frac{\Omega_1}{2J_{1,\mathrm{S}}}\right)\right) + \cos\left(\frac{\pi J_{12}}{2J_{1,\mathrm{S}}} + \pi J_{12}t_1\right)\left(2\mathrm{I}_{1x}\mathrm{S}_{4z}\cos\left(\frac{\Omega_1}{2J_{1,\mathrm{S}}}\right) - 2\mathrm{I}_{1y}\mathrm{S}_{4z}\sin\left(\frac{\Omega_1}{2J_{1,\mathrm{S}}}\right)\right)\right]. \tag{2}$$

It contains mixed absorptive and dispersive as well as single and double anti-phase Cartesian product operator terms depending on the chemical shift of I_1 as well as on the ratio of the homo- and heteronuclear coupling constants and modulated by homonuclear proton coupling during the evolution time t_1. Since both the heteronuclear and the homonuclear coupling constants typically encountered are in the same range and also highly variable, it is impossible to obtain pure-phase spectra in a general case. For these reasons, most basic HMBC experiments are only displayed in magnitude mode. The anti-phase character precludes decoupling during acquisition. In addition, homonuclear I-spin couplings split or broaden the line shapes in the indirect domain, as the heteronuclear two-spin coherence [a superposition of zero quantum coherence (0QC, ZQC) and double-quantum coherence ($\pm$2QC, DQC)] is evolving according to

$$2\mathrm{I}_{2x}\mathrm{S}_x \rightarrow -4\mathrm{I}_{1y}\mathrm{I}_{2z}\mathrm{S}_{4x}\sin(\pi J_{12}t_1)\cos(t_1\Omega_{\mathrm{S}}) - 4\mathrm{I}_{1y}\mathrm{I}_{2z}\mathrm{S}_{4y}\sin(\pi J_{12}t_1)\sin(t_1\Omega_{\mathrm{S}}) - 2\mathrm{I}_{1x}\mathrm{S}_{4y}\cos(\pi J_{12}t_1)\sin(t_1\Omega_{\mathrm{S}}) - 2\mathrm{I}_{1x}\mathrm{S}_{4x}\cos(\pi J_{12}t_1)\cos(t_1\Omega_{\mathrm{S}}). \tag{3}$$

If homonuclear coupling modulations need to be avoided, either HSQC-based experiments[13,14] or constant-time (CT) evolution modifications of HMBC can be used.[15] Further, due to the terms depending on the ratio of the heteronuclear and homonuclear coupling constants in Equations (1) and (2), phase errors are all but unavoidable. From these equations, it is also evident that additional heteronuclear

couplings from S- to I-spins, that, like I_3 in our example, are not homonuclearly coupled to the originating spin I_1, do not affect these basic spectra. Of course due to the absence of decoupling, all homo- and heteronuclear couplings of I_1 also contribute to its multiplet splitting in the directly detected dimension.

In the absence of homonuclear coupling, pure absorption line shapes can be obtained if a refocusing delay of duration Δ is inserted before acquisition.

Broadband decoupling of the S spin can then be used to obtain singlets in f_2 dimension. Many other improvements that have been proposed for HMBC and which will be mentioned in this text, therefore attempt to reduce the coupling constant dependence as well as improve the phase and line shapes to obtain better sensitivity and resolution. Refocusing of anti-phase terms to allow for heteronuclear decoupling during acquisition may also help, but this advantage needs to be balanced against potential relaxation losses.

The LPJF in the original HMBC sequence (Figure 1) suppresses one-bond couplings correlations originating from a different set of isotopomers, by converting anti-phase coherences for large coupling constants to unobservable multiple-quantum coherence (MQC). But it does not affect the long-range cross-peak appearance, apart from a usually negligible amplitude reduction of ca. 1% for typical ^{1}H–^{13}C or ^{1}H–^{15}N spectra, which is due to a factor of $\cos(\pi\,{}^nJ_{1,S}(2\,{}^1J_{IS})^{-1})$, as will be shown later.

The basic HMBC as well as HMQC[3] experiments are considered very robust ones due to the low number of rf-pulses, which in practice do not require a lot of adjustment during setup, especially as there are no π-pulses on the heteronuclei. This low complexity with just five pulses (Figure 1) leaves ample opportunity for extensions of the pulse sequence, which are in the focus of this review.

3. BASIC EXPERIMENTS

3.1. Classical HMBC

'Heteronuclear multiple-bond coherence' is an NMR technique first reported by Bax and Summers,[3] in which ^{1}H nuclei are correlated to remote ^{13}C nuclei (two or three bonds away) in a 2D experiment via their long-range heteronuclear J-couplings ($^nJ_{CH}$). The original experiment differs from the basic four-pulse HMQC experiment discussed above in three ways:

1. The defocusing delay is much longer [$(2\,{}^nJ_{CH})^{-1} > 50$ ms vs. $(2\,{}^1J_{CH})^{-1} \approx 3.3$ ms] to accommodate the small long-range coupling constants ($\sim$10 Hz or less vs. $\sim$150 Hz).
2. To avoid further loss of signal due to T_2 relaxation during an equally long refocusing delay, the refocusing delay at the end of the sequence is omitted. The observed ^{1}H signals are therefore in anti-phase with respect to the remote ^{13}C, and decoupling cannot be used during acquisition of the FID.
3. A $\pi/2$ ^{13}C pulse is inserted just 3.3 ms $= \Delta = 1/(2\,{}^1J_{CH})$ after the initial ^{1}H $\pi/2$-pulse, to convert anti-phase ^{1}H coherence due to one-bond coupled ^{13}C into multiple-quantum coherence (MQC), just as it is in the HMQC experiment. The

phase cycling of this pulse ensures that coherence transfer pathways through this coherence are cancelled out. This common pulse sequence building block is called a 'low-pass *J*-filter',[16] often abbreviated as LPJF: It attenuates or eliminates cross-peaks due to one-bond heteronuclear couplings. Several low-pass *J*-filters can be concatenated to achieve superior suppression (see, e.g. Ref. 17).

Using Cartesian product operator calculations, the basic low-pass *J*-filtered HMBC experiment (Figure 1) of a spin system consisting of a spin I_1 coupled through one-bond coupling ($J_{14} = {}^1J_{CH}$) to a rare nucleus S_4 and of another spin I_2 coupled through a long-range coupling to the same rare nucleus ($J_{24} = {}^nJ_{CH}$) is analysed. After the second pulse in the sequence of Figure 1, one obtains the density matrix of filtered terms:

$$\begin{aligned}\sigma_{\text{filter}} = {} & \cos\left(\frac{\pi J_{2,S}}{2J_{1,S}}\right)\sin\left(\frac{\Omega_2}{2J_{1,S}}\right)I_{2x} - 2\cos\left(\frac{\Omega_2}{2J_{1,S}}\right)\sin\left(\frac{\pi J_{2,S}}{2J_{1,S}}\right)S_{4y}I_{2x} \\ & - \cos\left(\frac{\pi J_{2,S}}{2J_{1,S}}\right)\cos\left(\frac{\Omega_2}{2J_{1,S}}\right)I_{2y} - 2\cos\left(\frac{\Omega_1}{2J_{1,S}}\right)I_{1x}S_{4y} \\ & -2\sin\left(\frac{\Omega_1}{2J_{1,S}}\right)I_{1y}S_{4y} - 2\sin\left(\frac{\pi J_{2,S}}{2J_{1,S}}\right)\sin\left(\frac{\Omega_2}{2J_{1,S}}\right)I_{2y}S_{4y}.\end{aligned} \tag{4}$$

All two-spin terms represent MQC and are cancelled out by phase cycling. This means that the only remaining terms for the defocusing delay $(2\,{}^nJ_{CH})^{-1}$ corresponds to spin I_2. Using pulsed field gradients (PFGs), more efficient low-pass filters are possible, as will be shown later in this review. The basic HMBC experiment is always recorded in magnitude mode because the lack of refocusing of ^{1}H chemical shift evolution during the long delay leads to substantial frequency-dependent phase shifts in the f_2 dimension. The obvious disadvantage of magnitude mode HMBC is that the peak shape is broad with long 'tails', leading to long ridges, sometimes extending to the margins of the spectrum for the most intense cross-peaks. Although this problem can be alleviated by the use of 'aggressive' window functions (e.g. a full sine bell) during processing, it represents a major disadvantage if both high resolution and high sensitivity are required. In addition, it is often difficult to identify weak cross-peaks, since both the signal and the noise as well as electronic artefacts appear positive. The anti-phase structure of HMBC cross-peaks, which is very useful for recognition of small peaks, is lost when calculating the magnitude, and this structure makes weak cross-peaks 'stand out' from noise.

3.2. Decoupled HMBC

HMBC suffers from relatively low sensitivity as compared to one-bond heteronuclear correlation techniques. The detection of cross-peaks becomes especially difficult with multiply split methylene proton signals, particularly if signals are

broad. Furihata et al. used the standard HMQC experiment, relabelled as decoupled HMBC (D-HMBC), to overcome such problems and obtained spectra with improved signal-to-noise ratio.[18,19] This improvement is due to the refocusing of the heteronuclear coupling as the generation of in-phase signals allows decoupling during acquisition, leading to narrower signals. Thus, the spectra can be acquired in the phase-sensitive mode by suppressing the decrease of signal-to-noise ratio due to poor digital resolution. The only difference to the previously described HMBC experiment is that wide-band decoupling sequences such as MPF[20] for the ^{13}C nucleus are employed in D-HMBC, particularly if quaternary carbonyl signals appearing at the highest frequencies must also be decoupled. The decoupling bandwidth required is wider (more than 230 ppm) than that used normally for HMQC, which can pose implementation problems on higher field instruments. A LPJF is not part of the original sequence, but can be implemented easily, if considered necessary. It is claimed that D-HMBC facilitates observation of ^{13}C–^{1}H long-range couplings with small coupling constants.[18,19] As an illustrative example, HMBC of the peptide derivative promothiocin B,[18] yielded information on long-range couplings between ^{13}C and ^{1}H separated by four to five bonds with fixed delay times Δ of 120 ms and 500 ms, respectively, as shown in Figure 3. In addition, very small long-range couplings through three bonds ($\leq$2 Hz), which could not be observed by standard HMBC, were detectable by

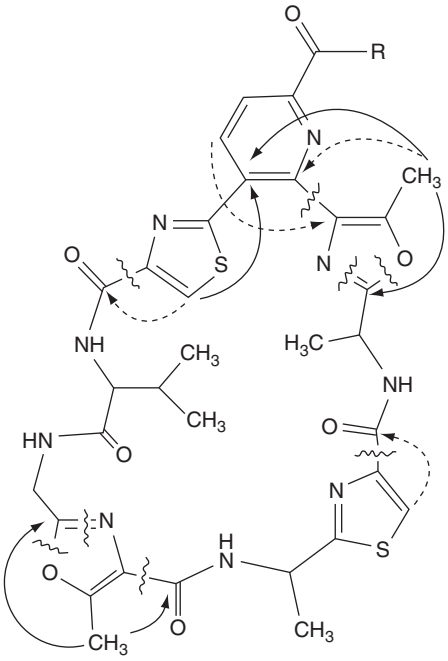

Figure 3 Long-range couplings observed in the D-HMBC spectra of promothiocin B. Correlations observed with coupling evolution time $\Delta = 120$ ms are indicated by dotted curved arrows and those with $\Delta = 500$ ms by full ones. Reprinted with permission from Ref. 18.

D-HMBC. The observation of such small long-range coupling correlations enabled the researchers to connect partial fragments delineated by conventional NMR techniques to the complete structure, as shown in Figure 3.

Decoupling during the acquisition time sometimes makes it more difficult to distinguish between one-bond and long-range coupling correlations, since the splitting information is missing. However, for certain applications like covariance processing (see Section 13.), it is a prerequisite.

3.3. Gradient HMBC

The major artefacts in the classical HMBC are noise ridges, which extend along the f_1 axis at the f_2 frequencies of all the intense proton resonances. Weak cross-peaks are therefore very difficult to detect on top of these ridges. These noise bands result from an imperfect cancellation of the signals of protons, which are not coupled to an indirectly detected heteronucleus and are therefore not labelled with its frequency. Selective inversion of the protons directly bound to an NMR inactive nucleus (e.g. via BIRD[21,22]) cannot be used, since this would apply to all protons of interest in a long-range correlation experiment.

An orders of magnitude improvement in the suppression of the noise ridges and a substantial breakthrough for the routine application of HMBC experiments, as compared to previous pulse sequences, was the introduction of PFGs,[23–25] since PFG techniques allow one to eliminate signals from undesired coherence transfer pathways in a single transient. The relative benefits of gradient-selected versus phase cycle-selected HMBC have been discussed earlier.[26]

In a basic ^{13}C-HMBC, this is typically achieved by three gradient pulses: in the first half of the evolution delay, in the second half and just before acquisition of the FID, with relative gradient strengths of 5, 3 and 4, respectively. This scheme selects double-quantum coherence during the evolution period and scrambles other coherence pathways (Figure 4).

Gradient HMBC spectra are virtually free of f_1 ridges. As an additional advantage, the receiver gain can be increased very much, because the undesired ^{1}H signals are cancelled within the sample. Phase cycling further reduces artefacts

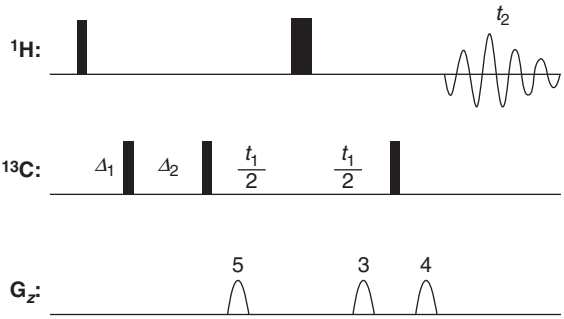

Figure 4 Magnitude gradient ^{1}H–^{13}C HMBC experiment. The Δ delays are the same as in Figure 1.

and accomplishes the LPJF to reject $^{1}J_{CH}$ correlations. Since this pulse sequence is based on the basic HMBC sequence,[3] the spectra still need to be displayed in magnitude mode.

3.4. Phase-sensitive gradient HMBC

Obtaining the advantages of phase-sensitive 2D NMR spectra requires us to avoid any net chemical shift evolution in either dimension, except during the evolution period. Net *J*-coupling evolution can only be suppressed for heteronuclear couplings but not for homonuclear couplings, in particular, ^{1}H–^{1}H. In an ideal phase-sensitive HMBC spectrum, f_2-cross-sections of any cross-peak should display absorptive line shape with normal *in-phase* homonuclear proton multiplet splitting, combined with *anti-phase* doublet splitting due to the active heteronuclear long-range coupling. The large chemical shift-dependent phase errors can be eliminated in both dimensions by refocusing all chemical shift evolution, except during t_1. The long-range HMQC pulse sequence[23] shown in Figure 5A uses a ^{13}C spin-echo period after the evolution time, assisted by a gradient in each half of the spin-echo.

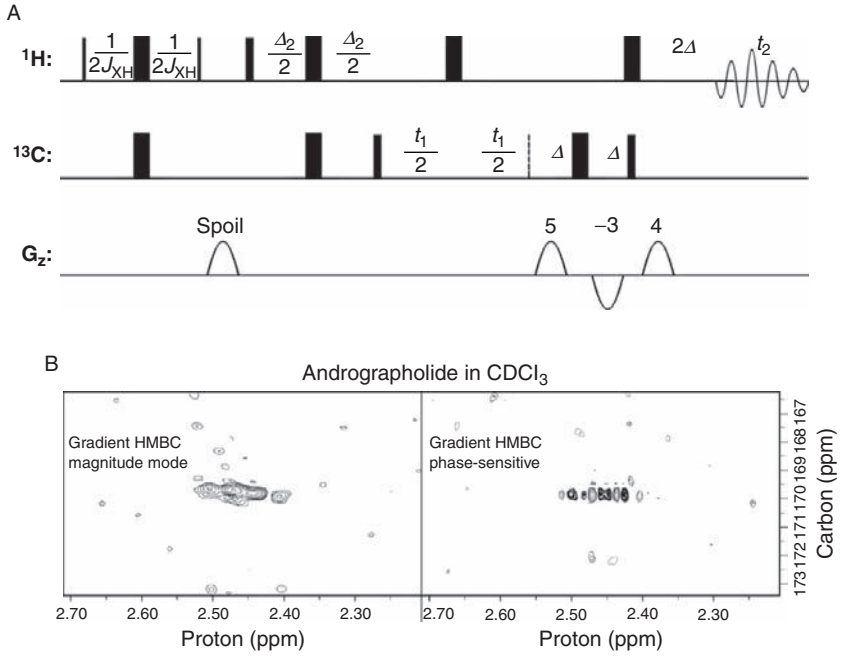

Figure 5 (A) Phase-sensitive gradient-selected HMBC pulse sequence.[23] This pulse sequence uses a TANGO element[27] as a LPJF, as discussed in the next section. Δ is a gradient accommodation delay. Δ_2 is set as in Figure 1. (B) Juxtaposition of a magnitude (left) and a phase-sensitive cross-peak (right) from HMBC spectra of andrographolide.[28] The phase-sensitive peak shown in the right pane 'stands out' from the noise much better because of its anti-phase character with positive (grey) and negative (black) multiplet components. (B) is reprinted with permission of John Wiley & Sons, Inc from Ref. 28.

During the first half of the spin-echo, the desired coherence is ^{1}H–^{13}C $\pm 2QC$, so that both ^{1}H and ^{13}C chemical shifts evolve [$\omega = \pm(\omega_H + \omega_C)$]. The ^{13}C π-pulse converts $\pm 2QC$ to 0QC [$\omega = \pm(\omega_H - \omega_C)$] so that at the end of the echo period the ^{13}C chemical shifts are refocused, ^{1}H chemical shift evolution is refocused in a second spin-echo, which uses the entire ^{13}C echo period as its first half. Simultaneously with the ^{1}H echo's π-pulse, a ^{13}C $\pi/2$-pulse converts 0QC to ^{1}H 1QC, so that only 1H chemical evolves during the second half of this outer spin-echo. A third gradient is placed in the second half of the ^{1}H spin-echo, ensure selection of the $\pm 2QC - 0QC - {}^{1}H - 1QC$ coherence pathway by the three gradients. Finally, ^{1}H chemical shifts during the long $(2^{n}J)^{-1}$ delay are refocused by simultaneous ^{1}H and ^{13}C π-pulses, but since the ^{1}H π-pulse affects all ^{1}H nuclei, the ^{1}H–^{1}H couplings are not refocused. A substantial advantage of this pulse sequence is that quadrature and phase-sensitive detection in both dimensions can be accomplished by echo/anti-echo gradient pathway selection, simply by swapping the first two gradients while repeating the experiment at each t_1 value. Product operator calculations (using the same definitions as used for Equation (4)) show that the remaining magnetization after combining ECHO and ANTI-ECHO pathway is either the term $2I_{2y}I_{4z}$ or $2I_{2x}I_{4z}$:

$$C_{\text{phase-sensitive HMBC ECHO}} = \left(-\frac{1}{2}\cos\left(\frac{\pi J_{2,S}}{J_{1,S}}\right)\cos(t_1\Omega_S) - \frac{1}{2}\cos(t_1\Omega_S)\right) I_{2x}S_{4z} + \left(\frac{1}{2}\cos\left(\frac{\pi J_{2,S}}{J_{1,S}}\right)\sin(t_1\Omega_S) + \frac{1}{2}\sin(t_1\Omega_S)\right) I_{2y}S_{4z}, \tag{5}$$

$$C_{\text{phase-sensitive HMBC ANTI-ECHO}} = \left(-\frac{1}{2}\cos\left(\frac{\pi J_{2,S}}{J_{1,S}}\right)\cos(t_1\Omega_S) - \frac{1}{2}\cos(t_1\Omega_S)\right) I_{2x}S_{4z} + \left(-\frac{1}{2}\cos\left(\frac{\pi J_{2,S}}{J_{1,S}}\right)\sin(t_1\Omega_S) - \frac{1}{2}\sin(t_1\Omega_S)\right) I_{2y}S_{4z}. \tag{6}$$

Phase-sensitive cross-peaks are narrower than their magnitude counterparts and have an anti-phase multiplet structure, which makes them 'stand out' from a noisy background, as demonstrated in Figure 5B.[28] Since curve fitting can be used to extract long-range coupling constants from the anti-phase splittings in f_2 slices from phase-sensitive HMBC, it is a valuable tool for conformational studies. This pulse sequence was enhanced by substituting broadband adiabatic pulses for the carbon π-pulses of the original sequence,[23] which improves performance in cases of wide ^{13}C spectral width, in particular, on high-field spectrometers. Further improvements, in particular, for the determination of long-range couplings, will be discussed in a later section of this review.

Phase-sensitive HMBC can also be achieved with phase cycling only, which has advantages over the gradient version, in cases where ultimate sensitivity is required, as discussed by Reynolds and Enriquez.[26]

4. STRATEGIES TO SUPPRESS UNDESIRED ONE-BOND CORRELATIONS

One-bond correlations may occur in HMBC spectra, and—depending on the application—may interfere with the intended purpose. Already, the initial HMBC pulse sequence of Figure 1 contains a basic LPJF. HMBC variants with improved LPJF efficiency such as the implementation of a BIRD-relaxation filter[29] or a TANGO filter[27,30] have been developed early. The original *J*-filtering approach can also be extended for broad-banded one-bond-coupling suppression, by using multiple $\pi/2$-pulses on the heteronucleus, as described in Refs. 17,31,32. Of course, most schemes for low-pass *J*-filtering can also be combined with more sophisticated HMBC variants than the ones presented in this section.

4.1. The TANGO HMBC experiment

The one-bond correlations can be eliminated in a single scan by inserting a basic TANGO excitation element[27] with two $\pi/4$-pulses for ^{13}C-bound ^{1}H, followed by a 'spoiler' gradient before the HMBC pulse sequence (Figure 6).[30] In this pulse sequence, chemical shift evolution during the gradient pulses in t_1 and immediately preceding acquisition causes large frequency-dependent phase shifts. Therefore, these spectra are usually displayed in magnitude mode.

Product operator calculations (using the same definitions as used for Equation (4)) show that the remaining magnetization after the TANGO element is

$$\begin{aligned} C_{\mathrm{TANGO}} = & \mathrm{I}_{1y} + \left(\frac{1}{2} - \frac{1}{2}\cos\left(\frac{\pi J_{2,\mathrm{S}}}{J_{1,\mathrm{S}}}\right)\right)\mathrm{I}_{2y} + \left(-\frac{1}{2}\cos\left(\frac{\pi J_{2,\mathrm{S}}}{J_{1,\mathrm{S}}}\right) - \frac{1}{2}\right)\mathrm{I}_{2z} \\ & + \sqrt{2}\sin\left(\frac{\pi J_{2,\mathrm{S}}}{J_{1,\mathrm{S}}}\right)\mathrm{I}_{2x}\mathrm{S}_{4z}. \end{aligned} \tag{7}$$

All terms except the I_{2z} are destroyed by a spoiler gradient. The output shows that all one-bond correlations are eliminated.

The TANGO element is followed by a magnitude gradient HMBC (as shown in Figure 4), leading to the following remaining product operator terms:

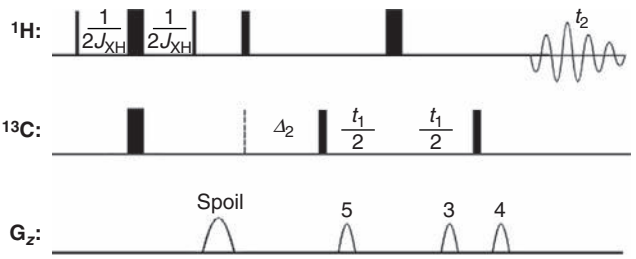

Figure 6 Magnitude gradient HMBC with TANGO[30] Δ_2 is set as in Figure 1.

$$C_{\text{gradHMBC with TANGO}} = \cos^2\left(\frac{\pi J_{2,S}}{2J_{1,S}}\right)\cos\left(\frac{\Omega_2}{2J_{2,S}} + t_1\Omega_S\right)I_{2x}S_{4z} - \cos^2\left(\frac{\pi J_{2,S}}{2J_{1,S}}\right)\sin\left(\frac{\Omega_2}{2J_{2,S}} + t_1\Omega_S\right)I_{2y}S_{4z}. \quad (8)$$

4.2. The BIRD-HMBC sequence

The basic BIRD-HMBC pulse sequence,[33] which implements efficient low-pass *J*-filtering and provides narrow line shapes in spite of magnitude mode spectral display, is shown in Figure 7.

Instead of the LPJF shown above, it incorporates a BIRD_y element,[21] with the delay $D_2 = (2\,{}^1J_{C,H})^{-1}$ adjusted for direct couplings and the delay $D_3 = (4\,{}^nJ_{C,H})^{-1}$ adjusted for long-range couplings, respectively. Product operator calculations (using the same definitions as used for Equation (4)) show that the remaining magnetization after the BIRD element is

$$C_{\text{BIRD}} = \sin\left(\frac{\Omega_1}{2J_{2,S}}\right)I_{1x} - \cos\left(\frac{\Omega_1}{2J_{2,S}}\right)I_{1y} + 2I_{2x}S_{4z}. \quad (9)$$

Neglecting homonuclear couplings, proton signals evolve in the course of the BIRD_y element under the influence of heteronuclear long-range coupling ${}^nJ_{C,H}$ into pure anti-phase coherence ($I_y \rightarrow 2\,{}^nI_xS_z$), whereas protons coupled via one-bond coupling constants ${}^1J_{C,H}$ are refocused to give pure in-phase coherence [${}^1I_y \rightarrow {}^1I_y\cos(2\omega_I D_3) + {}^1I_x\sin(2\omega_I D_3)$]. In principle, and as long as the condition $D_2 = (2\,{}^1J_{CH})^{-1}$ is fulfilled, solely long-range anti-phase coherence will be transformed into corresponding MQCs by a carbon $\pi/2$-pulse. Subsequently, ${}^{13}C$ chemical shifts label evolution in t_1, the coherence is transferred back into proton anti-phase coherence and could be detected immediately without ${}^{13}C$ decoupling. However, due to the non-uniformity of ${}^1J_{CH}$ coupling constants, the BIRD condition for D_2 may be violated, and low-pass *J*-filtering has to be introduced immediately after the BIRD_y element. The best results have been achieved with a filter

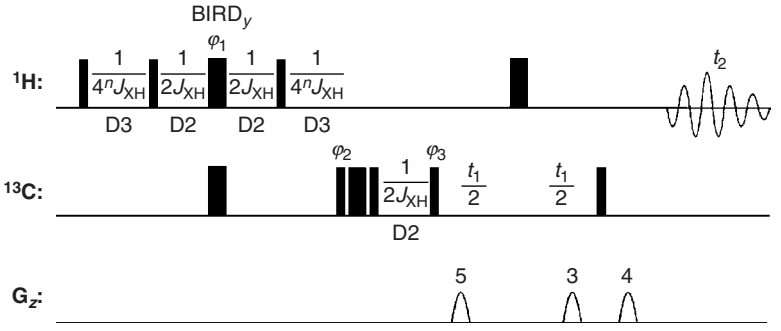

Figure 7 BIRD-HMBC pulse sequence for the detection of ${}^nJ_{CH}$ correlations with a single LPJF.[33]

element consisting of a $\pi/2_{\pm x}-\pi_y-\pi/2_x$ ^{13}C composite pulse, followed by a delay D_2 and applied with a one-step LPJF. The composite ^{13}C pulse allows $^nJ_{(C,H)}$ signals to be labelled selectively and differently ($\pm 2^nI_xS_z$) from scan to scan, and with the pulse and receiver phases set accordingly to be co-added. The signals of the bulk of $^1J_{(C,H)}$ coherences however, evolving into anti-phase coherence in the course of D_2 and, following the same pathway, detected together with the $^nJ_{(C,H)}$ signals, are cancelled in subsequent scans. $^1J_{CH}$ coherences, on the other hand, for which the condition $D_2=(2\,^1J_{CH})^{-1}$ is violated, evolve in the course of the BIRD$_y$ element partially and depending on the degree of violation into $2\,^1I_xS_z$, $2\,^1I_yS_z$ anti-phase coherence. These $^1J_{(C,H)}$ coherences are labelled together with long-range coherences and would give rise to unwanted $^1J_{(C,H)}$ residual peaks in the spectrum. In the course of the filter delay D_2, these $^1J_{(C,H)}$ anti-phase coherences evolve back for the most part into in-phase coherence (^1I_y, ^1I_x), are not transformed into multi-quantum coherence by the ^{13}C $\pi/2$-pulse and are filtered out. The high low-pass filter efficiency obtained by this simple procedure may be improved even more by implementing a second $\pi/2_{\pm x}-\pi_y-\pi/2_x-D_2$ LPJF element (Figure 8).

Taking advantage of the double-difference principle (implemented through phase cycling), this two-stage filter achieves very good $^1J_{CH}$ correlation suppression. ^{13}C broadband decoupling during acquisition can be used if either a refocusing delay of $(2^nJ_{CH})^{-1}$ or another BIRD$_y$ element are to be inserted prior to acquisition.

4.3. Clean HMBC

One often-neglected problem in low-pass *J*-filtered HMBC spectra, which can however lead to severe interpretation errors, is the occurrence of spurious correlations caused by strong homonuclear proton coupling. This effect has been investigated in detail by Würtz et al.[34] As a remedy, it is suggested that low-pass *J*-filtering be applied both in the initial and terminal parts of the pulse sequence, as shown in Figure 9.

Terminal low-pass *J*-filters[35] require additional repetitions of the pulse sequence. They may therefore increase to the total experimental time required.

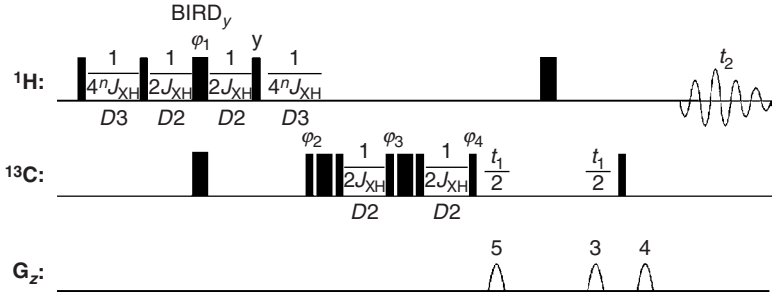

Figure 8 BIRD-HMBC pulse sequence for the detection of $^nJ_{CH}$ correlations with a two-step BIRD low-pass filter.[33]

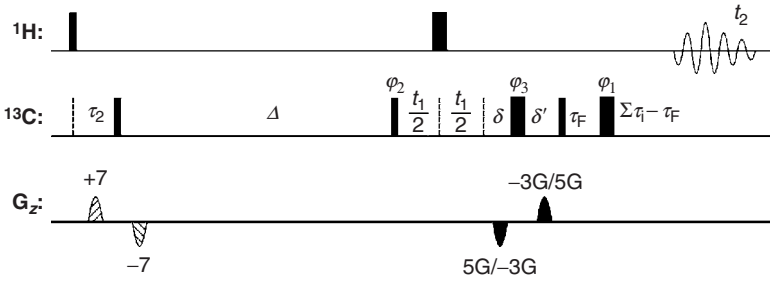

Figure 9 Clean HMBC pulse sequence.[34] With $\Delta = (2\,{}^{n}J_{IS})^{-1}$; the delays for the 3rd order LPJF are $\tau_1 = (1/2)\,[{}^{1}J_{min} + 0.07({}^{1}J_{max} - {}^{1}J_{min})]^{-1}$, $\tau_2 = ({}^{1}J_{max} + {}^{1}J_{min})^{-1}$, $\tau_3 = (1/2)\,[{}^{1}J_{max} - 0.07({}^{1}J_{max} - {}^{1}J_{min})]^{-1}$, δ is the gradient delay. For a second-order terminal filter, the sequence has to be repeated for four different values of τ_F, that is: $\tau_F = \{0, \tau_1, \tau_3, \tau_1 + \tau_3\}$. The first two gradients can be set in an order of magnitude weaker than the gradients used for the formation of heteronuclear gradient echoes.

This is not a problem when working with low sample amounts, since the intrinsically low sensitivity of the experiment usually requires large scan numbers anyways. Figure 10 shows an illustrative example of spectra from an oligosaccharide sample,[36] where the conventional HMBC is hampered with strong coupling artefacts, that are absent from the clean HMBC spectrum. To obtain this spectrum, an improved adiabatic version of the terminal LPJF[37] was employed.

5. HSQC-BASED MULTIPLE-BOND CORRELATIONS

5.1. Long-range HSQC and GSQMBC

Adapting the HSQC experiment for heteronuclear long-range coupling is straightforward and has been used earlier, for example, by Poppe and Van Halbeek[38] or Mattila et al.[39] without assigning any special name or acronym. While Mattila et al. used spatially inhomogeneous spin-lock pulses to disperse unwanted coherences, Marek et al.[40] described an experiment that utilizes PFGs for coherence selection. This experiment has been given the acronym GSQMBC (gradient-enhanced single-quantum multiple-bond correlation experiment; Figure 11).

The main difference to the standard (HMQC-based) HMBC experiments is that evolution of ^{1}H–^{1}H homonuclear couplings is avoided and that the acquisition of phase-sensitive spectra by the GSQMBC experiment allows for higher resolution and thus the measurement of very small coupling constants. The pulse sequence works just like a gradient-selected HSQC experiment without refocusing and decoupling. It is advisable that the π-pulses are applied as composite pulses to avoid off-resonance effects. The gradient ratios are adjusted using $G_2 - G_1 = (\gamma_H / \gamma_X)G_3$, with $G_2 > G_1$. The sign of G_3 is alternated to afford phase-sensitive spectra that need to be processed according to the echo/anti-echo protocol.[41] A GSQMBC example spectrum is shown in Figure 12.

Quick analysis of coupling constants can be achieved using a method developed by Prestegard and Kim,[42] which avoids overestimation of coupling constants that

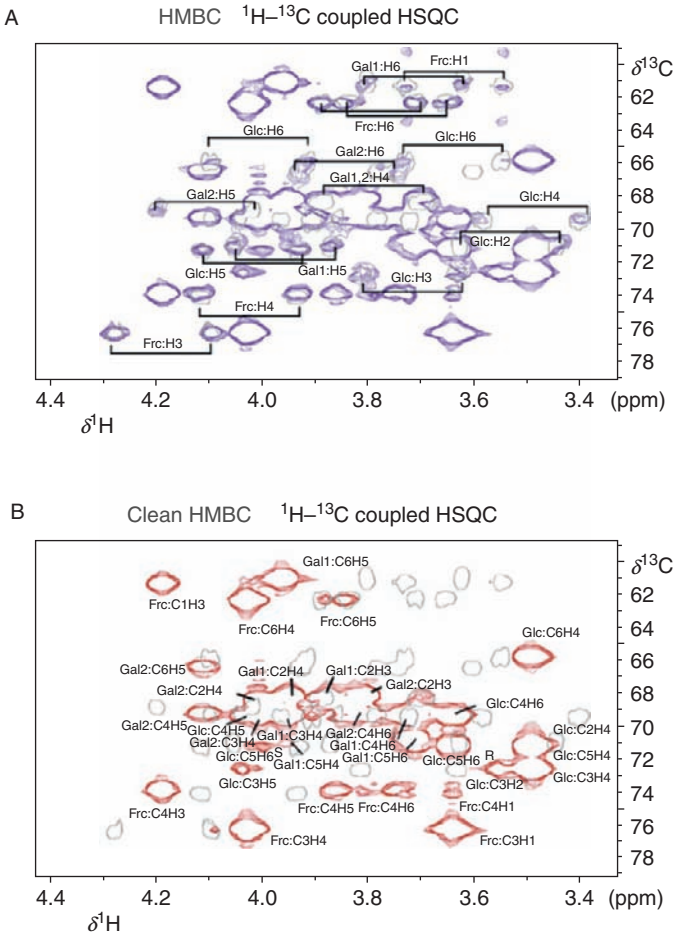

Figure 10 Comparison of conventional HMBC (A) and clean HMBC (B) of a 30-residue oligosaccharide from *Francisella victoria*. Spectra are overlaid in grey with HSQC spectra recorded without ^{13}C decoupling during acquisition of the proton dimension to indicate the positions of strong coupling-induced one-bond artefacts. These artefacts can significantly affect the spectral appearance even at a ^{1}H spectral frequency of 800 MHz and are effectively purged in the clean version (the figure is reproduced with permission from Ref. 36).

are similar to, or smaller than the line width. For this approach, the estimated coupling constant from the mostly absorptive, anti-phase (υ_a) doublet and the distance of the two extrema in the dispersive (υ_d, $\pi/2$ phase shifted) doublet are required. The coupling constant J is determined by solving Equation (10):

$$J^6 - \upsilon^2 J^4 + \left(9/4\upsilon_a^4 - 3/2\upsilon_a^2\upsilon_d^2 - 3/4\upsilon_d^2\right)J^2 + 81/64\upsilon_a^6 - 9/16\upsilon_a^4\upsilon_d^2 - 21/32\upsilon_a^2\upsilon_d^4 - 1/16\upsilon_d^6 + \upsilon_d^8/64\upsilon_a^2 = 0. \quad (10)$$

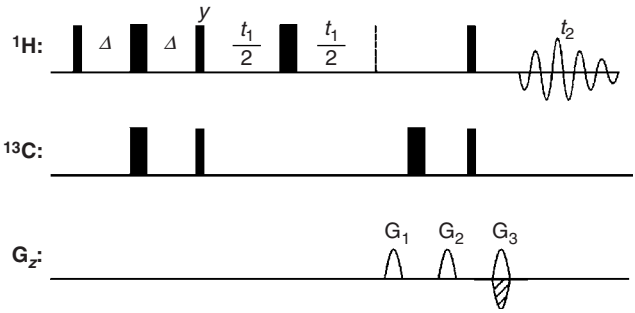

Figure 11 GSQMBC pulse sequence by Marek et al.,[40] $\Delta = (2\,{}^{n}J_{IS})^{-1}$.

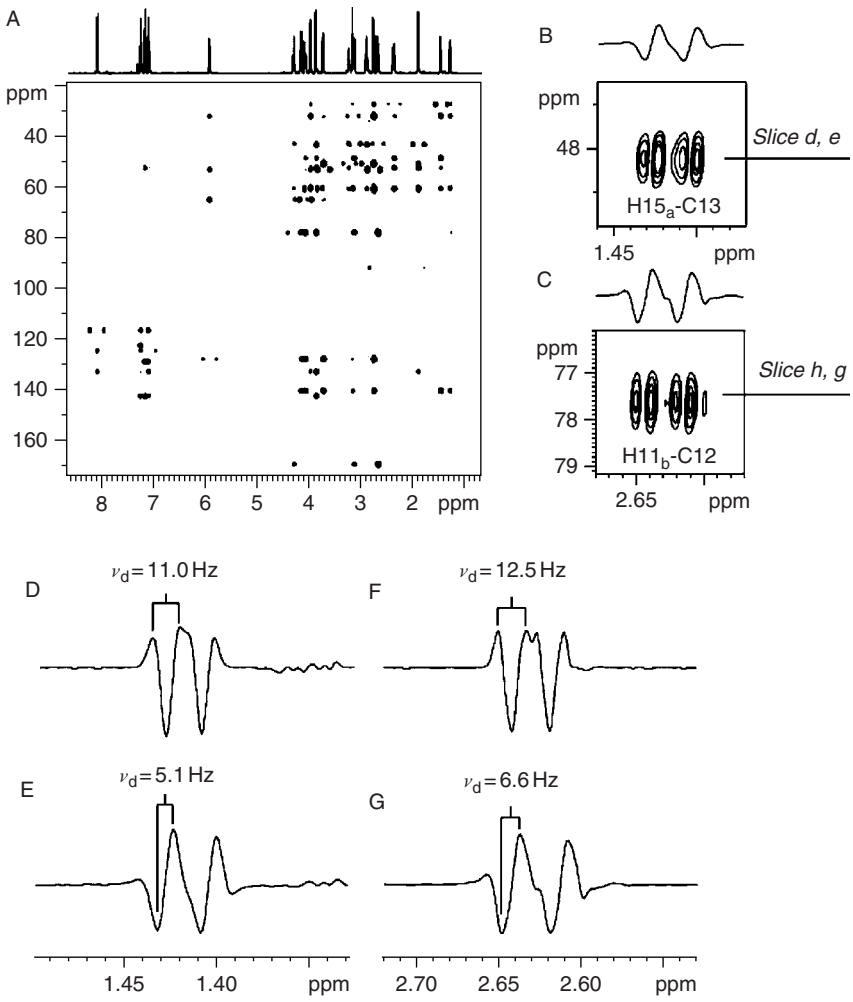

Figure 12 (A) GSQMBC spectrum of strychnine in $CDCl_3$ and the 1D-slices of the correlations H15a-C13 and H11b-C12 (D–G). Reprinted with permission of John Wiley & Sons, Inc. from Ref. 32.

Undesired $^1J_{CH}$ correlations can be suppressed by a TANGO-spin-lock-BIRD element[30,43] or by a G-BIRD$_{R,X}$ building block to remove unwanted direct correlations (see the following section).[44] Problems may arise from the dispersive contributions to the line shapes and preclude its use for analysis of moderate to complex multiplet structures. These dispersive contributions can be removed with a heteronuclear *z*,*z*-filter.[45,46] A peak-fitting approach is described by Keeler et al.[47] for psHMBC. In long-range HSQC experiments, the simultaneous evolution of homonuclear and heteronuclear coupling constants during the fixed delays may cause accidental disappearing of some peaks, that is, when one $\cos(\pi J\tau)$ factor becomes zero, a problem that can be overcome by using a small flip angle proton pulse at the end of the evolution.[48]

5.2. HSQMBC

A refined version of the HSQC-based GSQMBC pulse sequence discussed above is the HSQMBC experiment (Figure 13).[10,49] The HSQC pulse sequence is the fundamental building block.

The INEPT transfer produces single-quantum anti-phase coherence on the heteronuclei. This approach effectively removes homonuclear coupling evolution during t_1. A trim pulse is used (prior to transfer of magnetization to the *X* nuclei) to help diphase any unwanted magnetization and to aid with the suppression of H_2O. A ^{1}H π-pulse in the middle of t_1 effectively refocuses ^{1}H chemical shift and heteronuclear coupling. After t_1, an encoding gradient is applied, followed by a ^{13}C π-pulse to refocus chemical shift and coupling evolution during the first selection gradient. A *z*,*z*-filter gradient destroys the unwanted coherences, which could cause dispersive contributions to the line shape. After the magnetization is transferred back to protons by a $\pi/2$-pulse, a decoding gradient sequence prepares for detection.

All HSQC-based long-range correlation experiments can easily be modified for decoupling during acquisition, since the gradient refocusing delay can also serve to refocus the heteronuclear couplings if simultaneous π-pulses are applied on both nuclei and the delay ∂ is adjusted to ca. $\tau/4$. Such experiments, which are

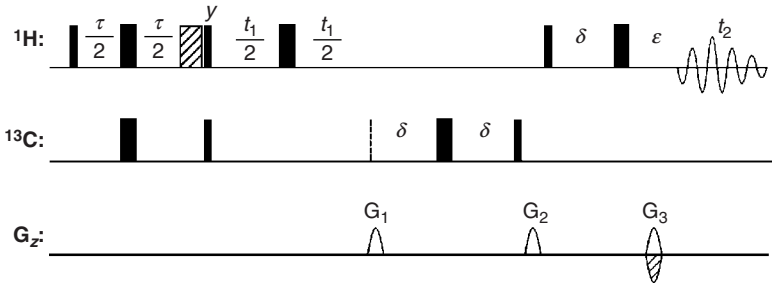

Figure 13 The HSQMBC experiment.[10] The hatched bar represents a trim pulse; $\tau = (2\ ^nJ_{X,H})^{-1}$; $\tau/2 = (4\ ^nJ_{X,H})^{-1}$; gradient values for the HSQMBC are G_1:G_2:G_3 = 80:10:±20.

essentially HSQC experiments with delays adjusted for long-range couplings, have been employed in cases where a wide range of homonuclear coupling constants cause a broadening in f_1 and superior resolution is required, as in carbohydrate derivatives.[50]

Without decoupling, these experiments allow accurate determination of heteronuclear long-range coupling constants using peak-fitting.[47] To increase sensitivity and efficiently suppress $^1J_{CH}$ correlations from the spectra, again a G-BIRD$_{R,X}$ filter can be incorporated in the initial INEPT transfer to decouple remote protons during the INEPT preparation (Figure 14).[32]

Based on this approach, like the G-BIRD$_{R,X}$–CPMG–HSQMBC pulse sequence,[51] (Figure 15) has been developed, which facilitates the direct determination of long-range couplings in the presence of homonuclear couplings by providing a more uniform phase behaviour.

The CPMG pulse train further eliminates phase distortions due to ^{1}H–^{1}H homonuclear couplings. Thus, the phase distortions arising from ^{1}H–^{1}H coupling evolution for both $^2J_{CH}$ and $^3J_{CH}$ cross-peaks to quaternary carbons can be suppressed.[32,51] This leads to very clean absorptive multiplet patterns for small molecules with extended homonuclear (proton) coupling networks, as exemplified by Figure 16, where coupling constants were determined with an accuracy of within ± 0.5 Hz.

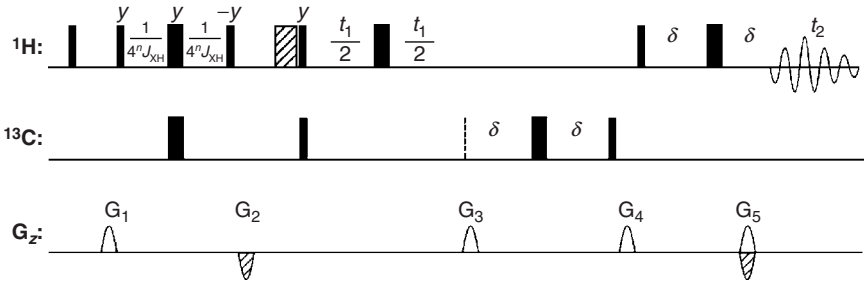

Figure 14 The G-BIRD$_R$-HSQMBC experiment. Gradient ratios are G_1:G_2:G_3:G_4:G_5 = 2.5:−2.5:8:1:±2.[32]

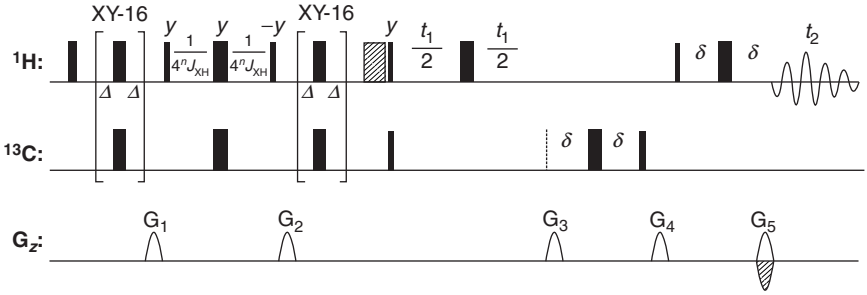

Figure 15 The G-BIRD$_{R,X}$–CPMG–HSQMBC pulse sequence.[51] Gradient ratios are G_1:G_2:G_3:G_4:G_5 = 2.5:2.5:8:1:±2, Δ = 200 μs, the delay ∂ is optimized for long-range coupling evolution.

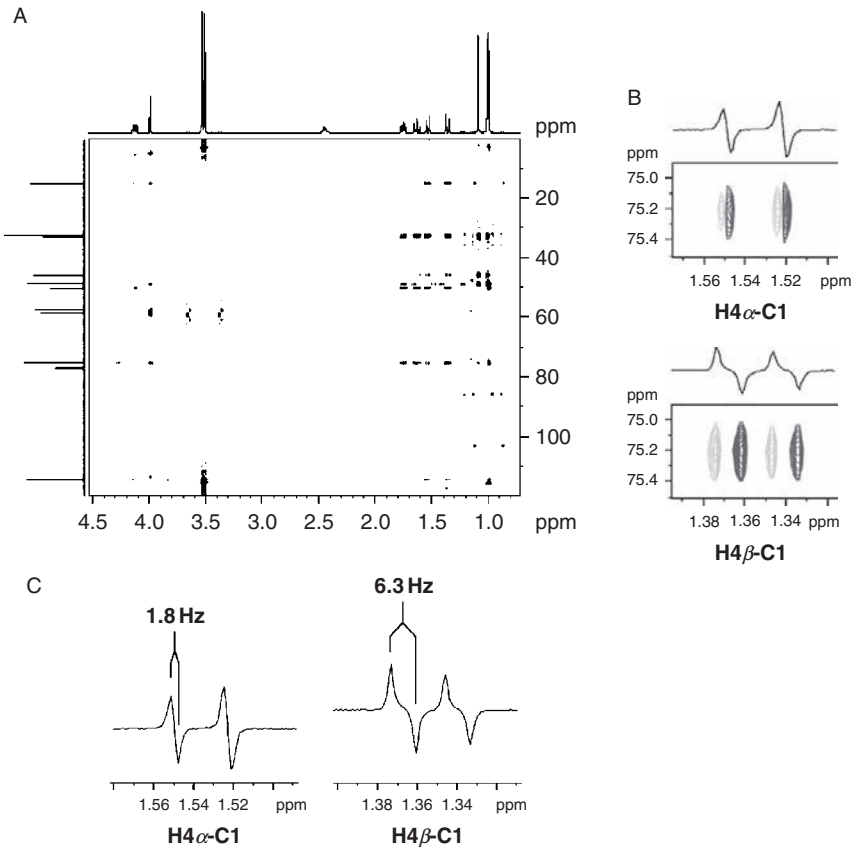

Figure 16 2D G-BIRD$_{R,X}$–CPMG–HSQMBC spectrum of a substituted cyclopentane derivative. (A) 2D spectrum; (B) expansion of the spectrum showing the H4α–C1 and H4β–C1 correlations; (C) slices through the H4α–C1 and H4β–C1 correlations, showing the measurements of the $^{3}J_{CH}$ coupling constants. The delay for long-range polarization transfer ∂ was set to ~31 ms, the trim pulse to 2 ms duration. The values of $^{2,3}J_{CH}$ were determined from direct measurement and subsequent manual peak-fitting analysis.[47] The figure is reproduced from Ref. 51 with permission.

In the context of accurate determination of residual dipolar couplings (RDC) superimposed on ^{n}J-couplings, a highly optimized variant of this sequence has been developed,[52] which will be discussed further below.

6. EXTENDING THE SCOPE OF LONG-RANGE COUPLING CONSTANTS

Depending on the settings for the long-range coupling evolution delay, important cross-peaks may be rather weak or may even be lost. One challenge for improved HMBC is therefore covering a wide range of long-range coupling

constants, which can span a range from ca. 1–25 Hz, in a single experiment. A common approach to increase the coupling constant band width is by systematically varying the originally fixed delay, for heteronuclear coupling evolution, alongside the evolution period.[18] Experiments like ACCORD-HMBC[53] with carbon decoupling and using purge pulses to remove direct $^{1}J_{CH}$ suffer from an undesirable skewed line shape caused by evolution of homonuclear couplings in t_1.[19] CT versions of this sequence have since been introduced to improve the quality of the resulting spectra.[23] The broadband HMBC experiment introduced by Meissner and Sørensen[35] is a very straightforward and effective method to improve the *J*-bandwidth of HMBC by co-adding spectra recorded with different delays.

In another approach, 3D-HMBC,[54,55] the coupling evolution delay is incremented independently so that each slice in such a pseudo 3D experiment corresponds to a 2D-HMBC spectrum optimized for a specific coupling situation. Thus, the *J* values are sampled by the different fixed precession periods. Albeit being demanding with respect to time and storage space requirements, the possibility to extract coupling information from the modulations along the third time domain yields an additional benefit. Other modifications of the basic HMBC pulse sequence have attempted to improve sensitivity. Furihata and Seto,[18] for example, obtained better sensitivity by refocusing the anti-phase signal and using carbon decoupling during acquisition, in cases where extra signal loss due to transverse relaxation during the added delay was small. This D-HMBC experiment, is *de facto* equivalent to a HMQC experiment[2] with fixed delays adjusted for long-range coupling.

The accordion principle used with the ACCORD-HMBC experiment to equalize cross-peak intensities for different $^{n}J_{C,H}$ coupling constants could also be incorporated. $^{n}J_{C,H}$ evolution delays D_3 are replaced by variable delays (v_d) and are simultaneously decremented from one t_1 increment to the next in the course of the experiment. The strategy outlined above deviates from the strategy followed with the HMBC experiment, the ACCORD-HMBC experiment and their variants. Instead of suppressing unwanted $^{1}J_{C,H}$ correlations by one or several filter elements in a single scan, one-bond coherences are preserved with the BIRD-HMBC experiment and are cancelled by subtraction from each other in subsequent scans.

Modifications of these HMBC experiments with a delay for refocusing long-range couplings allowing ^{13}C broadband decoupling have been proposed[18] and phase-sensitive approaches have been published.[40,56]

Variants of the pioneering ACCORD-HMBC[53] experiment like IMPEACH-MBC[57] and CIGAR-HMBC (*C*onstant-time *I*nverse-detected *G*radient *A*ccordion *R*escaled long-range HMBC)[58] effectively sample a wide range of long-range couplings in a systematic fashion and in a single experiment. Nevertheless, accordion evolution introduces modulation by ^{1}H–^{1}H couplings in the t_1-dimension. Since noise or spurious peaks are not modulated, the skew of long-range multiplets can advantageously be used to validate ambiguously weak responses. However, such signal distortion can also severely impede interpretation and assignment of accordion-type spectra.

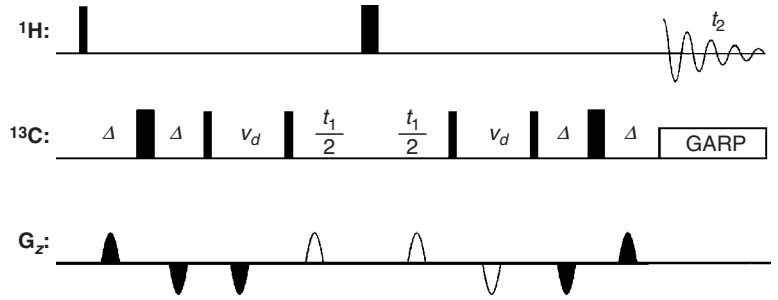

Figure 17 ACCORD-HMBC by Wagner and Berger,[53] $\Delta = (2^1J_{IS})^{-1}$, ν_d is varied in concert with t_1.

6.1. ACCORD-HMBC

Martin et al.[59] compared the ACCORD-HMBC (Figure 17) to related experiments using fixed delays, in order to assess the best way for observing a complete set of $^{2,3}J$ long-range ^{1}H–^{13}C couplings in a complex molecule.

Single fixed-delay experiments are obviously optimized for only one value of long-range coupling constant, whereas accordion-type experiments allow one to cover a range of coupling values. Therefore, one can observe correlations, which would otherwise be too weak to be unequivocally identifiable. The typical skewed appearance of cross-peak multiplet patterns in accordion-type experiments due to the scaled evolution of couplings during the accordion delay requires higher resolution in the indirect dimension to avoid ambiguities in interpretation. This additional fine structure can be beneficial in that it helps to differentiate 'real correlations' from noise or artefacts. A good comparison of the performance of HMBC, ACCORD-HMBC and BIRD-HMBC can be found in Ref. 33. While the same cross-peak patterns may be obtained with BIRD-HMBC and HMBC experiments, some cross-peaks are missing in the ACCORD-HMBC spectrum because of their lower intensity.

Similarly, narrow line shapes are obtained with HMBC and BIRD-HMBC experiments in contrast to the broadened shapes obtained with the ACCORD-HMBC experiment.

6.2. CIGAR-HMBC

Apart from the narrow range of *J*-couplings, there is another drawback associated with the PFG-HMBC experiments based on HMQC: ^{1}H homonuclear couplings cause splitting both in the direct and indirect dimensions. This severely limits the achievable resolution in the indirect dimension. CT experiments are an efficient remedy for this problem. The CIGAR-HMBC experiment, implemented by Hadden et al.[58] (Figure 18), suppresses homonuclear ^{1}H coupling modulation during the evolution time completely by CT evolution. This narrows peaks in the indirect dimension, but cannot prevent intensity loss due to an unfavourable magnitude of the homonuclear coupling. In addition, this experiment uses the accordion principle to average over a range of $^nJ_{CH}$ coupling constants just like the previously

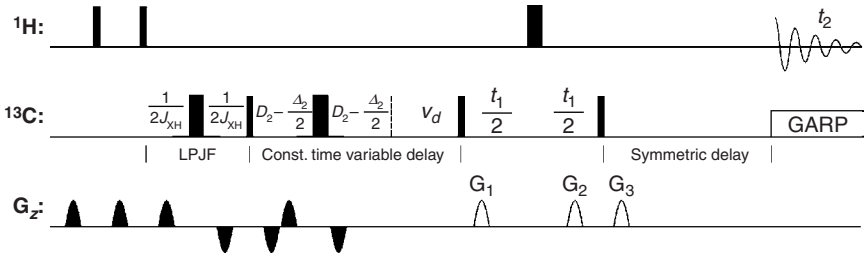

Figure 18 Pulse sequence of the CIGAR-HMBC experiment[58] designed to suppress homonuclear coupling evolution by constant-time evolution. The overall duration of the 'symmetric delay' is equal to the sum of the duration of the pulses, gradients and delays from the LPJF block and the constant-time–variable delay block. This delay is required to refocus magnetization if broadband decoupling during evolution is used.

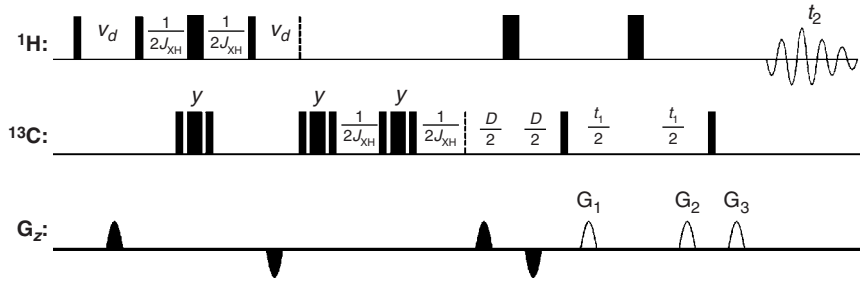

Figure 19 Accordion BIRD-HMBC experiment[60] The delay D is incremented from 0 to ($\tau_{max} - \tau_{min} - t_1$)$\times$ ni, where ni corresponds to the total number of t_1 increments, in concert with decrementing ν_d and with the incrementing of the evolution time t_1, thus making the experiment constant-time.

discussed ACCORD-HMBC. Furthermore, a two-fold LPJF suppresses $^1J_{CH}$ correlation signals effectively allowing broadband decoupling without introducing ambiguity between one-bond and long-range correlations.

The CIGAR-HMBC experiment addresses important deficiencies in the classical HMBC experiment: ambiguously weak or missing long-range correlations, residual $^1J_{CH}$ correlations and homonuclear coupling modulation. Modifications that increase the total duration of the pulse sequence may be problematic if transverse relaxation times are short. In addition, sensitivity losses due to the accordion element have to be taken into account. Bearing in mind that there is no single universally optimal pulse sequence for any long-range correlation problem, CIGAR-HMBC can be considered as one of the most practically useful broadbanded HMBC variants to date.

6.3. ACCORD-BIRD-HMBC

Furrer[60] combined the accordion technique with BIRD-HMBC providing ACCORD-HMBC-type spectra with reduced signal splitting in the indirect dimension and superior suppression of $^1J_{CH}$ cross-peaks. Figure 19 displays the

pulse sequence of the CT accordion BIRD-HMBC experiment. It starts with a $BIRD_{R,X}$ element,[61] as described above (Figures 14 and 15), with the delay δ adjusted for one-bond couplings. The systematically decremented delay (v_d) samples a range of potential heteronuclear long-range coupling constants. The $^1J_{CH}$ correlations are suppressed as follows: The $^1J_{CH}$ anti-phase coherences evolve together with the long-range couplings; but while the long-range couplings have evolved into pure anti-phase coherences after the second delay (v_d), the $^1J_{CH}$-dependent coherences are refocused into pure in-phase coherences, which are dephased by the gradients.[33]

The black gradient pairs flanking the BIRD and π-pulses (drawn in black) suppress possible MQC created by pulse imperfections. The suppression of one-bond couplings is owed to two LPJF elements, each consisting of a $\pi/2_{\pm x}-\pi-\pi/2_x$ ^{13}C composite pulse, immediately followed by a delay $\delta=(2\,^1J_{XH})^{-1}$. Due to the CT evolution, the ^1H–^1H coupling evolution is suppressed and only the desired long-range heteronuclear couplings are allowed to evolve over the variable delay (v_d). Finally, after the CT period, a $\pi/2$ ^{13}C pulse converts the anti-phase coherences into double-quantum coherences, which are allowed to evolve during the evolution time. The last $\pi/2$ ^{13}C pulse converts the double-quantum coherences into observable magnetization.

6.4. Broadband HMBC

In broadband HMBC experiments,[35] one avoids the problems of co-evolution and modulations during an accordion-type delay by using a small set of numerically optimized, to obtain a series of spectra, which are linearly combined, *a posteriori*. This approach is more economical in the use of spectrometer time than a 'brute-force' accordion setup. If the data are stored separately at acquisition, different linear combinations of the data allow one to control the bandwidth of the long-range correlations and of the low-pass *J*-filtering at processing time, independently. A number of advanced HMBC-variants discussed further below build upon this principle.

6.5. *J*-compensated HMBC

J-compensated pulse sequences represent a totally different approach from the accordion-type broadband HMBC experiments discussed so far in this section. They are magnetization transfer experiments designed from composite pulses by transferring the concept to bilinear rotations. *J*-compensated pulse sequences are ideally derived from short composite pulses, where each pulse is replaced by a bilinear rotation element of the same rotation angle, an approach first used in the broadband INEPT pulse sequence.[62,63] Composite pulses that are efficient in the presence of B_1-field inhomogeneity lead to *J*-compensated sequences that are effective over a wide range of *J* values.[64] *J*-compensation building blocks can replace the delay for spin–spin coupling evolution in many existing pulse methods. They effectively transform initial *z*-magnetization to heteronuclear anti-phase coherence over a wider range of *J*-couplings than the standard pulse-delay block at the

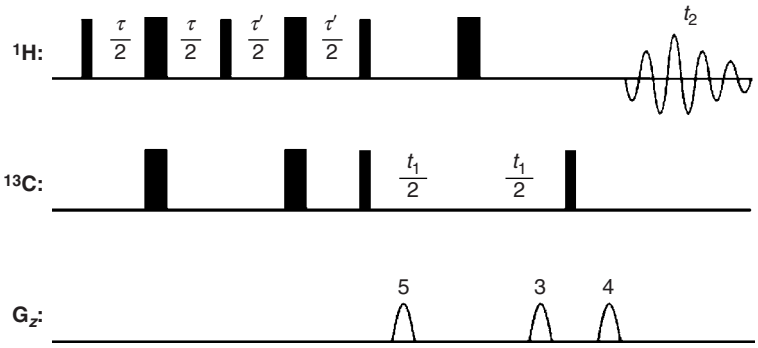

Figure 20 *J*-compensated HMBC.[66] The setting of the delays is discussed in the text.

beginning of the HMBC pulse sequence. This is similar to a composite pulse being more efficient in an inhomogeneous field than a single $\pi/2$-pulse. The pulse sequence of *J*-HMSQC is similar to the HSQC sequence, except for the two delays, τ', which are initially set equal to τ. Torres et al.[65] introduced the long-range version LR-HSMQC and the improved *J*-compensated HMBC sequence shown in Figure 20.

The conversion of in-phase to anti-phase coherence by spin–spin coupling can be conceived as a composite bilinear β pulse ($\beta = \gamma B_1 \tau$, with the magnetogyric ratio γ and the amplitude of the rf-field B_1, and pulse duration τ) usually set to $\pi/2$. The shortest composite pulse that can be used is a two-step pulse train of the form $(a\beta)_\Phi$ $(b\beta)_\varphi$, where a and b are amplitude coefficients of the first and second rf-pulses with nominal rotation β, while Φ and φ denote the corresponding phases. The three most popular composite pulses of this form are the $\beta_0(2\beta)_{120}$,[64,67] $\beta_0(\beta)_{90}$[68] and $\beta_0(2\beta)_{90}$.[69,70]

Torres et al.[66] also implemented this approach for common composite pulses and designed shorter versions for *J*-compensation by optimizing their efficiency in generating transverse magnetization.

Figure 21 compares theoretical and experimental signal-intensity profiles obtained with the standard pulse sequences and different *J*-compensated sequences from Ref. 66. The theoretical intensity profiles are presented for each sequence as a function of β, while the experimental profiles are shown for HMBC and corresponding *J*-compensated HMBC sequences as a function of β'. The experimental HMBC signal-intensity profiles were obtained by measuring anti-phase proton CH signal intensity from $CHCl_3$ for which β' or τ were set values relevant to the direct CH coupling ($^1J_{CH} = 209.3$ Hz). As can be seen in Figure 21, there is very good agreement between the theoretical and the experimental profiles. In the experimental comparison of HMBC sequences, sodium acrylate (Figure 22) served as a test sample, because it provides a wide range both for the J_{CH} values to the carboxyl carbon and for proton–proton coupling. Figure 22 compares cross-sections from the regular, and different *J*-compensated, HMBC. C1-H2 and C1-H3a correlations are visible in the standard HMBC experiment, but the C1-H3b ($^3J_{C1\text{-}H3b} = 14.1$ Hz corresponding to $\beta' \approx \pi$) is missing. All *J*-compensated sequences show this correlation, although its amplitude depends on the particular variant of the method.

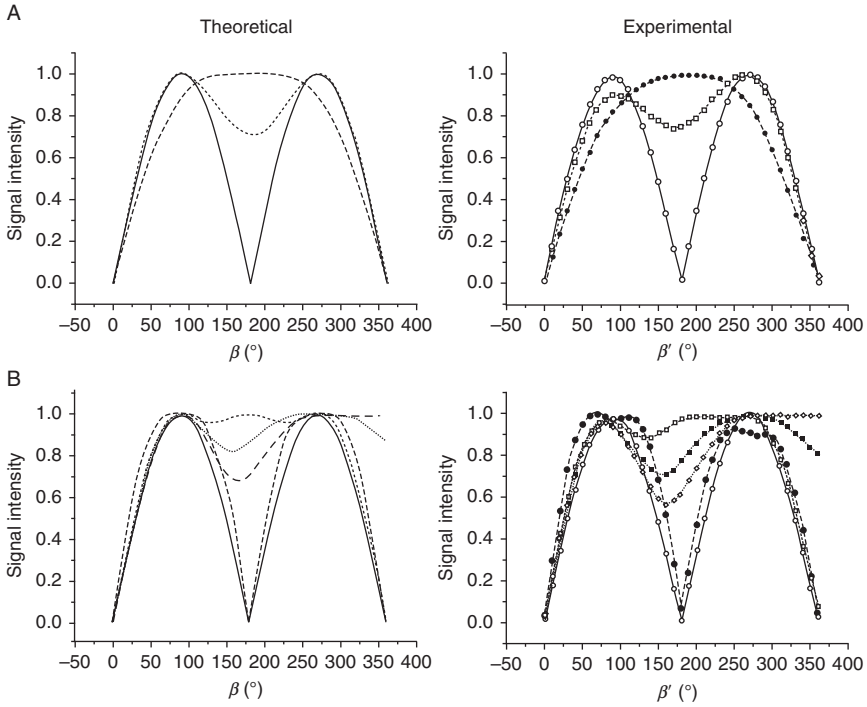

Figure 21 Comparison of the theoretical and experimental performance by relative signal amplitudes of regular and *J*-compensated HMBC sequences. Anti-phase coherence amplitude profiles for $CHCl_3$ were created from evolution of in-phase proton magnetization due to direct CH *J*-coupling using the HMBC pulse sequences presented in Figure 20. In all HMBC experiments, the τ delay was set for one-bond coupling ($^1J_{CH} = 209.3$ Hz) instead of long-range coupling. (A) Conventional HMBC (solid line), HMBC-*J*45 + 90A (dashed line), HMBC-*J*45 + 90B (dotted line). (B) Conventional HMBC (solid line), HMBC-*J*90 + 90 (long dashed line), HMBC-*J*90 + 45 (dotted line), HMBC-*J*90 + 30 (short dashed line) and HMBC-*J*90 + 22 (broken solid line). Reprinted with permission from Ref. 66.

7. HMBC EXPERIMENTS FOR DETERMINING COUPLING CONSTANTS

Accurate determination of long-range couplings is of prime importance for conformational analysis.[71–74] Proton-detected experiments have provided a tremendous advantage in this field, but the complex splitting pattern and mixed phase of HMBC cross-peaks also required considerable efforts to develop methods that allow or facilitate the extraction of accurate heteronuclear coupling constants from HMBC-type spectra. Usually, they are used in conjunction with fitting procedures.

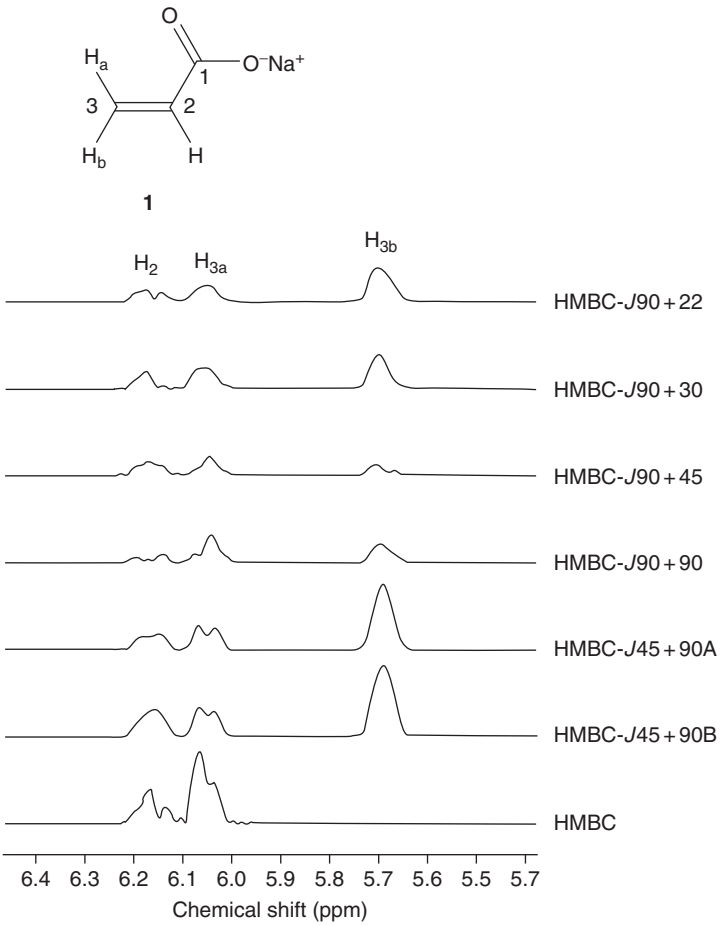

Figure 22 Selected f_2 slices from 2D maps of HMBC and *J*-compensated HMBC experiments with sodium acrylate. Each slice was obtained from the carboxyl carbon (C-1) cross-peak of the relevant spectrum. The f_2 slices are plotted at the same absolute intensity. Reprinted with permission from Torres et al.[66]

7.1. *J*-resolved HMBC

Furihata and Seto[75] developed a modified HMBC sequence, the *J*-resolved HMBC-1, which became the basis for a number of advanced techniques. It starts with a *J*-resolving building block and ends with a HMBC sequence. In *J*-resolved HMBC-1, t_1 is extended over 300–500 ms to enable the measurement of proton–carbon spin coupling constants in the f_1 dimension, and the spin evolution time (Δ_2) of the basic HMBC pulse sequence is replaced by a *J*-scaling element ($nt_1/2$–$\pi_{(H,C)}$–$nt_1/2$) (Figure 23).

As a result, the magnetization is evolved with t_1, $(n+1)t_1$ and nt_1 for chemical shift, proton–proton spin couplings and proton–carbon couplings, respectively,

and thus, the spin couplings, J_{HH} and J_{CH}, appear in the fl dimension as splittings of $(n+l)J_{HH}$ and ${}^{n}J_{CH}$. In 2D-*J*-resolved spectroscopy, $t_{1,max}$ must be larger than $1/J$. If $t_{1,max}$ is smaller than $1/J$, a condition required by the sampling theorem is not satisfied and the coupling constants cannot be determined. In *J*-resolved HMBC, the scaling factor n must be set so as to give an $nt_{lmax} > 1/J$, as in the evolution time of 2D-*J*-resolved spectroscopy. This requirement severely affects the sensitivity of the experiment, as compared to 'normal' HMBC.

The alternative experiment, *J*-resolved-HMBC-2[75] (Figure 24), introduces a 'variable delay–constant-time' element for balancing the homonuclear and heteronuclear coupling evolution.[32,76,77]

The positioning of the π-pulses in the 'constant-time–variable delay' achieves refocusing of both the homonuclear and heteronuclear couplings within an accordion-type pseudo-evolution time. The heteronuclear anti-phase magnetization is transferred back to the protons prior to detection. The scaling of homonuclear and heteronuclear coupling constants can be controlled independently by varying the

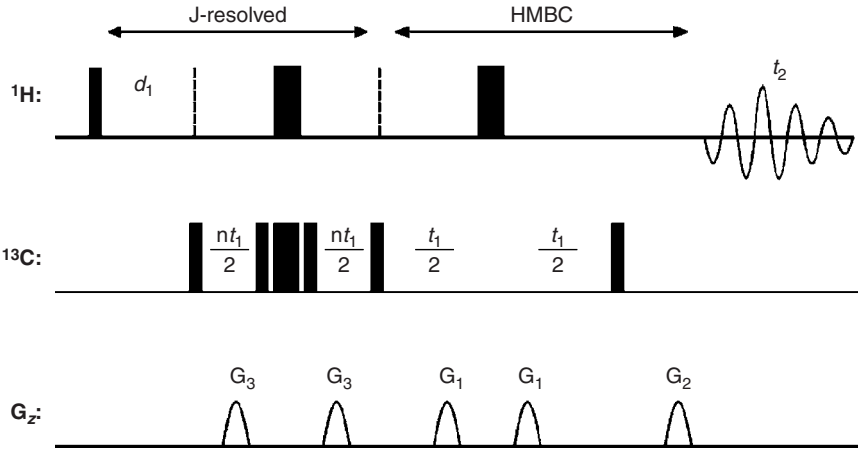

Figure 23 *J*-resolved HMBC-1 pulse sequence by Furihata and Seto[75] G_1:G_2 = 2:1, $G_2 \neq G_3 \neq G_1$.

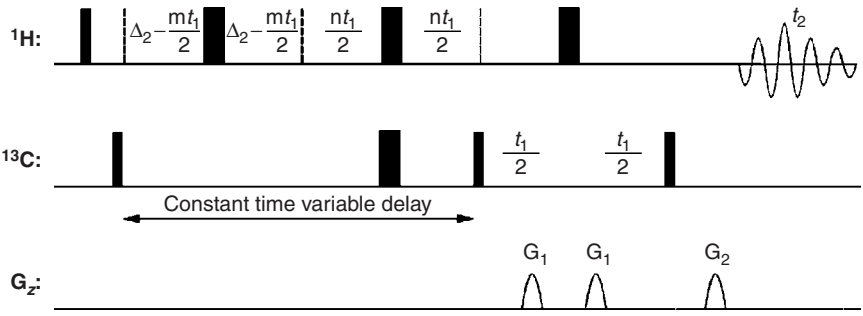

Figure 24 The *J*-resolved-HMBC-2 experiment.[75] The timing of the 'constant-time–variable delay' is detailed in the text, G_1:G_2 = 2:1.

values of n and m in the two variable delay periods. When m is set to $n+1$, homonuclear couplings are decoupled due to a net CT period throughout the accordion and t_1-elements. If m is set less than n, the heteronuclear couplings are scaled up by a factor n and homonuclear couplings are scaled down by $((n-1)-m)$. Although an increase in signal-to-noise can be attained by using a value of m smaller than n, in practical terms, the evolution of the homonuclear couplings could severely complicate the spectral analysis, generally not making this a preferred parameter selection. This problem is largely resolved in the recent selective *J*-resolved-HMBC experiment,[78] which employs a selective proton π-pulse to allow couplings to the affected spins to evolve in the *J*-resolving period and a CT evolution period to remove the J_{HH} splitting (Figure 25).

The selective *J*-resolved HMBC pulse sequence can be seen as being composed of a *J*-resolving building block and a CT-HMBC[79] part. In the *J*-resolving block (between points a and b in Figure 25), a selective-shaped ^{1}H π-pulse is used, which must be adjusted such as not to affect protons that should be decoupled, while keeping its duration as short as possible to limit signal loss due to T_2 relaxation. In *J*-resolved HMBC-1, the remaining two ^{1}H hard π-pulses cannot be replaced by selective ones, because application of a selective ^{1}H pulse in the evolution period would cause splitting due to the one-bond coupling to protons not involved in the MQC. In the CT-HMBC part (between points b and c in Figure 25), the ^{1}H–^{1}H spin couplings have no net evolution enabling straightforward determination of long-range CH coupling constants.

The cross-peak splittings are illustrated in the experimental spectra in Figure 26, where *J*-resolved HMBC-2 and selective *J*-resolved HMBC spectra are compared.

This figure not only illustrates the differences in multiplet patterns but also underscores the improved resolution in the carbon dimension of selective *J*-resolved HMBC.[78] The interpretation of small *J* values from these spectra is not fully quantitative but usually suitable for conformational analysis. Larger long-range J_{CH} are easily determined from the spacing of doublet cross-peaks, while cross-peaks with the long-range $^3J_{CH} \leq 3$ Hz appear as singlets, indicating *gauche* conformation of the pertinent fragment. Another important advantage of the selective *J*-resolved HMBC experiment is its higher sensitivity.

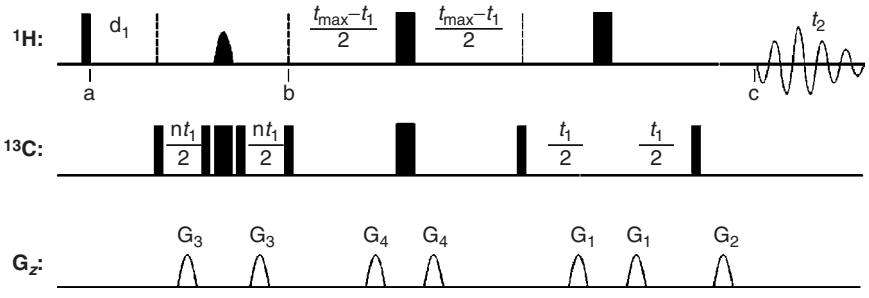

Figure 25 The selective *J*-resolved HMBC pulse sequence.[78] G_1:G_2 = 2:1, $G_2 \neq G_3 \neq G_1$, $G_2 \neq G_4 \neq G_1$, $G_4 \neq G_3$.

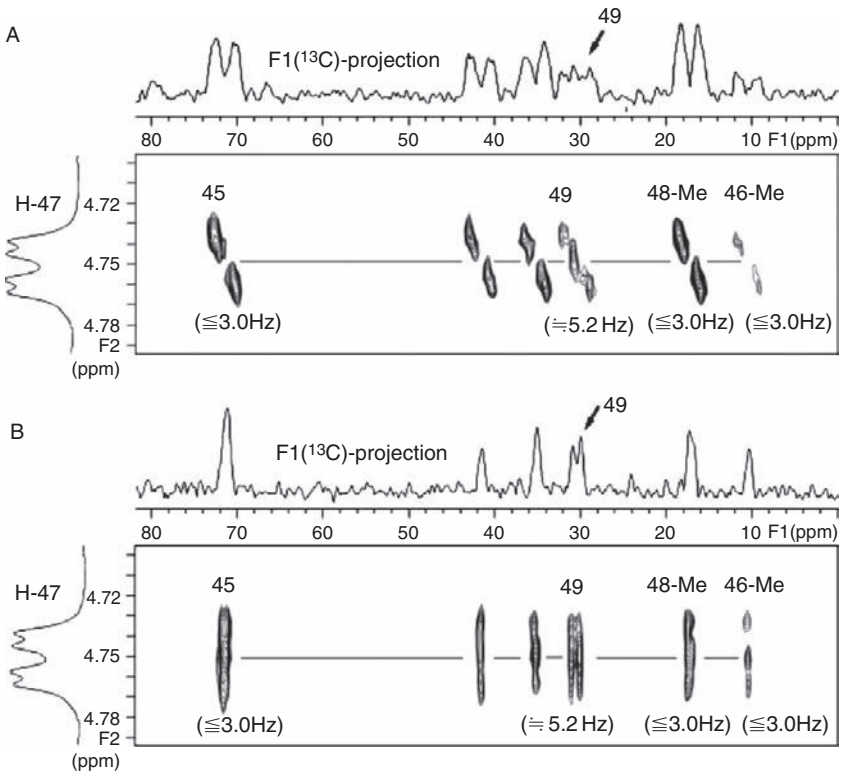

Figure 26 (A) The *J*-resolved HMBC-1 and (B) the selective *J*-resolved HMBC spectra of monazomycin. Reprinted from Ref. 78 with permission from John Wiley & Sons, Inc.

7.2. *J*-IMPEACH-MBC

The *J*-IMPEACH-MBC experiment[80] (Figure 27) was derived from IMPEACH-MBC[57] by omitting the refocusing prior to t_2. This allows for the scaled evolution of the heteronuclear couplings in f_1, while preventing homonuclear coupling evolution by using a CT delay. The spectra obtained with this pulse sequence are similar to those from the *J*-resolved HMBC-2. However, this experiment simplifies the *J*-resolved-HMBC-2 pulse sequence in that it merges several π-pulses throughout the experiment, yielding an increase in overall S/N. The key innovation in this experiment is the inclusion of a 'constant-time–variable delay element' $[D/2\text{-}\pi(^{13}\mathrm{C}) - D/2 - v_\mathrm{d}]$. This makes homonuclear couplings evolve in CT, thereby suppressing modulations that occur in the ACCORD-HMBC experiment discussed above.

At the same time, the CT element allows the evolution of heteronuclear couplings during t_1. By that varied delay and successive increments, a range of long-range couplings can be sampled. Subsequently, HMQC is created by a $\pi/2$ ^{13}C pulse. After this point, gradient selection and back transfer of magnetization to protons for detection are performed in the same way as for the normal

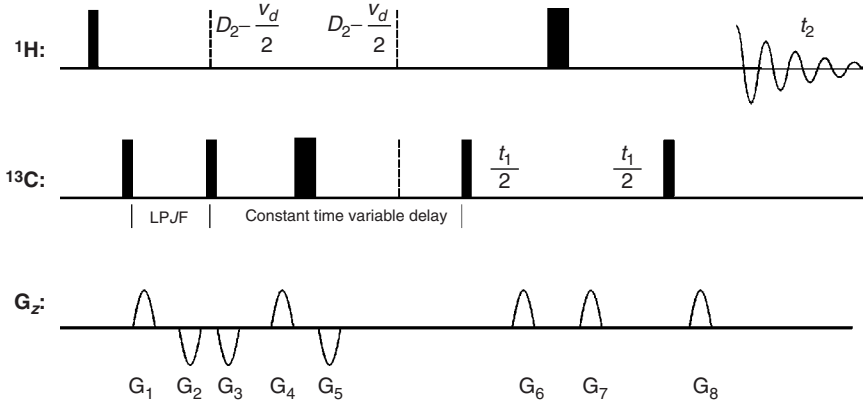

Figure 27 Pulse sequence for the *J*-IMPEACH-MBC experiment.[80]

gradient HMBC experiment (Figure 4).[25] An example spectrum of strychnine with expanded cross-peaks is shown in Figure 28.

The scaling of *J*, which is achieved by setting v_d a multiple (typically 30) of the maximum t_1, has perhaps an unexpected consequence. On low-field spectrometers, a long v_d is required, which causes relaxation lasses, while the sensitivity is better on higher field instruments, where v_d can be shorter. The *J*-resolved-HMBC-2 and the *J*-IMPEACH-MBC experiments are limited to a qualitative interpretation of the small heteronuclear. Both *J*-IMPEACH-MBC and the *J*-resolved HMBC-2 experiments allow data interpretation at a glance and are useful for semi-quantitative *J*-based conformational analysis, if sufficient sample is available (and soluble).[81]

7.3. IMPACT-HMBC

*Imp*roved and *a*ccelerated *c*onstant-*t*ime *h*eteronuclear *m*ultiple-*b*ond *c*orrelation (IMPACT-HMBC),[82] has recently been derived from the band-selective, CT-HMBC experiment introduced by Claridge and Pérez-Victoria.[15] The pulse sequence (Figure 29) starts with a ^{1}H cross-polarization (ASAP—*a*cceleration by *s*haring *a*djacent *p*olarization) period to accelerate recovery of longitudinal ^{1}H magnetization and to transfer polarization from close protons.[83] The ASAP 'mixing' reduces the 'f_1 ridges', a common problem with short recovery delays.

A third-order LPJF[35] precedes the long-range coupling evolution period Δ. The CT element for t_1-evolution avoids homonuclear proton and allows for phase-sensitive HMBC recording,[84]thus delivering very good ^{13}C resolution. ASAP[83] is also used in this sequence.

Figure 30 compares a standard low-pass filtered gradient-selected HMBC spectrum of cholesteryl acetate using the IMPACT-HMBC experiment.

The artefacts (f_1 ridges and residual $^1J_{CH}$ correlations), which can interfere with true long-range correlations, are significantly reduced in the IMPACT-HMBC spectrum as a consequence of the ASAP period and the *J*-filtering.

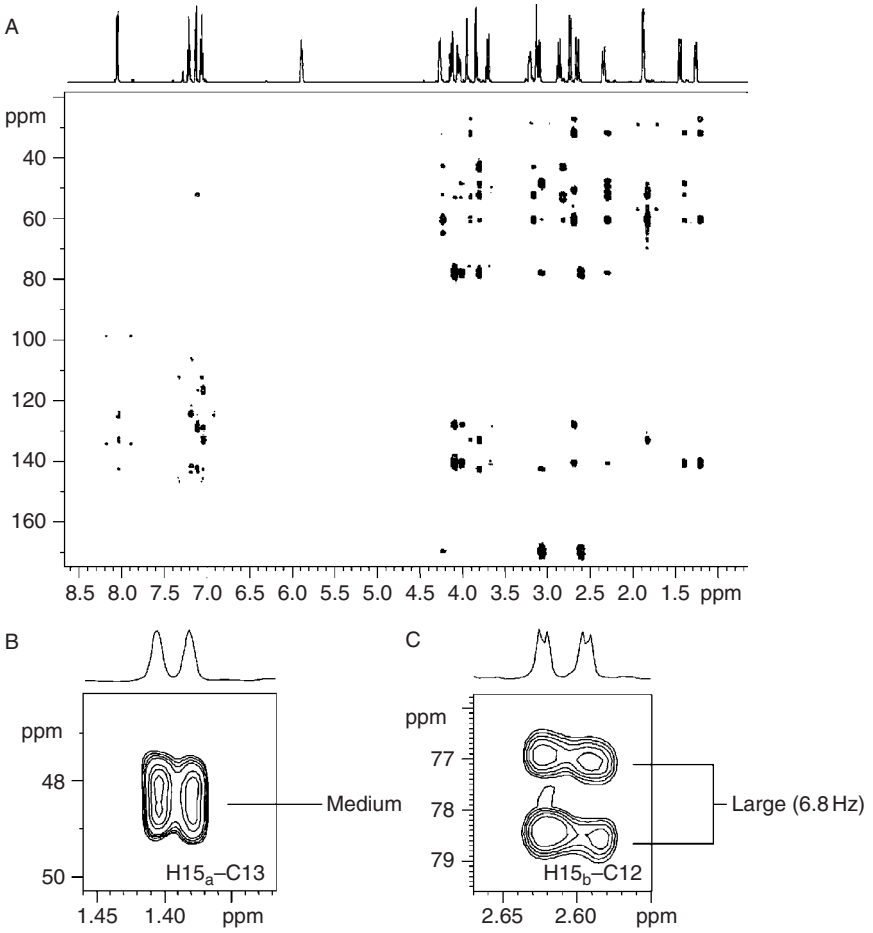

Figure 28 2D *J*-IMPEACH-MBC spectrum of strychnine in $CDCl_3$; (B) expansion of the 2D *J*-IMPEACH-MBC spectrum with the H-15a to C-13 correlation, showing the determination of the $^3J_{C,H}$ coupling constant; (C) expansion of the 2D *J*-IMPEACH-MBC spectrum showing the H-11b to C-12 correlation and the determination of the $^3J_{C,H}$ coupling constant. Reprinted with permission from Ref. 32.

7.4. Determination of RDCs

The emergence of RDC-based geometry determination also for small molecules[85] has spurred new applications of HMBC-derived NMR methods that allow accurate determination of small heteronuclear coupling constants. In principle, all the methods described above can be used for that purpose; however, the special accuracy requirements of RDC-experiments, and in addition, the need to determine the signs of the RDCs, require special attention.

The most accurate experiments for extraction of RDCs are based on the idea of using a reference experiment, where the coupling of interest does not cause a splitting.[86] The advantage of such an approach is that one does not need to determine the mixed phase contributions and pulse imperfection artefacts

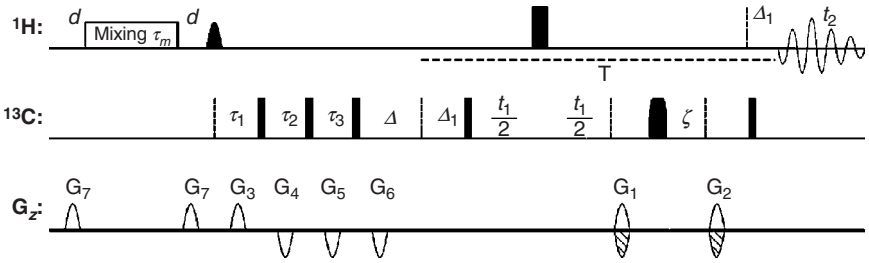

Figure 29 The IMPACT-HMBC pulse sequence.[82] The first pulse on the ^{1}H channel is shown as a sine shape and its length can be set according to the Ernst angle. The shaped π-pulse on the ^{13}C channel can be set as a broadband or band-selective pulse. $^1J_{CH}$ correlations are suppressed using a third-order LPJF and the delays as previously described in[35] $\Delta = (2\,{}^nJ_{IS})^{-1}$. The delays Δ_1 are decremented as t_1 is incremented such that the period T remains constant. Delay ζ is set to prevent ^{13}C chemical shift evolution for the first t_1 value, $\zeta = t_1(0) + \pi_H$ (duration of H π-pulse). The standard relaxation delay is replaced with a mixing sequence of length τ_m flanked by field gradients pulses and relaxation delays d.[83] Gradient ratios are G_1:G_2:G_3:G_4:G_5:G_6:G_7 = 5:3:4:2.5:1:0.5:1.5 (odd experiments) and 3:5:4:2.5:1:0.5:1.5 (even experiments). Further details can be found in the original publication.[82]

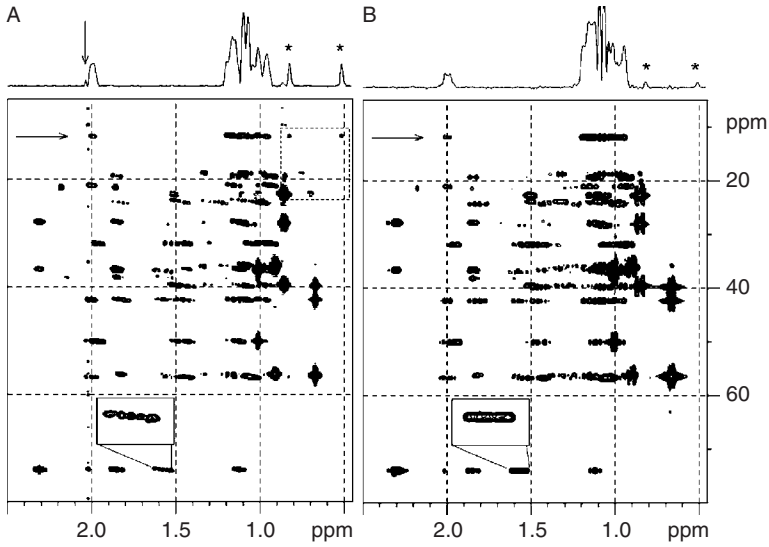

Figure 30 Aliphatic carbon region of HMBC spectra of cholesteryl acetate using (A) the standard low-pass-filtered gradient-selected HMBC and (B) the IMPACT-HMBC experiment. The enlarged cross-peaks in the inset boxes demonstrate the improved peak shape in the presence of strong homonuclear coupling. The traces above the spectra are 1D cross-sections at the position of the horizontal arrows showing the long-range correlations of the methyl C18. An f_1 noise ridge is indicated by the vertical arrow in (A) and residual $^1J_{CH}$ artefacts are denoted by asterisks and the dashed box.[82] Reproduced from Ref. 82 by permission of The Royal Society of Chemistry.

separately, since they are the same in the reference experiment. Based on an earlier method by Verdier et al.[87] Kobzar and Luy[52] have developed a particularly accurate set of experiments consisting of a CT-HMBC experiment, together with a reference CT-HSQC experiment, as shown in Figure 31.

The special advantage of their approach is that both line shapes and amplitudes can be used in the fitting procedure. On account of the CT evolution, the peaks are narrow in the indirect dimension and the line shapes are independent of the carbon chemical shift, as can be appreciated from the comparison in Figure 32.

The cross-peaks in HMBC and corresponding reference HSQC spectra only differ by the heteronuclear long-range splitting; therefore, the fit procedure only needs to vary this parameter. However, the sign of coupling constants cannot be determined in general cases with these experiments.[52]

8. Γ-HMBC

Schwalbe and co-workers[6] developed a method called Γ-HMBC, in which glycosidic torsion angles are determined from $^3J_{CH}$ couplings, together with dipolar cross-correlated relaxation rates $\Gamma_{C_iHi,C_iH_j}^{C}$. It relies on an original pulse sequence

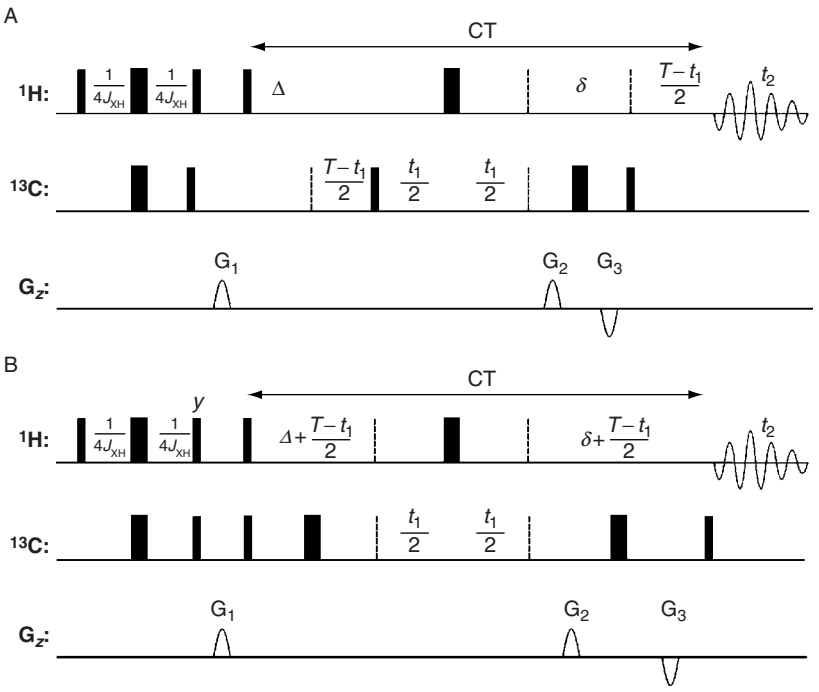

Figure 31 (A) Constant-time HMBC optimized for accurate determination of heteronuclear long-range couplings from proton multiplet patterns in conjunction with the reference HSQC experiment of exactly the same duration shown in (B). The gradient ratios are G_1:G_2:G_3 = 33:50:−30 (echo)/33:30:−50(anti-echo). Δ is adjusted for long-range evolution (ca. 62.5 ms).

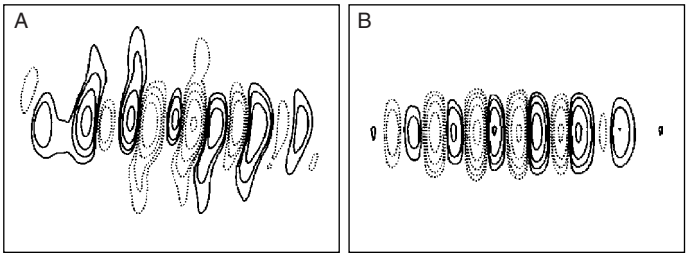

Figure 32 Comparison of typical phase-sensitive cross-peaks obtained with a conventional HMBC and the constant-time HMBC experiment from Figure 31. Reprinted from Ref. 52 with permission.

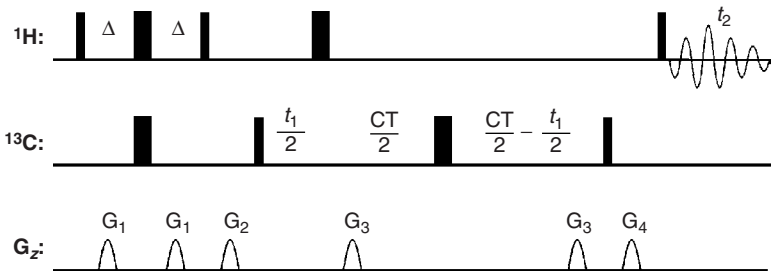

Figure 33 Pulse sequence on which the Γ-HMBC experiment is based.[88] The following parameters were used by Ilin et al.[6]: $\Delta = (2J)^{-1}$, CT = 30ms, $G_1 = 0.20$ T/m, $G_2 = 0.15$ T/m, $G_3 = 0.40$ T/m, $G_4 = 0.10$ T/m. CT is the constant-time delay.

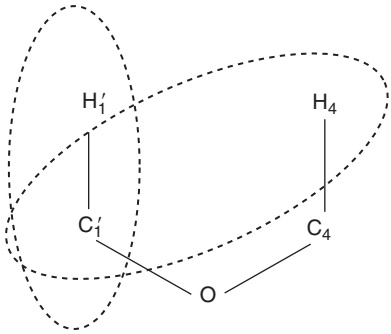

Figure 34 Numbering of atoms in a glycosidic fragment. The dashed ovals indicate the cross-correlated dipolar interactions causing the HMBC-like correlation in Γ-HMBC.

(Figure 33) by Vincent and Zwahlen[88], in which coherence transfer between hydrogen and carbon atoms across the glycosidic linkage is achieved by C–H-dipolar cross-correlated relaxation.

In this experiment, an initial anti-phase operator $2H1'_zC1'_x$ (for numbering See Figure 34) evolves into the operator $2H_{4z}C1'_x$ through cross-correlated dipole–dipole relaxation between two C–H dipoles centred on C1′.

During the CT delay, the Cartesian product operator term $2H_{4y}C_{1'z}$ evolves modulated by the $^3J_{C1'H4}$ coupling constant, which can then be determined by fitting cross-peaks multiplets with simulated line shapes. The method was used to determine the conformation around glycosidic bonds in a glycopeptide.[6] Cross-correlation effects between the CSA and DD relaxation mechanisms have also been observed in HMBC spectra.[7]

9. MULTIPLICITY EDITING OF HMBC SPECTRA

An improved edited HMBC experiment splits into two sub-spectra according to the number of protons attached to ^{13}C nuclei being odd or even.[17,89,90] Representative pulse sequences from Ref. 90 implementing this technique are depicted in Figure 35.

To produce the edited spectra, one combines the sub-spectra in the following manner: $^{13}C_q$ and $^{13}CH_2 = 2A - (B + C)$ and ^{13}CH and $^{13}CH_3 = 2A + (B + C)$. For optimal results, the sub-spectra should be acquired in an interleaved manner using twice the number of scans for A than for the others. In Figure 36, the $^{13}C_q$ and $^{13}CH_2$ spectrum (red) obtained with the method of Figure 35 is overlaid with the ^{13}CH and $^{13}CH_3$ spectrum (blue) of strychnine in $CDCl_3$.

10. INDENTIFYING TWO-BOND CORRELATIONS

Distinction of two- and three-bond H–C and H–N couplings is considered a very worthwhile goal. Although impossible for quaternary heteroatoms, it has become feasible in chains of protonated carbons through development of the concepts used in ACCORD-HMBC, IMPEACH-MBC and CIGAR-HMBC.

10.1. $^2J,^3J$-HMBC

The $^2J,^3J$-HMBC experiment[92] shown in Figure 37 includes a modification of the constant-time–variable delay, which was introduced in the IMPEACH experiment,[57] the so-called STAR (*S*electively *T*ailored *A*ccordion F_1 *R*efocusing) operator, which is an extension of the 'constant-time–variable delay' mentioned previously.

Due to differential behaviour of the two- and three-bond correlations, the corresponding 2D cross-peak multiplets vary in their shape. The differentiation of two- and three-bond heteronuclear couplings is based on the coevolution of the homonuclear proton couplings of directly attached protons during the STAR(R) operator building block. Since in a chain of three CH-groups $^4J_{HH}$ are usually much smaller than $^3J_{HH}$, only the homonuclear vicinal coupling $^3J_{HH}$ causes a skewing of the spitting about the chemical shift of the carbon to which the proton has a $^2J_{CH}$ heteronuclear coupling. By contrast, the $^3J_{CH}$ heteronuclear correlation cross-peak is not skewed, since $^4J_{HH}$ is usually small (Figure 38).

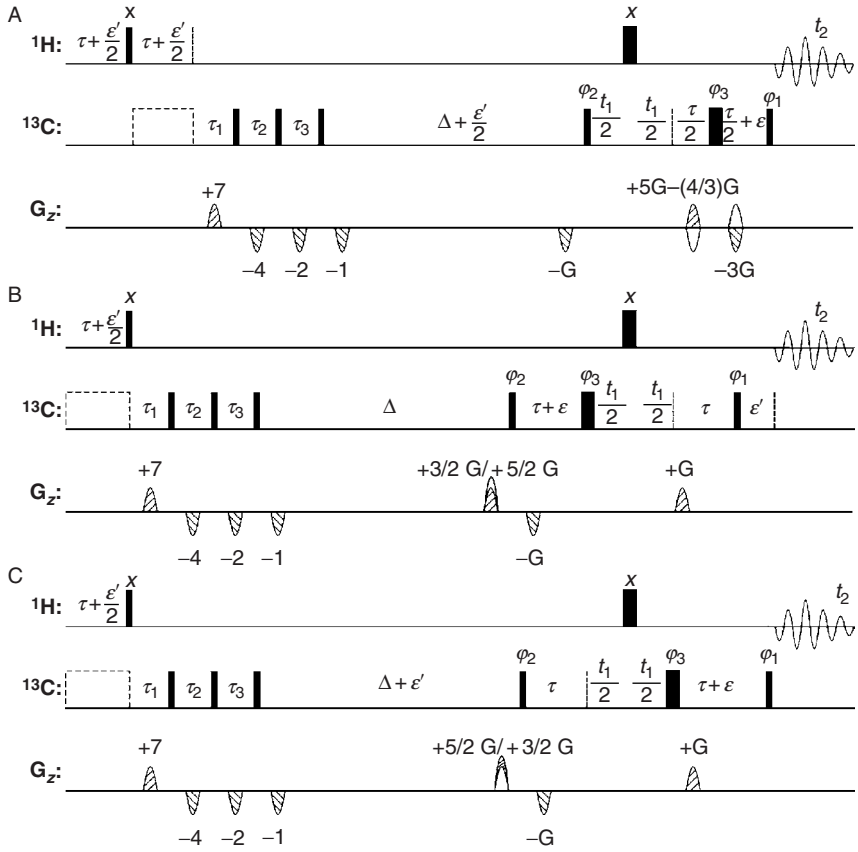

Figure 35 Pulse sequences for multiplicity editing of broadband HMBC spectra.[17] (A) Standard HMBC sequence, (B) Up–down− sequence, (C) Up–down+ sequence. The dashed boxes indicate GARP decoupling. All use a third-order LPJF,[35] with the delays $\tau_1 = ½\,[^1J_{min} + 0.07(^1J_{max} - {}^1J_{min})]^{-1}$, $\tau = \tau_2 = (^1J_{max} + {}^1J_{min})^{-1}$ and $\tau_3 = ½\,[^1J_{max} + 0.07(^1J_{max} - {}^1J_{min})]^{-1}$ adjusted for effective suppression of one-bond correlations over a range $^1J_{min}$–$^1J_{max}$ of coupling constants. Δ is adjusted for the evolution of long-range heteronuclear coupling. Separate sub-spectra for odd and even numbers of directly attached hydrogen atoms are obtained as the sum or difference, respectively, of (A) with (B) or (C). The delays ∂ (duration of a gradient pulse), ε (minimum t_1 time plus the duration of a proton π-pulse) and ε' (ε + the duration of a carbon π-pulse) are minor adjustments. The amplitudes of the initial four gradients of the LPJF may be an order of magnitude less than the other gradients. In sequences B and C, ^{13}CH and $^{13}CH_3$ peaks are inverted relative to the standard experiment. Recommended phase cycles are detailed in Ref. 90.

The different appearance of the cross-peaks occurs since the BIRD element only affects the two-bond correlation. This is further illustrated by the $^2J,^3J$-HMBC spectrum of strychnine in Figure 39, where the expansion showing the H11α-C13 and H11 α -C12 correlations represents a typical example of a $^2J,^3J$ distinction.

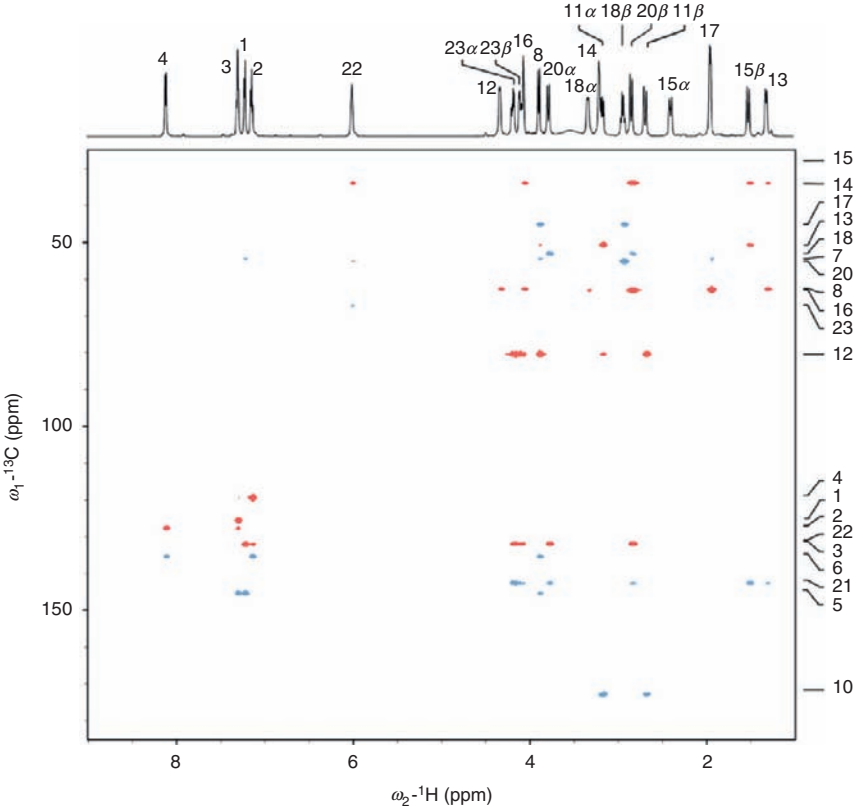

Figure 36 Multiplicity edited HMBC spectrum of strychnine using the pulse sequences in Figure 35 in an interleaved manner and with the GARP scheme[91] used for decoupling. Reprinted from Benie and Sørensen[90] with permission (For interpretation of the references to colour in this figure legend, the reader is referred to the Web version of this chapter.).

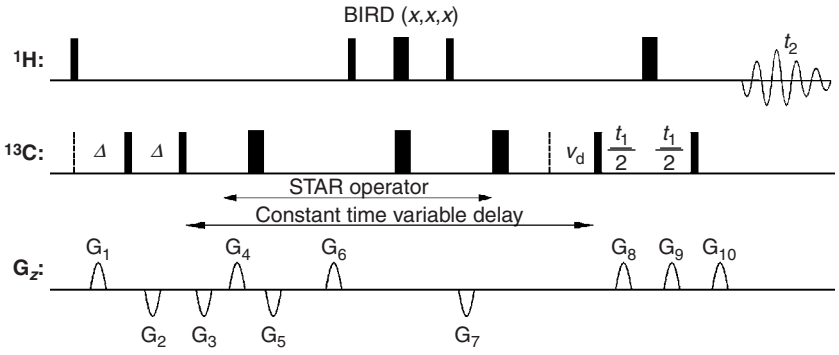

Figure 37 Pulse sequence of the ^2J,^3J-HMBC experiment.[92]

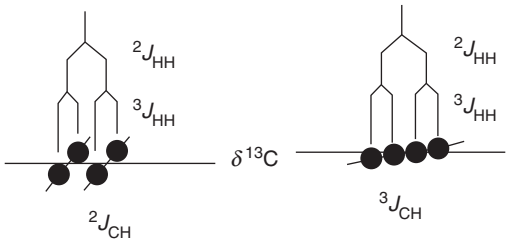

Figure 38 Scheme illustrating the discrimination of two-bond from three-bond correlations by the skew of cross-peak multiplet patterns in $^2J,^3J$-HMBC experiments. Reprinted with permission from Krishnamurthy et al.[92]

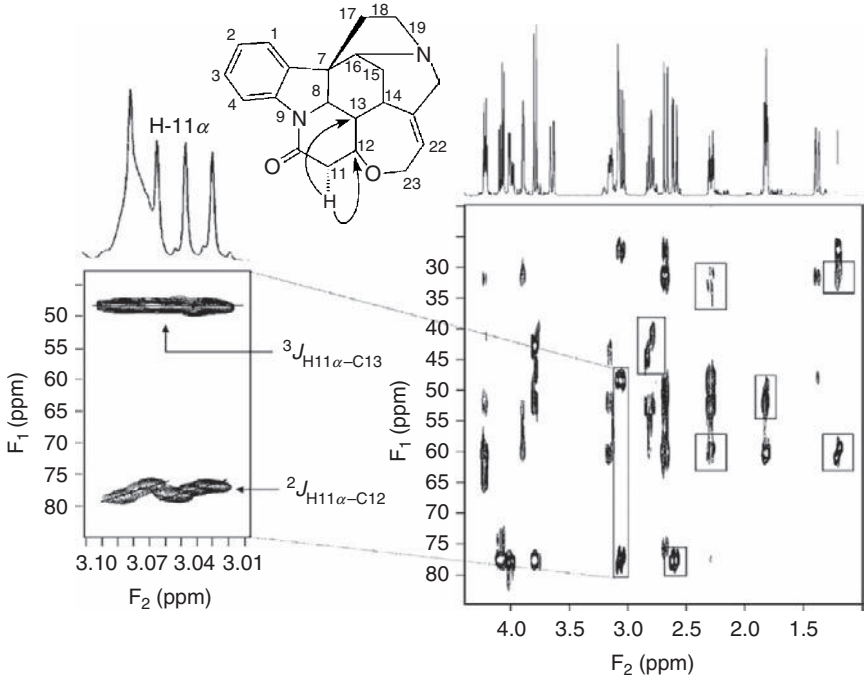

Figure 39 $^2J,^3J$-HMBC spectrum of strychnine with molecular structure diagram accordion optimized for long-range couplings between 6 and 10 Hz acquired with a *J*-scaling factor of 16. The expansion on the left illustrates how two- and three-bond heteronuclear correlations can be discriminated by the skew of the cross-peak multiplets. The delays within the constant-time STAR operator were varied in the following way: Δ_1 was incremented to 16 times t_{1max}, while Δ_2 was decremented to 0 synchronously. These manipulations keep the overall duration of the STAR operator constant over the course of the experiment. The delays D and ν_d were controlled such that for the final increment of the evolution time $D = 33.3$ ms and $\nu_d = 50$ ms. Reprinted from Ref. 92 with permission.

10.2. H2BC

The heteronuclear 2 bond correlation (H2BC) experiment by the group of Sørensen[36,93] takes a different approach to tackle the challenge of selective two-bond heteronuclear correlation. Strictly speaking, it is not an HMBC-type experiment, but the concept is based on a HMQC-COSY 'hyphenation' and therefore also restricted to C–H-chains. The information obtained is complementary to HMBC and even provides two-bond correlation information, if $^2J_{CH}$ is vanishingly small. The experiment can also be extended to a 3D version by allowing for chemical shift evolution of protons during a second split evolution period.[36] This experiment has also been combined recently with HMBC to the hybrid sequences HAT-HMBC.[37] The authors recommend it as an experiment to be performed after H2BC and regular HMBC to resolve possible open ends left by the spectra from these two experiments.

11. 3D NMR METHODS INVOLVING HMBC

While most 3D NMR methods find their primary motivation in reducing spectral overcrowding, in the case of HMBC (which often features sparsely populated 2D maps), a sensitivity issue was prevailing.

11.1. 3D-HMBC

The amplitude of HMBC cross-peaks is reduced significantly if a proton has multiple coupling partners; this being especially crucial with methylene proton signals in a complicated proton spin system. This phenomenon is caused by the fan-out of proton signals of concern due to coupling to many proton signals during the evolution period. Furihata and Seto[54] addressed this problem in a somewhat counter-intuitive fashion by developing the conventional 2D-HMBC into 3D-HMBC. The delay time Δ_2 and t_1 in the 2D-HMBC (Figure 1) are replaced by evolution times t_1 (*J*-dimension) and t_2 (chemical shift dimension), respectively, in the 3D-HMBC pulse sequence, with Δ_1 being set to 3.5 ms. Their results clearly show that 3D-HMBC is apparently more sensitive than it's 2D predecessor. In addition, the technique is very useful when the connectivity information of broad proton signals is obscured due to complex splitting patterns and due to fast transverse relaxation of methylene groups. Furihata and Seto[54] observed a substantial increase of the signal. It should be noted that in their original spectra, only four scans were used for taking each increment in the 3D experiment, as opposed to 64 scans per increment for the 2D experiment.

11.2. 3D-*J*-HMBC

In 1999, Sze et al.[55] published the so-called 3D-*J*-resolved HMBC. Application of this 3D-*J*-resolved HMBC experiment should facilitate spectral assignment and the measurement of long-range ^{1}H–^{13}C couplings, particularly in systems with

poor sensitivity and severe overlaps. The preparation period of the 2D-HMBC experiment is replaced by an evolution period for one-bond and multiple-bond *J*-couplings. Two advantages of this arrangement arise over the method proposed by Furihata and Seto[54]: The chemical shifts during the *J* evolution period are refocused so that the spectral width of this dimension is reduced to $^{1}J_{CH}$. Thus, possible peak cancellations due to spectral folding are avoided and the resolution is increased. The spectral width in the *J*-dimension can be further reduced to optimize the sensitivity per time and resolution as long as folded $^{1}J_{CH}$ peaks do not overlap with $^{n}J_{CH}$ cross-peaks.

Another advantage is that 2D HMQC and HMBC spectra, which are optimal in sensitivity for a wide range of $^{1}J_{CH}$ and $^{3}J_{CH}$ values, can be obtained by summing the sections of the 3D spectrum along the f_1-dimension corresponding to the well-separated one-bond and long-range *J*-couplings.

2D-HMBC spectra obtained in this way are free of interference from the one-bond correlation peaks. The separation of the one- and multiple-bond correlation peaks is more effective than that with the traditional LPJF methods, which cannot purge all one-bond ^{1}H–^{13}C correlation peaks completely due to the variations in $^{1}J_{CH}$ coupling constants.

11.3. COSY–HMBC

HMBC usually requires large spectral width in the indirect dimension. Apart from posing challenges for rf-pulse performance, the resolution requirements in the indirect dimension often preclude including an HMBC element in a 3D pulse sequence, except for 3D-*J*-resolved HMBC (described above), which require relatively few data points in the *J*-dimension. Random sampling (or non-uniform sampling—NUS)[94,95] in combination with processing methods like multi-dimensional Fourier transformation or maximum entropy[96] is advantageous for the processing of large multi-dimensional NMR data sets, particularly with sparse peak distribution.[97] This approach enables one to obtain highly resolved, aliasing-free 3D spectra at very low sampling density. Misiak et al. applied this technique to perform 3D COSY–HMBC experiments (Figure 40) and achieved complete assignments of organic molecules.[98–100]

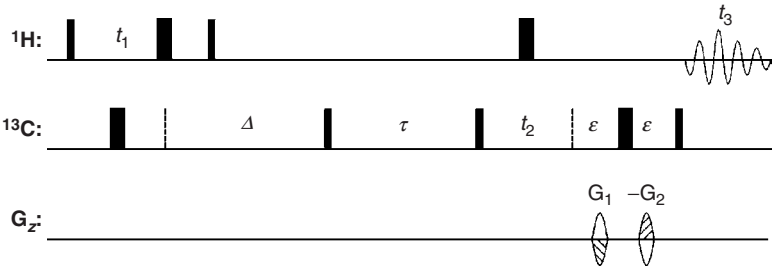

Figure 40 3D-COSY–HMBC pulse sequence.[98] $\Delta = (2\,^{1}J_{IS})^{-1}$, $\tau = (2\,^{n}J_{IS})^{-1}$, ε is used to accommodate the gradient pulses G_1:$G_2 = +(\gamma_H + \gamma_C)$:$-(\gamma_H - \gamma_C)$ and $-(\gamma_H - \gamma_C)$:$+(\gamma_H + \gamma_C)$ for echo and anti-echo, respectively.

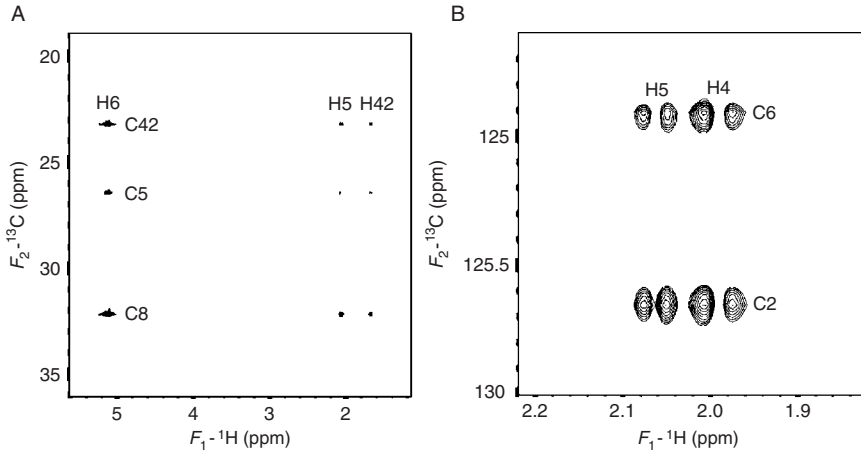

Figure 41 2D cross-sections from the 3D COSY–HMBC spectrum of the natural abundance prenol-10 recorded with the pulse sequence of Figure 40: (A) $^1H/^{13}C$ plane for F3(^1H) = 5.124 ppm (H-6); (B) $^1H/^{13}C$ plane for F3(^1H) = 1.990 ppm (H-4). Reprinted from Ref. 100 with permission.

In Figure 41, cross-sections of the 3D-COSY–HMBC spectrum of prenol-10 are displayed. This compound has many near degenerate chemical shifts and therefore represents a challenging assignment problem, which is conveniently solved by the application of 3D-COSY–HMBC.[100]

Random sampling of the evolution time space (NUS) used in this method allows one to obtain an excellent resolution, which is extremely important in cases of crowded spectra.

Another 3D experiment deserves to be mentioned here: 3D HSQC-HSQMBC[101] aimed at complex molecules with many protonated carbons and a narrow spread of ^{13}C chemical shifts like complex carbohydrates; it does not provide correlation of quaternary carbons, though. This type of experiment is likely to benefit much of the upcoming non-uniform sampling techniques.

12. NEW TECHNIQUES FOR EFFICIENT ACQUISITION

Considerable efforts have recently been made to make NMR spectroscopy more efficient, particularly for routine analysis. Among these approaches, multiplex spectra derive information from raw data containing super-positions of different types of information by a linear combination of subsets. Since these techniques require no additional hardware, they can be easily implemented on practically all modern pulse spectrometers.

12.1. Heteronuclear multiple-bond and single-bond connectivities (HMSC)

The first multiplex-type experiment delivering HMBC information as well as HSQC one-bond correlations was the MBOB experiment (Figure 42) by Meissner and Sørensen.[35,89]

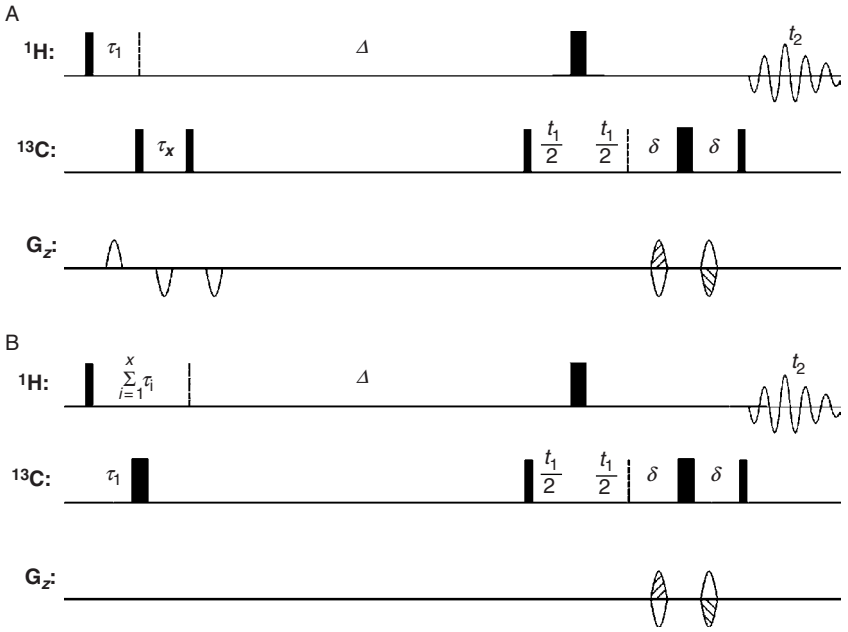

Figure 42 MBOB pulse sequence for simultaneous observation of one-bond and long-range correlations.[35]

Burger et al.[102] developed the similar HMSC technique for simultaneous determination of long-range and one-bond heteronuclear connectivities. The pulse sequence used for HMSC is identical to the one for BIRD-HMBC (Figure 10), but different data manipulation (i.e. separate storage of phase cycle steps) is required. Compared to two standard HSQC and HMBC experiments applied one after the other, the measuring time of the HSQC spectrum is economized, since the lower sensitivity of the HMBC experiment determines the total measurement time. At the same time, usually a higher SNR for the HSQC spectrum is achieved at no additional costs. The efficiency of the new pulse sequence and the quality of the resulting spectra were demonstrated using strychnine.[102] For HMSC, the pulse sequence originally developed for BIRD-HMBC (Figure 11) is used, but for each t_1 value, two t_2-FIDs with different phase settings $\Phi_2 = y, -x$ are acquired and stored separately ('interleaved' mode of detection). The residual phases in the experiment are cycled as follows: $\Phi_1 = y(-y)$; $\Phi_3 = x_2(-x)_2$; $\Phi_{REC} = x_2(-x)_2$.

Figure 43 shows one-bond and long-range correlation spectra of tetracycline obtained with a single MBOB experiment. The excellent discrimination between $^nJ_{CH}$ and $^1J_{CH}$ cross-peaks achieved with the optimized MBOB experiment with no residual cross-peaks of the other type left in the corresponding sub-spectra is evident.

12.2. Time-shared (TS) experiments

Other implementations of the multiplex principle, where different frequencies are allowed to precess simultaneously, have been dubbed 'TS' NMR experiments, recently reviewed by Parella and Nolis.[103] TS experiments have been proposed for

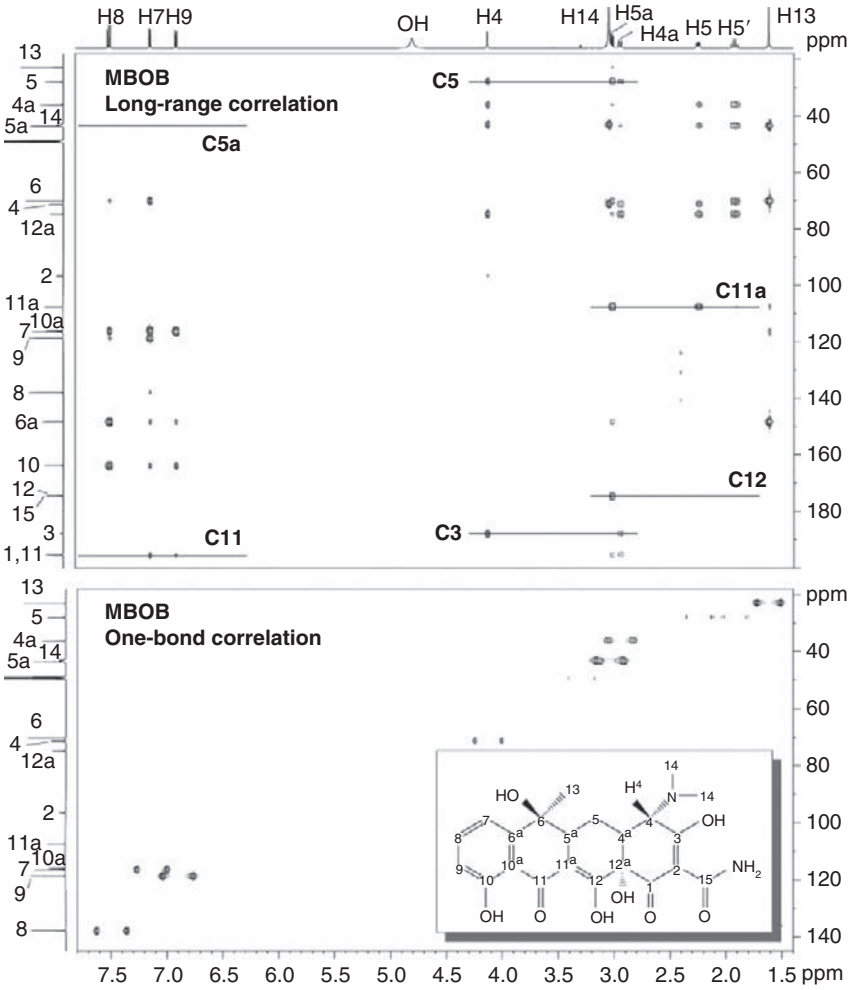

Figure 43 MBOB spectra of tetracycline hydrochloride in CD_3OD recorded with the pulse sequence in Figure 42A. A third-order *J*-filter was applied. Parameters: relaxation delay 2.4 s; $\tau_1 = 3.91$ ms, $\tau_2 = 3.45$ ms, $\tau_3 = 3.08$ ms (i.e. $J_{min} = 125$ Hz and $J_{max} = 165$ Hz); $\Delta = 97.4$, 80.0, 67.8 and 59.0; t_1 (max) = 4.21 ms; t_2 (max) = 376.7 ms; 8 scans per Δ value. Sine-shaped gradients of 1.0-ms duration and a unit strength of 5.0×10^{-2} T/m followed by a gradient recovery delay of 0.3 ms were applied. Two data sets, even and odd, were recorded and combined. The MBOB long-range correlation spectrum (top) results from addition of the odd and even data sets. The MBOB one-bond correlation spectrum (bottom) was obtained by subtraction of these two data sets. The signals are split by $^1J_{CH}$ in the F_2 dimension. Single-pulse 1D ^{1}H and ^{13}C are printed in place of projections next to the 2D spectra. Reprinted from Ref. 89 with permission.

different multinuclear applications, such as simultaneous ^{15}N and ^{13}C editing in NOESY-HSQC-type experiments,[104,105] simultaneous H_α and H_N detection in triple-resonance experiments[106] and simultaneous methyl and amide TROSY experiments of large deuterated proteins.[107]

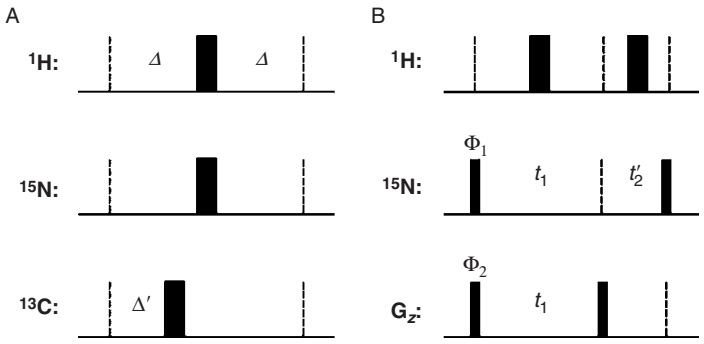

Figure 44 Pulse-sequence building blocks for time-shared experiments: (A) simultaneous evolution of *J*(CH) and *J*(NH) during a fixed defocusing period (B) simultaneous but independent frequency labelling by ^{13}C and ^{15}N chemical shift evolution.[108]

The TS CN-HMBC experiment achieves simultaneous correlation of ^{13}C–^{1}H and ^{15}N–^{1}H in HMBC spectra in such a multiplexed fashion.[108] The basic building blocks of TS NMR experiments are depicted in Figure 44. The pulse sequence element shown in Figure 44A allows the simultaneous evolution of the two different J_{CH} and J_{NH} couplings during a fixed defocusing period. The experiment can be optimized separately for different J_{CH} and J_{NH} by adjusting $\Delta = (4\ J_{CH})^{-1}$ and $\Delta' = (4\ J_{NH})^{-1}$.

The pulse sequence building block in Figure 44B is designed for the simultaneous, but independent frequency labelling by ^{13}C and ^{15}N frequency labelling during the incremented t_1 and t_1' evolution periods of the 2D experiment.

Spectral widths in the indirect dimension are independently adjustable for each heteronucleus. The t_1-increment is in the wider spectral width dimension (usually carbon) and is set to the reciprocal of the spectral width. The increment of the additional evolution period $\Delta t_1'$ is set to the difference of the reciprocal spectral widths of both nuclei. Other important aspects of time-shared experiments in general have recently been reviewed by Parella and Nolis.[103]

In TS experiments, the coherence pathways can be independently selected for ^{13}C and ^{15}N at natural isotope abundance, since the majority of protons coupled to ^{13}C is not coupled to ^{15}N.

The FID resulting from TS-HMBC experiments contains both ^{1}H–^{13}C and ^{1}H–^{15}N data that are encoded by phase cycling and can be unravelled by forming linear combinations of separately stored FIDs, thus delivering a multiplex advantage for the two correlation spectra. Two complementary data sets acquired with a π phase difference between C and N coherence pathways (controlled by the phase Φ_1 and Φ_2 in the element in Figure 35B) are acquired. The separate C and N subspectra are obtained by addition and subtraction of these data, respectively. Maximum sensitivity is retained through the multiplex advantage, as illustrated in Figure 45.

Time-shared experiments are special cases of multiplexed experiments,[109–112] which also include the MBOB and HMSC experiments described above. The analogy of 'time sharing' in computer science does not serve these experiments

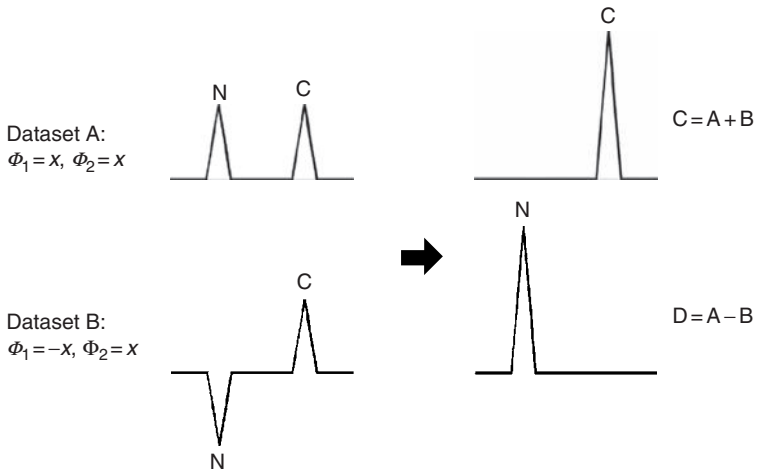

Figure 45 Scheme of data acquisition and data-processing procedures for nucleus editing in TS experiments. Two equivalent data sets (A and B) are separately collected in an interleaved mode with inversion of the phase Φ_1 (see Figure 44). After proper linear time-domain data combination, individual C and D spectra are obtained, retaining maximum sensitivity.[108]

right, since the term implies that the spectrometer time is shared between the experiments, dedicating only a fraction of its performance to each; but in these multiplex NMR experiments, the information from the parallel pathways is collected at the same time retaining the sensitivity of the individual experiments from which they are composed.

The fundamentals of the time-shared HMBC experiment shall be explained by way of a ^{1}H ^{13}C and ^{1}H ^{15}N TS-HMBC experiment (Figure 46). The single evolution delay Δ is optimized for a single 6–8 Hz coupling value because both long-range $^{n}J_{CH}$ and $^{n}J_{NH}$ ($n > 1$) coupling constants are in the range of 0–12 Hz. A LPJF only for ^{13}C, that is, $\Delta_1 = (2\,^{1}J_{CH})^{-1}$, is used to minimize direct correlation cross-peaks. Optionally, a ^{15}N-LPJF could also be incorporated.

The number of pulses and the duration of the sequence are exactly the same as the regular ^{15}N-HMBC, and the major difference is the addition of a t_1' period as compared to the basic ^{13}C-HMBC experiment. PFGs are placed and adjusted to simultaneously select both ^{13}C and ^{15}N coherence transfer pathways. The general equations for optimal refocusing condition in the TS-HMBC pulse sequence are described by Parella and Nolis[103] in their recent review article. A version with an optimized gradient ratio for both nuclei has been published by the same research group.[113]

A gradient ratio of 6:3:5:6 is one possible solution fulfilling the required relationships. The exact calculations of the gradient ratios are crucial when applying the TS-HMBC experiments for other nuclei. When setting up a TS-HMBC experiment, it may be necessary to adjust the relative resolution between the heteronuclei in the indirect dimension. A reduced ^{15}N spectral width (higher resolution) is achieved by increasing the $\Delta t_1'$ period, but this can incur ^{13}C sensitivity losses as compared to the standard experiment. By larger ^{15}N spectral

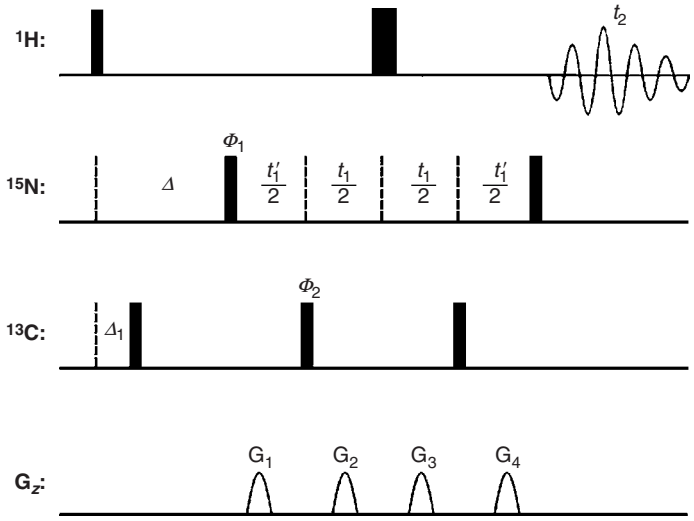

Figure 46 ^{1}H–^{13}C and ^{1}H–^{15}N TS-HMBC experiment.[108] The Δ and Δ1 delays are optimized to $\frac{1}{2}{}^nJ\ (6-8\,\text{Hz})$ and $\frac{1}{2}{}^1J_{(6-8\,\text{Hz})}$ (145 Hz), respectively. Gradients G_2 and G_3 are optimized to select ^{13}C magnetization, whereas all four G_1–G_4 gradients select the equivalent ^{15}N coherence pathway: G_1:G_2:G_3:G_4 = 60:50:30:60. Two different data sets are acquired and processed using the nucleus editing procedure described.[103]

widths, that is, shorter $\Delta t_1'$ periods, ^{13}C sensitivity losses due to relaxation can be minimized. In practice, a compromise needs to be made.

TS-HMBC experiments are recorded with the pulse sequence of Figure 46. Two complementary data sets are acquired in an interleaved fashion. The first experiment uses the same relative phases for ϕ_1 and ϕ_2 (data set A), while the second experiment inverts the phase ϕ_1 with respect to ϕ_2 (data set B). Addition (A + B) and subtraction (A − B) will afford the separate ^{13}C and ^{15}N spectra, retaining maximum sensitivity for both. Figure 47 shows the resulting TS-HMBC spectra for strychnine.

The relative sensitivity gains per time unit when running TS parallel acquisition versus separate acquisition of approximately $\sqrt{2}$ (141%) predicted by theory are confirmed by the experiments. Figure 48 underscores the total sensitivity per time gain achieved by using a two-nucleus TS-HMBC (CN-HMBC) experiment. The signal-to-noise ratio is the same as of two separate HMBC experiments requiring twice the total time.

Most variants of HMBC pulse sequences can be adopted as TS experiments (e.g. TS-HSQMBC[49]). The advantages of TS experiments can be combined with those of other independently accelerated NMR methods. With the MATS technique,[114] TS experiments can be combined with the multiple FID acquisition within the same scan to perform simultaneous acquisition of multiple and complementary NMR spectra, thus offering important spectrometer time savings. Figure 49 shows the MATS-HMBC pulse sequence that records 2D ^{1}H–^{13}C and ^{1}H–^{15}N HMBC as well as ^{1}H–^{13}C and ^{1}H–^{15}N HMBC-COSY spectra simultaneously.

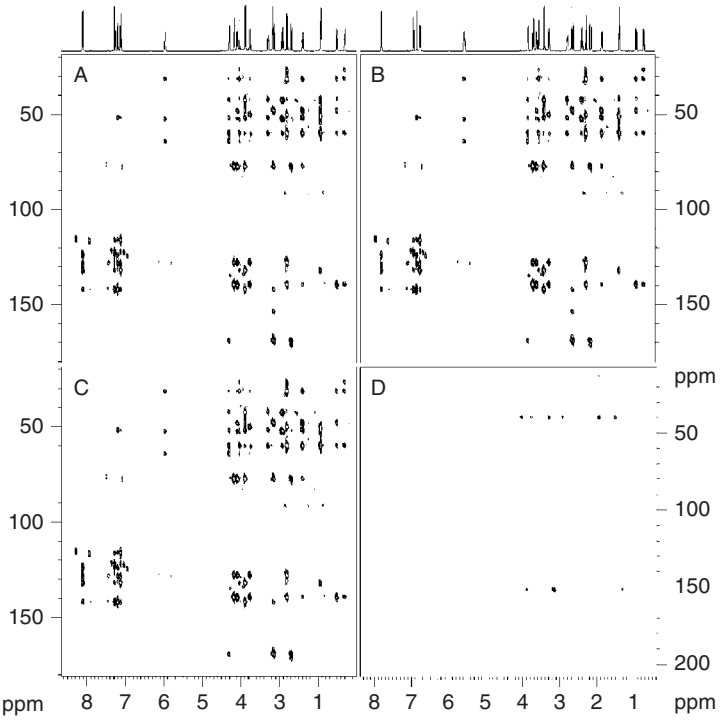

Figure 47 2D TS-HMBC (CN-HMBC) spectra of strychnine obtained using the sequence of Figure 45. HMBC spectra of strychnine showing the basic acquisition and processing steps: (A, B) Two complementary data sets are acquired with relative phases $\Phi_1 = x$ and $\Phi_1 = -x$, respectively. Appropriate linear combinations (A $\pm$ B) followed by conventional processing provide the two separate (C) C-HMBC and (D) N-HMBC spectra with enhanced sensitivity. Reprinted with permission from Ref. 108. Copyright 2007 American Chemical Society.

An example of four 2D spectra obtained by parallel acquisition using MATS-HMBC is shown in Figure 50.

It was reported that the measuring time with MATS is reduced by 75%, as compared to the separate acquisition of each data set by using conventional single-FID pulse programs.[114]

In principle, more than two parallel evolution channels are possible on spectrometers equipped with the appropriate probes and multi-channel receivers. Parallel acquisition (i.e. in the direct dimension) has recently become available on commercial spectrometers through parallel receivers and multiple detection coils. Recently, a series of experiments under the acronym PANSY (Parallel Acquisition NMR spectroscopy) have been proposed, allowing the simultaneous acquisition of FIDs of different nuclei. Simultaneously, proton-detected and fluorine-detected HMBC spectra have been demonstrated.[115,116] The highly multiplexed and parallelized PANACEA-experiment,[117] which promises 'Molecular Structure from a Single NMR Experiment', also includes a 3D-*J*-HMBC

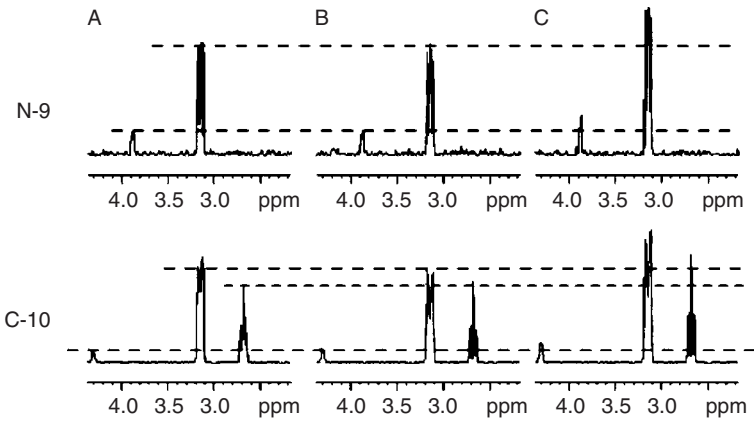

Figure 48 1D row sections taken at C-10 (172 ppm) and N-9 (151 ppm) of Figure 47. (A) individual slices extracted from 2D C- and N-HMBC spectra acquired separately; (B) individual slices extracted from the 2D CN-HMBC spectrum acquired with the same number of scans as each individual HMBC experiment shown in A; (C) Individual slices taken from the 2D CN-HMBC spectra acquired with the same total measuring time as both spectra in A. Reprinted with permission from Ref. 108.

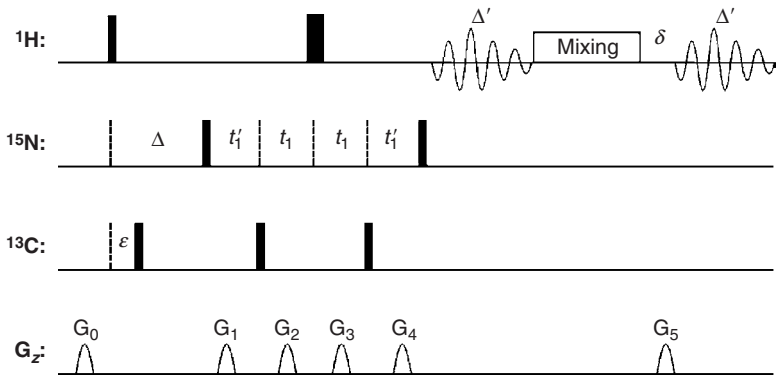

Figure 49 MATS-HMBC experiment, a basic single-pass pulse sequence for simultaneous recording of complementary HMBC spectra. The mixing process could be a COSY or a TOCSY process. Thus, multiple FID signals can be collected separately and stored in different memory blocks. Complete experimental details can be found in the original Ref. 114.

experiment. The verdict about the practical applicability of such parallel methods is however still missing due to the small number of spectrometers that are equipped in this manner.

12.3. Ultrafast HMBC

Ultrafast-NMR (UF-NMR) spectroscopy[118] alone or coupled with other pulse sequence building blocks has shown its capability of delivering virtually any type of multi-dimensional NMR spectrum in a single scan, exploiting spatial

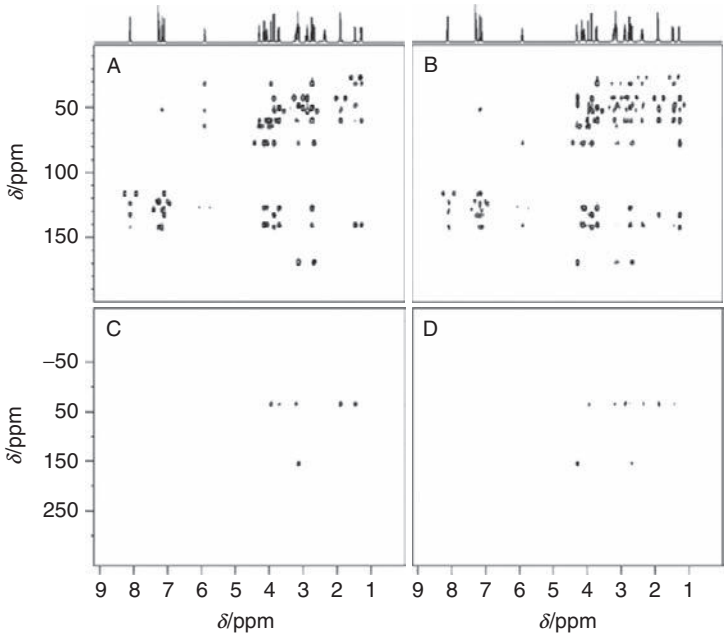

Figure 50 Complementary (A) $^{1}H–^{13}C$ HMBC, (B) $^{1}H–^{13}C$ HMBC-COSY, (C) $^{1}H–^{15}N$ HMBC and (D) $^{1}H–^{15}N$ HMBC-COSY spectra of strychnine obtained simultaneously by the MATS approach. Adopted from Ref. 114. Copyright Wiley-VCH Verlag GmbH & Co. KGaA. Reproduced with permission.

encoding of the indirect domain modulations.[119] Thus, real-time monitoring of dynamic chemical reactions by multi-dimensional NMR can be achieved on a time scale below one second, provided there is sufficient sensitivity.[120] The UF-HMBC experiment provides for real-time observation reactions.[121] It is most useful for reactions involving non-protonated centres such as of ketones or carboxylate-derivatives.

The pulse sequence depicted in Figure 51 consists of a continuous spatial encoding ultrafast HSQC sequence,[122] in which the delay d is set to accommodate long-range couplings.[121] In single-scan multi-dimensional NMR, contrary to traditional approaches, the spectral widths of the spatially encoded and of the directly detected dimensions are not independent of each other. The greater the spectral width in the spatially encoded dimension, the poorer the resolution becomes in the direct domain.[118,123] Furthermore, the spectral width and therefore the resolution in the indirect domain depend on the available gradient strength G_a and the duration T_a of the decoding gradients, which are both limited by practical and fundamental considerations. Because a wide spectral range in the indirect domain needed to be covered to detect the possible intermediates, Herrera et al.[121] monitored two different spectral windows by using two different indirect dimension frequency offsets on alternate transients, while monitoring the progress of the reaction.

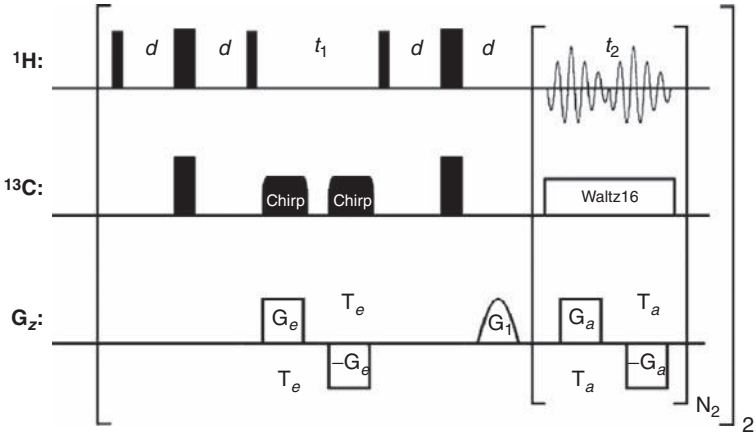

Figure 51 Ultrafast 2D HMBC used to monitor changes on the carbonyl carbon atom.[122]

Using this sequence, a total of 219 UF-HMBC spectra for each spectral window were recorded over a total time of 112 min. Each single spectrum was measured for 5.37 s, and a measurement was repeated every 10 s. Figure 52 shows a series of six representative 2D UF-HMBC spectra recorded (spectra 1–6).

These spectra correspond to the first frequency window studied. The ranges examined were 210–150 ppm for ^{13}C, which covers the carbonyl region and 9–2 ppm for ^{1}H. Spectra were numbered 1–6 (referred to as HMBC-1, etc.). Spectrum HMBC-1 (0.0 min) corresponds to the solution of ketone **1** (bold numerals in this paragraph refer to substances in Figure 52) in deuterated acetonitrile before the addition of Tf_2O. HMBC-1 shows a cross-peak at 198.9/2.56 ppm due to the ^{2}J coupling between the carbonyl carbon and the methyl protons of **1** (red arrow). The addition of Tf_2O produced a small change in the position of the cross-peak from **1**. In HMBC-2, taken 1.02 min after the addition, a new cross-peak appeared at 195.2–3.26 ppm (green arrow). This peak intensified in HMBC-3 (1.53 min), decreased clearly in HMBC-5 (33.2 min) and remained close to the detection limit in HMBC-6 (76.4 min). Simultaneously, the cross-peak (167.4–8.38, blue arrow) that belongs to the pyrimidine **5** increased its intensity (HMBC-3 to HMBC-6). The signal from **1** decreased (HMBC-1 to HMBC-5) and is absent in HMBC-6. The cross-peak emerging in the course of the reaction (green arrows) in Figure 52 belongs to the complex **2** formed from ketone **1** and triflic anhydride. The rise and fall of **2** during the reaction clearly shows its character as an intermediate. Structures of **1** and **2** are similar and therefore produce cross-peaks close to each other. Further mechanistic detail of that reaction can be found in the paper by Herrera et al.[121]

The full potential of single scan multi-dimensional NMR can probably only be realized in combination with dynamic nuclear polarization (DNP). Giraudeau et al.[124] have recently published a first example of a DNP-enhanced ultrafast HMBC experiment.

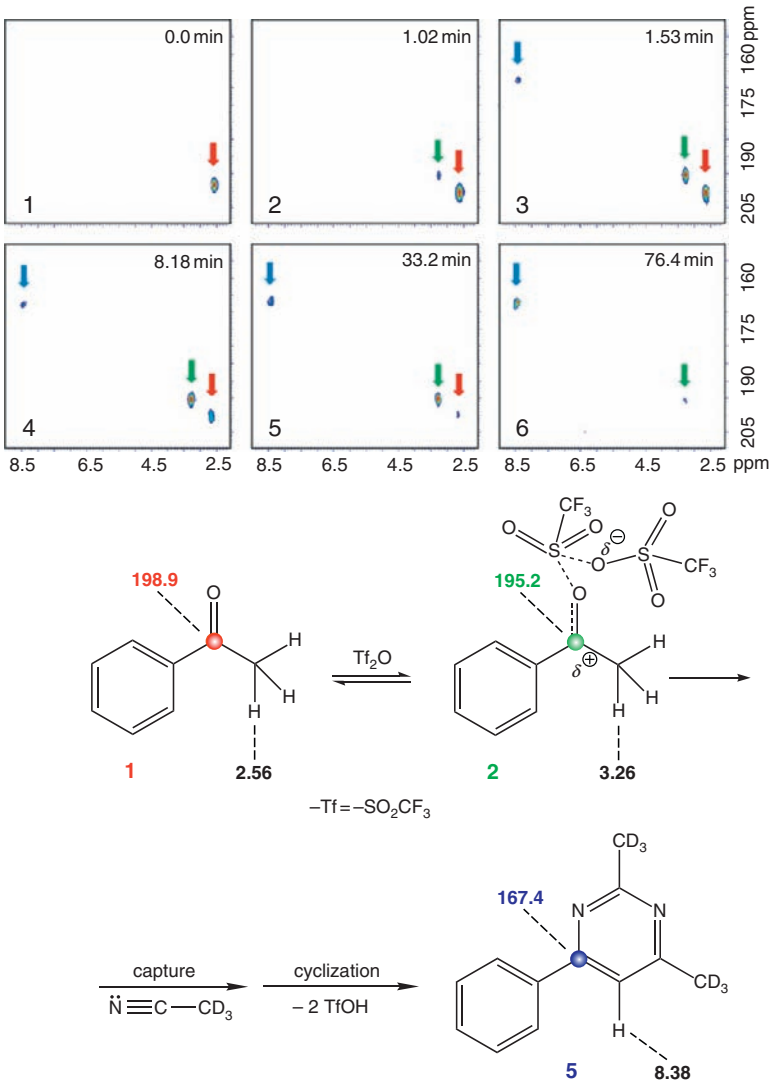

Figure 52 A series of six UF-HMBC experiments (1–6) taken at different times throughout the reaction and shifts from the participating reactant **1**, product **5** and intermediate **2**. Cross peaks colours match the corresponding atoms. Spectra reprinted with permission from Ref. 121. Copyright 2010 American Chemical Society. (For interpretation of the references to colour in this figure legend, the reader is referred to the Web version of this chapter.)

13. COVARIANCE PROCESSING OF HMBC SPECTRA

Covariance spectra resulting, for example, from ^{1}H–^{13}C HMBC experiments, provide information similar to ^{13}C–^{13}C INADEQUATE spectra.[125,126] Blinov et al.[127] have obtained ^{13}C–^{13}C COSY-like spectra using covariance processing of

HSQC-TOCSY experiments, which show connectivities between protonated carbons only. Furthermore, they introduced unsymmetrical indirect covariance processing and used it for the generation of carbon–carbon long-range correlation data from GHSQC and GHMBC spectra as well as HSQC-COSY-like correlations from COSY and HSQC experiments.[128] Zhang et al.[129] have already described the possibility of using the frequency domain response for calculation of the covariance matrix. While they used an INADEQUATE experiment for the source data, in our case, the covariance spectrum is computed from a long-range HSQC experiment after 2D Fourier transform. Both ^{13}C–^{13}C and ^{1}H–^{1}H multi-bond correlation spectra are thus obtained from a single experimental data set. To obtain the ^{1}H–^{1}H multi-bond correlation spectrum, it is necessary to transpose the long-range HSQC data prior to covariance processing. To demonstrate the potential and assess the scope and limitations of this new processing protocol, it was applied to a derivative of emodin (Figure 53).[130]

The experimental data were obtained from a single decoupled long-range HSQC spectrum with decoupling to avoid homonuclear ^{1}H–^{1}H *J*-splittings in ω_1. The raw data were Fourier-transformed in both dimensions and phase-corrected for pure absorption peaks. The dual absorptive quadrant $S(\omega_1, \omega_2)$ of the hypercomplex data matrix is then subjected to the covariance analysis as follows: The covariance matrix $C(\omega_1,\omega_2)$ is derived from the spectrum matrix $S(\omega_1,\omega_2)$ in the following way:

$$C\left(\omega_1, \omega_1^{'}\right) = \int S(\omega_1, \omega_2) S\left(\omega_1^{'}, \omega_2\right) \mathrm{d}\omega_2 = S \cdot S^{\mathrm{T}} \tag{11}$$

In practice, this equation is computed as the discrete sum of products of matrix elements. The elements of $C(\omega_1,\omega_1')$ then contain the covariance coefficients between pairs of rows of the original data set $S(\omega_1,\omega_2)$. To obtain the covariance spectrum, the square root of C is determined as follows: The positive definite Hermitian matrix C can be diagonalized by a unitary matrix U:

$$C = U^{\mathrm{T}} \mathrm{diag}(\lambda_1, \ldots, \lambda_n) U. \tag{12}$$

Here, $\lambda_1,\ldots, \lambda_n$ are the eigenvalues of C. The square root of the matrix C is computed as

$$C^{1/2} = U^{\mathrm{T}} \mathrm{diag}(\sqrt{\lambda_1}, \ldots, \sqrt{\lambda_n}) U. \tag{13}$$

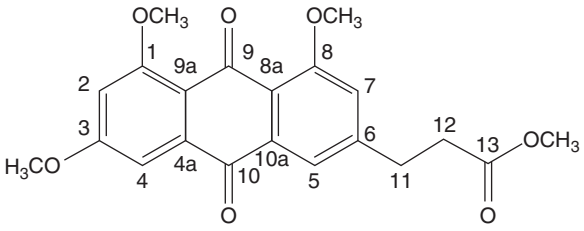

Figure 53 Structure and numbering of compounds of methyl-3-(1,6,8-trimethoxy-9,10-anthraquinon-3-yl)-propionate.

This operation yields the final covariance spectrum $F(\omega_1, \omega_1') = C^{1/2}$, which is symmetric, and thus correlates resonance frequencies sampled during the indirect detection period t_1 with each other via their common proton frequencies in t_2. The analogous procedure with interchanged ω_1 and ω_2 axes (i.e. starting with the transposed HMBC data matrix) can be used to obtain a covariance spectrum of the direct domain resonances $F(\omega_2, \omega_2')$. An example ^{13}C–^{13}C-correlation spectrum derived from a single long-range HSQC with decoupling is shown in Figure 54.

The analogous procedure with interchanged ω_1 and ω_2 axes (i.e. starting with the transposed HMBC data matrix) can be used to obtain a covariance spectrum of the direct domain resonances $F(\omega_2, \omega_2')$. In the resulting covariance spectra, one can see connectivities between spins with common heteronuclear long-range coupling partners, as exemplified in Figure 55.

We have recently used this approach also with a standard decoupled gradient-selected HMQC experiment for the ^{13}C assignment of very sparsely protonated-phenolic compounds and marine pigments.[131]

Asymmetrical covariance processing of multi-dimensional spectra of different nuclei with one common dimension allows for novel highly efficient strategies in structure elucidation; for example, ^{13}C–^{15}N correlation has been achieved by unsymmetrical indirect covariance processing of ^{1}H–^{13}C HSQC and ^{1}H–^{15}N IMPEACH.[132]

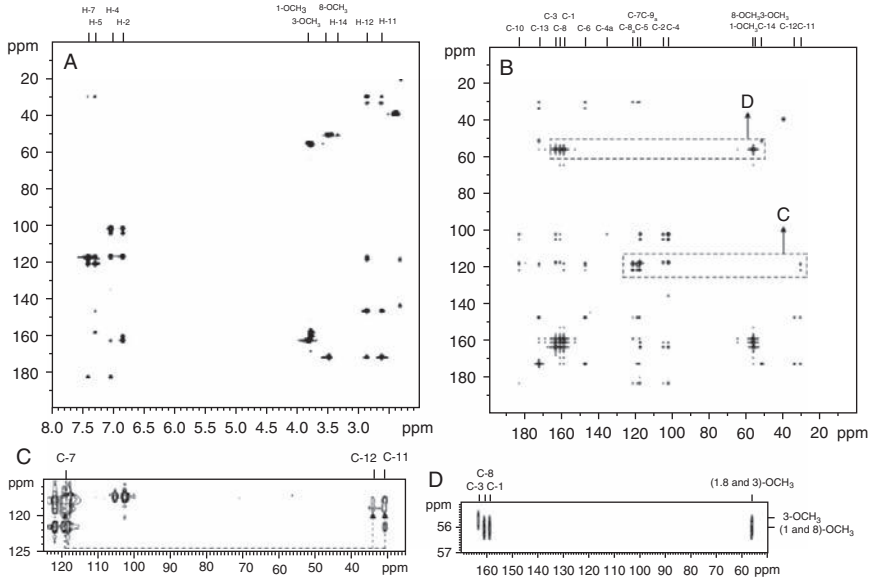

Figure 54 2D NMR spectra of the compound in Figure 53 **1**: (A) ^{1}H–^{13}C HMBC spectrum with ^{1}H-assignments given along the top edge; (B) ^{13}C–^{13}C covariance spectrum derived from A with ^{13}C assignments given along the top edge. (C) Expanded region from (B), containing cross-peaks from $-OCH_3$ to aromatic ^{13}C. (D) Expanded region from (B), containing cross-peaks between the aromatic C-7 (118.9 ppm) and the aliphatic carbons of the $-CH_2COOCH_3$ moiety (CH_3: 33.5 ppm and CH_2: 30.6 ppm). Reprinted with permission of John Wiley & Sons, Inc. from Ref. 130.

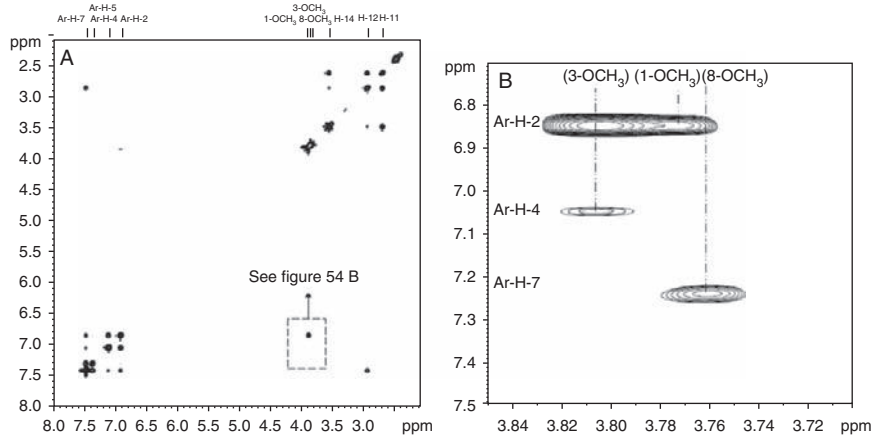

Figure 55 (A) Indirect ^{1}H–^{1}H covariance correlation spectrum derived from the same long-range HSQC spectrum as in Figure 54, with ^{1}H-assignments given on the top edge. The dashed box indicates the location of the enlarged region shown in (B) showing cross-peaks in the aromatic/OCH_3 region of the ^{1}H-HMBC covariance spectrum. Reprinted with permission of John Wiley & Sons, Inc from Ref. 130.

14. OTHER NUCLEI

Besides ^{13}C– or ^{15}N–^{1}H-HMBC, it is also possible to exploit and determine long-range coupling constants between protons and other heteronuclei, for example, ^{19}F,[133,134] ^{29}Si,[135,136] ^{31}P,[137,138] ^{77}Se,[139,140] ^{119}Sn,[141,142] ^{125}Te[139] or ^{187}Os.[143] As shown for tin,[144] this is straightforward by using the original pulse sequence proposed by Bax and Summers[3] and changing the delays to the values determined from the corresponding coupling constants. ^{19}F-^{13}C-CIGAR-HMBC experiments have been found to be a very useful tool for investigating fluorinated polymers.[145] More recently, measurement of long-range ^{1}H–^{29}Si couplings using a gradient-enhanced HMBC pulse sequence (as shown in Figure 4) without LPJF was carried out.[135] It should also be noted that in organometallic compounds ^{13}C–^{1}H, HMBC is a very useful technique to determine ^{1}H-metal and ^{13}C-metal coupling constants from the splitting patterns, for example, in tin complexes of crown ethers.[146]

In situations where routine application of multiple HMBC spectra with different nuclei are required (e.g. ^{19}F–^{13}C and ^{1}H–^{13}C), the newly introduced parallel acquisition techniques mentioned above may prove particularly useful.[116]

To conclude this short chapter, we wish to draw the attention on applications of the HMBC experiments for the determination of more unusual long-range coupling constants between a heteronucleus to other heteronuclei like $^{2,3}J$ (^{29}Si–^{13}C),[136,147–149] $^{2,3}J$(^{119}Sn–^{29}Si),[141] ^{2}J(^{207}Pb–^{29}Si)[150,151] or $^{2,3,n}J$(^{207}Pb–^{119}Sn, ^{31}P, ^{77}Se, ^{183}W, ^{195}Pt).[152]

Further examples of applications involving metal nuclei can be found in a recent review in this series.[153]

15. CONCLUSION AND OUTLOOK

From the basic HMBC technique, derivative pulse sequences have been developed and are still being developed incorporating many of the building blocks developed for other pulsed NMR applications. HMBC has become a pivotal and indispensable tool in the molecular structure analysis by NMR techniques for research and routine applications in academic labs and industry. Among the variety of NMR pulse sequences used today, the HMBC technique is a key tool for resonance assignment and structure elucidation, especially for compounds with non-protonated carbon or nitrogen. Currently, one can witness an increasing number of developments towards time-saving strategies in NMR, using approaches like multiple receivers,[115,116] multiplexed coherence transfer pathways[103] and non-uniform sampling.[94] Ultimately, these developments will lead to more efficient HMBC-type NMR experiments allowing users to utilize the NMR spectrometers more economically.

In addition to these 'economical' improvements, the introduction of dynamic nuclear polarization (DNP)[154–157] as a means of enhancing NMR-signals by orders of magnitude in concert with ultrafast NMR techniques, as introduced by the groups of Frydman[158,159] and Bodenhausen,[160] will not only speed up structure elucidation but also allow the real-time analysis of chemical reaction intermediates, as shown in very recent publications. A particularly elegant way of parallel encoding and ultrafast acquisition enhanced by DNP has been demonstrated by Giraudeau et al.,[124] which is considered a promising new instrument for improving the understanding of the pathways of chemical reactions involving non-protonated carbon or nitrogen atoms in diverse application areas like inorganic, organic and biological chemistry.

REFERENCES

1. G. E. Martin and A. J. Williams, Long-range $^{1}H–^{15}N$ heteronuclear shift correlation. *in*: Annual Reports on NMR Spectroscopy, (G. A. Webb ed.), **Vol. 55,** Academic Press, Oxford, 2005, p. 1.
2. L. Müller, *J. Am. Chem. Soc.*, 1979, **101,** 4481.
3. A. Bax and M. F. Summers, *J. Am. Chem. Soc.*, 1986, **108,** 2093.
4. G. E. Martin and R. C. Crouch, *J. Nat. Prod.*, 1991, **54,** 1.
5. R. Araya-Maturana, T. Delgado-Castro, W. Cardona and B. E. Weiss-López, *Curr. Org. Chem.*, 2001, **5,** 253.
6. S. Ilin, C. Bosques, C. Turner and H. Schwalbe, *Angew. Chem. Int. Ed.*, 2003, **42,** 1394.
7. S. Bouguet-Bonnet, S. Leclerc, P. Mutzenhardt and D. Canet, *J. Magn. Reson. A*, 2005, **173,** 29.
8. A. Bax, R. H. Griffey and B. L. Hawkins, *J. Magn. Reson.*, 1983, **55,** 301.
9. G. Bodenhausen and D. J. Ruben, *Chem. Phys. Lett.*, 1980, **69,** 185.
10. R. T. Williamson, B. L. Marquez, W. H. Gerwick and K. Köver, *Magn. Reson. Chem.*, 2000, **38,** 265.
11. P. Güntert, N. Schaefer, G. Otting and K. Wüthrich, *J. Magn. Reson. A*, 1993, **101,** 103.
12. P. Güntert, *Int. J. Quantum Chem.*, 2006, **106,** 344.
13. M. Wu, T. Okino, L. M. Nogel, B. L. Marquez, R. T. Williamson, N. Sitachitta, F. W. Berman, T. F. Murray, K. Mcgough, R. Jacobs, K. Colsen T. Asano, *et al.*, *J. Am. Chem. Soc.*, 2000, **122,** 12041.
14. A. M. Gronenborn and G. M. Clore, *Curr. Opin. Chem. Biol.*, 1998, **2,** 564.
15. T. D. W. Claridge and I. Pérez-Victoria, *Org. Biomol. Chem.*, 2003, **1,** 3632.
16. H. Kogler, O. W. Sørensen, G. Bodenhausen and R. R. Ernst, *J. Magn. Reson.*, 1983, **55,** 157.

17. N. T. Nyberg and O. W. Sørensen, *Magn. Reson. Chem.*, 2006, **44,** 451.
18. K. Furihata and H. Seto, *Tetrahedron Lett.*, 1995, **36,** 2817.
19. H. Seto, *Pure Appl. Chem.*, 1999, **71,** 1133.
20. T. Fujiwara, T. Anai, N. Kurihara and K. Nagayama, *J. Magn. Reson. A*, 1993, **104,** 103.
21. J. R. Garbow, D. P. Weitekamp and A. Pines, *Chem. Phys. Lett.*, 1982, **93,** 504.
22. A. Bax and S. Subramanian, *J. Magn. Reson.*, 1986, **67,** 565.
23. W. Willker, D. Leibfritz, R. Kerssebaum and W. Bermel, *Magn. Reson. Chem.*, 1993, **31,** 287.
24. J. Keeler, R. T. Clowes, A. L. Davis and E. D. Laue, *Methods Enzymol.*, 1994, **239,** 145.
25. R. E. Hurd and B. K. John, *J. Magn. Reson.*, 1991, **91,** 648.
26. W. F. Reynolds and R. G. Enriquez, *Magn. Reson. Chem.*, 2001, **39,** 531.
27. S. C. Wimperis and R. Freeman, *J. Magn. Reson.*, 1984, **58,** 348.
28. N. E. Jacobsen, *NMR Spectroscopy Explained: Simplified Theory, Applications and Examples for Organic Chemistry and Structural Biology*. John Wiley & Sons, Inc., Hoboken, NJ, 2007 (p. 510, Fig. 11.21.).
29. G. Martin and A. Zektzer, Phase sensitive HMBC with BIRD filter. *In* 2D NMR Methods for Establishing Molecular Connectivity VCH, Weinheim, 1988.
30. T. Parella, F. Sanchez-Ferrando and A. Virgili, *J. Magn. Reson. A*, 1995, **112,** 241.
31. A. Meissner and O. W. Sørensen, *Magn. Reson. Chem.*, 2001, **39,** 49.
32. B. L. Marquez, W. H. Gerwick and R. T. Williamson, *Magn. Reson. Chem.*, 2001, **39,** 499.
33. R. Burger, C. Schorn and P. Bigler, *Magn. Reson. Chem.*, 2000, **38,** 963.
34. P. Würtz, P. Permi, N. C. Nielsen and O. W. Sørensen, *J. Magn. Reson.*, 2008, **194,** 89.
35. A. Meissner and O. W. Sørensen, *Magn. Reson. Chem.*, 2000, **38,** 981.
36. S. Meier, B. O. Petersen, J.Ø. Duus and O. W. Sørensen, *Carbohydr. Res.*, 2009, **344,** 2274.
37. S. Meier, A. J. Benie, J.Ø. Duus and O. W. Sørensen, *Chemphyschem*, 2009, **10,** 893.
38. L. Poppe and H. Van Halbeek, *J. Magn. Reson. (1969)*, 1991, **92,** 636.
39. S. Mattila, A. M. P. Koskinen and G. Otting, *J. Magn. Reson. B*, 1995, **109,** 326.
40. R. Marek, L. Kralik and V. Sklenar, *Tetrahedron Lett.*, 1997, **38,** 665.
41. L. E. Kay, T. Keifer and T. Saaerinen, *J. Am. Chem. Soc.*, 1992, **114,** 10663.
42. J. H. Prestegard and Y. Kim, *J. Magn. Reson.*, 1989, **84,** 9.
43. P. J. Proteau, W. H. Gerwick, F. Garcia-Pichel and R. Castenholz, *Experientia*, 1993, **49,** 825.
44. S. Heikkinen and I. Kilpelainen, *J. Magn. Reson.*, 1999, **137,** 93.
45. D. Bruhwiler and G. Wagner, *J. Magn. Reson.*, 1986, **69,** 546.
46. B. K. John, D. Plant and R. E. Hurd, *J. Magn. Reson.*, 1992, **101,** 113.
47. J. Keeler, D. Neuhaus and J. J. Titman, *Chem. Phys. Lett.*, 1988, **146,** 545.
48. D. Stresinkova and N. Müller, *J. Magn. Reson. A*, 1996, **120,** 105.
49. P. Nolis, M. Perez and T. Parella, *Magn. Reson. Chem.*, 2006, **44,** 1031.
50. C. Schäffer, N. Müller, R. Christian, M. Graninger, T. Wugeditsch, A. Scheberl and P. Messner, Glycobiology 1999, **9,** 407; and C. Steindl, C. Schäffer, T. Wugetitsch, M. Graninger, I. Matecko, N. Müller, and P. Messner, *Biochem. J.*, 2002, **368,** 483.
51. V. Lacerda, G. V. J. D. Silva, M. G. Constantino, C. F. Tormena, R. Williamson and B. L. Marquez, *Magn. Reson. Chem.*, 2006, **44,** 95.
52. K. Kobzar and B. Luy, *J. Magn. Reson.*, 2007, **186,** 131.
53. R. Wagner and S. Berger, *Magn. Reson. Chem.*, 1998, **36,** 44.
54. K. Furihata and H. Seto, *Tetrahedron Lett.*, 1996, **37,** 8901.
55. K. H. Sze, X. Z. Yan, X. M. Kong, C. T. Che and G. Zhu, *Tetrahedron Lett.*, 1999, **40,** 5587.
56. S. Sheng and H. V. Halbeek, *J. Magn. Reson.*, 1998, **130,** 296.
57. C. E. Hadden, G. E. Martin and V. V. Krishnamurthy, *J. Magn. Reson.*, 1999, **140,** 274.
58. C. E. Hadden, G. E. Martin and V. V. Krishnamurthy, *Magn. Reson. Chem.*, 2000, **38,** 143.
59. G. E. Martin, C. E. Hadden, R. C. Crouch and V. V. Krishnamurthy, *Magn. Reson. Chem.*, 1999, **37,** 517.
60. J. Furrer, *Magn. Reson. Chem.*, 2006, **44,** 845.
61. D. Uhrin, T. Lipatj and K. E. Köver, *J. Magn. Reson. A*, 41.
62. S. Wimperis and G. Bodenhausen, *J. Magn. Reson.*, 1986, **69,** 264.
63. N. Müller and V. V. Lapachev, *Monatsh. Chem.*, 1987, **118,** 1201.
64. M. H. Levitt, *Prog. Nucl. Magn. Reson. Spectrosc.*, 1985, **18,** 61.
65. A. M. Torres, W. A. Bubb and P. W. Kuchel, *J. Magn. Reson.*, 2002, **156,** 249.

66. A. M. Torres, W. A. Bubb, D. J. Philp and P. W. Kuchel, *J. Magn. Reson.*, 2008, **194,** 81.
67. M. H. Levitt, *J. Magn. Reson.*, 1982, **48,** 234.
68. R. Freeman, S. P. Kempsell and M. H. Levitt, *J. Magn. Reson.*, 1980, **38,** 453.
69. O. W. Sørensen, J. C. Madsen, N. C. Nielsen, H. Bildsø and H. J. Jakobsen, *J. Magn. Reson.*, 1988, **77,** 170.
70. N. C. Nielsen, H. Bildsø, H. J. Jakobsen and O. W. Sørensen, *J. Magn. Reson.*, 1989, **85,** 359.
71. H. Kessler, C. Griesinger, J. Lautz, A. Mueller, W. F. V. Gunsteren and H. J. C. Berendsen, *J. Am. Chem. Soc.*, 1988, **110,** 3393.
72. P. Schmieder, M. Kurz and H. Kessler, *J. Biomol. NMR*, 1991, **1,** 403.
73. G. E. Martin, Qualitative and quantitative exploitation of heteronuclear coupling constants. *in*: Annual Reports on NMR Spectroscopy, (G. A. Webb ed.), **Vol. 46,** Academic Press, Oxford, 2002, p. 37.
74. R. Riccio, G. Bifulco, P. Cimino, C. Bassarello and L. Gomez-Paloma, *Pure Appl. Chem.*, 2003, **75,** 295.
75. K. Furihata and H. Seto, *Tetrahedron Lett.*, 1999, **40,** 6271.
76. G. Bodenhausen and R. R. Ernst, *J. Magn. Reson.*, 1982, **45,** 367.
77. G. Bodenhausen and R. R. Ernst, *J. Am. Chem. Soc.*, 1982, **104,** 1304.
78. K. Furihata, M. Tashiro and H. Seto, *Magn. Reson. Chem.*, 2009, **47,** 814.
79. K. Furihata and H. Seto, *Tetrahedron Lett.*, 1998, **39,** 7337.
80. R. T. Williamson, B. L. Marquez, W. H. Gerwick, G. E. Martin and V. V. Krishnamurthy, *Magn. Reson. Chem.*, 2001, **39,** 127.
81. M. Matsumori, D. Kaneno, M. Murata, H. Nakamura and K. Tachibana, *J. Org. Chem.*, 1999, **64,** 866.
82. J. Furrer, *Chem. Commun.*, 2010, **46,** 3396.
83. E. Kupce and R. Freeman, *Magn. Reson. Chem.*, 2007, **45,** 2.
84. D. O. Cicero, G. Barbato and R. Bazzo, *J. Magn. Reson.*, 2001, **148,** 209.
85. C. Thiele, *Concepts Magn. Reson. A*, 2007, **30A,** 65.
86. J. J. Titman, D. Neuhaus and J. Keeler, *J. Magn. Reson. (1969)*, 1989, **85,** 111.
87. L. Verdier, P. Sakhaii, M. Zweckstetter and C. Griesinger, *J. Magn. Reson.*, 2003, **163,** 353.
88. S. J. F. Vincent and C. Zwahlen, *J. Am. Chem. Soc.*, 2002, **122,** 8307.
89. T. Schulte-Herbrüggen, A. Meissner, A. Papanikos, M. Meldal and O. W. Sørensen, *J. Magn. Reson.*, 2002, **156,** 282.
90. A. J. Benie and O. W. Sørensen, *Magn. Reson. Chem.*, 2006, **44,** 739.
91. A. J. Shaka, P. B. Barker and R. Freeman, *J. Magn. Reson.*, 1985, **64,** 547.
92. V. V. Krishnamurthy, D. J. Russell, C. E. Hadden and G. E. Martin, *J. Magn. Res.*, 2000, **146,** 232.
93. N. T. Nyberg, J.Ø. Duus and O. W. Sørensen, *J. Am. Chem. Soc.*, 2005, **127,** 6154.
94. V. Y. Orekhov, I. V. Ibraghimov and M. Billeter, *J. Biomol. NMR*, 2001, **20,** 49.
95. V. Jaravine, I. Ibraghimov and V. Y. Orekhov, *Nat. Meth.*, 2006, **3,** 605.
96. M. Mobli, M. Maciejewski, M. Gryk and J. Hoch, *J. Biomol. NMR*, 2007, **39,** 133.
97. K. Kazimierczuk, W. Kozminski and I. Zhukov, *J. Magn. Reson.*, 2006, **179,** 323.
98. M. Misiak and W. Koźmiński, *Magn. Reson. Chem.*, 2009, **47,** 825.
99. M. Misiak and W. Koźmiński, *Magn. Reson. Chem.*, 2007, **45,** 171.
100. M. Misiak, W. Koźminski, M. Kwasiborska, J. Wojcik, E. Ciepichal and E. Swiezewska, *Magn. Reson. Chem.*, 2009, **47,** 825.
101. D. Uhrín, *J. Magn. Reson.*, 2002, **159,** 145.
102. R. Burger, C. Schorn and P. Bigler, *J. Magn. Reson.*, 2001, **148,** 88.
103. T. Parella and P. Nolis, *Concepts Magn. Reson. A*, 2010, **36A,** 1.
104. S. M. Pascal, D. R. Muhandiram, T. Yamazaki, J. Forman-Kay and L. E. Kay, *J. Magn. Reson. B*, 1994, **103,** 197.
105. D. P. Frueh, D. A. Volsburg, C. T. Walsh and G. Wagner, *J. Biomol. NMR*, 2006, **34,** 31.
106. D. P. Frueh, H. Arthanari and G. Wagner, *J. Biomol. NMR*, 2005, **33,** 187.
107. C. Guo, D. Zhang and V. Tugarinov, *J. Am. Chem. Soc.*, 2008, **130,** 10872.
108. M. Perez-Trujillo, P. Nolis and T. Parella, *Org. Lett.*, 2007, **9,** 29.
109. N. Ivchenko, C. E. Hughes and M. H. Levitt, *J. Magn. Reson.*, 2003, **160,** 52.
110. O. W. Sørensen, *J. Magn. Reson.*, 1990, **89,** 210.

111. J. Schlagnitweit, G. Zuckerstätter and N. Müller, *Magn. Reson. Chem.*, 2010, **48,** 1.
112. A. Z. Gurevich, I. L. Barsukov, A. S. Arseniev and V. F. Bystrov, *J. Magn. Reson.*, 1984, **56,** 471.
113. M. Perez-Trujillo, P. Nolis, W. Bermel and T. Parella, *Magn. Reson. Chem.*, 2007, **45,** 325.
114. P. Nolis, M. Perez-Trujillo and T. Parella, Multiple FID acquisition of complementary HMBC data. *Angew. Chem. Int. Ed.*, 2007, **46,** 7495–7497.
115. E. Kupce and R. Freeman, *J. Am. Chem. Soc.*, 2006, **128,** 9606.
116. E. Kupce, S. Cheatham and R. Freeman, *Magn. Reson. Chem.*, 2007, **45,** 378.
117. E. Kupce and R. Freeman, *J. Am. Chem. Soc.*, 2008, **130,** 10788.
118. M. Mishkovsky and L. Frydman, *Annu. Rev. Phys. Chem.*, 2009, **60,** 429.
119. A. Tal, B. Shapira and L. Frydman, *Angew. Chem. Int. Ed.*, 2009, **48,** 2732.
120. M. Gal, M. Mishkovsky and L. Frydman, *J. Am. Chem. Soc.*, 2006, **128,** 951.
121. A. Herrera, E. Fernandez-Valle, E. M. Gutierrez, R. Martınez-Alvarez, D. Molero, Z. D. Pardo and E. Saez, *Org. Lett.*, 2010, **12,** 144.
122. Y. Shrot, B. Shapira and L. Frydman, *J. Magn. Reson.*, 2004, **171,** 162.
123. L. Frydman, A. Lupulescu and T. Scherf, *J. Am. Chem. Soc.*, 2003, **125,** 9204.
124. P. Giraudeau, Y. Shrot and L. Frydman, *J. Am. Chem. Soc.*, 2009, **131,** 13902.
125. J. C. Hus and R. Brüschweiler, *J. Chem. Phys.*, 2002, **117,** 1166.
126. F. Zhang and R. Brüschweiler, *J. Am. Chem. Soc.*, 2004, **126,** 13180.
127. K. A. Blinov, N. I. Larin, A. J. Williams, M. Zell and G. E. Martin, *Magn. Reson. Chem.*, 2006, **44,** 107.
128. K. A. Blinov, N. I. Larin, A. J. Williams, K. A. Mills and G. E. Martin, *J. Heterocycl. Chem.*, 2006, **43,** 163.
129. F. Zhang, N. Trbovic, J. Wang and R. Brüschweiler, *J. Magn. Reson.*, 2005, **174,** 219.
130. W. Schoefberger, V. Smrecki, D. Vikic-Topic and N. Müller, *Magn. Reson. Chem.*, 2007, **45,** 583.
131. J. Mastelic, I. Jerkovic, I. Blazevic, M. Poljak-Blazi, S. Borovic, I. Ivancic-Bace, V. Smrecki, N. Zarkovic, K. Brcic-Kostic, D. Vikic-Topic, and N. Müller, *J. Agric. Food Chem.* **2008,** 56, 3989; and K. Wolkenstein, W. Schoefberger, and N. Müller T. *Oji J. Nat. Prod.*, 2009, **72,** 2036.
132. G. E. Martin, B. D. Hilton, P. A. Irish, K. A. Blinov and A. J. Williams, *J. Heterocycl. Chem.*, 2007, **44,** 1219.
133. M. Takasak, K. Kimura, K. Kawaguchi, A. Abe and G. Katagiri, *Macromolecules*, 2005, **38,** 6031.
134. M. Hennig, M. L. Munzarová, W. Bermel, L. G. Scott, V. Sklenár and J. R. Williamson, *J. Am. Chem. Soc.*, 2006, **128,** 5851.
135. S. Provera, S. Davalli, G. H. Raza, S. Contini and C. Marchioro, *Magn. Reson. Chem.*, 2001, **39,** 38.
136. B. Wrackmeyer and H. Oehme, *Z. Naturforsch. B*, 2001, **56,** 947.
137. M. Raab, G. Schick, R. Fondermann, M. Dolg, W. Henze, U. Weynand, R. M. Gschwind, K. Fischer, M. Schmidt and E. Niecke, *Angew. Chem.*, 2006, **118,** 3154.
138. R. M. Gschwind, M. Armbrüster and I. Z. Zubrzycki, *J. Am. Chem. Soc.*, 2004, **126,** 10228.
139. A. Levy, U. P. Biedermann, S. Cohen and I. Agranat, *Phosphorus Sulfur Silicon Rel. Elem.*, 1998, **136–138,** 139.
140. B. W. Tattershall and E. L. Sandham, *J. Chem. Soc. Dalton Trans.*, 2001, 1834.
141. B. Wrackmeyer, M. Vosteen and W. Storch, *J. Mol. Struct.*, 2002, **602–603,** 177.
142. M. Biesemans, J. C. Martins, R. Willem, A. Lycka, A. Ruzicka and J. Holecek, *Magn. Reson. Chem.*, 2002, **40,** 65.
143. R. Benn, E. Joussen, H. Lehmkuhl, F. Lopez Ortiz and A. Rufinska, *J. Am. Chem. Soc.*, 1989, **111,** 8754.
144. F. Kayser, M. Biesemans, M. Gielen and R. Willem, *J. Magn. Reson. A*, 1993, **102,** 249.
145. M. Takasaki, K. Kimura, K. Kawaguchi, A. Abe and G. Katagiri, *Macromolecules*, 2005, **38,** 6031.
146. M. Amini, A. Azadmher, H. Bijanzadeh and N. Hadipour, *J. Incl. Phenom. Macrocycl. Chem.*, 2006, **54,** 77.
147. R. K. Harris and C. T. G. Knight, *J. Chem. Soc. Faraday Trans.*, 1983, **79,** 1525.
148. H. B. Yokelson, A. J. Millevolte, G. R. Gillette and R. West, *J. Am. Chem. Soc.*, 1987, **109,** 6865.
149. E. Liepins, I. Birgele, E. Lukevics, E. T. Bogoradovsky and V. S. Zavgorodny, *J. Organomet. Chem.*, 1990, **393,** 11.
150. B. Wrackmeyer, K. Horchler and H. Zhou, *Spectrochim. Acta*, 1990, **46A,** 809.
151. B. Wrackmeyer and H. Zhou, *Spectrochim. Acta A Mol. Spectrosc.*, 1991, **47,** 849.

152. B. Wrackmeyer, Application of 207Pb NMR parameters. *in*: Annual Reports on NMR Spectroscopy, (G. A. Webb, ed.), **Vol. 47,** Academic Press, Oxford, 2002, p. 1.
153. J. A. Iggo, J. Liu and G. Overend, The indirect detection of metal nuclei by correlation spectroscopy (HSQC and HMQC). *in*: Annual Reports on NMR Spectroscopy, (G. A. Webb ed.), **Vol. 63,** Academic Press, Oxford, 2008, p. 179.
154. W. Müller-Warmuth and K. Meise-Gresch, *Adv. Magn. Reson.*, 1983, **11,** 1.
155. D. A. Hall, *Science*, 1997, **276,** 930.
156. C.-G. Joo, K.-N. Hu, J. A. Bryant and R. G. Griffin, *J. Am. Chem. Soc.*, 2006, **128,** 9428.
157. L. R. Becerra, *J. Magn. Reson. A*, 1995, **117,** 28.
158. M. Mishkovsky and L. Frydman, *Chemphyschem*, 2008, **9,** 2340.
159. L. Frydman and D. Blazina, *Nat. Phys.*, 2007, **3,** 415.
160. P. Pelupessy, E. Rennella and G. Bodenhausen, *Science*, 2009, **324,** 1693.

CHAPTER 2

Two-Dimensional Higher Quantum Correlation and Resolved Techniques for the Analyses of Complex ^{1}H NMR Spectra of Scalar-Coupled Spins

N. Suryaprakash

Contents

NMR Research Centre, Indian Institute of Science, Bangalore, India

Annual Reports on NMR Spectroscopy, Volume 72
ISSN 0066-4103, DOI: 10.1016/B978-0-12-385857-3.00002-5

© 2011 Elsevier Ltd.
All rights reserved.

Abstract The number of permitted single quantum (SQ) transitions in the ^{1}H NMR spectra of scalar-coupled spins increases rapidly with the increase in the number of interacting spins, thereby posing a challenge for their analyses. The numerous two-dimensional methodologies are available in the knowledge bank of NMR for the determination of spectral parameters and to obtain information on the molecular structure and conformation. The indirect detection of forbidden higher quantum NMR transitions, that is, other than those allowed by the normal selection rules for the detection of SQ frequencies, is one of the significant steps in this direction. The detection of higher quantum transitions of coupled spin 1/2 nuclei has been extensively employed for the study of molecules oriented in strong and weak aligning media, not only to simplify the analyses of complex NMR spectra but also to determine the molecular geometries. In this chapter, we discuss our recent studies on the development and applications of higher quantum correlation and resolved techniques for the analyses of complex ^{1}H NMR spectra of scalar-coupled spins. The behaviour of magnetization in the spin-selected and non-selected higher quantum is discussed using both product operator and polarization operator approaches for a weakly coupled AMX spin system. Subsequently, applications of these methodologies for the analyses of complex ^{1}H NMR spectra have been discussed with specific examples.

Key Words: Scalar couplings, Spectral simplification, Spin system filtering, Discerning of overlapped transitions, Signs of the couplings, Multiple quantum, Double quantum *J*-resolved, Spin-selective excitation, 2-Fluoropyridine, Halogenated benzanilides.

1. INTRODUCTION

The NMR spectroscopy is an indispensable technique for the elucidation of molecular structure and conformation.[1–6] The usefulness of the technique arises from the fact that the nucleus is very sensitive to any microscopic perturbation of

the electronic distribution around it. The significant shift in the resonance frequencies arising due to any such perturbations can be precisely detected. The detected frequencies and the intensities in the high-resolution single quantum (SQ) NMR spectra of diamagnetic materials depend on various interactions experienced by the spins such as chemical shifts (δ_i), dipolar couplings (D_{ij}), scalar couplings (J_{ij}) and quadrupolar couplings (Q_i). While dealing with the NMR spectra of spin 1/2 nuclei in solution state, the information on the molecular structure and conformation is generally obtained using chemical shifts and scalar couplings, whereas the relaxation parameters provide information on the dynamics of the molecules. For N non-equivalent spin 1/2 interacting nuclei, there are ${}^{2N}C_{N-1}$ theoretically possible transitions from which N chemical shifts and $N^*(N-1)/2$ scalar couplings are required to be determined. The number of spectral parameters required to be derived and the detected transitions depend on the chemical or magnetic equivalence of the nuclear spins in the molecules. The analysis of such spectra could be either first order or second order depending on whether the spin system is strongly or weakly coupled. The definition of strong and weak coupling is governed by the ratio of the spin–spin coupling to that of the chemical shift difference between the coupled spins. In weakly coupled spin systems, where the chemical shift separation between the interacting spins is several orders of magnitude larger than the spin–spin couplings, the spectra are first order and the simple and straightforward analyses give chemical shifts and spin–spin couplings.

For the measurement of homo- and heteroscalar couplings in small organic molecules or biomolecules, there are several reported methodologies, viz. *J*-resolved,[7–9] E-COSY type,[10–16] two-dimensional (2D) and quantitative *J* correlation[17–21] experiments, polarization-based resolved and correlation experiments[22–28] with several modified sequences for suppression of artefacts and to enhance sensitivity.[29–35] The derived spectral parameters, especially three bond J_{ij}s, are utilized for obtaining the dihedral angle restraints.[1–6] For the determination of the magnitudes and relative signs of the coupling constants, there are several techniques such as spin tickling,[36] double and triple resonance,[37] Z-COSY[38] and soft-COSY.[39] The phase-sensitive and spin-state-selective double quantum (DQ) and zero quantum (ZQ) coherence[40–42] studies, where the couplings evolve as sums and differences, respectively, also provide the magnitudes and signs of scalar couplings.

As the number of interacting spins in the molecule increases, there is also a stringent requirement on the spectral resolution, implying that the extraction of such information from very complex NMR spectra is always a challenging task. Usually detected SQ NMR transitions are highly redundant.[1] As an example in a network of six coupled spins, theoretically there are 792 allowed transitions from which only 6 chemical shifts and 15 scalar couplings are to be derived. All the transitions are not necessary to derive the spectral information. One of the ways of simplifying the spectrum is to detect few transitions that are sufficient to yield the desired information. This is achieved by the indirect detection of multiple quantum (MQ) NMR frequencies which are generally forbidden according to the well-known selection rules for NMR transitions. This reduces the redundancy in the

number of SQ transitions, thereby simplifying the analyses of complex NMR spectra. This method has found excellent applications in the study of structures of molecules oriented in liquid crystalline media.[43–48] In the isotropic solutions, the network of scalar-coupled spins is usually smaller and the MQ technique finds little use as far as the spectral simplification is concerned, although there are reported studies on spin topology filtering.[49,50] Nevertheless, the concept of MQ is employed in several multidimensional experiments such as INADEQUATE, where the correlation between coupled natural abundant ^{13}C spins is detected. For deeper discussion on the principles and applications of MQ NMR techniques, readers are referred to excellent reviews.[51,52]

In this chapter, our recent studies utilizing spin-selective and non-selective MQ correlation and resolved techniques are described. These methodologies when applied to scalar-coupled homo- and heteronuclear spin systems not only break the spectral complexity but also provide the relative signs and magnitudes of the couplings. After a very brief introduction to MQ, spin-state selection, pulse sequences for spin-selective and non-selective excitation and the application of these methodologies are discussed with specific examples.

1.1. Multiple quantum NMR

MQ coherence is a coherent superposition of energy states for which the total spin quantum number is anything other than ± 1. The allowed ZQ, SQ and DQ transitions for a weakly coupled two spin system are pictorially depicted in Figure 1. The ZQ and DQ excitation and detection fall under the category of MQ experiments. The spins that undergo transitions between the two states are referred to as *active spins* and all the remaining spins are said to be *passive*. The nature of the coherence depends both on the order of the quantum and on the properties of active spins and their nature of interactions with the passive spins. The collection of all the active spins can be construed as a super spin and the remaining passive spins as spectator spins. The active and passive spins in a group of coupled spins for single and multiple quantum excitations are pictorially depicted in Figure 2.

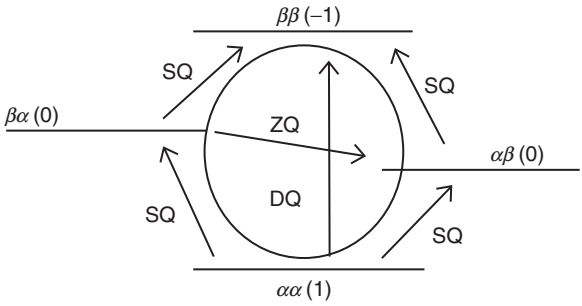

Figure 1 The energy level diagram for an AX spin system and the allowed zero quantum (ZQ), single quantum (SQ) and double quantum (DQ) transitions. The ZQ and DQ transitions represented in the circle are forbidden according to the selection rules of NMR transitions and are indirectly detected.

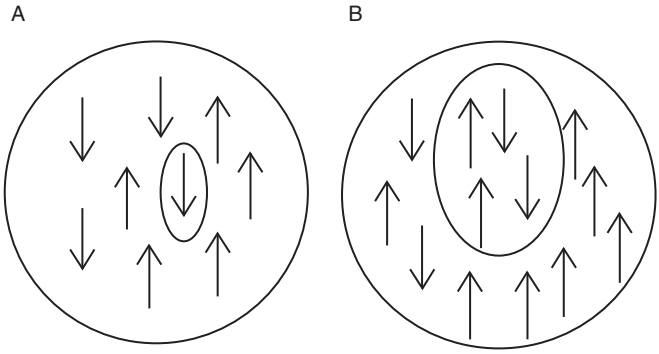

Figure 2 (A) The cartoon representation of an *N* coupled spin system. When a single spin represented in an inner circle is allowed to flip, the single quantum transitions are detected. The single spin is referred as active spin and the remaining ones are passive. (B) The schematic representation of higher quantum. In the inner circle, there is more number of spins compared to that in (A). When all these spins are allowed to spin simultaneously, multiple quantum coherence is detected. The group of active spins is called a super spin. As the number of active spins increases, correspondingly the number of spectator spins available for interaction with active spins and thereby the scalar fields get reduced.

In SQ, any one of the spins is flipped in the presence of scalar fields of the spectator spins (Figure 2A). Then the scalar fields from all the remaining spins are available for this single spin. As the size of the super spin increases, the number of spectator spins decreases and consequently the available scalar fields for interaction with active spins are reduced (Figure 2B). Hence, the multiplet pattern gets simplified at higher quantum. The number of allowed transitions for ZQ and MQ of N interacting spin 1/2 nuclei is given by

$$Z_0 = \frac{1}{2}\left[{}^{2N}C_N - 2N\right], \tag{1}$$

$$Z_m = \frac{2N!}{(N-m)!(N+m)!}, \tag{2}$$

where Z_0 refers to ZQ and Z_m refers to m^{th} quanta for non-zero m. Thus, for N non-equivalent spin 1/2 system, $N=m$ gives the highest quantum and it pertains to a situation wherein all the spins are participating spins and there will not be any spectator spins. This is a situation where all the N spins flip simultaneously from the spin state $|\alpha\rangle$ to spin state $|\beta\rangle$ or vice versa. This implies that there is no scalar field to influence the spectrum. According to Equation (2) this results in a single transition. Therefore, the highest quantum coherence is a situation where all the spins are active and results in flipping at their respective chemical shift positions. The single transition of the highest quantum thus resonates at the sum of their chemical shifts.

$N-1$ quantum is a situation in which $N-1$ spins are active and a single left over spin is a spectator. The super spin is then split by the scalar field of a single

spectator spin, resulting in a doublet centred at the sum of the chemical shift positions of the active spins. The doublet separation corresponds to the cumulative additive values of couplings between active spins and the passive spins. For N chemically non-equivalent spins, there are N doublets in the $N-1$ quantum. The $N-2$ quantum coherence is a situation where $N-2$ spins flip at a time in the presence of the remaining two spins. This will have more number of transitions than $N-1$ quantum, but significantly less compared to SQ transitions. The number of transitions and thereby the complexity of the spectrum increases on going to lower quantum. Furthermore, the precessional frequency of any higher quantum coherence is proportional to its order. Consequently, the field inhomogeneity also proportionally gets scaled up. Thus, the m^{th} quantum order is broadened by m times. However, the ZQ coherence is insensitive to the field inhomogeneity. Several reports discuss the excitation and detection of higher quantum coherence.[53–60]

1.2. Spin-state-selective detection

Another method of reducing spectral complexity is to detect transitions based on the spin states of the coupled nucleus. In the spin-state-selective detection of two coupled spins—the high-field and low-field components of the doublets—is either separated or individually detected. An example of the spin-state-selective detection for an AX spin system is pictorially represented in Figure 3. This method has been employed for the measurement of scalar couplings in biological macromolecules and also in high-resolution solid-state NMR studies. Spin-state-selective techniques are well documented in the literature.[61–83]

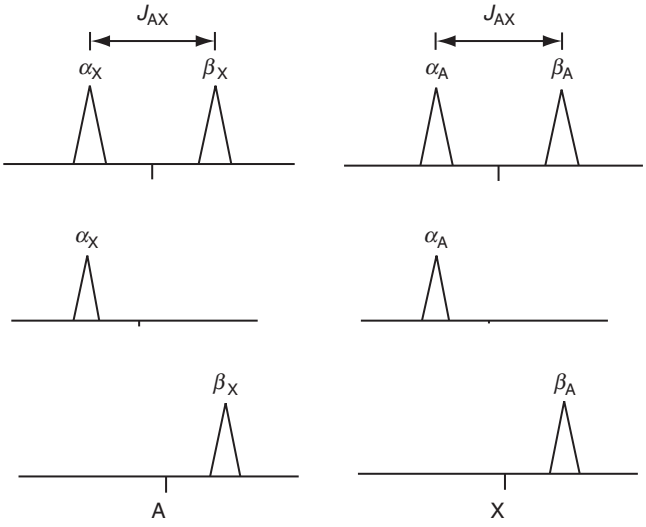

Figure 3 Schematic representation of spin-state selection in an AX spin system. The transition of a particular $|\alpha\rangle$ of $|\beta\rangle$ spin state is selectively detected.

1.3. Non-selective excitation of MQ

All the MQ experiments employ a three-pulse sequence. The MQ orders are created during the evolution period and are subsequently converted into detectable SQ coherence. Appropriate excitation and detection pulse sequences are constructed based on the information to be derived. Excitation and detection sequences are designed by using either spin-selective or non-selective pulses. The pulse sequences generally employed in spin-selective and non-selective MQ experiments are given in Figure 4. The detailed discussion on MQ spectrum of different types of spin systems is available in the literature.[60] For a homonuclear three-spin system of the type AMX, all the possible double and zero quantum transitions are depicted in Figure 5. This spin system is interesting as it has exact number of DQ and ZQ transitions as depicted in Figure 5A and B. One can non-selectively excite all the three possible DQ transitions, viz. AM DQ (where A and M spins are active spins), AX DQ (where A and X spins are active spins) and MX DQ (where M and X spins are active spins). In the DQ–SQ correlation experiment,

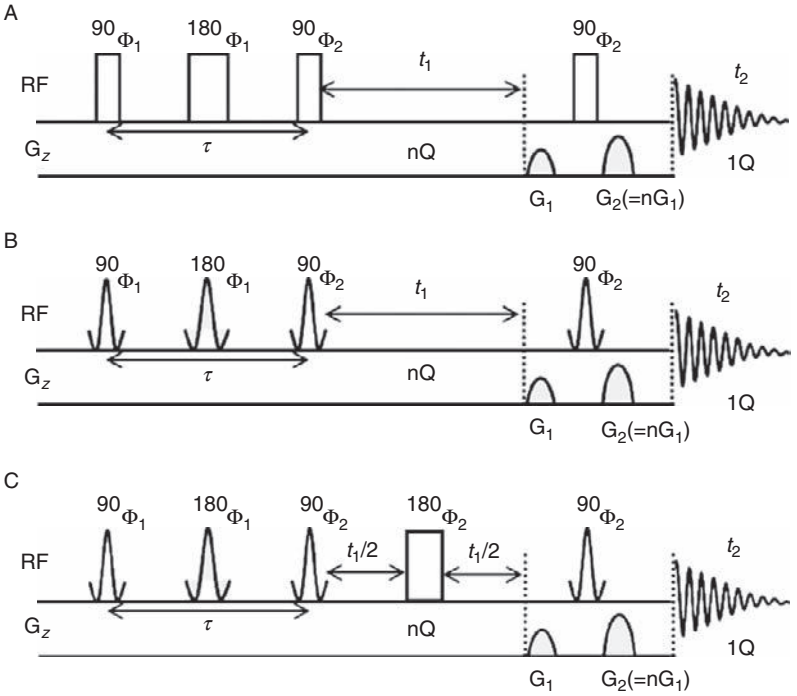

Figure 4 (A) The pulse sequence used for the non-selective MQ–SQ correlation experiments. The delay, τ, has to be optimized for the excitation of homonuclear MQ. The phases are $\Phi_1 = (p)x$, $\Phi_2 = \Phi_1 \pm (\pi/2)$, Φ_R(receiver phase) $= x$, where p is the order of coherence. (B) The pulse sequence used for the spin-selective MQ–SQ correlation experiments. All the pulses are selectively applied on chosen spins. (C) Pulse sequence used for MQ-*J*-resolved experiments, which is identical to (B), but the 180° pulse in the middle of the t_1 period, is non-selective.

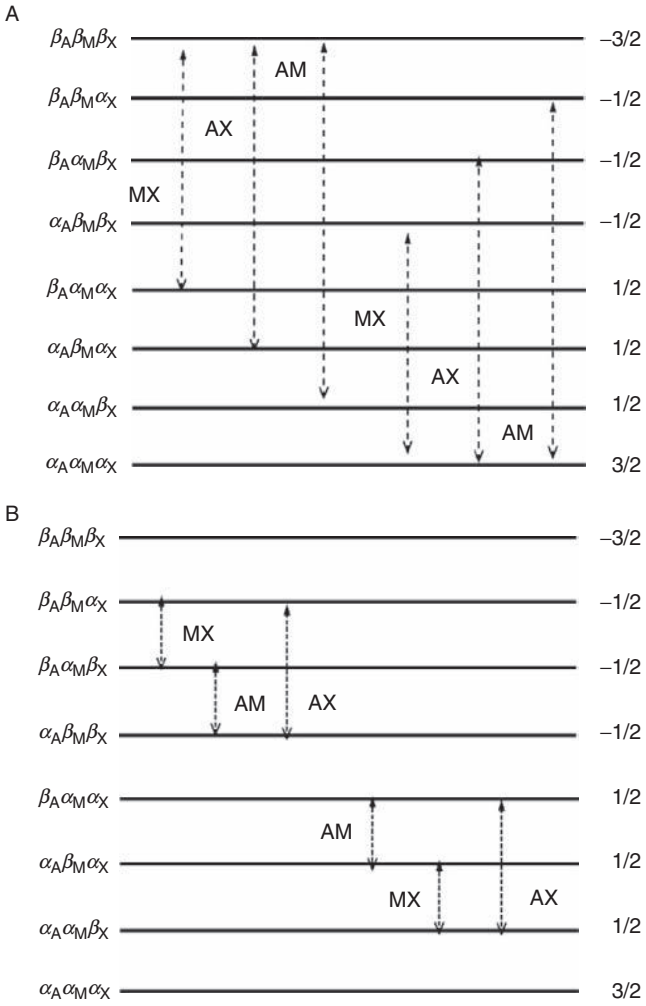

Figure 5 The schematic representation of energy states of an AMX spin system and the possible (A) DQ transitions and (B) ZQ transitions. AX, AM and MX transitions represented by double-headed vertical arrows correspond to simultaneous flipping of two chosen spins. In this specific spin system, there are two possible transitions for each DQ and ZQ coherences.

the DQ dimension provides three sets of doublets at the sum of the chemical shifts of the two active spins. The separation of the doublets pertains to the sum of passive couplings, viz. J_{AX+MX}, J_{AM+MX} and J_{AM+AX}, respectively, for AM, AX and MX DQ. Each component of these doublets corresponds to the $|\alpha\rangle$ and $|\beta\rangle$ states of the respective passive spin. The cross sections taken along the SQ dimension for any of the spin states of the passive spin give all the 12 transitions expected for an AMX spin system, whose intensities depend on the flip angle.[84] Thus in a non-selective detection, each $|\alpha\rangle$ and $|\beta\rangle$ spin state of passive spins correlates to all the allowed transitions in the SQ dimension.

1.4. Spin-state-selective detection of MQ

In the example of an AMX spin system discussed in the preceding section instead of non-selective excitation, if a pulse is applied selectively on any two spins and no pulse is applied on the third spin, then the states of the passive spin remain unperturbed both in DQ and in SQ dimensions. It may be emphasized that in the selective excitation, the spins must be weakly coupled. Due to large chemical shift difference, the heteronuclear spins are weakly coupled. The non-selective excitation of homonuclear highest quantum coherence in heteronuclear spin systems retains the spin states of heteronucleus undisturbed. This is analogous to the spin-selective excitation in a homonuclear spin system. In both the situations the passive spin(s) provide spin-state selection. Then the spin state of the passive spins in the DQ dimension encodes the spin states involved in the SQ transitions that arise only due to coupling among active spins and results in the selective detection of SQ transitions. The cross section taken along SQ dimension for any one of the passive spin states has less number of transitions compared to the normal SQ spectrum but suffice to determine the chemical shifts of active spins and the couplings among them. Thus in the selective AM DQ excitation of AMX spin system, the cross section taken along SQ dimension for each spin state of passive X spin provides only four transitions instead of eight. Therefore, the spin-state selection has a power of reducing the spectral complexity. The interesting feature of the experiment is that it also achieves, in homonuclear spin systems, separation of passive couplings and active couplings in the MQ and SQ dimensions, respectively. In the heteronuclear spin systems, it achieves separation of homo- and heteronuclear couplings in direct and indirect dimensions, respectively.

The selection of particular higher quantum is achieved by the application of pulse field gradients before and after the last pulse (G_1 and G_2 in Figure 4), which converts MQ coherence to detectable SQ coherence. The gradient ratio n (G_2/G_1) defines the order of the quantum to be detected. This also implies that ZQ selection is impossible by the application of gradients. The detection of ZQ coherence is achieved by phase cycling. In the following sections, the theoretical description of spin-selective MQ, applications for spectral simplification, spin system filtering and the utilization of higher quantum *J*-resolved techniques for the determination of scalar couplings of smaller magnitudes are discussed taking specific examples.

2. THEORETICAL DESCRIPTION OF SPIN DYNAMICS IN MQ EXCITATION

2.1. DQ excitation of an AMX spin system

For conceptual understanding of the spin dynamics in spin-selective and non-selective MQ, a weakly coupled AMX spin system is chosen because it gives identical number of ZQ and DQ transitions. The spin-selective and non-selective excitations of DQ in an AMX spin system have been reported.[85,86] While the DQ

coherence precess at the sum of the chemical shifts of two active spins, the two spin ZQ coherences precess at the difference of their chemical shifts. Except for this difference, the selective excitation of the ZQ coherence of any two spins—AM, AX or MX—and its correlation to SQ provides the spin-state selection analogous to that of DQ coherence. It is thus possible to separate active and passive couplings and derive the information which is possible from the selective DQ–SQ correlation spectrum. In the following sections, the dynamics of the spins under the application of the selective and non-selective pulses and the appearance of the ZQ and DQ spectra will be discussed using both product operator and polarization operator approaches. Subsequently, the experimental demonstration of such experiments is also discussed.

2.2. Product operator approach

The product operator formalism[87] is employed to discuss the evolution of magnetization at different stages of the pulse sequences given in Figure 4. The pulse sequences (Figure 4A and B) are utilized, respectively, for non-selective and selective excitation of both DQ and ZQ.

2.2.1. DQ excitation

In the pulse sequence given in Figure 4A, immediately after the second 90° pulse there are three kinds of DQ coherences, viz. AM, AX and MX, from the anti-phase magnetization. In the DQ dimension, the magnetization evolves at the sums of their respective chemical shifts under the additive value of the couplings of the active spins to the passive spin. For the conceptual development of theory, the discussion is restricted to AM DQ–SQ coherence. However, the discussion is equally valid for other two DQ coherences also.

The magnetization $-2I_{(\mathrm{A})\mathrm{X}}I_{(\mathrm{M})\mathrm{Y}}$ immediately after the second 90° pulse is written as a linear combination of DQ and ZQ terms of A and M spins as

$$-2I_{(\mathrm{A})\mathrm{X}}I_{(\mathrm{M})\mathrm{Y}} \rightarrow -\left(\mathrm{DQ}_{\mathrm{Y}}^{\mathrm{AM}} - \mathrm{ZQ}_{\mathrm{Y}}^{\mathrm{AM}}\right). \tag{3}$$

The evolution of DQ part under chemical shifts and couplings is relevant for the present discussion.

The chemical shift evolution of DQ terms in the DQ dimension is

$$\begin{aligned} -\left(\mathrm{DQ}^{\mathrm{AM}}\right)_{\mathrm{Y}} &\rightarrow -\left[\mathrm{DQ}_{\mathrm{Y}}^{\mathrm{AM}}\cos(\Omega_{\mathrm{A}}+\Omega_{\mathrm{M}})t_1 - \mathrm{DQ}_{\mathrm{X}}^{\mathrm{AM}}\sin(\Omega_{\mathrm{A}}+\Omega_{\mathrm{M}})t_1\right] \\ &= -\left[\mathrm{DQ}_{\mathrm{Y}}^{\mathrm{AM}}\cos(\Omega_{\mathrm{AM}}t_1) - \mathrm{DQ}_{\mathrm{X}}^{\mathrm{AM}}\sin(\Omega_{\mathrm{AM}}t_1)\right]. \end{aligned} \tag{4}$$

where $\Omega_{\mathrm{AM}}=\Omega_{\mathrm{A}}+\Omega_{\mathrm{M}}$.

The evolution of DQ terms under the sum of the passive couplings to X spin $K_{\mathrm{AM}}=J_{\mathrm{AX}}+J_{\mathrm{MX}}$ is

$$\begin{aligned} \rightarrow\ & \mathrm{DQ}_{\mathrm{Y}}^{\mathrm{AM}}\cos(\Omega_{\mathrm{AM}}t_1)\cos(\pi K_{\mathrm{AM}}t_1) - 2\mathrm{DQ}_{\mathrm{X}}^{\mathrm{AM}}I_{(\mathrm{X})\mathrm{Z}}\cos(\Omega_{\mathrm{AM}}t_1)\sin(\pi K_{\mathrm{AM}}t_1) \\ & - \mathrm{DQ}_{\mathrm{X}}^{\mathrm{AM}}\sin(\Omega_{\mathrm{AM}}t_1)\cos(\pi K_{\mathrm{AM}}t_1) - 2\mathrm{DQ}_{\mathrm{Y}}^{\mathrm{AM}}I_{(\mathrm{X})\mathrm{Z}}\sin(\Omega_{\mathrm{AM}}t_1)\sin(\pi K_{\mathrm{AM}}t_1). \end{aligned} \tag{5}$$

The expanded DQ_Y^{AM} and DQ_X^{AM} terms of the above equation are rewritten as

$$\begin{aligned}\rightarrow & \left[I_{(A)X}I_{(M)Y} + I_{(A)Y}I_{(M)X}\right]\cos(\Omega_{AM}t_1)\cos(\pi K_{AM}t_1)\\ & -2\left[I_{(A)X}I_{(M)X} - I_{(A)Y}I_{(M)Y}\right]I_{(X)Z}\cos(\Omega_{AM}t_1)\sin(\pi K_{AM}t_1)\\ & -\left[I_{(A)X}I_{(M)X} - I_{(A)Y}I_{(M)Y}\right]\sin(\Omega_{AM}t_1)\cos(\pi K_{AM}t_1)\\ & -2\left[I_{(A)X}I_{(M)Y} + I_{(A)Y}I_{(M)X}\right]I_{(X)Z}\sin(\Omega_{AM}t_1)\sin(\pi K_{AM}t_1).\end{aligned} \tag{6}$$

2.2.1.1. Case 1: When all the three pulses are non-selective: When all the pulses are non-selective, all the three possible DQ coherences are present and at the end of the third 90° pulse, the product operator terms present in the direct dimension of Equation (6) are

$$\begin{aligned}\rightarrow & \left[I_{(A)X}I_{(M)Z} + I_{(A)Z}I_{(M)X}\right]\cos(\Omega_{AM}t_1)\cos(\pi K_{AM}t_1)\\ & -2\left[I_{(A)X}I_{(M)X} - I_{(A)Z}I_{(M)Z}\right]\left(-I_{(X)Y}\right)\cos(\Omega_{AM}t_1)\sin(\pi K_{AM}t_1)\\ & -\left[I_{(A)X}I_{(M)X} - I_{(A)Z}I_{(M)Z}\right]\sin(\Omega_{AM}t_1)\cos(\pi K_{AM}t_1)\\ & -2\left[I_{(A)X}I_{(M)Z} + I_{(A)Z}I_{(M)X}\right]\left(-I_{(X)Y}\right)\sin(\Omega_{AM}t_1)\sin(\pi K_{AM}t_1).\end{aligned} \tag{7}$$

Using trigonometric identity, Equation (7) is rewritten as

$$\begin{aligned}\rightarrow & \frac{1}{2}\left[I_{(A)X}I_{(M)Z} + I_{(A)Z}I_{(M)X}\right]\left[\cos(\Omega_{AM} + \pi K_{AM})t_1 + \cos(\Omega_{AM} - \pi K_{AM})t_1\right]\\ & -\left[I_{(A)X}I_{(M)X} - I_{(A)Z}I_{(M)Z}\right]\left(-I_{(X)Y}\right)\left[\sin(\Omega_{AM} + \pi K_{AM})t_1 - \sin(\Omega_{AM} - \pi K_{AM})t_1\right]\\ & -\frac{1}{2}\left[I_{(A)X}I_{(M)X} - I_{(A)Z}I_{(M)Z}\right]\left[\sin(\Omega_{AM} + \pi K_{AM})t_1 + \sin(\Omega_{AM} - \pi K_{AM})t_1\right]\\ & -\left[I_{(A)X}I_{(M)Z} + I_{(A)Z}I_{(M)X}\right]\left(-I_{(X)Y}\right)\left[\cos(\Omega_{AM} - \pi K_{AM})t_1 - \cos(\Omega_{AM} + \pi K_{AM})t_1\right].\end{aligned} \tag{8}$$

The term $[I_{(A)X}I_{(M)Z} + I_{(A)Z}I_{(M)X}]$ is observable during t_2 and generates cross-peaks at Ω_A and Ω_M in F_2 dimension with anti-phase splitting of J_{AM}. The term $I_{(A)X}I_{(M)Z}$ has an in-phase splitting of J_{AX} in F_2 dimension. Both these peaks are shifted in F_1 dimension by $\Omega_A + \Omega_M$ and are referred to as *direct peaks*. The direct peaks have an in-phase splitting of K_{AM} in F_1 dimension. Therefore, the term $I_{(A)X}I_{(M)Z}$ in F_2 dimension is the doublet of a doublet. This is anti-phase with respect to J_{AM} and in phase with respect to J_{AX} at the chemical shift of A. Similarly, the term $I_{(A)Z}I_{(M)X}$ in F_2 dimension is a doublet of a doublet, anti-phase with respect to J_{AM} and in phase with respect to J_{MX} at the chemical shift of M.

The term $I_{(A)Z}I_{(M)Z}I_{(X)Y}$ represents an I_Y coherence anti-phase with respect to I_M and I_A in F_2 dimension and has doubly anti-phase dispersive line shape. The cross-peak has a chemical shift of Ω_X in F_2 and is modulated at the frequency $\Omega_A + \Omega_M$ in F_1 dimension. This is also dispersive in F_1 dimension and is denoted as a remote peak. In effect, the non-selective pulses create all the three DQ coherences and generate cross-peaks from all the coupled spins at both the spin states of the passive spin in the DQ dimension.

2.2.1.2. Case 2: When all the three pulses are applied on two selective spins: The discussion is restricted to the A and M spins selected DQ. However, the discussion is equally valid for AX- and MX-selected DQ excitations also. In the AM spins selected DQ coherence, all the three 90° pulses are applied only on A and M spins. It retains AM DQ term and the remaining two MX and AX DQ terms are absent. After the last selective 90° pulse, we have the following terms

$$\begin{aligned}
&\rightarrow \frac{1}{2}\left[I_{(A)X}I_{(M)Z} + I_{(A)Z}I_{(M)X}\right]\left[\cos(\Omega_{AM} + \pi K_{AM})t_1 + \cos(\Omega_{AM} - \pi K_{AM})t_1\right] \\
&-\left[I_{(A)X}I_{(M)X} - I_{(A)Z}I_{(M)Z}\right]\left(-I_{(X)Z}\right)\left[\sin(\Omega_{AM} + \pi K_{AM})t_1 - \sin(\Omega_{AM} - \pi K_{AM})t_1\right] \\
&-\frac{1}{2}\left[I_{(A)X}I_{(M)X} - I_{(A)Z}I_{(M)Z}\right]\left[\sin(\Omega_{AM} + \pi K_{AM})t_1 + \sin(\Omega_{AM} - \pi K_{AM})t_1\right] \\
&-\left[I_{(A)X}I_{(M)Z} + I_{(A)Z}I_{(M)X}\right]\left(-I_{(X)Z}\right)\left[\cos(\Omega_{AM} - \pi K_{AM})t_1 - \cos(\Omega_{AM} + \pi K_{AM})t_1\right].
\end{aligned} \tag{9}$$

It is obvious from the second term of Equation (9) that the relay peak from AM to X spin is absent in this situation.

Now the spectrum is a sum of the first and the fourth terms unlike in the non-selective case, where the spectrum is a result of first and second terms of Equation (8). The second and third terms are not detectable.

Assuming $J_{AM} > J_{AX}$, the appearance of the spectrum from the first term is schematically represented in Figure 6B. This spectrum displays the A part of the direct peak of a non-selective experiment. The doublet of doublet in SQ dimension is present in both the cross sections corresponding to the two DQ transitions in t_1 dimension. The identical spectrum appears in both the cross sections. The appearance of the spectrum from fourth term of Equation (9) is shown in Figure 6C. The final spectrum is the result of the sum of these two spectra which appears as shown in Figure 6D. The doublet of doublet of A is reduced to two doublets each in a different cross sections. Each doublet corresponds to the same spin state of the passive spin X. In other words, the spectrum of A is a doublet because of the $|\alpha\rangle$ and $|\beta\rangle$ spin states of spin M. There are two such doublets because of $|\alpha\rangle$ and $|\beta\rangle$ spin states of spin X but now they are present in separate cross sections rather than in a single cross section. This is because the spin states of the X spin are undisturbed in both the dimensions, a consequence of the spin-selective last 90° pulse of the sequence and retention of couplings to X spin in both dimensions. The selective pulse leads to spin-state-selective coherence transfer from DQ coherences to SQ coherences or in other words transfer is possible only between connected transitions. In energy level scheme shown for the three-spin system in Figure 6A, we have two DQ transitions A and A′ corresponding to $|\alpha\rangle$ and $|\beta\rangle$ spin states of spin X. Now, the DQ–SQ conversion leads to correlation between only DQ coherence corresponding to $|\alpha\rangle$ spin state of X and the SQ coherence corresponding to the same spin state of X, that is, A to A_1' and A_2. Similarly, the $|\beta\rangle$ DQ coherence correlates to only $|\beta\rangle$ SQ coherences, that is, A′ to A_1 and A_2'. Now, the spectrum in the SQ dimension can be visualized as two sub-spectra according to $|\alpha\rangle$ and $|\beta\rangle$

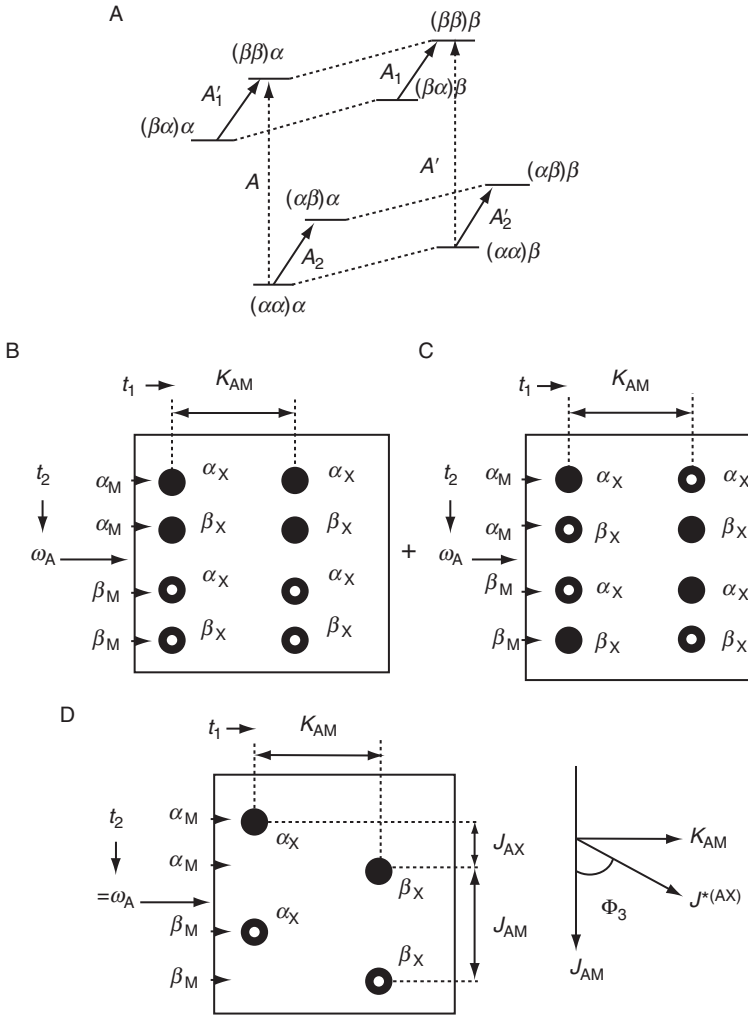

Figure 6 (A) The energy level diagram shown for the three-spin system. There are two DQ transitions A and A′ corresponding to $|\alpha\rangle$ and $|\beta\rangle$ spin states of spin X. Spin-state-selective DQ–SQ correlation leads to correlation between only DQ coherence corresponding to $|\alpha\rangle$ spin state of X and the SQ coherence corresponding to the same spin state of X, that is, A to A_1 and A_2. Similarly, the $|\beta\rangle$ DQ coherence correlates to only $|\beta\rangle$ SQ coherences, that is, A′ to A_1' and A_2'. Thus correlation between only connected transitions is observed. (B) The schematic representation of the appearance of the spectrum from the first term of Equation (9), (C) appearance of the spectrum from the fourth term of Equation (9) and (D) the spectrum from the sum of the first and the fourth terms of Equation (9). The figure on the right side of (D) is the displacement vector $J^{*}_{(AX)}$, connecting peaks of like signs. Tilt angle can be used to predict the relative signs of the passive coupling (reproduced with permission from American Institute of Physics).

spin states of spin X. Thus, reduced multiplicity resulting in high resolution and spectral simplification can be achieved in the cross sections along SQ dimension.

Another point to be highlighted is that the J_{AX} passive coupling can be measured from the displacement of the two doublets at the chemical shift position of A spin. Such a measurement is more precise because peak-to-peak separation is not subjected to systematic errors associated with the finite line width[88] and permits the determination of scalar couplings that are much smaller than line width. Similarly, J_{MX} passive coupling can be measured from the displacement of the two doublets at the chemical shift position of M spin. The entire discussion above for the detection of A part is also applicable for the detection of M part.

A displacement vector $J^{*(AX)}$, connecting peaks of like signs, as shown on the right side of Figure 6D, indicates the sign of passive coupling J_{AX}. If the angle Φ_3 between the vector J_{AM} and $J^{*(AX)}$ is less than 90°, then J_{AX} has a positive sign, else it has a negative sign. This approach can be utilized to determine the relative signs of hetero- and homonuclear couplings. It may be pointed out that this is analogous to an E-COSY spectrum,[11,14] where it has also been mentioned that similar information can be obtained from a small angle MQT. The small flip angle MQT suffers from considerable loss of signal intensity and provides intensity-dependent spin-state selection. However, such problems are not encountered in the present sequences as the applied flip angles are selective 90° resulting in no loss of sensitivity.

2.3. Polarization operator approach

Another approach to understand the spin dynamics is by the polarization operators.[6] The magnetization immediately after the second 90° pulse in Figure 4A is $-2I_X{}^A I_Y{}^M$. In terms of polarization operators, the terms $I_X{}^A$, $I_Y{}^M$ and E^X are written as

$$I_X^A = \frac{1}{2}\left(I_+^A + I_-^A\right), \quad I_Y^M = \frac{1}{2i}\left(I_+^M - I_-^M\right) \text{ and } \quad E^X \equiv \frac{1}{2}\left(I_\alpha^X + I_\beta^X\right). \tag{10}$$

Using the above SQ terms, the MQ (including ZQ and DQ) terms are written as

$$\left(I_X^A I_Y^M + I_Y^A I_X^M\right)E^X = \frac{1}{2i}\left(I_+^A I_+^M - I_+^A I_-^M + I_-^A I_+^M - I_-^A I_-^M\right)\frac{1}{2}\left(I_\alpha^X + I_\beta^X\right). \tag{11}$$

The term $\left(I_+^A I_+^M I_\alpha^{+X}\right.$ of the above equation has a coherence order $p=2$(a DQ coherence) and is converted into SQ by the last 90° pulse of the sequence. The effect of the application of a non-selective and a spin-selective pulse on this term is discussed below.

2.3.1. Effect of non-selective DQ–SQ conversion pulse

A non-selective DQ–SQ conversion by the application of hard 90° pulses on an AMX spin system leads to the following terms:

$$I_+^{\mathrm{A}} I_+^{\mathrm{M}} I_\alpha^{\mathrm{X}} \rightarrow \frac{1}{2}\left[I_+^{\mathrm{A}} + I_-^{\mathrm{A}} + \mathrm{i}\left(I_\alpha^{\mathrm{A}} - I_\beta^{\mathrm{A}}\right)\right]\frac{1}{2}\left[I_+^{\mathrm{M}} + I_-^{\mathrm{M}} + \mathrm{i}\left(I_\alpha^{\mathrm{M}} - I_\beta^{\mathrm{M}}\right)\right]$$
$$\frac{1}{2}\left[I_\alpha^{\mathrm{X}} + I_\beta^{\mathrm{X}} + \mathrm{i}\left(I_+^{\mathrm{X}} - I_-^{\mathrm{X}}\right)\right] = \frac{1}{4}\left[I_+^{\mathrm{A}} I_+^{\mathrm{M}} + I_+^{\mathrm{A}} I_-^{\mathrm{M}} + \mathrm{i}I_+^{\mathrm{A}}\left(I_\alpha^{\mathrm{M}} - I_\beta^{\mathrm{M}}\right)\right.$$
$$+I_-^{\mathrm{A}} I_+^{\mathrm{M}} + I_-^{\mathrm{A}} I_-^{\mathrm{M}} + \mathrm{i}I_-^{\mathrm{A}}\left(I_\alpha^{\mathrm{M}} - I_\beta^{\mathrm{M}}\right) + \mathrm{i}\left(I_\alpha^{\mathrm{A}} - I_\beta^{\mathrm{A}}\right)I_+^{\mathrm{M}} + \mathrm{i}\left(I_\alpha^{\mathrm{A}} - I_\beta^{\mathrm{A}}\right)$$
$$\left.I_-^{\mathrm{M}} + \mathrm{i}\left(I_\alpha^{\mathrm{A}} - I_\beta^{\mathrm{A}}\right)\mathrm{i}\left(I_\alpha^{\mathrm{M}} - I_\beta^{\mathrm{M}}\right)\right]\frac{1}{2}\left[I_\alpha^{\mathrm{X}} + I_\beta^{\mathrm{X}} + \mathrm{i}\left(I_+^{\mathrm{X}} - I_-^{\mathrm{X}}\right)\right]. \tag{12}$$

From the above terms, the SQ terms with the coherence order $p = -1$ is obtained as

$$\frac{1}{4}I_-^{\mathrm{A}}\left(I_\alpha^{\mathrm{M}} - I_\beta^{\mathrm{M}}\right)\frac{1}{2}\left(I_\alpha^{\mathrm{X}} + I_\beta^{\mathrm{X}}\right), \tag{13}$$

which has the frequency modulation:

$$\begin{aligned}&\exp(\mathrm{i}[\Omega_{\mathrm{A}} - \pi J_{\mathrm{AM}}])\{\exp(\mathrm{i}[\Omega_{\mathrm{A}} - \pi J_{\mathrm{AX}}]) + \exp(\mathrm{i}[\Omega_{\mathrm{A}} + \pi J_{\mathrm{AX}}])\}\\ &-\exp(\mathrm{i}[\Omega_{\mathrm{A}} + \pi J_{\mathrm{AM}}])\{\exp(\mathrm{i}[\Omega_{\mathrm{A}} - \pi J_{\mathrm{AX}}]) + \exp(\mathrm{i}[\Omega_{\mathrm{A}} + \pi J_{\mathrm{AX}}])\}.\end{aligned} \tag{14}$$

The overall transformation is given by

$$I_+^{\mathrm{A}} I_+^{\mathrm{M}} I_\alpha^{\mathrm{X}} \rightarrow \frac{1}{4}I_-^{\mathrm{A}}\left(I_\alpha^{\mathrm{M}} - I_\beta^{\mathrm{M}}\right)\frac{1}{2}\left(I_\alpha^{\mathrm{X}} + I_\beta^{\mathrm{X}}\right). \tag{15}$$

It can be observed from the frequency modulation that the cross section containing SQ frequencies in the direct dimension arising from DQ transition $I_+^{\mathrm{A}} I_+^{\mathrm{M}} I_\alpha^{\mathrm{X}}$ provides J_{AM} active coupling and J_{AX} passive coupling, which has anti-phase line shape with respect to J_{AM} coupling and in-phase line shape with respect to J_{AX} coupling. In other words, both $|\alpha\rangle$ and $|\beta\rangle$ spin states of X spin are present in the cross section corresponding to DQ transition $I_+^{\mathrm{A}} I_+^{\mathrm{M}} I_\alpha^{\mathrm{X}}$.

Similar analysis can be carried out for the DQ transition pertaining to $|\beta\rangle$ state of X spin, $I_+^{\mathrm{A}} I_+^{\mathrm{M}} I_\alpha^{\mathrm{X}}$:

$$I_+^{\mathrm{A}} I_+^{\mathrm{M}} I_\beta^{\mathrm{X}} \rightarrow \frac{1}{2}\left[I_+^{\mathrm{A}} + I_-^{\mathrm{A}} + \mathrm{i}\left(I_\alpha^{\mathrm{A}} - I_\beta^{\mathrm{A}}\right)\right]\frac{1}{2}\left[I_+^{\mathrm{M}} + I_-^{\mathrm{M}} + \mathrm{i}\left(I_\alpha^{\mathrm{M}} - I_\beta^{\mathrm{M}}\right)\right]\frac{1}{2}\left[I_\alpha^{\mathrm{X}} + I_\beta^{\mathrm{X}} - \mathrm{i}\left(I_+^{\mathrm{X}} - I_-^{\mathrm{X}}\right)\right]. \tag{16}$$

Here again, we arrive at the conclusion that the cross section containing SQ frequencies in SQ dimension arising from DQ transition $I_+^{\mathrm{A}} I_+^{\mathrm{M}} I_\beta^{\mathrm{X}}$ provides J_{AM} active coupling and J_{AX} passive coupling, which has anti-phase line shape with respect to J_{AM} coupling and in-phase line shape with respect to J_{AX} coupling. In other words, both $|\alpha\rangle$ and $|\beta\rangle$ spin states of X spin are present in the cross section corresponding to $|\beta\rangle$ spin state of the passive spin in DQ dimension. It implies that the non-selective DQ–SQ correlation results in non-selective DQ–SQ coherence transfer and does not provide any spin-state selection and spectral simplicity.

2.3.2. Effect of spin-selective DQ–SQ conversion pulse

AM spin-selective 90° pulse does not interact with the spin X. Therefore, in such a situation one obtains

$$I_+^{\mathrm{A}} I_+^{\mathrm{M}} I_\alpha^{\mathrm{X}} \rightarrow \frac{1}{2}\left[I_+^{\mathrm{A}} + I_-^{\mathrm{A}} + \mathrm{i}\left(I_\alpha^{\mathrm{A}} - I_\beta^{\mathrm{A}}\right)\right]\frac{1}{2}\left[I_+^{\mathrm{M}} + I_-^{\mathrm{M}} + \mathrm{i}\left(I_\alpha^{\mathrm{M}} - I_\beta^{\mathrm{M}}\right)\right]^{I_\alpha^{\mathrm{X}}}. \tag{17}$$

The term $\frac{1}{4} I_-^{\mathrm{A}}\left(I_\alpha^{\mathrm{M}} - I_\beta^{\mathrm{M}}\right)\frac{1}{2}\left(I_\alpha^{\mathrm{X}}\right)$ represents a coherence order of $p = -1$ and has the frequency modulation:

$$\exp(\mathrm{i}[\Omega_{\mathrm{A}} - \pi J_{\mathrm{AM}} - \pi J_{\mathrm{AX}}]) - \exp(\mathrm{i}[\Omega_{\mathrm{A}} + \pi J_{\mathrm{AM}} - \pi J_{\mathrm{AX}}]), \tag{18}$$

which implies that the cross section containing SQ frequencies in the direct dimension arising from the DQ transition $I_+^{\mathrm{A}} I_+^{\mathrm{M}} I_\alpha^{\mathrm{X}}$ provides J_{AM} active coupling which has anti-phase line shape with respect to J_{AM} coupling. However, the J_{AX} coupling is absent in this cross section. In other words, only $|\alpha\rangle$ spin state of the X spin is present in this cross section. Thus, the $|\alpha\rangle$ domain of A spin SQ transitions is obtained from $|\alpha\rangle$ domain of DQ transitions and gets separated from the $|\beta\rangle$ domain of A spin SQ transitions.

Similar analysis can be carried out for the term $I_+^{\mathrm{A}} I_+^{\mathrm{M}} I_\alpha^{\mathrm{X}}$. The term $\frac{1}{4} I_-^{\mathrm{A}}\left(I_\alpha^{\mathrm{M}} - I_\beta^{\mathrm{M}}\right)\frac{1}{2}\left(I_\beta^{\mathrm{X}}\right)$ represents a coherence order of $p = -1$ and has the frequency modulation:

$$\exp(\mathrm{i}[\Omega_{\mathrm{A}} - \pi J_{\mathrm{AM}} + \pi J_{\mathrm{AX}}]) - \exp(\mathrm{i}[\Omega_{\mathrm{A}} + \pi J_{\mathrm{AM}} + \pi J_{\mathrm{AX}}]), \tag{19}$$

which again implies that the cross section containing SQ frequencies in the direct dimension arising from the DQ transition $I_+^{\mathrm{A}} I_+^{\mathrm{M}} I_\beta^{\mathrm{X}}$ provides J_{AM} active coupling which has anti-phase line shape with respect to J_{AM} coupling and the J_{AX} coupling is absent in this cross section. In other words, only $|\beta\rangle$ spin state of the X spin is present in this cross section. The J_{AX} coupling can however be determined from the relative displacement of the doublet between the $|\alpha\rangle$ and $|\beta\rangle$ cross sections. Both these product operator and polarization operator approaches can also be employed for understanding the spin dynamics of spin-selective ZQ–SQ correlation experiments.

3. DQ EXPERIMENTS ON 2,3-DIBROMOPROPIONIC ACID

3.1. Non-selective DQ excitation

To corroborate the theoretical description for an AMX spin system, the ^{1}H NMR spectrum of the molecule 2,3-dibromopropionic acid has been studied.[85,86] The chemical structure and numbering of interacting spins of this molecule given in Figure 7A form a spin system of the type AMX. The 1D proton spectrum of this molecule reported in Figure 7B exhibits 12 transitions as expected for an AMX-type spin system with four transitions of equal intensity for each spin at their respective chemical shift positions. The non-selective DQ–SQ correlation spectrum of this molecule is reported in Figure 8. All the three types of DQ coherences

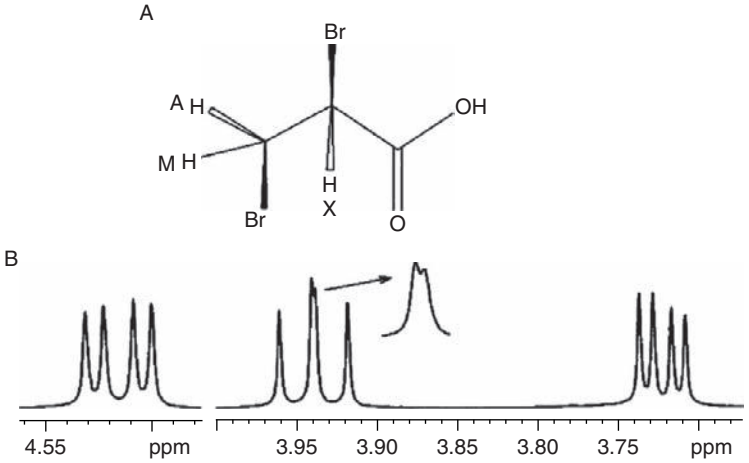

Figure 7 (A) The chemical structure and labelling of interacting spins in 2,3-dibromopropionic acid. The protons of the molecule form a weakly coupled spin system of the type AMX and the protons are accordingly labelled by alphabets. (B) The 500-MHz one-dimensional proton spectra of 2,3-dibromopropionic acid in the solvent $CDCl_3$ (reproduced with permission from American Institute of Physics).

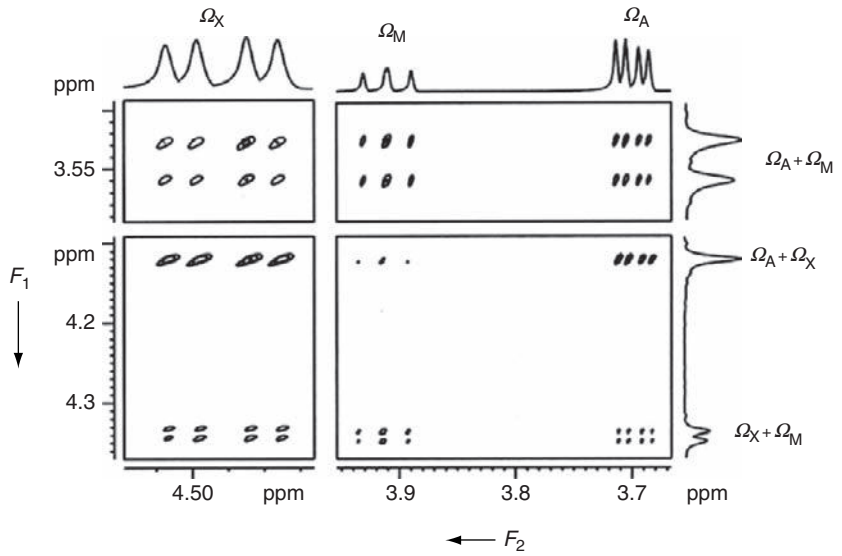

Figure 8 The 500-MHz two-dimensional spectrum correlating DQ coherence to its SQ coherence in 2,3-dibromopropionic acid. The corresponding F_1 and F_2 projections are also given. The DQ dimension pertains to the non-selective excitation of all the three double quanta using the pulse sequence given in Figure 4A. Ω_A, Ω_M and Ω_X correspond to chemical shifts of the protons A, M and X. Sum of the chemical shifts in the F_1 dimension identifies the different double quanta. The AX DQ–SQ spectrum has the doublet in the DQ dimension but is unresolved due to very small difference between J_{AM} and J_{AX} which are of opposite signs (reproduced with permission from American Institute of Physics).

(AM, AX and MX) are detected and the DQ dimension show doublets with separations corresponding to the sums of respective couplings of active spins to the passive spin. The F_2 cross section for any transition in the DQ dimension results in a conventional 1D spectrum. In all the three DQ coherences, each doublet component shows correlation to all the SQ transitions indicating the absence of any spin-state selection. It is interesting to note that AX DQ exhibited a singlet confirming that $J_{AM}+J_{MX}$ is negligibly small. This implies that each of these two couplings is either negligibly small or larger with nearly equal strengths of opposite signs. The determination of the signs of the couplings using spin-selective DQ (SSDQ) experiments resolves this ambiguity.

3.2. Spin-selective DQ–SQ excitation

It is possible to determine all the three scalar couplings of this molecule by the selective detection of ^{1}H SQ transitions using homonuclear proton DQ coherence edited with passive proton spin states. Any one of the possible three DQ–SQ experiments is sufficient to extract this information. For example, in an AM-selective DQ–SQ experiment, the doublet taken at any of the active spins provides J_{AM}. From the relative displacement of the peaks between the cross sections, the magnitudes and the relative signs of the couplings between active spins (A and M) and the passive spin (X), J_{AX} and J_{MX} could be determined. However, for the determination of the relative signs of J_{AM} and J_{AX} or J_{AM} and J_{MX}, any one of the remaining two spin DQ–SQ experiment is essential.

The selective excitation of AM DQ results in all the protons evolving at the sum of the resonance offset ($\Omega_A+\Omega_M$) under sum of passive couplings ($J_{AX}+J_{MX}$) in the DQ dimension. In the DQ dimension, AMX spin system behaves like an AX spin system, where proton A is the super spin (active spins A and M) and third proton X is the spectator (passive) spin. The DQ spectrum pertains to A part of this AX-type spectrum. In the spin product basis set, the spin states of X coupled to AM DQ states of proton $|\alpha_A\alpha_M\rangle$ and $|\beta_A\beta_M\rangle$ are written as $|\alpha_X\rangle$ and $|\beta_X\rangle$. The two transitions of the A spin in the DQ dimension correspond to these two passive spin states.

Figure 9A shows AM-selective DQ spectrum of 2,3-dibromopropionic acid along with F_1 and F_2 projections. The F_2 projection, the cross sections taken along SQ dimension at different spin states of DQ, and the selected region of the 1D spectrum are reported in Figure 9B. Each of these cross sections pertains to selectively detected SQ transitions originating from the initial second quantum state which has X spin, either in $|\alpha_X\rangle$ or in $|\beta_X\rangle$ state, and ends up in states where single proton spin (A or M) flips but still has X spin in its initial $|\alpha_X\rangle$ or $|\beta_X\rangle$ state. An example of such a transition is between the states $|\alpha_A\alpha_M\alpha_X\rangle$ and $|\beta_A\alpha_M\alpha_X\rangle$. Each cross section is a doublet, from which J_{AM} can be determined. It implies that as far as the determination of J_{AM} is concerned, the interference from passive coupling is removed. Both J_{AX} and J_{MX} can be extracted from the displacement of the cross-sections. The values of the scalar couplings determined (in Hz) are $J_{AX}=4.2$, $J_{AM}=10.1$ and $J_{MX}=11.2$.

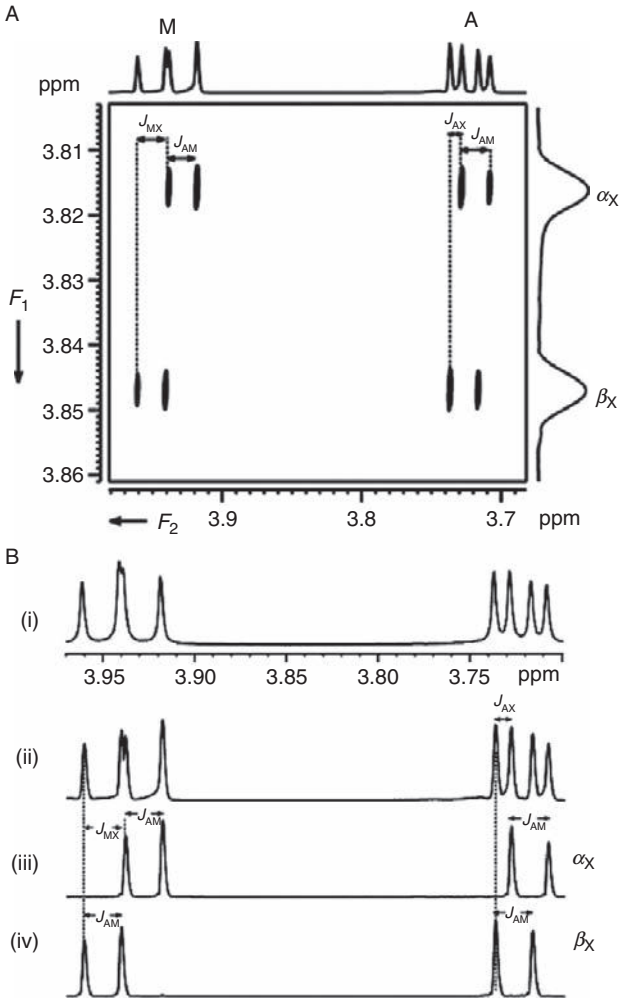

Figure 9 (A) The 500-MHz two-dimensional spectrum correlating AM spin-selective DQ coherence to its SQ coherence in an AMX spin system in 2,3-dibromopropionic acid along with the corresponding projections. The doublet separation in the F_1 dimension corresponds to $J_{AX} + J_{MX}$. $|\alpha_X\rangle$ and $|\beta_X\rangle$ correspond to spin states of X in the DQ dimension. The cross sections along the SQ dimension for any spin state of X in the DQ dimension provide the active coupling J_{AM} which is marked for one of the cross sections. The displacements of the doublets between the two F_1 cross sections provide passive couplings J_{AX} and J_{MX} which are also marked. Tilts of the displacement vectors for both A and M shown by dotted lines indicate that the relative signs of J_{AX} and J_{MX} are same. (B) (i) The 500-MHz ^{1}H spectrum of 2,3-dibromopropionic acid plotted for the spins A and M, (ii) the projection along SQ dimension of (A), (iii) the cross section taken along SQ dimension at the spin state $|\alpha_X\rangle$ of spin X in the DQ dimension and (iv) the cross section taken along SQ dimension at the spin state $|\beta_X\rangle$ of spin X in the DQ dimension (reproduced with permission from American Institute of Physics).

It is obvious from Figure 9A that the directions of the displacement vectors at the chemical shift positions of both A and M are identical, indicating that the relative signs of J_{AX} and J_{MX} are same. Therefore, in the AX DQ coherence, which evolves with the sum of the J_{AM} and J_{MX}, the doublet separation in the DQ dimension should be 21.3 Hz. However, in the non-selective DQ–SQ experiment (Figure 8), a singlet was detected for AX DQ. This implies that the signs of these two passive couplings must be opposite resulting in a singlet, which is nothing but an unresolved doublet with a separation of nearly 1 Hz. Another DQ–SQ experiment unequivocally establishes the relative signs of couplings. A DQ experiment with the selective excitation of spins M and X has therefore been carried out and this spectrum is reported in Figure 10. The analysis of this spectrum provided active (J_{MX}) and passive (J_{AX} and J_{AM}) couplings. But the interesting point to note is that the tilt of the displacement vector is negative at X spin chemical shift and positive at M spin chemical shift, indicating that J_{AM} is opposite in sign with respect to J_{AX} and J_{MX}. Combining the information from both AM and MX spin-selected DQ–SQ correlation experiments, the sign of J_{AM} has been assigned to be negative ($J_{AM} = -10.1$ Hz). The added advantage of this spin-selective excitation

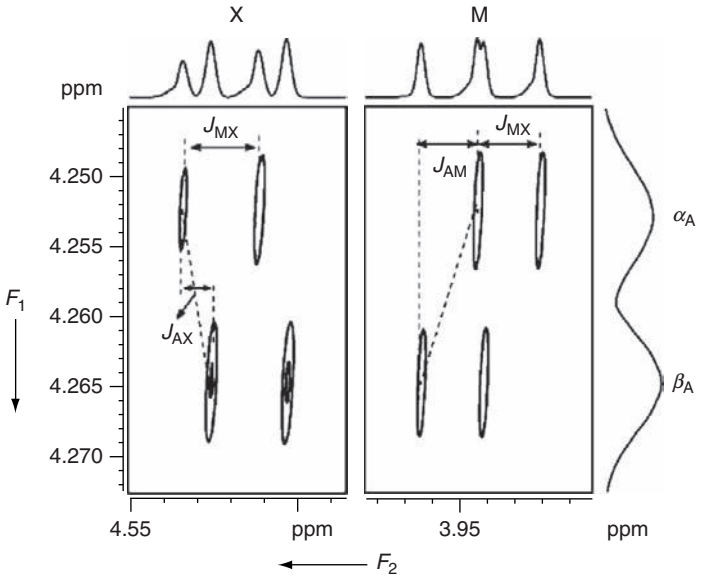

Figure 10 The 500-MHz two-dimensional spectrum correlating MX spin-selective DQ coherence to its SQ coherence in 2,3-dibromopropionic acid with the corresponding projections. The doublet separation in the F_1 dimension pertains to $J_{AM} + J_{AX}$. $|\alpha_A\rangle$ and $|\beta_A\rangle$ correspond to the two spin states of spin A in the DQ dimension. Ω_M and Ω_X refer to the chemical shift positions of spins M and X, respectively. The cross section along the SQ dimension for any spin state of spin A in the DQ dimension provides the active coupling J_{MX} which is marked for the cross section corresponding to the spin state $|\alpha_A\rangle$. The marked displacement of the doublets at chemical shift positions provides passive couplings J_{AM} and J_{AX}. The tilts of the displacement vectors for J_{AM} and J_{AX} are opposite, indicating that their relative signs are opposite (reproduced with permission from American Institute of Physics).

is that the total experimental time required for two experiments (0.5 h + 0.5 h) is less than one non-selective DQ experiment (3 h). This is due to the fact that in a non-selective experiment, the large spectral width is required to be covered in DQ dimension and demands more number of t_1 points. In the spin-selective experiment, only particular region is excited and the required number of t_1 points is less.

3.3. Spin-selected ZQ experiment

As discussed earlier in the theoretical section, the MX spin-selected ZQ experiment also exhibits spin-state selection. All the spectral information including the signs of the couplings that are derived from the MX DQ spectrum could be determined in these ZQ–SQ experiments also. The MX-selected ZQ–SQ correlation spectrum[85] is reported in Figure 11. It is interesting to note that in spite of the fact that spins evolve with the difference of $J_{AX} - J_{AM}$ in the ZQ dimension, the doublet separation is larger than that in the DQ evolution. This is attributed to opposite signs of the passive couplings and the separation now corresponds to $J_{AX} - J_{AM} = 4.2 - (-10.1) = 14.3$ Hz. This further supports the earlier interpretation of the negative sign for J_{AM}.

4. FILTERING OF SPIN SYSTEMS

The proton spectra could be complex due to numerous scalar couplings experienced by each interacting spin. The closely resonating protons present in the same molecule under different chemical environments result in severe overlap of transitions. Discerning of these overlapped transitions is a prerequisite for the spectral

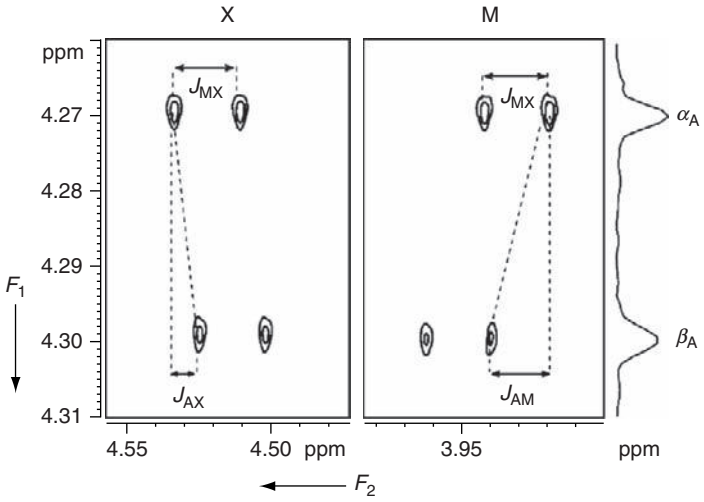

Figure 11 The 500-MHz two-dimensional ZQ–SQ spectrum of 2,3-dibromopropionic acid with selective excitation of spins M and X along with the F_1 and F_2 projections. Although the ZQ evolves with the difference of the passive couplings, as the signs of J_{AX} and J_{AM} are opposite, the doublet separation in the ZQ dimension is larger than that in Figure 10. This confirms that J_{AM} and J_{AX} are opposite (reproduced with permission from American Institute of Physics).

analyses. One of the ways of simplifying the analyses is the identification of spin-coupled networks of different topologies using MQ experiment.[49,50] The reported pulse schemes can distinguish molecular fragments containing same number of spins but different coupling topologies. It is also possible for the filtering of different spin systems in the molecules by employing non-selective excitation of highest quantum, provided the cumulative additive values of the chemical shifts of active spins are substantially different among different spin systems. Additional spectral simplification can also be achieved by the blend of the spin system filtering and spin-state selection.

4.1. Spin-selective homonuclear MQ in heteronuclear systems

In a heteronuclear spin system, the homonuclear spin-state selection is achieved by the pulse sequence depicted in Figure 4B. For the conceptual understanding of the methodology, an example of a selective excitation of proton DQ (spins A and K) in a weakly coupled spin system of the type AFKPX (where X = ^{19}F and the remaining spins are protons) is considered. Proton is detected in both F_1 and F_2 dimensions with ^{19}F decoupling in the F_1 dimension. The DQ excitation of spins A and K results in two energy states corresponding to $|\alpha\alpha\rangle$ and $|\beta\beta\rangle$ spin states. This is schematically depicted in Figure 12A. In the DQ dimension, each of these spin

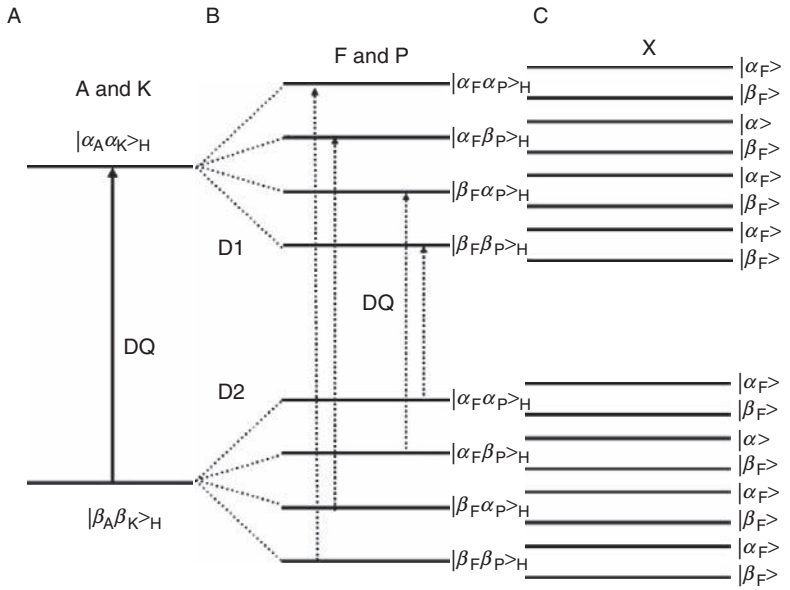

Figure 12 The schematic representation of energy level diagram depicting the proton-detected DQ–SQ correlation and the spin-state selection in a five-spin system of the type AFPKX, where X spin is ^{19}F and the remaining spins are protons. (A) Homonuclear active spin states in DQ dimension with the selective excitation of spins A and K, (B) spin-state selection resulting only from passive spin states $|\alpha_F\alpha_P\rangle$, $|\alpha_F\beta_P\rangle$, $|\beta_F\alpha_P\rangle$ and $|\beta_F\beta_P\rangle$ of protons F and P in the DQ dimension as ^{19}F is decoupled by a refocusing pulse and (C) each spin state in (B) splits into $|\alpha\rangle$ and $|\beta\rangle$ states of ^{19}F in the SQ dimension.

states is further split into four energy states corresponding to four possible spin states $|\alpha\alpha\rangle$, $|\alpha\beta\rangle$, $|\beta\alpha\rangle$ and $|\beta\beta\rangle$ of spins F and P, giving rise to two domains D1 and D2. The DQ dimension provides only four transitions, as depicted in Figure 12B. Consequent to ^{19}F decoupling in the F_1 dimension additional splitting is not detected. The protons F and P provide spin-state selection in the DQ dimension as the SQ transitions of each domain correlate with the corresponding spin states of A and K spins. However, when ^{19}F is allowed to couple with protons, each of four transitions in DQ is further split into doublets as depicted in Figure 12C, resulting in total of eight transitions. In the F_2 dimension, all the couplings are present and there will be 16 transitions for each A and K spins.

4.2. Non-selective homonuclear MQ in heteronuclear systems

In an AFKPX spin system discussed in the preceding section, the homonuclear highest quantum achievable is 4Q, where all the four protons are allowed to flip simultaneously. This pertains to a spin-selective excitation of 4Q. The heteronuclear spin provides spin-state selection and is depicted by an energy level diagram in Figure 13. All the active protons can be regarded as a super spin with two possible orientations, that is, $|\alpha\alpha\alpha\alpha\rangle_H$ and $|\beta\beta\beta\beta\rangle_H$ (Figure 13A). The two 4Q spin states are further split into a doublet due to $|\alpha\rangle$ and $|\beta\rangle$ spin states of passive ^{19}F (Figure 13B). The absence of any pulse on ^{19}F leaves its $|\alpha\rangle$ and $|\beta\rangle$ spin states unperturbed in both F_1 and F_2 dimensions. In 4Q dimension, the scalar

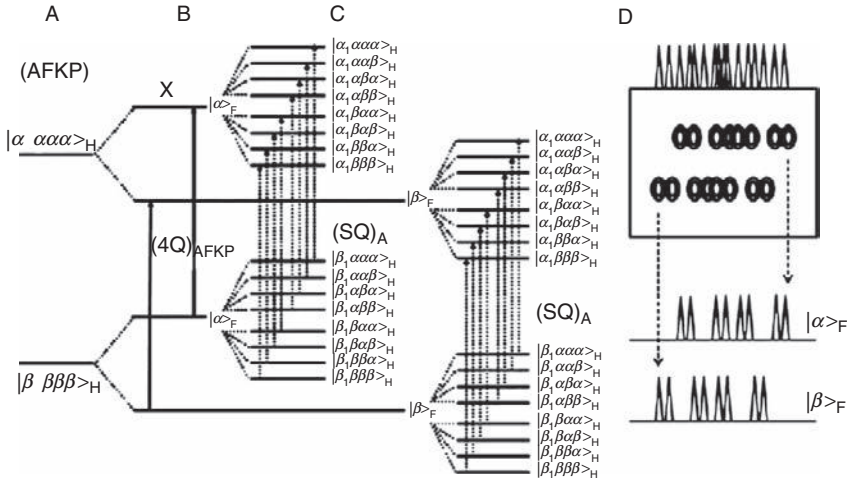

Figure 13 The schematic representation of energy level diagram depicting the 4Q–SQ correlation and the spin-state selection achieved in an AFKPX spin system, where X spin is ^{19}F and the remaining spins are protons. (A) 4Q excitation with simultaneous flipping of the spins AFKP, (B) spin-state selection resulting from the passive spin states $|\alpha\rangle$ and $|\beta\rangle$ of ^{19}F in 4Q dimension and (C) each $|\alpha\rangle$ and $|\beta\rangle$ spin states of ^{19}F in 4Q correlates to its corresponding $|\alpha\rangle$ and $|\beta\rangle$ states in the SQ dimension giving rise to spin-state selection. (D) Demonstration of spectral simplification by the passive spin states of ^{19}F.

coupling is absent among the protons and the spins do evolve at the cumulative additive values of individual chemical shifts. However, the active spins evolve with the sum of prevailing passive heteronuclear couplings (sum of J_{HF}s). From the first-order interpretation of spectrum, it is obvious that there are 16 transitions possible for each proton. The $|\alpha\rangle$ and $|\beta\rangle$ spin states of ^{19}F in 4Q dimension correlate, respectively, to the corresponding $|\alpha\rangle$ and $|\beta\rangle$ spin states of ^{19}F in the SQ dimension as depicted in Figure 13C. Thus for each proton, eight possible transitions are detected for each $|\alpha\rangle$ and $|\beta\rangle$ spin states of ^{19}F. Therefore, the SQ cross section for particular spin state of ^{19}F results in half the number of transitions, thereby reducing the redundancy in the number of SQ transitions by a factor of 2 as depicted in Figure 13D.

5. APPLICATION TO AROMATIC RING SYSTEMS CONTAINING A HETEROATOM

In single aromatic ring systems with a substituted NMR active heteronucleus, such as ^{31}P or ^{19}F, the spectral simplification is achieved by the non-selective excitation of homonuclear highest quantum coherence of protons. This is a situation where ^{19}F or ^{31}P acts as a passive spin providing spin-state selection. Such an application is discussed for five-spin systems of the type AFKPX.[85,86]

5.1. 4Q detection in 2-fluoropyridine

The protons and ^{19}F of the molecule 2-fluoropyridine, whose chemical structure and the numbering of interacting spins are given in Figure 14, form a weakly coupled five-spin system of the type AFKPX (where X pertains to ^{19}F and the remaining spins are protons). The ^{1}H-detected spectrum corresponds to AFKP part. The 2D spectrum correlating homonuclear fourth quantum (4Q) coherence of protons to its SQ coherence is reported in Figure 14 along with the corresponding projections on both the dimensions.[85,86] The 4Q excitation results in flipping of all the protons simultaneously.

For the analysis of 4Q spectrum, all the four protons can then be treated as a single spin A (super spin) and the fluorine as X spin. The spin system in the 4Q dimension can then be treated as the weakly coupled two spins of the type AX. The ^{1}H-detected 4Q is the A part of this AX spin system. The eigenstate of the active spin A is split due to scalar couplings with the passive spin (X), whose two possible spin states are $|\alpha\rangle$ and $|\beta\rangle$ resulting in a doublet for 4Q spectrum. The magnetization evolves in the t_1 dimension, under $\delta_3+\delta_4+\delta_5+\delta_6$ and $J_{23}+J_{24}+J_{25}+J_{26}$.

The cross sections taken along the SQ dimension at two different spin states in the 4Q dimension can be visualized analogous to that in 2,3-dibromopropionic acid. The projection along SQ dimension gives four groups of peaks at the chemical shift positions of the four protons. Previous published work[89,90] assisted in the assignment of chemical shifts of protons. Each proton has two cross sections corresponding to $|\alpha\rangle$ and $|\beta\rangle$ spin states of ^{19}F and the number of selectively

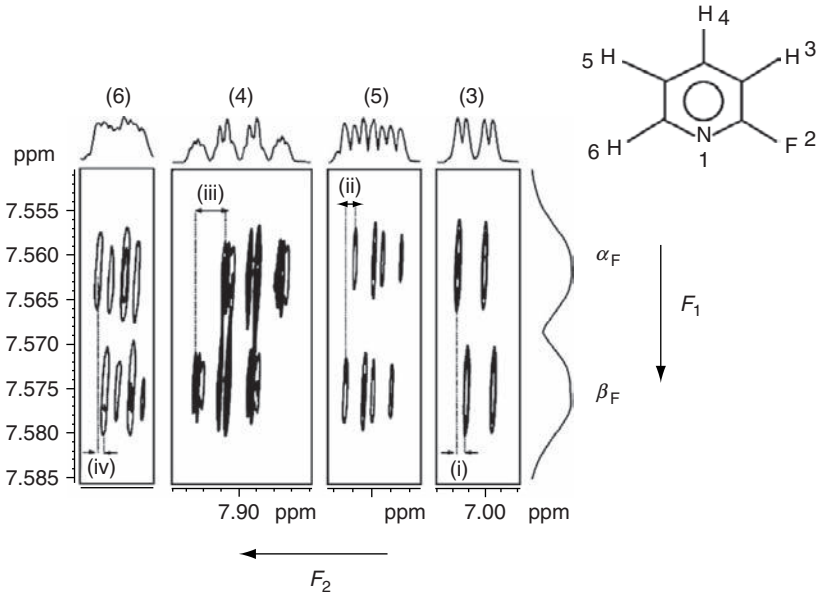

Figure 14 Molecular structure and numbering of interacting spins in 2-fluoropyridine and its ^{1}H 4Q–SQ spectrum recorded 500 MHz. Two signals along 4Q axis (F_1 dimension) corresponded to the $|\alpha\rangle$ and $|\beta\rangle$ spin states of ^{19}F separated by the sum of all J_{HF}. The assignment to different protons is also marked. It is evident from the 2D spectrum that the cross section taken along F_2 dimension reduces the spectral complexity by a factor of 2 due to spin-state selection (reproduced with permission from American Institute of Physics).

detected transitions in each cross section is half the normal spectrum but sufficient for the determination of all δ_H and J_{HH}. Thus, the experiment separated homonuclear and heteronuclear couplings in two dimensions. Although 4Q excitation is carried out with hard pulse, the situation is analogous to selectively excited DQ coherence of AMX spin system discussed earlier because the pulse is ineffective on ^{19}F and its spin state remains the same. Thus, the theoretical interpretation of selective excitation given earlier is applicable in this case also.

The displacement of the cross sections due to $|\alpha\rangle$ and $|\beta\rangle$ spin states of ^{19}F provides J_{HF}. The straight lines joining the displacement of the cross sections for both the spin states of the ^{19}F are reported in Figure 14. From the directions of the tilt, it is evident that the slope of the line is positive for the protons numbered 4 and 5 and negative for the protons numbered 3 and 6. This gives an idea of the relative signs of the couplings. Attributing the positive and negative signs, respectively, for the positive and negative slopes, the determined individual heteronuclear couplings (in Hz) are $J_{23} = -2.69$, $J_{24} = 8.4$, $J_{25} = 2.64$ and $J_{26} = -1.15$.

The doublet separation of the 4Q dimension corresponds to 7.1 Hz, which is equal to $J_{23} + J_{24} + J_{25} + J_{26}$. This value is in agreement with the above determined values when the appropriate signs are assigned for the couplings. If the sum of the heteronuclear couplings measured from the 4Q dimension is assigned the negative sign (-7.1 Hz), accordingly the signs of the individual J_{HF} given above are

reversed. The significant advantage of this experiment is the determination of the relative signs of the heteronuclear couplings in a single experiment unlike in some experiments where two experiments such as ZQ and DQ are added or subtracted.

5.2. 4Q detection in 1-chloro-2-fluorobenzene

The protons and fluorine in the molecule 1-chloro-2-fluorobenzene, whose chemical structure and the numbering of interacting spins are given in Figure 15, form a weakly coupled five-spin system of the type AFKPX.[85,86] The ^{1}H-detected spectrum pertains to AFKP part of AFKPX system. The homonuclear 4Q–SQ 2D spectrum is reported in Figure 15 along with the corresponding projections on both the dimensions. The analysis of this spectra is similar to the one discussed in the preceding section. The spectrum is well dispersed and the chemical shift of each proton has been assigned utilizing the reported values from the literature.[91] All the four groups of transitions are plotted with the expanded scale in Figures 16 and 17.

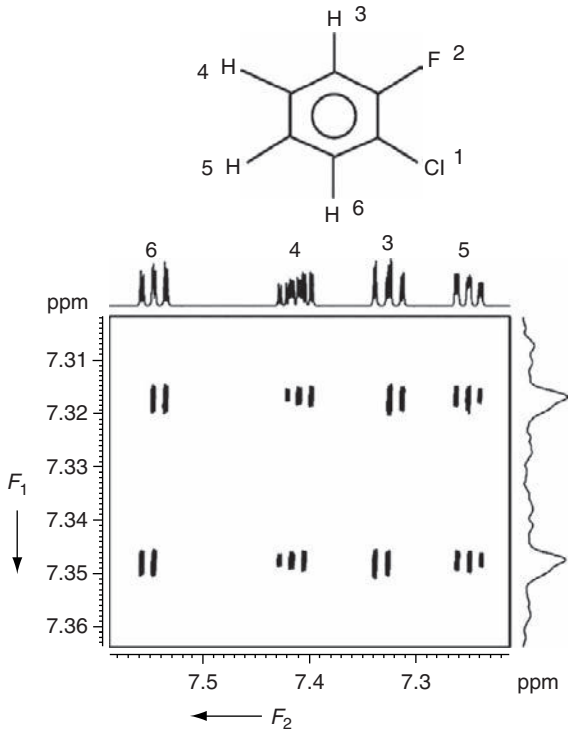

Figure 15 (A) Molecular structure and numbering of interacting spins in 1-chloro-2-fluorobenzene and its ^{1}H 4Q–SQ spectrum recorded at 500 MHz. Two signals along 4Q axis (F_1 dimension) corresponded to the $|\alpha\rangle$ and $|\beta\rangle$ spin states of ^{19}F separated by the sum of all J_{HF}. The assignment to different protons is also marked. It is clearly evident that the cross section taken along F_2 dimension reduces the spectral complexity by a factor of 2 due to spin-state selection (reproduced with permission from American Institute of Physics).

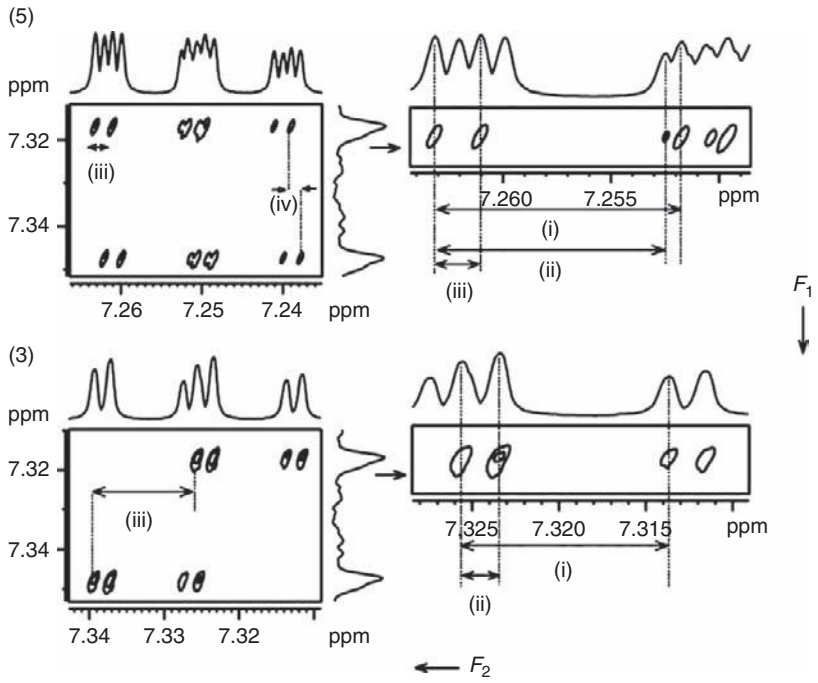

Figure 16 Expanded regions of spectrum corresponding to protons numbered H5 and H3 in Figure 15. The spectrum on the right side is the further expansion of part of the spectrum at one of the spin states in the 4Q dimension. From the separations marked (i), (ii) and (iii) on the right side of (5), one can determine J_{56}, J_{45} and J_{35}. From the separations marked (i) and (ii) on the right side of (3), one can determine J_{34} and J_{35}. It is difficult to determine J_{36} due to negligible strength which is comparable to line width (reproduced with permission from American Institute of Physics).

The additional expansion of the parts of the spectrum from the cross section of one of the spin state of ^{19}F is also given in Figures 16 and 17. The homonuclear couplings could be easily extracted from the cross sections as marked in the figures. The displacement vectors of various multiplets provided the signs and magnitudes of the heteronuclear couplings, viz. $J_{23} = 9.6$ Hz, $J_{24} = 4.98$ Hz, $J_{25} = -0.85$ Hz and $J_{26} = 7.6$ Hz. In this molecule also one of the heteronuclear couplings (J_{25}) has been shown to be negative. The doublet separation in the 4Q dimension is 21.3 Hz which is in agreement with the sum of heteronuclear couplings derived from the displacement vectors $(9.6 + 4.98 + (-0.85) + 7.6 = 21.38)$.

6. APPLICATION TO MOLECULES WITH TWO OR MORE PHENYL RINGS

In systems with limited spectral complexity, a single COSY spectrum allows the identification of coupled spin networks and also permits the measurement of all the coupling constants. In larger or complex spin systems, often COSY spectrum

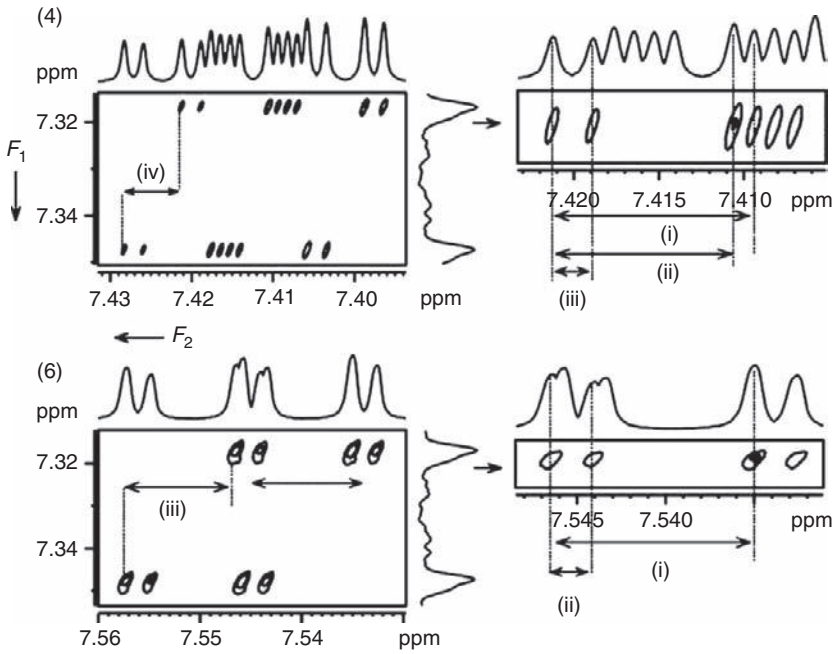

Figure 17 Expanded regions of spectrum corresponding to protons numbered H4 and H6 in Figure 15. The spectrum on the right side is the expansion of part of the spectrum at one of the spin state in the 4Q dimension. From the separations marked (i), (ii) and (iii) on the right side of (4), one can determine J_{34}, J_{45} and J_{46}. From the separations marked (i) and (ii) on the right side of (6), one can determine J_{56} and J_{46} (reproduced with permission from American Institute of Physics).

alone is not sufficient for the analyses. Such situations are most often encountered in molecules possessing more than one aromatic ring, where there will be severe overlap of numerous multiplet components arising from too many couplings of different magnitudes experienced by each interacting spin.[92–94] As an example, the 1D ^{1}H spectra of difluorinated benzanilides and their chemical structures are reported in Figure 18. Figure 18B–D contains the 1D spectra of 2-fluoro-*N*-(2-fluorophenyl)benzamide, 2-fluoro-*N*-(3-fluorophenyl)benzamide and 2-fluoro-*N*-(4-fluorophenyl)benzamide, respectively. In all these molecules, the coupling of NH proton with the remaining spins is undetectable and thus the proton NMR spectrum of each molecule pertains to the 10 interacting spins with 8 chemically inequivalent protons and 2 fluorines. The absence of symmetry element in the molecules indicates that the ^{1}H spectrum must display eight distinct proton chemical shifts. It is evident from Figure 18 that all the spectra are complex with many degenerate or near degenerate transitions from two phenyl rings, in addition to many short- and long-range scalar couplings experienced by each proton. Furthermore, many protons are resonating over a narrow spectral range. The severity of the spectral complexity is obvious from the 1D spectra (Figure 18C and D), especially in Figure 18D where the multiplets from five protons resonate within a spectral width of less than 0.12 ppm, depicting the

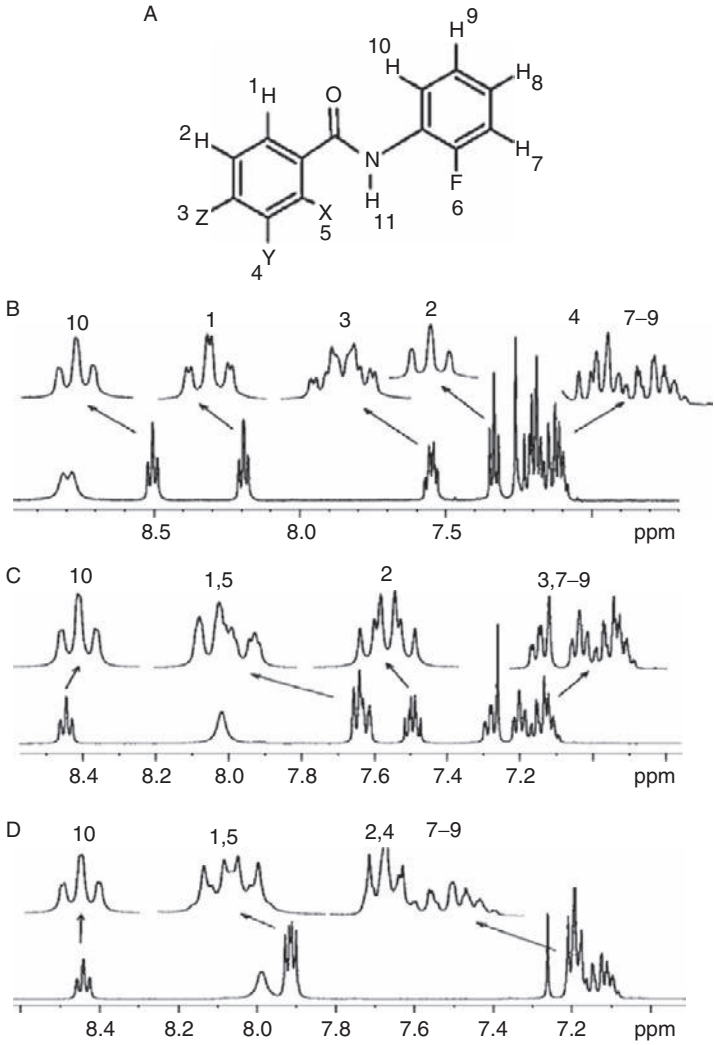

Figure 18 (A) The basic framework for the structures and numbering of interacting spins in difluorinated benzamides. The molecules are 2-fluoro-*N*-(2-fluorophenyl)benzamide (**1**), 2-fluoro-*N*-(3-fluorophenyl)benzamide (**2**) and 2-fluoro-*N*-(4-fluorophenyl)benzamide (**3**). In the basic molecular framework, for molecule (**1**) X = F and Y = Z = H, for molecule (**2**) X = Z = H and Y = F and for molecule (**3**) Z = F and X = Y = H; (B–D) 500-MHz ^{1}H NMR spectra of **1**, **2** and **3**, respectively, in the solvent $CDCl_3$. The expansions of the crowded regions are depicted by arrows (reproduced with permission from American Chemical Society).

significant loss of resolution and the challenging task in the resonance assignments. However, the interesting point is that the interacting spins between the two phenyl rings are separated by seven bonds and do not exhibit any detectable couplings among them. Hence, the spectrum of each molecule can be construed as an overlap of two independent five-spin spectra, one from each phenyl ring.

Nevertheless, for the unambiguous analyses, the identification of resonances pertaining to each phenyl ring and the unravelling of the overlapped transitions of four chemically inequivalent protons of each phenyl ring is a requirement.

The well-known 2D COSY spectrum can be employed to identify the coupled partners. The typical COSY spectrum of 2-fluoro-*N*-(4-fluorophenyl)benzamide (Figure 18D) is reported in Figure 19A. Though the COSY spectrum identifies the coupled partners it fails to discriminate the spin systems, especially those resonating in the high-field region. This is clear from the expanded region of the spectrum marked with a broken rectangle represented in Figure 19B. Since all the spins in each phenyl ring are coupled partners, the problem remains invariant even in the TOCSY spectra.

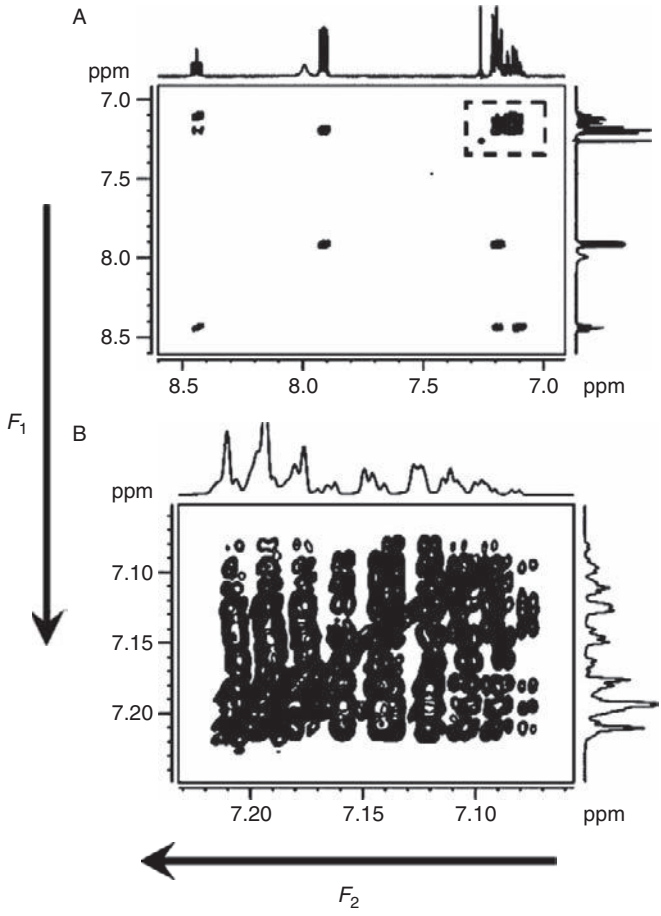

Figure 19 (A) The homonuclear ^1H–^1H COSY spectra of 2-fluoro-*N*-(4-fluorophenyl)benzamide (structure in Figure 18A) in the solvent $CDCl_3$, along with F_1 and F_2 projections. (B) The expanded region marked with broken rectangle in (A) indicates the spectral complexity and difficulty in identifying the coupled partners (reproduced with permission from American Chemical Society).

Therefore, the assignment of proton chemical shifts and the determination of coupling constants in such molecules are challenging tasks. Other techniques like soft-COSY, Z-COSY, etc., provide reduced multiplicity, but the problem of overlap of ^{1}H resonances from the two aromatic rings continues to persist. The MQ pulse sequence for spin topology filtering can also be explored. But the creation of MQ coherences is inhibited when the system departs from the specified topology. Also, MQ sequences for topological filtering can distinguish molecular fragments containing same number of spins but different coupling patterns and are applicable to molecules such as 3-fluoro-*N*-(4-fluorophenyl)benzamide. When the spin topological network of coupled protons is identical in both the rings as in the molecule 3-fluoro-*N*-(3-fluorophenyl)benzamide, the spin system filtering is difficult. Fluorine decoupling simplifies the spectrum but overlap of the spectra from two phenyl rings cannot be removed. In the following sections, several such examples where the MQ techniques can be exploited for the simplification of the analysis of such complex ^{1}H spectra are discussed.

6.1. Molecules containing two phenyl rings of identical spin topology

The two isomers of benzanilides, viz. 2-fluoro-*N*-(2-fluorophenyl)benzamide and 3-fluoro-*N*-(3-fluorophenyl)benzamide, fall under this category. The chemical structures with the numbering of interacting spins of these molecules are reported in Figure 20. The highest homonuclear MQ excitation possible in each of the two independent five-spin systems is fourth quantum of protons. The non-selective proton 4Q–SQ spectra of both the molecules are given below the respective chemical

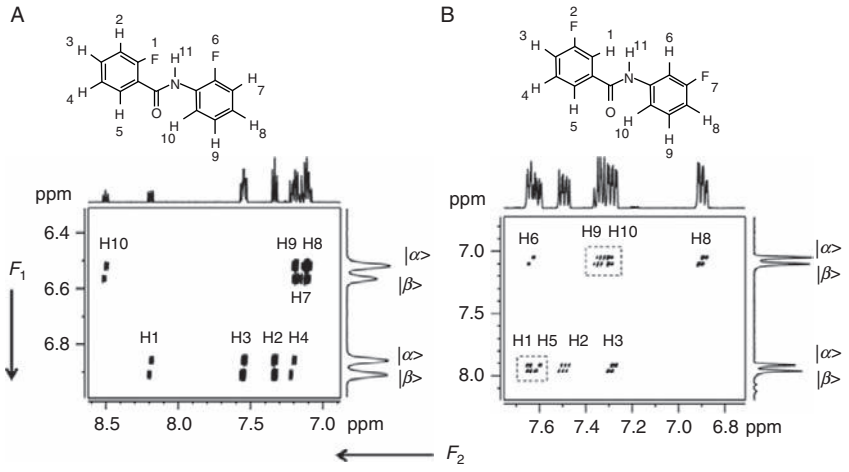

Figure 20 (A) The 500-MHz ^{1}H 4Q–SQ correlation spectra of the 2-fluoro-*N*-(2-fluorophenyl) benzamide along with F_1 and F_2 projections. (B) The 500-MHz ^{1}H 4Q–SQ correlation spectrum of 3-fluoro-*N*-(3-fluorophenyl)benzamide along with F_1 and F_2 projections. The four transitions in the 4Q dimension pertain to two spin states of ^{19}F of each phenyl ring marked as $|\alpha\rangle$ and $|\beta\rangle$, respectively. Chemical structure and numbering of interacting protons are given at the top of the 2D spectrum. Assignments of chemical shifts for different protons are also marked (reproduced with permission from American Chemical Society).

structures in Figure 20. Each molecule contains two phenyl rings of identical spin topology. The proton spectrum of the molecule pertains to 11 interacting spins with 9 protons and 2 fluorines. The NH proton of the molecule does not display any coupling with protons or fluorines, indicating that ^{1}H spectrum arises due to the interaction of eight chemically non-equivalent protons and two fluorines. The 1D ^{1}H spectrum does not display eight distinct chemical shifts in both the molecules (F_2 projections in Figure 20). For the unambiguous analyses of the spectrum, the unravelling of the overlapped transitions is a prerequisite. Being separated by seven bonds, the couplings between inter-ring spins are undetectable and hence the spectrum of each molecule can be construed as an overlap of two independent five-spin spectra. In both the molecules, four coupled protons and the fluorine of each phenyl ring pertain to the weakly coupled spin systems of the type AFKPX, where X is the ^{19}F spin and the remaining spins are protons. The ^{1}H-detected spectrum is the AFKP part of this AFKPX spin system. The 4Q–SQ correlation spectrum clearly identifies the sub-spectrum for each phenyl ring. In addition to filtering of the sub-spectrum for each spin system in the 4Q dimension, there is also additional splitting arising due to two spin states of ^{19}F. The sub-spectrum of each cross section contains only one-fourth the number of transitions compared to that of the 1D ^{1}H spectrum. Assignments to individual protons are significantly simplified after the separation of spectra for two independent spin systems. The assignment of peaks to the individual protons of the phenyl rings is straightforward and is marked in the figure. For both the molecules, cross section taken parallel to F_2 dimension at either $|\alpha\rangle$ or $|\beta\rangle$ spin state of ^{19}F for each phenyl ring position provides δ_{H} and J_{HH} pertaining to the particular phenyl ring.

In 2-fluoro-*N*-(2-fluorophenyl)benzamide (Figure 20A), the doublet near 6.88 ppm in the indirect dimension has been assigned to the phenyl ring with protons numbered H1–H5. Accordingly, the other doublet near 6.54 ppm is assigned to the phenyl ring with spins numbered H6–H10. The difference in the cumulative additive values of all the proton chemical shifts between two phenyl rings $[(\delta_{\mathrm{H1}}+\delta_{\mathrm{H2}}+\delta_{\mathrm{H3}}+\delta_{\mathrm{H4}})-(\delta_{\mathrm{H7}}+\delta_{\mathrm{H8}}+\delta_{\mathrm{H9}}+\delta_{\mathrm{H10}})]$ is 171.54 Hz and the corresponding value in the 4Q dimension is 171.43 Hz. The respective doublet separations in the 4Q dimension for these rings are 23.06 and 23.23 Hz. These values are the algebraic sums of all J_{HF} with appropriate sign combination. Similarly, for 3-fluoro-*N*-(3-fluorophenyl)benzamide (Figure 20B), the difference in sum of the chemical shifts $[(\delta_{\mathrm{H6}}+\delta_{\mathrm{H9}}+\delta_{\mathrm{H10}}+\delta_{\mathrm{H8}})-(\delta_{\mathrm{H1}}+\delta_{\mathrm{H5}}+\delta_{\mathrm{H2}}+\delta_{\mathrm{H3}})]$ between the phenyl rings is 435.11 Hz and the corresponding value in the 4Q dimension is 435.74 Hz. The doublet near 7.94 ppm is assigned to the phenyl ring which has protons numbered H1–H5 and the other doublet near 7.07 ppm is assigned to the phenyl ring which has protons numbered H6–H10.

6.2. Molecules containing two phenyl rings with different spin topologies

This section is focused on the analyses of the spectra of molecules with different spin topologies of the two phenyl rings. The chemical structures and the number of interacting spins, the corresponding 1D ^{1}H NMR spectra of molecules

belonging to this class, are already reported in Figure 18. The 4Q–SQ spectra of these molecules are reported in Figure 21. In 2-fluoro-*N*-(3-fluorophenyl)benzamide (Figure 21B), the nomenclature of spin systems in both the phenyl rings is AFKPX but with different topological network of coupled protons. However, in

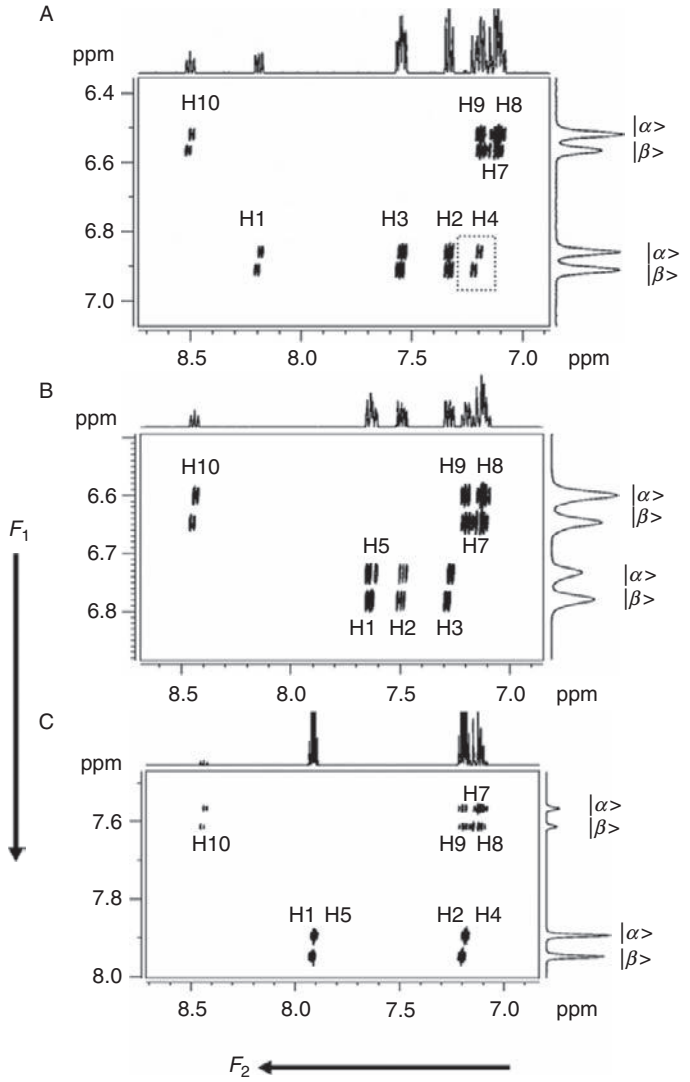

Figure 21 (A–C) The 500-MHz ^{1}H 4Q–SQ correlation spectra of the molecules 2-fluoro-*N*-(2-fluorophenyl)benzamide, 2-fluoro-*N*-(3-fluorophenyl)benzamide and 2-fluoro-*N*-(4-fluorophenyl) benzamide, respectively, along with F_1 and F_2 projections (structures are given in Figure 18A). The assignments of chemical shifts for different protons are also marked for each molecule. The four transitions in the 4Q dimension pertain to two spin states of ^{19}F of each phenyl ring marked $|\alpha\rangle$ and $|\beta\rangle$, respectively (reproduced with permission from Elsevier).

3-fluoro-*N*-(4-fluorophenyl)benzamide (Figure 21C), the spin systems are of the type AA′MM′X and AFKPX. It may be pointed out, though, that in spite of overlap of transitions the distinctly different peaks for both the phenyl rings have been filtered out in this molecule also. The first-order analyses of the spectra corresponding to both the phenyl rings in the molecule 2-fluoro-*N*-(3-fluorophenyl) benzamide and the ring with fluorine in the *meta*-position in the 3-fluoro-*N*-(4-fluorophenyl)benzamide molecule have been carried out analogous to the molecules discussed in the preceding section. The protons of the phenyl ring with fluorine in the *para*-position form ''nearly'' an AA′XX′ spin system due to accidental equivalence of protons and the first-order analysis of the spectrum of this strongly coupled spin system is not possible. The cross section taken along the SQ dimension at any spin states of ^{19}F in the 4Q dimension has provided a deceptively simple spectrum with only four transitions of significant intensity. Although heteronuclear couplings with the relative signs have been determined precisely for this ring, three homonuclear couplings have only been estimated.

6.3. Application to dihalogenated benzanilides

In this section, we concentrate on the spectra of dihalogen-substituted benzanilides. The molecules chosen for the study are 3-chloro-*N*-(2-fluorophenyl)benzamide, 3-bromo-*N*-(2-fluorophenyl)benzamide, 2-chloro-*N*-(2-fluorophenyl) benzamide and 2-bromo-*N*-(2-fluorophenyl)benzamide. Though the basic molecular framework is similar to difluorinated benzanilides discussed in the previous sections, the substitution of different halogens at different positions of the phenyl ring drastically alters the spectral complexity.[94] This is evident from the 1D spectra of these molecules given in Figure 22, especially for 3-chloro-*N*-(2-fluorophenyl)benzamide and 2-bromo-*N*-(2-fluorophenyl)benzamide. Moreover, the identification of peaks corresponding to the fluorinated phenyl ring is another task in these classes of molecules. The 4Q–SQ spectra of these molecules reported in Figure 23 have been employed to simplify the analyses of the 1D spectra.

The analyses of the MQ spectra of these molecules are similar to those discussed earlier. However, it may be pointed out that the spin-state selection is achieved only for the ring with ^{19}F substitution and is absent for the phenyl rings substituted with halogens. The 4Q dimension has three peaks, one of which is from the non-fluorinated ring and other are the doublets arising due to heteronuclear splitting with ^{19}F. This enables the discrimination of the peaks for fluorinated and non-fluorinated rings. The first-order analyses of these spectra are pretty straightforward and all the parameters have been determined precisely.

Therefore, in all the examples discussed in the previous sections, the higher quantum correlation studies have several distinct advantages, viz., (a) filter the sub-spectra for different spin systems, (b) identify the transitions belonging to fluorinated and non-fluorinated rings, (c) reduce the redundancy in the SQ transitions for each spin state of ^{19}F, (d) provide relative signs of couplings and (e) simplify the complexity of the spectrum by a factor of 2, as far as the

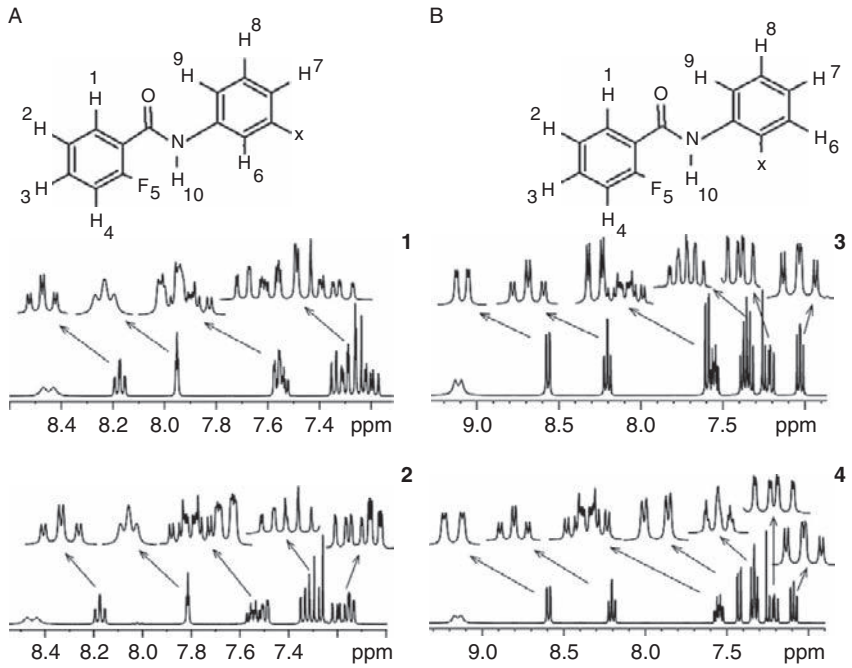

Figure 22 Molecular frame and the numbering of interacting spins, where X = Cl for the molecules 3-chloro-*N*-(2-fluorophenyl)benzamide (**1**) and 2-chloro-*N*-(2-fluorophenyl)benzamide (**3**) and X = Br for the molecules 3-bromo-*N*-(2-fluorophenyl)benzamide (**2**) and 2-bromo-*N*-(2-fluorophenyl)benzamide (**4**). The 400-MHz one-dimensional ^{1}H NMR spectra of molecules (A) 3-chloro-*N*-(2-fluorophenyl)benzamide and 3-bromo-*N*-(2-fluorophenyl)benzamide and (B) 2-chloro-*N*-(2-fluorophenyl)benzamide and 2-bromo-*N*-(2-fluorophenyl)benzamide. The expansions of the crowded regions are depicted by arrows (reproduced with permission from Wiley Interscience).

determination of the scalar couplings between the protons of the ^{19}F-substituted phenyl ring is concerned. All these advantages simplify the spectral analyses.

6.4. Relative signs of the couplings in halogenated benzanilides

The expanded regions of the 4Q–SQ spectrum (Figure 20B) pertaining to protons numbered H9 and H10 and for the protons numbered H1 and H5 are reported in Figure 24 for the molecule 3-fluoro-*N*-(3-fluorophenyl)benzamide. The opposite directions of tilts in (i) and (ii) in Figure 24A indicate that the relative signs of two J_{HF} (J_{79} and $J_{7,10}$) values are opposite. This is true even in Figure 24B and the signs of couplings J_{12} and J_{25} are opposite. However, due to negligibly small strengths of couplings, the opposite directions of tilts are not clearly evident in (i). Figure 24C contains the cross sections taken parallel to the F_2 dimension corresponding to spin states $|\alpha\rangle$ and $|\beta\rangle$ of ^{19}F of phenyl rings where the displacements of cross sections for peaks (i), (ii), (iii) and (iv) are for the spins numbered H10, H9, H6 and H8, respectively. In Figure 24D, the cross sections taken parallel to the F_2

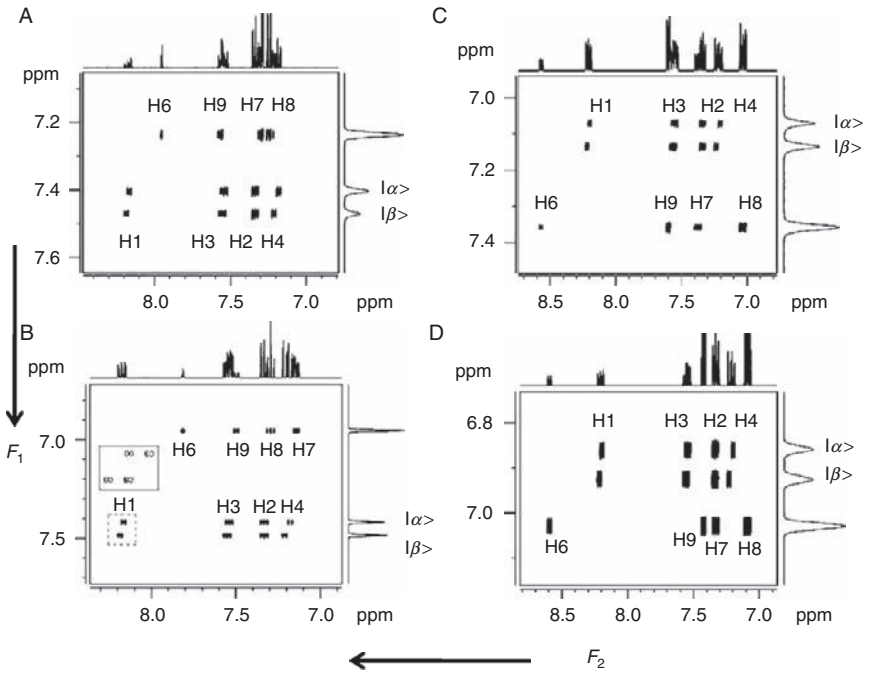

Figure 23 (A–D) The 400-MHz ^{1}H 4Q–SQ correlation spectra of molecules 3-chloro-*N*-(2-fluorophenyl)benzamide, 3-bromo-*N*-(2-fluorophenyl)benzamide, 2-chloro-*N*-(2-fluorophenyl)benzamide and 2-bromo-*N*-(2-fluorophenyl)benzamide, respectively, along with F_1 and F_2 projections. The two transitions in the 4Q dimension pertaining to two spin states of ^{19}F of the phenyl ring are marked as $|\alpha\rangle$ and $|\beta\rangle$, respectively. The assignments of chemical shifts for different protons are also marked (reproduced with permission from Wiley Interscience).

dimension corresponding to spin states ^{19}F of phenyl rings for the protons numbered H1–H5 are reported. The marked directions of displacements (i), (ii), (iii) and (iv) correspond to protons H1, H5, H2 and H3, respectively. The directions of tilt of the displacement vectors indicate that two J_{HF} are opposite in signs with respect to others. Another example of the molecule whose 4Q–SQ spectrum is reported in Figure 23B is plotted with an expanded scale in Figure 25. It is clear that even in this molecule, the tilt of the displacement vector for the proton H3 is opposite to that of the remaining three, indicating that the coupling J_{25} is opposite in sign relative to J_{15}, J_{35} and J_{45}.

7. SPIN-STATE-SELECTED DQ-*J*-RESOLVED SEQUENCE

In the previous sections the spin system filtering and the spin-state selection aided the analyses of the spectra and permitted the precise measure of spectral parameters. When the couplings are very small and comparable to line width, it is difficult to extract them from the cross sections of the 4Q spectrum due to the

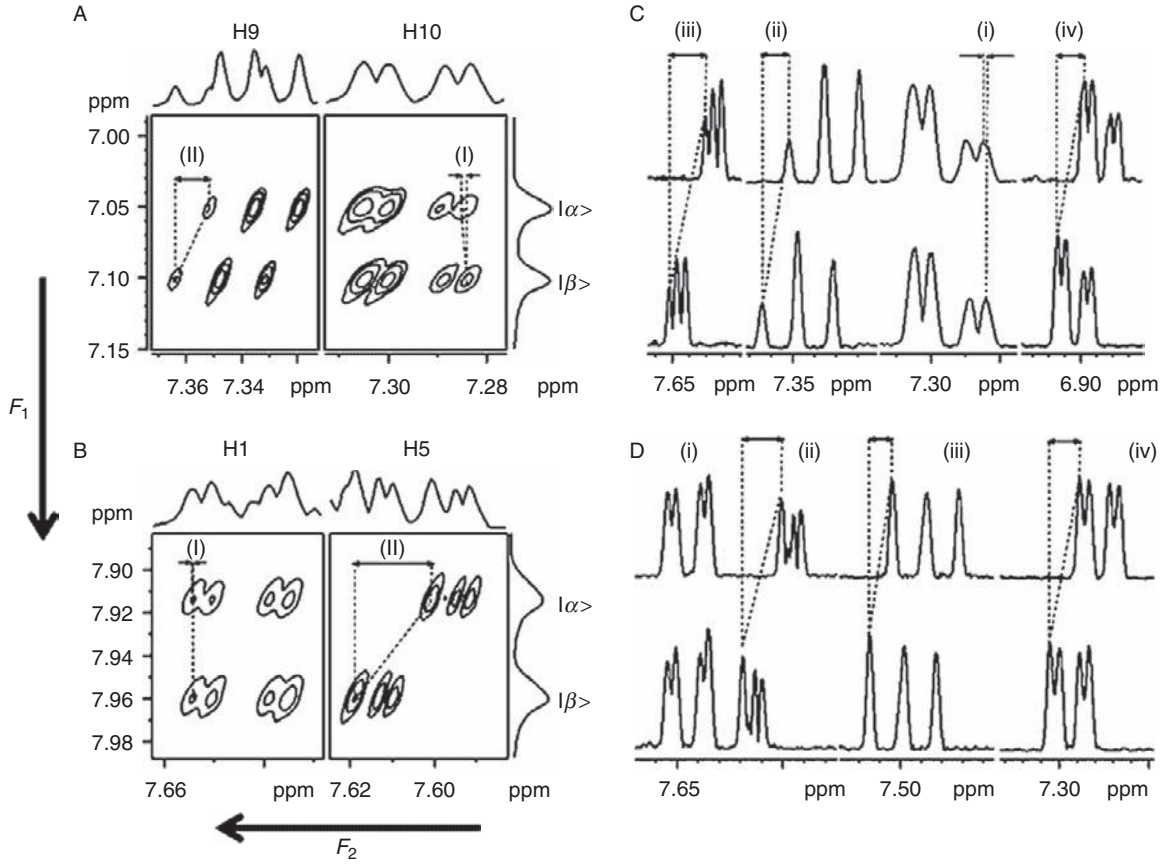

Figure 24 (A, B) Expansion of regions marked with broken rectangles in Figure 20B. (A) Expanded region for the protons numbered H9 and H10 and (B) expanded region for the protons numbered H1 and H5. The opposite direction of tilt in (i) and (ii) in (A) indicates that the relative signs of these two J_{HF} are opposite. This is true even in (B), but due to negligibly small couplings the opposite direction of tilt is not clearly evident. (C) The cross sections taken parallel to F_2 dimension corresponding to spin states $|\alpha\rangle$ and $|\beta\rangle$ of ^{19}F of phenyl rings where the displacements of cross sections for the peaks marked as (i), (ii), (iii) and (iv) are for the spins numbered 10, 9, 6 and 8, respectively; and (D) the cross sections taken parallel to F_2 dimension corresponding to spin states $|\alpha\rangle$ and $|\beta\rangle$ of ^{19}F of phenyl rings for the protons numbered H1, H2, H3 and H5. The marked directions of displacements (i), (ii), (iii) and (iv) correspond to protons H1, H5, H2 and H3, respectively (reproduced with permission from Wiley Interscience).

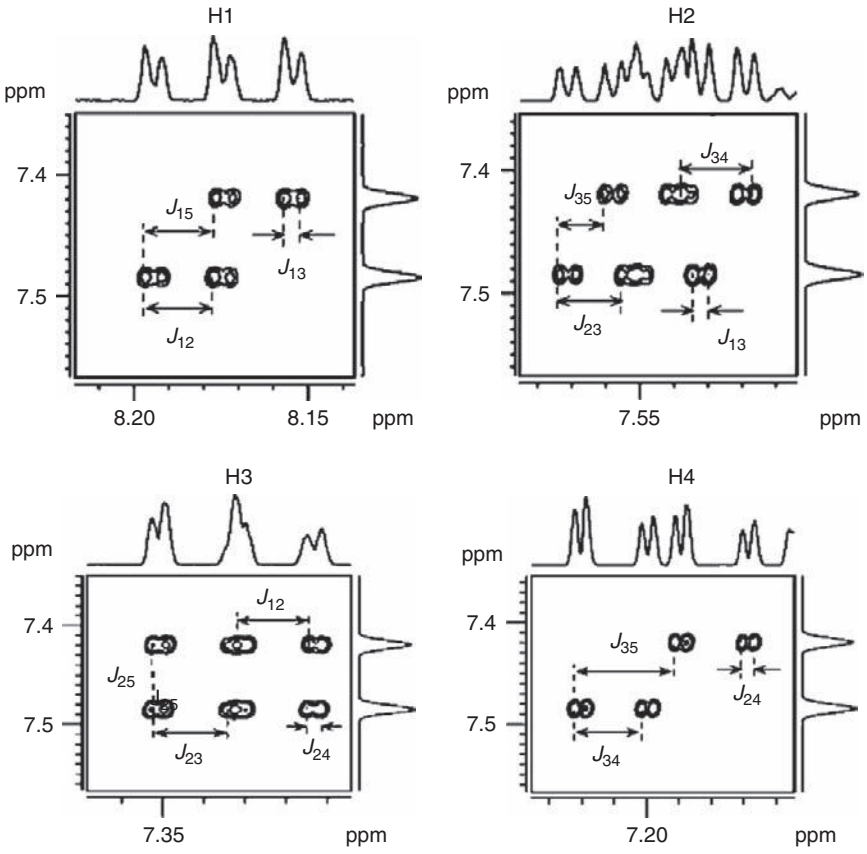

Figure 25 (A–D) The expanded regions of Figure 23A corresponding to protons H1–H4. The cross sections taken at the two spin states of ^{19}F and the displacements of cross sections giving J_{HF} are marked. It is clear that the tilt of the displacement for the proton H3 is opposite to that of the remaining three, indicating that this coupling is opposite in sign (reproduced with permission from Elsevier).

presence of all the homonuclear couplings and the complexity of the multiplet. However, it is possible to measure very small displacements between multiplets in different cross sections. In the spin-state-selective correlation experiment, the passive couplings are responsible for the displacements of the multiplets rather than splitting. Therefore, one of the approaches in measuring small couplings is to make these couplings passive and responsible for the displacement of cross sections. In achieving this goal, a method has been developed to separate the homonuclear couplings. The technique cited as DQ-*J*-resolved has been applied to many spin systems to determine scalar couplings of very low magnitudes.[85,86] The pulse sequence employs the DQ detection of any two proton spins. In the molecules containing ^{19}F, the complete decoupling of fluorine to all the protons in the DQ dimension will be an added advantage. This is achieved by a non-selective ^{1}H

pulse in the middle of DQ dimension, which however retains their couplings to passive proton spins for spin-state selection. In such a situation, the remaining two passive protons mimic the heteronuclei. The application of such pulse sequences is feasible in situations when the excitation profile does not interfere with the closely resonating spins.

7.1. Application of DQ-*J*-resolved experiment to 2-fluoropyridine

The DQ-*J*-resolved experiment with selective excitation and detection of DQ of protons H3 and H5 in 2-fluoropyridine (structure in Figure 14) and the simultaneous application of a non-selective 180° pulse on protons in the middle of t_1 dimension has been carried out. This retains only the sum of passive couplings to protons H4 and H6, while the sum of passive couplings to fluorine spin is refocused. Figure 26 shows this selective DQ-*J*-resolved spectrum. The experiment results in the spin-state selection of protons H4 and H6. The DQ dimension

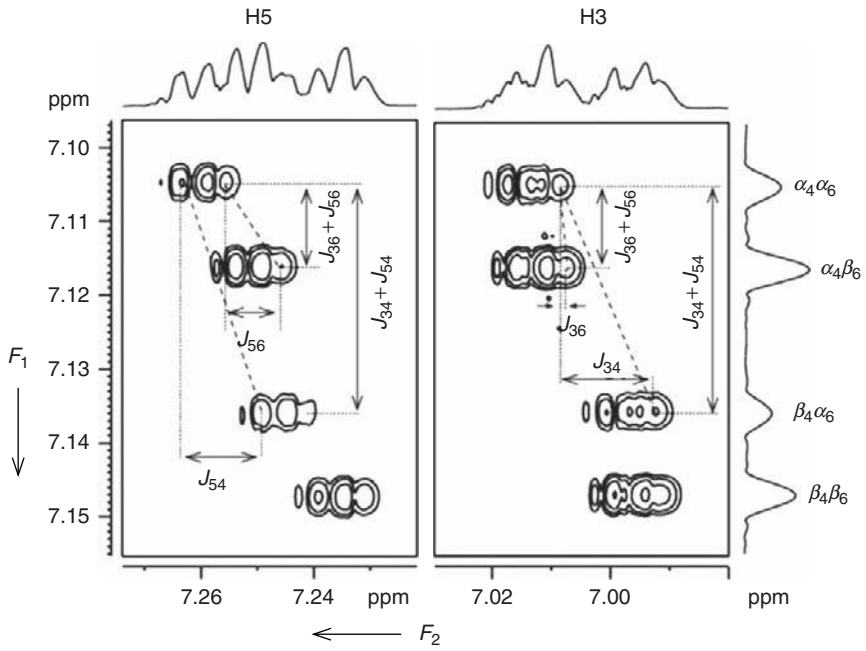

Figure 26 The 500-MHz two-dimensional spin-state-selected DQ-*J*-resolved spectrum of 2-fluoropyridine in actone-d_6. The protons numbered H3 and H5 are selectively excited and detected for DQ–SQ correlation. A non-selective 180° pulse is applied on protons in the middle of t_1 dimension to retain only the sum of passive couplings to protons numbered H4 and H6, while the sum of passive couplings to ^{19}F is refocused. The region of the spectrum is plotted only for H3 and H5. Two doublets in DQ dimension provide $J_{36}+J_{56}$ and $J_{34}+J_{45}$ as indicated. The two displacement vectors indicated for proton H3 provide J_{34} and J_{36}. The displacement vectors indicated for proton H5 provide J_{45} and J_{56} (reproduced with permission from American Institute of Physics).

provides the couplings of active protons H3 and H5 to passive protons H4 and H6. Each of these protons has spin states $|\alpha\rangle$ and $|\beta\rangle$ and in the spin product basis has four eigenstates $|\alpha_4\alpha_6\rangle$, $|\alpha_4\beta_6\rangle$, $|\beta_4\alpha_6\rangle$ and $|\beta_4\beta_6\rangle$, where the subscripts refer to protons H4 and H6, respectively. The DQ dimension in such a case is a doublet of a doublet with the large doublet separation providing $J_{34}+J_{54}$, while small doublet separation provides $J_{36}+J_{56}$ at the chemical shift positions of spins H3 and H5. In the SQ dimension, there are two displacement vectors for each of the spins H3 and H5. At the chemical shift position of H5, two displacements can be utilized to determine individual values of J_{56} and J_{45} as shown in Figure 26. The displacements at the chemical shift position of H3 can be exploited to derive individual values of J_{36} and J_{34}. Therefore, from a single experiment, the individual couplings J_{56}, J_{34} and J_{54} have been determined in the SQ dimension in addition to J_{36} which was difficult to extract from both 1D and 4Q–SQ experiments.

Application of 180° pulse in the middle of t_1 dimension removes the field inhomogeneity contributions. The DQ-*J*-resolved pulse sequence has several distinct advantages, viz., (a) separates very small proton couplings by sum of passive couplings, (b) reduces complexity by spin-state selection, (c) simultaneously decouples the fluorine to all the protons in DQ dimension, (d) displacement vectors provide relative signs of the homonuclear couplings and (e) overcomes the problem of field inhomogeneity. This technique has been further extended to complex molecules and they are discussed in the following sections.

7.2. DQ-*J*-resolved experiments on molecules containing two phenyl rings

In the 4Q–SQ spectrum of the molecule 3-fluoro-*N*-(3-fluorophenyl)benzamide reported in Figure 20B, the F_2 cross section at $|\alpha\rangle$ or $|\beta\rangle$ positions of ^{19}F reveals a triplet pattern for proton H9. The topology of the spin system suggests that $^3J_{89}$ and $^3J_{9,10}$ are of comparable magnitudes and can account for such a triplet. The long-range coupling $^5J_{69}$ responsible for additional splitting is not detected because of very small magnitude and hidden within the natural line width. This implies that cross sections of 4Q–SQ spectrum do not permit the measure of such smaller remote couplings. To measure all the remote couplings, two independent SSDQ-*J*-resolved experiments have been performed on this molecule. Figure 27A contains the SSDQ-*J*-resolved spectrum with selective excitation of protons H9 and H10 and with the simultaneous application of a non-selective 180° pulse on protons in the middle of t_1 dimension. In the DQ dimension, the pulse sequence retains only the sum of passive couplings to protons H6 and H8 (i.e. $J_{69}+J_{6,10}$ and $J_{89}+J_{8,10}$), while the couplings to fluorine spin are completely refocused. Each H6 and H8 has spin states $|\alpha\rangle$ and $|\beta\rangle$ and in the spin product basis has four eigenstates $|\alpha_6\alpha_8\rangle$, $|\alpha_6\beta_8\rangle$, $|\beta_6\alpha_8\rangle$ and $|\beta_6\beta_8\rangle$, where the subscript refers to protons H6 and H8. Thus, the DQ dimension will have four transitions with the large doublet separation providing $J_{89}+J_{8,10}$, while the smaller doublet separation provides $J_{69}+J_{6,10}$. The separation in the DQ dimension would be identical at the chemical shift positions of both the active spins. In the SQ dimension, there are two

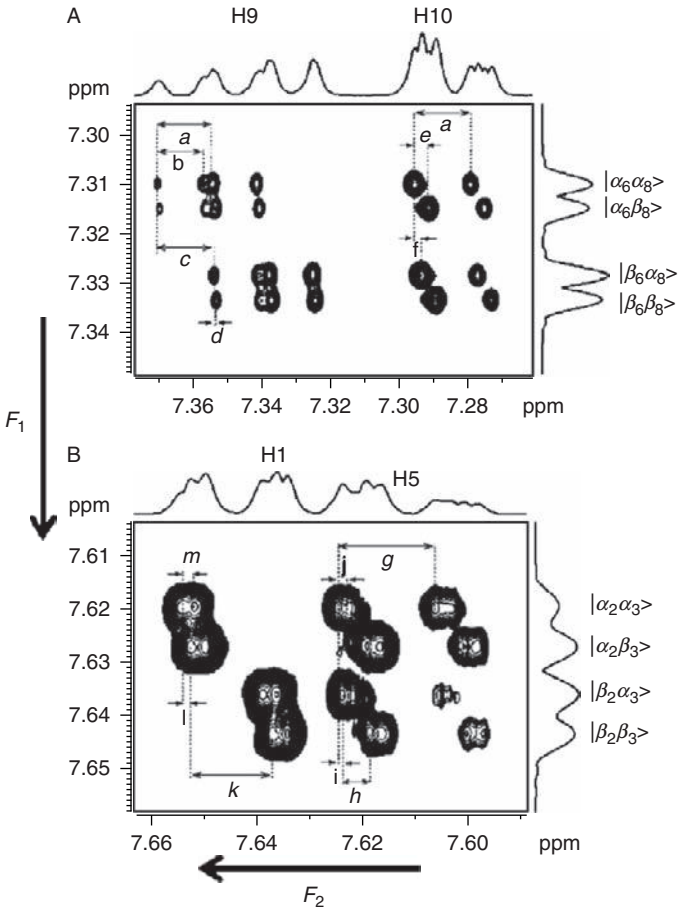

Figure 27 The SSDQ-*J*-resolved spectra of 3-fluoro-*N*-(3-fluorophenyl)benzamide in the isotropic solvent $CDCl_3$. (A) Spectrum corresponding to the selective double quantum excitation of protons H9 and H10. The displacements providing the coupling information are $a = J_{9,10}$, $b = J_{79}$, $c = J_{89}$, $d = J_{69}$, $e = J_{8,10}$ and $f = J_{6,10}$. The marked spin states in the DQ dimension correspond to the passive spins H6 and H8. (B) The spectrum corresponding to the selective excitation of protons H1 and H5. The marked spin states in the DQ dimension correspond to the passive protons H2 and H3. The displacements providing the coupling information are $g = J_{45}$, $h = J_{35}$, $i = J_{25}$, $j = J_{15}$, $k = J_{12}$, $l = J_{13}$ and $m = J_{15}$. Notice the advantage of the experiment in measuring the precise values of the smaller couplings (J_{13}, J_{25}, J_{69} and $J_{6,10}$) which were difficult to measure from the other experiments (reproduced with permission from Elsevier).

displacement vectors for each of the protons H9 and H10 which provide both active and passive couplings. The two displacements at the chemical shift position of proton H9 can be utilized to determine individual values of J_{89} and J_{69}. The displacements at the chemical shift position of proton H10 can be exploited to derive individual values of $J_{8,10}$ and $J_{6,10}$. Thus from SSDQ-*J*-resolved experiment, the couplings which were difficult to extract from the 4Q–SQ experiment have

been determined more precisely. Figure 27B contains similar DQ-*J*-resolved experiment with selective excitations of protons H1 and H5. In this situation the protons H2 and H3 are passive. The different displacements providing the coupling information from both these experiments are marked with alphabets. Figure 28 contains the two different DQ-*J*-resolved spectra, with selective

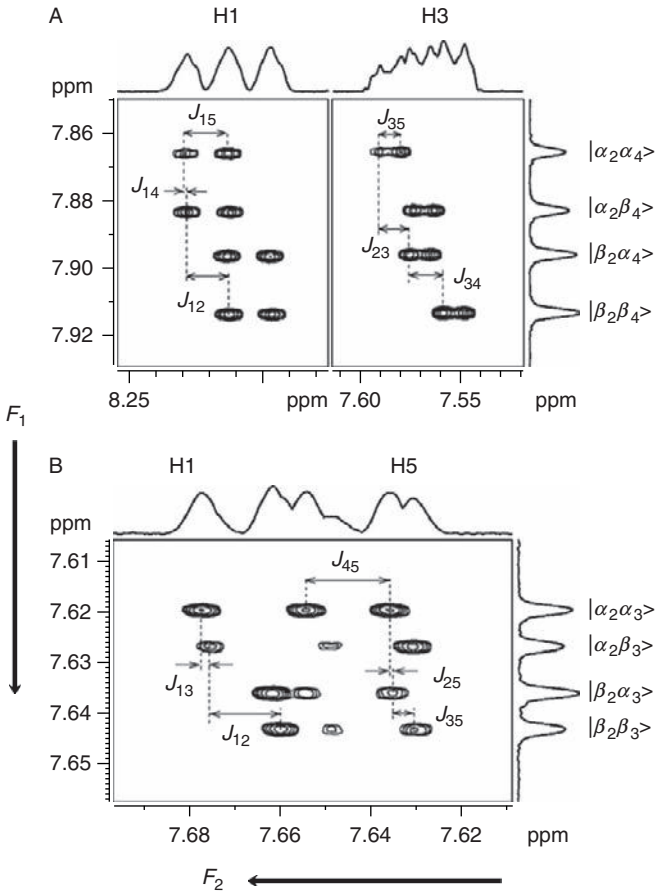

Figure 28 (A) The SSDQ-*J*-resolved spectra of 2-fluoro-*N*-(2-fluorophenyl)benzamide (structure is given in Figure 20) in the isotropic solvent $CDCl_3$ with the biselective excitation of protons H1 and H3. The marked spin states in the DQ dimension correspond to the passive spins H2 and H4. The separations providing the coupling information have been marked. Notice the smaller values of the coupling (J_{14}) that could be measured from this experiment which were hindered in the 4Q–SQ correlation experiment. (B) The SSDQ-*J*-resolved spectra of 2-fluoro-*N*-(3-fluorophenyl)benzamide in the isotropic solvent $CDCl_3$ with the selective excitation of protons H1 and H5. The marked spin states in the DQ dimension correspond to the passive spins H2 and H3. The separations providing the coupling information have been marked. Notice the smaller values of the couplings (J_{13} and J_{25}) that could be measured from this experiment which were hindered in the 4Q–SQ correlation experiment (reproduced with permission from Elsevier).

excitations of protons H1 and H3 and also H1 and H5 of another molecule, 2-fluoro-*N*-(2-fluorophenyl)benzamide (Figure 20A). In the first experiment (Figure 28A), the passive spins are H2 and H4 and in the second experiment (Figure 28B) the passive spins are H2 and H3. The separations and the displacements of cross sections providing various couplings have been marked in the figures. These experiments also permitted the determination of negligibly smaller couplings.

8. SPIN-SELECTED 3Q-*J*-RESOLVED EXPERIMENTS

As discussed in the preceding section, the DQ-*J*-resolved experiment provided remote couplings in case of phenyl rings in 2-fluoro-*N*-(2-fluorophenyl)benzamide.[93,94] For the extraction of remote couplings among protons in one of the phenyl rings is very tedious due to severe overlap of the transitions from the protons H7, H8 and H9. Therefore, the selective excitation of any two protons of this ring is impossible without disturbing the remaining protons. However, selective excitation of three protons H7, H8 and H9 is not precluded. Therefore, analogous to SSDQ-*J*-resolved experiment, another spin-selective 3Q (SS3Q)-*J*-resolved experiment has been carried out[93,94] on both of these molecules. The decoupling of ^{19}F by the π pulse in the t_1 dimension provided a doublet in the 3Q dimension due to splitting from the $|\alpha\rangle$ and $|\beta\rangle$ spin states of passive proton H10 with a separation equal to $J_{7,10}+J_{8,10}+J_{9,10}$. The displacement of cross sections aided the direct measurement of $^3J_{HH}$, $^4J_{HH}$ and $^5J_{HH}$ to proton H10. The displacements and the peak separations providing the couplings are marked in Figure 29. The inspection of the directions of the tilts marked in the figure also reveals that $^3J_{HH}$, $^4J_{HH}$ and $^5J_{HH}$ have similar signs. The application of 4Q–SQ correlated, SSDQ-*J*-resolved and SS3Q-*J*-resolved spectra has provided the precise values of long-range couplings in the investigated molecules.

9. OPTIMIZATION OF τ DELAY IN SSMQ-*J*-RESOLVED EXPERIMENTS

The complex situations are encountered in the molecules 3-chloro-*N*-(2-fluorophenyl)benzamide and 3-bromo-*N*-(2-fluorophenyl)benzamide for the selective excitation of any two protons without disturbing the spins from the other ring as the transitions are severely overlapped. For example, in the 4Q–SQ spectrum of molecule 3-bromo-*N*-(2-fluorophenyl)benzamide (Figure 23D), the transitions from the protons H2, H3 and H4 of one ring, H7, H8 and H9 of the other ring are severely overlapped. Thus, the derivation of remote couplings by selective DQ excitation in such a situation is challenging. In combating this difficulty, the knowledge of approximate coupling strengths has been utilized for the optimization of the τ delay for selective excitation of protons in the crowded region.[94] The bunch of resonances (H7 and H8) is dominated by scalar coupling J_{78} (nearly 8 Hz) rather than J_{24} (nearly 2 Hz). The τ delay has been appropriately optimized for the DQ excitation of protons H7 and H8. There is an excellent suppression of the

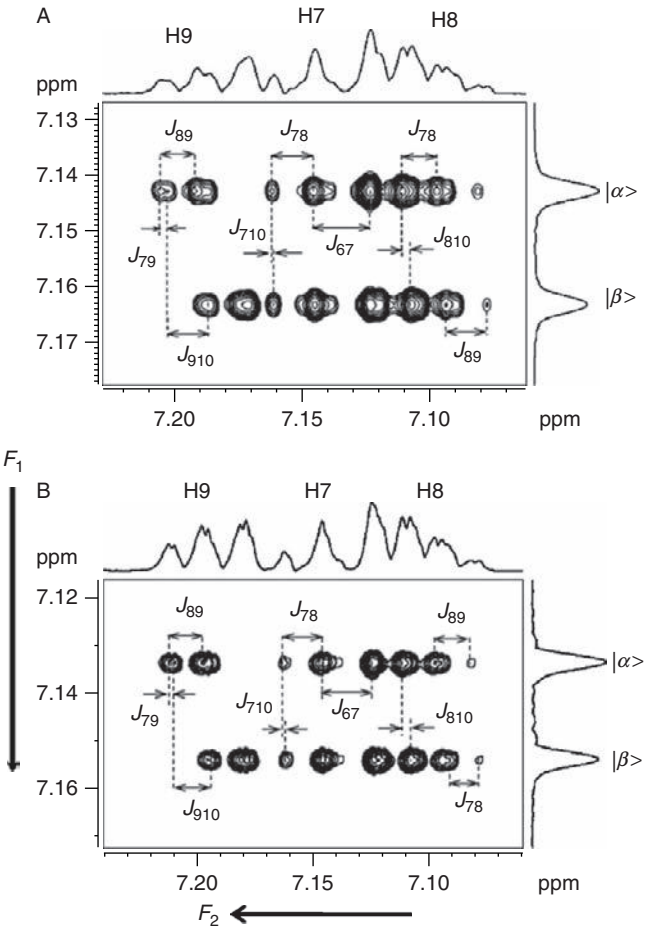

Figure 29 (A, B) The SS3Q-*J*-resolved spectra of 2-fluoro-*N*-(2-fluorophenyl)benzamide and 2-fluoro-*N*-(4-fluorophenyl)benzamide (structures are given in Figure 18), respectively, in the isotropic solvent $CDCl_3$ with the selective excitation of protons H7, H8 and H9. The marked spin states $|\alpha\rangle$ and $|\beta\rangle$ in the 3Q dimension correspond to the passive spin states of proton H10. For 2-fluoro-*N*-(2-fluorophenyl)benzamide, the separations providing the coupling information have been identified. Notice the smaller values of the coupling ($J_{7,10}$) that could be measured from this experiment which was difficult to obtain from the other experiments. The direction of the tilts indicates that the couplings $J_{7,10}$, $J_{8,10}$ and $J_{9,10}$ have similar signs (reproduced with permission from Elsevier).

transitions pertaining to the protons H2 and H4 as the strength of coherence transfer is insufficient to enhance the signal intensity. This is clearly evident from the 2D spectrum given in Figure 30A. Moreover, the signals along DQ axis are distinctly separated to provide the required coupling information. Precise long-range couplings that were difficult to extract from the 1D spectrum have been determined. Similar experiment on the molecule 3-chloro-

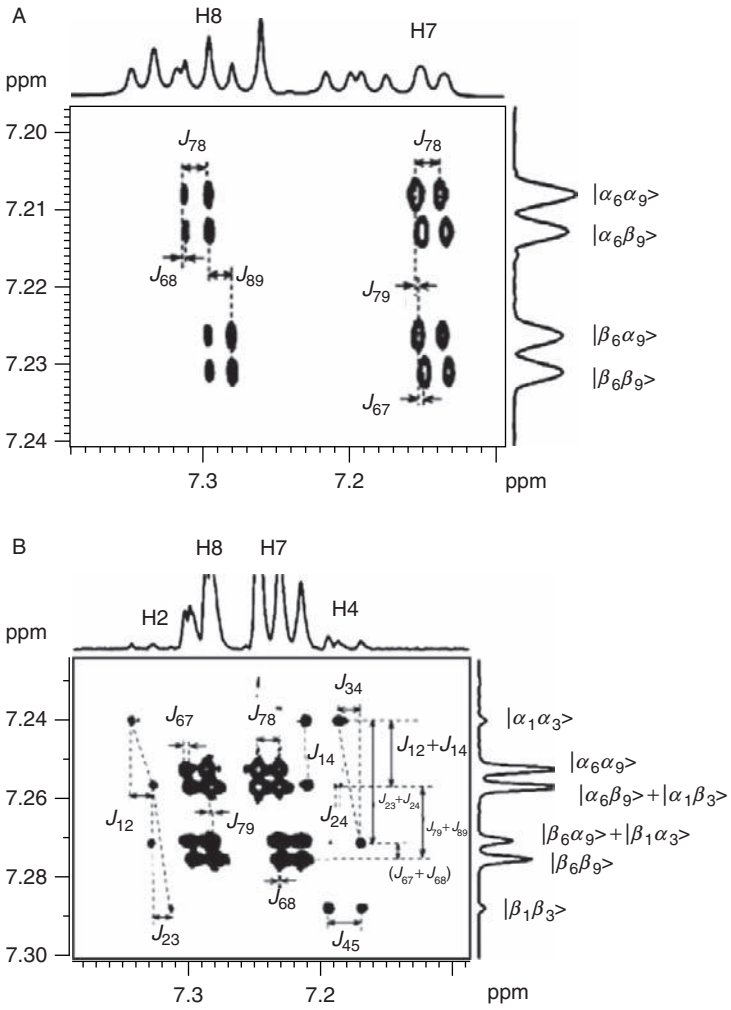

Figure 30 (A) The spectrum corresponding to the selective excitation of protons H7 and H8 in the molecule 3-bromo-*N*-(2-fluorophenyl)benzamide (structure is given in Figure 22). The marked spin states in the DQ dimension correspond to the passive spins H6 and H9. The marked separations provide the couplings, viz. J_{67}, J_{68}, J_{78} and J_{89}. Notice the advantage of the experiments in measuring the precise values of the smaller couplings (J_{68}) which are difficult to measure from other experiments. (B) The SSDQ-*J*-resolved spectra of molecule 3-chloro-*N*-(2-fluorophenyl) benzamide with the selective excitation of protons H2, H4, H7 and H8 adapting the strategy of optimizing the τ value for excitation of coherences of selected coupled partners (reproduced with permission from Wiley Interscience).

N-(2-fluorophenyl)benzamide has also been carried out on protons H7 and H8. The chemical shift difference between two protons is much less compared to the previously discussed molecule and the DQ excitation of these protons is even more challenging. The τ delay was optimized for the simultaneous and selective

excitation of H7 and H8 as well as H2 and H4 protons, although the intensity for the DQ excitation of H2 and H4 protons is relatively weak. This spectrum is reported in Figure 30B. The measurable couplings are marked in the figure.

10. CONCLUSIONS

Excitation of homonuclear highest quantum coherence in a heteronuclear spin system or by $N-1$ or lower order ($N \neq 1$) spin-selective excitation of MQ in homonuclear N spin system results in a situation where each state of the passive spins in the MQ dimension encodes the spin states involved in the SQ transitions that arise only due to coupling between active spins. This results in the spin-state-selective detection of SQ transitions based on the spin state of passive spin(s) in MQ dimension. The cross section taken along SQ dimension for any one of the passive spin state has sufficient number of transitions essential to determine the couplings between the active spins. Further active and passive couplings are separated from each other in different dimensions. The individual passive couplings can be determined from the displacements of the multiplets in the SQ dimension. Thus, the redundancy in the number of transitions required to extract the active couplings is significantly reduced. The dynamics of the spins in the spin-selective and non-selective excitations of DQ is discussed for a weakly coupled AMX spin system using both product operator and polarization operator formalisms. The effect of magnetic field inhomogeneity has also been suppressed in the selective excitation experiments. The pulse sequence for double and triple quantum selective *J*-resolved experiments not only decouples the heteronuclei but also permits the measure of small proton couplings in the MQ dimension. The experiments serve as invaluable tools to simplify the analyses of complex ^{1}H NMR spectra of scalar-coupled spins.

ACKNOWLEDGEMENT

Author gratefully acknowledges the financial support by the Department of Science and Technology, New Delhi for the Grant No. SR/S1/PC-13/2008.

REFERENCES

1. R. R. Ernst, G. Bodenhausen and A. Wokaun, Principles of Nuclear Magnetic Resonance in One and Two Dimensions. Clarendon Press, Oxford, 1991.
2. J. Cavanagh, W. J. Fairbrother, A. G. Palmer, III, M. Rance and N. J. Skelton, NMR Spectroscopy: Principles and Practice. 2nd ed. Elsevier Academic Press, Amsterdam, 2007.
3. G. S. Rule and T. K. Hitchens, Fundamentals of Protein NMR Spectroscopy. Springer, The Netherlands, 2006.
4. T. D. W. Claridge, High Resolution NMR Techniques in Organic Chemistry. 2nd ed. Elsevier, Amsterdam, 2009.
5. H. Günther, NMR Spectroscopy: Basic Principles, Concepts, and Applications in Chemistry. John Wiley and Sons, New York, 1992.
6. J. Keeler, Understanding NMR Spectroscopy. John Wiley and Sons, England, 2005.

7. D. Neuhaus, G. Wagner, M. Vasak, J. H. R. Kaegi and K. Wuthrich, Systematic application of high-resolution, phase-sensitive two-dimensional ^{1}H-NMR techniques for the identification of the amino-acid-proton spin systems in proteins: Rabbit metallothionein-2. *Eur. J. Biochem.*, 1985, **151,** 257.
8. L. E. Kay and A. Bax, New methods for the measurement of NH—CαH coupling constants in ^{15}N-labeled proteins. *J. Magn. Reson.*, 1990, **86,** 110.
9. S. Heikkinen, H. Aitio, P. Permi, R. Folmer, K. Lappalaonen and I. Kilpelainen, J-multiplied HSQC (MJ-HSQC): A new method for measuring ^{3}J(HNHα) couplings in^{15}N-labeled proteins. *J. Magn. Reson.*, 1999, **137,** 243.
10. A. Bax and R. Freeman, Investigation of complex networks of spin-spin coupling by two-dimensional NMR. *J. Magn. Reson.*, 1981, **44,** 542.
11. C. Griesinger, O. W. Sorensen and R. R. Ernst, Correlation of connected transitions by two-dimensional NMR spectroscopy. *J. Chem. Phys.*, 1986, **85,** 6837.
12. G. T. Montelione, M. E. Winker, P. Rauenbuehler and G. Wagner, Accurate measurements of long-range heteronuclear coupling constants from homonuclear 2D NMR spectra of isotope-enriched proteins. *J. Magn. Reson.*, 1989, **82,** 198.
13. O. W. Sørensen, Three- and four-dimensional NMR experiments for measurement of spin-spin coupling constants. *J. Magn. Reson.*, 1990, **90,** 433.
14. C. Griesinger, O. W. Sørensen and R. R. Ernst, Two-dimensional correlation of connected NMR transitions. *J. Am. Chem. Soc.*, 1985, **107,** 6394.
15. U. Eggenberger, Y. Karimi-Nejad, H. Thüring, H. Rüterjans and C. Griesinger, Determination of Hα, Hβ and Hβ, C′ coupling constants in ^{13}C-labeled proteins. *J. Biomol. NMR*, 1992, **2,** 583.
16. J. M. Schmidt, R. R. Ernst, S. Aimoto and M. Kainosho, Determination of heteronuclear three-bond J-coupling constants in peptides by a simple heteronuclear relayed E.COSY experiment. *J. Biomol. NMR*, 1995, **6,** 95.
17. P. Andersson, K. Nordstrand, M. Sunnerhagen, E. Liepinsh, I. Turovskis and G. Otting, Heteronuclear correlation experiments for the determination of one-bond coupling constants. *J. Biomol. NMR*, 1998, **11,** 445.
18. M. D. Sørensen, J. J. Led and O. W. Sørensen, A new 2D NMR method for measurement of J_{HH} coupling constants. *J. Biomol. NMR*, 1994, **4,** 135.
19. A. Bax, D. Max and D. Zax, Measurement of long-range ^{13}C-^{13}C J couplings in a 20-kDa protein-peptide complex. *J. Am. Chem. Soc.*, 1992, **114,** 6923.
20. B. Reif, M. Köck, R. Kerssebaum, J. Schleucher and C. Griesinger, Determination of ^{1}J, ^{2}J, and ^{3}J Carbon–Carbon Coupling Constants at Natural Abundance. *J. Magn. Reson. B*, 1996, **112,** 295.
21. J. S. Hu and A. Bax, Determination of ϕ and χ_1 Angles in Proteins from ^{13}C$-^{13}$C Three-Bond J Couplings Measured by Three-Dimensional Heteronuclear NMR. How Planar Is the Peptide Bond? *J. Am. Chem. Soc.*, 1997, **119,** 6360.
22. K. Furihata and H. Seto, A new NMR method for measuring proton–proton spin coupling constants: J-resolved HMQC. *Tetrahedron Lett.*, 2001, **42,** 899.
23. M. L. Liu, R. D. Farrant, J. M. Gillam, J. K. Nicholson and J. C. Lindon, Selective inverse-detected long-range heteronuclear J-resolved NMR spectroscopy and its application to the measurement of ^{3}JCH. *J. Magn. Reson. B*, 1995, **109,** 275.
24. K. Furihata and H. Seto, J-Resolved HMBC, a new NMR technique for measuring heteronuclear long-range coupling constants. *Tetrahedron Lett.*, 1999, **40,** 6271.
25. A. Mucci, F. Parenti and L. Schenetti, On the Recovery of $^{3}J_{H,H}$ and the Reduction of Molecular Symmetry by Simple NMR Inverse Detection Experiments. *Eur. J. Org. Chem.*, 2002, 938.
26. K. E. Kover and K. Feher, Measurement of one-bond heteronuclear dipolar coupling contributions for amine and diastereotopic methylene protons. *J. Magn. Reson.*, 2004, **168,** 307.
27. V. Rutar and T. C. Wong, Utilization of the improved resolution in two-dimensional polarization transfer NMR. *J. Magn. Reson.*, 1983, **53,** 495.
28. G. A. Morris, Indirect two-dimensional J spectroscopy: Measurement of proton multiplet structure via carbon-13 signals. *J. Magn. Reson.*, 1981, **44,** 277.
29. A. Bax, R. Freeman and G. A. Morris, A simple method for suppressing dispersion-mode contributions in NMR spectra: The ''pseudo echo'' *J. Magn. Reson.*, 1981, **43,** 333.

30. A. J. Pell and J. Keeler, Two-dimensional J-spectra with absorption-mode lineshapes. *J. Magn. Reson.*, 2007, **189,** 293.
31. M. J. Thrippleton, R. A. E. Edden and J. Keeler, Suppression of strong coupling artefacts in J-spectra. *J. Magn. Reson.*, 2005, **174,** 97.
32. B. Luy, Adiabatic z-filtered J-spectroscopy for absorptive homonuclear decoupled spectra. *J. Magn. Reson.*, 2009, **201,** 18.
33. G. Bodenhausen, R. Freeman and D. L. Turner, Two-dimensional J spectroscopy: Proton-coupled carbon-13 NMR. *J. Chem. Phys.*, 1976, **65,** 839.
34. L. Muller, A. Kumar and R. R. Ernst, Two-dimensional carbon-13 spin-echo spectroscopy. *J. Magn. Reson.*, 1977, **25,** 383.
35. P. Bachmann, W. P. Aue, L. Muller and R. R. Ernst, Phase separation in two-dimensional spectroscopy. *J. Magn. Reson.*, 1977, **28,** 29.
36. R. Freeman, The relative signs of N.M.R. spin coupling constants from double irradiation experiments. *Mol. Phys.*, 1961, **4,** 385.
37. W. S. Brey, L. W. Jaques and H. J. Jakobsen, A ^{13}C-{^{1}H} double resonance study of the signs of ^{1}H-^{19}F and ^{13}C-^{19}F spin coupling constants in fluorobenzenes and 2-fluoropyridine. *Org. Magn. Reson.*, 1979, **12,** 243.
38. H. Oschkinat, A. Pastor, P. Pfändler and G. Bodenhausen, Two-dimensional correlation of directly and remotely connected transitions by z-filtered COSY. *J. Magn. Reson.*, 1986, **69,** 559.
39. R. Brüschweiler, J. C. Madsen, C. Griesinger, O. W. Sørensen and R. R. Ernst, Two-dimensional NMR spectroscopy with soft pulses. *J. Magn. Reson.*, 1987, **73,** 380.
40. J. Jarvet and P. Allard, Phase-sensitive two-dimensional heteronuclear zero- and double-quantum-coherence spectroscopy. *J. Magn. Reson. B*, 1996, **112,** 240.
41. N. C. Nielsen, H. Thøgersen and O. W. Sørensen, A systematic strategy for design of optimum coherent experiments applied to efficient interconversion of double- and single- quantum coherences in nuclear magnetic resonance. *J. Chem. Phys.*, 1996, **105,** 3962.
42. G. Otting, A DQ/ZQ NMR experiment for the determination of the signs of small J(^{1}H,^{13}C) coupling constants in linear spin systems. *J. Magn. Reson.*, 1997, **124,** 503.
43. G. K. Pierens, T. A. Carpenter, L. D. Colebrook, L. D. Field and L. D. Hall, Selection of multiple-quantum spectra of molecules in liquid-crystalline solution using pulsed magnetic field gradients. *J. Magn. Reson.*, 1969, **99,** 398.
44. J. M. Polson and E. E. Burnell, A multiple-quantum ^{1}H NMR study of partially oriented biphenylene. *J. Magn. Reson. A*, 1994, **106,** 223.
45. J. C. T. Rendell and E. E. Burnell, Frequency-selective excitation in multiple-quantum NMR. *J. Magn. Reson. A*, 1995, **112,** 1.
46. T. Chandrakumar, J. M. Polson and E. E. Burnell, A multiple-quantum^{1}H NMR study of conformational biasing of biphenyl in a nematic liquid crystal. *J. Magn. Reson. A*, 1996, **118,** 264.
47. G. Celebre, F. Castiglione, M. Longeri and J. W. Emsley, The NMR spectra of samples dissolved in liquid-crystalline phases. automatic analysis with the aid of multiple-quantum spectra. *J. Magn. Reson. A*, 1996, **121,** 139.
48. J. M. Polson and E. E. Burnell, Conformational equilibrium and orientational ordering: ^{1}H-nuclear magnetic resonance of butane in a nematic liquid crystal. *J. Chem. Phys.*, 1995, **103,** 6891.
49. M. H. Levitt and R. R. Ernst, Spin-pattern recognition in high-resolution proton NMR spectroscopy. *Chem. Phys. Lett.*, 1983, **100,** 119.
50. M. H. Levitt and R. R. Ernst, Multiple-quantum excitation and spin topology filtration in high-resolution NMR. *J. Chem. Phys.*, 1985, **83,** 3297.
51. T. J. Norwood, Multiple-quantum NMR methods. *Prog. NMR Spectrosc.*, 1992, **24,** 295.
52. G. Bodenhausen, Multiple-quantum NMR. *Prog. NMR Spectrosc.*, 1980, **14,** 137.
53. W. S. Warren and A. Pines, Analogy of multiple-quantum NMR to isotopic spin labeling. *J. Am. Chem. Soc.*, 1981, **103,** 1613.
54. W. S. Warren, J. B. Murdoch and A. Pines, Computer simulations of multiple-quantum NMR experiments. II. Selective excitation. *J. Magn. Reson.*, 1984, **60,** 236.
55. W. S. Warren and A. Pines, Experiments on selective excitation of multiple-quantum transitions in NMR spectroscopy. *J. Chem. Phys.*, 1981, **74,** 2808.

56. W. S. Warren and A. Pines, Simple pulse sequences for selective multiple-quantum excitation. *Chem. Phys. Lett.*, 1982, **88,** 441.
57. D. P. Weitekamp, J. R. Garbow and A. Pines, Determination of dipole coupling constants using heteronuclear multiple quantum NMR. *J. Chem. Phys.*, 1982, **77,** 2870.
58. J. B. Murdoch, W. S. Warren, D. P. Weitekamp and A. Pines, Computer simulations of multiple-quantum NMR experiments. I. Nonselective excitation. *J. Magn. Reson.*, 1984, **60,** 205.
59. M. Munowitz and A. Pines, Multiple-quantum nuclear magnetic resonance spectroscopy. *Science*, 1986, **233,** 525.
60. L. Braunschweiler, G. Bodenhausen and R. R. Ernst, Analysis of networks of coupled spins by multiple quantum N.M.R.. *Mol. Phys.*, 1983, **48,** 535.
61. P. Permi and A. Annila, Transverse relaxation optimised spin-state selective NMR experiments for measurement of residual dipolar couplings. *J. Biomol. NMR*, 2000, **16,** 221.
62. A. Meissner, J.Ø. Duus and O. W. Sørensen, Spin-state-selective excitation. Application for E.COSY-type measurement of J_{HH} coupling constants. *J. Magn. Reson.*, 1997, **128,** 92.
63. A. Meissner, J.Ø. Duus and O. W. Sørensen, Integration of spin-state-selective excitation into 2D NMR correlation experiments with heteronuclear ZQ/2Q Π rotations for $^1J_{XH}$. *J. Biomol. NMR*, 1997, **10,** 89.
64. M. D. Sørensen, A. Meissner and O. W. Sørensen, Spin-state-selective coherence transfer via intermediate states of two-spin coherence in IS spin systems: Application to E.COSY-type measurement of J coupling constants. *J. Biomol. NMR*, 1997, **10,** 181.
65. A. Meissner, T. Schulte-Herbrüggen and O. W. Sørensen, Spin-state-selective polarization or excitation for simultaneous E.COSY-type measurement of $^3J(C',H^\alpha)$ and $^3J(H^N,H^\alpha)$ Coupling Constants with Enhanced Sensitivity and Resolution in multidimensional NMR spectroscopy of $^{13}C,^{15}N$-labeled proteins. *J. Am. Chem. Soc.*, 1998, **120,** 3803.
66. J. Briand and O. W. Sørensen, Simultaneous and independent rotations with arbitrary flip angles and phases for I, IS^α, and IS^β spin systems. *J. Magn. Reson.*, 1998, **135,** 44.
67. P. Nolis and T. Parella, Simultaneous α/β spin-state selection for ^{13}C and ^{15}N from a time-shared HSQC-IPAP experiment. *J. Biomol. NMR*, 2007, **37,** 65.
68. L. Duma, S. Hediger, A. Lesage and L. Emsley, Spin-state selection in solid-state NMR. *J. Magn. Reson.*, 2003, **164,** 187.
69. P. Nolis, J. F. Espinosa and T. Parella, Optimum spin-state selection for all multiplicities in the acquisition dimension of the HSQC experiment. *J. Magn. Reson.*, 2006, **180,** 39.
70. T. Parella and M. Gairi, Simultaneous Recording of Spin-State-Selective NMR Spectra for Different I_nS Spin Systems. *J. Am. Chem. Soc.*, 2004, **126,** 9821.
71. G. Guichard, A. Violette, G. Chassaing and E. Miclet, Solution structure determination of oligoureas using methylene spin state selective NMR at ^{13}C natural abundance. *Magn. Reson. Chem.*, 2008, **46,** 918.
72. A. Rexroth, P. Schmidt, S. Szalma, T. Geppert, H. Schwalbe and C. Griesinger, New principle for the determination of coupling constants that largely suppresses differential relaxation effects. *J. Am. Chem. Soc.*, 1995, **117,** 10389.
73. P. Anderson, J. Weigelt and G. Otting, Spin-state selection filters for the measurement of heteronuclear one-bond coupling constants. *J. Biomol. NMR*, 1988, **12,** 435.
74. B. Brutscher, Accurate measurement of small spin–spin couplings in partially aligned molecules using a novel J-mismatch compensated spin-state-selection filter. *J. Magn. Reson.*, 2001, **151,** 332.
75. P. Permi, Determination of three-bond scalar coupling between $^{13}C'$ and $^1H^\alpha$ in proteins using an iHN(CA),CO(α/β-J-COHA) experiment. *J. Magn. Reson.*, 2003, **163,** 114.
76. L. Duma, S. Hediger, B. Brutscher, A. Böckmann and L. Emsley, Resolution Enhancement in Multidimensional Solid-State NMR Spectroscopy of Proteins Using Spin-State Selection. *J. Am. Chem. Soc.*, 2003, **125,** 11816.
77. R. Verel, T. Manolikas, A. B. Siemer and B. H. Meier, Improved resolution in ^{13}C solid-state spectra through spin-state-selection. *J. Magn. Reson.*, 2007, **184,** 322.
78. P. Permi and A. Annila, A new approach for obtaining sequential assignment of large proteins. *J. Biomol. NMR*, 2001, **20,** 127.
79. P. Permi, A spin-state-selective experiment for measuring heteronuclear one-bond and homonuclear two-bond couplings from an HSQC-type spectrum. *J. Biomol. NMR*, 2002, **22,** 27.

80. D. Lee, B. Vögeli and K. Pervushin, Detection of C′,C^{α} correlations in proteins using a new time- and sensitivity-optimal experiment. *J. Biomol. NMR*, 2005, **31,** 273.
81. P. Würtz, K. Fredriksson and P. Permi, A set of HA-detected experiments for measuring scalar and residual dipolar couplings. *J. Biomol. NMR*, 2005, **31,** 321.
82. G. C. R. Rani and R. Riek, Pseudomultidimensional NMR by spin-state selective off-resonance decoupling. *J. Am. Chem. Soc.*, 2003, **125,** 16104.
83. P. R. Vasos, J. B. Hall and D. Fushmann, Spin-state selection for increased confidence in cross-correlation rates measurements. *J. Biomol. NMR*, 2005, **31,** 149.
84. N. Murali, Y. V. S. Ramakrishna, K. Chandrasekhar, M. Albert Thomas and A. Kumar, Flip angle dependence in two-dimensional multiple quantum coherence NMR spectroscopy. *Pramana*, 1984, **23,** 547.
85. B. Bikash and N. Suryaprakash, Spin selective multiple quantum NMR for spectral simplification, determination of relative signs, and magnitudes of scalar couplings by spin state selection. *J. Chem. Phys.*, 2007, **127,** 214510.
86. B. Bikash, Ph.D. Thesis, Indian Institute of Science, Bangalore, 2008.
87. O. W. Sørenson, G. W. Eich, M. H. Levitt, G. Bodenhausen and R. R. Ernst, Product operator formalism for the description of NMR pulse experiments. *Prog. NMR Spectrosc.*, 1984, **16,** 163.
88. Y. Kim and J. H. Prestegard, Measurement of vicinal couplings from cross peaks in COSY spectra. *J. Magn. Reson.*, 1989, **84,** 9.
89. W. A. Thomas and G. E. Griffin, The NMR spectra of some fluorinated pyridine derivatives. *Org. Magn. Reson.*, 1970, **2,** 503.
90. W. B. Smith and J. L. Roark, Proton magnetic resonance spectra of several 2-substituted pyridines. *J. Phys. Chem.*, 1969, **73,** 1049.
91. J. E. Loemker, J. M. Read, Jr. and J. H. Goldstein, Nuclear magnetic resonance analyses and parameters for some monohalosubstituted fluorobenzenes. *J. Phys. Chem.*, 1968, **72,** 991.
92. B. Bikash, G. N. Manjunatha Reddy, R. P. Uday, T. N. Guru Row and N. Suryaprakash, Simplifying the complex ^{1}H NMR spectra of fluorine-substituted benzamides by spin system filtering and spin-state selection: multiple-quantum-single-quantum correlation. *J. Phys. Chem. A*, 2008, **112,** 10526.
93. G. N. Manjunatha Reddy, T. N. Guru Row and N. Suryaprakash, Discerning the degenerate transitions of scalar coupled ^{1}H NMR spectra: Correlation and resolved techniques at higher quantum. *J. Magn. Reson.*, 2009, **196,** 119.
94. G. N. Manjunatha Reddy, S. K. Nayak, T. N. Guru Row and N. Suryaprakash, Proton NMR studies of dihalogenated phenylbenzamides: Two-dimensional higher quantum methodologies. *Magn. Reson. Chem.*, 2009, **47,** 684.

CHAPTER 3

High-Resolution Magic Angle Spinning—Enabling Applications of NMR Spectroscopy to Semi-Solid Phases

William P. Power*

Contents

Abstract

High-resolution magic angle spinning (HRMAS) is the combined application of high-resolution NMR experiments with dipolar- and susceptibility-reducing sample rotation to viscous or gel-like samples. It has generated significant insights into questions of structure in systems ranging from polymeric, inorganic and environmental samples, to foodstuffs, to whole cells and tissues, particularly in the burgeoning field of metabolite profiling. This review provides an updated look at the applications arising over the 8 years that have passed, from 2003 to 2009, since our initial survey.

Key Words: High-resolution magic angle spinning, Nuclear magnetic resonance, Polymers, Metabolic profiling, Metabolomics, Metabonomics, Membranes, Peptides, Proteins, Whole cells, Tissues.

* Department of Chemistry, University of Waterloo, Waterloo, Ontario, Canada

Annual Reports on NMR Spectroscopy, Volume 72
ISSN 0066-4103, DOI: 10.1016/B978-0-12-385857-3.00003-7

© 2011 Elsevier Ltd.
All rights reserved.

1. INTRODUCTION

In an initial review prepared some 8 years ago,[1] we described the initial stages of development of a novel marriage of the specificity afforded by high-resolution NMR experiments with the line-narrowing advantages of magic angle spinning (MAS) from solid-state techniques. Over the ensuing time, this marriage has fostered an explosion of interest in the application of NMR spectroscopy to the study of heterogeneous systems that lie between pure solution and pure solid phases. The diversity of information available from elucidating molecular details in these complex matrices, ranging from swollen polymers to human tissues, has proved valuable to our understanding of the physics, chemistry and biology that underpins their unique behaviour, whether it is beneficial, in the case of a supported catalyst, or detrimental, as encountered in many diseases including cancer. Particular emphasis has arisen in the use of high-resolution magic angle spinning (HRMAS) as a complement to *in vivo* magnetic resonance spectroscopy (MRS), to understand the metabolic nature of many different biological assemblies. It is the purpose of this review to update our previous survey, chronicling the use of HRMAS from 2003 to 2009, and capture the great diversity in application with which HRMAS has contributed to our growing knowledge of complicated semi-solid systems.

2. NATURE OF THE SAMPLES AND SPECTROSCOPY

Originally applied as a means to provide high-resolution spectra of polymer-supported species such as those encountered in solid-phase organic and peptide chemistry, HRMAS is now widely applied to a wide range of samples exhibiting moderate line broadening resulting from magnetic susceptibility differences and residual dipolar couplings. Covering a diverse spectrum from viscous ionic liquids to whole cells and mammalian tissues, such samples share an unstructured matrix of relatively rigid and more freely flowing constituents that cannot be treated as purely solution or solid-state phases. The restricted motion inherent within these matrices ensures that the dipolar coupling between the magnetic nuclei in the sample is not completely removed by diffusion and tumbling. In addition, though often less considered in NMR experiments of single-phase samples, the magnetic susceptibility of the samples changes at the interfaces between components of the samples, whether they are particles, polymers, membranes or fluids. As there are many such interfaces within these samples, these susceptibility differences cause broadening of the resulting NMR signals, particularly if the most abundant nucleus, ^{1}H, is chosen as the preferred NMR probe, often the case for reasons of sensitivity and simplicity. In the vast majority of articles covered in this review, ^{1}H HRMAS NMR is indeed the technique of choice—where it is not, the nucleus of interest will be emphasized. The challenges resulting from the observation of this strong and abundant nucleus in these types of samples are summarized and resolved in brief here; more extensive discussion is available in the previous review.[1]

Central to all applications covered in this review is the dependence of dipolar and magnetic susceptibility broadening on $P_2(\cos\theta) = \frac{1}{2}(3\cos^2\theta - 1)$, the second-order Legendre polynomial. This function has a value of 0 when the angle θ, which represents the angle between the dipolar vector between two coupled nuclei and the vector representing the direction of the applied magnetic field, adopts a value of $\cos^{-1}(1/\sqrt{3})$ or 54.74°. The technique of MAS relies on reorienting a sample at this angle at a rate that is faster than the interaction which is causing the broadening. The resulting time average from this macroscopic sample manipulation can be understood by the property of a Legendre polynomial that it can be decomposed into products of other Legendre polynomials. By choosing the spinning axis to lie at 54.74° with respect to the applied magnetic field, hence making one term zero, the product of the two factors within the time average must be zero as well, and the broadening is removed. This is illustrated in Figure 1—the ''dashed'' dipolar vector in the rotor on the left of the figure has had its orientation dependence detailed to the right. This occurs for *all* vectors regardless of their orientations in the rotor, denoted by the angle β, as long as the rate of rotation is greater than the strength of the interaction expressed in hertz.

Dipolar broadening arises in samples where the timescale of the random (often Brownian) motion between two (or more) magnetic nuclei is less than timescale of their through-space interaction as magnetic dipoles. At one extreme, in a fixed crystalline environment common to solids, the dipolar coupling can dominate the NMR spectra of, in particular, ^{1}H nuclei, due to their high abundance and strong magnetic moment. Restricted or oriented motion often leads a reduction in the

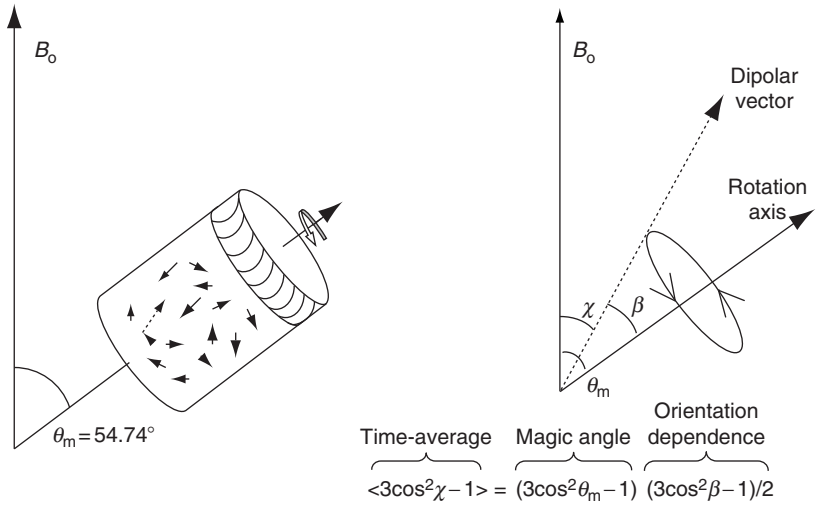

Figure 1 Magic angle spinning and its effect on anisotropic interactions. The dashed vector, denoting one particular dipolar interaction, or some other measure of molecular orientation, is shown on the right in terms of the geometry of sample spinning. By rotating the sample rapidly about an appropriate axis, the anisotropy or broadening experienced by the nucleus can be reduced to zero.

strength of the coupling from this extreme, but not enough to remove its influence entirely (even in solution under rapid molecular tumbling, its influence survives, though often only observable indirectly through its contribution to relaxation). It is in this restricted regime where many of the sample types encountered in the articles of this review fall. The challenge remains to remove, or at least substantially attenuate, the dipolar broadening, but without resort to techniques such as decoupling which would make ready observation of ^{1}H nuclei more technically demanding. Fortunately, MAS at relatively modest rates (2–5 kHz) is often sufficient to satisfy the desired high-resolution conditions.

Broadening arising from magnetic susceptibility differences within a sample can only be addressed by MAS. Interfaces between solution-like and solid-like domains within a heterogeneous sample, whether it is a tissue, a cell, or a swollen polymer, give rise to changes in magnetic susceptibility that cannot be addressed by careful calibration of magnetic field or RF homogeneity—they are inherent to the sample itself and not a feature of poor experimental set-up.

Hardware, in particular NMR probes and their controllers, facilitating MAS NMR is routinely available in most NMR facilities, due to the increasing interest in and access to solid-state NMR techniques. While specialized HRMAS probes provide higher ultimate resolution due to more careful design and construction, even MAS probes meant for studies of rigid solids have been used with great success in HRMAS applications. Sample containers, or rotors, typically can be specially ordered or modified to prevent leakage of liquid components from the samples of interest.[2]

3. EXTENDING HRMAS TECHNIQUES

Attempts to improve the quality and information content of 2D HRMAS NMR spectra have been reported by several groups, either through additional spectral analysis or through specially tailored pulse sequences. The use of constant-time experiments and BIRD pulses increased the quality of HMQC and HMBC spectra for polymer-supported peptides, by reducing ^{1}H–^{1}H modulation and sample spinning artefacts.[3] Higher quality through-bond 2D correlated spectra were obtained using TOBSY, a solid-state NMR symmetry-based pulse sequence, rather than TOCSY, as was the inclusion of adiabatic inversion pulses such as WURST.[4,5] Measurement of apparent equilibrium dissociation constants K_d for iodobenzamide-based drugs to synthetic melanin has been measured via the line broadening induced by complex formation on the HRMAS spectra.[6] Magnetization transfer from bulk H_2O to macromolecules in tissue samples via *z*-spectroscopy has been used to identify interacting species via the asymmetry introduced to their $^{1}H_2O$ line shape at MAS rates above 10 kHz.[7] Summaries of the ''best practices'' for both shimming[8] and RF pulse design[9] in HRMAS have been recently provided.

Approaches that exploit the semi-solid nature of the samples that are most commonly investigated permits application of techniques from solid-state NMR as well as classical high-resolution NMR. Dipolar recoupling techniques[10] use coherent polarization transfer via dipolar or *J*-coupling, rather than relying on

incoherent relaxation-derived exchange, as NOESY does. In fact, the dipolar and *J*-coupling evolutions could be separated, providing very useful structural information. It should be noted that this approach provides more direct information on distances than that typically available from NOE measurements. Rotor-frequency-driven dipolar recoupling, RFDR, common in the solid-state NMR of ^{13}C-enriched proteins, has been applied to both peptides bound to polymer supports[11] and membrane-bound proteins.[12] This approach yielded more specific correlations and was less dependent on the length of the mixing time for the observation of them, compared to NOESY. Surfactant templates trapped in the pores of mesoporous silica were best characterized with more solid-state techniques such as rotational resonance, rather than NOESY HRMAS, due to the spin diffusion that occurs in these more rigid frameworks.[13]

Ionic liquids are a new area of application for HRMAS. A particularly good example of its utility is provided by a recent study of organic solutes and reactions within ionic liquids; the line narrowing afforded by MAS of the viscous systems is quite impressive (see Figure 2).[14] Line narrowing only occurs after approximately 10 min of sample rotation, indicating perhaps some mechanical or phase separation process is responsible for the narrowing, rather than an inherent anisotropy within the sample. Solvation of CO_2 has shed light on the acid/base solvation within ionic liquids using ^{13}C HRMAS.[15]

The availability of gradient coils in many newer HRMAS probes has brought new applications as well. In favourable circumstances, where sensitivity is not a limiting factor, the application of gradients can be used to permit single-scan 2D experiments, resulting incredibly short experiment times.[16] This is only advantageous for samples that have very strong signals, providing all the required sensitivity in a single scan, hence likely limited to relatively uncomplicated ^{1}H spectra.

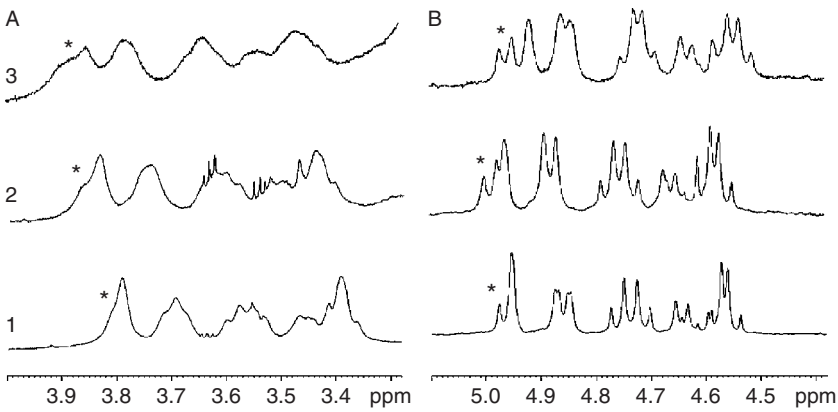

Figure 2 Ionic liquid spectra contrasting resolution of methyl 2,3,4,6-tetra-*O*-benzyl-α-D-glucopyranoside dissolved in three ionic liquids: **1**, 1-butyl-3-methylimidazolium hexafluorophosphate; **2**, 1-hexyl-3-methylimidazolium hexafluorophosphate and **3**, 1-octyl-3-methylimidazolium hexafluorophosphate afforded by (A) standard high-resolution and (B) HRMAS techniques. The benzylic H signal is indicated by the asterisk. Reprinted with permission from Rencurosi et al.[14] Copyright The Royal Society of Chemistry 2007.

Foremost among the new gradient techniques has been the development of chromatographic NMR, which uses the presence within a sample of a stationary phase used in chromatography to permit spectral discrimination of small molecules in solution by amplifying the differences in their diffusion coefficients. Use of DOSY-type NMR techniques permits these small molecules to be ''resolved'' spectroscopically.[17–19] It has also been applied to the measurement of diffusion coefficients of liquid crystals.[20] This area has been recently reviewed.[21] This approach has been extended to direct analysis of TLC spots by placing them directly into HRMAS rotors for spectral analysis.[22] A recent application of this chromatographic NMR analysed green tea extracts for catechins, using β-cyclodextrin and bovine serum albumin as resolution agents in the DOSY-based experiments.[23] More fundamental investigations of the microscopic origin of chromatographic separations have also been performed *in situ* on a number of stationary phases. *p*-Xylene has been found to exist in two domains when eluted through a C18-bonded silica column, within and surrounding the alkyl chains and in slow exchange between these two.[24] Alkyl chain conformation, as determined by ^{13}C HRMAS, was the dominating influence in molecular shape recognition in polymer-based stationary phases on silica.[25] Hydrophobic interactions were believed to be responsible for observed affinities for a series of steroids with a cholesterol-based stationary phase.[26] However, molecular shape was also important in reverse-phase HPLC separations of tocopherol isomers in C30-based columns, as evident from saturation-transfer difference NMR experiments.[27] Chiral stationary phases showed NOESY NMR changes with different analytes consistent with selectivity for *R* and *S* isomers.[28,29]

Some of the more novel extensions have come through modification of the sample spinning conditions of the experiments. Bulky samples that may not be amenable to the geometry and constraints of a standard HRMAS experimental set-up, with rotation of the sample at 54.7°, can be subjected to similar high-resolution conditions through *projected MAS*. Here, in a 2D experiment, the sample is subjected to rotation at two different but complementary angles that result in the removal of any line broadening, under suitable evolution times at each of the angles.[30] Sample rotation rates have been a concern for several groups, although there is little evidence so far that rotation of the samples described in this review at moderate rates up to 6 kHz causes any degradation of them. Slow spinning at 600–700 Hz has been proposed as a more moderate demand on sample integrity, when combined with spinning-rate variation to identify the isotropic peaks (spinning sidebands appears at multiple of the spinning frequency so are readily identified if the spinning rate is varied).[31,32] Reliable spectra including intensities could be obtained from such spectra compared to the spinning-sideband-free spectra obtained at 3 kHz.

A more extreme example of slow spinning experiments has been provided by the work of Robert Wind and his group, recently reviewed by him.[33] Slow MAS, at 40 Hz, in combination with the 2D PASS (phase-alternated spinning sidebands) technique to provide the required spectral resolution, has been applied to living bacterial cells where their survival was not compromised by rapid rotation[34] and yielded evidence of new peaks in the spectra of postmortem rabbit[35] and rat[36]

tissue as a function of pH—signals that were not evident in normal HRMAS. Upon even slower spinning, so-called magic angle turning, or MAT, at 1 Hz, using a 2D technique called PHORMAT to obtain high-resolution spectra from such low rotation rates, was applied to rat liver tissue,[37] and assessed versus PASS.[38] Indeed, at such low spinning rates, live animals become accessible to this technique and a live mouse was successfully subjected to PHORMAT HRMAS at 1.5 Hz.[39] Greater spectral definition of the mouse organs of interest resulted from the addition of gradients (similar to imaging experiments) to select specific regions of the mouse under MAT, in an experiment coined LOCMAT, or localized MAT,[40] one example of which is given in Figure 3. This opens the door to possible *in vivo* applications of HRMAS-like conditions through, perhaps, slow turning of the static magnetic field rather than of sceptical or uncooperative patients.

Finally, an area of much future promise in terms of sensitivity enhancement of HRMAS experiments is that of microcoils, where very small nanolitre-volume samples are placed directly within a microcoil that inductively couples with the main coil of a MAS NMR probe.[41,42] Applications to tissue samples have been recently reported, with increases in sensitivity of a factor of 10, due to the high filling factor afforded by this technique.[43]

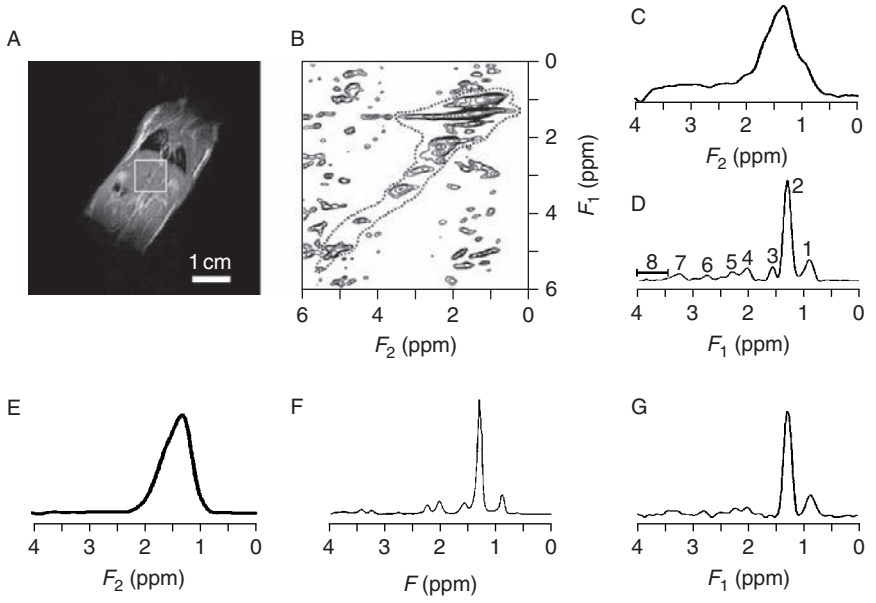

Figure 3 (A) 85 MHz *in vivo* ^{1}H MRI of a mouse with $8 \times 8 \times 8$ mm volume of liver depicted in LOCMAT spectra (B)–(E) indicated by the box; (B) 2D LOCMAT spectrum; (C) anisotropic projection of (B); (D) isotropic spectrum; (E) anisotropic spectrum corresponding to the lipid aliphatic methylene signal, labelled **2** in (D); (F) 300 MHz *ex vivo* ^{1}H PASS NMR at 40 Hz rotation of excised mouse liver tissue, which compares well with (D); and (G) 85 MHz ^{1}H isotropic LOCMAT spectrum of a $6 \times 6 \times 6$ mm volume of liver, where the signals fall to the level of noise, establishing the functional limit of detection. Reprinted with permission from Wind et al.[40] Copyright Wiley-Liss, Inc. 2005.

4. APPLICATIONS TO POLYMERS, POLYMER-SUPPORTED SYSTEMS AND MEMBRANES

Characterization of polymers has been an ongoing application of HRMAS, providing information on the distribution of segments as a function of degree of cross-linking in both polyamidoamines[44] and polyethylenimine hydrochloride[45] membranes. Polymerization reactions have been assessed *in situ*, providing reactivity ratio estimates for acrylate/methacrylate copolymers[46] as well as side reaction identification in the hyperbranched polycondensation of 2,2-bis(hydroxymethyl)propionic acid.[47] Novel polymers incorporating biological feedstocks have been characterized structurally, including the synthesis of starch–graft–polycaprolactone networks,[48] as well as the use of phosphine-oxide-modified vegetable oils copolymerized with acrylates in terms of their thermal and thermo-oxidative degradation via ^{31}P HRMAS.[49] Thermal properties of other polymers have also been investigated using HRMAS, providing information on the phase transitions of polyacrylamides composed of three different cross-linking agents.[50] However, it has been noted that melt-state MAS at $T_g + 150$ °C, rather than HRMAS of the same swollen polymer, provides better quantification of branching in poly(*n*-alkyl)acrylates.[51]

Hydrogels, and related systems, are quite amenable to HRMAS characterization and NMR has been used extensively in studies of these systems. A series of hydrogels based on oxazoline polymers have been reported,[52,53] and extended to amphigels and lypogels.[54] Hydrogels from polyacrylamides with different cross-linkers have been assessed.[55] The potential use of hydrogels from polyacrylic acid sodium salts as clathrate hydrates for H_2 storage has been analysed using HRMAS.[56] Alkyne–benzylazide reactions within cryogels have been monitored and their progress evaluated by HRMAS detection of the reaction participants *in situ*.[57]

The ability of polymers to interact with other species is often an important component of its use. For example, Hyflon® membranes are used as gas separation membranes due to their gas transport properties and moderate selectivity. However, increasing solvent content of these membranes inhibits their selectivity and increases gas permeability. HRMAS NMR was used to attempt to elucidate specific interactions between this fluorinated polymer and its fluorinated solvents but none were found.[58] Degradation of a nerve agent mimic, diisopropyl fluorophosphate, on specially prepared polyacrylonitrile fibre mats was assessed using ^{31}P HRMAS.[59] The relative affinity of a template-induced methacrylate polymer to reincorporate its template selectively compared to a non-templated but otherwise identical polymer was determined using saturation-transfer-difference (STD) NMR at the template site, showing the specifics of the template binding.[60]

A focus of the previous review,[1] the use of HRMAS to characterize species attached to polymeric supports, such as those encountered in solid-phase chemistry, continues to be an area of activity. Solid-phase organic chemistry, a key component of combinatorial chemistry, makes extensive use of HRMAS to characterize and perfect reaction pathways and products. A series of disubstituted benzoates were quantified while still attached to a polystyrene support through

reference to a convenient ''internal standard'', the methylene protons from the linker group in Wang resin.[61] Direct O-glycosylation of *N*α-Fmoc amino acids on Tantagel was confirmed by HRMAS.[62] Enrichment with ^{13}C labels permitted characterization of saccharides attached to a polystyrene resin, via the increased spectral resolution afforded by ^{13}C chemical shifts in INADEQUATE and HSQC HRMAS spectra—information that was not readily discerned from the overlapping ^{1}H signals.[63] Addition of a diffusion filter in gradient HRMAS experiments to distinguish covalent from included products aided in the elucidation of enolate chemistry directly on a polymer support.[64] ''Traceless'' solid-phase chemistry using Te and Se linker atoms between the polymer support and reactive species has been analysed in detail,[65] where ''traceless'' means that the linker group leaves no ''legacy'' functionality on the synthesized product due to its attachment to the polymer. The successful extension of this technique with ''green'' cleavage agents has been subsequently demonstrated.[66] A synthetic strategy to simultaneously attach amino acids to a tripeptide ''core'' element through both its C and N termini was followed sequentially by HRMAS to demonstrate the success of the approach, and to identify and subsequently eliminate side reactions that occur.[67] Chiral-derivatizing agents attached to a support were characterized by HRMAS prior to their use in a novel and simple ''one-pot'' high-resolution NMR experiment that yields optical configuration without tedious purification and separation.[68]

The influence of the polymer support on the HRMAS NMR spectral characteristics, particularly increased ^{1}H linewidths, of attached species has been demonstrated to occur through the magnetic susceptibility of aromatic components of polystyrene-based resins[69] as well as slow resin dynamics affecting T_2.[70]

Larger assemblies have been attached to polymer supports and successfully characterized using, among other techniques, HRMAS, although HRMAS appears to be the most widely applicable structural tool. Catalysts based on organotin chloride have been prepared[71] and their catalytic reactions monitored using HRMAS *in situ*.[72] Diffusion filters using gradient techniques and ^{119}Sn HRMAS NMR as well as ^{1}H has been used in these and subsequent[73,74] studies, to great effect. Catalytic polystyrene resins containing prolinamide were characterized and their utility established for stereoselective aldol reactions.[75] Supramolecular assemblies attached to polymer supports have also been prepared and characterized, including such moieties as catenanes and rotaxanes,[76] as well as crown ethers and porphyrins.[77] The thermodynamic control of the formation of complexes involving these polymer-supported assemblies was demonstrated by NMR to conform to the behaviour of their free analogues.[78] ''Threading'' of macrocycles onto indolocarbazole ''axles'' via anionic templating has been well characterized through distinctive high-frequency shifts ($\sim$4 ppm) of the $N^{1}H$ signals, clearly visible in Figure 4.[79]

Analogies between free solution structure and structure of polymer-supported species have received some interest. Vancomycin bound to a solid support was validated as a useful screening technique upon confirmation by HRMAS NMR of its similar structure in both free and bound forms.[80] Novel model peptides incorporating α-aminoisobutyric acid (AiB) have been shown to adopt a 3_{10}

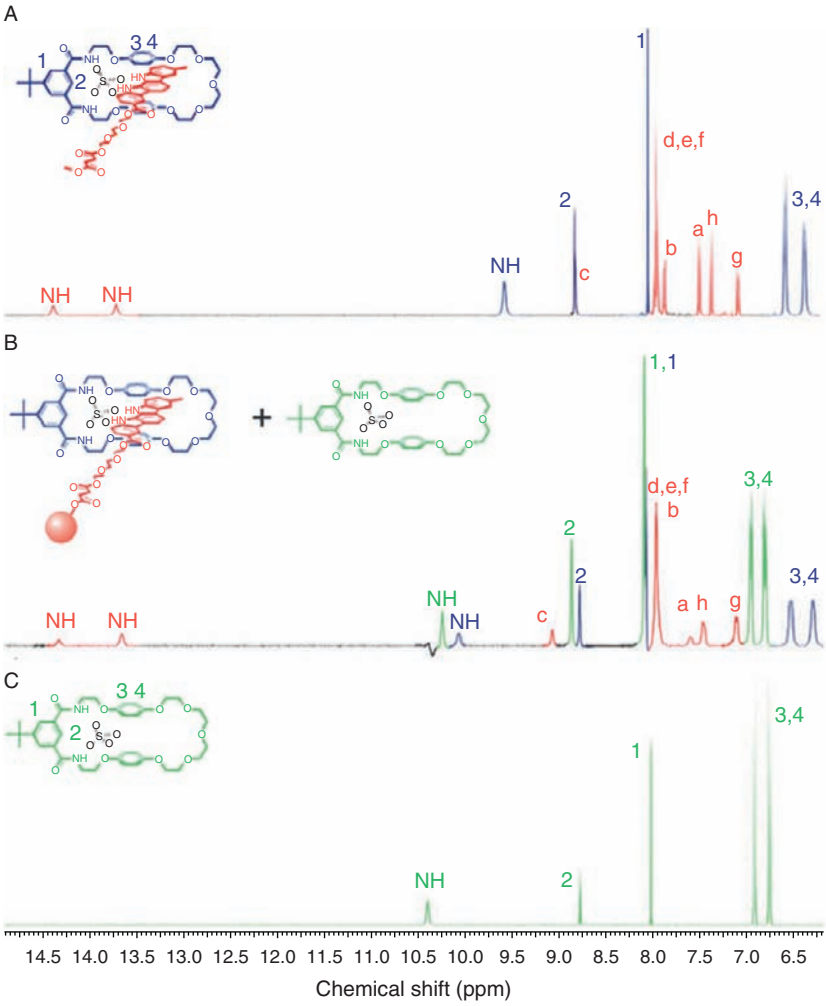

Figure 4 ^{1}H NMR spectra of (A) an indolocarbazole (peaks labeled with lower-case letters and the two NH peaks at 13.7 and 14.5 ppm) with a macrocycle (peaks labeled with numbers and NH peak at 9.6 ppm) and tetrabutylammonium sulfate in equimolar ratio in acetonitrile solution, (B) the same indolocarbazole tethered to TantaGel^{TM}resin with excess macrocycle and tetrabutylammonium sulfate, and (C) only free macrocycle and tetrabutylammonium sulfate in equimolar ratio in acetonitrile solution. Spectrum C permits identification of free uncomplexed macrocycle in the mixture, spectrum B. Reprinted with permission from Zhao et al.[79] Copyright The Royal Society of Chemistry and the Centre National de la Recherche Scientifique 2009. (The reader is referred to the colour version of this figure in the Web version of this chapter, where the peaks arising from the indolocarbazole, complexed macrocycle and free macrocycle are identified in red, blue and green, respectively, for greater clarity.)

helix in polymer-bound form close to that found in solution.[81] Structures novel to polymer supports have also been characterized. Inhibitor screening phases were developed from α-ketoamino acids,[82] as were affinity phases for cytochrome

P450,[83] both characterized using HRMAS. Oligoureas grown on poly(oxyethylene) supports were found, using HRMAS NOESY, to exhibit a 2.5 helical conformation.[84] Attachment to a polymer support was used to prevent aggregation so that the monomeric structure of a prion fragment could be determined by HRMAS.[85]

Oxide supports are also amenable to HRMAS investigation, although solid-state NMR approaches still dominate, as evident in a recent review.[86] A mixed metal Pd/Cu cross-coupling catalyst formed by phosphine linkers on a silica support was swollen in acetone and the ^{31}P HRMAS spectra were used to characterize the individual Pd and Cu metal sites.[87] In the functioning mixed catalyst, no distinct molecular aggregate of the two sites could be determined, and there was some evidence of Pd hopping among the available sites. The role of the $MgCl_2$ support in a Ziegler–Natta catalyst was studied using diffusion-filtered ^{1}H HRMAS of added long-chain silanes.[88] The catalytic reaction was followed, its mechanism deduced and the reaction conditions optimized using *in situ* HRMAS NMR of the sulphuric acid-catalysed conversion of anthranilamide and acetone to a quinazolin-4(3H)-one.[89]

Increasing interest is being paid to functionalization of the surfaces of nanoparticles. Peptides originally attached to PVDF films that maintained their antigen specificity upon attachment[90] have now been similarly attached to PVDF nanoparticles.[91] PVDF is an ideal substrate as it is a biocompatible fluorinated thermoplastic polymer; HRMAS is an essential tool to determine the level and nature of attachment. It has also been used to determine the surface coverage of β-D-glucose on biocompatible nanoparticles composed of polyesters and lactic and glycolic acid copolymers.[92] Other nanoparticles, particularly Au-based, have been studied using HRMAS techniques; these and other NMR investigations have been recently reviewed.[93] Organic ligands on Au nanoparticles show a characteristic loss of ^{1}H signals in 1D and 2D HRMAS spectra when they lie very close to the Au surface.[94] Thiol binding of a cysteine-containing 15-mer peptide was confirmed by HRMAS characterization of the attached peptide.[95] Even paramagnetic nanoparticles are amenable to NMR analysis under MAS; ^{1}H spectra of organic ligands attached to superparamagnetic iron oxide nanoparticles could be resolved.[96] Ligand attachment was confirmed by used of a diffusion-ordered experiment. Solvent choice was key to success, with the polarity rather than solvation characteristics of the solvent most important.

The structure and dynamics of lipid membranes, and interactions between membranes and molecules, peptides and proteins embedded in them, continue to be a focus of HRMAS studies, due to its ability to provide high-resolution NMR spectra of the viscous, orientationally ordered environment of such systems; this area has been recently reviewed.[97] Bicelles have comprised a large number of such investigations, due to the orientational control afforded by such systems.[98]

Technically, issues of sample conditions and integrity have been addressed, including the expected observation that higher field (e.g. 800 MHz) is beneficial for HRMAS NMR of bicelle systems, but so too are higher rotation rates, up to 10 kHz, which did not have deleterious effects on them.[99] Such higher sample rotation rates were also possible without damaging the samples with a new glass-plate rotor system for oriented membrane studies, which worked with 4 mm rotors.[100] Switched angle spinning of bicelles has been used to retain anisotropic

information from the high-resolution spectra, providing ready access to residual dipolar couplings for structural determination.[101] A combination of HRMAS and high-resolution NMR spectra has been used to resolve residual dipolar couplings from *J*-coupling, which greatly facilitates the accuracy of structural factors available from the technique without having to resort to multiple bicelle orientation to deduce such information.[102]

Differences in phases of surfactant and model membrane phases are amenable to characterization by HRMAS. Phase transitions in an alkyl dioxyethylene sulphate/alkylbetaine system could only be resolved from T_2 measurements by the increased resolution and selectivity afforded by HRMAS.[103] The multi-lamellar vesicles formed by combining two different phosphatidyl nucleosides were shown to be an intimate mixture rather than two separate domains by HRMAS NOESY spectroscopy.[104] Compared to small and large unilamellar vesicles, multilamellar vesicles of 1-palmitoyl-2-oleoyl-*sn*-glycero-3-phospatidylcholine (POPC) were more amenable to HRMAS analyses, requiring lower sample rotation rates (3 vs. 12 kHz) for complete averaging of the broadened lines.[105] Of the large and small unilamellar vesicles, large vesicles were preferred, since they act as a better model for real membranes. The better orientation of tethered versus adsorbed lipid bilayers within nanotubes has been characterized by ^{2}H HRMAS.[106]

Interactions with small molecules, peptides and proteins have been characterized, but many of these studies are giving way to more realistic ones involving whole cells and tissues (*vide infra*). Addition of a relaxation agent, Gd^{3+}, to egg yolk lecithin systems incorporating the antibacterial agents (+)-totarol[107] and triclosan[108] permitted ^{13}C relaxation measurements to locate the area in which these agents associate with the membrane; in each case, they are found to lie close to the head group. The possibilities for 3D structure determination of peptides and proteins have been sampled in phosphatidylcholine bicelles. Application of HRMAS NOESY experiments provided some structural data regarding the orientation of a pentapeptide in the bicelle.[109] A larger 25-residue fragment peptide from a kinase substrate was both oriented and located with a model bilayer plasma membrane using both NOESY and cross-relaxation rate data.[110] Use of gradient techniques, especially diffusion filters, has assisted in characterizing diffusion of small molecules within membranes,[111] including several studies of cholesterol and related sterols,[112,113] ibuprofen[114] and a series of five similar flavonoids.[115] The role of cholesterol in dynamics of phospholipid phases has also been delineated using magnetization transfer techniques.[116]

5. APPLICATIONS TO PROTEINS, WHOLE CELLS AND TISSUES

While more rigid proteins are best characterized by modern solid-state NMR techniques employing ^{13}C-enriched samples, mobile domains of otherwise rigid protein assemblies have been analysed with HRMAS to great effect. Melanin, a complex protein that has eluded definitive characterization to date, has had some structural components determined by use of gradient-assisted HMQC and HMBC of swollen melanin.[117] The phospholipid metabolism in melanoma cells has been

followed *in situ* before and after treatment with chloroethylnitrosourea, an antineoplastic, showing a large increase in phosphoethanolamine after treatment.[118] More recently, the incorporation of ^{13}C-labelled substrates, such as L-DOPA, mannose and glucose through melanin biosynthesis by *Cryptococcus neoformans* has provided further insight,[119] including changes in glucose and sodium acetate metabolism upon melanogenesis.[120] The mobile regions of tau protein filaments[121] and the prion protein fragment HET-s(218–289),[122] both implicated in Alzheimer's disease, have been characterized by HRMAS. Of note, in the tau study, electron microscopy was used in evaluating the effect of sample spinning on the protein filaments. Although some ''fuzziness'' of the filament images was observed after spinning at rates beyond 1 kHz, there was no discernable change in the NMR spectra, indicating no distinct structural changes. The mobile residues observed by HRMAS for the prion fragment had been previously undetected in solid-state NMR studies, indicating the utility of HRMAS as a complementary structural probe in such systems. Microtubule formation by tau proteins within oocyte cells has also been followed by HRMAS.[123]

One of the key advantages HRMAS has brought to the fields of cell and systems biology is the ability to characterize structures and processes within whole cells and organisms. Cellular metabolism, including the action of drugs, cell-wall elucidation and molecular phenotyping and taxonomy have been very active areas of research over the past decade; recent reviews and methods have been provided by Grivet,[124] Nothaft[125] and Brisson.[126] One of the first notable aspects of ^{1}H HRMAS NMR spectra of whole cells in water is the separation of the $^{1}H_2O$ peak into two signals, one broad with the other narrow (see Figure 5), that arise from phase separation of the water into two components due to the rapid spinning of the sample.[127] The narrow line corresponds to cell-free water along the centre of the rotor, the other to water containing cells along the rotors walls. This effect has been used to measure the uptake of MRI contrast agents by red and white blood cells using HRMAS.[128] The peak separation depended on the actual cell line, and correlated roughly with the protein content of the cells,[127] an effect later attributed to hydrogen bonding with the proteins.[129] Magnetization transfer experiments were used to study in greater detail the nature of water interactions with lipids, proteins, and metabolites in cells and tissue samples; phospholipids were found to interact more strongly than proteins.[130] Robust cell lines, like human red blood cells, were relatively immune to physical damage from spinning, while more fragile cells, such as rat hepatocytes, were quite susceptible.[127] The cell-free water linewidth could be correlated with cell lysis; when it was greater than 2.5 Hz, significant cell lysis had occurred, the cellular components diffusing into the cell-free water phase causing the line broadening. The phase separation could be eliminated by adding albumin to samples, which acted as a network limiting the diffusion of cells to the outer walls.[131] Under this ''stabilized'' condition, the water exchange time between intracellular and extracellular regions across red blood cell membranes was estimated to be in the order of 10 ms, in accord with estimates from other techniques. The effects of cell handling and storage on cell integrity in HRMAS NMR studies have been explored for various cell lines, including tumour cells and amniocytes; fresh cells and cryoprotected

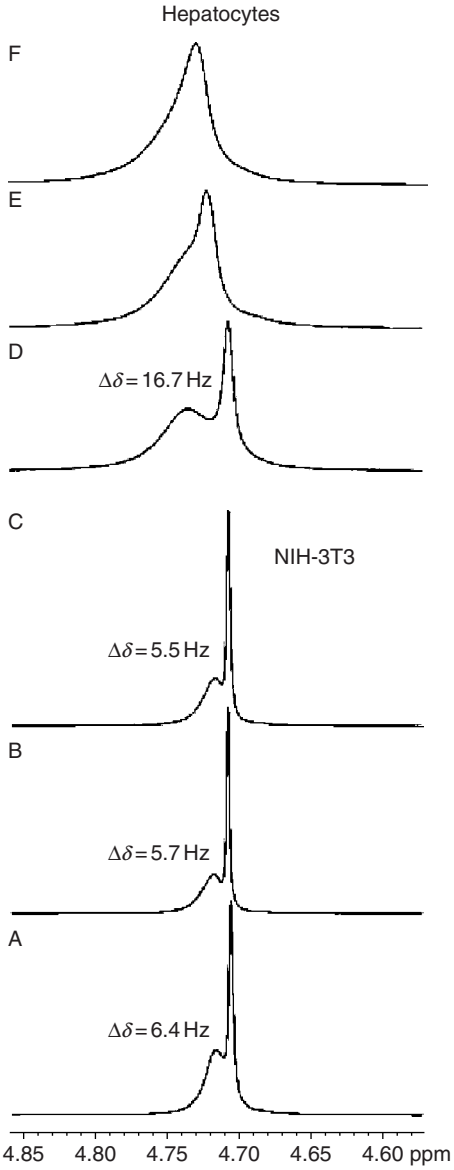

Figure 5 600 MHz ^{1}H HRMAS NMR spectra of (A)–(C) mouse fibroblast and (D)–(F) rat hepatoma cells. The three spectra for each cell line represent initial spectra at 1.5 kHz MAS (A, D) followed by MAS at 4 kHz (B, E) then returned to MAS at 1.5 kHz (C, F). Note that initially the ^1H_2O signal shown is split into two due to fractionation of the suspension, with the narrow line corresponding to free water. The rat hepatoma cells undergo lysis at the higher MAS rate, resulting in loss of the narrow ^1H_2O line due to distribution of cell components throughout the solution; no such disruption occurs with the mouse fibroblast suspension. Reprinted with permission from Aime et al.[127] Copyright Wiley-Liss, Inc. 2005.

frozen cells maintained their integrity fairly well, whole frozen non-protected cells were fully lysed by the time the analysis was initiated.[132]

HRMAS NMR of brain cells (neuronal and glial) provides evidence that *in vivo* MRS may be missing important lipid signals due to the T_2-weighted editing that is commonly applied in the MRS.[133] Creatine levels in particular did not behave in HRMAS as expected from the *in vivo* studies. The increased *de novo* synthesis of fatty acids in cells subjected to elevated glucose levels, mimicking diabetes mellitus, has been observed directly in whole cells by HRMAS.[134]

The action of drugs can be followed *in situ* once NMR spectroscopy of whole cells is possible. Among the first of these applications was Chen[135] who monitored the efficacy of thiazolidinedione on liposarcoma cells by measuring the ratio of phosphatidylcholine to phosphocholine. Similarly, treatment of endometrial cells with tamoxifen indicated changes in RNA transcription and cell membrane turnover by characterization of the metabolites in the cell via HRMAS.[136] The action of ethionamide[137,138] on mycobacteria was followed by use of diffusion filters to selectively observe intracellular components; unfortunately, the precise structure of the active metabolized drug agent within the cell could not be determined. Such downstream effects are likely the mode of action for the drugs bezafibrate and medroxyprogesterone acetate on acute myeloid leukaemia cell lines, as there were no obvious changes on the metabolites visible under HRMAS after 24 h.[139] Higher resolution is likely necessary before any conclusions can be drawn on the differences between film and free forms of *Pseudomonas aeruginosa* survival rates under antibiotic treatments, where the film-formed bacterium is known to be more resistant to treatment.[140] Binding of one of the three anti-apoptosis agents, imidazo[1,2-a]pyridine derivatives, to myelomonocytic cells was directly detected using HRMAS.[141]

The validity of the whole-cell approach was verified by comparing the metabolite profiles of the microalgae *Thalassiosira pseudonana* from both whole-cell samples and cell extracts each subjected to HRMAS NMR; the results from whole cells were very good, with high resolution.[142] Another microalgae, *Chaetoceros muelleri*, has had its storage polysaccharides and other components identified by ^{1}H[143] and ^{13}C[144] HRMAS NMR, including DEPT. The biocontrol agent that limits mould in grain storage, the yeast *Pichia anomala*, has been studied under the effects of oxygen limitation, a condition common in its use.[145]

The ability to identify the cell-wall components, particularly lipopolysaccharides, *in situ* using whole cells has been an important contribution. One of the first applications of HRMAS to this area was reported by Szymanski[146] who used HRMAS (Figure 6) to establish the conservation of a heptasaccharide on the cell walls of two different *Campylobacter* lines, a main cause of gastroenteritis. The enzyme responsible for cell-surface carbohydrate production in *Campylobacter jejuni* was subsequently identified,[147] as was this cell's biosynthetic mechanism for N-linked glycans.[148] The presence of a phosphoramidate on its cell surface was detected by HRMAS, and posited as a possible marker for diagnosis and treatment.[149–151] HRMAS NMR has also been used to identify similarities in the cell-wall lipopolysaccharides of strains of *Hafnia alvei* bacteria,[152] the differences between two strains of *Bordetella pertussis* in the presence of a particular

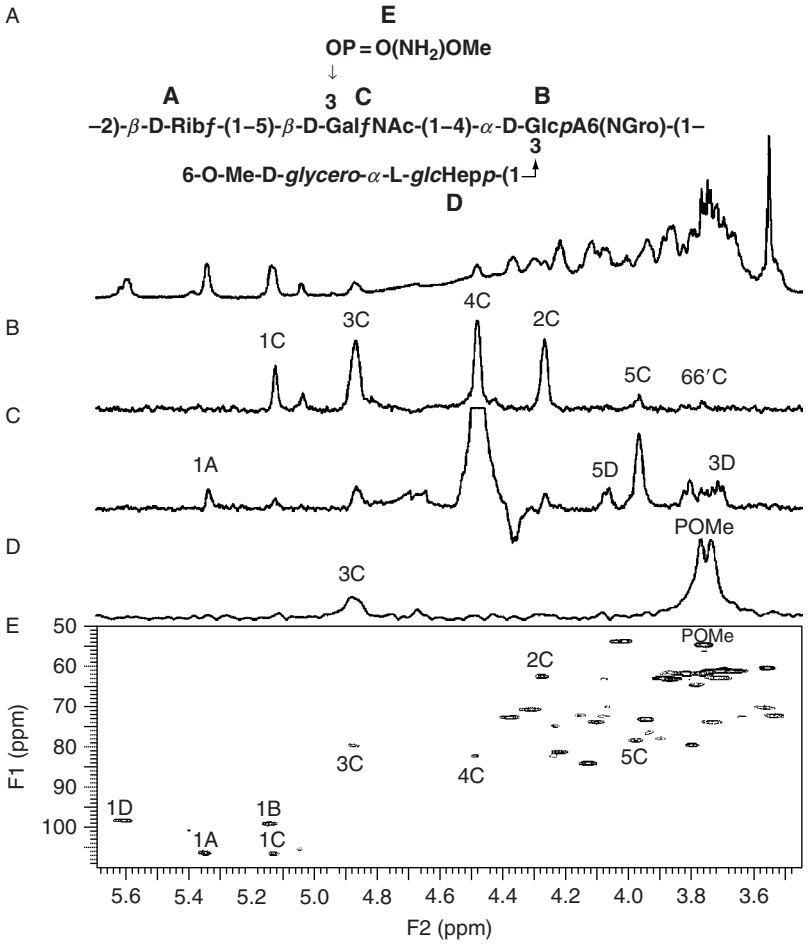

Figure 6 600 MHz ^{1}H HRMAS NMR spectra of the capsular polysaccharide of a variant of *Campylobacter jejuni*. The structure of the capsular polysaccharide is given at the top with the five main residues labelled **A–E**. (A) ^{1}H spectrum of the purified polysaccharide; (B) selective TOCSY used for assignment of residue **C**; (C) selective NOESY to detect **C** and **D** inter-residue contacts; (D) slice from ^{1}H–^{31}P HMQC to establish attachment of **E**; and (E) ^{1}H–^{13}C HMQC showing assignments for residue **C**. Reprinted with permission from Szymanski et al.[146] Copyright The American Society for Biochemistry and Molecular Biology, Inc. 2003.

pentasaccharide on their cell surfaces[153] and the structure of cell-wall polysaccharides of *Neisseria meningitidis*[154] and *Plesiomonas shigelloides*.[155]

Identification of cell-wall components leads naturally to the more precise observation of the effects of therapeutic agents in dealing with many of these infectious organisms. Mycobacteria, the cause of tuberculosis, have attracted numerous studies that use HRMAS to determine the action of drugs on their cells. The fate of ethambutol[156,157] and thiacetazone[158] administered to mycobacteria has been followed in efforts to determine their mode of action. Sophisticated 2D

and 3D HCCH-TOCSY and HCCH-COSY HRMAS techniques together with ^{13}C-enriched substrates have been developed to establish cell-wall structures,[157] and the challenges and promise of this approach have been highlighted.[159,160] Selective COSY was used to great effect to quantify the extent of cyclopropanation on mycobacterial cell surfaces, which is a hallmark of pathogenicity in these organisms.[158]

Characterization of metabolites within cells as well as in cell-wall components permits identification of different types of organisms, resulting in a phenotyping or taxonomy by NMR; this application is becoming more common. Chauton identified four marine microalgae (phytoplankton) through analysis and classification of the HRMAS spectra.[161] ''Silent'' mutations in different *Caenorhabditis elegans* phenotypes have been detected through analysis of their metabolites.[162] The NMR method and its limits have been well explored,[163] as have the statistical approaches used in the differentiation.[164] The toxic strains of *Candida albicans* were identified through the determination of β-mannoside saccharides on their cell surfaces. HRMAS has been used with MALDI-TOF mass spectrometry to identify marine bacteria under minimal and enriched growth conditions successfully.[165] When compared to FT-IR classifications of lichen taxa, HRMAS NMR was not as accurate, consistent in only most of the samples with a few classification errors.[166]

6. ENVIRONMENTAL AND FOOD APPLICATIONS OF HRMAS

The complex mixtures of materials that make up our environment have proven to be ripe for analysis using NMR, with HRMAS providing the resolution for distinct chemical signatures and interactions to be detected. While coal has long been investigated by traditional solid-state techniques, its putative origin in microalgae has been more recently of interest. The structure of the biopolymeric algaenan from *Botryococcus braunii* was characterized by NMR in terms of its size (roughly 40 carbons) and functional groups (aldehydes and unsaturated hydrocarbons).[167] The thermal decomposition has been monitored through two subsequent studies.[168,169] Other marine sediments have been characterized, providing evidence of trapping of nitrogen by peptidic material,[170] correlation of lower and higher gas hydrate concentrations with increased proteinaceous and increased lipid levels, respectively,[171] and revealing a 6-kDa cutin-like biopolymer that is believed to be responsible for Pu and other heavy metal transport.[172]

Soils and clays are another area of interest, with particular emphasis on the fate of organic compounds, including pesticides and pollutants, within these heterogeneous materials. Sorption of humic acid to clay mineral surfaces results in uptake of aromatics and proteins in montmorillonite, and aliphatic groups in kaolinite.[173,174] Carbohydrates and amino acids were not present in the ^{1}H HRMAS NMR spectra of these materials, however.[175] Application of HRMAS provided useful distinguishing information concerning the uptake of three pesticides in clays, in contrast to inconclusive results using solid-state CPMAS techniques. Soil moisture and solvent used for swelling the soil samples are key factors to successful HRMAS analyses.[176]

With foodstuffs, HRMAS holds the promise to provide information on molecular structure without destroying the pristine form of the food by complicated separations or pretreatments. A particularly troublesome component of vegetable products, the insoluble cutin protein, has been characterized by ^{1}H HRMAS—it is predominantly an aliphatic polyester with some alcohol functionality.[177] Its insolubility is believed to arise from cross-linking due to α-branched fatty acids and esters that were evident in the NMR spectra. The cutin from *Agave americana* leaves was found to be highly crystalline.[178] Different strains or places of origin for lamb meat[179] and cheese[180] have been distinguished by their HRMAS NMR spectra. Use of 2D HRMAS techniques permitted the origin or ''hard'' potatoes to be deduced as due to intercellular adhesion that results from biopolyesters bound to the cell walls.[181] The effects of stress, such as drought, salt exposure or pressure, have been evaluated by HRMAS of rice,[182] wheat[183] and strawberries,[184] by analysing directly the stressed sample. The effects of baking on flour and the resulting breads could be determined as an increase in the concentration of simple acids (succinic, lactic and acetic) with heat.[185] In some cases, interference effects from the matrix preclude HRMAS analyses; alginates, used as a stabilizer in food and drugs, were best analysed by CPMAS due to their calcium-rich nature.[186]

Several examples of drug preparations and interactions have been established as well. The herbal aphrodisiac catuaba from several commercial sources was analysed for active ingredients successfully.[187] The fermentation precipitate of the Hib vaccine could be analysed directly to confirm the presence of the bacterial capsular polysaccharide.[188] The binding of neurotensin to a detergent-stabilized receptor could be monitored directly though the ^{13}C chemical shift changes that occur in the HRMAS spectra.[189] Drug delivery efficiencies between topical and injection applications have been contrasted using HRMAS of skin and muscle tissue of rats subjected to both dosing methods with benzoic acid.[190]

7. METABOLIC PROFILING

By far the greatest area of application of HRMAS in recent years has been in metabolic profiling, also known as metabolomics and metabonomics.[191] The ability of HRMAS to resolve narrow lines in spite of heterogeneous matrix, such as those found in biological tissues, permits the identification and quantification of various molecular and macromolecular components of the matrix.[192,193] This approach is particularly well suited to biopsies in a clinical setting, as other methods, such as tissue extracts, require significant pretreatment before analysis.[194] With the robustness of HRMAS to sample composition, such pretreatment is not required and samples may be analysed directly, often with the addition of a reference material to ensure accurate chemical shifts and/or quantitation. A prototype rotor to facilitate quantitation has been described,[195] as have algorithms for automated quantitation of HRMAS spectra.[196,197] Metabolites have been analysed in a wide range of materials, ranging from plants and animal tissues to biopsies of human cancers. In particular, the higher resolution afforded by HRMAS has made it a useful complement to *in vivo* MRS.[198]

8. HUMAN METABOLITES

Establishing convenient biomarkers for cancer in its various forms among cellular metabolites is an area of prolific research. Several recent reviews highlight the impact of metabolic profiling in cancer research.[199–201] Brain tumours have attracted considerable attention, notably in attempts to classify tumours based on the ratios of various metabolites, usually in concert with *in vivo* spectroscopy.[202,203] Glycine emerged as a promising biomarker for tumour aggressiveness[204]; similar conclusions were drawn from an earlier MRS and HRMAS study of neurocytomas.[205] Application of HRMAS to paediatric brain tumours[206] and glioma biopsy samples[207,208] permitted resolution of choline and two derivatives, phosphocholine and glycerophosphocholine, that is not possible *in vivo*; this permitted grading of the tumours based on high phosphocholine levels in high-grade tumours, while low-grade tumours exhibited elevated glycerophosphocholine.[207] An increase in malignancy was correlated with higher levels of choline, myo-inositol, alanine, taurine and glycine.[208] In the childhood brain tumours, degree of tumour necrosis and proportion of cancerous tissue could be assessed based on the metabolite ratios.[206] A more recent study of childhood brain tumours both *in vivo* and *ex vivo* found 8 of 12 metabolites that were useful in assessing the tumours; both HRMAS and MRS yielded similar results, although quantification and resolution were better under HRMAS, evident in Figure 7.[209] Taurine levels were found to correlate with apoptotic cell density in biopsies of gliomas.[210] Elevated creatine and glutamine levels, among other metabolic changes, were used to classify various tumours with over 90% accuracy on their metabolic profiles alone.[211] Metabolite profiles were found to be useful in tumour grading and tracked patient evolution better than traditional histopathological analysis.[212] A detailed assessment of 37 metabolites has been performed on glioblastoma brain tumour tissue; maintenance of the sample at 4 °C during analysis limited sample degradation,[213] and quantification of concentrations was successful using an electronically generated reference signal.[214] When combined with genomics, as little as 2 mg of tissue was all that was required to classify brain tumour biopsies; the non-destructive nature of HRMAS permitted the genomic analysis to use the NMR sample after spectral acquisition without difficulty.[215] Meningiomas have characterized in terms of a range of metabolites by *ex vivo* HRMAS, facilitating better *in vivo* analysis[216]; subsequent work has found these tumours to exhibit different levels of glutathione, glutamine, glutamate, phosphocholine and phosphoethanolamine based on the tumour class, while in this case alanine was not a useful discriminator.[217] Care must be exercised when using biopsy samples, as it has been noted that anaerobic glycolysis during biopsy reduces glucose levels and increases alanine and lactate; other metabolite concentrations were not affected.[218]

Higher molecular weight components have also been used to characterize tumours. Proton signals from small molecules bound to lipids or protein matrices are invisible to MRS due to their short transverse relaxation times and are only observable under HRMAS.[219] Metastases of brain tumours have been correlated with, in particular, the tumour lipid signals and validated by following the clinical outcomes; survival could be predicted based on a statistical analysis of the

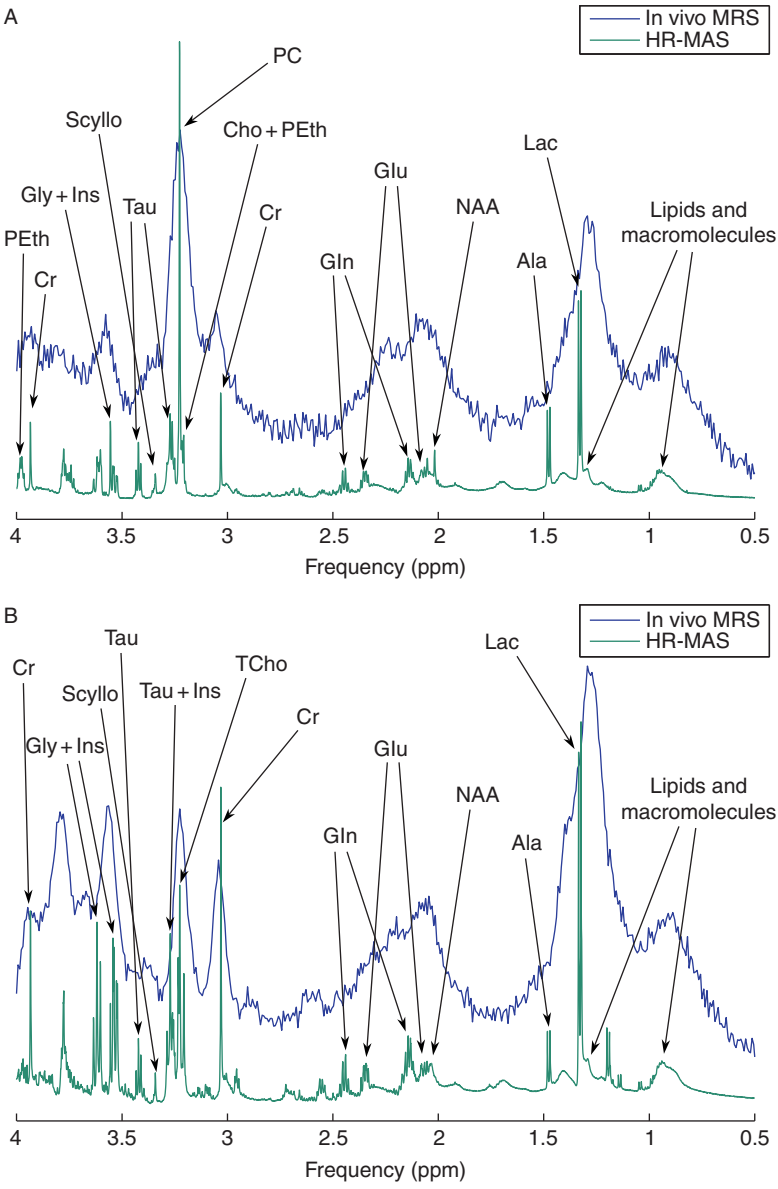

Figure 7 Comparison of ^{1}H *in vivo* MRS spectra at 1.5 T (upper traces) and *ex vivo* HRMAS NMR spectra at 14.1 T (lower traces) of (A) medulloblastoma tumour and (B) ependymoma tumour. Note the difference in resolutions available from each technique, although at a near 10-fold difference in applied magnetic field. Reprinted with permission from Wilson et al.[209] Copyright John Wiley and Sons, Ltd 2009.

metabolites.[220] Lipid signals in brain tumour tissue have been correlated with lipid droplets that arise from the cytoplasm and precede necrosis.[221] Interactions between small metabolites and macromolecules in tissues induce small shifts that need to be accounted for in analytical models.[222] It has been noted that, in cases where only small metabolites need to be characterized, MAS may not be necessary if a simple dilution of the brain tissue with excess D_2O is followed by high-resolution NMR, as concentrations of small metabolites were found to be consistent between the two methods.[223] Characterization of metabolite levels has advanced sufficiently that a secure clinical network has been outlined, based on pattern recognition of MRS, HRMAS and DNA microarray data for brain tumour diagnosis and prognosis.[224]

Other brain disorders besides cancer have been analysed using metabolic profiling; a recent review has highlighted the use of HRMAS in studies of neurodegenerative disorders.[225] *N*-acetyl-aspartate levels correlated with neuronal density; its ratio to creatine, among other metabolite ratios, could be used to distinguish normal brain tissue from that of Alzheimer's patients.[226] HRMAS and MRS could both be used to demonstrate decreased levels of *N*-acetyl-aspartate, γ-aminobutyric acid, glutamine and glutamate, as well as increased inositols, in the inherited brain disorder, infantile neuronal ceroid lipofuscinoses; however, no such metabolic changes were observed in the juvenile form of the same disorder.[227]

Breast cancer has been studied extensively by magnetic resonance imaging and MRS, and HRMAS is beginning to be applied to assist with *in vivo* analyses.[228,229] The advantages of direct HRMAS of tissues compared to perchloric acid extracts of them were detailed earlier.[230] Clinical profiles of large and small tumours showed higher levels of choline and glycine in large tumours, with the increased resolution afforded by HRMAS demonstrating that the relative intensities of the choline derivatives, choline, phosphocholine and glycerophosphocholine, unresolved in MRS, distinguished cancerous from healthy tissue.[231] Lower levels of glycine have been correlated with better patient prognoses in a correlation between multiple metabolite levels quantified with an external electronically generated input and patients' 5-year health status.[232] Biopsies from breast tumours have been assessed for histological grade, hormone status and lymphatic spread using various multivariate models of the metabolite concentrations and their extension to MRS has been proposed.[233] The response of human breast cancer tissue in a mouse model to docetaxel treatment showed a significant decrease in choline metabolite levels, suggesting that NMR could be used as an early drug treatment monitor.[234]

Similar approaches have been pursued with cervical cancer. Cervical cancer biopsies could be classified based on levels of lipids, choline and creatine.[235] Compared to tissue extracts, metabolite levels determined via HRMAS performed well, correlating degree of malignancy with elevated choline and amino acids, and decreased glucose.[236] Subsequently, lipid levels in cervical cancer cells have been correlated specifically with apoptosis, while choline, creatine, taurine, glucose and lactate levels indicated both tumour cell fraction and cell density.[237] Diffusion-weighted HRMAS was used to detect mobile lipid signals, indicating they

accumulate during tumourigenesis.[238] The pre-invasive to invasive transition in cervical cancer has been characterized through elevated choline-containing metabolites in invasive cancers observed using both ^{1}H and ^{31}P HRMAS NMR of biopsies,[239] with these elevated levels appearing in adjacent healthy tissue as well.[240]

Early work on HRMAS of prostate cancer tissues suggested that spermine could be used as a metabolic marker,[241] and that prostate cancer assessment can be improved by HRMAS metabolite profiling.[242] Healthy tissue could be distinguished from cancerous tissue through lower levels of citrate and polyamines, and higher concentrations of choline metabolites; greater changes in these levels correlated with aggressive cancers.[243] However, recent work has indicated that HRMAS fails to detect polyamines including spermine in both human prostate biopsies and mouse xenografts.[244] Choline degradation in tissue samples was minimized by performing HRMAS at 1 °C, essential if choline levels are to be used as a metabolic marker of disease.[245] High resolution afforded by the *ex vivo* analysis permitted phosphocholine increases and phosphoethanolamine decreases to be used as specific markers of cancer presence.[246] Increased lactate and alanine levels have also been proposed, where increases in their concentration were indicative of as low as 5% cancer in the tissue sample.[247] Choline, citrate and lactate levels have been used to assess Gleason scores in prostate needle biopsies, in their ratios to creatine.[248] Polyunsaturated omega-6 fatty acids have been detected in advanced prostate tumours, while they were absent in normal and early-stage cancerous tissues.[249] Freezing of tissue samples at −80 °C over a 12- to 16-h period for later HRMAS analysis was generally not detrimental to accurate metabolite analysis, although citrate and acetate levels were somewhat affected[250]; after 32 months, however, there was no observable differences in metabolites of these same specimens once sampling issues were accounted for.[251] It is important to note, though, that these two studies of tissue storage effects did not include any cancerous tissue, which may be more susceptible to changes under storage.[251] The complementarity of HRMAS to MRS in obtaining molecular information concerning prostate cancer has been reviewed.[203] In related work, testicular biopsies have been used to characterize metabolic signatures of infertile men, with phosphocholine emerging as a convenient marker.[252]

Among other applications is the discrimination of two types of lymphoma through alanine and taurine levels.[253] Gastrointestinal disorders have been studied; gastric adenocarcinoma is accompanied by high levels of triglycerides.[254] Increases in choline, glycine, alanine as well as triglycerides were observed during gastric carcinogenesis.[255] Metabolic characterization of five distinct regions of a normal gastrointestinal tract has been completed, with clear distinction in their profiles, including ^{1}H and ^{31}P HRMAS data.[256,257] Biopsies of ulcerative colitis exhibited elevated antioxidants and amino acids with decreased lipids, glycerophosphocholine, myo-inositol and betaine; colonocytes showed only these depressed levels, with no metabolite elevated.[258] Increases in taurine, glutamate, aspartate and lactate, with decreased levels of myo-inositol and glucose, have been identified as markers of colorectal cancer[259]; others have noted increases in lipids, acetate and lactate as well, even in tissues 15 cm from the tumour.[260] When

compared to colorectal cancer biopsies, one of the three particular mouse xenograft models has been found to be most similar to actual human cancers, in their lipid, lactate and choline metabolite levels most notably.[261] Combined analysis with GCMS and HRMAS NMR of biopsies has been proposed as a new diagnostic tool for colorectal cancer.[262]

In phase 1 of a clinical trial, HRMAS NMR of renal tissue has correctly identified absence of disease when compared to histology and imaging.[263] Fifty metabolites have been characterized in lung cancer biopsies, with increased lactate, phosphocholine and glycerophosphocholine found in tumour tissue; care was taken to complete HRMAS analyses within 2 h to minimize post-biopsy conversion of phosphocholine and glycerophosphocholine to choline.[264] Detection of lung cancer prior to onset of clinical symptoms may be possible using HRMAS of serum samples; relative volumes of tumours and discrimination of types of cancer were evident from the analyses.[265]

Intervertebral disc analysis by imaging and MRS has been recently reviewed[266]; the degree of vertebrate disc degeneration correlated with *N*-acetylaspartate:choline and choline:carbohydrate ratios, but no relaxation differences, a tool proposed for imaging analyses, were evident.[267,268] Changes in cartilage metabolites have been proposed as markers for degenerative joint diseases.[269] The creatine and phosphocreatine signals in skeletal muscle have been resolved by HRMAS.[270] When treated with the chemotherapeutic agent chloroethylnitrosourea, liver and bone cancer cell lines were observed to undergo changes to their mitochondrial oxidative phosphorylation mechanism in order to promote cancer cell survival.[271] Liver function both pre- and post-transplant has been monitored by following lipid composition *ex vivo*[272]; 22 metabolites have been characterized in liver needle biopsies.[273] Presence of liver cancer, as well as its grade, can be determined from the levels of lactate, amino acids, phosphoethanolamine and choline metabolites in liver tissues.[274] Choline levels in amniotic fluid were used as a probe of fetal lung maturity in an effort to prevent neonatal morbidity and mortality.[275]

9. ANIMAL AND PLANT METABOLITES

More controlled systems of disease and metabolism are available through the use of animal models, and numerous studies of metabolite profiles have utilized HRMAS to elucidate these. Rats and mice are particularly common choices for the study of disease, due to variants that have genetic predispositions to display or resist certain metabolic traits or pathways, and the ease with which these can be stressed, modified, contrasted or subjected to putative treatment.

Brain metabolism under a variety of conditions has been evaluated. Apoptosis-induced changes in metabolite levels in rat glioma cells have been well characterized, noting in particular the increase in lipid concentrations.[276–279] Using a number of ^{1}H and ^{13}C HRMAS, *in vivo* and transcriptional analyses, the increase has been shown to arise from a non-membrane source, and choline derivatives, a common marker, showed no changes. Subsequently, the higher resolution

afforded by *ex vivo* HRMAS showed that choline derivatives differed in their response to gene therapy-induced apoptosis in rat gliomas.[280] Choline was also found to behave differently between brain tissues and tissue extracts in SIV-infected macaques, while six other metabolites compared well[281]; the difference in choline levels was attributed to an inability to detect membrane-bound choline in HRMAS or to a baseline artefact. Long periods of MAS were found to release creatine from membranes to an NMR-visible form, while delayed freezing of rat brain tissues caused changes in glycolysis metabolites.[282] It was recently discovered that fatty acid metabolism is altered in rat glioma cells treated with an antimitotic oleyl glycoside, leading to apoptosis, highlighting the use of HRMAS to monitor the actions of therapeutic agents on cancer cell functions.[283]

Natural abundance ^{13}C HRMAS of brain tissue yielded best results for small metabolites using the high-resolution DEPT sequence exploiting indirect coupling for sensitivity enhancement, while more motionally restricted lipid signals were best observed using the dipolar coupling-dependent cross-polarization technique.[284] Injection of ^{13}C-enriched glucose followed by ^{13}C HRMAS of brain tissue indicates even incorporation of the isotopic label into glutamate, glutamine, aspartate and γ-aminobutyric acid, and compared well to results from tissue extracts (see Figure 8).[285]

A survey of rat brain metabolites in different regions, including the stem, cerebellum, frontal cortex and hippocampus, demonstrated clear differences in the levels of key metabolites,[286] are also evident as a function of age,[287] and served

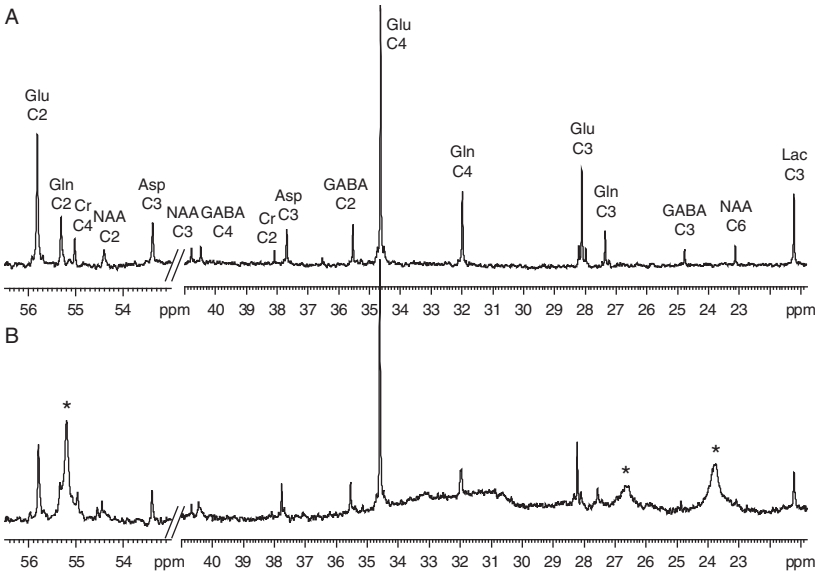

Figure 8 Comparison of ^{13}C NMR spectra of rat thalamus tissue (A) extracted with perchloric acid and obtained in solution and (B) obtained directly on the tissue sample using HRMAS 15 min after injecting the rats with [1,6-^{13}C]-glucose. Asterisks indicate lipid signals. Reprinted with permission from Risa et al.[285] Copyright John Wiley and Sons, Ltd 2009.

as a baseline for a follow-up study on the changes that result in each region when Huntington's disease symptoms were induced using 3-nitropropionic acid, most notably a universal, dose-dependent increase in succinate.[288] Vitamin A deficiency in young rats resulted in lower *N*-acetyl-aspartate, creatine and phosphocreatine, with increased myo-inositol, although anatomical changes in the brain were evident earlier than these metabolic differences.[289] The schizophrenia drug haloperidol showed no effect of *N*-acetyl-aspartate levels in rat brain.[290] Rat hippocampus regions showed decreased *N*-acetyl-aspartate and increased choline derivatives, consistent with neuronal loss and cell breakdown, after treatment with kainic acid.[291] Sleep deprivation in rats changes the levels of glutamate in different regions of their brains.[292] A slight decrease in phosphocholine was noted in the hippocampus regions of rats exposed to pyridostigmine bromide, an anti-nerve agent and purported contributor to Gulf War Illness.[293]

Electrically stimulated epileptic seizures showed early increases in total creatine, choline and alanine levels in rats' brains,[294] while exposing rats to soman to induce epileptic-like symptoms resulted in increased alanine and acetate, as well as lactate, glycerophosphocholine and glutamine, with reduced levels of myo-inositol and *N*-acetyl-aspartate.[295] In mice, soman-induced seizures increased and decreased the same metabolites as well as increasing the levels of choline and γ-aminobutyric acid.[296] In mice with the cerebral metabolic defects associated with Batten disease, a childhood neurodegenerative disorder, changes in lipid deposition in the cortex were detected only by HRMAS of brain tissue.[297] Mice exhibiting ataxia were found to have increased levels of glutamine and decreased γ-aminobutyric acid, choline, phosphocholine and lactate.[298] The effects of neonatal alcohol exposure,[299] as well as toluene inhalation on juvenile[300] and older rats,[301] demonstrated different changes in metabolites across different brain regions, and at different ages of the animals.

The effect of dietary toxins often is most noticeable in liver and kidney before effects are apparent in other organs, hence a popular area has been that of animal models of biochemical toxicology in determining the precise metabolic action in these organs through *ex vivo* HRMAS of tissues directly, rather than tissue extracts.[302] The toxin D-galactosamine increased cholesterol and esters in the livers of rats, with tissues cultured in spheroids rather than monolayers.[303] The toxicity of acetaminophen in mouse liver was correlated with an increase in liver triglycerides and monosaturated fatty acids, with a decrease of polyunsaturated fatty acids, phospholipids, glucose and glycogen, which was taken as a sign of increased glycolysis.[304] The toxicity of a HIV therapy drug candidate was also shown to be due to an impaired fatty acid metabolism, resulting in an increase in liver triglyceride levels.[305] The effects of hydrazine treatment on rat liver metabolic profiles were amplified through spectral editing and pattern recognition techniques applied to liver tissues; elevated lipids and alanine, decreased glycogen, choline, taurine, trimethylamine-*N*-oxide and glucose were evident.[306] Similar effects were observed in the kidneys of rats exposed to $HgCl_2$, especially in the renal cortex.[307] Heavy-metal toxins, $La(NO_3)_3$ and $Ce(NO_3)_3$, resulted in elevated triglycerides in both liver and kidney tissues in rats, with the liver noted as the main target of the toxicity.[308,309] The time course of metabolites in rat liver, as well

as plasma and urine, after exposure to the liver toxin allyl formate indicated mitochondrial impairment and increased glucose utilization in the liver.[310] A coincident increase in liver lipids with decreased plasma lipids demonstrated that changes were occurring in lipid transport as a result.

Isochronous signals in fatty rat liver tissue could be resolved based on changes in the measured diffusion coefficients from a gradient HRMAS measurement; an increase in the diffusion coefficient of the signal arising from co-resonant glucose, betaine and trimethylamine-*N*-oxide indicated an increase in the levels of the smallest contributor, trimethylamine-*N*-oxide.[311] The livers of type 2 diabetic mice showed elevated triglycerides and bile acids, with reduced levels of trimethylamine-*N*-oxide and choline derivatives, while their kidneys showed no clear changes in metabolite levels.[23] The complicated metabolism of the conception and hormone replacement therapeutic agent, medroxyprogesterone acetate, by P450 enzymes in pig liver were determined to result mainly in 6β-, 1β- and 2β-hydroxy derivatives. Hypercholesterolaemic pigs were subjected to two high-fibre diets based on either wheat or rye to evaluate their liver response.[312] Pigs on the rye diet reduced their cholesterol through a liver cholesterol metabolism. Normal and hypertensive rat kidney tissue showed marked differences in the metabolite levels of their cortex regions, in particular.[313]

The development of the rat intestinal tract has been followed for young rats through monitoring changes in metabolite levels. Both the ileum and jejunum showed increases in lipids, lactate, taurine and creatine with age, while glycerophosphocholine decreased.[314] Gastrointestinal tumours in mice have shown early decreases in glycerophosphocholine and dimethylamine, with increase in lactate and myo-inositol.[315] When mice with colon cancer were treated with omega-3 fatty acids, such as fish oil, tumour growth was reduced compared to mice fed corn oil, and phosphocholine levels were lower.[316] The benefits of probiotic *Lactobacilli* on intestinal tissue have been evaluated; homocysteine and ascorbate metabolism were most influenced by their presence, in a fairly comprehensive survey of metabolic changes in adrenal glands, kidneys, pancreas, plasma, liver, faeces and urine of mice.[317,318]

The effects of ultraviolet radiation on animal eyes, specifically the lens and cornea, have been studied extensively, with particular emphasis on determining the metabolic changes associated with the onset of cataracts. The metabolic profile of rat lens after exposure showed non-dose-dependent increases in alanine and adenosine–monophosphate, with 13 other water-soluble metabolites decreasing.[319] When followed over time, phenylalanine increased 125 h after exposure, while all others were lower; after 625 h, most metabolites had recovered to normal levels.[320] These metabolic changes occurred over a much longer time scale than was evident from light scattering of the lenses. Another contributor to the onset of cataracts, long-term steroid use, was evaluated in rabbit lenses where the rabbits were exposed to the steroid dexamethasone.[321–323] The metabolites glutathione, inositol, taurine, lactate and ascorbate all decreased after steroid treatment; glucose increased. Single and repeated exposures to UV radiation resulted in similar changes in the cornea, with decreases noted previously and increases in both glucose and betaine.[324] Selenite-induced cataracts in rat lenses correlated with

increases in amino acid levels, and significant decreases in glutathione, succinate and phosphocholine; these changes correlated with lens opacification.[325] These changes could be separated from maturing effects in lenses of rats, which were largely increases in taurine, hypotaurine and myo-inositol.[326] A complete metabolic profile of the four different regions of the rat lens after UV radiation exposure has also been completed.[327]

Initial work on rat heart tissues indicated that mitochondrial metabolites are often invisible to NMR where intact membranes were present; tissue extracts were found to be more reliable[328] More recently, the effects of methamphetamine on rat heart wall metabolites showed decreases in serotonin and choline, while carnitine levels increased, consistent with an increase in fatty acid metabolism.[329] Discrimination between pancreatic cancer and chronic pancreatitis in rats has been established based on HRMAS metabolite profiles.[330] The cancer had lower levels of choline derivatives and higher levels of amino acids and lipids; pancreatitis demonstrated reverse changes. The best markers of cancer were noted as decreased levels of phosphocholine and glycerophosphocholine. Treatment of melanoma in mice with cystemustine resulted in changes in the phospholipid metabolism within the tumours geared towards tumour survival, characterized by increases in phosphocholine and phosphoethanolamine.[331] Similarly, treatment with chloroethylnitrosourea resulted in an initial increase in glucose, glutamine and aspartate levels as the tumour growth was inhibited, followed by increases in polyunsaturated fatty acids and reduced utilization of glucose as tumour growth recovered.[332] The methionine metabolism in these tumours was elucidated by using L-(methyl-^{13}C)methionine as a feedstock and following its fate in the tumours.[333] Others have noted that the use of ^{31}P-based HRMAS methods could be particularly useful in following the levels and fates of phosphorus-containing metabolites associated with cancer.[334,335]

Mice with an inability to biosynthesize creatine due to a guanidinoacetate methyltransferase deficiency showed no metabolic changes in *in vivo* MRS; however, HRMAS of excised muscle tissue showed a notable increase in guanidinoacetate levels.[336] The effects of burn trauma on mice muscle were characterized both *in vivo* and *ex vivo*, showing a similar increase in lipids and resulting apoptosis.[337] Treatment of mouse fibrosarcomas with a vascular-disrupting agent showed a decrease in phosphocholine and glycerophosphocholine levels, which was consistent with reduced cell membrane turnover; this was proposed as a sensitive biomarker for monitoring the response to treatment.[338] The time course of cartilage degradation in guinea pigs over a 120-day period showed the cascade leading to breakdown; an initial increase in proteoglycans was followed by a sharp increase in signals from chondrocyte membrane lipids and finally an increase in mobile methyl signals due to collagen breakdown.[339] Testicular tissue from rats exposed to the spermatocyte toxicant ethyleneglycol monomethylether showed effects consistent with perturbation of their energy supply, suppression of the citric acid cycle or oxidative stress.[340]

Finally, several novel organisms have had their metabolic profiles studied. Earthworms have been characterized in terms of their metabolites as a function of body part; the low toxicity of the herbicide glyphosate on earthworm was

confirmed in profiles of exposed and pristine specimens.[341] Two types of poplar tree have been profiled in terms of their growth process metabolic changes; the authors noted that detection and understanding of different lignification processes may be possible through HRMAS.[342] The efficiency of different solvents used in plant tissue extraction has been verified through HRMAS of the plant residues.[343]

REFERENCES

1. W. P. Power, High resolution magic angle spinning—applications to solid phase synthetic systems and other semi-solids. *Annu. Rep. NMR Spectrosc.*, 2003, **51,** 261–295.
2. S. Hayashi, Sealing effect of magic-angle-spinning rotors in solid-state NMR. *Anal. Sci.*, 2009, **25,** 133–136.
3. T. R. Ramadhar, F. Amador, M. J. T. Ditty and W. P. Power, Inverse H–C ex situ HRMAS NMR experiments for solid-phase peptide synthesis. *Magn. Reson. Chem.*, 2008, **46,** 30–35.
4. A. S. Zektzer, M. G. Swanson, S. Jarso, S. J. Nelson, D. B. Vigneron and J. Kurhanewicz, Improved signal to noise in high-resolution magic angle spinning total correlation spectroscopy studies of prostate tissues using rotor-synchronized adiabatic pulses. *Magn. Reson. Med.*, 2005, **53,** 41–48.
5. O. C. Andronesi, D. Mintzopoulos, J. Struppe, P. M. Black and A. A. Tzika, Solid-state NMR adiabatic TOBSY sequences provide enhanced sensitivity for multidimensional high-resolution magic-angle-spinning ^{1}H MR spectroscopy. *J. Magn. Reson.*, 2008, **193,** 251–258.
6. M. Borel, D. Lafarge, M. F. Moreau, M. Bayle, L. Audin, N. Moins and J. C. Madelmont, High resolution magic angle spinning NMR spectroscopy used to investigate the ability of drugs to bind to synthetic melanin. *Pigment Cell Res.*, 2005, **18,** 49–54.
7. R. Avni, O. Mangoubi, R. Bhattacharyya, H. Degani and L. Frydman, Magnetization transfer magic-angle-spinning z-spectroscopy of excised tissues. *J. Magn. Reson.*, 2009, **199,** 1–9.
8. M. Piotto, K. Elbayed, J. M. Wieruszeski and G. Lippens, Practical aspects of shimming a high resolution magic angle spinning probe. *J. Magn. Reson.*, 2005, **173,** 84–89.
9. K. Elbayed, B. Dillmann, J. Raya, M. Piotto and F. Engelke, Field modulation effects induced by sample spinning: application to high-resolution magic angle spinning NMR. *J. Magn. Reson.*, 2005, **174,** 2–26.
10. K. Thieme and I. Schnell, Determination of long-range distances and dynamic order parameters by dipolar recoupling in high-resolution magic-angle spinning NMR spectroscopy. *J. Am. Chem. Soc.*, 2003, **125,** 12100–12101.
11. J. Raya, A. Bianco, J. Furrer, J. P. Briand, M. Piotto and K. Elbayed, Proton dipolar recoupling in resin-bound peptides under high-resolution magic angle spinning. *J. Magn. Reson.*, 2002, **157,** 43–51.
12. D. Aucoin, D. Camenares, X. Zhao, J. Jung, T. Sato and S. O. Smith, High-resolution ^{1}H MAS RFDR NMR of biological membranes. *J. Magn. Reson.*, 2009, **197,** 77–86.
13. C. Sizun, J. Raya, K. Elbayed, A. Intasiri and A. Boos, Investigation of the surfactants in CTAB-templated mesoporous silica by ^{1}H HRMAS NMR. *Microporous Mesoporous Mater.*, 2003, **66,** 27–36.
14. A. Rencurosi, L. Lay, G. Russo, D. Prosperi, L. Poletti and E. Caneva, HRMAS NMR analysis in neat ionic liquids: a powerful tool to investigate complex organic molecules and monitor chemical reactions. *Green Chem.*, 2007, **9,** 216–218.
15. P. J. Carvalho, V. H. Alvarez, B. Schroeder, A. M. Gil, I. M. Marrucho, M. Aznar, L. M. Santos and J. A. Coutinho, Specific solvation interactions of CO_2 on acetate and trifluoroacetate imidazolium based ionic liquids at high pressures. *J. Phys. Chem.*, 2009, **113,** 6803–6812.
16. M. Gala, C. Melianb, D. E. Demcob, B. Blmichb and L. Frydman, Solid-state single-scan 2D NMR under magic-angle-spinning. *Chem. Phys. Lett.*, 2008, **459,** 188–193.
17. S. Viel, G. Excoffier, G. Pags, F. Ziarelli, C. Delaurent and S. Caldarelli, Combined use of pulsed gradient spin echo and high resolution magic angle spinning to investigate solutes diffusion in presence of a chromatographic stationary phase. *Diffus. Fundam.*, 2007, **6,** 7.1–7.2.

18. G. Pages, C. Delaurent and S. Caldarelli, Investigation of the chromatographic process via pulsed-gradient spin-echo nuclear magnetic resonance. Role of the solvent composition in partitioning chromatography. *Anal. Chem.*, 2006, **78,** 561–566.
19. S. Viel, F. Ziarelli and S. Caldarelli, Enhanced diffusion-edited NMR spectroscopy of mixtures using chromatographic stationary phases. *Proc. Natl. Acad. Sci. USA*, 2003, **100,** 9696–9698.
20. E. E. Romanova, F. Grinberg, A. Pampel, J. Karger and D. Freude, Diffusion studies in confined nematic liquid crystals by MAS PFG NMR. *J. Magn. Reson.*, 2009, **196,** 110–114.
21. S. Caldarelli, Chromatographic NMR: a tool for the analysis of mixtures of small molecules. *Magn. Reson. Chem.*, 2007, **45,** S48–S55.
22. S. A. Bradley and R. L. McLaughlin, High-resolution magic-angle spinning NMR for the identification of reaction products directly from thin-layer chromatography spots. *Magn. Reson. Chem.*, 2007, **45,** 814–818.
23. J. Xu, T. Tan, L. Kenne and C. Sandstrom, The use of diffusion-ordered spectroscopy and complexation agents to analyze mixtures of catechins. *New J. Chem.*, 2009, **33,** 1057–1063.
24. M. Coen, I. D. Wilson, J. K. Nicholson, H. Tang and J. C. Lindon, Probing molecular dynamics in chromatographic systems using high-resolution ^{1}H magic-angle-spinning NMR spectroscopy: interaction between *p*-xylene and C18-bonded silica. *Anal. Chem.*, 2004, **76,** 3023–3028.
25. C. Meyer, U. Skogsberg, N. Welsch and K. Albert, Nuclear magnetic resonance and high-performance liquid chromatographic evaluation of polymer-based stationary phases immobilized on silica. *Anal. Bioanal. Chem.*, 2005, **382,** 679–690.
26. V. Friebolin, S. Marten and K. Albert, Characterization of binding affinities in a chromatographic system by suspended state HR/MAS NMR spectroscopy. *Magn. Reson. Chem.*, 2009, **48,** 111–116.
27. S. Schauff, V. Friebolin and M. D. Grynbaum, Monitoring the interactions of tocopherol homologues with reversed-phase stationary HPLC phases by ^{1}H suspended-state saturation transfer difference high-resolution/magic angle spinning NMR spectroscopy. *Anal. Chem.*, 2007, **79,** 8323–8326.
28. U. Skogsberg, H. Hndel, D. Sanchez and K. Albert, Comparisons of the interactions between two analytes and two structurally similar chiral stationary phases using high-performance liquid chromatography, suspended-state high-resolution magic angle spinning nuclear magnetic resonance and solid-state nuclear magnetic resonance spectroscopy. *J. Chromatogr. A*, 2004, **1023,** 215–223.
29. C. Hellriegel, U. Skogsberg, K. Albert, M. Lammerhofer, N. M. Maier and W. Lindner, Characterization of a chiral stationary phase by HR/MAS NMR spectroscopy and investigation of enantioselective interaction with chiral ligates by transferred NOE. *J. Am. Chem. Soc.*, 2004, **126,** 3809–3816.
30. R. W. Martin, R. C. Jachmann, D. Sakellariou, U. G. Nielsen and A. Pines, High-resolution nuclear magnetic resonance spectroscopy of biological tissues using projected magic angle spinning. *Magn. Reson. Med.*, 2005, **54,** 253–257.
31. M. A. Burns, J. L. Taylor, C. L. Wu, A. G. Zepeda, A. Bielecki, D. Cory and L. L. Cheng, Reduction of spinning sidebands in proton NMR of human prostate tissue with slow high-resolution magic angle spinning. *Magn. Reson. Med.*, 2005, **54,** 34–42.
32. J. L. Taylor, C. L. Wu, D. Cory, R. G. Gonzalez, A. Bielecki and L. L. Cheng, High-resolution magic angle spinning proton NMR analysis of human prostate tissue with slow spinning rates. *Magn. Reson. Med.*, 2003, **50,** 627–632.
33. R. A. Wind and J. Z. Hu, In vivo and ex vivo high-resolution ^{1}H NMR in biological systems using low-speed magic angle spinning. *Prog. Nucl. Magn. Reson. Spectrosc.*, 2006, **49,** 207–259.
34. J. Z. Hu, R. A. Wind, J. McLean, Y. A. Gorby, C. T. Resch and J. K. Fredrickson, High-resolution ^{1}H NMR spectroscopy of metabolically active microorganisms using non-destructive magic angle spinning. *Spectroscopy*, 2004, **19,** 98–103.
35. H. C. Bertram, J. Z. Hu, D. N. Rommereim, R. A. Wind and H. J. Andersen, Dynamic high-resolution ^{1}H and ^{31}P NMR spectroscopy and ^{1}H T_2 measurements in postmortem rabbit muscles using slow magic angle spinning. *J. Agric. Food Chem.*, 2004, **52,** 2681–2688.
36. H. C. Bertram, H. J. Jakobsen and O. B. Nielsen, Origin of the high-frequency resonances in ^{1}H NMR spectra of muscle tissue: an in vitro slow magic-angle spinning study. *J. Agric. Food Chem.*, 2005, **53,** 3229–3234.

37. J. Z. Hu, D. N. Rommereim and R. A. Wind, High-resolution ^{1}H NMR spectroscopy in rat liver using magic angle turning at a 1 Hz spinning rates. *Magn. Reson. Med.*, 2002, **47,** 829–836.
38. J. Z. Hu and R. A. Wind, The evaluation of different MAS techniques at low spinning rates in aqueous samples and in the presence of magnetic susceptibility gradients. *J. Magn. Reson.*, 2002, **159,** 92–100.
39. R. A. Wind, J. Z. Hu and D. N. Rommereim, High-resolution ^{1}H NMR spectroscopy in a live mouse subjected to 1.5 Hz magic angle spinning. *Magn. Reson. Med.*, 2003, **50,** 1113–1119.
40. R. A. Wind, J. Z. Hu and P. D. Majors, Localized in vivo isotropic-anisotropic correlation ^{1}H NMR spectroscopy using ultraslow magic angle spinning. *Magn. Reson. Med.*, 2005, **55,** 41–49.
41. A. S. Edison and J. R. Long, The magic of solenoids. *Nature*, 2007, **447,** 646–647.
42. D. Sakellariou, G. Le Goff and J. F. Jacquinot, High-resolution, high-sensitivity NMR of nanolitre anisotropic samples by coil spinning. *Nature*, 2007, **447,** 694–697.
43. A. Wong, P. M. Aguiar and D. Sakellariou, Slow magic-angle coil spinning: a high-sensitivity and high-resolution NMR strategy for microscopic biological specimens. *Magn. Reson. Med.*, 2010, **63,** 269–274.
44. R. Annunziata, J. Franchini, E. Ranucci and P. Ferruti, Structural characterisation of poly(amidoamine) networks via high-resolution magic angle spinning NMR. *Magn. Reson. Chem.*, 2007, **45,** 51–58.
45. G. A. Giffin, F. Y. Castillo, R. Frech, D. T. Glatzhofer and C. M. Burba, Spectroscopic investigation of proton-conducting, cross-linked linear poly(ethylenimine) hydrochloride membranes. *Polymer*, 2009, **50,** 171–176.
46. N. Sahloul, A. Emwas, W. Power and A. Penlidis, Ethyl acrylate–hydroxyethyl acrylate and hydroxyethyl acrylate–methacrylic acid: reactivity ratio estimation from cross-linked polymer using high resolution magic angle spinning spectroscopy. *J. Macromol. Sci. A: Pure Appl. Chem.*, 2005, **42,** 1369–1385.
47. H. Komber, A. Ziemer and B. Voit, Etherification as side reaction in the hyper-branched polycondensation of 2,2-bis(hydroxymethyl)propionic acid. *Macromolecules*, 2002, **35,** 3514–3519.
48. L. Najemi, T. Jeanmaire, A. Zerroukhi and M. Raihane, Isocyanate-free route to starch-graft-polycaprolactone via carbonyldiimidazole (CDI)-mediated end group conversion. *Starch*, 2010, **62,** 90–101.
49. L. Montero De Espinosa, J. C. Ronda, M. Gali and V. Cdiz, A straightforward strategy for the efficient synthesis of acrylate and phosphine oxide-containing vegetable oils and their crosslinked materials. *J. Polym. Sci. A: Polym. Chem.*, 2009, **47,** 4051–4063.
50. G. Ru, N. Wang, S. Huang and J. Feng, ^{1}H HRMAS NMR study on phase transition of poly(*N*-isopropylacrylamide) gels with and without grafted comb-type chains. *Macromolecules*, 2009, **42,** 2074–2078.
51. P. Castignolles, R. Graf, M. Parkinson, M. Wilhelm and M. Gaborieau, Detection and quantification of branching in polyacrylates by size-exclusion chromatography (SEC) and melt-state ^{13}C NMR spectroscopy. *Polymer*, 2009, **50,** 2373–2383.
52. J. Rueda, R. Suica, H. Komber and B. Voit, Synthesis of new polymethyloxazoline hydrogels by the ''macroinitiator'' methods. *Macromol. Chem. Phys.*, 2003, **204,** 954–960.
53. J. C. Rueda, H. Komber, B. Voit, J. C. Cedrn and G. Shevtsova, Synthesis of new hydrogels by copolymerization of poly(2-methyl-2-oxazoline) bis(macromonomers) and *N*-vinylpyrrolidone. *Macromol. Chem. Phys.*, 2003, **204,** 947–953.
54. J. C. Rueda, H. Komber and B. Voit, Synthesis of new amphiphilic and lypophilic polymer networks containing 2-methyl- and 2-nonyl-2-oxazoline by the macroinitiator method. *J. Polym. Sci. A: Polym. Chem.*, 2005, **43,** 122–128.
55. J. C. Cuggino, C. I. A. Igarzabal, J. C. Rueda, L. M. Quinzani, H. Komber and M. C. Strumia, Synthesis and characterization of new hydrogels through copolymerization of *N*-acryloyl-tris-(hydroxymethyl)aminomethane and different crosslinking agents. *Eur. Polym. J.*, 2008, **44,** 3548–3555.
56. F. Su, C. L. Bray, B. O. Carter, G. Overend, C. Cropper, J. A. Iggo, Y. Z. Khimyak, A. M. Fogg and A. I. Cooper, Reversible hydrogen storage in hydrogel clathrate hydrates. *Adv. Mater.*, 2009, **21,** 2382–2386.

57. W. V. Camp, T. Dispinar, B. Dervaux, F. E. du Prez, J. C. Martins and B. Fritzinger, Click functionalization of cryogels conveniently verified and quantified using high-resolution MAS NMR spectroscopy. *Macromol. Rapid Commun.*, 2009, **30,** 1328–1333.
58. M. Macchione, J. C. Jansen, G. De Luca, E. Tocci, M. Longeri and E. Drioli, Experimental analysis and simulation of the gas transport in dense Hyflon® AD60X membranes: influence of residual solvent. *Polymer*, 2007, **48,** 2619–2635.
59. X. Chen, M. Lin, Z. Chen and J. Zhong, Fast acquisition scheme for achieving high-resolution MRS with J-scaling under inhomogeneous fields. *Magn. Reson. Med.*, 2009, **61,** 775–784.
60. U. Skogsberg, C. Meyer, J. Rehbein, G. Fischer, S. Schauff, N. Welsch, K. Albert, A. J. Hall and B. Sellergren, A solid-state and suspended-state magic angle spinning nuclear magnetic resonance spectroscopic investigation of a 9-ethyladenine molecularly imprinted polymer. *Polymer*, 2007, **48,** 229–238.
61. J. Blas, A. Rivera-Sagredo, R. Ferritto and J. F. Espinosa, Structural characterization and quantitation of compound loading of disubstituted benzoates bound to Wang resin through high-resolution magic angle spinning NMR spectroscopy. *Magn. Reson. Chem.*, 2004, **42,** 950–954.
62. N. H. Yao, W. Y. He, K. S. Lam and G. Liu, Solid-phase synthesis of *O*-glycosylated *N*α-Fmoc amino acids and analysis by high-resolution magic angle spinning NMR. *J. Comb. Chem.*, 2004, **6,** 214–219.
63. N. M. Loening, T. Kanemitsu, P. H. Seeberger and R. G. Griffin, Solid-phase synthesis and ^{1}H and ^{13}C high-resolution magic angle spinning NMR of ^{13}C-labeled resin-bound saccharides. *Magn. Reson. Chem.*, 2004, **42,** 453–458.
64. J. S. Fruchart, G. Lippens, C. Kuhn, H. Gras-Masse and O. Melnyk, Solid-phase enolate chemistry investigated using HR-MAS NMR spectroscopy. *J. Org. Chem.*, 2002, **67,** 526–532.
65. T. Ruhland, J. Torang, H. Pedersen, J. C. Madsen and K. S. Bang, Traceless solid phase synthesis with polystyrene-bound tellurium and in comparison with polystyrene-bound selenium. *Synthesis*, 2004, **14,** 2323–2328.
66. T. Ruhland, J. Torang, H. Pedersen, J. C. Madsen and K. S. Bang, Green traceless cleavage from resin-bound selenium and tellurium and analysis by 2D $^{29}Si/^{1}H$ HR-MAS NMR spectroscopy. *Synthesis*, 2005, **10,** 1635–1640.
67. L. Taboada, L. Prieto, P. Vidal, J. F. Espinosa and J. A. Erickson, Solid-phase synthesis of novel trimers containing a phenylstatine core and analysis by high-resolution magic angle spinning. *J. Comb. Chem.*, 2007, **9,** 748–755.
68. S. Porto, J. M. Seco, J. F. Espinosa, E. Quinoa and R. Riguera, Resin-bound chiral derivatizing agents for assignment of configuration by NMR spectroscopy. *J. Org. Chem.*, 2008, **73,** 5714–5722.
69. J. Furrer, K. Elbayed, M. Bourdonneau, J. Raya, D. Limal, A. Bianco and M. Piotto, Characterization of Italian durum wheat semolina by means of chemical analytical and spectroscopic determinations. *Magn. Reson. Chem.*, 2002, **40,** 123–132.
70. G. Lippens, G. Chessari and J. M. Wieruszeski, Resin dynamics contributes to the NMR line broadening of organic molecules grafted onto a polystyrene resin. *J. Magn. Reson.*, 2002, **156,** 242–248.
71. J. C. Martins, F. A. Mercier, A. Vandervelden, M. Biesemans, J. M. Wieruszeski, E. Humpfer, R. Willem and G. Lippens, Fine-tuned characterization at the solid/solution interface of organotin compounds grafted onto cross-linked polystyrene by using high-resolution MAS NMR spectroscopy. *Chem. Eur. J.*, 2002, **8,** 3431–3441.
72. G. Deshayes, K. Poelmans, I. Verbruggen, C. Camacho-Camacho, P. Dege, V. Pinoie, J. C. Martins, M. Piotto, M. Biesemans, R. Willem and P. Dubois, Polystyrene-supported organotion dichloride as a recyclable catalyst in lactone ring-opening polymerization: assessment and catalysis monitoring by high-resolution magic-angle-spinning NMR spectroscopy. *Chem. Eur. J.*, 2005, **11,** 4552–4561.
73. K. Poelmans, V. Pinoie, I. Verbruggen, M. Biesemans, R. Willem, G. Deshayes, E. Duquesne, C. Delcourt, P. Dege, P. Dubois and H. E. Miltner, Undecyltin trichloride grafted onto cross-linked polystyrene: an efficient catalyst for ring-opening polymerization of ε-caprolactone. *Organometallics*, 2008, **27,** 1841–1849.
74. V. Pinoie, K. Poelmans, I. Verbruggen, M. Biesemans, R. Willem, H. Miltner, G. Van Assche, B. Van Mele and J. Martins, A polystyrene-supported tin trichloride catalyst with a C11-spacer.

Catalysis monitoring using high-resolution magic angle spinning NMR. *Organometallics*, 2007, **26,** 6718–6725.
75. M. Gruttadauria, F. Giacalone, A. M. Marculesu, A. M. P. Salvo and R. Noto, Stereoselective aldol reaction catalyzed by a highly recyclable polystyrene supported substituted prolinamide catalyst. *ARKIVOC*, 2009, **8,** 5–15.
76. K. D. Johnstone, N. Bampos, J. K. M. Sanders and M. J. Gunter, Gel-phase HR-MAS ^{1}H NMR spectroscopy as a probe for solid-tethered diimide rotaxanes and catenanes. *New J. Chem.*, 2006, **30,** 861–867.
77. K. M. Mullen, K. D. Johnstone, D. Nath, N. Bampos, J. K. M. Sanders and M. J. Gunter, Crown-ether- and porphyrin-attached gel-phase resins in thermodynamically controlled rotaxane assembly. *Org. Biomol. Chem.*, 2009, **7,** 293–303.
78. K. M. Mullen, K. D. Johnstone, M. Webb, N. Bampos, J. K. M. Sanders and M. J. Gunter, Monitoring the thermodynamically-controlled formation of diimide-based resin-attached rotaxanes by gel-phase HR MAS ^{1}H NMR spectroscopy. *Org. Biomol. Chem.*, 2008, **6,** 278–286.
79. L. Zhao, K. M. Mullen, M. J. Chmielewski, A. Brown, N. Bampos, P. D. Beer and J. J. Davis, Anion templated assembly of an indolocarbazole containing pseudorotaxane on beads and silica. *New J. Chem.*, 2009, **33,** 760–768.
80. N. H. Yao, W. Y. He, K. S. Lam and G. Liu, Conformational studies of resin-bound vancomycin and the complex of vancomycin and Ac_2-L-Lys-D-Ala-D-Ala. *J. Comb. Chem.*, 2005, **7,** 123–129.
81. N. Lancelot, K. Elbayed, J. Raya, M. Piotto, J. P. Briand, F. Formaggio, C. Toniolo and A. Bianco, Characterization of the 3_{10}-helix in model peptides by HRMAS NMR spectroscopy. *Chem. Eur. J.*, 2003, **9,** 1317–1323.
82. A. Papanikos and M. Meldal, Alpha-keto amide peptides: a synthetic strategy to resin-bound peptide isosteres for protease inhibitor screening on solid support. *J. Comb. Chem.*, 2004, **6,** 181–195.
83. L. H. Lucas, M. A. Cerny, Y. M. Koen, R. P. Hanzlik and C. K. Larive, ^{1}H high-resolution magic-angle spinning (HR-MAS) NMR analysis of ligand density on resins using a resin internal standard. *Anal. Bioanal. Chem.*, 2004, **380,** 627–631.
84. A. Violette, N. Lancelot, A. Poschalko, M. Piotto, J. P. Briand, J. Raya, K. Elbayed, A. Bianco and G. Guichard, Exploring helical folding of oligoureas during chain elongation by high-resolution magic-angle-spinning (HRMAS) NMR spectroscopy. *Chem. Eur. J.*, 2008, **14,** 3874–3882.
85. S. B. Andrey, M. L. Chan and W. P. Power, HRMAS ^{1}H NMR conformational study of the resin-bound amyloid-forming peptide GNNQQNY from the yeast prion Sup35. *J. Phys. Chem. A*, 2010, **114,** 3457–3465.
86. J. Blumel, Linkers and catalysts immobilized on oxide supports: new insights by solid-state NMR spectroscopy. *Coord. Chem. Rev.*, 2008, **252,** 2410–2423.
87. T. Posset and J. Bluemel, New mechanistic insights regarding Pd/Cu catalysts for the Sonogashira reaction: HRMAS NMR studies of silica-immobilized systems. *J. Am. Chem. Soc.*, 2006, **128,** 8394–8395.
88. V. Busico, M. Caus, R. Cipullo, R. Credendino, F. Cutillo, V. Van Axel Castelli, N. Friederichs, R. Lamanna and A. Segre, Periodic DFT and high-resolution magic-angle-spinning (HR-MAS) ^{1}H NMR investigation of the active surfaces of $MgCl_2$-supported Ziegler–Natta catalysts. The $MgCl_2$ matrix. *J. Phys. Chem. C*, 2008, **112,** 1081–1089.
89. A. D. Roy, K. Jayalakshmi, S. Dasgupta, R. Roy and B. Mukhopadhyay, Real time HR-MAS NMR: application in reaction optimization, mechanism elucidation and kinetic analysis for heterogeneous reagent catalyzed small molecule chemistry. *Magn. Reson. Chem.*, 2008, **46,** 1119–1126.
90. M.-C. Clochard, N. Betz, M. Goncalves, C. Bittencourt, J. J. Pireaux, K. Gionnet, G. Deleris and A. Le Moel, Peptide immobilization onto radiation grafted PVDF-g-poly(acrylic acid) films. *Nucl. Instrum. Meth. Phys. Res. B*, 2005, **236,** 208–215.
91. S. Deshayes, V. Maurizot, M. Clochard, T. Berthelot, C. Baudin and G. Deleris, Synthesis of specific nanoparticles for targeting tumor angiogenesis using electron-beam irradiation. *Radiat. Phys. Chem.*, 2010, **79,** 208–213.
92. L. Costantino, F. Gandolfi, L. Bossy-Nobs, G. Tosi, R. Gurny, F. Rivasi, M. A. Vandelli and F. Forni, Nanoparticulate drug carriers based on hybrid poly(D,L-lactide-coglycolide)-dendron structures. *Biomaterials*, 2006, **27,** 4635–4645.

93. F. Du, B. Zhang, H. Zhou, B. Yin and L. Chen, Structure elucidation of nanoparticle-bound organic molecules by ^{1}H NMR. *Trends Anal. Chem.*, 2009, **28,** 88–95.
94. H. Zhou, F. Du, X. Li, B. Zhang, W. Li and B. Yan, Characterization of organic molecules attached to gold nanoparticle surface using high resolution magic angle spinning ^{1}H NMR. *J. Phys. Chem. C*, 2008, **112,** 19360–19366.
95. Z. Krpetic, P. Nativo, F. Porta and M. Brust, A multidentate peptide for stabilization and facile bioconjugation of gold nanoparticles. *Bioconjug. Chem.*, 2009, **20,** 619–624.
96. L. Polito, M. Colombo, D. Monti, S. Melato, E. Caneva and D. Prosperi, Resolving the structure of ligands bound to the surface of superparamagnetic iron oxide nanoparticles by high-resolution magic-angle spinning NMR spectroscopy. *J. Am. Chem. Soc.*, 2008, **130,** 12712–12724.
97. C. Ader, R. Schneider, K. Seidel, M. Etzkorn and M. Baldus, Magic-angle-spinning NMR spectroscopy applied to small molecules and peptides in lipid bilayers. *Biochem. Soc. Trans.*, 2007, **35,** 991–995.
98. A. Diller, C. Loudet, F. Aussenac, G. Raffard, S. Fournier, M. Laguerre, A. Grelard, S. J. Opella, F. M. Marassi and E. J. Dufourc, Bicelles: a natural 'molecular goniometer' for structural, dynamical and topological studies of molecules in membranes. *Biochimie*, 2009, **91,** 744–751.
99. C. Carlotti, F. Aussenac and E. J. Dufourc, Towards high-resolution ^{1}H-NMR in biological membranes: magic angle spinning of bicelles. *Biochim. Biophys. Acta*, 2002, **1564,** 156–164.
100. C. Sizun and B. Bechinger, Bilayer sample for fast or slow magic angle oriented sample spinning solid-state NMR spectroscopy. *J. Am. Chem. Soc.*, 2002, **124,** 1146–1147.
101. G. Zandomeneghi, P. T. Williamson, A. Hunkeler and B. H. Meier, Switched-angle spinning applied to bicelles containing phospholipid-associated peptides. *J. Biomol. NMR*, 2003, **25,** 125–132.
102. C. G. Canlas, D. Ma, P. Tang and Y. Xu, Residual dipolar coupling measurements of transmembrane proteins using aligned low-q bicelles and high-resolution magic angle spinning NMR spectroscopy. *J. Am. Chem. Soc.*, 2008, **130,** 13294–13300.
103. M. N. Triba, M. Trakia, D. E. Warschawski, L. Nicolas-Morgantini, A. Lety, P. Gilard and P. F. Devaux, Proton magic-angle spinning-NMR investigation of surfactant aqueous suspensions. *J. Colloid Interface Sci.*, 2004, **274,** 341–345.
104. O. Cruciani, L. Mannina, A. P. Sobolev, A. Segre and P. Luisi, Multilamellar liposomes formed by phosphatidyl nucleosides: an NMR-HR-MAS characterization. *Langmuir*, 2004, **20,** 1144–1151.
105. O. Cruciani, L. Mannina, A. P. Sobolev, C. Cametti and A. Segre, An improved NMR study of liposomes using 1-palmitoyl-2-oleoyl-sn-glycero-3-phospatidylcholine as model. *Molecules*, 2006, **11,** 334–344.
106. O. Wattraint, D. E. Warschawski and C. Sarazin, Tethered or adsorbed supported lipid bilayers in nanotubes characterized by deuterium magic angle spinning NMR spectroscopy. *Langmuir*, 2005, **21,** 3226–3228.
107. A. Bernabeu, S. Shapiro and J. Villalan, A MAS-NMR study of the location of (+)-totarol, a diterpenoid bioactive molecule, in phospholipid model membranes. *Chem. Phys. Lipids*, 2002, **119,** 33–39.
108. J. Guillen, A. Bernabeu, S. Shapiro and J. Villalan, Location and orientation of triclosan in phospholipid model membranes. *Eur. Biophys. J.*, 2004, **33,** 448–453.
109. C. Sizun, F. Aussenac, A. Grelard and E. J. Dufourc, NMR methods for studying the structure and dynamics of oncogenic and antihistaminic peptides in biomembranes. *Magn. Reson. Chem.*, 2004, **42,** 180–186.
110. W. Zhang, E. Crocker, S. McLaughlin and S. O. Smith, Binding of peptides with basic and aromatic residues to bilayer membranes: phenylalanine in the myristoylated alanine-rich c kinase substrate effector domain penetrates into the hydrophobic core of the bilayer. *J. Biol. Chem.*, 2003, **278,** 21459–21466.
111. A. Pampel, Pulsed field gradient NMR in combination with magic angle spinning—new possibilities for studying diffusion in lipid membranes and heterogeneous materials. *Diffus. Fundam.*, 2005, **2,** 128.1–128.2.
112. H. A. Scheidt, D. Huster and K. Gawrisch, Diffusion of cholesterol and its precursors in lipid membranes studied by ^{1}H pulsed field gradient magic angle spinning NMR. *Biophys. J.*, 2005, **89,** 2504–2512.

113. O. Soubias, M. Piotto, O. Saurel, O. Assemat, V. Rat and A. Milon, Detection of natural abundance ^{1}H–^{13}C correlations of cholesterol in its membrane environment using a gradient enhanced HSQC experiment under high resolution magic angle spinning. *J. Magn. Reson.*, 2003, **165,** 303–308.
114. H. C. Gaede and K. Gawrisch, Multi-dimensional pulsed field gradient magic angle spinning NMR experiments on membranes. *Magn. Reson. Chem.*, 2004, **42,** 115–122.
115. H. A. Scheidt, A. Pampel, L. Nissler, R. Gebhardt and D. Huster, Investigation of the membrane localization and distribution of flavonoids by high-resolution magic angle spinning NMR spectroscopy. *Biochim. Biophys. Acta*, 2004, **1663,** 97–107.
116. D. E. Warschawski and P. F. Devaux, ^{1}H–^{13}C polarization transfer in membranes: a tool for probing lipid dynamics and the effect of cholesterol. *J. Magn. Reson.*, 2005, **177,** 166–171.
117. S. Tian, J. Garcia-Rivera, B. Yan, A. Casadevall and R. E. Stark, Unlocking the molecular structure of fungal melanin using ^{13}C biosynthetic labeling and solid-state NMR. *Biochemistry*, 2003, **42,** 8105–8109.
118. D. Morvan, A. Demidem, J. Papon and J. C. Madelmont, Quantitative HRMAS proton total correlation spectroscopy applied to cultured melanoma cells treated by chloroethyl nitrosourea: demonstration of phospholipid metabolism alterations. *Magn. Reson. Med.*, 2003, **49,** 241–248.
119. J. Zhong, S. Frases, H. Wang, A. Casadevall and R. E. Stark, Following fungal melanin biosynthesis with solid-state NMR: biopolymer molecular structures and possible connections to cell-wall polysaccharides. *Biochemistry*, 2008, **47,** 4701–4710.
120. W. Li, R. Slominski and A. T. Slominski, High-resolution magic angle spinning nuclear magnetic resonance analysis of metabolic changes in melanoma cells after induction of melanogenesis. *Anal. Biochem.*, 2009, **386,** 282–284.
121. A. Sillen, J. M. Wieruszeski, A. Leroy, A. B. Younes, I. Landrieu and G. Lippens, High-resolution magic angle spinning NMR of the neuronal tau protein integrated in Alzheimer's-like paired helical fragments. *J. Am. Chem. Soc.*, 2005, **127,** 10138–10139.
122. A. B. Siemer, A. A. Arnold, C. Ritter, T. Westfeld, M. Ernst, R. Riek and B. H. Meier, Observation of highly flexible residues in amyloid fibrils of the HET-s prion. *J. Am. Chem. Soc.*, 2006, **128,** 13224–13228.
123. J. Bodart, J. Wieruszeski, L. Amniai, A. Leroy, I. Landrieu, A. Rousseau-Lescuyer, J. Vilain and G. Lippens, NMR observation of tau in xenopus oocytes. *J. Magn. Reson.*, 2008, **192,** 252–257.
124. J. Grivet and A. Delort, NMR for microbiology: in vivo and in situ applications. *Prog. Nucl. Magn. Reson. Spectrosc.*, 2009, **54,** 1–53.
125. H. Nothaft, X. Liu, D. J. McNally and C. M. Szymanski, *N-Linked Protein Glycosylation in a Bacterial System*. Functional Glycomics: Methods in Molecular Biology 2010, Vol. 600. Humana Press, Clifton, NJ, 2010, pp. 227–243.
126. J. Brisson, E. Vinogradov, D. J. McNally, N. H. Khieu, I. C. Schoenhofen, S. M. Logan and H. Jarrell, *The Application of NMR Spectroscopy to Functional Glycomics*. Functional Glycomics: Methods in Molecular Biology 2010, Vol. 600. Humana Press, Clifton, NJ, 2010, pp. 155–173.
127. S. Aime, E. Bruno, C. Cabella, S. Colombatto, G. Digilio and V. Mainero, HR-MAS of cells: a ''cellular water shift'' due to water–protein interactions? *Magn. Reson. Med.*, 2005, **54,** 1547–1552.
128. L. Calabi, G. Alfieri, L. Biondi, M. De Miranda, L. Paleari and S. Ghelli, Application of high-resolution magic-angle spinning NMR spectroscopy to define the cell uptake of MRI contrast agents. *J. Magn. Reson.*, 2002, **156,** 222–229.
129. T. J. Larkin, W. A. Bubb and P. W. Kuchel, Water chemical shift in ^{1}H NMR of red cells: effects of ph when transmembrane magnetic susceptibility differences are low. *Magn. Reson. Med.*, 2008, **59,** 707–711.
130. J. H. Chen, E. B. Sambol, P. Decarolis, R. O'Connor, R. C. Geha, Y. V. Wu and S. Singer, High-resolution MAS NMR spectroscopy detection of the spin magnetization exchange by cross-relaxation and chemical exchange in intact cell lines and human tissue specimens. *Magn. Reson. Med.*, 2006, **55,** 1246–1256.
131. E. Bruno, G. Digilio, C. Cabella, A. de Reggi, S. Baroni, V. Mainero and S. Aime, Water exchange across the erythrocyte plasma membrane studied by HR-MAS NMR spectroscopy. *Magn. Reson. Med.*, 2006, **56,** 978–985.
132. I. F. Duarte, J. Marques, A. F. Ladeirinha, C. Rocha, I. Lamego, R. Calheiros, T. M. Silva, M. P. M. Marques, J. B. Melo, I. M. Carreira and A. M. Gil, Analytical approaches toward

successful human cell metabolome studies by NMR spectroscopy. *Anal. Chem.*, 2009, **81,** 5023–5032.
133. J. L. Griffin, M. Bollard, J. K. Nicholson and K. Bhakoo, Spectral profiles of cultured neuronal and glial cells derived from HRMAS ^{1}H NMR spectroscopy. *NMR Biomed.*, 2002, **15,** 375–384.
134. H. K. Nyblom, L. I. Nord, R. Andersson, L. Kenne and P. Bergsten, Glucose-induced de novo synthesis of fatty acyls causes proportional increases in INS-1E cellular lipids. *NMR Biomed.*, 2008, **21,** 357–365.
135. J. H. Chen, B. M. Enloe, P. Weybright, N. Campbell, D. Dorfman, C. D. Fletcher, D. G. Cory and S. Singer, Biochemical correlates of thiazolidinedione-induced adipocyte differentiation by high-resolution magic angle spinning NMR spectroscopy. *Magn. Reson. Med.*, 2002, **48,** 602–610.
136. J. L. Griffin, J. C. Pole, J. K. Nicholson and P. L. Carmichael, Cellular environment of metabolites and a metabonomic study of tamoxifen in endometrial cells using gradient high resolution magic angle spinning ^{1}H NMR spectroscopy. *Biochim. Biophys. Acta*, 2003, **1619,** 151–158.
137. X. Hanoulle, J. M. Wieruszeski, P. Rousselot-Pailley, I. Landrieu, C. Locht, G. Lippens and A. R. Baulard, Selective intracellular accumulation of the major metabolite issued from the activation of the prodrug ethionamide in mycobacteria. *J. Antimicrob. Chemother.*, 2006, **58,** 768–772.
138. X. Hanoulle, J. M. Wieruszeski, P. Rousselot-Pailley, I. Landrieu, A. R. Baulard and G. Lippens, Monitoring of the ethionamide pro-drug activation in mycobacteria by ^{1}H high resolution magic angle spinning NMR. *Biochem. Biophys. Res. Commun.*, 2005, **331,** 452–458.
139. S. Tiziani, A. Lodi, F. L. Khanim, M. R. Viant, C. R. Brunce and U. L. Gunther, Metabolomic profiling of drug responses in acute myeloid leukaemia cell lines. *PLoS ONE*, 2009, **4,** e4251.
140. E. L. Gjersing, J. L. Herberg and J. Horn, NMR metabolomics of planktonic and biofilm modes of growth in *Pseudomonas aeruginosa*. *Anal. Chem.*, 2007, **79,** 8037–8045.
141. S. Follot, J. Debouzy, D. Crouzier, C. Enguehard-Gueiffier, A. Gueiffier, F. Nachon, B. Lefebvre and F. Fauvelle, Physicochemical properties and membrane interactions of anti-apoptotic derivatives 2-(4-fluorophenyl)-3-(pyridin-4-yl)imidazo[1,2-a]pyridine depending on the hydroxyalkylamino side chain length and conformation: an NMR and ESR study. *Eur. J. Med. Chem.*, 2009, **9,** 3509–3518.
142. M. S. Chauton, G. Johnsen and T. R. Storseth, High-resolution magic angle spinning ^{1}H NMR analysis of whole cells of *Thalassiosira pseudonana* (Bacillariophyceae): broad range analysis of metabolic composition and nutritional value. *J. Appl. Phycol.*, 2003, **15,** 533–542.
143. T. R. Storseth, K. Hansen, J. Skjermo and J. Krane, Characterization of a beta-D-(1→3)-glucan from the marine diatom *Chaetoceros muelleri* by high-resolution magic-angle spinning NMR spectroscopy on whole algal cells. *Carbohydr. Res.*, 2004, **339,** 421–424.
144. M. S. Chauton, T. R. Storseth and J. Krane, High-resolution magic angle spinning NMR analysis of whole cells of *Chaetoceros muelleri* (Bacillariophyceae) and comparison with ^{13}C-NMR and distortionless enhancement by polarization transfer ^{13}C-NMR analysis of lipophilic extracts. *J. Phycol.*, 2004, **40,** 611–618.
145. E. Fredlund, A. Broberg, M. E. Boysen, L. Kenne and J. Schnurer, Metabolite profiles of the biocontrol yeast *Pichia anomala* J121 grown under oxygen limitation. *Appl. Microbiol. Biotechnol.*, 2004, **64,** 403–409.
146. C. M. Szymanski, F. S. Michael, H. C. Jarrell, J. Li, M. Gilbert, S. Larocque, E. Vinogradov and J. R. Brisson, Detection of conserved N-linked glycans and phase-variable lipooligosaccharides and capsules from *Campylobacter* cells by mass spectrometry and high resolution magic angle spinning NMR spectroscopy. *J. Biol. Chem.*, 2003, **278,** 24509–24520.
147. S. Bernatchez, C. M. Szymanski, N. Ishiyama, J. Li, H. C. Jarrell, P. C. Lau, A. M. Berghuis, N. M. Young and W. W. Wakarchuk, A single bifunctional UDP-GlcNAc/Glc 4-epimerase supports the synthesis of three cell surface glycoconjugates in *Campylobacter jejuni*. *J. Biol. Chem.*, 2005, **280,** 4792–4802.
148. J. Kelly, H. Jarrell, L. Millar, L. Tessier, L. M. Fiori, P. C. Lau, B. Allan and C. M. Szymanski, Biosynthesis of the N-linked glycan in *Campylobacter jejuni* and addition onto protein through block transfer. *J. Bacteriol.*, 2006, **188,** 2427–2434.
149. D. J. McNally, M. P. Lamoureux, L. M. Fiori, J. Li, R. A. Coleman, N. H. Khieu, J. Brisson, H. C. Jarrell, C. M. Szymanski, A. Karlyshev, G. Thacker and B. Wren, Commonality and

biosynthesis of the *O*-methyl phosphoramidate capsule modification in *Campylobacter jejuni*. *J. Biol. Chem.*, 2007, **282,** 28566–28576.
150. D. J. McNally, M. Lamoureux, J. J. Li, J. Kelly, J. R. Brisson, C. M. Szymanski and H. C. Jarrell, HR-MAS NMR studies of N-15-labeled cells confirm the structure of the *O*-methyl phosphoramidate CPS modification in *Campylobacter jejuni* and provide insight into its biosynthesis. *Can. J. Chem.*, 2006, **84,** 676–684.
151. D. J. McNally, H. C. Jarrell, N. H. Khieu, J. Li, E. Vinogradov, D. M. Whitfield, C. M. Szymanski and J. R. Brisson, The HS:19 serostrain of *Campylobacter jejuni* has a hyaluronic acid-type capsular polysaccharide with a nonstoichiometric sorbose branch and *O*-methyl phosphoramidate group. *FEBS J.*, 2006, **273,** 3975–3989.
152. S. Dag, T. Niedziela, M. Dzieciatkowska, J. Lukasiewicz, W. Jachymek, C. Lugowski and L. Kenne, The *O*-acetylation patterns in the *O*-antigens of *Hafnia alvei* strains PCM 1200 and 1203, serologically closely related to PCM 1205. *Carbohydr. Res.*, 2004, **339,** 2521–2527.
153. T. Niedziela, I. Letowska, J. Lukasiewicz, M. Kaszowska, A. Czarnecka, L. Kenne and C. Lugowski, Epitope of the vaccine-type *Bordetella pertussis* strain 186 lipooligosaccharide and antiendotoxin activity of antibodies directed against the terminal pentasaccharide-tetanus toxoid conjugate. *Infect. Immun.*, 2005, **73,** 7381–7389.
154. S. K. Gudlavalleti, C. M. Szymanski, H. C. Jarrell and D. S. Stephens, In vivo determination of *Neisseria meningitidis* serogroup A capsular polysaccharide by whole cell high-resolution magic angle spinning NMR spectroscopy. *Carbohydr. Res.*, 2006, **341,** 557–562.
155. A. Maciejewska, J. Lukasiewicz, T. Niedziela, Z. Szewczuk and C. Lugowski, Structural analysis of the O-specific polysaccharide isolated from *Plesiomonas shigelloides* O51 lipopolysaccharide. *Carbohydr. Res.*, 2009, **344,** 894–900.
156. R. E. Lee, W. Li, D. Chatterjee and R. E. Lee, Rapid structural characterization of the arabinogalactan and lipoarabinomannan in live mycobacterial cells using 2D and 3D HR-MAS NMR: structural changes in the arabinan due to ethambutol treatment and gene mutation are observed. *Glycobiology*, 2005, **15,** 139–151.
157. W. Li, R. E. Lee, R. E. Lee and J. Li, Methods for acquisition and assignment of multidimensional high-resolution magic angle spinning NMR of whole cell bacteria. *Anal. Chem.*, 2005, **77,** 5785–5792.
158. A. Alahari, X. Trivelli, Y. Gurardel, L. G. Dover, G. S. Besra, J. C. Sacchettini, R. C. Reynolds, G. D. Coxon and L. Kremer, Thiacetazone, an antitubercular drug that inhibits cyclopropanation of cell wall mycolic acids in mycobacteria. *PLoS ONE*, 2007, **2,** 1343.
159. Y. Li, B. J. Wylie and C. M. Rienstra, Selective refocusing pulses in magic-angle spinning NMR: characterization and applications to multi-dimensional protein spectroscopy. *J. Magn. Reson.*, 2006, **179,** 206–216.
160. J. Alper, Hitting the magic angle for cell wall analysis. *Anal. Chem.*, 2005, **77,** 371A.
161. M. S. Chauton and T. F. Storseth, *HR MAS NMR Spectroscopy of Marine Microalgae, Part 1: Classification and Metabolite Composition from HR MAS ^{1}H NMR Spectra and Multivariate Analysis*. Springer, Netherlands, 2006, pp. 947–951.
162. B. J. Blaise, J. Giacomotto, B. Elena, M. E. Dumas, P. Toullhoat, L. Segalat and L. Emsley, Metabotyping of *Caenorhabditis elegans* reveals latent phenotypes. *Proc. Natl. Acad. Sci. USA*, 2007, **104,** 19808–19812.
163. B. J. Blaise, J. Giacomotto, M. N. Triba, P. Toulhoat, M. Piotto, L. Emsley, L. Segalat, M. E. Dumas and B. Elena, Metabolic profiling strategy of *Caenorhabditis elegans* by whole-organism nuclear magnetic resonance. *J. Proteome Res.*, 2009, **8,** 2542–2550.
164. B. J. Blaise, L. Shintu, B. Elena, L. Emsley, M. Dumas and P. Toulhoat, Statistical recoupling prior to significance testing in nuclear magnetic resonance based metabonomics. *Anal. Chem.*, 2009, **81,** 6242–6251.
165. S. Salaun, N. Kervarec, P. Potin, D. Haras, M. Piotto and S. La Barre, Whole-cell spectroscopy is a convenient tool to assist molecular identification of cultivatable marine bacteria and to investigate their adaptive metabolism. *Talanta*, 2010, **80,** 1758–1770.
166. G. B. Alcantara, A. G. Ferreira, N. K. Honda and M. M. C. Ferreira, Chemometric analysis applied in ^{1}H HR-MAS NMR and FT-IR data for chemotaxonomic distinction of intact lichen samples. *Anal. Chim. Acta*, 2007, **595,** 3–8.

167. A. J. Simpson, X. Zang, R. Kramer and P. G. Hatcher, New insights on the structure of algaenan from *Botryoccocus braunii race* A and its hexane insoluble botryals based on multidimensional NMR spectroscopy and electrospray-mass spectrometry techniques. *Phytochemistry*, 2003, **62,** 783–796.
168. E. Salmon, F. Behar, F. Lorant, P. G. Hatcher, P. Metzger and P. Marquaire, Thermal decomposition processes in algaenan of *Botryococcus braunii race* L. Part 1: experimental data and structural evolution. *Org. Geochem.*, 2009, **40,** 400–415.
169. E. Salmon, F. Behar, F. Lorant, P. G. Hatcher and P. Marquaire, Early maturation processes in coal. Part 1: pyrolysis mass balance and structural evolution of coalified wood from the Morwell Brown Coal seam. *Org. Geochem.*, 2009, **40,** 500–509.
170. J. M. de la Rosa, J. A. Gonzalez-Perez, R. Gonzalez-Vazquez, T. Verdejo, J. R. de Andres, L. Sanchez-Garcia, P. G. Hatcher, H. Knicker, A. Teran, O. Polvillo and F. J. Gonzalez-Vila, Detection of nitrogen stable forms in marine sediments by high resolution magic angle spinning (HRMAS) ^{1}H nuclear magnetic resonance (NMR). *Geophys. Res. Abstr.*, 2006, **8,** 03925.
171. B. P. Kelleher, W. L. Kingery, R. E. Rogers, J. Dearman and A. J. Simpson, Effects of natural organic matter from sediments on the growth of marine gas hydrates. *Mar. Chem.*, 2007, **103,** 237–249.
172. C. Xu, P. H. Santschi, J. Y. Zhong, P. G. Hatcher, A. J. Francis, C. J. Dodge, K. A. Roberts, C. C. Hung and B. D. Honeyman, Colloidal cutin-like substances cross-linked to siderophore decomposition products mobilizing plutonium from contaminated soils. *Environ. Sci. Technol.*, 2008, **42,** 8211–8217.
173. X. Feng, A. J. Simpson and M. J. Simpson, Investigating the role of mineral-bound humic acid in phenanthrene sorption. *Environ. Sci. Technol.*, 2006, **40,** 3260–3266.
174. X. Feng, A. J. Simpson and M. J. Simpson, Chemical and mineralogical controls on humic acid sorption to clay mineral surfaces. *Org. Geochem.*, 2005, **36,** 1553–1566.
175. A. J. Simpson, M. J. Simpson, W. L. Kingery, B. A. Lefebvre, A. Moser, A. J. Williams, M. Kvasha and B. P. Kelleher, The application of ^{1}H high-resolution magic-angle spinning NMR for the study of clay-organic associations in natural and synthetic complexes. *Langmuir*, 2006, **22,** 4498–4503.
176. A. Shirzadi, M. J. Simpson and R. Kumar, Molecular interactions of pesticides at the soil-water interface. *Environ. Sci. Technol.*, 2008, **42,** 5514–5520.
177. A. P. Deshmukh, A. J. Simpson and P. G. Hatcher, Evidence for cross-linking in tomato cutin using HR-MAS NMR spectroscopy. *Phytochemistry*, 2003, **64,** 1163–1170.
178. A. P. Deshmukh, A. J. Simpson, C. M. Hadad and P. G. Hatcher, Insights into the structure of cutin and cutan from *Agave americana* leaf cuticle using HRMAS NMR spectroscopy. *Org. Geochem.*, 2005, **36,** 1072–1085.
179. D. Sacco, M. A. Brescia, A. Buccolieri and A. C. Jambrenghi, Geographical origin and breed discrimination of Apulian lamb meat samples by means of analytical and spectroscopic determinations. *Meat Sci.*, 2005, **71,** 542–548.
180. L. Shintu, F. Ziarelli and S. Caldarelli, Is high-resolution magic angle spinning NMR a practical speciation tool for cheese samples? Parmigiano Reggiano as a case study. *Magn. Reson. Chem.*, 2004, **42,** 396–401.
181. B. Yu, G. Vengadesan, H. Wang, L. Jashi, T. Yefremov, S. Tian, V. Gaba, I. Shomer and R. E. Stark, Magic-angle spinning NMR studies of cell wall bound aromatic-aliphatic biopolyesters associated with strengthening of intercellular adhesion in potato (*Solanum tuberosum* L.) tuber parenchyma. *Biomacromolecules*, 2006, **7,** 937–944.
182. E. Fumagalli, E. Baldoni, P. Abbruscato, P. Piffanelli, A. Genga, R. Lamanna and R. Consonni, NMR techniques coupled with multivariate statistical analysis: tools to analyse *Oryza sativa* metabolic content under stress conditions. *J. Agron. Crop Sci.*, 2009, **195,** 77–88.
183. H. Winning, N. Viereck, B. Wollenweber, F. H. Larsen, S. Jacobsen, I. Sndergaard and S. B. Engelsen, Exploring abiotic stress on asynchronous protein metabolism in single kernels of wheat studied by NMR spectroscopy and chemometrics. *J. Exp. Bot.*, 2009, **60,** 291–300.
184. L. Otero and G. Prstamo, Effects of pressure processing on strawberry studied by nuclear magnetic resonance. *Innovative Food Sci. Emerg. Technol.*, 2009, **10,** 434–440.

185. M. A. Brescia, A. Sgaramella, S. Ghelli and A. Sacco, ^{1}H HR-MAS NMR and isotopic investigation of bread and flour samples produced in southern Italy. *J. Sci. Food Agric.*, 2003, **83,** 1463–1468.
186. T. Salomonsen, H. M. Jensen, F. H. Larsen, S. Steuernagel and S. B. Engelsen, Alginate monomer composition studied by solution- and solid-state NMR—a comparative chemometric study. *Food Hydrocolloids*, 2009, **23,** 1579–1586.
187. C. Daolio, F. L. Beltrame, A. G. Ferreira, Q. B. Cass, D. A. G. Cortez and M. M. C. Ferreira, Classification of commercial catuaba samples by NMR, HPLC and chemometrics. *Phytochem. Anal.*, 2008, **19,** 218–228.
188. J. M. Wieruszeski, P. Talaga and G. Lippens, Development of a high-resolution magic-angle spinning nuclear magnetic resonance identity assay of the capsular polysaccharide from *Haemophilus influenzae* type b present in cetavlon precipitate. *Anal. Biochem.*, 2005, **338,** 20–25.
189. P. T. Williamson, S. Bains, C. Chung, R. Cooke and A. Watts, Probing the environment of neurotensin whilst bound to the neurotensin receptor by solid state NMR. *FEBS Lett.*, 2002, **518,** 111–115.
190. L. H. Lucas, S. F. Wilson, C. E. Lunte and C. K. Larive, Concentration profiling in rat tissue by high-resolution magic-angle spinning NMR spectroscopy: investigation of a model drug. *Anal. Chem.*, 2005, **77,** 2978–2984.
191. S. Carraro, G. Giordano, F. Reniero, G. Perilongo and E. Baraldi, Metabolomics: a new frontier for research in pediatrics. *J. Pediatr.*, 2009, **154,** 638–644.
192. J. C. Lindon, O. P. Beckonert, E. Holmes and J. K. Nicholson, High-resolution magic angle spinning NMR spectroscopy: application to biomedical studies. *Prog. Nucl. Magn. Reson. Spectrosc.*, 2009, **55,** 79–100.
193. J. L. Griffin, Metabonomics: NMR spectroscopy and pattern recognition analysis of body fluids and tissues for characterisation of xenobiotic toxicity and disease diagnosis. *Curr. Opin. Chem. Biol.*, 2003, **7,** 648–654.
194. J. L. Griffin and J. P. Shockcor, Metabolic profiles of cancer cells. *Nat. Rev. Cancer*, 2004, **4,** 551–561.
195. R. Holly, A. Damyanovich and H. Peemoeller, NMR high-resolution magic angle spinning rotor design for quantification of metabolic concentrations. *Rev. Sci. Instrum.*, 2006, **77,** 054301.
196. D. Stefan, F. D. Cesare, A. Andrasescu, E. Popa, A. Lazariev, E. Vescovo, O. Strbak, S. Williams, Z. Starcuk, M. Cabanas, D.v. Ormondt and D. Graveron-Demilly, Quantitation of magnetic resonance spectroscopy signals: the jMRUI software package. *Meas. Sci. Technol.*, 2009, **20,** 104035.
197. G. Reynolds, M. Wilson, A. Peet and T. N. Arvanitis, An algorithm for the automated quantitation of metabolites in in vitro NMR signals. *Magn. Reson. Med.*, 2006, **56,** 1211–1219.
198. Alan Dove, The big picture. *Nat. Med.*, 2005, **11,** 111–112.
199. R. Canese, E. Iorio, A. Ricci, M. E. Pisanu, M. Giannini and F. Podo, Free content metabolite quantification in tumours by magnetic resonance spectroscopy: objectives, results and perspectives. *Curr. Med. Imaging Rev.*, 2009, **5,** 110–127.
200. J. L. Spratlin, N. J. Serkova and S. G. Eckhardt, Clinical applications of metabolomics in oncology: a review. *Clin. Cancer Res.*, 2009, **15,** 431–440.
201. B. Sitter, T. F. Bathena, M. Tessema and I. S. Gribbestad, High resolution magic angle spinning (HR MAS) MR spectroscopy in metabolic characterization of human cancer. *Prog. Nucl. Magn. Reson. Spectrosc.*, 2009, **54,** 239–254.
202. N. P. Davies, M. Wilson, L. M. Harris, K. Natarajan, S. Lateef, L. Macpherson, S. Sgouros, R. G. Grundy, T. N. Arvanitis and A. C. Peet, Identification and characterisation of childhood cerebellar tumours by in vivo proton MRS. *NMR Biomed.*, 2008, **21,** 908–918.
203. B. Celda, D. Monleon, M. C. Martinez-Bisbal, V. Esteve, B. Martinez-Granados, E. Pinero, R. Ferrer, J. Piquer, L. Marti-Bonmati and J. Cervera, MRS as endogenous molecular imaging for brain and prostate tumors: FP6 project ''eTUMOR'' *New Trends in Cancer for the 21st Century*. Springer, New York, 2006, pp. 285–302.
204. N. P. Davies, M. Wilson, K. Natarajan, Y. Sun, L. MacPherson, M.-A. Brundler, T. N. Arvanitis, R. G. Grundy and A. C. Peet, Non-invasive detection of glycine as a biomarker of malignancy in childhood brain tumours using in-vivo ^{1}H MRS at 1.5 tesla confirmed by ex-vivo high-resolution magic-angle spinning NMR. *NMR Biomed.*, 2009, **23,** 80–87.

205. I. B. Yeh, M. Xu, W. H. Ng, J. Ye, D. Yang and C. C. T. Lim, Central neurocytoma: typical magnetic resonance spectroscopy findings and atypical ventricular dissemination. *Magn. Reson. Imaging*, 2008, **26,** 59–64.
206. A. A. Tzika, L. L. Cheng, L. Goumnerova, J. R. Madsen, D. Zurakowski, L. G. Astrakas, M. K. Zarifi, R. M. Scott, D. C. Anthony, R. G. Gonzalez and P. M. Black, Biochemical characterization of pediatric brain tumors by using in vivo and ex vivo magnetic resonance spectroscopy. *J. Neurosurg.*, 2002, **96,** 1023–1031.
207. V. Righi, J. M. Roda, J. Paz, A. Mucci, V. Tugnoli, G. Rodriguez-Tarduchy, L. Barrios, L. Schenetti, S. Cerdán and M. L. García-Martín, ^{1}H HR-MAS and genomic analysis of human tumor biopsies discriminate between high and low grade astrocytomas. *NMR Biomed.*, 2009, **22,** 629–637.
208. W. Tan, Y. Ke and G. Wu, Preliminary study in vitro brain tumor with high resolution magic angle spinning proton magnetic resonance spectroscopy. *Chinese-German J. Clin. Oncol.*, 2008, **7,** 103–106.
209. M. Wilson, N. P. Davies, R. G. Grundy and A. C. Peet, A quantitative comparison of metabolite signals as detected by in vivo MRS with ex vivo ^{1}H HR-MAS for childhood brain tumours. *NMR Biomed.*, 2009, **22,** 213–219.
210. K. S. Opstad, B. A. Bell, J. R. Griffiths and F. A. Howe, Taurine: a potential marker of apoptosis in gliomas. *Br. J. Cancer*, 2009, **100,** 789–794.
211. M. Wilson, N. P. Davies, M. Brundler, C. McConville, R. G. Grundy and A. C. Peet, High resolution magic angle spinning ^{1}H NMR of childhood brain and nervous system tumours. *Mol. Cancer*, 2009, **8**(6), 1–11.
212. G. Erb, K. Elbayed, M. Piotto, J. Raya, A. Neuville, M. Mohr, D. Maitrot, P. Kehrli and I. J. Namer, Toward improved grading of malignancy in oligodendrogliomas using metabolomics. *Magn. Reson. Med.*, 2008, **59,** 959–965.
213. M. C. Martinez-Bisbal, L. Marti-Bonmati, J. Piquer, A. Revert, P. Ferrer, J. L. Llacer, M. Piotto, O. Assemat and B. Celda, ^{1}H and ^{13}C HR-MAS spectroscopy of intact biopsy samples ex vivo and in vivo ^{1}H MRS study of human high grade gliomas. *NMR Biomed.*, 2004, **17,** 191–205.
214. M. C. Martinez-Bisbal, D. Monleon, O. Assemat, M. Piotto, J. Piquer, J. L. Llacer and B. Celda, Determination of metabolite concentrations in human brain tumour biopsy samples using HR-MAS and ERETIC measurements. *NMR Biomed.*, 2009, **22,** 199–206.
215. A. A. Tzika, L. Astrakas, H. H. Cao, D. Mintzopoulos, O. C. Andronesi, M. Mindrinos, J. W. Zhang, L. G. Rahme, K. D. Blekas, A. C. Likas, N. P. Galatsanos R. S. Carroll, *et al.*, Combination of high-resolution magic angle spinning proton magnetic resonance spectroscopy and microscale genomics to type brain tumor biopsies. *Int. J. Mol. Med.*, 2007, **20,** 199–208.
216. V. Tugnoli, L. Schenetti, A. Mucci, F. Parenti, R. Cagnoli, V. Righi, A. Trinchero, L. Nocetti, C. Toraci, L. Mavilla, G. Trentini E. Zunarelli, *et al.*, Ex vivo HR-MAS MRS of human meningiomas: a comparison with in vivo ^{1}H MR spectra. *Int. J. Mol. Med.*, 2006, **18,** 859–869.
217. D. Monleon, J. M. Morales, J. Gonzalez-Darder, F. Talamantes, O. Cortes, R. Gil-Benso, C. Loezin-Gines, M. Cerda-Nicolas and B. Celda, Benign and atypical meningioma metabolic signatures by high-resolution magic-angle spinning molecular profiling. *J. Proteome Res.*, 2008, **7,** 2882–2888.
218. K. S. Opstad, A. J. Wright, B. A. Bell, J. R. Griffiths and F. A. Howe, Correlations between in vivo ^{1}H MRS and ex vivo ^{1}H HRMAS metabolite measurements in adult human gliomas. *J. Magn. Reson. Imaging*, 2010, **31,** 289–297.
219. A. Ramani, A. E. Aliev, G. J. Barker and P. S. Tofts, Another approach to protons with constricted mobility in white matter: pilot studies using wideline and high-resolution NMR spectroscopy. *Magn. Reson. Imaging*, 2003, **21,** 1039–1043.
220. T. E. Sjobakk, R. Johansen, T. F. Bathen, U. Sonnewald, R. Juul, S. H. Torp, S. Lundgren and I. S. Gribbestad, Characterization of brain metastases using high-resolution magic angle spinning MRS. *NMR Biomed.*, 2008, **21,** 175–185.
221. K. S. Opstad, B. A. Bell, J. R. Griffiths and F. A. Howe, An investigation of human brain tumour lipids by high-resolution magic angle spinning ^{1}H MRS and histological analysis. *NMR Biomed.*, 2008, **21,** 677–685.
222. K. S. Opstad, B. A. Bell, J. R. Griffiths and F. A. Howe, Toward accurate quantification of metabolites, lipids, and macromolecules in HRMAS spectra of human brain tumor biopsies using LCModel. *Magn. Reson. Med.*, 2008, **60,** 1237–1242.

223. M. Xu, J. Ye, D. Yang, X. Xu, T. T. Yeo, W. H. Ng and C. C. Lim, Ex-vivo NMR of unprocessed tissue in water: a simplified procedure for studying intracranial neoplasms. *Anal. Bioanal. Chem.*, 2007, **389,** 2153–2159.
224. H. Gonzalez-Velez, M. Mier, M. Julia-Sape, T. N. Arvanitis, J. M. Garcia-Gomez, M. Robles, P. H. Lewis, S. Dasmahapatra, D. Dupplaw, A. Peet, C. Arus B. Celda, *et al.*, Healthagents: distributed multi-agent brain tumor diagnosis and prognosis. *Appl. Intell.*, 2009, **30,** 191–202.
225. E. Holmes, T. M. Tsang and S. J. Tabrizi, The application of NMR-based metabonomics in neurological disorders. *NeuroRx*, 2006, **3,** 358–372.
226. L. L. Cheng, K. Newell, A. E. Mallory, B. T. Hyman and R. G. Gonzalez, Quantification of neurons in Alzheimer and control brains with ex vivo high resolution magic angle spinning proton magnetic resonance spectroscopy and stereology. *Magn. Reson. Imaging*, 2002, **20,** 527–533.
227. B. Sitter, T. Autti, J. Tyynela, U. Sonnewald, T. F. Bathen, J. Puranen, P. Santavuori, M. J. Haltia, A. Paetau, T. Polvikoski, I. S. Gribbestad and A. M. Hakkinen, High-resolution magic angle spinning and ^{1}H magnetic resonance spectroscopy reveal significantly altered neuronal metabolite profiles in CLN1 but not in CLN3. *J. Neurosci. Res.*, 2004, **77,** 762–769.
228. U. Sharma and N. R. Jagannathan, Biochemical characterization of breast tumors by in vivo and in vitro magnetic resonance spectroscopy (MRS). *Biophys. Rev.*, 2009, **1,** 21–26.
229. K. Glunde, M. A. Jacobs, A. P. Pathak, D. Artemov and Z. M. Bhujwalla, Molecular and functional imaging of breast cancer. *NMR Biomed.*, 2009, **22,** 92–103.
230. B. Sitter, U. Sonnewald, M. Spraul, H. E. Fjosne and I. S. Gribbestad, High-resolution magic angle spinning MRS of breast cancer tissue. *NMR Biomed.*, 2002, **15,** 327–337.
231. B. Sitter, S. Lundgren, T. F. Bathen, J. Halgunset, H. E. Fjosne and I. S. Gribbestad, Comparison of HR MAS MR spectroscopic profiles of breast cancer tissue with clinical parameters. *NMR Biomed.*, 2006, **19,** 30–40.
232. B. Sitter, T. F. Bathen, T. E. Singstad, H. E. Fjosne, S. Lundgren, J. Halgunset and I. S. Gribbestad, Quantification of metabolites in breast cancer patients with different clinical prognosis using HR MAS MR spectroscopy. *NMR Biomed.*, 2010, **23,** 424–431.
233. T. F. Bathen, L. R. Jensen, B. Sitter, H. E. Fjoesne, J. Halgunset, D. E. Axelson, I. S. Gribbestad and S. Lundgren, MR-determined metabolic phenotype of breast cancer in prediction of lymphatic spread, grade, and hormone status. *Breast Cancer Res. Treat.*, 2007, **104,** 181–189.
234. L. R. Jensen, E. M. Huuse, T. F. Bathen, P. E. Goa, A. M. Bofin, T. B. Pedersen, S. Lundgren and I. S. Gribbestad, Assessment of early docetaxel response in an experimental model of human breast cancer using DCE-MRI, ex vivo HR MAS, and in vivo ^{1}H MRS. *NMR Biomed.*, 2010, **23,** 56–65.
235. M. M. Mahon, N. M. deSouza, R. Dina, W. P. Soutter, G. A. McIndoe, A. D. Williams and I. J. Cox, Preinvasive and invasive cervical cancer: an ex vivo proton magic angle spinning magnetic resonance spectroscopy study. *NMR Biomed.*, 2004, **17,** 144–153.
236. B. Sitter, T. Bathen, B. Hagen, C. Arentz, F. E. Skjeldestad and I. S. Gribbestad, Cervical cancer tissue characterized by high-resolution magic angle spinning MR spectroscopy. *Magn. Reson. Mater. Phys. Biol. Med.*, 2004, **16,** 174–181.
237. H. Lyng, B. Sitter, T. F. Bathen, L. R. Jensen, K. Sundfr, G. B. Kristensen and I. S. Gribbestad, Metabolic mapping by use of high-resolution magic angle spinning ^{1}H MR spectroscopy for assessment of apoptosis in cervical carcinomas. *BMC Cancer*, 2007, **7,** 11.
238. D. Zietkowski, R. L. Davidson, T. R. Eykyn, S. S. De Silva, N. M. deSouza and G. S. Payne, Detection of cancer in cervical tissue biopsies using mobile lipid resonances measured with diffusion-weighted ^{1}H magnetic resonance spectroscopy. *NMR Biomed.*, 2010, **23,** 382–390.
239. S. S. De Silva, G. S. Payne, V. Thomas, Paul G. Carter, T. E. J. Ind and N. M. deSouza, Investigation of metabolite changes in the transition from pre-invasive to invasive cervical cancer measured using ^{1}H and ^{31}P magic angle spinning MRS of intact tissue. *NMR Biomed.*, 2009, **22,** 191–198.
240. S. S. De Silva, G. S. Payne, V. A. Morgan, T. E. J. Ind, J. H. Shepherd, D. P. J. Barton and N. M. deSouza, Epithelial and stromal metabolite changes in the transition from cervical intraepithelial neoplasia to cervical cancer: an in vivo ^{1}H magnetic resonance spectroscopic imaging study with ex vivo correlation. *Eur. Radiol.*, 2009, **19,** 2041–2048.

241. J. Kurhanewicz, M. G. Swanson, S. J. Nelson and D. B. Vigneron, Combined magnetic resonance imaging and spectroscopic imaging approach to molecular imaging of prostate cancer. *Magn. Reson. Imaging*, 2002, **16,** 451–463.
242. L. L. Cheng, M. A. Burns, J. L. Taylor, W. He, E. F. Halpern, W. S. McDougal and C. L. Wu, Metabolic characterization of human prostate cancer with tissue magnetic resonance spectroscopy. *Cancer Res.*, 2005, **65,** 3030–3034.
243. M. G. Swanson, D. B. Vigneron, Z. L. Tabatabai, R. G. Males, L. Schmitt, P. R. Carroll, J. K. James, R. E. Hurd and J. Kurhanewicz, Proton HR-MAS spectroscopy and quantitative pathologic analysis of MRI/3D-MRSI-targeted postsurgical prostate tissues. *Magn. Reson. Med.*, 2003, **50,** 944–954.
244. N. G. Spencer, T. R. Eykyn, N. M. deSouza and G. S. Payne, The effect of experimental conditions on the detection of spermine in cell extracts and tissues. *NMR Biomed.*, 2010, **23,** 163–169.
245. M. G. Swanson, A. S. Zektzer, Z. L. Tabatabai, J. Simko, S. Jarso, K. R. Keshari, L. Schmitt, P. R. Carroll, K. Shinohara, D. B. Vigneron and J. Kurhanewicz, Quantitative analysis of prostate metabolites using ^{1}H HR-MAS spectroscopy. *Magn. Reson. Med.*, 2006, **55,** 1257–1264.
246. M. G. Swanson, K. R. Keshari, Z. L. Tabatabai, J. P. Simko, K. Shinohara, P. R. Carroll, A. S. Zektzer and J. Kurhanewicz, Quantification of choline- and ethanolamine-containing metabolites in human prostate tissues using ^{1}H HR-MAS total correlation spectroscopy. *Magn. Reson. Med.*, 2008, **60,** 33–40.
247. M. Tessem, M. G. Swanson, K. R. Keshari, M. J. Albers, D. Joun, Z. Laura Tabatabai, J. P. Simko, K. Shinohara, S. J. Nelson, D. B. Vigneron, I. S. Gribbestad and J. Kurhanewicz, Evaluation of lactate and alanine as metabolic biomarkers of prostate cancer using ^{1}H HR-MAS spectroscopy of biopsy tissues. *Magn. Reson. Med.*, 2008, **60,** 510–516.
248. J. J. A. van Asten, V. Cuijpers, C. Hulsbergen-van de Kaa, C. Soede-Huijbregts, J. A. Witjes, A. Verhofstad and A. Heerschap, High resolution magic angle spinning NMR spectroscopy for metabolic assessment of cancer presence and Gleason score in human prostate needle biopsies. *Magn. Reson. Mater. Phys. Biol. Med.*, 2008, **21,** 435–442.
249. K. Stenman, J. B. Hauksson, G. Grobner, P. Stattin, A. Bergh and K. Riklund, Detection of polyunsaturated omega-6 fatty acid in human malignant prostate tissue by 1D and 2D high-resolution magic angle spinning NMR spectroscopy. *Magn. Reson. Mater. Phys. Biol. Med.*, 2009, **22,** 327–331.
250. C. L. Wu, J. L. Taylor, W. He, A. G. Zepeda, E. F. Halpern, A. Bielecki, R. G. Gonzalez and L. L. Cheng, Proton high-resolution magic angle spinning NMR analysis of fresh and previously frozen tissue of human prostate. *Magn. Reson. Med.*, 2003, **50,** 1307–1311.
251. K. W. Jordan, W. He, E. F. Halpern, C. Wu and L. L. Cheng, Evaluation of tissue metabolites with high resolution magic angle spinning MR spectroscopy human prostate samples after three-year storage at −80°C. *Biomark. Insights*, 2007, **2,** 147–154.
252. D. S. Aaronson, R. Iman, T. J. Walsh, J. Kurhanewicz and P. J. Turek, A novel application of ^{1}H magnetic resonance spectroscopy: non-invasive identification of spermatogenesis in men with non-obstructive azoospermia. *Hum. Reprod.*, 2010, **25,** 847–852.
253. I. Barba, C. Sanz, A. Barbera, G. Tapia, J. Mate, D. Garcia-Dorado, J. Riberia and A. Oriol, Metabolic fingerprinting of fresh lymphoma samples used to discriminate between follicular and diffuse large B-cell lymphomas. *Exp. Hematol.*, 2009, **37,** 1259–1265.
254. V. Tugnoli, A. Mucci, L. Schenetti, V. Righi, C. Calabrese, A. Fabbri, G. Di Febo and M. R. Tosi, Ex vivo HR-MAS magnetic resonance spectroscopy of human gastric adenocarcinomas: a comparison with healthy gastric mucosa. *Oncol. Rep.*, 2006, **16,** 543–553.
255. C. Calabrese, A. Pisi, G. Di Febo, G. Liguori, G. Filippini, M. Cervellera, V. Righi, P. Lucchi, A. Mucci, L. Schenetti, V. Tonini, M. R. Tosi and V. Tugnoli, Biochemical alterations from normal mucosa to gastric cancer by ex vivo magnetic resonance spectroscopy. *Cancer Epidemiol. Biomark. Prev.*, 2008, **17,** 1386–1395.
256. Y. Wang, O. Cloarec, H. Tang, J. C. Lindon, E. Holmes, S. Kochhar and J. K. Nicholson, Magic angle spinning NMR and ^{1}H-^{31}P heteronuclear statistical total correlation spectroscopy of intact human gut biopsies. *Anal. Chem.*, 2008, **80,** 1058–1066.
257. Y. Wang, E. Holmes, E. M. Comelli, G. Fotopoulos, G. Dorta, H. Tang, M. J. Rantalainen, J. C. Lindon, I. E. Corthsy-Theulaz, L. B. Fay, S. Kochhar and J. K. Nicholson, Topographical

variation in metabolic signatures of human gastrointestinal biopsies revealed by high-resolution magic-angle spinning ^{1}H NMR spectroscopy. *J. Proteome Res.*, 2007, **6,** 3944–3951.
258. J. T. Bjerrum, O. H. Nielsen, F. Hao, H. Tang, J. K. Nicholson, Y. Wang and J. Olsen, Metabonomics in ulcerative colitis: diagnostics, biomarker identification, and insight into the pathophysiology. *J. Proteome Res.*, 2010, **9,** 954–962.
259. M. Piotto, F.-M. Moussallieh, B. Dillmann, A. Imperiale, A. Neuville, C. Brigand, J.-P. Bellocq, K. Elbayed and I. J. Namer, Metabolic characterization of primary human colorectal cancers using high resolution magic angle spinning ^{1}H magnetic resonance spectroscopy. *Metabolomics*, 2009, **5,** 292–301.
260. V. Righi, C. Durante, M. Cocchi, C. Calabrese, G. D. Febo, F. Lecce, A. Pisi, V. Tugnoli, A. Mucci and L. Schnetti, Discrimination of healthy and neoplastic human colon tissues by ex vivo HR-MAS NMR spectroscopy and chemometric analyses. *J. Proteome Res.*, 2009, **8,** 1859–1869.
261. T. Seierstad, K. Re, B. Sitter, J. Halgunset, K. Flatmark, A. H. Ree, D. R. Olsen, I. S. Gribbestad and T. F. Bathen, Principal component analysis for the comparison of metabolic profiles from human rectal cancer biopsies and colorectal xenografts using high-resolution magic angle spinning ^{1}H magnetic resonance spectroscopy. *Mol. Cancer*, 2008, **7,** 33.
262. E. C. Y. Chan, P. K. Koh, M. Mal, P. Y. Cheah, K. W. Eu, A. Backshall, R. Cavill, J. K. Nicholson and H. C. Keun, Metabolic profiling of human colorectal cancer using high-resolution magic angle spinning nuclear magnetic resonance (HR-MAS NMR) spectroscopy and gas chromatography mass spectrometry (GC/MS). *J. Proteome Res.*, 2009, **8,** 352–361.
263. J. M. Stern, M. E. Merritt, I. Zeltser, J. D. Raman and J. A. Cadeddu, Phase one pilot study using magnetic resonance spectroscopy to predict the histology of radiofrequency-ablated renal tissue. *Eur. Urol.*, 2009, **55,** 433–440.
264. C. M. Rocha, A. S. Barros, A. N. Gil, B. J. Goodfellow, E. Humpfer, M. Spraul, I. M. Carreira, J. B. Melo, J. Bernardo, A. Gomes, V. Sousa, L. Carvalho and I. F. Duarte, Metabolic profiling of human lung cancer tissue by ^{1}H high resolution magic angle spinning (HRMAS) NMR spectroscopy. *J. Proteome Res.*, 2010, **9,** 319–332.
265. K. W. Jordan, C. B. Adkins, L. Su, E. F. Halpern, E. J. Mark, D. C. Christiani and L. L. Cheng, Comparison of squamous cell carcinoma and adenocarcinoma of the lung by metabolomic analysis of tissue-serum pairs. *Lung Cancer*, 2010, **68,** 44–50.
266. S. Majumdar, Magnetic resonance imaging and spectroscopy of the intervertebral disc. *NMR Biomed.*, 2006, **19,** 894–903.
267. K. R. Keshari, J. C. Lotz, J. Kurhanewicz and S. Majumdar, Correlation of HR-MAS spectroscopy derived metabolite concentrations with collagen and proteoglycan levels and Thompson grade in the degenerative disc. *Spine*, 2005, **30,** 2683–2688.
268. K. R. Keshari, A. S. Zektzer, M. G. Swanson, S. Majumdar, J. C. Lotz and J. Kurhanewicz, Characterization of intervertebral disc degeneration by high-resolution magic angle spinning (HR-MAS) spectroscopy. *Magn. Reson. Med.*, 2005, **53,** 519–527.
269. W. Ling, R. R. Regatte, M. E. Schweitzer and A. Jerschow, Characterization of bovine patellar cartilage by NMR. *NMR Biomed.*, 2008, **21,** 289–295.
270. J. Chen, Y. V. Wu, P. DeCarolis, R. O'Connor, C. J. Somberg and S. Singer, Resolution of creatine and phosphocreatine ^{1}H signals in isolated human skeletal muscle using HR-MAS ^{1}H NMR. *Magn. Reson. Med.*, 2008, **59,** 1221–1224.
271. D. Loiseau, D. Morvan, A. Chevrollier, A. Demidem, O. Douay, P. Reynier and G. Stepien, Mitochondrial bioenergetic background confers a survival advantage to HepG2 cells in response to chemotherapy. *Mol. Carcinog.*, 2009, **48,** 733–741.
272. I. F. Duarte, E. G. Stanley, E. Holmes, J. C. Lindon, A. M. Gil, H. Tang, R. Ferdinand, C. G. McKee, J. K. Nicholson, H. Vilca-Melendez, N. Heaton and G. M. Murphy, Metabolic assessment of human liver transplants from biopsy samples at the donor and recipient stages using high-resolution magic angle spinning ^{1}H NMR spectroscopy. *Anal. Chem.*, 2005, **77,** 5570–5578.
273. B. Martinez-Granados, D. Monleon, M. C. Martinez-Bisbal, J. M. Rodrigo, J. del Olmo, P. Lluch, A. Ferrandez, L. Marti-Bonmati and B. Celda, Metabolite identification in human liver needle biopsies by high-resolution magic angle spinning ^{1}H NMR spectroscopy. *NMR Biomed.*, 2006, **19,** 90–100.

274. Y. Yang, C. Li, X. Nie, X. Feng, W. Chen, Y. Yue, H. Tang and F. Deng, Metabonomic studies of human hepatocellular carcinoma using high-resolution magic-angle spinning ^{1}H NMR spectroscopy in conjunction with multivariate data analysis. *J. Proteome Res.*, 2007, **6,** 2605–2614.
275. B. N. Joe, K. Vahidi, A. Zektzer, M. Chen, M. S. Clifton, T. Butler, K. Keshari, J. Kurhanewicz, F. Coakley and M. G. Swanson, ^{1}H HR-MAS spectroscopy for quantitative measurement of choline concentration in amniotic fluid as a marker of fetal lung maturity: inter- and intraobserver reproducibility study. *J. Magn. Reson. Imaging*, 2008, **28,** 1540–1545.
276. J. L. Griffin, C. Blenkiron, P. K. Valonen, C. Caldas and R. A. Kauppinen, High-resolution magic angle spinning ^{1}H NMR spectroscopy and reverse transcription-PCR analysis of apoptosis in a rat gliomas. *Anal. Chem.*, 2006, **78,** 1546–1552.
277. J. L. Griffin and O. Corcoran, High-resolution magic-angle spinning ^{13}C NMR spectroscopy of cerebral tissue. *Magn. Reson. Mater. Phys. Biol. Med.*, 2005, **18,** 51–56.
278. J. L. Griffin, K. K. Lehtimaeki, P. K. Valonen, O. H. Groehn, M. I. Kettunen, S. Ylae-Herttuala, A. Pitkaenen, J. K. Nicholson and R. A. Kauppinen, Assignment of ^{1}H nuclear magnetic resonance visible polyunsaturated fatty acids in BT4C gliomas undergoing ganciclovir-thymidine kinase gene therapy-induced programmed cell death. *Cancer Res.*, 2003, **63,** 3195–3201.
279. K. K. Lehtimaeki, P. K. Valonen, J. L. Griffin, T. H. Vaeisaenen, O. H. Groehn, M. I. Kettunen, J. Vepsaelaeinen, S. Ylae-Herttuala, J. Nicholson and R. A. Kauppinen, Metabolite changes in BT4C rat gliomas undergoing ganciclovir-thymidine kinase gene therapy-induced programmed cell death as studied by ^{1}H NMR spectroscopy in vivo, ex vivo, and in vitro. *J. Biol. Chem.*, 2003, **278,** 45915–45923.
280. P. K. Valonen, J. L. Griffin, K. K. Lehtimaeki, T. Liimatainen, J. K. Nicholson, O. H. J. Groehn and R. A. Kauppinen, High-resolution magic-angle-spinning ^{1}H NMR spectroscopy reveals different responses in choline-containing metabolites upon gene therapy-induced programmed cell death in rat brain glioma. *NMR Biomed.*, 2005, **18,** 252–259.
281. E. M. Ratai, S. Pilkenton, M. R. Lentz, J. B. Greco, R. A. Fuller, J. P. Kim, J. He, L. L. Cheng and R. G. Gonzlez, Comparisons of brain metabolites observed by HRMAS ^{1}H NMR of intact tissue and solution ^{1}H NMR of tissue extracts in SIV-infected macaques. *NMR Biomed.*, 2005, **18,** 242–251.
282. K. S. Opstad, B. A. Bell, J. R. Griffiths and F. A. Howe, An assessment of the effects of sample ischaemia and spinning time on the metabolic profile of brain tumour biopsy specimens as determined by high-resolution magic angle spinning ^{1}H NMR. *NMR Biomed.*, 2008, **21,** 1138–1147.
283. I. Garcia-Alvarez, L. Garrido, E. Doncel-Perez, M. Nieto-Sampedro and A. Fernandez-Mayoralas, Detection of metabolite changes in C6 glioma cells cultured with antimitotic oleyl glycoside by ^{1}H MAS NMR. *J. Med. Chem.*, 2009, **52,** 1263–1267.
284. Y. Yang, L. Chen, H. Gao, D. Zeng, Y. Yue, M. Liu, H. Lei, F. Deng and C. Ye, High-resolution magic-angle spinning ^{13}C spectroscopy of brain tissue at natural abundance. *Magn. Reson. Chem.*, 2006, **44,** 263–268.
285. O. Risa, T. M. Melo and U. Sonnewald, Quantification of amounts and ^{13}C content of metabolites in brain tissue using high-resolution magic angle spinning ^{13}C NMR spectroscopy. *NMR Biomed.*, 2009, **22,** 266–271.
286. T. M. Tsang, J. L. Griffin, J. Haselden, C. Fish and E. Holmes, Metabolic characterization of distinct neuroanatomical regions in rats by magic angle spinning ^{1}H nuclear magnetic resonance spectroscopy. *Magn. Reson. Med.*, 2005, **53,** 1018–1024.
287. X. Zhang, H. Liu, J. Wu, X. Zhang, M. Liu and Y. Wong, Metabonomic alterations in hippocampus, temporal and prefrontal cortex with age in rats. *Neurochem. Int.*, 2009, **54,** 481–487.
288. T. M. Tsang, J. N. Haselden and E. Holmes, Metabonomic characterization of the 3-nitropropionic acid rat model of Huntington's disease. *Neurochem. Res.*, 2009, **34,** 1261–1271.
289. N. Ghenimi, M. Beauvieux, M. Biran, V. Pallet, P. Higueret and J. Gallis, Vitamin A deficiency in rats induces anatomic and metabolic changes comparable with those of neurodegenerative disorders. *J. Nutr.*, 2009, **139,** 696–702.
290. J. Bustillo, R. Barrow, R. Paz, J. Tang, N. Seraji-Bozorgzad, G. J. Moore, F. Bolognani, J. Lauriello, N. Perrone-Bizzozero and M. Galloway, Long-term treatment of rats with haloperidol: lack of an effect on brain *N*-acetyl aspartate levels. *Neuropsychopharmacology*, 2006, **31,** 751–756.
291. H. Mao, D. Toufexis, X. Wang, A. Lacreuse and S. Wu, Changes of metabolite profile in kainic acid induced hippocampal injury in rats measured by HRMAS NMR. *Exp. Brain Res.*, 2007, **183,** 477–485.

292. B. M. Cortese, T. R. Mitchell, M. P. Galloway, K. E. Provost, J. Fang, G. J. Moore and T. W. Uhde, Region-specific alteration in brain glutamate: possible relationship to risk-taking behavior. *Physiol. Behav.*, 2010, **99,** 445–450.
293. I. Lamproglou, L. Barbier, M. Diserbo, F. Fauvelle, W. Fauquette and C. Amourette, Repeated stress in combination with pyridostigmine. Part I: long-term behavioural consequences. *Behav. Brain Res.*, 2009, **197,** 301–310.
294. H. L. Liu, F. Fang, H. Zhu, S. A. Xia, D. Han, L. Hu, H. Lei and M. L. Liu, Metabolic changes in temporal lobe structures measured by HR-MAS NMR at early stage of electrogenic rat epilepsy. *Exp. Neurol.*, 2008, **212,** 377–385.
295. F. Fauvelle, F. Dorandeu, P. Carpentier, A. Foquin, H. Rabeson, D. Graveron-Demilly, P. Arvers and G. Testylier, Changes in mouse brain metabolism following a convulsive dose of soman: a proton HRMAS NMR study. *Toxicology*, 2010, **267,** 99–111.
296. H. Rabeson, F. Fauvelle, G. Testylier, A. Foquin, P. Carpentier, F. Dorandeu, D. van Ormondt and D. Graveron-Demilly, Quantitation with QUEST of brain HRMAS-NMR signals: application to metabolic disorders in experimental epileptic seizures. *Magn. Reson. Med.*, 2008, **59,** 1266–1273.
297. M. R. Pears, D. Rubtsov, H. M. Mitchison, J. D. Cooper, D. A. Pearce, R. J. Mortishire-Smith and J. L. Griffin, Strategies for data analyses in a high resolution ^{1}H NMR based metabolomics study of a mouse model of Batten disease. *Metabolomics*, 2007, **3,** 121–136.
298. J. L. Griffin, C. K. Cemal and M. A. Pook, Defining a metabolic phenotype in the brain of a transgenic mouse model of spinocerebellar ataxia 3. *Physiol. Genomics*, 2004, **16,** 334–340.
299. S. K. O'Leary-Moore, A. P. McMechan, M. P. Galloway and J. H. Hannigan, Neonatal alcohol-induced region-dependent changes in rate brain neurochemistry measured by high-resolution magnetic resonance spectroscopy. *Alcohol. Clin. Exp. Res.*, 2008, **32,** 1–11.
300. S. K. O'Leary-Moore, M. P. Galloway, A. P. McMechan, J. H. Hannigan and S. E. Bowen, Region-dependent alterations in glutamate and GABA measured by high-resolution magnetic resonance spectroscopy following acute binge inhalation of toluene in juvenile rats. *Neurotoxicol. Teratol.*, 2007, **29,** 466–475.
301. S. K. O'Leary-Moore, M. P. Galloway, A. P. McMechan, S. Irtenkauf, J. H. Hannigan and S. E. Bowen, Neurochemical changes after acute binge toluene inhalation in adolescent and adult rats: a high-resolution magnetic resonance spectroscopy study. *Neurotoxicol. Teratol.*, 2009, **31,** 382–389.
302. N. J. Waters, E. Holmes, C. J. Waterfield, R. D. Farrant and J. K. Nicholson, NMR and pattern recognition studies on liver extracts and intact livers from rats treated with α-naphthylisothiocyanate. *Biochem. Pharmacol.*, 2002, **64,** 67–77.
303. M. E. Bollard, J. Xu, W. Purcell, J. L. Griffin, C. Quirk, E. Holmes and J. K. Nicholson, Metabolic profiling of the effects of D-galactosamine in liver spheroids using ^{1}H NMR and MAS-NMR spectroscopy. *Chem. Res. Toxicol.*, 2002, **15,** 1351–1359.
304. M. Coen, E. M. Lenz, J. K. Nicholson, I. D. Wilson, F. Pognan and J. C. Lindon, An integrated metabonomic investigation of acetaminophen toxicity in the mouse using NMR spectroscopy. *Chem. Res. Toxicol.*, 2003, **16,** 295–303.
305. R. J. Mortishire-Smith, G. L. Skiles, J. W. Lawrence, S. Spence, A. W. Nicholls, B. A. Johnson and J. K. Nicholson, Use of metabonomics to identify impaired fatty acid metabolism as the mechanism of a drug-induced toxicity. *Chem. Res. Toxicol.*, 2004, **17,** 165–173.
306. Y. Wang, M. E. Bollard, H. Keun, H. Antti, O. Beckonert, T. M. Ebbels, J. C. Lindon, E. Holmes, H. Tang and J. K. Nicholson, Spectral editing and pattern recognition methods applied to high-resolution magic-angle spinning ^{1}H nuclear magnetic resonance spectroscopy of liver tissues. *Anal. Biochem.*, 2003, **323,** 26–32.
307. Y. Wang, M. E. Bollard, J. K. Nicholson and E. Holmes, Exploration of the direct metabolic effects of mercury II chloride on the kidney of Sprague–Dawley rats using high-resolution magic angle spinning ^{1}H NMR spectroscopy of intact tissue and pattern recognition. *J. Pharm. Biomed. Anal.*, 2006, **40,** 375–381.
308. H. F. Wu, X. Y. Zhang, X. J. Li, Z. F. Li, P. Q. Liao, W. S. Li, Y. J. Wu and F. K. Pei, Investigation on acute biochemical effects of $Ce(NO_3)_3$ on liver and kidney tissues by MAS ^{1}H NMR spectroscopic-based metabonomic approach. *J. Rare Earths*, 2006, **24,** 357–363.

309. H. Wu, X. Zhang, X. Li, Y. Wu and F. Pei, Acute biochemical effects of $La(NO_3)_3$ on liver and kidney tissues by magic-angle spinning ^1H nuclear magnetic resonance spectroscopy and pattern recognition. *Anal. Biochem.*, 2005, **339,** 242–248.
310. I. K. Yap, T. A. Clayton, H. Tang, J. R. Everett, G. Hanton, J. P. Provost, J. L. Le Net, C. Charuel, J. C. Lindon and J. K. Nicholson, An integrated metabonomic approach to describe temporal metabolic disregulation induced in the rat by the model hepatotoxin allyl formate. *J. Proteome Res.*, 2006, **5,** 2675–2684.
311. O. M. Rooney, J. Troke, J. K. Nicholson and J. L. Griffin, High-resolution diffusion and relaxation-edited magic angle spinning ^1H NMR spectroscopy of intact liver tissue. *Magn. Reson. Med.*, 2003, **50,** 925–930.
312. H. C. Bertram, I. F. Duarte, A. M. Gil, K. E. Knudsen and H. N. Laerke, Metabolic profiling of liver from hypercholesterolemic pigs fed rye or wheat fiber and from normal pigs. High-resolution magic angle spinning ^1H NMR spectroscopic study. *Anal. Chem.*, 2007, **79,** 168–175.
313. S. D. Huhn, C. M. Szabo, J. H. Gass and A. E. Manzi, Metabolic profiling of normal and hypertensive rat kidney tissues by HRMAS-NMR spectroscopy. *Anal. Bioanal. Chem.*, 2004, **378,** 1511–1519.
314. Y. Wang, H. Tang, E. Holmes, J. C. Lindon, M. E. Turini, N. Sprenger, G. Bergonzelli, L. B. Fay, S. Kochhar and J. K. Nicholson, Biochemical characterization of rat intestine development using high-resolution magic-angle-spinning ^1H NMR spectroscopy and multivariate data analysis. *J. Proteome Res.*, 2005, **4,** 1324–1329.
315. A. Backshall, D. Alferez, F. Teichert, I. D. Wilson, R. W. Wilkinson, R. A. Goodlad and H. C. Keun, Detection of metabolic alterations in non-tumor gastrointestinal tissue of the Apc(Min/+) mouse by ^1H MAS NMR spectroscopy. *J. Proteome Res.*, 2009, **8,** 1423–1430.
316. T. F. Bathen, K. Holmgren, A. G. Lundemo, M. H. Hjelstuen, H. E. Krokan, I. S. Gribbestad and S. A. Schnberg, Omega-3 fatty acids suppress growth of SW620 human colon cancer xenografts in nude mice. *Anticancer Res.*, 2008, **28,** 3717–3724.
317. F. J. Martin, N. Sprenger, I. K. S. Yap, Y. Wang, R. Bibiloni, F. Rochat, S. Rezzi, C. Cherbut, S. Kochhar, J. C. Lindon, E. Holmes and J. K. Nicholson, Panorganismal gut microbiome-host metabolic crosstalk. *J. Proteome Res.*, 2009, **8,** 2090–2105.
318. F. P. Martin, Y. Wang, N. Sprenger, E. Holmes, J. C. Lindon, S. Kochhar and J. K. Nicholson, Effects of probiotic *Lactobacillus paracasei* treatment on the host gut tissue metabolic profiles probed via magic-angle-spinning NMR spectroscopy. *J. Proteome Res.*, 2007, **6,** 1471–1481.
319. O. Risa, O. Saether, S. Loefgren, P. G. Soederberg, J. Krane and A. Midelfart, Metabolic changes in rat lens after in vivo exposure to ultraviolet irradiation: measurements by high resolution MAS ^1H NMR spectroscopy. *Invest. Ophthalmol. Vis. Sci.*, 2004, **45,** 1916–1921.
320. O. Risa, O. Saether, M. Kakar, V. Mody, S. Loefgren, P. G. Sderberg, J. Krane and A. Midelfart, Time dependency of metabolic changes in rat lens after in vivo UVB irradiation analysed by HR-MAS ^1H NMR spectroscopy. *Exp. Eye Res.*, 2005, **81,** 407–414.
321. M. Fris, J. Cejkova and A. Midelfart, The effect of single and repeated UVB radiation on rabbit lens. *Graefes Arch. Clin. Exp. Ophthalmol.*, 2008, **246,** 551–558.
322. O. Saether, J. Krane, O. Risa, J. Cejkova and A. Midelfart, High-resolution MAS ^1H NMR spectroscopic analysis of rabbit cornea after treatment with dexamethasone and exposure to UV-B radiation. *Curr. Eye Res.*, 2005, **30,** 1041–1049.
323. O. Saether, O. Risa, J. Cejkova, J. Krane and A. Midelfart, High-resolution magic angle spinning ^1H NMR spectroscopy of metabolic changes in rabbit lens after treatment with dexamethasone combined with UVB exposure. *Graefes Arch. Clin. Exp. Ophthalmol.*, 2004, **242,** 1000–1007.
324. M. Fris, M. B. Tessem, J. Cejkova and A. Midelfart, The effect of single and repeated UVB radiation on rabbit cornea. *Graefes Arch. Clin. Exp. Ophthalmol.*, 2006, **244,** 1680–1687.
325. M. Fris, M. B. Tessem, O. Saether and A. Midelfart, Biochemical changes in selenite cataract model measured by high-resolution MAS ^1H NMR spectroscopy. *Acta Ophthalmol. Scand.*, 2006, **84,** 684–692.
326. M. Fris and A. Midelfart, Postnatal biochemical changes in rat lens: an important factor in cataract models. *Curr. Eye Res.*, 2007, **32,** 95–103.
327. M. B. Tessem, T. F. Bathen, S. Loefgren, O. Saether, V. Mody, L. Meyer, X. Dong, P. G. Soederberg and A. Midelfart, Biological response in various compartments of the rat lens after in vivo exposure to UVR-B analyzed by HR-MAS ^1H NMR spectroscopy. *Invest. Ophthalmol. Vis. Sci.*, 2006, **47,** 5404–5411.

328. M. E. Bollard, A. J. Murray, K. Clarke, J. K. Nicholson and J. L. Griffin, A study of metabolic compartmentation in the rat heart and cardiac mitochondria using high-resolution magic angle spinning ^{1}H NMR spectroscopy. *FEBS Lett.*, 2003, **553,** 73–78.
329. S. A. Perrine, M. S. Michaels, F. Ghoddoussi, E. M. Hyde, M. E. Tancer and M. P. Galloway, Cardiac effects of MDMA on the metabolic profile determined with ^{1}H-magnetic resonance spectroscopy in the rats. *NMR Biomed.*, 2009, **23,** 419–425.
330. F. Fang, X. H. He, H. W. Deng, Q. Chen, J. P. Lu, M. Spraul and Y. H. Yu, Discrimination of metabolic profiles of pancreatic cancer from chronic pancreatitis by high-resolution magic angle spinning ^{1}H nuclear magnetic resonance and principal components analysis. *Cancer Sci.*, 2007, **98,** 1678–1682.
331. D. Morvan, A. Demidem, J. Papon, M. De Latour and J. C. Madelmont, Melanoma tumors acquire a new phospholipid metabolism phenotype under cystemustine as revealed by high-resolution magic angle spinning proton nuclear magnetic resonance spectroscopy of intact tumor samples. *Cancer Res.*, 2002, **62,** 1890–1897.
332. D. Morvan and A. Demidem, Metabolomics by proton nuclear magnetic resonance spectroscopy of the response to chloroethylnitrosourea reveals drug efficacy and tumor adaptive metabolic pathways. *Cancer Res.*, 2007, **67,** 2150–2159.
333. D. Morvan, A. Demidem, S. Guenin and J. C. Madelmont, Methionine-dependence phenotype of tumors: metabolite profiling in a melanoma model using l-[methyl-^{13}C]methionine and high-resolution magic angle spinning ^{1}H–^{13}C nuclear magnetic resonance spectroscopy. *Magn. Reson. Med.*, 2006, **55,** 984–996.
334. M. Coen, Y. S. Hong, O. Cloarec, C. M. Rhode, M. D. Reily, D. G. Robertson, E. Holmes, J. C. Lindon and J. K. Nicholson, Heteronuclear ^{1}H–^{31}P statistical total correlation NMR spectroscopy of intact liver for metabolic biomarker assignment: application to galactosamine-induced hepatotoxicity. *Anal. Chem.*, 2007, **79,** 8956–8966.
335. G. S. Payne, H. Troy, S. J. Vaidya, J. R. Griffiths, M. O. Leach and Y. L. Chung, Evaluation of ^{31}P high-resolution magic angle spinning of intact tissue samples. *NMR Biomed.*, 2006, **19,** 593–598.
336. W. K. Renema, A. Schmidt, J. J. van Asten, F. Oerlemans, K. Ullrich, B. Wieringa, D. Isbrandt and A. Heerschap, MR spectroscopy of muscle and brain in guanidinoacetate methyltransferase (GAMT)-deficient mice: validation of an animal model to study creatine deficiency. *Magn. Reson. Med.*, 2003, **50,** 936–943.
337. L. G. Astrakas, I. Goljer, S. Yasuhara, K. E. Padfield, Q. Zhang, S. Gopalan, M. N. Mindrinos, G. Dai, Y. M. Yu, J. A. Martyn, R. G. Tompkins, L. G. Rahme and A. A. Tzika, Proton NMR spectroscopy shows lipids accumulate in skeletal muscle in response to burn trauma-induced apoptosis. *FASEB J.*, 2005, **19,** 1431–1440.
338. B. Madhu, J. C. Waterton, J. R. Griffiths, A. J. Ryan and S. P. Robinson, The response of RIF-1 fibrosarcomas to the vascular-disrupting agent ZD6126 assessed by in vivo and ex vivo ^{1}H magnetic resonance spectroscopy. *Neoplasia*, 2006, **8,** 560–567.
339. M. Borel, P. Pastoureau, J. Papon, J. Madelmont, N. Moins, J. Maublant and E. Miot-Noirault, Longitudinal profiling of articular cartilage degradation in osteoarthritis by high-resolution magic angle spinning ^{1}H NMR spectroscopy: experimental study in the meniscectomized guinea pig models. *J. Proteome Res.*, 2009, **8,** 2594–2600.
340. T. Yamamoto, I. Horii and T. Yoshida, Integrated NMR-based metabonomic investigation of early metabolic effects of ethylene glycol monomethyl ether (EGME) on male reproductive organs in rats. *J. Toxicol. Sci.*, 2007, **32,** 515–528.
341. D. Bon, V. Gilard, S. Massou, G. Prs, M. Malet-Martino, R. Martino and F. Desmoulin, In vivo ^{31}P and ^{1}H HR-MAS NMR spectroscopy analysis of the unstarved *Aporrectodea caliginosa* (Lumbricidae). *Biol. Fertil. Soils*, 2006, **43,** 191–198.
342. S. Wiklund, M. Karlsson, H. Antti, D. Johnels, M. Sjstrm, G. Wingsle and U. Edlund, A new metabonomic strategy for analysing the growth process of the poplar tree. *Plant Biotechnol. J.*, 2005, **3,** 353–362.
343. Y. Sekiyama, E. Chikayama and J. Kikuchi, Profiling polar and semipolar plant metabolites throughout extraction processes using a combined solution-state and high-resolution magic angle spinning NMR approach. *Anal. Chem.*, 2010, **82,** 1643–1652.

CHAPTER 4

Accurate Measurement of Small *J* Couplings

Zhong Chen, Yuqing Huang, Yanqin Lin, and **Shuhui Cai**

Contents

Abstract

Small *J* coupling constants are closely relevant to the assignment of conformational preferences for medium- to large-sized molecules and the valuable structural information about the backbone dihedral angles of biological molecules. Thus, accurate measurement for small *J* coupling constants is extremely important, which has long been recognized. However, the accurate measurement of small *J* coupling constants is limited by the natural linewidth since the line splitting arising from small *J* couplings are usually merged into the related peaks. A cornucopia of NMR spectral techniques has been designed for the achievement of small *J* coupling information. Generally, the existing techniques can be divided into two types. One is to directly

Department of Physics, Fujian Key Laboratory of Plasma and Magnetic Resonance, State Key Laboratory of Physical Chemistry of Solid Surfaces, Xiamen University, Xiamen, China

Annual Reports on NMR Spectroscopy, Volume 72
ISSN 0066-4103, DOI: 10.1016/B978-0-12-385857-3.00004-9

© 2011 Elsevier Ltd.
All rights reserved.

extract small *J* coupling constants without *J* multiplication, while another is on the basis of *J* multiplication. Performance of the existing techniques has been evaluated and the results show that these approaches can be adapted for a wide range of samples, ranging from complex chemical molecules to biological samples, even for the samples under inhomogeneous magnetic fields. These spectral editing techniques provide complementary strategies for the quantification of small *J* coupling constants. In this review, the mechanisms of these approaches are presented with the analysis of their corresponding applicability and efficiencies.

Keywords: NMR, *J* coupling constants, Accurate measurement, Scaling, Intermolecular multiple-quantum coherences, Inhomogeneous fields.

1. INTRODUCTION

High-resolution nuclear magnetic resonance (NMR) spectroscopy is arguably a powerful and non-invasive tool for the analysis of molecular structures, conformations, compositions, and dynamics.[1–5] From biomolecules to living organisms, from nanoparticles to materials, it has provided a wealth of invaluable information. A modern high-resolution NMR spectrum generally contains the information of chemical shifts, *J* coupling constants, multiplet patterns, and peak intensities, which constitute a 'detector' for every molecule and then permit the identification and quantification for the complex chemical and biological samples.[6,7] Concretely, the values of chemical shifts are related to inequivalent atomic nuclei (e.g. protons) in a molecule, while *J* coupling constants, multiplet patterns, and peak intensities provide the structural information for the molecule.[8,9] In general, it is easy to obtain accurate information of chemical shift, multiplet pattern, and peak intensity of every atomic nuclei in a small molecule in liquid state by using conventional single-quantum coherence (SQC) high-resolution NMR spectroscopy. Even for the solution with large molecules such as biological samples, the basic spectral information is still accessible. Moreover, the development of multidimensional NMR spectroscopy provides a significant way to achieve sufficient dispersion of chemical shifts and avoid severe peak overlap in the spectra of large molecules.[10]

The measurement of *J* coupling constants for scalar-coupled spin systems is usually feasible through the conventional SQC high-resolution spectra. However, it is difficult to extract the accurate small *J* coupling information for weakly scalar-coupled spin systems even under extremely homogeneous magnetic fields. Compared to the strongly scalar-coupled spin systems, the small *J* coupling splitting originated from two atomic nuclei connected by long-range bonds are usually hidden within the natural linewidth (LW). Figure 1 shows the 1D conventional SQC spectra of 3-fluoro-*N*-(3-fluorophenyl)benzamide and 3-fluoro-*N*-(4-fluorophenyl)benzamide.[11] The experiments were performed at a shimmed magnetic field with a strength of 11.3 T. Both of these chemical samples contain the phenyl ring in their molecular structure. The unambiguous analysis of these spectra is

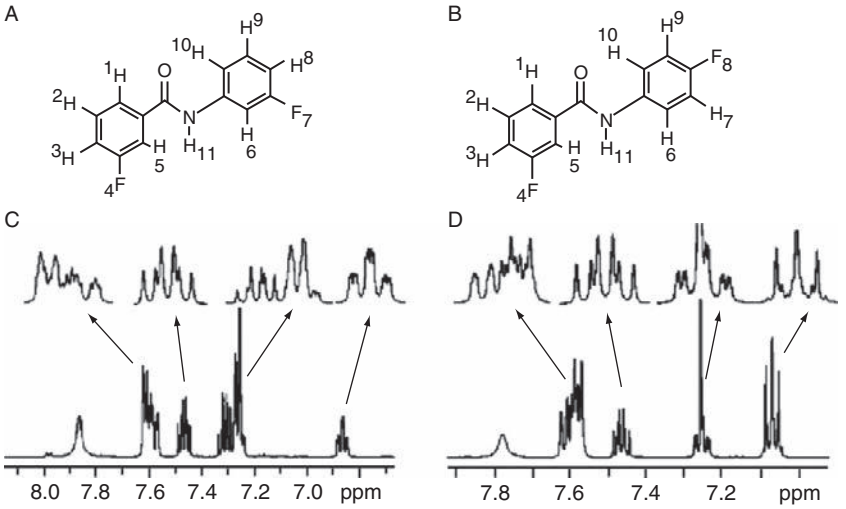

Figure 1 (A and B) Structures of 3-fluoro-*N*-(3-fluorophenyl)benzamide and 3-fluoro-*N*-(4-fluorophenyl)benzamide, together with the numbering of interacting spins. (C and D) ^{1}H NMR spectra (500 MHz) of compounds in (A) and (B), respectively, in the solvent $CDCl_3$. The expansions of the crowded regions are depicted by arrows. (Source: Adapted from Ref. 11.)

extremely difficult due to the severe overlap of proton resonances. From the expansions of the crowded regions, it can be seen that the *J* couplings from long-range bonds are too small in magnitude in comparison with the natural LW to be detectable, such as $^{5}J_{69}$ separated by five bonds.

The importance of accurate measurement of small *J* coupling constants has long been recognized. The homonuclear *J* coupling constants are widely applied to assign conformational preferences of medium- to large-sized molecules and provide valuable structural information about the backbone dihedral angles in biological molecules. For example, the homonuclear $^{3}J(H^{N}H^{\alpha})$ coupling constants are correlated with the torsion angles in the polypeptide backbone by a parameterized Karplus equation.[12–14] However, accurate determination of these *J* couplings in proteins is limited by the small magnitudes of couplings relative to the natural proton LW. It is important for spectroscopists to obtain the accurate values of *J* coupling constants and chemical shifts, which are often required for spectral fitting in *in vivo* spectral analysis.[15,16] However, besides the *J* coupling constants with large magnitudes, the measurement of small *J* couplings is influenced by the intrinsic natural LW of spectral peaks and may become inaccurate or even impossible under *in vivo* conditions. Moreover, *J* coupling constants and chemical shifts may vary from *in vitro* to *in vivo* due to the changes of molecular environment, cation binding, temperature, ionic strength, and pH,[17] which deteriorates the accurate measurement of small *J* couplings.

The development of shimming techniques[18–20] is advantageous to the detection of *J* couplings since it can partially enhance the spectral resolution. However, the spectral resolution is still not enough for accurate measurement of small

J couplings since the natural LW caused by transverse relaxation cannot be narrowed by any methods. Besides the improvements in hardware, a number of spectral editing techniques have been developed for accurate measurement of small *J* couplings. In this report, we give an overview of the mechanisms and practical implementations of the methodologies for accurate detection of small *J* coupling constants, and put in perspective for their applicabilities and efficiencies. These spectroscopic techniques can generally be classified into two classes. One class is to extract the small *J* coupling constants without *J* multiplication, such as selective *J*-resolved spectroscopy,[21–23] spin selective *n*-quantum *J*-resolved (SSnQ-*J*-resolved) spectroscopy,[11,24,25] which play a great role in accurate measurement of small *J* couplings. Another class is on the basis of *J* multiplication, such as *J*-multiplied HSQC[26] and HMQC[27,28] spectroscopy, *J*-scaled COSY,[29–31] *J*-scaled intermolecular multiple-quantum coherence (iMQC) spectroscopy.[32,33] The *J*-scaled iMQC spectroscopy (JSIS) is intrinsically insensitive to the magnetic field inhomogeneities since distant dipolar field (DDF) is utilized. The details and underlying mechanisms of these methods are discussed in the following sections.

2. *J*-RESOLVED SPECTROSCOPY FOR ACCURATE MEASUREMENT

2.1. *J*-resolved spectroscopy

The conventional 2D *J*-resolved spectroscopy is the first choice for quantitative detection of *J* coupling constants. 2D *J*-resolved spectroscopy[8] is one of the first 2D NMR techniques. In the family of 2D NMR techniques, *J*-resolved spectroscopy plays an important role in spectral analysis since it separates the joint effects of chemical shifts and *J* couplings (either homo- or heteronuclear) by storing them into two different spectral dimensions. The homonuclear pulse sequence, $(\pi/2) - t_1/2 - (\pi) - t_1/2 - t_2$, produces a spectrum $S(\omega_1,\omega_2)$ with the hyperfine structure relative to each chemical shifted signal tilted by 45° in the (ω_1,ω_2) plane. The transformation from $S(\omega_1,\omega_2)$ to $S(J,\delta)$ can be realized by additional post-processing. A completely decoupled spectrum is then obtained along the direct dimension (F2 axis). The *J* coupling information is distributed along the indirect dimension (F1 axis), which provides an easy way for direct detection of *J* coupling constants. 2D *J*-resolved spectroscopy is an important tool for the analysis of complex chemical and biological materials.[34–38] A number of modified versions have been developed to enhance the ability of 2D *J*-resolved spectroscopy.[39–43] However, it is noticed that the conventional 2D *J*-resolved spectroscopy and its related modified versions[39–43] are usually not suitable to the situation when the magnetic fields are inhomogeneous. Unfortunately, there are many circumstances where the magnetic fields cannot be perfect for sample tests. The inhomogeneous line broadening would hamper the spectral resolution of 2D *J*-resolved spectra. Although spin echo in the *J*-resolved pulse sequence can remove the inhomogeneous line broadening in the F1 dimension, the influence of inhomogeneous fields remains in the F2 dimension, which results in the loss of exact chemical shift and *J* coupling information and even overlapping of

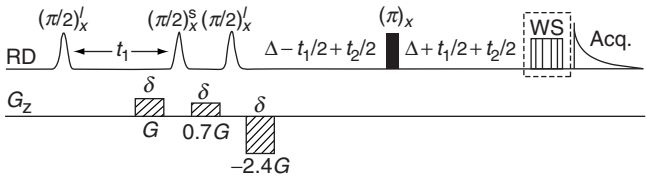

Figure 2 ISQC-*J*RES sequence for high-resolution 2D *J*-resolved spectra in inhomogeneous fields via 3D acquisition. Full vertical bars stand for non-selective RF pulse. Gaussian-shaped pulses are selective RF pulses. Dashed rectangles represent coherence-selection gradients, 'WS' is the spare module for solvent suppression. (Source: Adapted from Ref. 44.)

spectral peaks. Recently, a pulse sequence, iSQC-*J*RES,[44] has been proposed by our group to obtain high-resolution 2D *J*-resolved spectra in inhomogeneous fields via 3D acquisition.[45] This method is based on intermolecular single-quantum coherences (iSQCs). Two indirect-detection periods are the iSQC evolution period and spin echo evolution period, respectively. Since the iSQC evolution period and spin echo evolution period in iSQC-*J*RES sequence are intrinsically insensitive to magnetic field inhomogeneities, high-resolution 2D *J*-resolved spectra can be recovered from nuclei in inhomogeneous fields by projecting the 3D data onto the 2D plane. This method may be used to study complex chemical materials and biological metabolites in inhomogeneous fields.

The iSQC-*J*RES sequence is shown in Figure 2. The first and third RF pulses are solvent-selective, while the second RF pulse is solute-selective. To select the coherence-transfer pathway $0 \rightarrow +1 \rightarrow +2 \rightarrow +1 \rightarrow -1$, three linear coherence-selection gradients (CSGs) with an area ratio of $1:0.7:-2.4$ are applied. The experimental results of butyl methacrylate in methanol are presented in Figure 3. The conventional 2D *J*-resolved spectrum of the sample in a homogeneous magnetic field is shown in Figure 3A. The 2D *J*-resolved spectrum obtained in the inhomogeneous field using the conventional method is shown in Figure 3B. The iSQC-*J*RES projection spectrum obtained in the same inhomogeneous field is shown in Figure 3C. It can be seen that a high-resolution 2D *J*-resolved spectrum can be recovered from the inhomogeneous field by using the iSQC-*J*RES sequence.

Although conventional 2D *J*-resolved spectroscopy and its related modified versions can provide hyperfine pattern for normal spin systems, even under inhomogeneous fields (iSQC-*J*RES sequence), they do not allow accurate determination of small coupling constants. In the *J*-resolved spectra acquired from these approaches, all the couplings are active and evolve simultaneously in the indirect dimension. The spectral window in the *J*-dimension is limited by the widest multiplet pattern, which lowers the resolution necessary for accurate measurement of small *J* coupling constants.

2.2. Selective *J*-resolved spectroscopy

Selective *J*-resolved spectroscopy is an approach that can overcome the resolution problem in *J* coupling dimension for accurate measurement of small *J* couplings. Firstly, the spin pair with mutual small *J* coupling should be identified. This single

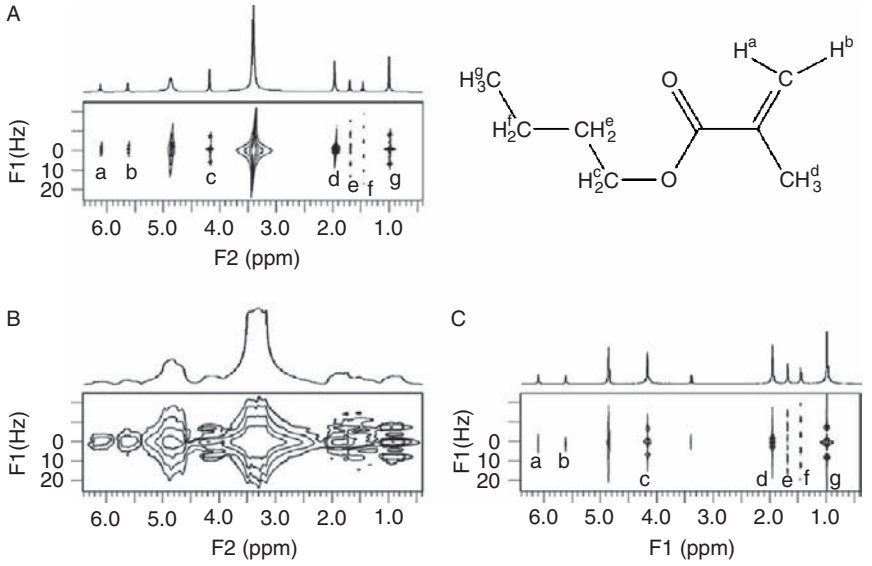

Figure 3 2D *J*-resolved spectra of a solution of butyl methacrylate in methanol. (A) Conventional spectrum with a clockwise rotation of 45° in a well-shimmed field and its projection along the F2 axis, (B) conventional spectrum of spins in an inhomogeneous field with the linewidth of solvent peak of 200 Hz (absolute-valued mode), (C) iSQC-*J*RES projection spectrum under the same inhomogeneous field and its projection along the F1 axis. The structure of butyl methacrylate is shown on the top left of the frame, together with proton labels. (Source: Adapted from Ref. 44.)

spin pair is then selectively excited by specific selective pulses, which means that only the mutual *J* coupling between this spin pair is active and evolves in the indirect evolution period. The spectral window in the *J*-dimension is only related to the multiplet pattern of the selective spin pair, which permits adequate resolution necessary for measuring small *J* coupling constants. In addition, the spectrum is simplified by the exclusion of unwanted spins, which is useful for complex chemical or biological samples. The SERF method was proposed based on this concept.[21] However, the SERF method greatly relies on the selective pulses for both the excitation of the target resonance and the selective refocusing of the partner, which makes its practical implementation sensitive to the phase behaviour of selective pulses. Combining the excitation sculpting[46] and double-quantum filtration, Bourg and Nuzillard proposed a biselective *J*-resolved pulse sequence to produce the same information as SERF more robustly.[22] Similarly, Rastrelli and co-workers proposed a biselective *J*-resolved pulse sequence based on the DPFGSE approach to allow for the accurate measurement of small *J* couplings.[23] This method does not produce so-called 'strong coupling artifacts' typically observed when soft pulses are employed, and is quite tolerant to pulse miscalibration as well. Therefore, it is more applicable for organic chemistry, ranging from complex natural substances to molecules of biological interest. In the following, we will focus on the biselective *J*-resolved experiment based on DPFGSE approach.

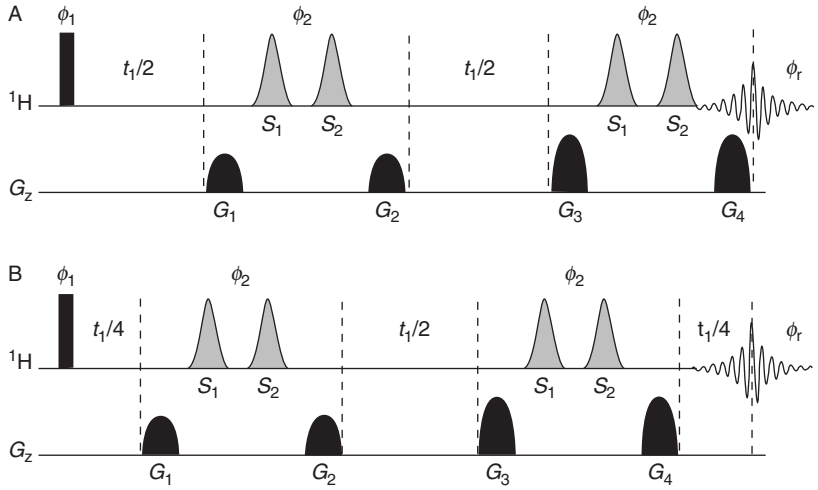

Figure 4 Pulse sequences for bioselective *J*-resolved experiments. (A) Single spin-echo; (B) double spin-echo. Block rectangles represent $\pi/2$ hard pulses; soft π pulses S_1 and S_2 (in grey) are generically represented as Gaussian envelopes. Gradient pairs are set to $G_1 = G_2$ and $G_3 = G_4$. (Source: Adapted from Ref. 23.)

The pulse sequences for the biselective *J*-resolved experiment are shown in Figure 4. Figure 4A and B is for single spin-echo and double spin-echo, respectively.[23] Both strategies lead to a biselective *J*-resolved spectrum where the signals of a spin pair evolve under their mutual *J* coupling in the indirect dimension. The double spin-echo *J*-resolved experiment performs well in the reduction of unwanted 'strong coupling artifacts'. An example result from strychnine dissolved in $CDCl_3$ shows the ability of the biselective *J*-resolved spectroscopy in extracting the small *J* coupling constant (Figure 5).[23] In order to achieve the maximum possible resolution in the indirect dimension for this small ^{1}H–^{1}H long-range coupling (0.7 Hz), a spectral window of 20 Hz was set and 64 t_1 increments were collected.

2.3. SSnQ-*J*-resolved spectroscopy

2D NMR techniques, such as COSY, TOCSY, *J*-resolved spectroscopy, have been applied for the analysis of ^{1}H NMR spectra of complex molecules. The identification of the spin resonances of different protons, the information of their structural network, and the accurate magnitudes of *J* couplings can be extracted from these 2D spectroscopy. It is known that these conventional techniques are usually not suitable for the measurement of accurate magnitudes of small *J* couplings.[23] To overcome this problem, spin state selective detection was proposed,[47–57] where the high field and low field components of both resolved and unresolved multiplets were separated and individually detected. Incorporation of spin state selective detection and *n*-quantum filtering gives the SSnQ-*J*-resolved spectroscopy.[24] It can aid in discerning degenerate transitions and simplifying complex ^{1}H NMR spectra, thus providing accurate magnitudes of small *J* couplings. The single-quantum NMR spectra of weakly-coupled spin system are invariant to the change of relative

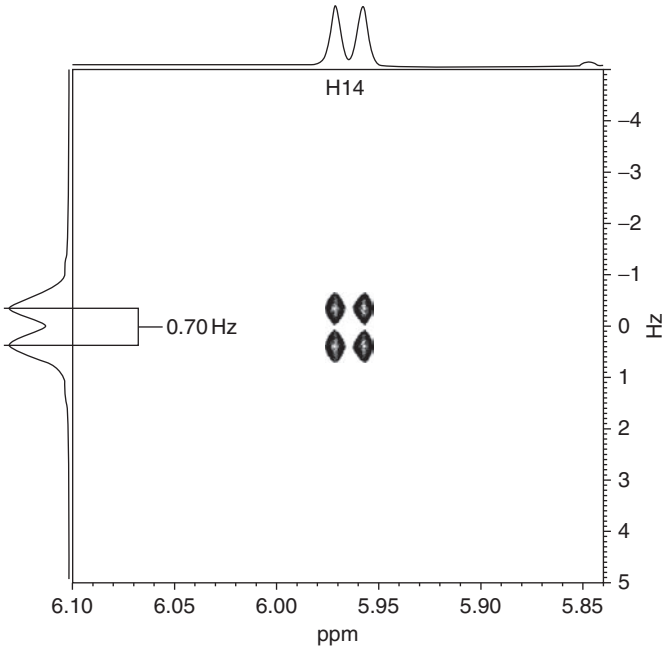

Figure 5 Expanded region of the selective *J*-resolved spectrum obtained by selective refocusing of protons H_{14} and H_{11} in the sample of strychnine dissolved in $CDCl_3$. (Source: Adapted from Ref. 23.)

signs of couplings.[58,59] However, both the magnitudes and signs of couplings play dominant roles in assessing the stereochemistry and the conformation of biomolecules. Besides the exact values of small *J* coupling constants, their relative signs can also be obtained from the SSnQ-*J*-resolved spectroscopy. Both double- and triple-quantum *J*-resolved techniques have several distinct advantages. For example, they can (a) separate very small proton couplings into different dimensions, (b) reduce spectral complexity by spin state selection, (c) provide relative signs of homonuclear couplings, and (d) overcome the influence of field inhomogeneity via the π pulse in the middle of the t_1 dimension.[11,24]

The pulse sequence for the SSnQ-*J*-resolved spectroscopy is shown in Figure 6.[24] The selective seduce shaped 90° and 180° RF pulses selectively excite the interested spins. The gradient pulse G_1 and G_2 are set to $G_2 = nG_1$ for homonuclear *n*-quantum of protons. The delay τ is optimized for the excitation of proton homonuclear *n*-quantum. The phases of RF pulse (Φ_1) and receiver (Φ_R) are both set to zero. The capability of this sequence has been tested by the chemical samples with fluorine-substituted phenyl ring, such as 2-fluoro-*N*-(2-fluorophenyl)benzamide, 2-fluoro-*N*-(3-fluorophenyl)benzamide, and 2-fluoro-*N*-(4-fluorophenyl)benzamide.[24] The conventional 1D ^{1}H NMR spectra of these samples are so complex that most small *J* coupling information is submerged in the spectral structure and natural LW. The SSnQ-*J*-resolved spectroscopy can simplify the spectral information and recover the small *J* coupling information by selectively

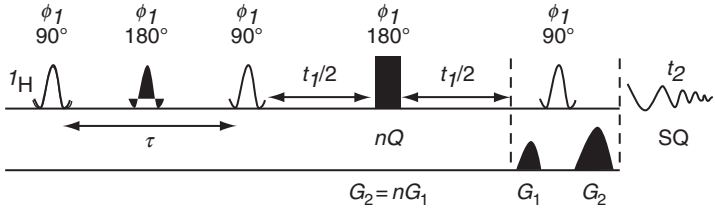

Figure 6 Pulse sequence for SSnQ-*J*-resolved experiments. (Source: Adapted from Ref. 24.)

exciting given spins. In general, the digital resolution in the *J* coupling dimension of SSnQ-*J*-resolved spectra can reach 0.04 Hz, which is good to the measurement of very small *J* coupling constants.

3. *J*-SCALED SPECTROSCOPY FOR ACCURATE MEASUREMENT

3.1. *J*-multiplied HSQC and HMQC spectroscopy

J-multiplication is another way to extract the small *J* coupling information. The apparent *J* coupling constants are magnified to overcome the influence of natural LW. The accurate *J* coupling constants can then be obtained by dividing the apparent *J* coupling constants by the magnified factor. The *J*-multiplied HSQC (MJ-HSQC[26]) and HMQC (JM-HMQC[27] and MJ-HMQC[28]) methods were proposed for the determination of homonuclear $^3J(H^NH^\alpha)$ coupling constants in ^{15}N-labelled small proteins. They multiply the *J* coupling in the indirectly detected dimension. For the MJ-HSQC method,[26] the time increment for the homonuclear *J* coupling evolution period is chosen to be a suitable multiple ($2N \times t_1$) of the corresponding increment for ^{15}N chemical shift evolution. This results in the splitting of the HSQC correlation in the F1 dimension by $2N \times {}^3J(H^NH^\alpha)$ and then allows direct observation of the $^3J(H^NH^\alpha)$ coupling constants. Compared to 3D experiments, the MJ-HSQC method is simpler and needs shorter measurement time but has good water suppression. However, the line broadening in the F1 dimension cannot be avoided since the *J* coupling evolution is incremented simultaneously with the chemical shift evolution. So an improved method, *J*-multiplied HMQC,[27,28] was proposed. This method benefits from the slower relaxation rate of heteronuclear multiple-quantum coherence. In addition, it combines the incrementation periods for *J*-multiplication and ^{15}N chemical shift evolution, thus reducing the length of overall pulse sequence. The favourable relaxation properties of multiple-quantum coherence result in narrower LW in the F1 dimension and enhanced sensitivity, which suggests that the *J*-multiplied HMQC is more suitable for slightly larger proteins than *J*-multiplied HSQC.

The MJ-HSQC and JM-HMQC sequences are presented in Figure 7. In the following, we take the JM-HMQC sequence[27] (Figure 7B) for analysis. The pulse sequence starts with the creation of heteronuclear multiple-quantum coherence in the usual HMQC way. The product operator analysis[60] was performed for the $H^NH^\alpha N$ spin system and the desired terms was obtained as

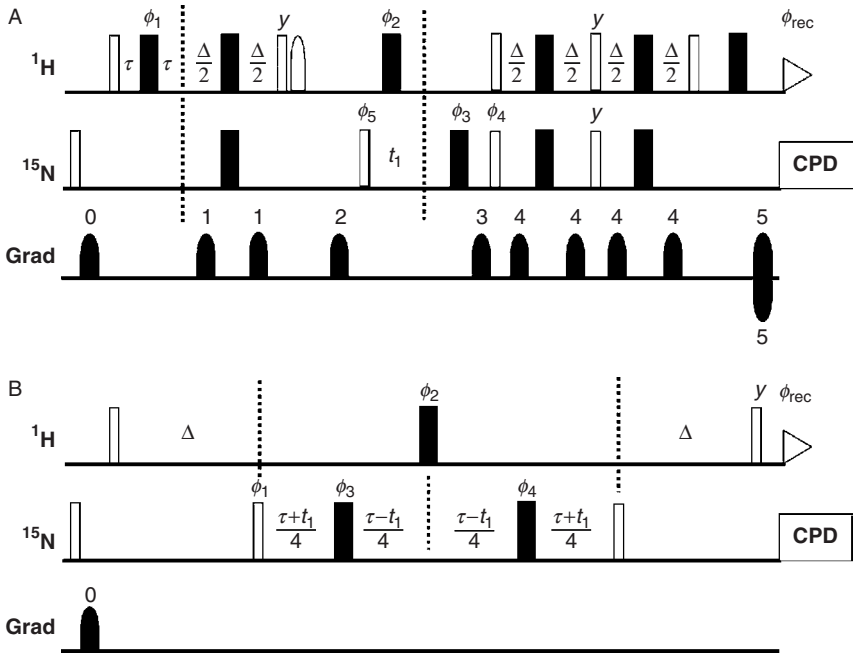

Figure 7 (A) *J*-multiplied sensitivity-enhanced HSQC (MJ-HSQC) pulse sequence. Narrow white bars and wide black bars indicate 90° and 180° hard rectangular pulses, respectively. Gradient pulses are represented by grey half-ellipses and selective 90° pulse on water resonance by a white half-ellipse. (B) *J*-multiplied HMQC sequence. Water suppression was achieved using WET solvent suppression scheme. (Source: Adapted from Refs. 26 and 27.)

$$\left\{\mathrm{H}_y^{\mathrm{N}}\mathrm{H}_I^{\alpha}\mathrm{H}_I \cos\left[N^3J\left(\mathrm{H}^{\mathrm{N}}\mathrm{H}^{\alpha}\right)\pi t_1\right] + \mathrm{H}_z^{\mathrm{N}}\mathrm{H}_x^{\alpha}\mathrm{H}_I \sin\left[N^3J\left(\mathrm{H}^{\mathrm{N}}\mathrm{H}^{\alpha}\right)\pi t_1\right] \cos(\Omega_{\mathrm{N}}t_1)\right\}. \quad (1)$$

The desired terms are cosine modulated by $N^3J(\mathrm{H}^{\mathrm{N}}\mathrm{H}^{\alpha})\pi t_1$ in the F1 dimension, where N denotes the multiplication factor of *J*-modulation, which can be any positive number. Therefore, the measurement of small J coupling constants can benefit from this *J*-modulation. This method was tested with human ubiquitin (16 residues, 8.6 kDa) (VLI Research).[27] From the result (Figure 8), we can see that the small J couplings which are usually covered by the natural LWs can be well resolved. The *J*-multiplied HSQC (MJ-HSQC[26]) and HMQC approaches are more suitable for the measurement of small J couplings in small proteins.

3.2. *J*-scaled COSY

Two-dimensional homonuclear correlated spectroscopy (COSY), which was firstly proposed by Jeener,[61] was widely applied in the fields of chemistry and biology. Its pulse sequence is $\pi/2{-}t_1{-}\pi/2{-}t_2$, where t_1 and t_2 are evolution and

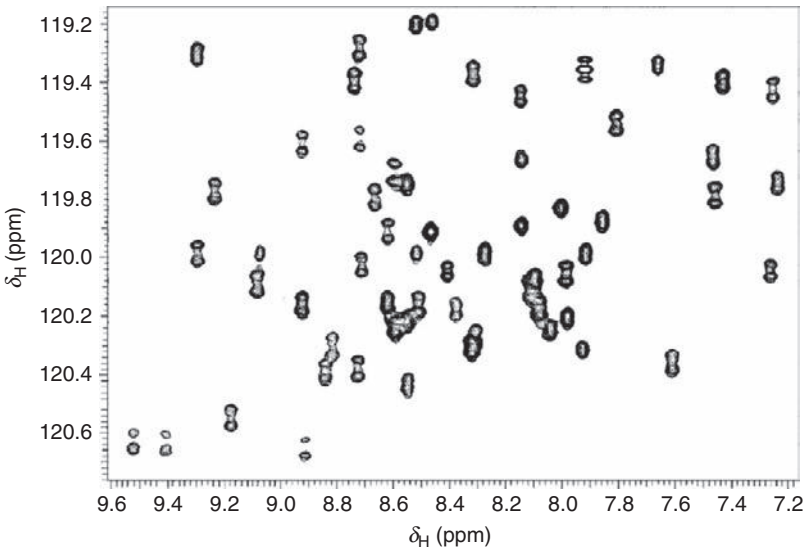

Figure 8 Representative expansion of three times *J*-multiplied $^{3}J(H^{N}H^{\alpha})$ ^{15}N–^{1}H correlation spectrum obtained using JM-HMQC pulse sequence with 32 scans per FID. (Source: Adapted from Ref. 27.)

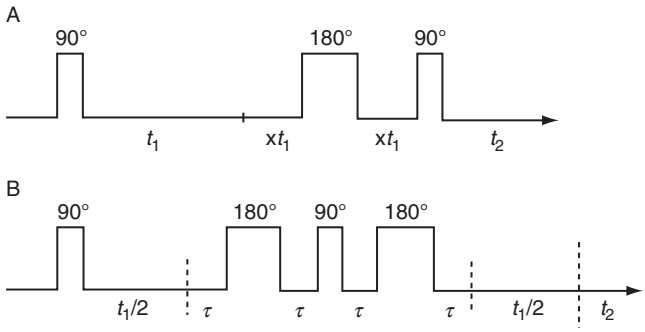

Figure 9 (A) *J*-scaled COSY pulse sequence, (B) *J*-scaled SECSY pulse sequence. (Source: Adapted from Refs. 30 and 31.)

detection periods, respectively. When the resolution of the COSY spectrum is poor, the *J* coupling constants cannot be well recognized. Two *J*-scaled pulse sequences based on COSY[29] and spin echo resolved spectroscopy (SECSY)[30] were developed to scale up *J* coupling constants. The pulse sequences are shown in Figure 9. *J*-scaling is achieved in the F1 dimension. This is useful for the observation of small *J* coupling constants.

For scheme A, the scaling factor (SF) for *J* coupling constants is $1+2x$, and for LWs is $1+2xT_2^*/T_2$, where T_2 is the intrinsic transverse relaxation time, and T_2^* is the transverse relaxation time including the effect of field inhomogeneity.[31] Since T_2^* is always smaller than T_2, the SF for LWs is smaller than that for *J* coupling

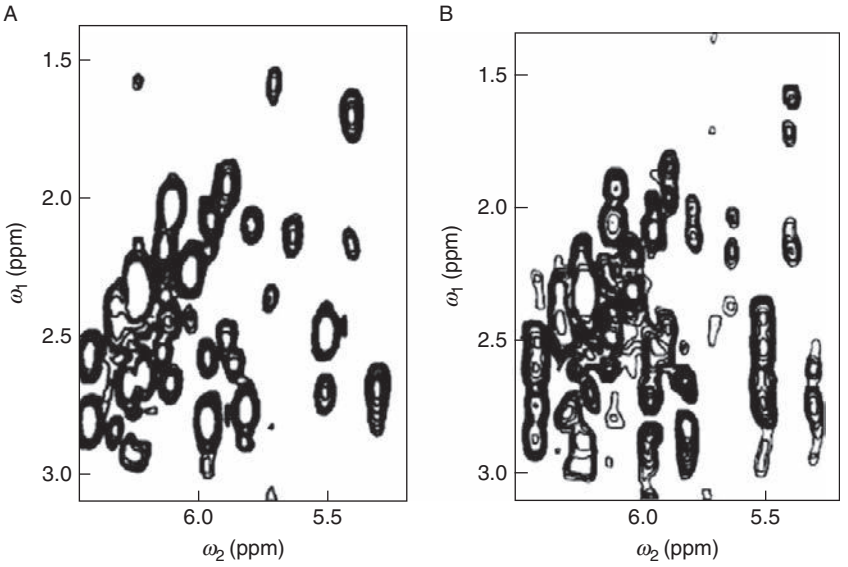

Figure 10 Parts of two-dimensional NMR spectra for identical portions acquired from a mixture of oligonucleotides using normal COSY (A) and *J*-scaled COSY (B). *J* values were scaled by a factor of two in (B). (Source: Adapted from Ref. 31.)

constants. Therefore, the resolution will be enhanced. For scheme B, $\tau = xt_1/2$. The SF for J coupling constants and LWs are $1+2x$ and $1+2xT_2^*/T_2$, respectively.[30] This is similar to the case of scheme A. Thus, the sensitivity is also enhanced. The SF for J coupling constants should be selected optimally so that the separations between peaks get enhanced and the overlap of peaks along the F1 dimension is avoided as far as possible. It is noted that for both schemes, spin systems evolve only under the influence of J coupling Hamiltonian in the evolution time other than t_1, and are not affected by the Zeeman Hamiltonian.

Figure 10 shows a comparison of the spectra obtained from the pulse sequences of normal COSY and *J*-scaled COSY, respectively. It can be seen that the spectrum in Figure 10B has higher resolution than that in Figure 10A. The spectrum of cytosine shown in Figure 11 was obtained using the *J*-scaled SECSY with a SF of 9. The effect caused by *J*-scaling can be clearly seen from the expansion of a peak (Figure 11).

4. *J*-SCALED IMQC SPECTROSCOPY IN INHOMOGENEOUS FIELDS

All the techniques mentioned above provide various ways for different spin systems to extract small J coupling information in homogeneous magnetic fields. In the circumstances where the magnetic field homogeneity is degraded or the testing objects are subject to intrinsic variation in magnetic susceptibility over the sample volume and among various structural components, line broadening due to

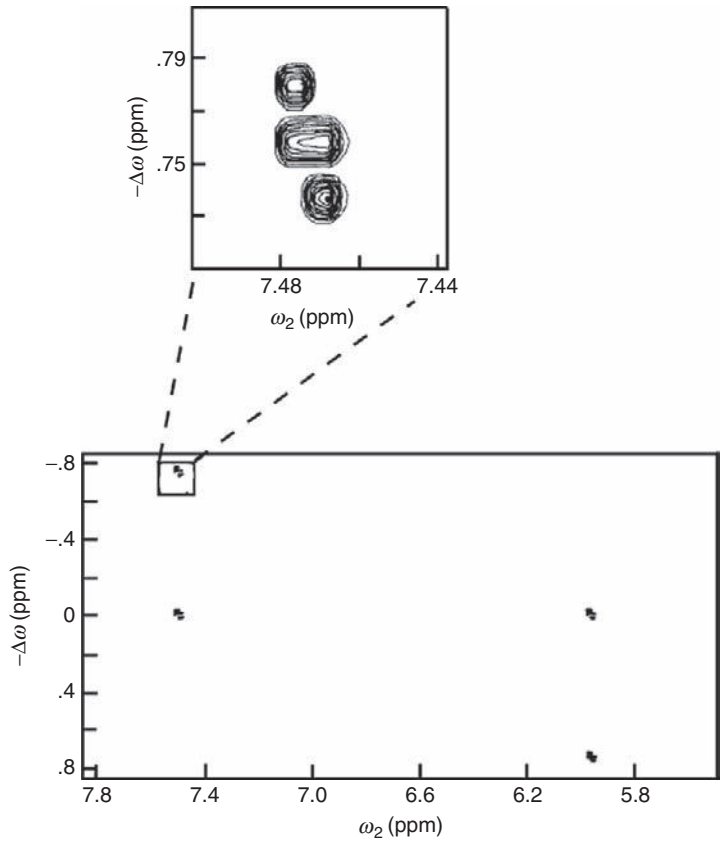

Figure 11 *J*-scaled SECSY spectrum of cytosine (an AX spin system) with a *J* scaling factor of 3. (Source: Adapted from Ref. 30.)

inhomogeneous field would lead to severe signal overlap and loss of fine spectral features, which precludes the NMR spectral analysis and hampers the accurate determination of small *J* coupling constants. To overcome this problem, some methods combined iMQCs with *J*-multiplication were proposed. It can be applied to obtain accurate small *J* coupling constants in inhomogeneous fields since iMQCs are intrinsically insensitive to magnetic field inhomogeneities and the measurement of small *J* coupling constants benefits from the *J*-multiplication.

4.1. Origin of *J*-scaled iMQC spectroscopy

iMQCs caused by long-range dipolar interactions among spins in different molecules have generated tremendous interests.[62–77] When two RF pulses separated by a time interval was applied to a highly polarized spin system, multiple iMQC signals were observed in the presence of magnetic field gradients.[62–64] Nowadays, the pulse sequences for creating iMQCs are mostly based on COSY Revamped with Asymmetric Z-gradient Echo Detection (CRAZED).[63] They usually contain

pulse field gradients or background magnetic field gradients that modulate the transverse magnetization into a helical structure. Two superficially quite different frameworks, classical DDF treatment[62,68] and quantum-mechanical density matrix treatment,[64] can be applied to analyze the iMQC phenomena. Although the classical and quantum-mechanical treatments are based on totally different physical mechanisms, they both lead to same predictions for the signals derived from the pulse sequences. Taking the intrinsic properties, iMQCs have been applied in many important fields, ranging from NMR spectral editing to magnetic resonance imaging (MRI).[78–97] High-resolution NMR spectroscopy in inhomogeneous fields based on iMQCs is one of the most important applications. Since intermolecular dipolar interactions are effective within the range of 10–100 μm, far smaller than a typical sample dimension, it is intuitively attractive to apply iMQCs to NMR spectroscopy in inhomogeneous fields. The main advantage of iMQC methods lies on its ability to detect identical interactions for different spin groups in a molecule, therefore simultaneously retaining all desired spectral features. Many pulse sequences have been proposed. Warren and co-workers proposed some sequences based on intermolecular zero-quantum coherences (iZQCs): HOMOGENIZED (HOMOGeneity Enhancement by Intermolecular ZEro-quantum Detection),[78] composite CPMG-HOMOGENIZED,[80] and ultrafast iZQC 2D spectroscopy technique.[81] Our group proposed iDQF-HOMOGENIZED[96] based on iZQCs, and IDEAL[90] (Intermolecular Dipolar-interaction Enhanced All Lines, also referred to as IDEAL-I) and IDEAL-II[91] based on intermolecular double-quantum coherences (iDQCs), and iSQC-JRES. All these approaches[78,80,81,96] can retain useful spectral information, and the apparent *J* coupling constants remain the same value as conventional *J* coupling constants except for the IDEAL-I and IDEAL-II, from which the apparent *J* coupling constants are magnified by a factor of 3 relative to the conventional *J* values. However, they are still unable to identify fine structures when the spectrum is crowded and/or when the *J* coupling constants are smaller than spectral resolution.

Inspired by these iMQC schemes, two *J*-scaled iMQC sequences, *J*-scaled iMQC-1[32] and JSIS,[33] were proposed to permit the achievement of apparent homonuclear *J* coupling constants with a SF variable in a large range while retaining all the high-resolution spectral information of chemical shifts, multiplet patterns, and relative peak areas from liquid samples under inhomogeneous fields. They allow accurate measurement of small *J* coupling constants no matter the magnetic field homogeneity is perfect or not. Both sequences were designed based on the iMQC 2D acquisition with three evolution periods. The apparent *J* coupling constants with a SF can be obtained from the 1D projection spectrum. For the *J*-scaled iMQC-1 sequence shown in Figure 12A, three gradient pulses with an area ratio of 2:1:4 are used to select the coherence transfer path $0\rightarrow+1\rightarrow+2\rightarrow-1$ during the evolution periods. The variable m is limited in the range of $0 < m \leq 1/2$ and controls the SF value from 3 to infinity. Three selective RF pulses are used to excite solute spins, solvent spin, and solvent spin, respectively. In practice, the requirement for accurate selective excitation, especially for solute spins, is usually hard to achieve. Therefore, the results may suffer from reduced signal intensity and artifacts, which imposes an obstacle for the potential practical application of

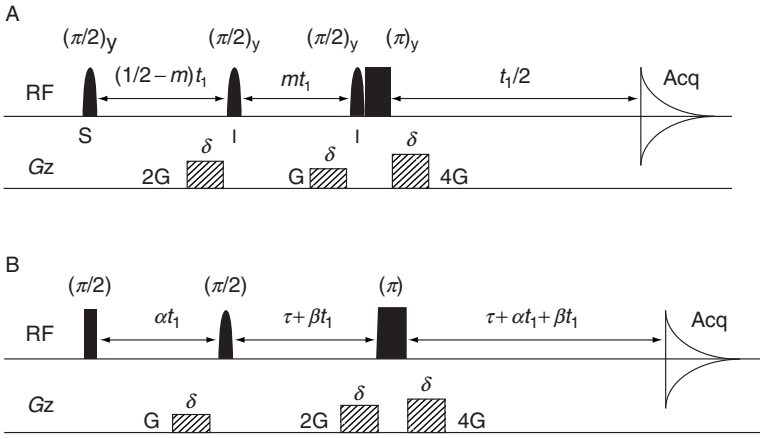

Figure 12 *J*-scaled iMQC pulse sequences. (A) *J*-scaled iMQC-1 sequence; (B) JSIS sequence. Full vertical bars stand for non-selective RF pulses, Gauss-shaped pulses are solvent- or solute-selective, and dash rectangles represent coherence selective gradients. (Source: Adapted from Refs. 32 and 33.)

the sequence. The JSIS sequence shown in Figure 12B overcomes this problem and makes the iMQC *J*-scaling technique more applicable for practical samples. Moreover, the SF can vary from zero to infinity, more flexible than the *J*-scaled iMQC-1 sequence. For the JSIS sequence, there are still three indirect evolution periods, and each involves a pulsed field gradient. The gradient pulses with an area ratio of 2:1:4 select the coherence transfer path of $0\rightarrow+2\rightarrow+1\rightarrow-1$. Only a solvent-selective pulse is used in this sequence. The variables α and β are limited in the ranges of $\alpha > 0$ and $\beta \geq -1.5\alpha$. The constant τ is set to zero and $(\alpha+\beta)$ is confined to 1/2 when β is not smaller than zero. When β is smaller than zero, the minimum value for τ is $-\beta t_1{}^{\max}$. Similar to other iMQC high-resolution approaches, the fundamental requirement of the *J*-scaled iMQC approaches is that one component of the sample (e.g. solvent) should contain a concentrated proton density in order to create a DDF for iMQC signals. This requirement may limit the effects of *J*-scaled iMQC approaches in some samples. However, solution state chemical or biological samples usually contain concentrated solvent, which provides a natural DDF source for the application of the sequences. In the following, the theoretical analysis of the *J*-scaled iMQC sequences is presented.

4.2. Theoretical analysis of *J*-scaled iMQC pulse sequences

The quantum-mechanical density matrix treatment is applied to analyze the *J* coupling magnification mechanism of the *J*-scaled iMQC pulse sequences. A homogeneous liquid mixture consisting of an AX spin-1/2 system of *S* component (including S_k and S_l spins with a scalar coupling constant J_{kl}) and a single spin-1/2 system of *I* component is considered. It is assumed that *I* spin (corresponding to solvent) is abundant and *S* spin (corresponding to solute) is either abundant or dilute. Assume that ω_m is the frequency offset of spin m ($m = I$, S_k, S_l) in the rotating frame in the absence of field inhomogeneity, and $\Delta B(\boldsymbol{r})$ is the

field inhomogeneity at position $\boldsymbol{r}$. The frequency offset, Ω_m, of the spin m in the inhomogeneous field, Ω_m, is given by

$$\Omega_m(\mathbf{r}) = \omega_m + \gamma \cdot \Delta B(\mathbf{r}), \quad m = I, S_k, S_l, \tag{2}$$

where γ is the gyromagnetic ratio of the nuclei. Equation (2) suggests that the magnetic field inhomogeneity causes a shift of angular frequency from the resonance frequency ω_m. For simplicity, the effects of radiation damping, diffusion, and relaxation are ignored, and the CSGs are applied along z direction. The expression for the signal from S spin after the JSIS sequence is deduced to be:[33]

$$\begin{aligned}\sigma_{\text{eff}} = -\frac{1}{8} i \sum_{i=1}^{N_S} \sum_{j=1}^{N_I} S_{ki}^{-} \sin\left[1.5 D_{ij}(\alpha t_1 + 2\beta t_1 + 2\tau + t_2)\right] \cos[\pi J_{kl}(2\alpha t_1 + 2\beta t_1 + 2\tau + t_2)] \\ \times e^{-i\left[-\varphi(r_i)+\varphi(r_j)\right]} e^{-i\left[\Omega_{I_j}(r_j)\right]\alpha t_1} e^{i[\Omega_{S_{ki}}(r_i)]t_2}\end{aligned} \tag{3}$$

where N_S and N_I are the molecular numbers of the S and I components, respectively. $\varphi(r_i) = \gamma G \delta s_i$ and $\varphi(r_j) = \gamma G \delta s_j$ are the phases accumulated at positions $\boldsymbol{r}_i$ and $\boldsymbol{r}_j$ due to the first CSG, where $\boldsymbol{s}_i$ and $\boldsymbol{s}_j$ are the locations of the ith S_k spin and the jth I spin along the gradient direction $\boldsymbol{s}$, respectively.

$$D_{ij} = \frac{\mu_0}{4\pi} \frac{\gamma^2 \hbar}{4 r_{S_{ki}I_j}^3} \left(1 - 3\cos^2 \theta_{S_{ki}I_j}\right)$$

is the residual intermolecular dipolar coupling constant, in which μ_0 is the vacuum permeability, $r_{S_{ki}Ij}$ is the distance between the S_{ki} spin and the I_j spin, and $\theta_{S_{ki}Ij}$ is the angle between the S_{ki} and I_j internuclear vector and the static magnetic field. Since D_{ij} is very small in usual cases, we have $\sin[1.5D_{ij}(\alpha t_1 + 2\beta t_1 + 2\tau + t_2)] \approx 1.5D_{ij}(\alpha t_1 + 2\beta t_1 + 2\tau + t_2)$ when $1.5D_{ij}(\alpha t_1 + \beta t_1 + 2\tau + t_2) \ll 1$. Therefore, Equation (3) can be simplified to

$$\begin{aligned}\sigma_{\text{eff}} = -\frac{3}{16} i(\alpha t_1 + 2\beta t_1 + 2\tau + t_2) \sum_{i=1}^{N_S} \sum_{j=1}^{N_I} S_{ki}^{-} D_{ij} \cos[\pi J_{kl}(2\alpha t_1 + 2\beta t_1 + 2\tau + t_2)] \\ \times e^{-i\left[-\varphi(r_i)+\varphi(r_j)\right]} e^{-i\left[\Omega_{I_j}(r_j)\right]\alpha t_1} e^{i[\Omega_{S_{ki}}(r_i)]t_2}\end{aligned} \tag{4}$$

For simplicity, we only consider the case of an isotropic sample in a small linear inhomogeneous magnetic field along the CSG direction. We then have

$$\begin{aligned}\sigma_{\text{eff}} = \frac{i}{16} \frac{(\alpha t_1 + 2\beta t_1 + 2\tau + t_2)\Delta_s}{\tau_d^I} \left(\frac{kT}{\hbar \omega_I}\right) M_{S_k}^{-} \\ \left\{ e^{-i[\alpha\omega_I - \pi J_{kl}(2\alpha+2\beta)]t_1} e^{i\left(\omega_{S_k} + \pi J_{kl}\right)t_2} e^{i2\pi J_{kl}\tau} + e^{-i[\alpha\omega_I + \pi J_{kl}(2\alpha+2\beta)]t_1} e^{i\left(\omega_{S_k} - \pi J_{kl}\right)t_2} e^{-i2\pi J_{kl}\tau} \right\}\end{aligned} \tag{5}$$

where $\frac{kT}{\hbar\omega_I}$ is the reciprocal of Boltzmann factor; $\tau_d^I \equiv 1/(\gamma\mu_0 M_0^I)$ is the dipolar demagnetizing time, in which M_0^I is the magnetization of I spin at equilibrium state, and $\Delta_s \equiv \left[3(\hat{s}\cdot\hat{z})^2 - 1\right]/2$.

Equation (5) provides a quantitative description of consequential apparent J coupling constants. It shows that the centers of intermolecular cross-peaks in the resulting 2D NMR spectrum locate at $(\alpha\omega_I - \pi J_{kl}(2\alpha+2\beta), \omega_{S_k} + \pi J_{kl})$ and $(\alpha\omega_I + \pi J_{kl}(2\alpha+2\beta), \omega_{S_k} - \pi J_{kl})$, respectively. If the frequency offset of I spin is set to zero, that is, $\omega_I = 0$, the intermolecular cross-peaks between I and S spins will centre at $(-\pi J_{kl}(2\alpha+2\beta), \omega_{S_k} + \pi J_{kl})$ and $(\pi J_{kl}(2\alpha+2\beta), \omega_{S_k} - \pi J_{kl})$. In inhomogeneous fields, due to the broadening of spectral peaks along both F1 and F2 dimensions, all the peaks appear as separate streaks along the direction $\phi = \text{arctg}(\alpha)$, where ϕ is the angle of spectral peaks with respect to the F2 axis. When the streaks are projected onto the F2 dimension after a counterclockwise rotation of $\pi/2 - \phi$ degree (this rotation transforms the data matrix (ω_2, ω_1) to $[\omega_2 - (\text{ctg}\phi)\omega_1, \omega_1]$), a high-resolution 1D spectrum can be obtained. The apparent J coupling constants are scaled by a factor of

$$\text{SF} = 3 + 2\beta/\alpha \tag{6}$$

It can be noticed that the SF of apparent J coupling constants is determined by the variables α and β. When $\alpha > 0$ and $-\alpha \geq \beta \geq -1.5\alpha$, the SF is in the range of 0 and 1. When $\alpha > 0$ and $0 \geq \beta \geq -\alpha$, the SF is in the range of 1 and 3. When $\alpha > 0$ and $\beta \geq 0$, the SF is in the range of 3 and infinity. The SF variable from 1 to infinity provides an effective and flexible way for accurate measurement of small J coupling constants.

Similarly, the expression for the signal from S spin using the J-scaled iMQC-1 sequence can be given as:

$$\sigma_{\text{eff}} = \frac{(0.5t_1 + t_2)\Delta_s}{16\tau_d^I}\left(\frac{kT}{\hbar\omega_I}\right) M_{S_k}^- \left\{ e^{-i[m\omega_I - \pi J_{kl}]t_1} e^{i\left(\omega_{S_k} + \pi J_{kl}\right)t_2} + e^{-i[\omega_I + \pi J_{kl}]t_1} e^{i\left(\omega_{S_k} - \pi J_{kl}\right)t_2} \right\} \tag{7}$$

Equation (7) shows that the centers of intermolecular cross-peaks in the resulting 2D NMR spectrum locate at $(m\omega_I - \pi J_{kl}, \omega_{S_k} + \pi J_{kl})$ and $(m\omega_I + \pi J_{kl}, \omega_{S_k} - \pi J_{kl})$, respectively. If the frequency offset of I spin is set to zero, the intermolecular cross-peaks between I and S spins will centre at $(-\pi J_{kl}, \omega_{S_k} + \pi J_{kl})$ and $(\pi J_{kl}, \omega_{S_k} - \pi J_{kl})$. In inhomogeneous fields, due to the broadening of spectral peaks along both F1 and F2 dimensions, all the peaks appear as separate streaks along the direction $\phi = \text{arctg}(m)$, where ϕ is the angle of spectral peaks with respect to the F2 axis. The apparent J coupling constants can be obtained with a SF $= 1 + 1/m$ $(0 < m \leq 1/2)$ when the streaks are projected onto the F2 dimension after a counterclockwise rotation of $\pi/2 - \phi$.

According to the above analysis, J-scaled iMQC pulse sequences are based on the 2D acquisition. A 1D high-resolution projection spectrum can be obtained from the 2D spectrum after a specific counterclockwise rotation. Although all the signals suffer from the inhomogeneous broadening along the F1 and F2 dimensions, the

spectral information can be preserved in the 1D projection spectrum. Moreover, the apparent *J* coupling constants in the 1D projection spectrum can be obtained with a SF. An accurate measurement of small *J* coupling constants can be achieved by adjusting m or α and β to appropriate value(s). In the following, two experiments are presented to illustrate the capability of *J*-scaled iMQC sequences in accurate measurement of small *J* coupling constants.

4.3. Results of *J*-scaled iMQC spectroscopy

Experiments were performed at 298 K using a Varian NMR System 500 MHz spectrometer with a 5 mm indirect detection probe with three-dimensional gradient coils. The experimental results of a sample of mixture of methyl ethyl ketone (MEK, $CH_3COCH_2CH_3$, solute) and cyclohexane (C_6H_{12}, solvent) with about 20% (by volume) acetone-d_6 are presented in Figure 13 to show the ability of the JSIS sequence in scaling the *J* coupling constants. The experimental results of a sample of histidine aqueous solution are presented in Figures 14 and 15 to show the ability of the *J*-scaled iMQC-1 sequence in the measurement of small *J* coupling constants.

For the sample of the mixture of MEK and cyclohexane, a conventional 1D spectrum in a homogeneous magnetic field was first acquired (Figure 13A). The magnetic field was then intentionally deshimmed to produce a LW of $\sim$30 Hz (phased mode). The resulting 1D spectrum is illustrated in Figure 13B. In the same inhomogeneous field, 2D spectra were acquired. The α and β were set to 1/6, 1/4, 1/4, 1/3 and $-1/4$, $-1/4$, $-1/8$, 1/6, respectively. Their 1D projections onto the F2 dimension are shown in Figure 13C–F, respectively. The corresponding simulated spectra are shown in Figure 13C′–F′. Compared to Figure 13A, the *J* splitting distances are 0- (completely decoupled), 1- (unchanged), 2- and 4-fold magnified in Figure 13C–F and Figure 13C′–F′, respectively, in good agreement with the theoretical predictions. A magnification of *J* splitting distances allows more accurate measurement of small *J* coupling constants. This, however, also aggravates overlap of spectral peaks in strongly coupled systems. Therefore, a proper SF is required for different systems.

For the sample of histidine aqueous solution, the conventional 1D high-resolution spectrum acquired in a well-shimmed field and the 1D spectrum acquired in an inhomogeneous field of about 30 Hz LW (phase mode) are shown in Figure 14A and B. There are five multiplets in the conventional spectrum (denoted as A, B, C, D, and E in Figure 14A). Scalar couplings exist between A and B, B and D, B and E, C and D, C and E, and D and E. The coupling constants J_{AB}, J_{BD}, J_{BE} are small, while J_{CD}, J_{CE}, J_{DE} are large. The small *J* coupling constants usually cannot be obtained from the conventional high-resolution spectrum in well-shimmed fields, to say nothing of in inhomogeneous fields. The results from the *J*-scaled iMQC-1 pulse sequence with SF = 11 in an inhomogeneous field are shown in Figure 15. We can see that the small *J* couplings J_{AB}, J_{BD}, J_{BE} can be well resolved from this spectrum since all the apparent *J* coupling constants are magnified to 11 times. The *J* coupling constants are measured as $J_{AB} = 1.38$ Hz, $J_{BD} = 1.09$ Hz, and $J_{BE} = 0.91$ Hz.

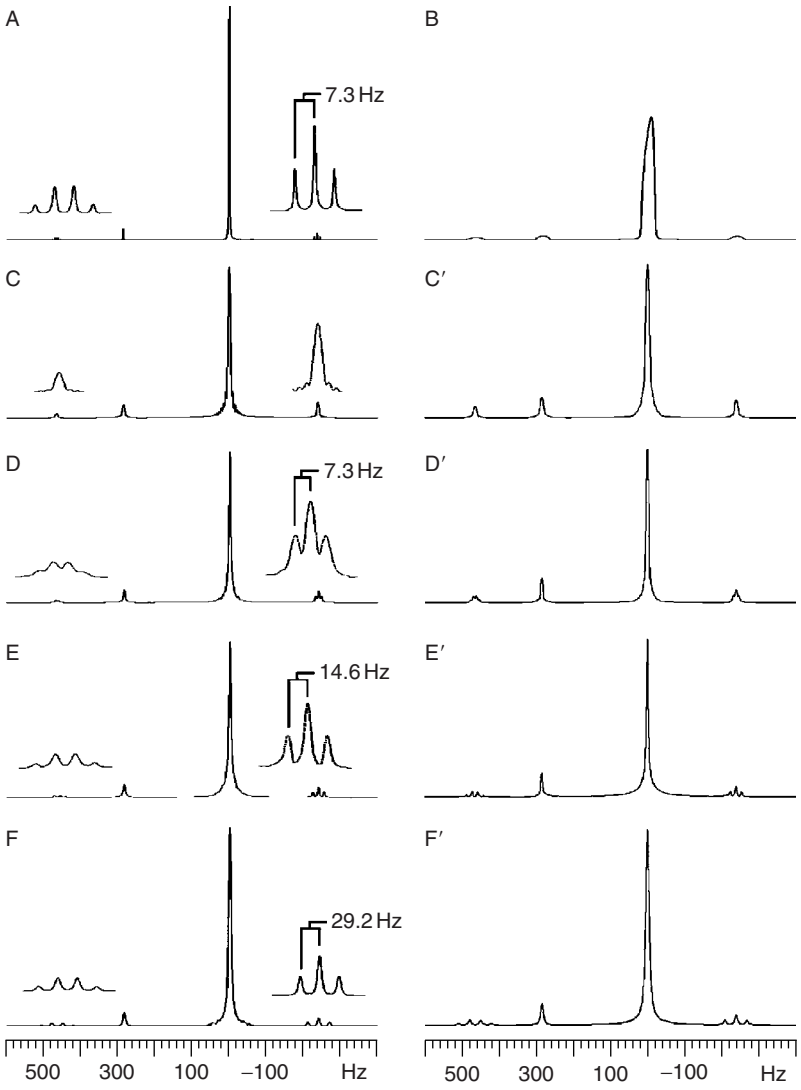

Figure 13 1D ^{1}H NMR spectra of the mixture of methyl ethyl ketone ($CH_3COCH_2CH_3$) and cyclohexane (C_6H_{12}). (A) Conventional 1D high-resolution spectrum acquired in a well-shimmed field, (B) 1D spectrum acquired in an inhomogeneous field of about 30 Hz linewidth, (C)–(F) accumulated projections onto the F2 dimension acquired from JSIS sequence. (C′)–(F′) Are simulation results corresponding to (C)–(F). (A) and (B) are displayed in phase mode, while (C)–(F) and (C′)–(F′) are absolute-valued projection spectra. Insets are magnified in both vertical and horizontal directions. Expansion factor is the same when expanded regions are from the same spectrum. (Source: Adapted from Ref. 33.)

4.4. Influence of scaling factor on the linewidth

The LWs in the spectra acquired from the *J*-scaled iMQC pulse sequences are related to the SF. In general, the LW in the indirect dimension of an iMQC spectrum depends on several factors, including transverse relaxation time T_2,

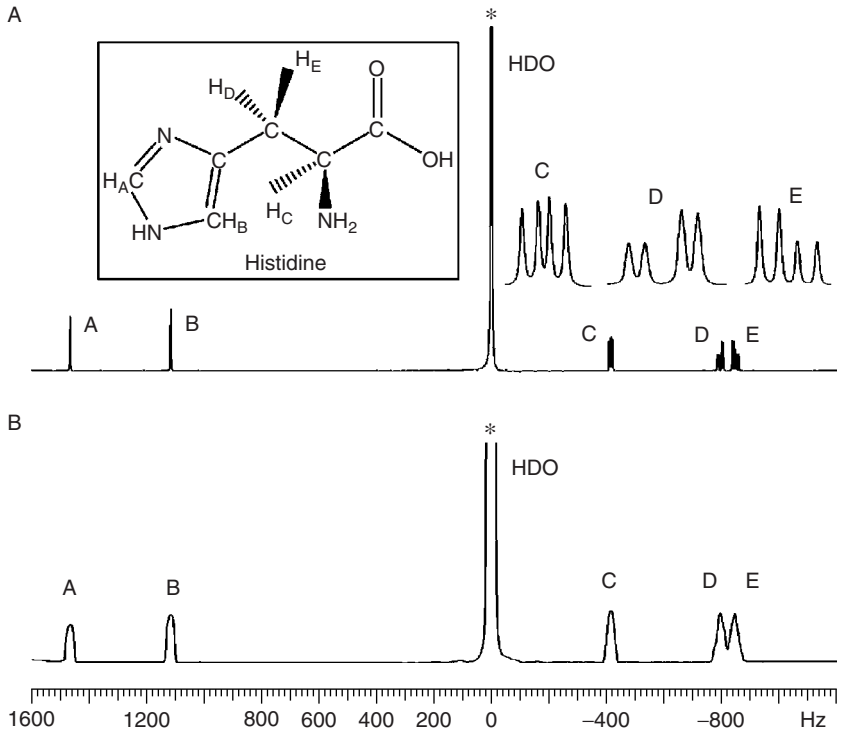

Figure 14 1D ^{1}H NMR spectra of histidine aqueous solution. (A) Conventional 1D high-resolution spectrum acquired in a well-shimmed field, and (B) 1D spectrum in an inhomogeneous field of about 30 Hz linewidth (phase mode). The peaks marked by * are truncated due to their strong intensities. Insets are magnified in both vertical and horizontal directions. The structure of histidine is shown in the block on the top left. (Source: Adapted from Ref. 32.)

background inhomogeneous field, diffusion and dipolar field. However, it is difficult to obtain an exact expression for the LW when all these factors are considered. Assuming that the inhomogeneous field is completely refocused by DDF and the effects of diffusion and dipolar field on signal amplitude can be neglected, here we make a simple analysis by considering only the effect of transverse relaxation attenuation during the JSIS sequence with SF $\geq$ 3. It is noted that the dependence of iMQC signal attenuation on indirect evolution time t_1 and T_2 is different from that of the conventional SQC signal in the cases of inhomogeneous fields.[96] For the JSIS sequence, the echo forms at $(3\alpha+2\beta)t_1$. The LW in the indirect dimension would be proportional to

$$\mathrm{LW} \propto \left[(3\alpha + 2\beta){R_2}^S + \alpha {R_2}^I\right] \tag{8}$$

where R_2 is the transverse relaxation rate, the reciprocal of T_2. As we have mentioned in the above section, the streaks tilt with an angle ϕ relative to the F2 axis. After the streaks have been rotated counterclockwise, the LW along the F2 axis which we are more concerned about is

$$\mathrm{LW} \propto \left[(3 + 2\beta/a){R_2}^S + {R_2}^I\right] \tag{9}$$

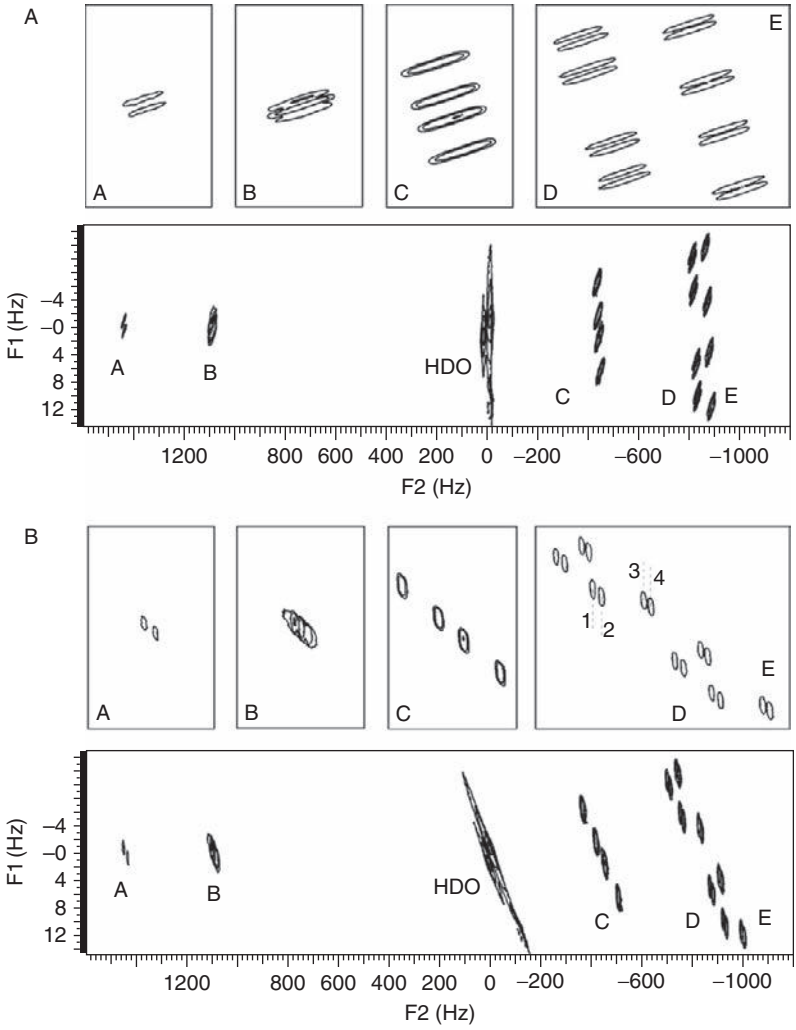

Figure 15 2D ^{1}H NMR spectra of histidine aqueous solution using the *J*-scaled iMQC-1 pulse sequence with $m = 1/10$ in the same inhomogeneous field as Figure 11B. (A) Experimental spectrum, (B) sheared spectrum of (A) after a counterclockwise rotation of 84.29°. Regions A, B, C, D, and E are magnified in both vertical and horizontal directions in both (A) and (B). (Source: Adapted from Ref. 32.)

The ratio between the increased normalized SF and the LW, which we define as increased resolution (IR) is then

$$IR = \frac{\text{SF / reference SF}}{\text{linewidth / reference linewidth}} \tag{10}$$

It can be seen that IR increases with the increase of SF. Therefore, the spectral resolution will increase consequently without overlap of spectral peaks. Note that

the IR increases rapidly at small SF and increases slowly at relatively large SF according to both theoretical data and experimental results. However, the signal-to-noise ratio (SNR) of the iMQC signals from the *J*-scaled iMQC pulse sequences is still much lower than that of conventional SQC signals, which may limit the practical application of these sequences. Improvement of the pulse sequences and optimization of the experimental parameters are still necessary for practical application.

5. CONCLUSION

Conventional 2D *J*-resolved spectroscopy provides hyperfine pattern for the *J*-coupled spin systems. However, it does not allow accurate determination of small *J* couplings since the spectral window along the *J*-dimension is limited by the widest multiplet pattern, which lowers the necessary spectral resolution for the small *J* couplings. To obtain small *J* coupling information, many NMR spectral editing techniques have been proposed. Selective *J*-resolved spectroscopy can overcome the resolution problem in *J* coupling dimension by selectively exciting the interested spin pair, thus providing a promising way for accurate measurement of small *J* couplings. The SSnQ-*J*-resolved spectroscopy can simplify the complex spectral information and provide the accurate information of small *J* couplings by exciting the interested spin states. However, it is impossible for these two techniques to obtain all the small *J* coupling constants in a sample from a single experiment due to the selective excitation. Based on the manipulation of evolution periods, *J*-multiplied HSQC and HMQC methods and *J*-scaled COSY are capable of yielding a spectrum with magnified apparent *J* coupling constants, which is useful for the accurate measurement of small *J* couplings. Combined *J*-multiplication with iMQCs, *J*-scaled iMQC pulse sequences were designed for the accurate measurement of small *J* coupling constants in inhomogeneous fields, which possess bright perspective in the detection of *in vivo* metabolites with small *J* couplings. However, the intrinsic low SNR is an obstacle for the practical application of *J*-scaled iMQC approaches. The SNR may be enhanced by combination with the dynamic nuclear polarization (DNP) technique.[98,99] Since there is not a method suitable for all kinds of situations, the existing methods play a complementary role in the accurate measurement of small *J* couplings.

ACKNOWLEDGEMENTS

This work was partially supported by the NNSF of China under Grants 10774125 and 10974164, and the Research Fund for the Doctoral Program of Higher Education of China under Grant 200803840019.

REFERENCES

1. S. Frank and P. C. Lauterbur, Voltage-sensitive magnetic gels as magnetic resonance monitoring agents. *Nature*, 1993, **363,** 334.
2. M. J. Shapiro and J. S. Gounarides, High resolution MAS-NMR in combinatorial chemistry. *Biotechnol. Bioeng.*, 2000, **71,** 130.

3. B. Ancian, NMR studies for mapping structure and dynamics of nucleosides in water. *Annu. Rep. NMR Spectrom.*, 2010, **69,** 39.
4. I. Tkac, P. G. Henry, P. Andersen, C. D. Keene, W. C. Low and R. Gruetter, Highly resolved *in vivo* ^{1}H NMR spectroscopy of the mouse brain at 9.4 T. *Magn. Reson. Med.*, 2004, **52,** 478.
5. P. Pelupessy, E. Rennella and G. Bodenhausen, High-resolution NMR in magnetic fields with unknown spatiotemporal variations. *Science*, 2009, **324,** 1693.
6. R. R. Ernst, G. Bodenhausen and A. Wokaun, Principles of Nuclear Magnetic Resonance in One and Two Dimensions. Clarendon Press, Oxford, 1991.
7. J. Keeler, Understanding NMR Spectroscopy. Wiley, England, 2005.
8. W. P. Aue, E. Bartholdi and R. R. Ernst, Two-dimensional spectroscopy. Application to nuclear magnetic resonance. *J. Chem. Phys.*, 1976, **64,** 2229.
9. K. Nagayama, K. Wuthrich and R. R. Ernst, Two-dimensional spin echo correlated spectroscopy (SECSY) for ^{1}H NMR studies of biological macromolecules. *Biochem. Biophys. Res. Commun.*, 1979, **90,** 305.
10. G. M. Clore and A. M. Gronenborn, Structures of larger proteins in solution: Three- and four-dimensional heteronuclear NMR spectroscopy. *Science*, 1991, **252,** 1390.
11. B. Baishya, G. N. M. Reddy, U. R. Prabhu, T. N. G. Row and N. Suryaprakash, Simplifying the complex ^{1}H NMR spectra of fluorine-substituted benzamides by spin system filtering and spin-state selection: Multiple-quantum−single-quantum correlation. *J. Phys. Chem. A*, 2008, **112,** 10526.
12. G. W. Vuister and A. Bax, Quantitative *J* correlation: A new approach for measuring homonuclear three-bond $J(H^{N}H^{\alpha})$ coupling constants in ^{15}N-enriched proteins. *J. Am. Chem. Soc.*, 1993, **115,** 7772.
13. L. E. Kay and A. Bax, New methods for the measuring of NH-C_{α}H coupling constants in ^{15}N-labelled proteins. *J. Magn. Reson.*, 1990, **86,** 110.
14. V. F. Bystrov, Spin-spin coupling and the conformational states of peptide systems. *Prog. NMR Spectrosc.*, 1976, **10,** 41.
15. F. J. Cooke, A. M. Blamire, D. N. Manners, P. Styles and B. Rajagopalan, Quantitative proton magnetic resonance spectroscopy of the cervical spinal cord. *Magn. Reson. Med.*, 2004, **51,** 1122.
16. A. A. Maudsley, S. K. Hilal, W. H. Perman and H. E. Simon, Spatially resolved high resolution spectroscopy by ''four-dimensional'' NMR. *J. Magn. Reson.*, 1983, **51,** 147.
17. R. A. de Graaf, D. L. Rothman and K. L. Behar, High resolution NMR spectroscopy of rat brain *in vivo* through indirect zero-quantum-coherence detection. *J. Magn. Reson.*, 2007, **187,** 320.
18. K. M. Koch, L. I. Sacolick, T. W. Nixon, S. McIntyre, D. L. Rothman and R. A. de Graaf, Dynamically shimmed multivoxel ^{1}H magnetic resonance spectroscopy and multislice magnetic resonance spectroscopic imaging of the human brain. *Magn. Reson. Med.*, 2007, **57,** 587.
19. K. M. Koch, S. McIntyre, T. W. Nixon, D. L. Rothman and R. A. de Graaf, Dynamic shim updating on the human brain. *J. Magn. Reson.*, 2006, **180,** 286.
20. K. M. Koch, P. B. Brown, D. L. Rothman and R. A. de Graaf, Sample-specific diamagnetic and paramagnetic passive shimming. *J. Magn. Reson.*, 2006, **182,** 66.
21. T. Facke and S. Berger, SERF, a new method for H-H spin-coupling measurement in organic chemistry. *J. Magn. Reson.*, 1995, **113,** 114.
22. S. Bourg and J. M. Nuzillard, In-phase double selective excitation of coupled spin systems using excitation sculpting. *J. Magn. Reson.*, 1998, **133,** 173.
23. F. Rastrelli and A. Bagno, Selective *J*-resolved spectra: A double pulsed field gradient spin-echo approach. *J. Magn. Reson.*, 2006, **182,** 29.
24. G. N. M. Reddy, T. N. G. Row and N. Suryaprakash, Discerning the degenerate transitions of scalar coupled ^{1}H NMR spectra: Correlation and resolved techniques at higher quantum. *J. Magn. Reson.*, 2009, **196,** 119.
25. B. Baishya and N. Suryaprakash, Spin selective multiple quantum NMR for spectral simplification, determination of relative signs, and magnitudes of scalar couplings by spin state selection. *J. Chem. Phys.*, 2007, **127,** 214510.
26. S. Hekkinen, H. Aitio, P. Permi, R. Folmer, K. Lappalainen and I. Klpelanen, *J*-multiplied HSQC (MJ-HSQC): A new method for measuring $^{3}J(H^{N}H^{\alpha})$ couplings in^{15}N-labeled proteins. *J. Magn. Reson.*, 1999, **137,** 243.

27. P. Permi, I. Klpelanen and S. Hekkinen, An improved *J*-multiplied method for the measurement of $^{3}J(H^{N}, H^{\alpha})$ from the two-dimensional ^{15}N -^{1}H correlation spectrum. *Magn. Reson. Chem.*, 1999, **37,** 821.
28. Y. Xia, X. G. Kong, N. Ip and G. Zhu, A *J*-multiplied HMQC (MJ-HMQC) experiment for measuring $^{3}J_{HNH\alpha}$ coupling constants. *J. Magn. Reson.*, 2000, **146,** 228.
29. R. V. Hosur, K. V. R. Chary and M. R. Kumar, *J*-scaling in two-dimensional homonuclear correlated spectroscopy for enhancement of cross peak intensities. *Chem. Phys. Lett.*, 1985, **116,** 105.
30. A. Sheth, M. Ravikumar and R. V. Hosur, Application of *J* scaling in two-dimensional spin-echo-correlated spectroscopy to observation of small coupling correlations. *J. Magn. Reson.*, 1986, **70,** 213.
31. M. Ravikumar, A. Sheth and R. V. Hosur, Analysis of resolution and sensitivity enhancements in two-dimensional scaling experiments. *J. Magn. Reson.*, 1986, **69,** 418.
32. Y. Q. Lin, Z. Chen, S. H. Cai and J. H. Zhong, Accurate measurements of small *J* coupling constants under inhomogeneous fields *via* intermolecular multiple-quantum coherences. *J. Magn. Reson.*, 2008, **190,** 298.
33. Y. Q. Lin, Z. Chen, S. H. Cai and J. H. Zhong, High-resolution *J*-scaling nuclear magnetic resonance spectra in inhomogeneous fields via intermolecular multiple-quantum coherences. *Appl. Spectrosc.*, 2009, **63,** 585.
34. M. G. Swanson, D. B. Vigneron, T. K. C. Tran, N. Sailasuta, R. E. Hurd and J. Kurhanewicz, Single-voxel oversampled J-resolved spectroscopy of in vivo human prostate tissue. *Magn. Reson. Med.*, 2001, **45,** 973.
35. S. L. Peng, C. H. Ye and M. L. Liu, Quantitative estimation of property parameters of crude oil using two-dimensional ^{13}C-^{1}H J-resolved nuclear magnetic resonance spectroscopy (HET-JRES). *Appl. Spectrosc.*, 2003, **57,** 1190.
36. E. Adalsteinsson, R. E. Hurd, D. Mayer, N. Sailasuta, E. V. Sullivan and A. Pfefferaum, *In vivo* 2D *J*-resolved magnetic resonance spectroscopy of rat brain with a 3-T clinical human scanner. *NeuroImage*, 2004, **22,** 381.
37. A. Khatib, E. G. Wilson, H. K. Kim, A. W. M. Lefeer, C. Erkelens, Y. H. Choi and R. Verpoorte, Assessment of elemental mobility in soil using a fluidised bed approach with on-line ICP-MS analysis. *Anal. Chim. Acta*, 2006, **599,** 264.
38. K. Lymer, K. Haga, I. Marshall, N. Sailasuta and J. Wardlaw, Reproducibility of GABA measurements using 2D J-resolved magnetic resonance spectroscopy. *Magn. Reson. Imaging*, 2007, **25,** 634.
39. M. L. Mai and X. Zhang, Multiple-quantum J-resolved NMR spectroscopy (MQ-JRES): Measurement of multiple-quantum relaxation rates and relative signs of spin coupling constants. *J. Magn. Reson.*, 2000, **146,** 277.
40. B. Baishya, U. R. Prabhu and N. Suryaprakash, Spin state selective coherence transfer: A method for discrimination and complete analyses of the overlapped and unresolved H-1 NMR spectra of enantiomers. *J. Magn. Reson.*, 2008, **192,** 101.
41. G. N. M. Reddy, T. N. G. Row and N. Suryaprakash, Discerning the degenerate transitions of scalar coupled ^{1}H NMR spectra: Correlation and resolved techniques at higher quantum. *J. Magn. Reson.*, 2009, **196,** 119.
42. P. Giraudeau and S. Akoka, A new detection scheme for ultrafast 2D *J*-resolved spectroscopy. *J. Magn. Reson.*, 2007, **186,** 352.
43. P. Giraudeau and S. Akoka, Resolution and sensitivity aspects of ultrafast *J*-resolved 2D NMR spectra. *J. Magn. Reson.*, 2008, **190,** 339.
44. Y. Q. Huang, S. H. Cai, Y. Q. Lin and Z. Chen, An intermolecular single-quantum coherence detection scheme for high-resolution two-dimensional *J*-resolved spectroscopy in inhomogeneous fields. *Appl. Spectrosc.*, 2010, **64,** 235.
45. Y. Q. Huang, X. Chen, S. H. Cai, C. B. Cai and Z. Chen, High-resolution two-dimensional correlation spectroscopy in inhomogeneous fields: New application of intermolecular zero-quantum coherences. *J. Chem. Phys.*, 2010, **132,** 134507.
46. T. L. Hwang and A. J. Shaka, Water suppression that works. Excitation sculpting using arbitrary wave-forms and pulsed-field gradients. *J. Magn. Reson.*, 1995, **112,** 275.
47. W. S. Brey, L. W. Jaques and H. J. Jakobsen, A ^{13}C -{^{1}H} double resonance study of the signs of ^{1}H -^{19}F and^{13}C -^{19}F spin coupling constants in fluorobenzenes and 2-fluoropyridine. *Org. Magn. Reson.*, 1979, **12,** 243.

48. A. Rexroth, P. Schmidt, S. Szalma, T. Geppert, H. Schwalbe and C. Griesinger, New principle for the determination of coupling constants that largely suppresses differential relaxation effects. *J. Am. Chem. Soc.*, 1995, **117,** 10389.
49. P. Anderson, J. Weigelt and G. Otting, Spin-state selection filters for the measurement of heteronuclear one-bond coupling constants. *J. Biomol. NMR*, 1998, **12,** 435.
50. L. Duma, S. Hediger, A. Lesage and L. Emsley, Spin-state selection in solid-state NMR. *J. Magn. Reson.*, 2003, **164,** 187.
51. L. Duma, S. Hediger, B. Brutscher, A. Bockmann and L. Emsley, Resolution enhancement in multidimensional solid-state NMR spectroscopy of proteins using spin-state selection. *J. Am. Chem. Soc.*, 2003, **125,** 11816.
52. P. Permi and A. Annila, A new approach for obtaining sequential assignment of large proteins. *J. Biomol. NMR*, 2001, **20,** 127.
53. P. Permi, A spin-state-selective experiment for measuring heteronuclear one-bond and homonuclear two-bond couplings from an HSQC-type spectrum. *J. Biomol. NMR*, 2002, **22,** 27.
54. C. R. R. Grace and R. Riek, Pseudomultidimensional NMR by spin-state selective off-resonance decoupling. *J. Am. Chem. Soc.*, 2003, **125,** 16104.
55. L. Braunschweiler, G. Bodenhausen and R. R. Ernst, Analysis of networks of coupled spins by multiple quantum NMR. *Mol. Phys.*, 1983, **48,** 535.
56. J. M. Polson and E. E. Burnell, A multiple-quantum ^{1}H NMR study of partially oriented biphenylene. *J. Magn. Reson.*, 1994, **106,** 223.
57. J. C. T. Rendell and E. E. Burnell, Frequency-selective excitation in multiple-quantum NMR. *J. Magn. Reson.*, 1995, **112,** 1.
58. C. Griesinger, O. W. Sorensen and R. R. Ernst, Two-dimensional correlation of connected NMR transitions. *J. Am. Chem. Soc.*, 1985, **107,** 6394.
59. H. J. Jakobsen, T. Bundgaard and R. S. Hansen, Assignments and signs of ^{13}C-^{31}P coupling constants from off-resonance proton decoupled ^{13}C spectra. *Mol. Phys.*, 1972, **23,** 197.
60. O. W. Sorensen, G. W. Eich, M. H. Levitt, G. Bodenhausen and R. R. Ernst, Product operator formalism for the description of NMR pulse experiments. *Prog. Nucl. Magn. Reson. Spectrosc.*, 1984, **16,** 163.
61. J. Jeener, Proceedings of the lecture presented at the Ampere International Summer School, Basko Polje, Yugoslavia, 1971 (unpublished).
62. R. Bowtell, R. M. Bowley and P. J. Glover, Multiple spin echoes in liquids in a high magnetic field. *J. Magn. Reson.*, 1990, **88,** 643.
63. W. S. Warren, W. Richter, A. H. Andreotti and B. T. Farmer, Generation of impossible cross-peaks between bulk water and biomolecules in solution NMR. *Science*, 1993, **262,** 2005.
64. S. Lee, W. Richter, S. Vathyam and W. S. Warren, Quantum treatment of the effects of dipole–dipole interactions in liquid nuclear magnetic resonance. *J. Chem. Phys.*, 1996, **105,** 874.
65. A. Jerschow, Multiple echoes initiated by a single radio frequency pulse in NMR. *Chem. Phys. Lett.*, 1998, **296,** 466.
66. Y. Y. Lin, N. Lisitza, S. D. Ahn and W. S. Warren, Resurrection of crushed magnetization and chaotic dynamics in solution NMR spectroscopy. *Science*, 2000, **290,** 118.
67. S. Capuani, F. Curzi, F. M. Alessandri, B. Maraviglia and A. Bifone, Characterization of trabecular bone by dipolar demagnetizing field MRI. *Magn. Reson. Med.*, 2001, **46,** 683.
68. J. Jeener, Dynamical effects of the dipolar field inhomogeneities in high-resolution NMR: Spectral clustering and instabilities. *Phys. Rev. Lett.*, 1999, **82,** 1772.
69. G. Deville, M. Bernier and J. M. Delrieux, NMR multiple echoes observed in solid ^{3}He. *Phys. Rev. B*, 1979, **19,** 5666.
70. J. Jeener, A. Vlassenbroek and P. J. Broekaert, Unified derivation of the dipolar field and relaxation terms in the Bloch -Redfield equations of liquid NMR. *Chem. Phys.*, 1995, **103,** 1309.
71. A. Vlassenbroek, J. Jeener and P. J. Broekaert, Macroscopic and microscopic fields in high-resolution liquid NMR. *Magn. Reson.*, 1996, **118,** 234.
72. M. H. Levitt, Demagnetization field effects in two-dimensional solution NMR. *Concepts Magn. Reson.*, 1996, **8,** 77.
73. Z. Chen and J. H. Zhong, Unconventional diffusion behaviors of intermolecular multiple-quantum coherences in nuclear magnetic resonance. *J. Chem. Phys.*, 2001, **114,** 5642.

74. Z. Chen, Z. W. Chen and J. H. Zhong, Quantitative characterization of intermolecular dipolar interactions of two-component systems in solution nuclear magnetic resonance. *J. Chem. Phys.*, 2001, **115,** 10769.
75. Z. Chen, Z. W. Chen and J. H. Zhong, Observation and characterization of intermolecular homonuclear single-quantum coherences in liquid nuclear magnetic resonance. *J. Chem. Phys.*, 2002, **117,** 8426.
76. D. Z. Balla and C. Faber, Intermolecular zero-quantum coherence NMR spectroscopy in the presence of local dipole fields. *J. Chem. Phys.*, 2008, **128,** 154522.
77. C. Faber, C. Heil, B. Zaheisen, D. Balla and R. Bowtell, Sensitivity to local dipole fields in the CRAZED experiment: An approach to bright spot MRI. *J. Magn. Reson.*, 2006, **182,** 315.
78. S. Vathyam, S. Lee and W. S. Warren, Homogeneous NMR spectra in inhomogeneous fields. *Science*, 1996, **272,** 92.
79. W. S. Warren, S. Ahn, M. Mescher, M. Garwood, K. Ugurbil, W. Richter, R. R. Rizi, J. Hopkins and J. S. Leigh, MR imaging contrast enhancement based on intermolecular zero quantum coherences. *Science*, 1998, **281,** 247.
80. Y. Y. Lin, S. Ahn, N. Murali, W. Brey, C. R. Bowers and W. S. Warren, High-resolution, >1 GHz NMR in unstable magnetic fields. *Phys. Rev. Lett.*, 2000, **85,** 3732.
81. G. Galiana, R. T. Branca and W. S. Warren, Ultrafast intermolecular zero quantum spectroscopy. *J. Am. Chem. Soc.*, 2005, **127,** 17574.
82. J. H. Zhong, Z. Chen and E. Kwok, In *vivo* intermolecular double-quantum imaging on a clinical 1.5 T MR scanner. *Magn. Reson. Med.*, 2000, **43,** 335.
83. I. Ardelean, E. Kossel and R. Kimmich, Attenuation of homo- and heteronuclear multiple spin echoes by diffusion. *J. Chem. Phys.*, 2001, **114,** 8520.
84. P. L. de Sousa, D. Gounot and D. Grucker, Flow effects in long-range dipolar field MRI. *J. Magn. Reson.*, 2003, **162,** 356.
85. G. D. Charles-Edwards, G. S. Payne, M. O. Leach and A. Bifone, Effects of residual single-quantum coherences in intermolecular multiple-quantum coherence studies. *J. Magn. Reson.*, 2004, **166,** 215.
86. P. L. de Sousa, D. Gounot and D. Grucker, Observation of diffraction-like effects in Multiple Spin Echoe (MSE) experiments in structured samples. *C. R. Chim.*, 2004, **7,** 31.
87. C. Faber, E. Pracht and A. Haase, Resolution enhancement in *in vivo* NMR spectroscopy: Detection of intermolecular zero-quantum coherences. *J. Magn. Reson.*, 2003, **161,** 265.
88. D. Balla and C. Faber, Solvent suppression in liquid state NMR with selective intermolecular zero-quantum coherences. *Chem. Phys. Lett.*, 2004, **393,** 464.
89. Z. Chen, T. Hou, Z. W. Chen, D. W. Hwang and L. P. Hwang, Selective intermolecular zero-quantum coherence in high-resolution NMR under inhomogeneous fields. *Chem. Phys. Lett.*, 2004, **386,** 200.
90. Z. Chen, Z. W. Chen and J. H. Zhong, High-resolution NMR spectra in inhomogeneous fields via IDEAL (intermolecular dipolar-interaction enhanced all lines) method. *J. Am. Chem. Soc.*, 2004, **126,** 446.
91. Z. Chen, S. H. Cai, Z. W. Chen and J. H. Zhong, Fast acquisition of high-resolution NMR spectra in inhomogeneous fields via intermolecular double-quantum coherences. *J. Chem. Phys.*, 2009, **130,** 084504.
92. W. Barros and D. F. Gochberg, Fast single-gradient simultaneous measurement of D and T2 in liquids via the distant dipolar field. *Chem. Phys. Lett.*, 2006, **431,** 174.
93. W. Barros, J. C. Gore and D. F. Gochberg, Simultaneous measurement of D and T_2 using the distant dipolar field. *J. Magn. Reson.*, 2006, **178,** 166.
94. C. Faber, Resolution enhancement in in *vivo* NMR spectroscopy. *Annu. Rep. NMR Spectro.*, 2007, **61,** 1.
95. P. P. Zanker, J. Schmiedeskamp, H. W. Spiess and R. H. Acosta, Distant dipolar fields in laser-polarized gases on macroscopic scales. *Phys. Rev. Lett.*, 2008, **100,** 213001.
96. X. Chen, M. J. Lin, Z. Chen, S. H. Cai and J. H. Zhong, High-resolution intermolecular zero-quantum coherence spectroscopy under inhomogeneous fields with effective solvent suppression. *Phys. Chem. Chem. Phys.*, 2007, **9,** 6231.

97. S. Chen, S. H. Cai and Z. Chen, Intermolecular multiple-quantum coherences between spin 1/2 and quadrupolar nuclei in liquid nuclear magnetic resonance. *Chem. Phys. Lett.*, 2008, **458,** 368.
98. E. R. Jenista, R. T. Branca and W. S. Warren, Hyperpolarized carbon–carbon intermolecular multiple quantum coherences. *J. Magn. Reson.*, 2009, **196,** 74.
99. M. Mishkovsky, U. Eliav, G. Navon and L. Frydman, Nearly 10^6-fold enhancements in intermolecular ^{1}H double-quantum NMR experiments by nuclear hyperpolarization. *J. Magn. Reson.*, 2009, **200,** 142.

This page intentionally left blank

CHAPTER 5

High-Resolution ^{1}H NMR Spectroscopy of Solids

Paul Hodgkinson

Contents

Abstract

Driven both by technological and methodological advances, major progress has been made over the past decade in improving the quality of ^{1}H NMR spectra in the solid state. Traditionally high-resolution solid-state ^{1}H NMR involved specialised and often challenging techniques, but the advent of fast magic-angle spinning (MAS) probes, higher magnetic fields, and RF decoupling schemes that complemented, rather than competed with, MAS has considerably simplified the task of obtaining useful ^{1}H spectra from solids. After introducing the factors that determine resolution in ^{1}H NMR and the approaches used to narrow ^{1}H linewidths, the relevant literature over the past

Department of Chemistry, Durham University, Durham, United Kingdom

Annual Reports on NMR Spectroscopy, Volume 72
ISSN 0066-4103, DOI: 10.1016/B978-0-12-385857-3.00005-0

© 2011 Elsevier Ltd.
All rights reserved.

decade is reviewed. The final section presents a selection of applications, highlighting the different areas to which resolved ^{1}H NMR spectra can now be applied.

Key Words: 1-H, Solid state, Resolution, Decoupling, Magic-angle spinning, Materials.

1. INTRODUCTION

While ^{1}H NMR is the cornerstone of solution-state NMR spectroscopy, the information content of ^{1}H NMR spectra of organic solids is usually limited, and most studies focus on ^{13}C NMR, despite its much lower overall receptivity. This is essentially due to the strong dipolar interactions between the abundant ^{1}H nuclei, which are efficiently averaged out in the solution state by rapid isotropic tumbling. In solids, the dipolar couplings experience little motional averaging, and the multiple, strong couplings between the different ^{1}H nuclei result in broad and featureless lines, typically about 50 kHz wide. Although ^{13}C nuclei in the solid state are also affected by anisotropic interactions, such as the heteronuclear couplings to ^{1}H and the chemical shift anisotropy (CSA), these interactions (or more precisely their effects on spectral resolution) can be efficiently suppressed by the combination of heteronuclear decoupling and magic-angle spinning (MAS).

Nevertheless, considerable progress has been made towards achieving high-resolution ^{1}H spectra from solid materials. After introducing the different strategies that have been used to improve ^{1}H spectral resolution, the relevant literature over the past decade is reviewed, and a selection of literature examples of the use of resolved ^{1}H spectra to different chemical problems presented.

1.1. Origins of linewidths in ^{1}H solid-state NMR spectra

The factors that determine resolution of NMR spectra can be divided into 'inhomogeneous' and 'homogeneous' factors. The homogeneous linewidth is the intrinsic linewidth associated with an idealised isolated resonance, while inhomogeneous factors modify the effective NMR frequency, leading to a broadening of the overall lineshape. A spin–echo experiment (largely) distinguishes these factors, as only inhomogeneous contributions are refocussed by the echo. Note that this separation is not so clear cut if the homogeneous linewidth contains 'mixed' terms, for example, cross-terms between the dipolar and CSA interactions; the decay observed in the spin–echo experiment may then not perfectly correspond to the homogeneous linewidth in the NMR spectrum.

In the case of isolated molecules tumbling in isotropic solution, the inhomogeneous line-broadening is purely determined by instrumental factors, and can be reduced to less than the relaxation-limited linewidth. In contrast, inhomogeneous distributions of NMR frequencies are almost inevitable in solid-state NMR, and these often prove to be the limiting factor on resolution. For example, the

impressive resolutions that now can be achieved in ^{13}C NMR of microcrystalline protein samples are in large part due to developments in sample preparation techniques leading to higher quality microcrystals (see, for example Ref. 1). Such good crystallinity ensures that equivalent sites *in an individual crystallite* have the same NMR frequency. This is not, however, sufficient to eliminate inhomogeneous line-broadening since susceptibility variations mean that the local magnetic field within different crystallites may not be identical, leading to a broadening of the NMR lineshape. These susceptibility effects are not fully averaged by MAS,[2–5] and the anisotropy of the sample's bulk magnetic susceptibility (ABMS) can often be limiting factor on spectral resolution for powdered solid sample. For example, amongst systems we have examined, ABMS is the dominant contribution to the ^{19}F linewidth (at about 1 ppm) in octafluoronaphthalene[6] and to the ^{1}H linewidth in hexamethylbenzene.[7] Density functional theory (DFT) calculations of the magnetic susceptibility tensor suggest that ABMS is the dominant line-broadening mechanism in diverse systems such as the small molecule drug, terbutaline sulphate,[8] malonic acid,[9] as well as inorganic phosphates.[10] Fortunately many important systems are less affected by ABMS broadenings, and inhomogeneous broadenings of 0.2 ppm or less have been reported in several solid-state NMR studies of proteins.[11,12] Nevertheless, given the limited shift range of ^{1}H NMR, even 0.2 ppm of broadening represents a significant limitation on resolution.

In the case of ^{1}H solid-state NMR, however, the inhomogeneous contribution to linewidth is usually dwarfed by the homogeneous linewidth due to the homonuclear ^{1}H dipolar couplings. Unfortunately MAS is only moderately effective in averaging out these couplings. MAS is most effective for interactions such as the CSA or (first order) quadrupolar coupling, where the lineshape breaks up under MAS into sharp spinning sidebands (whose linewidth is determined by inhomogeneous factors). Corresponding behaviour is also observed for dipolar couplings between isolated pairs of spins. However, the homonuclear dipolar coupling Hamiltonian between one pair of spins, say A and B, does not commute with coupling Hamiltonian involving a third spin (e.g. A and C). As discussed by Maricq and Waugh,[13] this failure of different coupling terms of the Hamiltonian to commute means that the spin dynamics do not refocus over a rotation cycle (except for special geometries in which all couplings share the same principal axis system). Instead, the rotor echoes decay in intensity and the spectrum is correspondingly broadened. In a confusing overlap with the terminology used for lineshape contributions, Hamiltonians which do not commute over the rotor cycle in this way are termed 'homogeneous', while the Hamiltonians for single-spin interactions (such as the CSA and quadrupolar coupling) or couplings between *heteronuclei* are termed 'inhomogeneous'. In contrast to the spinning sidebands associated with inhomogeneous Hamiltonians, the sidebands in MAS spectra of systems with homogeneous Hamiltonians narrow with increasing spinning rate. However, the linewidth only decreases as the inverse of the spinning rate, and very high MAS rates are required to achieve substantial narrowing. Nevertheless, fast MAS is proving a viable approach to high-resolution ^{1}H NMR, as discussed in Section 2.

The factors determining ^{1}H resolution under MAS have been extensively analysed by Zorin et al.,[7] and investigated experimentally in peptide[11] and

molecular organic solids.[9] The homogeneous ^{1}H linewidth, determined from spin–echo experiments, is found to be fully determined by the dipolar coupling network, which can be effectively parameterised in terms of the effective coupling strength and geometrical factors. The effective coupling strength for a given spin, j, is determined by the root-sum-square coupling to its neighbours,[14] k:

$$d_{\mathrm{rss},j} = \sqrt{\sum_{k \neq j} d_{jk}^2}. \tag{1}$$

While the details of the spin dynamics depend on the magnitude of the individual couplings, d_{jk}, and the relative orientations of their tensors, d_{rss} sets an effective scaling factor. Specifically, the linewidth as a function of spinning rate follows the relation:

$$\mathrm{FWHM} \approx G \frac{d_{\mathrm{rss}}^2}{\upsilon_{\mathrm{r}}}, \tag{2}$$

where υ_{r} is the MAS rate, and G is a dimensionless coefficient that depends on the geometry of the coupling network. This relationship is illustrated in Figure 1, which shows how data from systems with similar 'geometries' but very different coupling strengths can be superimposed when d_{rss} is used as a scaling factor. The slope of the plotted of (scaled) linewidth versus (scaled) MAS rate, which corresponds to G in Equation (1), is largest for geometries with clear 3D character and becomes very small for quasi-one-dimensional systems (corresponding to the

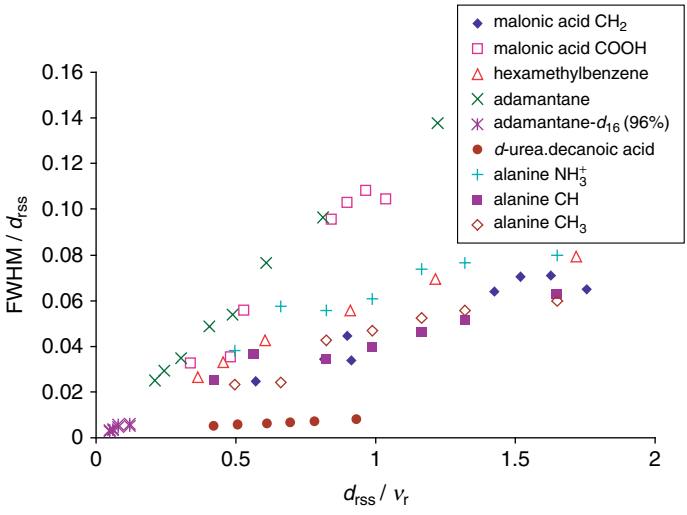

Figure 1 Plot of homogeneous ^{1}H linewidth as a function of MAS rate for a number of ^{1}H resonances, normalised by the root-sum-square coupling for the different sites. The linewidth scales inversely with spinning rate, with the constant of proportionality depending on the local network geometry. Plot adapted from results published in Ref. 7.

special case of a common principle axis system referred to above). Note how different G values may be observed for different resonances in the same system, depending on the nature of local coupling network, for example, the acid proton versus the CH_2 resonance of malonic acid.

The homogeneous nature of the Hamiltonian for a network of homonuclear dipolar couplings means that the problem of ^{1}H linewidths is intrinsically a multi-spin one. However, the spin dynamics can still be calculated exactly, provided a large enough spin system can be simulated. Figure 2 compares an experimental ^{1}H spectrum of adamantane under MAS with the results of a simulation involving a system of nine spins whose geometry and d_{rss} was matched with that of adamantane. Periodic boundary conditions and an artificial geometry were used in order to have a good model for the infinite lattice of the real system. The quality of agreement is remarkable considering the idealised nature of the simulated network and the absence of free parameters. While this nine-spin model works well for the simulation of the normal single-quantum (SQ) spectra, it will clearly be less satisfactory for predicting the dynamics of higher-order coherences; Ref. 15 and references therein discuss this distinct problem.

It is important to emphasise that the continuous spectra shown in Figure 2 are the sum of a very large number of individual transitions, and are not simply broadened versions of idealised spinning sideband manifolds. It may be convenient to describe the evolution of the ^{1}H magnetisation in a dipolar network in terms of 'spin diffusion', but diffusion rates and 'T_2 times' extracted from coupled systems are phenomenological quantities. The decay of initial transverse magnetisation results from a coherent spreading out into the large 'phase space' of accessible zero-quantum coherences, rather than a true (incoherent) relaxation process. The task of achieving high-resolution ^{1}H spectra is to manipulate the spin dynamics, for example, by spinning and/or RF irradiation in order to slow down this dephasing.

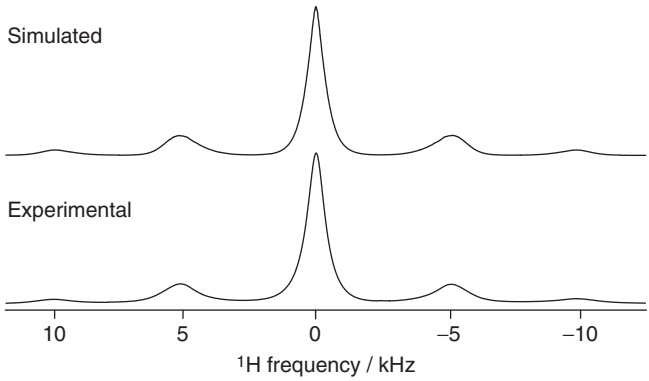

Figure 2 Experimental and numerically simulated ^{1}H spectra of powdered adamantane spinning at 5 kHz (^{1}H Larmor frequency of 499.7 MHz). Note the slight asymmetry of the spinning sidebands. Simulation details are given in Ref. 7.

1.1.1. Rotational resonance

Provided the sites involved are coupled, 'rotational resonance' effects are observed when spinning sideband of one resonance overlaps with another transition frequency in an MAS spectrum. These effects were observed in Andrew's pioneering work on MAS,[16] and subsequently analysed in detail by several research groups. They are not typically observed in ^{1}H NMR since the high MAS rates required for adequate resolution, coupled with the limited ^{1}H frequency range, means that centrebands and sidebands are unlikely to overlap. Similarly so-called '$n = 0$' rotational resonance effects,[13] associated with spins that have the same isotropic shift but are not strictly equivalent, are rarely observed. It has been shown in simulation that such effects are suppressed in multi-spin homogeneous systems.[7] However, ^{1}H $n = 0$ rotational resonance has been observed in silicate systems,[17] where the ^{1}H spins are relatively dilute. The resulting, potentially misleading, splittings in the MAS spectrum can be distinguished from genuine frequency differences by their sensitivity to MAS rate.

1.1.2. Orientation effects

The discussion above focusses on the overall resolution in spectra from microcrystalline powder samples. It is important to note that the MAS spectra from individual crystallites are not identical and will in general differ in both overall width and centreband width.[7] (There will also be very small differences in isotropic shift due to the effects of ABMS discussed above.) When considering the coupling network for individual crystallites, it is necessary to incorporate the orientational dependence of the coupling. Hence, the root-sum-square coupling qualified by crystallite orientation, Ω, becomes:

$$d_{\mathrm{rss},j}^{\Omega} = \sqrt{\sum_{k \neq j} \left[\frac{(3\cos^2\theta - 1) d_{jk}^2}{2} \right]}. \qquad (3)$$

The sub-spectra and values of $d_{\mathrm{rss},j}^{\Omega}$ associated with different crystallite orientations are quite different, even for relatively 'isotropic' distributions of spins such as cubic lattices.[7,15] The ^{1}H magnetisation will dephase more slowly for orientations associated with weaker overall coupling strength, that is, lower $d_{\mathrm{rss},j}^{\Omega}$, and the associated spectra will also be narrower. As illustrated in Figure 3, ^{1}H spectra acquired after spin–echo periods of increasing duration generally show improved ^{1}H resolution.[18] Delayed acquisition, and related 'constant time' experiments, thus potentially provide improved resolution at the cost of decreased sensitivity,[19] and can dramatically improve information content in some cases, for example, in applications to surface-adsorbed species[20,21] or polymeric systems.[22] Similar improvements in linewidths have also been observed in inverse detection experiments compared to pulse-and-acquire spectra, in which no selective dephasing is occurring.[23]

1.1.3. Heteronuclear couplings

Finally it is worth noting that coupling to nuclei other than ^{1}H may make a significant contribution to ^{1}H linewidths. Although heteronuclear dipolar couplings are generally averaged out by MAS, MAS is only partially effective in

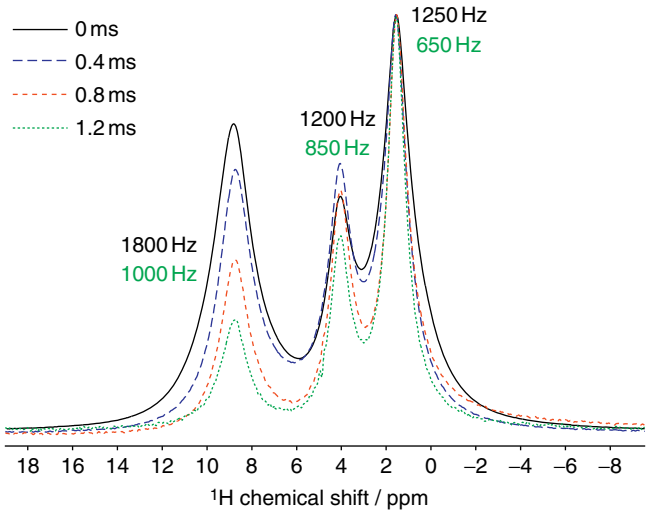

Figure 3 ^{1}H MAS 500 MHz NMR spectra acquired as a function of total spin–echo period (2τ) for powdered samples of alanine under 30 kHz MAS. The vertical scale is set so that the least-decayed signal (here the methyl resonance) has the same height. The figures give FWHM linewidths (to the nearest 50 Hz) for each peak in the spectra acquired with 0 (top) and 1.2 ms (bottom) echo periods. Figure derived from results published in Ref. 18.

averaging out interactions with nuclei with large quadrupole moments.[24] Particularly at lower magnetic fields, where such second-order effects are stronger, line-broadenings of resonances corresponding to hydrogens bonded to ^{14}N are readily observed.[25] ^{14}N decoupling using a train of ^{14}N pulses has recently been shown to substantially reduce linewidths for such resonances.[26] As noted in Section 2, decoupling, for example, of ^{15}N, may also be useful in isotopically enriched samples.[27,28]

1.2. Overview of homonuclear dipolar decoupling

As discussed above, MAS is much less effective for suppressing homonuclear dipolar couplings in comparison to inhomogeneous interactions such as the CSA. The design of so-called ultra-fast MAS modules has allowed spinning rates in excess of 60 kHz, but this is insufficient to suppress the dipolar broadening in typical organic solids, where static lineshapes in excess of 50 kHz are the norm. Moreover, the very small sample volumes of the rotors required (typically a few microlitres) make dilute spin NMR, such as ^{13}C and ^{15}N, very challenging at natural abundance. Hence, alternatives to MAS are often required.

In MAS, the spatial component of the NMR interactions is made time dependent through the physical rotation of the sample, such that anisotropic terms average out in the 'average Hamiltonian' over the rotor period. An alternative is to use periodic RF irradiation to manipulate the spin coherences such that the unwanted dipolar coupling terms are similarly averaged away over the period

of the RF. There are, however, some major differences between MAS and decoupling using RF irradiation.

In MAS, all the anisotropic interactions share the same orientation dependence on $3(\cos^2\theta - 1)/2$, where θ is the angle between the magnetic field and the principal axis of relevant rank 2 tensor. In contrast, RF irradiation works with the spin terms of the Hamiltonian and so scales the different NMR interactions differently. An ideal homonuclear decoupling sequence will scale the spin term of homonuclear coupling Hamiltonian to zero, but the averaged Hamiltonian for spin terms such as the CSA and *heteronuclear* dipolar coupling will be non-zero. As a result, RF homonuclear decoupling is generally combined with MAS in order to average out all the anisotropic interactions. Traditionally such CRAMPS[29] (combined rotation and multiple pulse spectroscopy) experiments have been performed using spinning rates of a few kilohertz, for which the MAS period is much larger than the period of the RF irradiation cycle. The dipolar Hamiltonian can be assumed to be constant over the RF period in this 'quasi-static' limit, which simplifies the task of devising suitable averaging sequences. Low MAS rates are essential when employing such decoupling sequences as resonant-like effects cause a collapse in performance when the MAS rotor period and RF cycle periods become synchronous (see Section 3.1).

The partial averaging of the chemical shift component of the Hamiltonian by the RF irradiation creates significant drawbacks for RF versus fast MAS-based approaches to obtaining high-resolution ^{1}H spectra. Writing the chemical shift Hamiltonian in the absence of RF decoupling as $H = \Omega\hat{I}_z$, where Ω is the precession frequency (in the rotating frame of reference), the average Hamiltonian (to first order) will have the form

$$\bar{H} = \mathbf{\Omega}\left(\lambda_x\hat{I}_x + \lambda_y\hat{I}_y + \lambda_z\hat{I}_z\right). \tag{4}$$

Note that this averaged Hamiltonian, $\bar{H}$, does not in general contain only an $\hat{I}_z$ term (corresponding to precession about z), but usually corresponds to precession about a tilted axis, z'. The averaged Hamiltonian in this tilted frame is

$$\bar{H}' = \lambda\Omega\hat{\mathbf{I}}'_z \quad \text{where } \lambda^2 = \lambda_x^2 + \lambda_y^2 + \lambda_z^2, \tag{5}$$

where λ is an effective scaling factor on the rate of precession, Ω. Tilted axis precession, illustrated in Figure 4A, significantly complicates the acquisition of artefact-free spectra.[30] Moreover, the scaling factor, λ, is very sensitive to the experimental conditions, in particular, the calibration of the RF nutation frequency (and indeed may vary with the offset Ω[31–33]). Hence, the frequency scale of CRAMPS spectra generally needs to be calibrated using a known system.

Figure 4 also illustrates different approaches used to observe the ^{1}H magnetisation under homonuclear decoupling. For direct acquisition (Figure 4B), the ^{1}H magnetisation is first tilted on to the tilted precession plane using a $\pi/2$ pulse (with phase matching the ϕ angle describing the orientation of the precession axis in xy so that the initial magnetisation is perpendicular to the precession axis). The NMR signal is then acquired in gaps ('windows') in the RF decoupling.

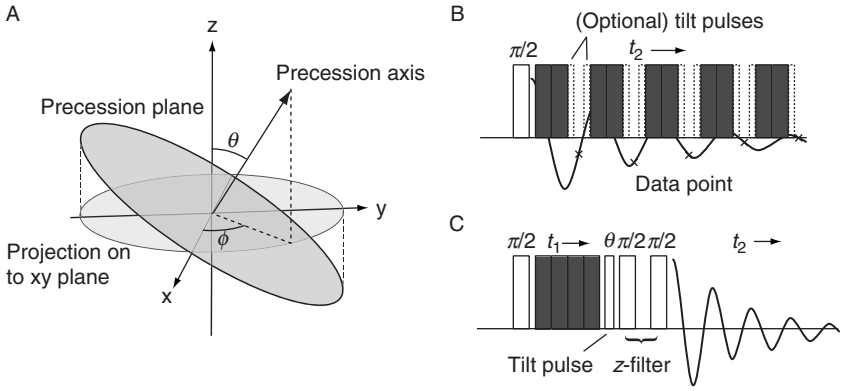

Figure 4 (A) Schematic of tilted axis precession under RF decoupling. The orientation of the precession axis, defined by the spherical angles θ and ϕ, varies with the decoupling sequence. (B) Schematic illustrating direct acquisition of the ^{1}H NMR signal using 'windows' inserted within blocks of windowless RF decoupling (grey blocks). (C) Acquisition under RF decoupling in the indirect dimension of a 2D experiment.

Windowed sequences, such as WHH-4,[34] contain delay periods which are sufficiently long for data acquisition. In contrast, 'windowless' sequences involve continuous irradiation and so acquisition windows must be inserted between decoupling blocks (illustrated as grey blocks in Figure 4). Tilted axis precession means that the magnetisation traces out an ellipse in the laboratory frame xy plane (Figure 4A), which leads to quadrature errors in the spectrum (i.e. artefact peaks at $-f$ for each genuine signal at frequency f). Quadrature artefacts can potentially be reduced by adding 'tilt' pulses either side of the acquisition, which temporarily restore the precession plane to xy prior to detection, although such pulses have been shown to have a deleterious effect on the decoupling.[35] Better alternatives include using phase cycling[30] or simply acquiring off-resonance and discarding the half of the spectrum containing the quadrature artefacts.

Correcting for the tilted axis precession is more straightforward if homonuclear decoupling is used in indirect dimensions. Figure 4C shows a typical pulse sequence for acquiring a high-resolution spectrum in f_1 (correlated with a normal MAS spectrum in f_2). As the decoupling is applied in a single block during t_1, there is no requirement to insert acquisition windows (or tilt pulses) in windowless decoupling schemes. Since inserting gaps without decoupling generally degrades performance, it is usually possible to achieve higher resolution spectra in indirect dimensions, at the expense of significantly increased experiment time. A subtle potential drawback of the sequence shown in Figure 4C is that the RF load (and consequent RF heating) changes as a function of t_1. Constant RF load sequences have been proposed to improve stability and reduce t_1 noise.[32]

It is also important to note that RF irradiation is subject to various experimental limitations that can have a significant impact on achievable resolution.[36–38] Inhomogeneity of the B_1 field means that the RF nutation rate cannot be set uniformly over an extended sample. This affects both the quality of decoupling, but also the λ

scaling factor; non-uniformity of λ will directly reduce the overall spectral resolution. The impact of RF inhomogeneity on CRAMPS experiments run in the quasi-static regime is typically minimised by constricting the sample to the central, homogeneous region of the coil, although there is evidence that MAS can strongly reduce the overall impact of RF inhomogeneity when used with sequences that are compatible with moderate to fast MAS rates.[35]

Another RF-related feature of homonuclear decoupling experiments is the presence of transient responses of the RF transmitter circuit to phase and/or amplitude changes. These transient responses, which have been measured directly and modelled for an RF irradiation scheme used for dipolar recoupling,[39] can be decomposed into a component with the same phase as the desired phase, and a 'quadrature' component 90° out of phase. The in-phase component leads to finite rise and fall times for amplitude of RF pulses. This does not itself significantly modify the spin dynamics, and the effects of the in-phase response are effectively folded into the optimisation of the RF nutation frequency. A significant quadrature component, however, will substantially modify the spin dynamics, and special 'tune up' sequences have often been used to help minimise the quadrature transient. The transient responses have an increasingly large impact on the overall pulse profile as ν_{rf} increases and individual pulses become shorter. This perhaps helps to explain the why a degradation of decoupling performance is commonly observed at very high nutation rates.[35,40] An extensive investigation of RF transients and their effects has been reported by Vega,[31] and it is also worth noting recent efforts to actively compensate for transient effects in order to generate more ideal pulse profiles.[41,42]

Given the number of features in play when RF homonuclear decoupling is being employed, the setup and optimisation of such experiments can be non-trivial, and a number of publications provide useful practical guides on classic CRAMPS experiments in the context of ^{19}F NMR,[43] and more recent experiments using ^{1}H homonuclear decoupling at higher MAS rates.[32,44,45] It is important to point out, however, that improvements in spectrometer technology have steadily simplified the task of effectively employing ^{1}H homonuclear decoupling. For example, relative phase accuracy[46] no longer needs to be adjusted. We also ignore here so-called console delays which result in an effective lag between phase and amplitude changes,[31,35] as these do not appear to be significant for current spectrometer designs. Finally, it is important to remember that homonuclear RF decoupling is still the approach of choice when optimal resolution is required. Figure 5 shows the resolution that can be achieved by applying RF decoupling in both direct and indirect dimensions compared to using fast (30 kHz) MAS.

2. HIGH-RESOLUTION ^{1}H SPECTRA WITHOUT RF DECOUPLING

In many important cases useful ^{1}H resolution can be obtained without RF homonuclear decoupling. This is more easily achieved for systems containing relatively dilute proton coupling networks (considered below) and/or using 'fast' or 'ultra-fast' MAS rates.

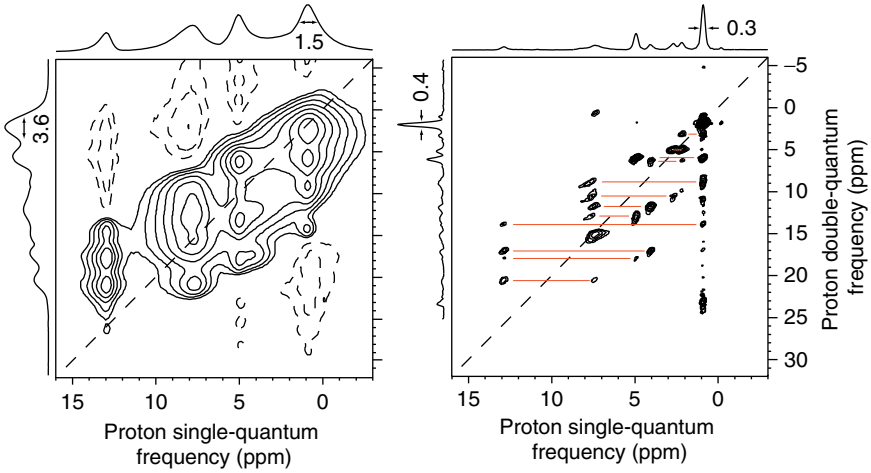

Figure 5 DQ/SQ ^{1}H correlation experiments on a small dipeptide using (left) 30 kHz MAS, and (right) 12.5 kHz + homonuclear decoupling (DUMBO) in both dimensions. See Section 4.3 for discussion of DQ/SQ correlation experiments. Figure adapted from results published in Ref. 47.

The technology for 'fast' MAS (up to 35 kHz), based on rotors of 2.5 mm external diameter, became available in the late 1990's.[48,49] Samoson and co-workers helped to drive progress to successively smaller and faster spinning modules.[9,50–52] Commercial MAS probes are now available, based on rotors with an external diameter of 1.3 mm, that have specified MAS rates of up to 67 kHz. Figure 6 shows an example of the resolution improvement that can be obtained from such ultra-fast MAS. Although the spectrum is far from liquid like, the different chemical sites are clearly resolved.

Fast MAS is particularly effective for samples where the coupling network is relatively weak in comparison with the dispersion of chemical shifts. In the limit where the difference in NMR frequencies exceeds the homogeneous linewidth, the linewidth is expected to decrease as the inverse *square* of the spinning rate.[53] For example, dramatic improvements in resolution as a function of MAS rate are often observed for paramagnetic systems (cf. Section 4.1), due to large paramagnetic contact shifts. High static magnetic fields also spread the range of frequencies and provide significant resolution improvements when coupled with fast MAS.[9,54] Very weak coupling networks are found in gel-like systems in which anisotropic molecular re-orientation almost averages out the anisotropic interactions. In these cases, only modest MAS of a few kilohertz is required to suppress the residual dipolar couplings and the susceptibility broadenings due to sample heterogeneity. Specialised HR-MAS (high-resolution magic-angle spinning) probes were initially developed to study organic molecules tethered to polymer beads[55] but are now routinely used to obtain high-resolution spectra from tissue samples[56] and food stuffs.[57] HR-MAS applications are not considered further.

A related route to obtaining high-resolution ^{1}H spectra is to weaken the dipolar coupling network by isotopic substitution with ^{2}H.[58,59] As predicted on theoretical grounds[7] and observed experimentally,[11] proton linewidths (or rather

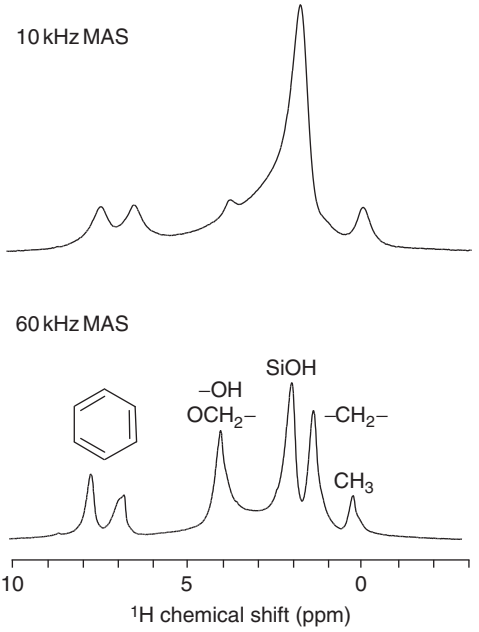

Figure 6 Illustration of the improved resolution obtained using ultra-fast (60 kHz) MAS on the ^{1}H spectrum of an organic fragment incorporated into a silica framework. Figure, which is based on results in course of publication, kindly supplied by Anne Lesage.

their homogeneous components) are found to depend approximately linearly on the proton density (expressed as a fraction of H sites), although the actual linewidth will depend on the exact pattern of isotopic substitution of nearby H sites. Reducing proton density by random isotopic substitution will naturally reduce the overall ^{1}H signal intensity (although this will be largely compensated by the reduced linewidth). In contrast, targeted substitution schemes can improve resolution without significantly compromising signal intensity. For example, an effective strategy in peptides is to make use of fully deuterated starting materials, but back-substitute exchangeable hydrogens (i.e. mostly amide NH in the backbone) by exchange in H_2O solution. ^{1}H spectra can then be obtained with excellent resolution from the amide protons with only minor loss of overall intensity.[27,60,61] Figure 7 illustrates the resolution improvements obtained on a model dipeptide. Note that it is necessary to apply broadband decoupling to ^{15}N for maximum resolution, using broadband sequences such as GARP[27] or WALTZ-16,[28] to remove the ^{15}N,^{1}H *J*-coupling. Additional gains in resolution (at the cost of sensitivity) have been obtained using H_2O/D_2O mixtures for the back-substitution and so diluting the ^{1}H coupling network further, with ^{1}H linewidths of less than 20 Hz reported.[12] Recent work has investigated the optimal conditions for the best overall resolution and sensitivity.[62] Alternative targeted substitution strategies for high-resolution ^{1}H NMR have also been proposed that do not involve exchangeable hydrogens.[63,64]

Finally it is worth noting alternative strategies to motional averaging. For example, the particles in colloidal suspensions may be sufficiently small that

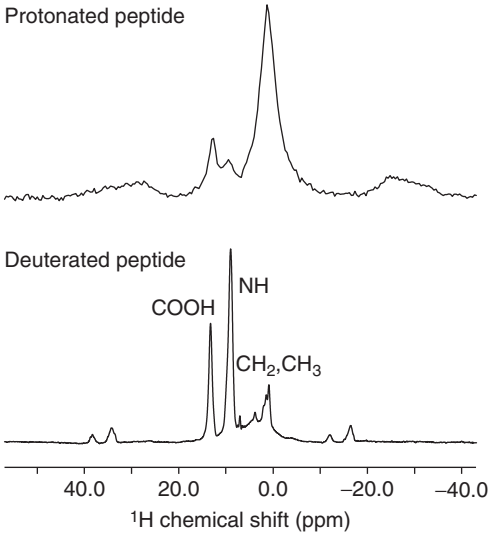

Figure 7 Enhanced resolution of exchangeable H sites obtained using deuterated peptides followed by back-substitution of ^{1}H. Figure based on results published in Ref. 60.

motional averaging leads to liquid-like spectra even though the NMR spectrum is of the solid material.[65] The difficulties of obtaining colloidal suspensions from general materials, however, limit the generality of this approach. Mounting a polymer sample on a piezoelectric oscillator plate has been shown to reduce ^{1}H NMR linewidths,[66] although the reductions were very modest in comparison to those achievable by MAS.

3. HIGH-RESOLUTION ^{1}H SPECTRA USING RF DECOUPLING

As discussed above, the best possible ^{1}H resolution for typical rigid solids at natural isotopic abundance is obtained using RF homonuclear decoupling, and considerable work has been done in the past decade to improve experimental methodology and understand the issues involved in obtaining high-quality ^{1}H spectra.[33,67] ^{1}H homonuclear decoupling is also important in other classes of experiments, such as Separated Local Field experiments to measure dipolar couplings involving ^{1}H nuclei,[68–70] but these other applications are not considered here.

3.1. General considerations

Before discussing individual RF decoupling sequences, we review recent literature covering theoretical methods and the general principles involved in analysing homonuclear decoupling sequences. The mechanics of the theoretical tools available have been discussed in detail by Vinogradov et al.[67] and only the key results are presented here. The focus is on decoupling schemes that are suitable for

moderate to fast MAS, which accounts for a large majority of solid-state NMR studies; 'classic' CRAMPS sequences designed for static or very slowly spinning samples such as BLEW-12[71] and BR-24[72] are much less effective under these conditions. It is, however, worth noting the more recent MSHOT[73,74] and EMSL-30 sequences,[75] which are designed for static or quasi-static applications. As well as being highly compensated, these sequences have the desirable property that the effective spin-lock axis is aligned along the z-axis, eliminating the problems associated with titled axis precession discussed in Section 1.2.

3.1.1. Design of homonuclear decoupling sequences for use under MAS

The traditional tool for the design and analysis of homonuclear decoupling sequences has been average Hamiltonian theory (AHT).[38,76,77] AHT was key to the development of decoupling sequences for the quasi-static regime, from relatively simple sequences such as WHH-4 to elaborate, 'supercycled' sequences such as BR-24.[72] This allows AHT to be used in a sequential fashion, that is, first evaluating the average Hamiltonian over the shorter timescale (of the RF), and then including the effect of the sample spinning. Under faster MAS the cycle times for the RF decoupling and sample rotation become similar, and it is no longer possible to decouple the timescales in this way.

Sequences intended to be used outside this quasi-static regime fall into one of two categories: those that are explicitly synchronised with MAS, with AHT being applied over the complete RF + spinning cycle, and non-synchronous sequences where more complex analytical tools, such as bimodal Floquet theory are required (see below). Levitt and co-workers have developed a useful formalism for the analysis of RF pulse sequences which involve explicit synchronisation of RF and rotation periods and which are based on a repeated phase-incremented pulse sequence element. A given sequence is characterised by a set of 'symmetry numbers'; XN_{κ}^{χ} denotes a basic element, X, that is repeated N times over κ rotor periods, with a phase increment of $2\pi\chi/N$. It is possible to select for and select against different NMR interactions in the final average Hamiltonian by appropriate choice of symmetry numbers. Although not in itself predictive of performance, this formalism provides a useful categorisation for rotor-synchronised sequences. For example, a semi-windowless WHH-4 sequence repeated four times per rotor period[78] would be classified $C4_1^0$, where the C ('cycle') indicates a base sequence with a net 0° rotation.

3.1.2. Analysis of homonuclear decoupling using Floquet theory

Many of the most widely applied homonuclear decoupling sequences are, however, not synchronised with rotation period. In the absence of a common repeat period, it is necessary to use some form of Floquet theory to analyse the spin dynamics.

In cases involving sample spinning alone, the Hamiltonian can be expressed as a simple Fourier series:

$$H(t) = \sum_{n=-2}^{2} H_n \mathrm{e}^{in\omega_r t}, \tag{6}$$

where the range of index n is appropriate for rank 2 spatial tensors, and $\omega_r = 2\pi\nu_r$ is the spinning frequency in angular units. In the presence of a periodic RF with cycle frequency ω_c, two indices are required:

$$\widetilde{H}(t) = \sum_{n=-2}^{2} \sum_{k=-\infty}^{\infty} \widetilde{H}_{n,k} e^{i(n\omega_r + k\omega_c)t}, \tag{7}$$

where k is the index for the Fourier series corresponding to the time-dependent RF. $\widetilde{H}$ indicates that the Hamiltonian is generally expressed in terms of an 'interaction frame' with respect to the RF (which is assumed to be the dominant term in the Hamiltonian). This involves using an axis system which is rotated in line with the effect of the RF. Generally RF pulse sequences for homonuclear decoupling are chosen to be 'cyclic' in the sense that this interaction frame returns to its starting point over the course of a full RF period, which ensures that the spin dynamics can be described by a well-defined effective Hamiltonian over the RF period. AHT is then used to determine analytical approximations to this effective Hamiltonian. Evaluating the spin dynamics is considerably more involved for non-cyclic sequences.[79]

Hence 'bimodal' Floquet theory has been widely to describe the spin dynamics for homonuclear decoupling using cyclic RF irradiation and sample spinning, although combinations of AHT and Floquet theory have also been used for cases where the evolution is sampled stroboscopically with the RF period.[80,81] The application of bimodal Floquet theory to homonuclear decoupling has been extensively described by Vega and co-workers[67,82–85] and so the details will not be discussed here. It is useful, however, to note some general features which emerge from these analyses. The resonance frequencies associated with a Hamiltonian of the form of Equation (7) will satisfy

$$\Delta\omega = \lambda_p - \lambda_{p'} + \nu\omega_r + \kappa\omega_c, \tag{8}$$

where p, p' are indices over the Hilbert space, λ_i are the eigenvalues of the Floquet Hamiltonian, and ν and κ are integers. This corresponds to a set of base frequencies and spinning/decoupling sidebands separated by multiples of both the spinning frequency and RF cycle frequency.

The Floquet treatment naturally explains the various 'resonance' conditions that can occur when multiple time dependencies are present.[82] One set of such conditions corresponds to

$$\nu\omega_r + \kappa\omega_c = 0, \tag{9}$$

that is commensurate relationships between spinning and RF cycle frequencies. Decoupling performance may be strongly degraded across the spectrum in this case. Figure 8 shows the simulated linewidth for a nine spin ^{1}H system under FSLG decoupling (cf. Section 3.2) and MAS. The unfavourable resonance conditions are sharp for ratios ω_c/ω_r of 3 and 4, while the resonances conditions at 1 and 2 are much broader and more difficult to avoid. Note that a multi-spin system is required for such simulations in order to reproduce the homogeneous character of the ^{1}H coupling network.

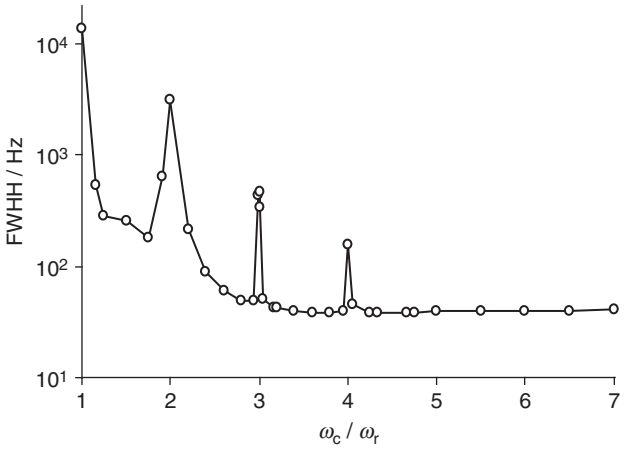

Figure 8 Linewidth of a simulated ^{1}H spectrum under $\nu_{rf} = 100$ kHz FSLG decoupling as a function of the ratio of RF cycle rate and MAS rotation rate. Figure adapted from results published in Ref. 35.

More perniciously, artefacts can also arise at specific frequencies satisfying

$$\nu\omega_r + \kappa\omega_c = \lambda_p - \lambda_{p'}, \tag{10}$$

that is where a line frequency coincides with a combination of rotor and cycle frequencies. This is analogous to 'rotational resonance' effects discussed in Section 1.1. These 'RF-rotor frequency' (RRF) lines are, however, more difficult to avoid and lead to additional sharp features interfering with genuine spectral features. These different resonant effects have been extensively analysed and investigated for the PMLG decoupling sequence,[82,83] but are expected to apply to all decoupling sequences. Indeed, RRF features can also be observed for rotor-synchronised sequences.[86]

3.1.3. Simulation of homonuclear decoupling

While Floquet theory is a powerful analytical tool for the treatment of periodic problems, it is less suited to spectral simulation.[67,87] Instead most simulations of RF decoupling employ direct integration of the density matrix propagator.[87–91] Where the Hamiltonian is continuously time dependent due to sample spinning, small timesteps (typically 1 μs) must be used to reproduce the spin dynamics faithfully. Since reproducing the homogeneous character of ^{1}H coupling networks requires the simulation of several spins, simulations of homonuclear decoupling under MAS are relatively expensive computationally, and most calculations have been performed with specialised codes that are optimised for large problems, such as SPINEVOLUTION[91] and pNMRsim.[92] A number of efficient algorithms have been developed to handle the time dependencies due to both RF decoupling and sample spinning.[35,93] In favourable cases, the RF and rotation cycle periods, τ_c and τ_r, are synchronous and it is sufficient to evaluate density matrix propagators

over the common period in order to characterise the spin dynamics, rather than integrate the density matrix evolution laboriously over each sampling dwell time. Where there is no obvious synchronisation between RF and rotation, it is generally possible to find an integer ratio M:N which is close to the desired ratio, τ_c/τ_r. The evolution can then be evaluated over the period $M\tau_r = N\tau_c$. This is particularly advantageous when simulating continuous phase-modulated decoupling sequences, since the evolution can be integrated over a single rotor period for a single reference phase, and the necessary step propagators obtained by 'phase shifts'.[35] As a result, it is now feasible to complement analytical explorations of decoupling on small spin system models with exact numerical simulations on larger, more realistic, spin systems.[35,83]

Note that multi-spin simulations are only required for modelling those aspects of the homonuclear decoupling experiment that involve the ^{1}H coupling network. Features, such as the direction of the effective spin-lock axis and chemical shift scaling under decoupling can be examined efficiently using single-spin simulations. For example, A. Vega analysed the effect of experimental imperfections on a variety of decoupling schemes, BLEW-12, DUMBO-1 and (in particular) PMLG, using single-spin simulations, concluding that the dominant factor determining ^{1}H resolution was the combined effect of pulse transients (specifically antisymmetric phase transients) and RF inhomogeneity.[31]

3.2. Decoupling with FSLG, PMLG and variants

The rest of this section focusses on the two most widely used and extensively studied families of decoupling sequences.

Lee-Goldburg (LG) decoupling involves RF irradiation that is $\Delta\nu = \nu_{rf}/\sqrt{2}$ off-resonance with respect to the ^{1}H NMR frequency, where ν_{rf} is the RF nutation rate. This results in a spin-lock axis inclined at the magic angle to the z-axis, and an effective precession rate of $\nu_{eff} = \sqrt{3/2}\nu_{rf}$. Basic LG decoupling only suppresses the homonuclear couplings to first order, and performance is considerably improved by alternating the sign of the frequency offset and inverting the RF phase after an integral number of precession cycles (duration $\tau_{LG} = 1/\nu_{eff}$). Not all spectrometer hardware can provide the necessary phase coherence through the frequency changes, and so this Frequency-Switched Lee-Goldburg (FSLG) decoupling is often implemented with a fixed on-resonance transmitter frequency and using explicit linear phase ramps to create the required frequency offsets.[68] As illustrated in Figure 10, the accumulated phase shift over a single LG step is $\tau_{LG}\nu_{eff} = 207.8^\circ$. Switching the sign of the offset reverses this phase trajectory after the 180° phase jump.

FSLG was initially applied in the context of heteronuclear problems, that is, observation of the heteronucleus while decoupling ^{1}H, with frequency switching every complete LG cycle.[94] Applications to directly detected ^{1}H spectroscopy, using windows inserted in a sequence with frequency switches after three LG cycles and performed under 3 kHz MAS, were less successful than existing CRAMPS sequences.[95] However, the short cycle of the FSLG sequence was subsequently shown to be compatible with moderately fast MAS (13 kHz), allowing

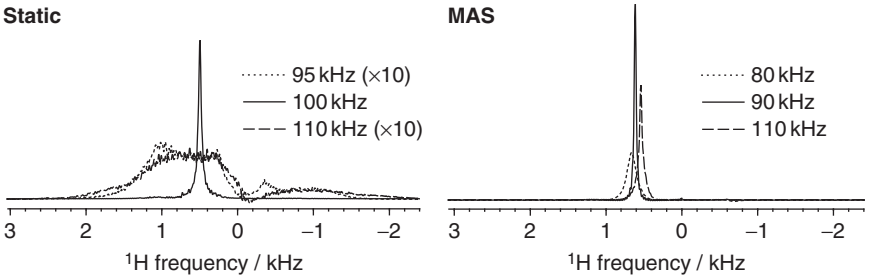

Figure 9 Simulation of the effects of deviation of the RF field strength from its nominal value on the ^{1}H spectrum of an adamantane-like spin system under FSLG decoupling: (left) static conditions, (right) under magic-angle spinning at 12 kHz. Timing parameters and RF offsets were set for $\nu_{rf} = 100$ kHz. Figure adapted from results published in Ref. 35.

well-resolved ^{1}H spectra to be obtained in the indirect dimension of HETCOR spectra[96] without the extensive tune-up associated with classic CRAMPS experiments. As shown in Figure 9, the performance of FSLG under static conditions is highly sensitive to the actual value of ν_{rf}, which translates to a high sensitivity to RF inhomogeneity.[95] These effects are greatly reduced when the sample is subject to MAS. Note how the optimum performance under MAS is obtained when the actual RF nutation rate is 'misset' (here by $\sim -10\%$) from expected value (although other studies have observed optimal nutation rates at higher ν_{rf}[97,98]).

Interest in LG decoupling was increased by the observation of S. Vega and co-workers that relatively coarse phase ramps were sufficient to obtain good decoupling performance from its on-resonance implementation.[99] This was termed PMLG*n* (Phase Modulated Lee-Goldburg), where *n* refers to the number of phase steps over the basic LG element. Effective ^{1}H resolution was observed for phase ramps as short as $n = 3$[82] over the phase excursion of 207.8°. Note that the scaling factor and precession axis orientation increasingly differ from their FSLG limits as *n* is decreased. The interaction between PMLG decoupling and MAS was extensively analysed using bimodal Floquet theory,[83] with the conclusion that the ratio of RF cycle and sample rotation frequencies, ω_c/ω_r, should exceed 3 to completely avoid resonant broadening effects (cf. Section 3.1).

Acquisition windows can be inserted between FSLG[100] or PMLG cycles[101] in order to obtain well-resolved directly acquired ^{1}H spectra under the conditions of moderately fast MAS with minor resolution loss. Although the performance losses for windowed PMLG (wPMLG) are relatively small, the addition of gaps into the continuous decoupling pulse train increases the impact of transient effects (cf. Section 1.2). The effects of such RF imperfections have been carefully analysed using numerical simulation of a model windowed PMLG sequence.[102] Strong deviations of the scaling factor and precession axis orientation were observed, both in simulation and experiment, for ^{1}H frequencies close to resonance. These effects were strongly asymmetrical, and markedly different spectral resolutions and artefact levels were observed depending on the position of the RF transmitter relative to the ^{1}H spectrum. Most notably, constructive interaction between the RF imperfections and decoupling at certain offsets resulted in an effective precession

axis close to the *z*-axis and improved resolution. Similar observations have been made by A. Vega in the context of PMLG applied in indirect dimensions,[31] implying that this is not purely an artefact of the acquisition windows in wPMLG. The interaction between RF irradiation, MAS, and RF imperfections for wPMLG were subsequently investigated in detail by both Floquet theory and extensive experimentation.[84] Although changing the sign of the transmitter offset and reversing the sense of the PMLG phase trajectory is expected to give equivalent overall decoupling performance, it was observed that better resolution was obtained with the transmitter to low frequency of the spectrum and an initial clockwise phase trajectory (the reverse of the trajectories shown in Figure 10). In this case, the difficult-to-decouple CH_2 resonances are well sited for the constructive interaction of RF imperfections and resonance offset.

It was subsequently determined that the favourable features associated with the constructive interaction of RF imperfections and decoupling could be selected for by combining two wPMLG blocks with inverted initial phases. As illustrated

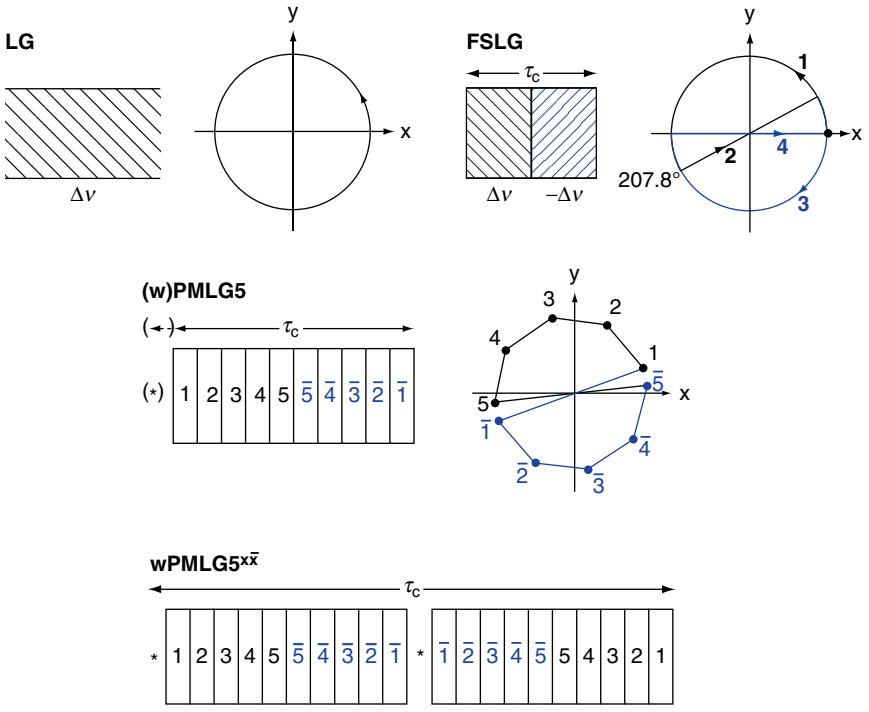

Figure 10 Schematic illustration of the family of LG decoupling sequences: LG, continuous off-resonance decoupling; FSLG, blocks with alternated sign of offset (and phase); (windowed) PMLG5, an on-resonance implementation of FSLG using five discrete phase steps per LG cycle (with optional acquisition window); wPMLG$^{x\bar{x}}$, windowed PMLG5 with phase-shifted initial signs (but consistent direction of phase increment). Asterisks mark acquisition windows. The diagram also illustrates the trajectories of the RF phase (with respect to the RF transmitter), that is, LG and FSLG involve continuous phase evolution, which is discretised in PMLG. Figure adapted from Ref. 33.

in Figure 10, wPMLG$^{x\bar{x}}$ involves an initial PMLG cycle starting with a phase of x followed by a subsequent PMLG cycle starting with $-x$ (but with the same sign of phase increment). This 'supercycle' resulted in a scaling factor and z-oriented precession axis which were essentially independent of offset,[103,104] and increased robustness with respect to variables such as resonance offset. The drawbacks are additional averaging resulting in a lower scaling factor of about 0.45 (compared to 0.61 for wPMLG[101]) and increased susceptibility to RRF artefacts (due to the longer cycle time). 'Supercycling' with steps of 120° changes the ω_c/ω_r ratio and leads to a pattern of interferences that is largely complementary to that associated with 180° phase steps.[113] Refs. 45 and 32 contain practical examples of using different LG-based decoupling sequences, together with helpful practical implementation details.

Finally, PMLG decoupling has been investigated at very fast sample spinning rates[105] (up to 65 kHz). Good decoupling could be obtained even at the highest spinning rates, although the RF nutation rate for optimal decoupling performance was found to increase monotonically with spinning rate, for example, $\nu_{rf} = 216$ kHz at 65 kHz MAS compared to 131 kHz at 35 kHz MAS. As shown in Figure 11, very similar resolution was observed for supercycled PMLG (wPMLG$^{x\bar{x}}$) and a supercycled version of DUMBO-1 (see below). Similar observations have been made in systematic studies of resolution at different static fields and spinning rates of up to 35 kHz,[54] with windowed wDUMBO tending to outperform wPMLG3. The reasons why PMLG decoupling is still effective at these high MAS rates has been investigated analytically and via numerical

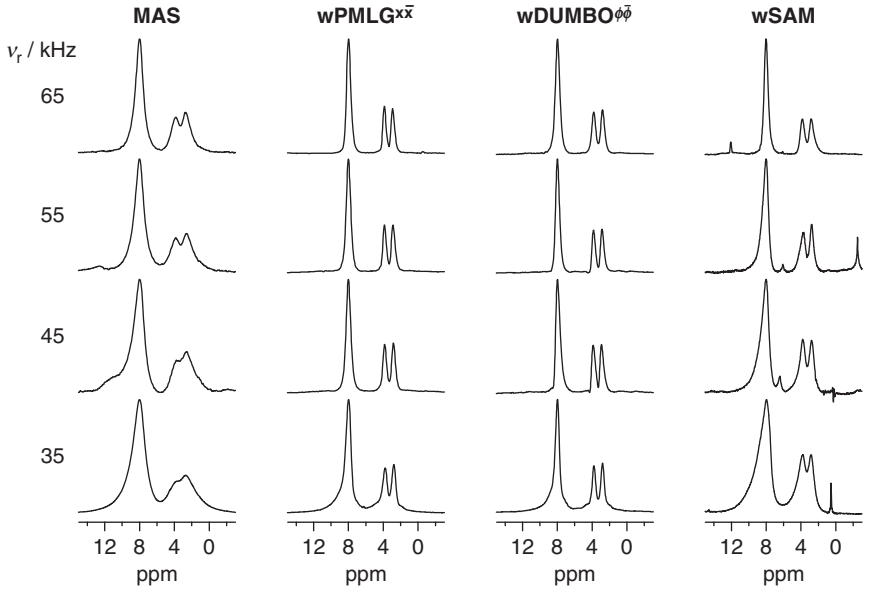

Figure 11 Decoupling performance as a function of MAS rate for supercycled versions of wPMLG5 and windowed DUMBO-1, plus the SAM scheme (see Section 3.4). Figure adapted from results published in Ref. 105. Note that the decoupling parameters (including RF nutation rate) were independently optimised for each spectrum.

simulation.[97] While the analysis shows an abundance of potentially deleterious resonance conditions when the RF cycle period is longer than MAS period ($\omega_c/\omega_r < 1$), simulations show that these resonance conditions become narrower and hence easier to avoid at fast spinning rates. Good resolution is obtained, for instance, at $\omega_c/\omega_r = 0.775$, that is, close to resonance conditions at 3/4 and 4/5. Although the resolution is not noticeably improved by the faster MAS, the viability of homonuclear decoupling under these conditions is important, as very fast MAS is required in some cases (e.g. paramagnetic systems considered in Section 4.1). Increasing RF nutation rates to stay within a quasi-static limit, say $\omega_c/\omega_r > 3$, is impractical both in terms of the power handling limits of the probes and the artefact levels expected with extremely short pulses (e.g. less than 200 ns for PMLG5 at $\omega_c/2\pi = 210$ kHz).

3.3. Decoupling with DUMBO and e-DUMBO

The other widely used sequence for homonuclear decoupling under MAS is the DUMBO sequence and its variants. The DUMBO sequences are windowless phase-modulated sequences, with the phase modulation, $\phi(t)$, described by a Fourier series

$$\phi(0 \le t \le \tau) = 360^\circ \left[C_0 + \sum_{n=1}^{N} C_n \cos\frac{2\pi n t}{\tau} + S_n \cos\frac{2\pi n t}{\tau} \right], \qquad (11)$$

where C_n and S_n are the Fourier coefficients (typically for $n = 1 \ldots 6$). C_0 determines the overall phase shift and is not relevant to the decoupling performance. In order to ensure cyclicity, the second half of the DUMBO phase modulation repeats the first half in reverse and phase shifted by 180°,

$$\phi(\tau + t) = \phi(\tau - t) + 180^\circ, \qquad (12)$$

with the overall duration of the DUMBO sequence being $\tau_c = 2\tau$. The time-reversal symmetry also ensures that odd-order terms in the Average Hamiltonian for the sequence are eliminated.[38] Note that the sequence is optimised in terms of discrete timesteps (typically 64 over τ_c), and a given set of coefficients is not necessarily optimal for a different discretisation.

The DUMBO-1 sequence[106] was obtained by optimising the simulated decoupling performance in a static two-spin simulation, starting from random coefficients, using a fixed cycle time of 30 μs at $\nu_{rf} = 100$ kHz (corresponding to a 6π overall rotation). This overall timing is the same as BLEW-12,[71] but the sequences are otherwise independent. The final optimisation measured decoupling performance (defined by the ratio of desirable to undesirable terms in the effective Hamiltonian over the cycle period) over a range of dipolar coupling values and RF nutation rates (corresponding to ±20% RF inhomogeneity). Although optimised for quasi-static conditions, and despite having a relatively long cycle time in comparison with FSLG and related sequences, DUMBO-1 has been found to be effective at relatively fast MAS rates; indeed signal intensities (although not

resolution) were found to increase by more than a factor of 3 on going from 10 kHz MAS ($\omega_c/\omega_r = 3.1$) to 22 kHz MAS ($\tau_c/\tau_r = 1.4$).[44] These gains in signal intensity could partially result from improvements in lineshape,[107,108] but are suggested to mostly result from suppression of decoupling sidebands.[109,110] Ref. 44 provides a helpful practical guide to the optimisation of homonuclear decoupling experiments involving tilted axis precession, with the focus on DUMBO.

Given the number of factors determining the performance of homonuclear decoupling, including experimental features such as pulse transients, there are significant advantages to optimising decoupling sequences directly on the spectrometer. This is particularly natural for sequences parameterised in terms of Fourier series, as previously demonstrated for heteronuclear decoupling.[111] For simplicity, initial optimisations of DUMBO-type sequences were performed using observation of a $^1J_{CH}$ coupling on ^{13}C, and optimising the overall intensity and 'quality' of the J doublet.[112] Refinement of the DUMBO-1 coefficients at 22 kHz MAS produced a phase modulation, e-DUMBO-1_{22}, that was effective over a range of MAS rates, and provided improved resolution (down to 0.2 ppm at a ^1H frequency of 700 MHz) compared to DUMBO-1.

The performance of e-DUMBO-1_{22} and DUMBO-1 has also been evaluated under ultra-fast (65 kHz) MAS and $\nu_{rf} = 170$ kHz. Note that experimental optimisation suggested a significantly shorter cycle time than that expected from the quasi-static limit (20 vs. 30 μs). The shorter cycle time and the ability of ultra-fast MAS probes to support high ν_{rf} values meant that the ω_c/ω_r ratio was only 0.77 at the fastest MAS rate. As observed for PMLG decoupling,[97] resolution at 65 kHz was at least no worse than at more modest spinning rates. DUMBO sequences can also be 'supercycled'[97,113] to create z-rotation sequences, although the scaling factor is strongly reduced, making it difficult to match the resolution of spectra obtained with conventional DUMBO-1.

3.4. Other approaches to homonuclear decoupling under MAS

In one of the earliest studies of homonuclear decoupling under moderate to fast MAS, Hafner and co-workers tested various pulse sequences with short cycle times under conditions of moderate (14.3 kHz) MAS.[114] Respectable performance was obtained using semi-windowless WHH-4 in an indirect dimension, without extensive spectrometer tune up or particularly strong RF nutation rates ($\nu_{rf} = 93$ kHz), relying instead on MAS to suppress incompletely averaged dipolar couplings and to compensate for the lack of supercycling. This was later extended to direct CRAMPS-style acquisition.[78] The interaction between the MAS and decoupling was analysed more formally, using a combined AHT-Floquet theory approach,[80] where it was demonstrated experimentally that MAS had a favourable impact on resolution up to ratios of RF cycle time to rotor periods of $\omega_c/\omega_r \approx 3$, with a complete breakdown of decoupling at $\omega_c \approx 2\omega_r$. The AHT-Floquet theory approach was more successful in describing the experimental results than simple AHT, although quantitative agreement was not expected due to the assumptions involved, for example, delta-function pulses. This approach to homonuclear decoupling has been summarised and reviewed in Ref. 81.

A number of groups have tackled the problem within the framework of the Levitt's symmetry approach to the design of rotation synchronised pulse sequences (cf. Section 3.1). The initial 'C' sequences were designed for homonuclear recoupling,[115] but C-type sequences based on 2π rotation elements that eliminate the homonuclear couplings also suppress chemical shift evolution from the average Hamiltonian, making them unsuitable for obtaining resolved ^{1}H NMR spectra.[67] Subsequent 'R' sequences, based on composite-pulse inversion pulses, were argued to be better suited to decoupling applications,[116] including under fast[117] and ultra-fast[186] MAS conditions, Simultaneous L^{12}.

These R sequences are found to give comparable performance to wPMLG$^{x\bar{x}}$. While the z rotation axis of wPMLG$^{x\bar{x}}$ is convenient for direct detection experiments, the x rotation axis of these R sequences is convenient for indirectly acquired spectra.[185] Other sequences have been developed of the type $CN_{\kappa}^{N/2}$, where the C element involves an overall 0° rotation. This rotation is implemented as either a pair of matched pulses of opposite phase,[118] or using a 'smooth amplitude modulated' (denoted SAM) variant in which the amplitude is cosine modulated.[119] This reduces both the pulse transients associated with 180° phase changes and the root-mean-square RF power required. These sequences also have an effective spin-lock axis aligned with the z-axis. In contrast to phase-modulated sequences, in which the chemical shift scaling factor is essentially fixed, the scaling factor of these amplitude modulated sequences is strongly dependent on the RF nutation frequency (which determines the depth of the modulation), and there is an optimum ν_{rf} which balances the efficiency of homonuclear decoupling against the chemical shift scaling factor. This approach has been analysed in detail in Ref. 86, focussing on fast (>30 kHz) MAS.

4. TECHNIQUES AND APPLICATIONS

4.1. Applications

The limited resolution of ^{1}H spectra in typical organic solids has often restricted ^{1}H solid-state NMR to wideline measurements of relaxation times, or using the width of the ^{1}H spectrum as a metric of dynamics. The resolution improvements provided by higher static magnetic fields, fast MAS and efficient, robust homonuclear decoupling sequences mean that useful resolution can now be obtained without considerable experimental effort. ^{1}H NMR has been used as a characterisation tool for a wide range of materials, and this section highlights a selection of applications where the advantages of ^{1}H NMR are especially evident. See also Ref. 120 for an excellent overview of the range of applications of ^{1}H and other spin-1/2 NMR in studies of the solid materials and Ref. 121 for a comprehensive review of applications of spin-1/2 NMR to polymeric and supramolecular systems.

4.1.1. Paramagnetic materials

The combination of large hyperfine shifts with intrinsically broad lines due to homonuclear dipolar coupling has generally meant that ^{1}H NMR of paramagnetic systems has been relatively uninformative; spectra obtained with moderate MAS

are dominated by extensive spinning sideband manifolds, while the wide frequency dispersion has limited the effectiveness of typical ^{1}H homonuclear decoupling schemes. However, Ishii and co-workers demonstrated that very fast MAS (greater than 20 kHz) allowed useful resolution to be obtained for the dilute spins of paramagnetic compounds without the use of RF decoupling.[122] As shown in Figure 12, dramatic improvements in ^{1}H resolution were also observed under these conditions.[123] The rapid sharpening of the spectrum with increasing MAS rate, coupled with intrinsically short spin–lattice relaxation times, meant that spectra with good sensitivity could be acquired in a short period. Moreover, the RF efficiency of ultra-fast MAS probes permits the use of very short duty cycles without the risk of excessive RF heating, which, combined with the very small sample volumes required, is a major advantage for studies of paramagnetic protein samples.[124]

Magnetic susceptibilities are often strongly anisotropic in paramagnetic complexes, and so the ABMS (cf. Section 1.1), rather than short T_2 relaxation times, is frequently the dominant source of ^{1}H linewidths. Heteronuclear correlation spectra are then particularly useful in resolving the features of the ^{1}H spectrum.[125] Although suitably adapted pulse sequences are required, for example, for broadband inversion,[126] to deal with the wide frequency ranges encountered, considerable progress now has been made in obtaining high-resolution ^{1}H 1D and 2D spectroscopy of paramagnetic solids.[127]

4.1.2. Materials characterisation

^{1}H is a particularly useful NMR nucleus for the study of hydrogen-containing species on surfaces of porous materials, such as zeolites, due to its high receptivity and the relatively dilute nature of the homonuclear coupling network. For example, ^{1}H spectra from olefin metathesis catalysts absorbed on silica could be

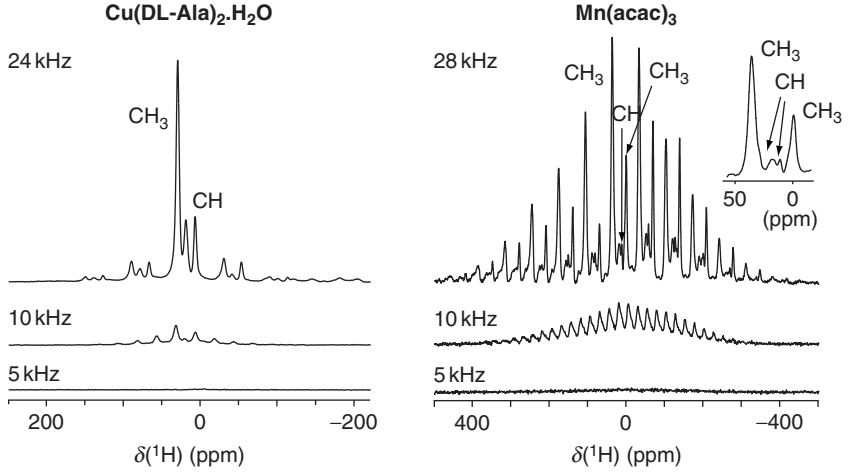

Figure 12 ^{1}H NMR spectra of two solid paramagnetic complexes as a function of magic-angle spinning rate. Figure adapted from data published in Ref. 123.

obtained using just MAS at 12.5 kHz.[21] A combination of experiments, including ^{15}N,^{1}H HETCOR, ^{1}H double-quantum (DQ)/SQ and triple-quantum (TQ)/SQ correlation spectra (see Section 4.3), have been used to probe the mechanism of supported organometallic catalyst.[128]

Similarly hybrid materials produced from sol-gel synthesis and related self-assembly techniques are excellent targets for high-resolution ^{1}H NMR studies, not least because such materials generally lack the long-range ordering required for Bragg diffraction. NMR can provide valuable local information, including about interactions between the organic guest and inorganic host. For instance, ^{1}H DQ/SQ correlation spectra have been used to reveal interaction between surfactant H sites and silanol protons on self-assembled silicate films,[129] and hydrogen bonding in self-assembled monolayers,[130] while ^{1}H spin diffusion has been used to explore longer range distances in inorganic/organic hybrid materials.[131] Figure 13 illustrates the resolution can be obtained using fast MAS in this type of sample.

^{1}H resolution using fast MAS is also important in ^{1}H,^{13}C correlation experiments on functionalised mesoporous silicas,[133] including spectra obtained with increase sensitivity by inverse detection on ^{1}H[134,135] (cf. Section 4.2). Solid-state NMR studies, including ^{1}H NMR, for sol-gel-derived materials have recently been reviewed,[136] while techniques for probing H,H proximity have been extensively reviewed by Brown.[137]

Gels themselves are also attractive subjects for ^{1}H NMR studies due to the partial averaging of dipolar coupling network due to molecular motion. For example, in one recent study moderate (10 kHz) MAS resolved ^{1}H signals from

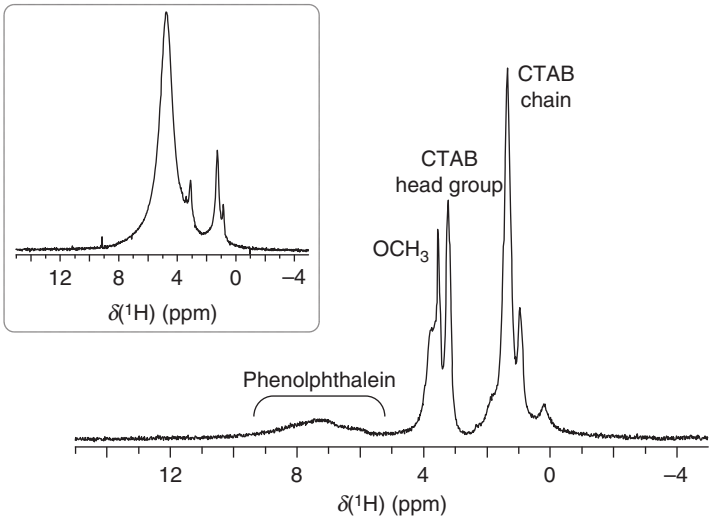

Figure 13 ^{1}H MAS spectra of a hybrid material formed between an organic pH indicator (phenolphthalein), a silica matrix and an amphiphile (CTAB) obtained at 14.1 T and $\nu_r = 30$ kHz. The combination of fast MAS and high static field significantly improves the ^{1}H resolution over the spectrum obtained at 7 T and $\nu_r = 15$ kHz MAS (inset), especially for the more mobile amphiphilic component. Figure adapted from data published in Ref. 132.

polymer host and small molecule guest.[138] wPMLG homonuclear decoupling provided further line narrowing of the polymer resonances, whose resolution is largely limited by inhomogeneous factors. Having resolved host and guest resonances, spin diffusion build-ups could then be used to probe host-guest interaction.

4.1.3. Characterisation of hydrogen bonding

Another major strength of NMR over X-ray diffraction studies is its sensitivity to hydrogen bonding,[139] which plays in crucial structural role in a wide variety of chemical systems. The single electron of the hydrogen atoms means that H atoms are easily misplaced, while NMR spectra, coupled with first principles calculation, can readily distinguish between incorrect and correct sitings.[8] ^{1}H NMR has also been widely used to probe hydrogen bonding in non-crystalline systems, including in complex polymer systems containing exchangeable water.[22,140] O···H hydrogen bonds are especially amenable to ^{1}H NMR studies as their shifts are usually distinctive; indeed the lack of chemical exchange in the solid state means that δ_H values in excess of 20 ppm may be observed, with the exact shift value depending on the strength of the hydrogen bond. Correlations between ^{1}H NMR parameters and O···O and H···O distances in O–H···O, in particular, have been extensively studied and reviewed.[141–143]

While compilations of observed shifts for a variety of systems have been the primary source of such correlations, advances in DFT-based first principles calculation mean that it is now feasible to establish more detailed and precise relationships between structure and NMR observables for individual chemical systems. Structural hypotheses can then be tested against ^{1}H NMR data, as demonstrated for a number of macromolecular systems by Spiess and co-workers.[49,144] Other examples of the use of first principles calculations include characterising silanol resonances in polysiloxane networks,[145] probing the effects of hydrogen bond directionality,[146] investigating weak hydrogen bonding[147] and characterising host-guest interactions using ^{1}H shifts.[148]

This is illustrated in Figure 14 for N–H···O hydrogen bonding. A subtle, but distinct, difference (of 0.5 ppm) is noted in the shift of the resonance corresponding to the hydrogen bond formed between molecular dimers in the two polymorphic forms of methylnitroacetanilide (MNA). Calculation of the ^{1}H shift as a function of the hydrogen position within the N–H···O bond provided a calibration curve yielding N–H distances of 1.03 Å (white) and 0.99 Å (yellow) with an estimated accuracy of ± 2 pm. This calibration was verified using the ^{1}H spectrum of histidine hydrochloride (Figure 14B); the predicted distances of 1.08 and 1.015 Å for the two distinct hydrogen bonds were in excellent agreement with neutron diffraction studies. Note that the corresponding distances determined by X-ray diffraction were systematically too short, and better agreement was obtained with the neutron diffraction results using the ^{1}H chemical shifts in this way than from earlier solid-state NMR studies measuring ^{15}N,^{1}H dipolar couplings.

Note that intermolecular hydrogen bonding is, by definition, very sensitive to intermolecular interactions and so it is generally necessary to use codes that include the periodicity of the crystal lattice using periodic boundary conditions.[151]

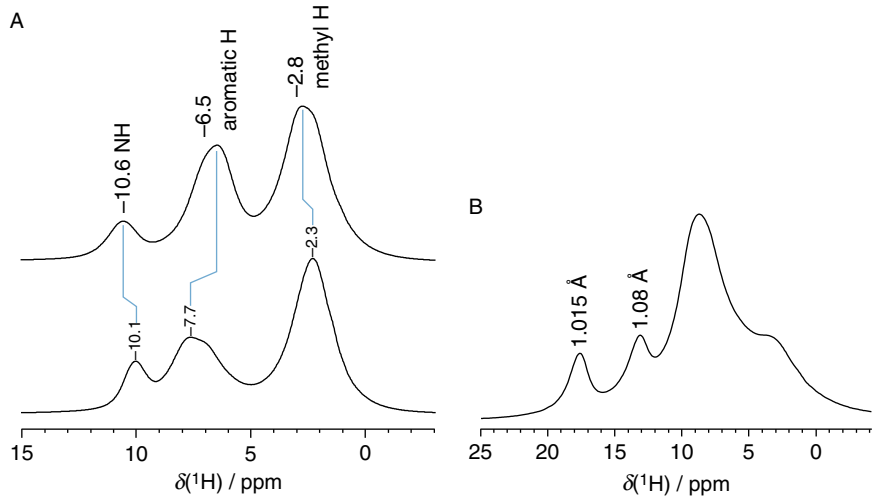

Figure 14 (A) ^{1}H NMR spectra of (top) white and (bottom) yellow forms of methylnitroacetanilide (MNA) obtained at 500 MHz and a spinning rate of 27 kHz. (B) ^{1}H spectrum of L-histidine hydrochloride hydrate obtained under the same conditions. Figures in (B) show estimated N–H hydrogen bond distances for the two distinct hydrogen bonds in the structure, using a calibration curve determined from calculations on the MNA dimer. Figure adapted from data published in Refs. 149 and 150.

For example, calculation of the ^{1}H spectrum of L-histidine hydrochloride considering an isolated molecule was much less successful, in particular for the hydrogen-bonded sites, than a calculation using periodic boundary conditions.[152]

4.1.4. Structure determination from ^{1}H NMR data

One of the most intriguing applications of the resolved ^{1}H solid-state NMR spectra is to the determination of crystal structures using microcrystalline powder samples. Determining structures of molecular solids from X-ray powder diffraction (XRPD) data is extremely challenging for all the simplest cases with few degrees of freedom. While considerable progress has been made towards establishing protein structures by solid-state NMR, obtaining crystal structures for small organic molecules is arguably a harder task. Isotopic enrichment is rarely realistic for synthetic small molecules, and the central problem is to establish sufficient intramolecular relationships to determine the 3D packing rather than just determining molecular conformation (the essential requirement for protein structures is to establish the fold, e.g. using intramolecular proximity information). ^{1}H NMR is well placed to determine these intramolecular relationships; ^{1}H shifts, and in particular those affected by hydrogen bonding, are expected to be sensitive to molecular packing, while dipolar couplings can potentially provide estimates of intermolecular distances or indicate 'contacts'.

The complementary information content of ^{1}H versus ^{13}C chemical shifts means that ^{1}H, ^{13}C correlation spectra are invaluable tools to assigning spectra

from molecular organic solids at natural abundance. Considerable progress has been made towards developing experimental protocols for the assignment of ^{1}H and ^{13}C spectra.[153,154] Provided sufficient ^{1}H sites can be resolved and assigned, it is then feasible to use spin diffusion rates as a proxy for distance information.[155] Exact modelling of spin diffusion in extended networks is a formidable challenge, but it was found that the spin diffusion build-up curves could be fitted well in terms of an exchange matrix K with elements $K_{ij} = d_{\mathrm{rss},ij}{}^{2}$, where $d_{\mathrm{rss},ij}{}^{2}$ is the root-sum-square dipolar coupling between sites of type i and type j.[156] Although phenomenological, this model is consistent with the use of d_{rss} as a metric of local coupling strength[14] and with theoretical work on spin diffusion. The d_{rss} values were calculated from the known crystal structure of the dipeptide model, and it was found that couplings up to a distance of 6 Å (or up to 15 Å in a later study on thymol[157]) needed to be included in order to converge the root-sum-square coupling and obtain good fits for the experimental build-up curves. Using information on the geometry and symmetry of the unit cell (which can often be obtained from XRPD, even in cases where the structure cannot be solved), a molecular modelling protocol was used to find candidate arrangements of the dipeptide with the unit cell that were consistent with the proton spin diffusion data. The ensemble of 16 lowest energy structures was in general agreement with the known crystal structure, although some regions, such as carboxylic acid groups, were poorly constrained by the spin diffusion data. However, subsequent refinement of these structures using DFT-based first principle calculations[158] yielded a final solution that was in excellent agreement (0.13 Å rms deviation) with structure determined by X-ray diffraction. This overall 'protocol' for structure determination using ^{1}H spin diffusion, molecular modelling and first principles calculation was subsequently demonstrated on thymol.[157] It was noted that the ^{1}H data were key to correctly describing the hydrogen-bonding arrangement and for providing good starting points for the final DFT refinement step.

Advances in computation of chemical shifts referred to above make it feasible to calculate expected NMR parameters for potential structures, and the direct use of ^{1}H and ^{13}C shifts in the *ab initio* determination of the crystal structures has recently been demonstrated.[159] Crystal structure prediction (CSP) protocols were used to generate plausible crystal structures for thymol (assuming only that there is a single molecule in the asymmetric unit and limiting the space groups considered to the seven most commonly encountered). ^{1}H and ^{13}C chemical shifts were calculated for the 23 lowest energy structures and the root-mean-square deviation between calculated and experimental shifts determined. One structure clearly provided the best match with the experimental shifts. This was not the lowest energy structure predicted by CSP, but it agreed perfectly with the XRD structure (0.29 Å rms deviation) and with the previous study incorporating spin diffusion data noted above. As shown in Figure 15, the ^{1}H shifts exhibited a much larger dispersion as a fraction of the shift range and were significantly more determinant. This is consistent with the idea that ^{1}H is highly sensitive to intermolecular interactions. Note that assignment of the ^{1}H resonances was not required, but obviously high-resolution ^{1}H spectrum is essential (in this case provided by MAS at 60 kHz at a nominal frequency of 900 MHz).

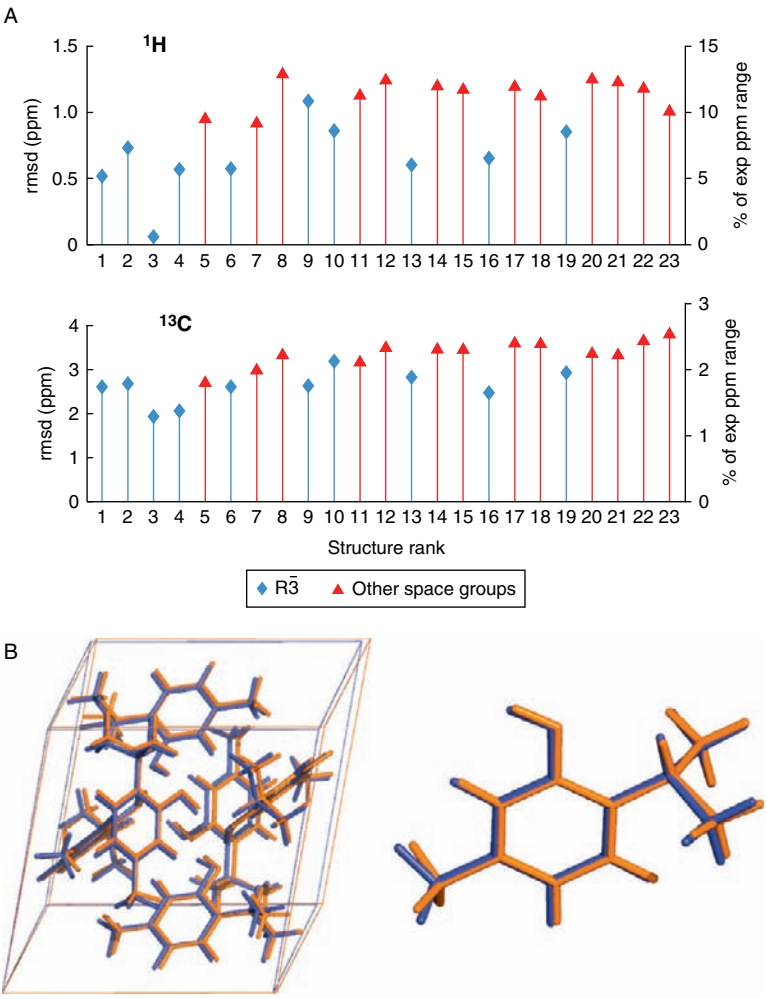

Figure 15 Crystal structure prediction of thymol on the basis of ^{1}H and ^{13}C chemical shifts. (A) RMS deviation between calculated and experimental shifts for different energetically plausible structures derived from *ab initio* CSP. (B) Comparison of the structure predicted by CSP + solid-state NMR (blue) with the known structure (orange). Figure adapted from data published in Ref. 159. (For interpretation of the references to colour in this figure legend, the reader is referred to the Web version of this chapter.)

4.2. Inverse detection to enhance sensitivity

It is common in solution-state NMR for nuclei such as ^{13}C to be detected indirectly, that is, magnetisation is transferred onto ^{1}H and detected at the ^{1}H frequency rather than directly at the ^{13}C frequency. The 'enhancement factor' of the spectral sensitivity for such 'inverse' detection has the functional dependence[160]

$$\zeta \propto \left(\frac{\gamma_H}{\gamma_C}\right)^{3/2}\left(\frac{W_C}{W^H}\right)^{1/2}, \tag{13}$$

where γ_X and W_X are the magnetogyric ratio and linewidth of nucleus X. The large magnetogyric ratio of ^{1}H leads to a significant sensitivity advantage for indirect detection, provided that $W_C \sim W_H$. In solid-state NMR, however, the much greater linewidths of ^{1}H resonances have meant that indirect detection is actually less efficient than simple direct detection.

If, however, the ^{1}H linewidth is sufficiently reduced by fast MAS and/or dilution of the coupling network, inverse detection may become a viable alternative. A number of researchers have investigated these potential sensitivity advantages, particularly in the context of heteronuclear correlation experiments on biomolecular solids. In principle, RF decoupling could also be used for linewidth narrowing. However, the use of CRAMPS-style acquisition is generally associated with significantly increased noise levels[120] and the literature examples to date have exclusively used fast MAS to achieve the necessary ^{1}H resolution.

Rienstra and co-workers obtained sensitivity enhancements of a factor of 18 using inverse detection and a probe optimised for ^{1}H detection to acquire highly resolved 3D spectra from less a micromole of an isotopically diluted protein sample.[161] Noting that ^{1}H back-substitution is not always practical for some protein systems, the same group obtain a factor of 14 enhancement in a fully protonated protein sample spinning at 40 kHz[162] (using a conventional solenoid coil). Reif and Griffin[27] observed enhancement factors of greater than 5 for ^{15}N inverse detection on isotopically diluted samples at a modest MAS rate of 13.5 kHz. Intermediate enhancements have been observed at 20 kHz MAS[28] and using heteronuclear recoupling sequences to transfer coherences,[163] an approach which is readily combined with heteronuclear distance measurement.[164]

As would be expected, more modest enhancements are observed for inverse detection of ^{13}C, due to its larger magnetogyric ratio, but these are still sufficient to result in reductions of experiment time of the order of 5–10.[134,165] Very similar improvements were observed in experiments using coherence transfers based on J rather than dipolar couplings.[166] Since J-based coherence transfers (here using refocussed INEPT) involve longer mixing periods, fast MAS is essential to slow down the dephasing of ^{1}H spin system; it was estimated here that the increase in ^{1}H decay rates in lowering the MAS rate from 40 to 20 kHz would have eliminated the advantage of inverse detection. The sensitivity advantage of inverse detection has also been used to obtain ^{13}C,^{1}H HETCOR experiments from very small quantities (4 mg) of pharmaceutical materials at natural isotropic abundance.[167] ^{13}C,^{1}H inverse spectroscopy has also been demonstrated using solely ultra-fast (60 kHz) MAS for ^{1}H decoupling.[23] The shorter INEPT sequence is more efficient than refocussed INEPT, but precludes heteronuclear decoupling (beyond a simple refocussing pulse) in t_1. The resulting loss of resolution largely negates the advantage of inverse detection for normal crystalline solids, but this is much less relevant to samples where the ^{13}C linewidth is largely determined by inhomogeneous factors; enhancements of an order of magnitude were observed on a

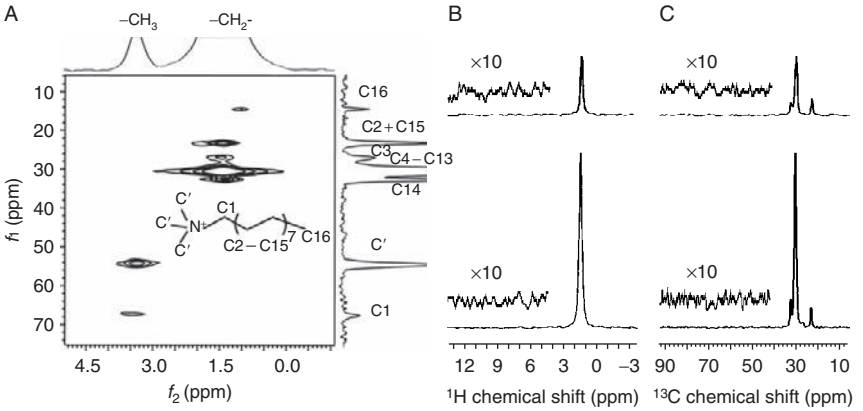

Figure 16 (A) ^{1}H-detected ^{1}H, ^{13}C correlation spectrum of a surfactant templated mesoporous silica obtained in 50 min at 40 kHz MAS and using refocussed INEPT for polarisation transfer. Cross-sections along (B) ^{1}H and (C) ^{13}C dimensions show the improved sensitivity of indirectly detected spectra (bottom traces) over the corresponding ^{13}C-detected spectra (top traces). Figure adapted from results published in Ref. 135.

sample of spider silk.[23] As shown in Figure 16, an INEPT-based ^{1}H-detected experiment provided significant (factor of 3) sensitivity gains for an inorganic/organic hybrid material at $\nu_r = 40$ kHz,[135] where inhomogeneous contributions to linewidth are also expected to be significant. Indirect detection on extremely small (nanolitre) samples has also been demonstrated in experiments with microcoils under MAS.[40] Note that care is required to minimise t_1 noise in inverse detection experiments, for example, by suppressing the substantial ^{1}H background signal and maximising RF stability.[28,134,167,168]

4.3. Multiple-quantum spectroscopy

The strong dipolar coupling network present in typical organic molecules is largely responsible for the difficulty of obtaining high-resolution ^{1}H spectra in solids. On the other hand, these same dipolar couplings are a potentially rich source of information about spatial proximity.[137,169] The most straightforward means of obtaining such information is via the excitation of multiple-quantum coherences, particularly DQ coherences. The strong dependence of the dipolar coupling with distance (as $1/r^3$) means that DQ coherence is only created between ^{1}H pairs that are in close proximity. In typical organic compounds, this implies that correlation peaks will only be observed for interproton distances up to about 3 Å,[137,170,171] with the strength of the dipolar coupling controlling the initial build-up rate of the correlation peak intensity.

The most common means of exploiting DQ coherences is via DQ/SQ correlation experiments. The pulse sequence for this experiment is illustrated schematically in Figure 17A. 'Recoupling' sequences designed to re-introduce dipolar couplings under MAS are used to convert initial equilibrium z-magnetisation into DQ coherence; the DQ coherence evolves during t_1 before being reconverted

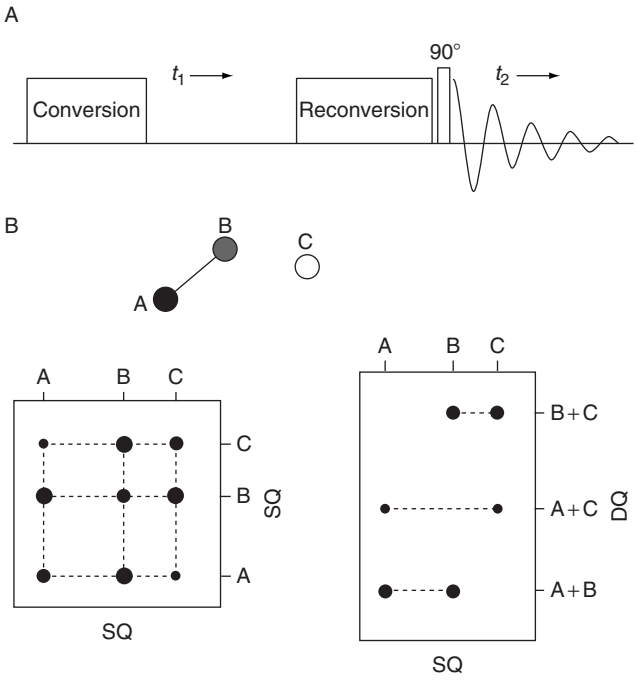

Figure 17 (A) Schematic of pulse sequence used to obtain DQ/SQ correlation spectra. (B) Illustration of the different correlation patterns obtained using SQ/SQ versus DQ/SQ correlation experiments. The size of the correlation spots indicates the dependence of the intensity of the correlation peaks on dipolar coupling (and hence distance) between the spins involved.

to z-magnetisation by a second, matching recoupling block. A 90° read pulse transfers this z-magnetisation into observable -1 coherence for detection. The conversion between z-magnetisation and DQ coherence is never 100% efficient, not least because it is impossible to optimise conversion simultaneously for all crystallites, but high receptivity of ^{1}H means that this is not a significant drawback. The excitation of multiple-quantum coherences using recoupling sequences and the quantitative applications of multi-quantum spectroscopy are not considered here (see Refs. 121,137,172,173 and references contained within).

Figure 17B contrasts the appearance of DQ/SQ spectra with SQ/SQ correlation spectra from EXSY/NOESY-like experiments. Unless DQ filtration is used,[17] SQ/SQ experiments always contain diagonal peaks. Given the limited resolution of solid-state ^{1}H spectra, these are likely to overlap with correlation peaks of interest. In contrast, only correlation peaks appear in DQ/SQ spectra. Diagonal (autocorrelation) peaks will only be observed if a DQ coherence can be created between a pair of like spins. Similarly TQ coherences are only generated between triples of adjacent spins, and TQ/SQ correlation experiments can provide further complementary information.[128,170,174,175]

The factors determining resolution in the DQ dimension are essentially the same as those considered above, and various combinations of fast MAS and/or RF

decoupling have been used to obtain useful 2D spectra. Incorporating windowless decoupling sequences into the indirect, DQ dimension is straightforward, but, as previously illustrated in Figure 5, the best possible resolution is obtained using CRAMPS in both dimensions.[47,176] Figure 18 illustrates the information content of the resulting 'DQ CRAMPS' experiments, showing how a pair of pseudopolymorphs can be readily distinguished using the 2D correlation pattern. This pattern is also easily observed in the formulated product, where the presence of additional peaks from the excipients would make identification of the polymorph less than certain. Similar information would be provided by ^{13}C spectra, but the DQ CRAMPS experiment has the merit of also providing direct information about the different pattern of hydrogen bonding in the two forms (giving rise to the highlighted correlation peaks at DQ frequencies of 18.0 vs. 20.1 ppm).

Note that 1D multiple-quantum filtered spectrum, which corresponds to only acquiring the first row of a multiple-quantum/SQ correlation experiment, can be a valuable tool in itself for heterogeneous systems. The DQ filtered (DQF) spectrum will be dominated by more rigid components with relatively strong dipolar couplings in comparison with normal SQ experiment. For example, 1D and 2D

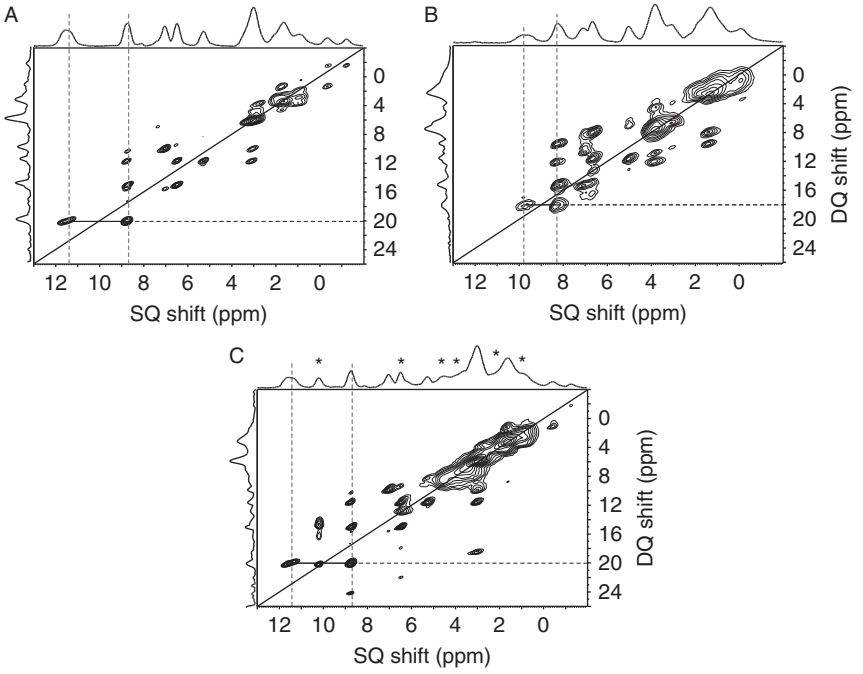

Figure 18 DQ/SQ CRAMPS spectra of (A) the anhydrous and (B) the monohydrate of a pharmaceutical API, and (C) a crushed tablet containing the API plus excipients (resonances marked by asterisks). The 2D spectra readily allow the forms and different hydrogen bonding patterns to be distinguished, including in the heterogeneous sample. The acquisition time for each spectrum was 105 min using 30 mg of sample. e-DUMBO-1_{22} homonuclear decoupling was applied in t_1 and windowed DUMBO-1 in t_2. Figure reproduced from Ref. 171.

DQF spectra have been used, in conjunction with fast MAS, to investigate structure and dynamics in proton-conducting polymer materials.[51,177–180]

5. OUTLOOK

The high receptivity of ^{1}H and the potential usefulness of information from ^{1}H chemical shifts and dipolar couplings means that ^{1}H has always been an attractive target for solid-state NMR. But the difficulty of obtaining resolved spectra has discouraged many spectroscopists.

This situation has changed significantly over the past decade. The advent of probes capable of spinning samples at speeds of 30 kHz and above, coupled with the use of higher field magnets, has allowed well-resolved spectra to be obtained, particularly for systems where the dipolar coupling is relatively weak (e.g. due to isotopic dilution). This in turn has enabled the use of inverse detection techniques to boost the sensitivity of detection of more dilute spins in 2D correlation experiments.

Suppressing the ^{1}H dipolar couplings via RF homonuclear decoupling is still necessary to obtain well-resolved spectra for typical molecular organic solids. However, increased understanding of the interaction between MAS and RF irradiation has allowed experimental protocols to be greatly simplified; good resolution can be obtained under moderate to fast MAS without significant time spent 'tuning up', as is necessary for CRAMPS experiments performed under static or slow MAS conditions. We can expect to see steady improvement of RF decoupling schemes optimised for faster MAS and/or low RF loading.

Looking ahead, developments in probe technology have the potential to carry ^{1}H solid-state NMR into new areas. A number of research groups have demonstrated the use of small RF coils in combination with MAS, either 'piggy-backing' the microcoil on a conventional MAS rotor[40,181,182] or inductively coupling to a coil inserted *inside* the MAS rotor.[183,184] Small RF coils allow good sensitivity to be obtained from sample volumes of the order of nanolitres, and extremely high RF ^{1}H nutation rates (in excess of 1 MHz) have been demonstrated. High RF nutation do not directly translate into good decoupling performance, as transient effects become very significant, recent work to actively compensate for transients[41,42] may provide at least a partial solution.

Even considering the advances made to date, it is clear that ^{1}H NMR will have an increasingly important role in the characterisation of solid materials, from complex biomolecules (Section 2), to surface-absorbed and hybrid materials, and molecular organic solids (Section 4.1).

ACKNOWLEDGEMENTS

Colleagues are warmly thanked for the generous permission to adapt their original artwork for inclusion in this review. The Engineering and Physical Sciences Research Council is thanked for funding of past and present projects investigating ^{1}H resolution in solids (GR/S56993/01 and EP/H023291/1).

REFERENCES

1. A. Detken, E. H. Hardy, M. Ernst, M. Kainosho, T. Kawakami, S. Aimoto and B. H. Meier, *J. Biomol. NMR*, 2001, **20,** 203.
2. D. L. VanderHart, W. L. Earl and A. N. Garroway, *J. Magn. Reson.*, 1981, **44,** 361.
3. A. N. Garroway, D. L. VanderHart and W. L. Earl, *Philos. Trans. R. Soc. Lond. A*, 1981, **299,** 609.
4. M. Alla and E. Lippmaa, *Chem. Phys. Lett.*, 1982, **87,** 30.
5. D. L. VanderHart, *in*: Encyclopaedia of Nuclear Magnetic Resonance, D. M. Grant and R. K. Harris (eds.), Wiley, New York, 1996, pp. 2938–2946.
6. A. J. Robbins, W. T. K. Ng, D. Jochym, T. W. Keal, S. J. Clark, D. J. Tozer and P. Hodgkinson, *Phys. Chem. Chem. Phys.*, 2007, **9,** 2389.
7. V. E. Zorin, S. P. Brown and P. Hodgkinson, *J. Chem. Phys.*, 2006, **125,** 144508:1.
8. R. K. Harris, P. Hodgkinson, V. Zorin, J.-N. Dumez, B. Elena, L. Emsley, E. Salager and R. Stein, *Magn. Reson. Chem.*, 2010, **48,** S103.
9. A. Samoson, T. Tuherm and Z. Gan, *Solid State Nucl. Magn. Reson.*, 2001, **20,** 130.
10. S. E. Lister, A. Soleilhavoup, R. L. Withers, P. Hodgkinson and J. S. O. Evans, *Inorg. Chem.*, 2010, **49,** 1188.
11. D. H. Zhou, D. T. Graesser, W. T. Franks and C. M. Rienstra, *J. Magn. Reson.*, 2006, **178,** 297.
12. V. Chevelkov, K. Rehbein, A. Diehl and B. Reif, *Angew. Chem. Int. Ed.*, 2006, **45,** 3878.
13. M. M. Maricq and J. S. Waugh, *J. Chem. Phys.*, 1979, **70,** 3300.
14. V. E. Zorin, S. P. Brown and P. Hodgkinson, *Mol. Phys.*, 2006, **104,** 293.
15. H. Cho, T. D. Ladd, J. Baugh, D. G. Cory and C. Ramanathan, *Phys. Rev. B*, 2005, **72,** 54427.
16. E. R. Andrew, S. Clough, L. F. Farnell, T. D. Gledhill and I. Roberts, *Phys. Lett.*, 1966, **21,** 505.
17. X. Xue, M. Kanzaki and A. Shatskiy, *Am. Mineral.*, 2008, **93,** 1099.
18. V. E. Zorin, B. Elena, A. Lesage, L. Emsley and P. Hodgkinson, *Magn. Reson. Chem.*, 2007, **45,** S93.
19. A. Lesage, L. Duma, D. Sakellariou and L. Emsley, *J. Am. Chem. Soc.*, 2001, **123,** 5747.
20. F. Blanc, C. Copéret, J. Thivolle-Cazat, J.-M. Basset, A. Lesage, L. Emsley, A. Sinha and R. R. Schrock, *Inorg. Chem.*, 2006, **45,** 9587.
21. F. Blanc, J. Thivolle-Cazat, J.-M. Basset, C. Copéret, A. S. Hock, Z. J. Tonzetich and R. R. Schrock, *J. Am. Chem. Soc.*, 2007, **129,** 1044.
22. B. Li, L. Xu, Q. Wu, T. Chen, P. Sun, Q. Jin, D. Ding, X. Wang, G. Xue and A.-C. Shi, *Macromolecules*, 2007, **40,** 5776.
23. G. P. Holland, B. R. Cherry, J. E. Jenkins and J. L. Yarger, *J. Magn. Reson.*, 2010, **202,** 64.
24. R. K. Harris and A. C. Olivieri, *Prog. Nucl. Magn. Reson. Spectrosc.*, 1992, **24,** 435.
25. A. Naito, A. Root and C. A. McDowell, *J. Phys. Chem.*, 1991, **95,** 3578.
26. R. S. Stein, B. Elena and L. Emsley, *Chem. Phys. Lett.*, 2008, **458,** 391.
27. B. Reif and R. G. Griffin, *J. Magn. Reson.*, 2003, **160,** 78.
28. E. K. Paulson, C. R. Morcombe, V. Gaponenko, B. Dancheck, R. A. Byrd and K. W. Zilm, *J. Am. Chem. Soc.*, 2003, **125,** 15831.
29. B. C. Gerstein, *in*: Encyclopaedia of Nuclear Magnetic Resonance, D. M. Grant and R. K. Harris (eds.), Wiley, New York, 2002.
30. H. Cho, *J. Magn. Reson. Ser. A*, 1996, **121,** 8.
31. A. J. Vega, *J. Magn. Reson.*, 2004, **170,** 22.
32. C. R. Morcombe, E. K. Paulson, V. Gaponenko, R. A. Byrd and K. W. Zilm, *J. Biomol. NMR*, 2005, **31,** 217.
33. P. K. Madhu, *Solid State Nucl. Magn. Reson.*, 2009, **35,** 2.
34. J. S. Waugh, L. M. Huber and U. Haeberlen, *Phys. Rev. Lett.*, 1968, **20,** 180.
35. V. E. Zorin, M. Ernst, S. P. Brown and P. Hodgkinson, *J. Magn. Reson.*, 2008, **192,** 183.
36. W.-K. Rhim, D. D. Elleman and R. W. Vaughan, *J. Chem. Phys.*, 1973, **59,** 3740.
37. W.-K. Rhim, D. D. Elleman, L. B. Schreiber and R. W. Vaughan, *J. Chem. Phys.*, 1974, **60,** 4595.
38. U. Haerberlen, *Adv. Magn. Reson.*, 1976, **Suppl. 1**.
39. M. Carravetta, M. Edén, O. G. Johannessen, H. Luthman, P. J. E. Verdegem, J. Lugtenburg, A. Sebald and M. H. Levitt, *J. Am. Chem. Soc.*, 2001, **123,** 10628.
40. A. Brinkmann, S. K. Vasa, H. Janssen and A. P. M. Kentgens, *Chem. Phys. Lett.*, 2010, **485,** 275.
41. K. Takeda, Y. Tabuchi, M. Negoro and M. Kitagawa, *J. Magn. Reson.*, 2008, **197,** 242.

42. Y. Tabuchi, M. Negoro, K. Takeda and M. Kitagawa, *J. Magn. Reson.*, 2010, **204,** 327.
43. P. Jackson and R. K. Harris, *Magn. Reson. Chem.*, 1988, **26,** 1003.
44. A. Lesage, D. Sakellariou, S. Hediger, B. Elena, P. Charmont, S. Steuernagel and L. Emsley, *J. Magn. Reson.*, 2003, **163,** 105.
45. C. Coelho, J. Rocha, P. K. Madhu and L. Mafra, *J. Magn. Reson.*, 2008, **194,** 264.
46. D. P. Burum, M. Linder and R. R. Ernst, *J. Magn. Reson.*, 1981, **43,** 463.
47. S. P. Brown, A. Lesage, B. Elena and L. Emsley, *J. Am. Chem. Soc.*, 2004, **126,** 13230.
48. I. Schnell, S. P. Brown, H. Yee-Low, H. Ishida and H. W. Spiess, *J. Am. Chem. Soc.*, 1998, **120,** 11784.
49. S. P. Brown and H. W. Spiess, *Chem. Rev.*, 2001, **101,** 4125.
50. M. Ernst, M. A. Meier, T. Tuherm, A. Samoson and B. H. Meier, *J. Am. Chem. Soc.*, 2004, **126,** 4764.
51. J. W. Traer, E. Montoneri, A. Samoson, J. Past, T. Tuherm and G. R. Goward, *Chem. Mater.*, 2006, **18,** 4747.
52. A. Samoson, T. Tuherm, J. Past, A. Reinhold, T. Anupõld and I. Heinmaa, New techniques in solid-state NMR. *Top. Curr. Chem.*, 2005, **246,** 15–31.
53. M. H. Levitt, D. P. Raleigh, F. Creuzet and R. G. Griffin, *J. Chem. Phys.*, 1990, **92,** 6347.
54. L. Mafra, C. Coelho, R. Siegel and J. Rocha, *J. Magn. Reson.*, 2009, **197,** 20.
55. W. L. Fitch, G. Detre, C. P. Holmes, J. N. Shoolery and P. A. Keifer, *J. Org. Chem.*, 1994, **59,** 7955.
56. J. C. Lindon, O. P. Beckonert, E. Holmes and J. K. Nicholson, *Prog. Nucl. Magn. Reson. Spectrosc.*, 2009, **55,** 79.
57. L. Shintu, F. Ziarelli and S. Caldarelli, *Magn. Reson. Chem.*, 2004, **42,** 396.
58. A. E. McDermott, F. J. Creuzet, A. C. Kolbert and R. G. Griffin, *J. Magn. Reson.*, 1992, **98,** 408.
59. L. Zheng, K. W. Fishbein, R. G. Griffin and J. Herzfeld, *J. Am. Chem. Soc.*, 1993, **115,** 6254.
60. B. Reif, C. P. Jaroniec, C. M. Rienstra, M. Hohwy and R. G. Griffin, *J. Magn. Reson.*, 2001, **151,** 320.
61. M. Hologne, V. Chevelkov and B. Reif, *Prog. Nucl. Magn. Reson. Spectrosc.*, 2006, **48,** 211.
62. Ü. Akbey, S. Lange, W. T. Franks, R. Linser, K. Rehbein, A. Diehl, B. J. van Rossum, B. Reif and H. Oschkinat, *J. Biomol. NMR*, 2010, **46,** 67.
63. V. Agarwal, A. Diehl, N. Skrynnikov and B. Reif, *J. Am. Chem. Soc.*, 2006, **128,** 12620.
64. H. Takahashi, M. Kainosho, H. Akutsu and T. Fujiwara, *J. Magn. Reson.*, 2010, **203,** 253.
65. J. P. Yesinowski, *J. Am. Chem. Soc.*, 1981, **103,** 6266.
66. A. Tomeda, S. Morisaki, K. Watanabe, S. Kuroki and I. Ando, *Chem. Phys. Lett.*, 2003, **376,** 346.
67. E. Vinogradov, P. K. Madhu and S. Vega, *Top. Curr. Chem.*, 2004, **246,** 33.
68. B. M. Fung, K. Ermolaev and Y. Yu, *J. Magn. Reson.*, 1999, **138,** 28.
69. S. J. Opella and F. M. Marassi, *Chem. Rev.*, 2004, **104,** 3587.
70. A. Ramamoorthy, Y. Wei and D. Lee, *Ann. Rep. NMR Spectrosc.*, 2004, **52,** 1.
71. D. P. Burum, M. Linder and R. R. Ernst, *J. Magn. Reson.*, 1981, **44,** 173.
72. D. P. Burum and W. K. Rhim, *J. Chem. Phys.*, 1979, **71,** 944.
73. M. Hohwy, P. V. Bower, H. J. Jakobsen and N. C. Nielsen, *Chem. Phys. Lett.*, 1997, **273,** 297.
74. M. Hohwy and N. C. Nielsen, *J. Chem. Phys.*, 1997, **106**.
75. H. Cho, *J. Magn. Reson.*, 1999, **141,** 164.
76. P. Mansfield, *Prog. Nucl. Magn. Reson. Spectrosc.*, 1972, **8,** 43.
77. M. Mehring, *Principles of High Resolution NMR in Solids*. 2nd edn. Springer-Verlag, Berlin, 1983.
78. S. Hafner and H. W. Spiess, *Solid State Nucl. Magn. Reson.*, 1997, **8,** 17.
79. I. Scholz, P. Hodgkinson, B. H. Meier and M. Ernst, *J. Chem. Phys.*, 2009, **114510,** 1.
80. C. Filip and S. Hafner, *J. Magn. Reson.*, 2000, **147,** 250.
81. S. Hafner and D. E. Demco, *Solid State Nucl. Magn. Reson.*, 2002, **22,** 247.
82. E. Vinogradov, P. K. Madhu and S. Vega, *Chem. Phys. Lett.*, 2000, **329,** 207.
83. E. Vinogradov, P. K. Madhu and S. Vega, *J. Chem. Phys.*, 2001, **115,** 8983.
84. M. Leskes, P. K. Madhu and S. Vega, *J. Chem. Phys.*, 2006, **125,** 124506.
85. S. Vega, *in*: Encyclopaedia of Nuclear Magnetic Resonance, D. M. Grant and R. K. Harris (eds.), Wiley, Chichester, 1996, pp. 2011–2025.
86. O. Lafon, Q. Wang, B. Hu, J. Trébosc, F. Deng and J.-P. Amoureux, *J. Chem. Phys.*, 2009, **130,** 014504.
87. P. Hodgkinson and L. Emsley, *Prog. Nucl. Magn. Reson. Spectrosc.*, 2000, **36,** 201.
88. M. Bak, J. T. Rasmussen and N. C. Nielsen, *J. Magn. Reson.*, 2000, **147,** 296.
89. M. Edén, *Concepts Magn. Reson.*, 2003, **17A,** 117.
90. M. Edén, *Concepts Magn. Reson.*, 2003, **18A,** 1.

91. M. Veshtort and R. G. Griffin, *J. Magn. Reson.*, 2006, **178,** 248.
92. P. Hodgkinson. pNMRsim: a general simulation program for large problems in solid-state NMR. http://www.durham.ac.uk/paul.hodgkinson/pNMRsim.
93. M. Veshtort, *Numerical simulations in Nuclear Magnetic Resonance: Theory and Applications,* 2003. [Ph.D. thesis Massachusetts Institue of Technology].
94. A. Bielecki, A. C. Kolbert and M. H. Levitt, *Chem. Phys. Lett.*, 1989, **155,** 341.
95. M. H. Levitt, A. C. Kolbert, A. Bielecki and D. J. Ruben, *Solid State Nucl. Magn. Reson.*, 1993, **2,** 151.
96. B.-J. van Rossum, H. Förster and H. J. M. de Groot, *J. Magn. Reson.*, 1997, **124,** 516.
97. M. Leskes, P. K. Madhu and S. Vega, *J. Magn. Reson.*, 2009, **199,** 208.
98. K. Mao and M. Pruski, *J. Magn. Reson.*, 2010, **203,** 144.
99. E. Vinogradov, P. K. Madhu and S. Vega, *Chem. Phys. Lett.*, 1999, **314,** 443.
100. K. Yamauchi, S. Kuroki and I. Ando, *J. Mol. Struct.*, 2002, **602,** 9.
101. E. Vinogradov, P. K. Madhu and S. Vega, *Chem. Phys. Lett.*, 2002, **354,** 193.
102. L. Bosman, P. Madhu, S. Vega and E. Vinogradov, *J. Magn. Reson.*, 2004, **169,** 39.
103. M. Leskes, P. K. Madhu and S. Vega, *Chem. Phys. Lett.*, 2007, **447,** 370.
104. M. Leskes, P. K. Madhu and S. Vega, *J. Chem. Phys.*, 2008, **128,** 052309.
105. M. Leskes, S. Steuernagel, D. Schneider, P. K. Madhu and S. Vega, *Chem. Phys. Lett.*, 2008, **466,** 95.
106. D. Sakellariou, A. Lesage, P. Hodgkinson and L. Emsley, *Chem. Phys. Lett.*, 2000, **319,** 253.
107. A. Detken, E. H. Hardy, M. Ernst and B. H. Meier, *Chem. Phys. Lett.*, 2002, **356,** 298.
108. P. Hodgkinson, *Prog. Nucl. Magn. Reson. Spectrosc.*, 2005, **46,** 197.
109. J. R. Sachleben, S. Caldarelli and L. Emsley, *J. Chem. Phys.*, 1996, **104,** 2518.
110. J. R. Sachleben, J. Gaba and L. Emsley, *Solid State Nucl. Magn. Reson.*, 2006, **29,** 30.
111. G. De Paëpe, P. Hodgkinson and L. Emsley, *Chem. Phys. Lett.*, 2003, **376,** 259.
112. B. Elena, G. De Paëpe and L. Emsley, *Chem. Phys. Lett.*, 2004, **398,** 532.
113. S. Paul, R. S. Thakur, M. Goswami, A. C. Sauerwein, S. Mamone, M. Concistrè, H. Förster, M. H. Levitt and P. K. Madhu, *J. Magn. Reson.*, 2009, **197,** 14.
114. S. Hafner and H. W. Spiess, *J. Magn. Reson. Ser. A*, 1996, **121,** 160.
115. Y. K. Lee, N. D. Kurur, M. Helme, O. G. Johannessen, N. C. Nielsen and M. H. Levitt, *Chem. Phys. Lett.*, 1995, **242,** 304.
116. P. K. Madhu, X. Zhao and M. H. Levitt, *Chem. Phys. Lett.*, 2001, **346,** 142.
117. S. Paul, R. S. Thakur and P. K. Madhu, *Chem. Phys. Lett.*, 2008, **456,** 253.
118. J.-P. Amoureux, B. Hu, J. Trébosc, Q. Wang, O. Lafon and F. Deng, *Solid State Nucl. Magn. Reson.*, 2009, **35,** 19.
119. J.-P. Amoureux, B. Hu and J. Trébosc, *J. Magn. Reson.*, 2008, **193,** 305.
120. A. Lesage, *Phys. Chem. Chem. Phys.*, 2009, **11,** 6876.
121. S. P. Brown, *Macromol. Rapid Commun.*, 2009, **30,** 688.
122. Y. Ishii, N. P. Wickramasinghe and S. Chimon, *J. Am. Chem. Soc.*, 2003, **125,** 3438.
123. N. P. Wickramasinghe, M. Shaibat and Y. Ishii, *J. Am. Chem. Soc.*, 2005, **127,** 5796.
124. I. Bertini, L. Emsley, M. Lelli, C. Luchinat, J. Mao and G. Pintacuda, *J. Am. Chem. Soc.*, 2010, **132,** 5558.
125. G. Kervern, G. Pintacuda, Y. Zhang, E. Oldfield, C. Roukoss, E. Kuntz, E. Herdtweck, J.-M. Basset, S. Cadars, A. Lesage and C. Copéret, *J. Am. Chem. Soc.*, 2006, **128,** 13545.
126. G. Kervern, G. Pintacuda and L. Emsley, *Chem. Phys. Lett.*, 2007, **435,** 157.
127. N. P. Wickramasinghe, M. A. Shaibat, C. R. Jones, L. B. Casabianca, A. C. De Dios, J. S. Harwood and Y. Ishii, *J. Chem. Phys.*, 2008, **128,** 052210.
128. P. Avenier, A. Lesage, M. Taoufik, A. Baudouin, A. De Mallmann, S. Fiddy, M. Vautier, L. Veyre, J.-M. Basset, L. Emsley and E. A. Quadrelli, *J. Am. Chem. Soc.*, 2007, **129,** 176.
129. T. M. Alam and H. Fan, *Macromol. Chem. Phys.*, 2003, **204,** 2023.
130. S. Pawsey, M. McCormick, S. De Paul, R. Graf, Y. S. Lee, L. Reven and H. W. Spiess, *J. Am. Chem. Soc.*, 2003, **125,** 4174.
131. D. Massiot, B. Alonso, F. Fayon, F. Fredoueil and B. Bujoli, *Solid State Sci.*, 2001, **3,** 11.
132. L. Camus, V. Goletto, J. Maquet, C. Gervais, C. Bonhomme, F. Babonneau and D. Massiot, *J. Sol-Gel Sci. Technol.*, 2003, **26,** 311.
133. J. Trebosc, J. W. Wiench, S. Huh, S.-Y. L. Victor and M. Pruski, *J. Am. Chem. Soc.*, 2005, **127,** 7587.
134. J. W. Wiench, C. E. Bronnimann, S. Y. Victor and M. Pruski, *J. Am. Chem. Soc.*, 2007, **129,** 12076.

135. K. Mao, J. W. Wiench, V. S.-Y. Lin and M. Pruski, *J. Magn. Reson.*, 2009, **196,** 92.
136. C. Bonhomme, C. Coelho, N. Baccile, C. Gervais, T. Azais and F. Babonneau, *Acc. Chem. Res.*, 2007, **40,** 738.
137. S. P. Brown, *Prog. Nucl. Magn. Reson. Spectrosc.*, 199.
138. A. Domján, E. Geissler and K. László, *Soft Matter*, 2010, **6,** 247.
139. S. P. Brown, *in*: NMR Crystallography, R. K. Harris, R. E. Wasylishen and M. J. Duer (eds.), Wiley, Chichester, 2009, pp. 321–339.
140. M. McCormick, R. N. Smith, R. Graf, C. J. Barrett, L. Reven and H. W. Spiess, *Macromolecules*, 2003, **36,** 3616.
141. R. K. Harris, P. Jackson, L. H. Merwin, B. J. Say and G. Hägele, *J. Chem. Soc., Faraday Trans. 1*, 1988, **84,** 3649.
142. A. E. Aliev and K. D. M. Harris, *in*: Supramolecular Assembly via Hydrogen Bonds I, (D. M. P. Mingos ed.), 2004, Vol. 108, Springer, Berlin, 2004, pp. 1–53.
143. X. Xue and M. Kanzaki, *J. Am. Ceram. Soc.*, 2009, **92,** 2803.
144. G. R. Goward, D. Sebastiani, I. Schnell, H. W. Spiess, H. D. Kim and H. Ishida, *J. Am. Chem. Soc.*, 2003, **125,** 5792.
145. J. Brus and J. Dybal, *Macromolecules*, 2002, **35,** 10038.
146. J. R. Yates, T. N. Pham, C. J. Pickard, F. Mauri, A. M. Amado, A. M. Gil and S. P. Brown, *J. Am. Chem. Soc.*, 2005, **127,** 10216.
147. A. C. Uldry, J. M. Griffin, J. R. Yates, M. Pérez-Torralba, M. D. Santa María, A. L. Webber, M. L. L. Beaumont, A. Samoson, R. M. Claramunt, C. J. Pickard and S. P. Brown, *J. Am. Chem. Soc.*, 2008, **130,** 945.
148. D. H. Brouwer, S. Alavi and J. A. Ripmeester, *Phys. Chem. Chem. Phys.*, 2008, **10,** 3857.
149. R. K. Harris, P. Y. Ghi, R. B. Hammond, C.-Y. Ma and K. J. Roberts, *Chem. Commun.*, 2834.
150. R. K. Harris, *Solid State Sci.*, 2004, **6,** 1025.
151. R. K. Harris, P. Hodgkinson, C. J. Pickard, V. Zorin and J. R. Yates, *Magn. Reson. Chem.*, 2007, **45,** S174.
152. J. Schmidt, A. Hoffmann, H. W. Spiess and D. Sebastiani, *J. Phys. Chem. B*, 2006, **110,** 23204.
153. J. Brus and A. Jegorov, *J. Phys. Chem. A*, 2004, **108,** 3955.
154. N. Mifsud, B. Elena, C. Pickard, A. Lesage and L. Emsley, *Phys. Chem. Chem. Phys.*, 2006, **8,** 3418.
155. J. Brus, H. Petříčková and J. Dybal, *Monatsh. Chem.*, 2002, **133,** 1587.
156. B. Elena and L. Emsley, *J. Am. Chem. Soc.*, 2005, **127,** 9140.
157. E. Salager, R. S. Stein, C. J. Pickard, B. Elena and L. Emsley, *Phys. Chem. Chem. Phys.*, 2009, **11,** 2610.
158. C. J. Pickard, E. Salager, G. Pintacuda, B. Elena and L. Emsley, *J. Am. Chem. Soc.*, 2007, **129,** 8932.
159. E. Salager, G. M. Day, R. S. Stein, C. J. Pickard, B. Elena and L. Emsley, *J. Am. Chem. Soc.*, 2010, **132,** 2564.
160. Y. Ishii and R. Tycko, *J. Magn. Reson.*, 2000, **142,** 199.
161. D. H. Zhou, J. J. Shea, A. J. Nieuwkoop, W. T. Franks, B. J. Wylie, C. Mullen, D. Sandoz and C. M. Rienstra, *Angew. Chem. Int. Ed.*, 2007, **46,** 8380.
162. D. H. Zhou, G. Shah, M. Cormos, C. Mullen, D. Sandoz and C. M. Rienstra, *J. Am. Chem. Soc.*, 2007, **129,** 11791.
163. I. Schnell, B. Langer, S. H. M. Söntjens, M. H. P. van Genderen, R. P. Sijbesma and H. W. Spiess, *J. Magn. Reson.*, 2001, **150,** 57.
164. I. Schnell and K. Saalwächter, *J. Am. Chem. Soc.*, 2002, **124,** 10938.
165. Y. Ishii, J. P. Yesinowski and R. Tycko, *J. Am. Chem. Soc.*, 2001, **123,** 2921.
166. K. Mao and M. Pruski, *J. Magn. Reson.*, 2009, **201,** 165.
167. D. H. Zhou and C. M. Rienstra, *Angew. Chem. Int. Ed.*, 2008, **47,** 7328.
168. V. Chevelkov, B. J. van Rossum, F. Castellani, K. Rehbein, A. Diehl, M. Hohwy, S. Steuernagel, F. Engelke, H. Oschkinat and B. Reif, *J. Am. Chem. Soc.*, 2003, **125,** 7788.
169. H. W. Spiess, *in*: Encyclopaedia of Nuclear Magnetic Resonance, D. M. Grant and R. K. Harris (eds.), Wiley, Chichester, 2002.
170. I. Schnell and H. W. Spiess, *J. Magn. Reson.*, 2001, **151,** 153.
171. J. M. Griffin, D. R. Martin and S. P. Brown, *Angew. Chem. Int. Ed.*, 2007, **46,** 8036.
172. I. Schnell, *Prog. Nucl. Magn. Reson. Spectrosc.*, 2004, **45,** 145.

173. L. Mafra, R. Siegel, C. Fernandez, D. Schneider, F. Aussenac and J. Rocha, *J. Magn. Reson.*, 2009, **199,** 111.
174. U. Friedrich, I. Schnell, D. E. Demco and H. W. Spiess, *Chem. Phys. Lett.*, 1998, **285,** 49.
175. M. Leskes and S. Vega, *J. Chem. Phys.*, 2009, **130,** 124506.
176. P. K. Madhu, E. Vinogradov and S. Vega, *Chem. Phys. Lett.*, 2004, **394,** 423.
177. G. R. Goward, M. F. H. Schuster, D. Sebastiani, I. Schnell and H. W. Spiess, *J. Phys. Chem. B*, 2002, **106,** 9322.
178. B. R. Cherry, C. H. Fujimoto, C. J. Cornelius and T. M. Alam, *Macromolecules*, 2005, **38,** 1201.
179. G. Ye, N. Janzen and G. R. Goward, *Macromolecules*, 2006, **39,** 3283.
180. G. Ye, C. A. Hayden and G. R. Goward, *Macromolecules*, 2007, **40,** 1529.
181. H. Janssen, A. Brinkmann, E. R. H. van Eck, P. J. M. van Bentum and A. P. M. Kentgens, *J. Am. Chem. Soc.*, 2006, **128,** 8722.
182. A. P. M. Kentgens, J. Bart, P. J. M. van Bentum, A. Brinkmann, E. R. H. van Eck, J. G. E. Gardeniers, J. W. G. Janssen, P. Knijn, S. Vasa and M. H. W. Verkuijlen, *J. Chem. Phys.*, 2008, **128,** 052202.
183. D. Sakellariou, G. Le Goff and J.-F. Jacquinot, *Nature*, 2007, **447,** 694.
184. M. Inukai and K. Takeda, *J. Magn. Reson.*, 2010, **202,** 274.
185. S. Paul, R. S. Thakur, M. H. Levitt and P. K. Madhu, *J. Magn. Reson.*, 2010, **205,** 269.
186. S. Paul, D. Schneider and P. K. Madhu, *J. Magn. Reson.*, 2010, **206,** 241.

This page intentionally left blank

CHAPTER 6

Multiple-Wave-Vector Diffusion-Weighted NMR

Jürgen Finsterbusch

Contents

Abstract

Since their introduction by Stejskal and Tanner, pulsed-field-gradient diffusion-weighted NMR experiments have been applied to characterize condensed matter ranging from liquids and rocks to biological tissue

Department of Systems Neuroscience, University Medical Center Hamburg-Eppendorf, Hamburg, Germany

Annual Reports on NMR Spectroscopy, Volume 72
ISSN 0066-4103, DOI: 10.1016/B978-0-12-385857-3.00006-2

© 2011 Elsevier Ltd.
All rights reserved.

in vivo. In spite of their outstanding success, for example, in biomedical research and clinical diagnosis, the technique faces some inherent limitations, for instance the inability to detect diffusion anisotropy present on a microscopic scale in a macroscopically isotropic sample. Thus, the interest in an extended version of the diffusion-weighted NMR experiment where two (or more) diffusion-weighting periods are applied successively in a single acquisition has emerged in the past few years. Such experiments, sometimes referred to as two- or multiple-wave-vector experiments, have been shown to be a promising tool to investigate diffusion in confined geometries. They are able to assess information difficult or impossible to achieve with standard diffusion-weighting experiments and, thus, may help to provide deeper insight into the sample's microstructure. In this work, current developments in the theoretical modelling of multiple-wave-vector experiments and recent experimental results demonstrating the potential of the technique are summarized.

Key Words: Multiple-wave-vector diffusion weighting, Double-wave-vector diffusion weighting, Double-pulsed-field gradient, Double-pulsed-field-gradient spin-echo, Pore size, Cell size, Pore eccentricity, Cell eccentricity, Microscopic diffusion anisotropy.

1. INTRODUCTION

Since the first experiments to investigate diffusion properties by means of pulsed-field-gradient NMR by Stejskal and Tanner[1] in 1965, this method has rapidly developed to an indispensable tool to study diffusion and motion, for example, in gases, fluids, porous media, and biological tissue, which is of considerable interest in geology, material science, hydrodynamics, biomedical research and medicine. For instance, the observation of a reduced diffusion coefficient in infarcted brain tissue at a very early stage[2] and the ability to use diffusion-tensor imaging[3] to track nerve fibres *in vivo*[4] had a tremendous impact on clinical diagnostics and neuroscientific research.

Experiments involving two diffusion-weighting periods in a single acquisition were first proposed by Cory et al.[5] in 1991. Their idea was that investigating the combined effect of two successive diffusion-weighting periods could reveal temporal or spatial correlations of the diffusion displacements occurring during these periods, for example, to detect pore leakage. When using the first diffusion weighting to dephase spins in free compartments or within larger pores, the displacement profiles obtained from the second diffusion weighting can be assigned to spins that were in a small, confined geometry during the first diffusion weighting. If it yields displacements larger than this pore dimension at longer diffusion times, this would be an indicator of pore leakage.

They also pointed out that if the two diffusion-weighting periods are applied in orthogonal directions, the experiment could be used to measure the superposition of the displacement profiles in two dimensions. Comparing this

superposition to the displacement profile obtained from a standard experiment, should reveal the eccentricity of the compartment present on a microscopic scale. Thus, such a experiment could detect diffusion anisotropy present on a microscopic scale, for example, due to pore eccentricity, in a sample that macroscopically and in a standard diffusion-weighted experiment appears isotropic, for example, because the pores are randomly oriented.

A few years later, Callaghan and Manz[6] presented a more specific analysis of the signal behaviour together with first experimental results. They considered a pulse sequence with two diffusion- or motion-encoding gradient pairs of identical encoding times that are separated by an exchange time and whose amplitude are varied independently yielding a two-dimensional experiment. The signal amplitude was shown to depend on the conditional probability to observe a displacement $\Delta\mathbf{r}_2$ during the second encoding period if a displacement $\Delta\mathbf{r}_1$ occurred during the first. Because these displacements differ if the velocities of the spins have changed during the exchange time, the term velocity exchange spectroscopy (VEXSY) was used for the method. As noted by the authors, such an exchange can only be reliably observed if the two encodings are collinear. Experiments demonstrating Gaussian displacement profiles for freely diffusing water and the velocity changes of a fluid between two cylinders with the inner rotating at constant angular velocity (Couette flow) were presented and showed a very good agreement with theoretical expectations.[6]

A first theoretical consideration for fully restricted diffusion was performed by Mitra[7] in 1995. He could show that in randomly oriented, isolated pores a modulation of the signal is expected when varying the angle between the two diffusion weightings. Thereby, the shape of the corresponding curves depends on (i) the time between the two diffusion-weighting periods, the so-called mixing time, and (ii) the shape of the compartment. For long diffusion times that were also assumed by Cory et al., a signal difference between parallel and orthogonal diffusion weightings is expected for eccentric pores, that is, if the diffusion locally is anisotropic. This means that an acquisition with parallel diffusion weightings can be used as a reference to an experiment with orthogonal orientations which is more elegant because systematic errors introduced by the second diffusion weighting would not show up in a control experiment with only one diffusion weighting.

Mitra also found that a modulation with a cos-shaped dependency appears for short mixing times, that is, if both diffusion weightings are applied in direct succession. Thereby, the modulation amplitude does not directly depend on the pore shape but increases with the pore size. Thus, experiments with more than one diffusion-weighting period may provide direct access to the microstructure of a sample and may yield information beyond that achievable with standard diffusion-weighting experiments.

The first experiment to observe local diffusion anisotropy in a macroscopically isotropic sample was performed by Cheng and Cory.[8] They observed the signal difference between parallel and orthogonal diffusion weightings caused by the prolate shape of treated yeast cells. Based on signal calculations for ellipsoidal cells, they were able to estimate the cells' size and eccentricity quite well as confirmed by light microscopy.

These results triggered the interest in experiments with multiple diffusion weightings, in particular regarding biological tissue. Estimating the cell size and shape with NMR methods could help to characterize and differentiate tissue and pathologies non-invasively and *in vivo*. In particular, complementing diffusion-tensor imaging which is applied very successfully to estimate the macroscopic diffusion anisotropy and white matter fibre orientations in the central nervous system, by a method assessing the microscopic diffusion anisotropy, for example, to characterize grey matter integrity, could have a considerable impact on biomedical research and clinical diagnostics.

Thus, in the last few years, many studies were performed to demonstrate the feasibility and describe, improve, validate and apply two-diffusion-weighting experiments and even revealed a new aspect of the diffusion–diffraction which has been reported by Özarslan and Basser.[9] These developments seem to confirm that the potential of such experiments to study the microstructure is very promising and it seems to be appropriate to give an overview of the progress obtained so far.

This overview will focus on two aspects that have been investigated extensively in the last few years due to their relevance for *in vivo* applications: the signal modulation with the angle between the diffusion weightings as described by Mitra[7] and the specific diffraction effect discovered by Özarslan and Basser.[9] However, a short summary of earlier developments and their current applications is given as well. The first part (Section 2) will give a short overview of the relevant principles including a short summary of earlier developments and their current applications (Section 2.1) and a simple theoretical approach to derive signal expressions that describe the specific effects covered (Section 2.4). It is followed by a summary of the extensions and generalizations developed for the theoretical description of the experiments (Section 3). Sections 4 and 5 present the experimental studies investigating the signal modulation with the angle between the diffusion weightings and the, so-called ''negative'', diffraction effect observed when the diffusion weighting is increased. The chapter closes with a summary (Section 6) and a conclusion (Section 7).

2. PRINCIPLES

In this section, the basic principles of experiments with multiple diffusion weightings are summarized. It starts with a very condensed overview of earlier developments and their current applications that are not covered in detail in the remaining chapter (Section 2.1). This section is followed by a short clarification of the nomenclature used in the field and in the present work (Section 2.2) and the pulse sequences considered (Section 2.3). A first theoretical approach for restricted diffusion is presented in Section 2.4 to demonstrate the basic signal properties, the angular modulations and the specific diffusion–diffraction effects. In Section 2.5, an excursion to the phase evolution is performed that may help to understand an, at a first glance surprising, effect observable in the experiments, the signal difference between parallel and antiparallel diffusion weightings.

The section closes with condensed summaries of the diffusion propagator (Section 2.6) and approaches to solve the Bloch–Torrey equation (Section 2.7) on which current theoretical considerations (Section 3) are based.

2.1. Background

Based on the ideas of Cory et al.,[5] Callaghan and Manz[6] and Mitra[7] sketched in Section 1, different NMR methods with more than one diffusion- or motion-encoding gradient pair were developed. The basic methods will be presented here very shortly, roughly categorized according to their dimensionality and the sample properties investigated.

In the simplest experiments, two motion-encoding or diffusion-weighting periods are applied successively with an exchange time in-between and the gradient amplitudes of both periods are stepped in unison (e.g. Refs. 10,11). Such experiments are one-dimensional and imply that the gradient pairs are collinear, that is, parallel or antiparallel, in order to detect changes in the displacement or velocity occurring between the different encoding periods. Depending on the relative orientations of the two encodings, the pulse sequences are flow-rephased or not which means that they reflect velocity or flow changes during the exchange time or a mean displacement over both periods, respectively.[10–12] Although such 1D sequences have been discussed in the literature (e.g. Refs. 10–13), they have not been widely used and, if applied, often aimed to realize flow rephasing in a diffusion-weighted experiment (e.g. Ref. 14), that is, without exploiting the effect of an exchange or the specific properties of multiple diffusion weightings. However, with the discovery of the specific diffraction properties present for multiple diffusion weightings by Özarslan and Basser[9] new interest in such experiments has risen as will be outlined in detail in this chapter.

Alternatively, the angle of the encoding gradient pairs can be varied while using fixed amplitudes, for example, as proposed by Cory et al.[5] and Mitra.[7] This also yields a 1D experiment where the modulation amplitude can reflect the pore size or locally anisotropic diffusion as is present in eccentric pores. Despite of their appealing simplicity and the promising results of Cheng and Cory[8] sketched in Section 1, only in the past few years corresponding studies have been reported, however, this field is increasing rapidly and is one of the main topics of this chapter.

In the two-dimensional variants, the gradient amplitudes are stepped independently, the VEXSY being a prominent example.[6] If the encoding periods are sufficiently short, the signal amplitude is only affected by any variation occurring in the exchange time, for example, due to a change of the orientation or magnitude of the velocity. A two-dimensional Fourier transformation then can be used to resolve temporal and spatial coherences of flow or diffusion as demonstrated in the examples reported, self-diffusion of water and Couette flow.[6] This approach has found broad applications, in particular in the study of flow phenomena (e.g. Refs. 11,15–18).

A slightly more general variant, acronymed as SERPENT, has been investigated by Stapf et al.[19,20] where three or more gradient pulses are applied such that

their vector sum is zero in order to end up with a measurable MR signal. It was setup to sequentially rephase the dephasing effect of the first gradient with the succeeding ones and can be considered as a special case of the general experiment considered by Mitra.[7] The experiment also has several encoding periods like VEXSY, however, the encodings are not independent and separated but interleaved, the shorter one being incorporated into the longer ones. Thus, the successively increasing displacements are encoded and can also be analyzed by a Fourier transformation. It has been shown that the three-pulse variant effectively is identical to a VEXSY sequence without exchange time, that is, with overlapping gradient pulses.[21]

Recently, a 2D variant combining motion and displacement encoding has been presented.[22] It involves a double-PGSE motion-encoding with the gradients stepped in unison, but these gradient pulses are superimposed by a displacement-encoding gradient pair that dephases during the first motion-encoding period and rephases during the second one. By independently stepping the encoding amplitude, velocity changes can be correlated with displacements which was used to study the non-local dispersion tensor in Couette flow and flow in porous media.[22,23]

For the investigation of diffusion properties, methods for diffusion–diffusion exchange spectroscopy (DEXSY) and diffusion–diffusion correlation spectroscopy (DDOSY) were introduced.[24] The DEXSY pulse sequence is essentially identical to the VEXSY sequence, however, the data analysis is usually performed with a Laplace transformation to resolve different exponential signal decays and derive the distribution of diffusion coefficients.[24] This method aims to detect a change of the diffusion coefficients during the exchange time which implies that the diffusion weightings are applied collinear. It can, for instance, detect pore leakage in the broadest sense, for example, spins moving in or out of a compartment of confined geometry like inter-pore diffusion in porous media. The leakage is represented by off-diagonal peaks (''cross-peaks'') after the Laplace transformation where the position of the cross-peaks relative to the corresponding diagonal peaks reflects the affected volume fraction.[25] The DEXSY method has been applied to study various exchange processes, for instance in emulsions (e.g. Ref. 26) and water diffusion in liquid crystals (e.g. Refs. 25,27–29) and microporous materials.[30]

The DDOSY method[24] targets diffusion correlations in different spatial directions which implies that the second diffusion weighting is applied in a direction orthogonal to the first one and that the exchange time is minimized to avoid pore leakage. It also usually is analyzed with a 2D Laplace transformation where cross-peaks now reflect locally anisotropic diffusion that may appear even if the sample macroscopically appears isotropic. Thus, DDOSY can be considered as the 2D variant of the experiment proposed by Cory et al.[5] and considered in more detail by Mitra[7] for fully restricted diffusion. Applications involved the detection of local diffusion anisotropy in liquid crystals (e.g. Refs. 25,27,28) and plant tissue.[31]

In the remaining of this chapter, one-dimensional experiments investigating the *angular* modulation of the signal amplitude are covered in detail in the context of restricted diffusion. They were inspired by the ideas of Cory et al.[5] and Mitra[7] and deal with two observations considered in detail in Section 2.4: (i) the signal

difference between parallel and antiparallel diffusion weightings to estimate pore sizes (''restriction effect'') and (ii) the signal difference between parallel and orthogonal diffusion weightings in the presence of locally anisotropic diffusion, for example, as in eccentric pores (''anisotropy effect''). Furthermore, a specific diffusion pattern occurring in experiments with two diffusion weightings recently discovered by Özarslan and Basser[9] is covered because it represents a novel feature that may help to improve the feasibility of diffraction experiments.

2.2. Nomenclature

Experiments with several successively applied diffusion-weighting periods are sometimes referred to as ''multiple-wave-vector'' diffusion-weighting experiments. This term, introduced by Mitra,[7] reflects the equivalence of a diffusion-weighting period to a scatter event which is characterized by a wave vector.[32] In the context of diffusion-weighted NMR experiments, this wave vector can be defined as $\mathbf{q} = \gamma\delta\,\mathbf{G}$, where γ is the gyromagnetic ratio, δ the pulse duration and $\mathbf{G}$ the magnetic field gradient. Standard diffusion-weighting experiments with a single de- and rephasing gradient can be described by a single-wave vector $\mathbf{q}$ and are equivalent to a simple scatter event. Accordingly, experiments with more than one diffusion weighting are characterized by multiple wave vectors.

Due to the scattering analogy, the expression ''multiple-scattering'' experiments has also been used.[8] In the literature, the terms ''double-pulsed-field-gradient'' (d-PFG) (e.g. Ref. 33) or ''double-pulsed-field-gradient spin-echo'' (d-PGSE) experiments (e.g. Refs. 10,34) are also often used. They have been chosen to be in line with the ''pulsed-field gradient'' (PFG) used for a standard diffusion-weighting experiment.

Herein, we will use the terms ''multiple-wave-vector'' (MWV) and, for its simplest version with two wave vectors, ''double-wave-vector'' (DWV) experiments. They will be distinguished from the standard, single-wave-vector experiments that involve only a single diffusion-weighting period.

Another ambiguity exists in the literature concerning the expression ''microscopic diffusion anisotropy''. In this chapter, the term will be used for diffusion that is anisotropic on a pore level, for example, diffusion in eccentric pores or cells, which is, for example, in accordance with Refs. 25,34. This means that restricted diffusion in spherical pores is considered to have no microscopic diffusion anisotropy. This is different from Ref. 35 where the term ''compartment shape anisotropy'' was introduced for the diffusion anisotropy in eccentric pores instead and microscopic diffusion anisotropy refers to the asymmetry of the diffusion propagator in the presence of a restricting boundary and, thus, also appears in spherical pores.

Due to the sign reversal occurring in DWV diffraction experiments (see, e.g. Section 2.4.4), the term ''negative diffraction'' effect has been introduced. It will also be used in this chapter to distinguish the DWV-specific effects from the diffraction patterns of standard, single-wave-vector experiments.

''Ideal'' timing parameters refer to short gradient pulses ($\delta \to 0$), long diffusion times ($\Delta \to \infty$) and short or long mixing times ($\tau_m \to 0$ or $\tau_m \to \infty$, respectively).

Under these assumptions, the derivation of signal expressions is straightforward (see Section 2.4) and the specific MWV effects are most pronounced.

2.3. Basic pulse sequences

An example of a MWV pulse sequence is shown in Figure 1A. In this most general case, each gradient pulse with wave vector $\mathbf{q}_j$ has its own gradient amplitude G_j, direction $\mathbf{G}_j/G_j$ and pulse duration δ_j. Furthermore, $n-1$ different diffusion times Δ_j are defined between the wave vectors. To generate a measurable NMR signal, rephasing is required, that is, $\sum_j (-1)^{(j-1)} \mathbf{q}_j = 0$, where the sign reflects the effect of the refocusing RF pulses as shown in Figure 1A. Thus, only $n-1$ independent wave vectors can be chosen.

A more specific experiment is shown in Figure 1B. It involves n independent diffusion-weighting periods consisting of a de- and rephasing gradient pulse of equal duration and amplitude. Each period is characterized by a wave vector $\mathbf{q}_j$ and a diffusion time Δ_j. The times between the diffusion weightings are termed mixing times τ_m. This variant is the ''classical'' MWV experiment which was analyzed in more detail for $n=2$ (Figure 1C) by Mitra and represents the basic experiment considered in this chapter. If the mixing time is set to 0, the intermediate gradient pulses overlap as shown in Figure 1D for the DWV experiment.

Figure 1E presents an extension of the pulse sequence shown in Figure 1C where the two diffusion-weighting periods of a DWV experiment are applied multiple times. These experiments with so-called ''multiple concatenations'' of the two wave vectors represent a special case of the MWV experiments shown in Figure 1B with only two different wave vectors, for example, applied in an alternating manner. However, as such experiments do not exploit the full flexibility of a general MWV experiment with different $\mathbf{q}_j$, they will be considered as DWV experiments. Note that these experiments may also be performed with a half-integral number of concatenations, that is, terminating with an incomplete cycle where only the first wave vector is applied.

For clarity, the pulse sequences shown in Figure 1 represent extensions of the standard pulsed-field-gradient spin-echo (PGSE) experiment.[1] However, it should be emphasized that the MWV experiments are defined based on the diffusion weightings, that is, they are not limited to spin echoes or the combinations of RF pulses shown in Figure 1 but can be applied with any RF pulse sequence including free induction decays or stimulated echoes.

Note that ''parallel'' and ''antiparallel'' wave-vector orientations considered in this chapter refer to the PGSE-based sequences shown in Figure 1. In the ''parallel'' orientation ($\mathbf{G}_1/G_1 = \mathbf{G}_2/G_2$), the overlapping gradient pulses in Figure 1D add up to yield a pulse with a larger amplitude. For the ''antiparallel'' orientation ($\mathbf{G}_1/G_1 = -\mathbf{G}_2/G_2$), their sum yields a reduced or even cancelled intermediate gradient pulse. This amplitude amplification and reduction are the criteria for parallel and antiparallel wave-vector orientations, respectively.

The pulse sequence with vanishing mixing times (Figure 1D) has a diffusion-weighting b value[1] of

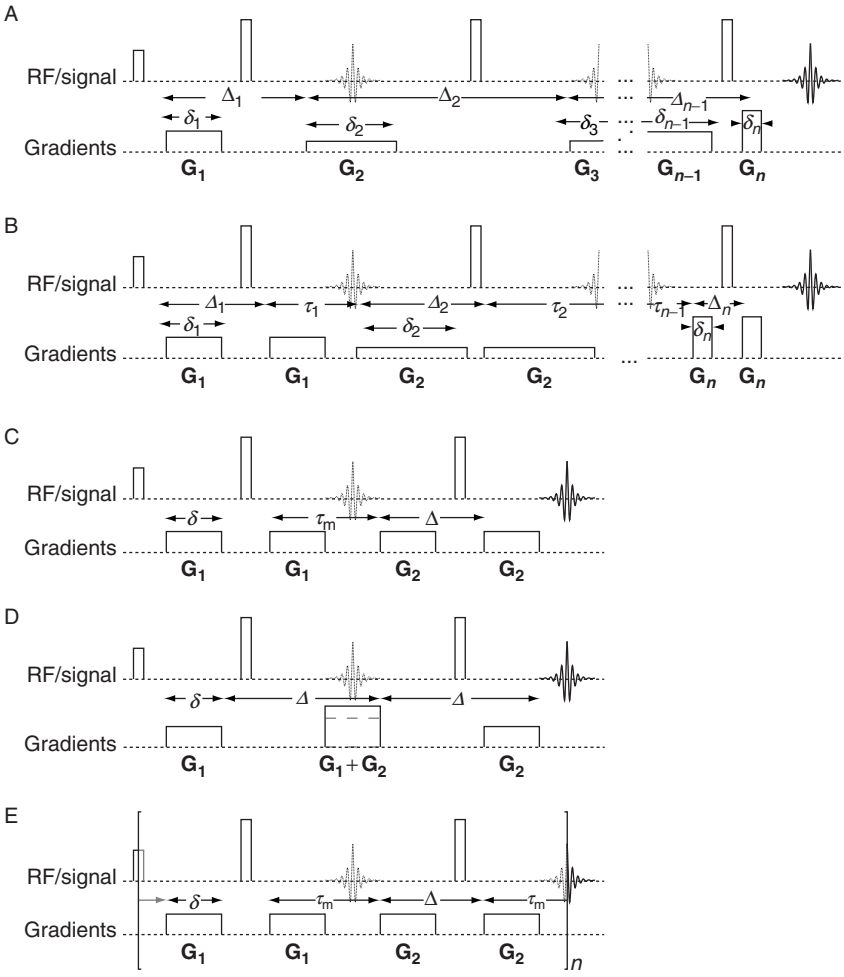

Figure 1 Basic pulse sequences for multiple-wave-vector diffusion-weighting experiments. (A) Most general case with different gradient amplitudes and directions, pulse durations and diffusion times. To ensure a proper rephasing, only $n-1$ independent wave vectors can be chosen. (B) "Classical" MWV experiment with n diffusion-weighting periods, each described by a wave vector. The times τ_m between the diffusion weightings are the so-called mixing times. (C, D) Double-wave-vector variants ($n=2$) of (B) with a fixed pulse duration and constant wave vector magnitudes and (C) a mixing time larger than the pulse duration and (D) a vanishing mixing time ($\tau_m=0$), that is, overlapping gradient pulses. The amplitude of the overlapping pulses shown in (D) corresponds to a parallel wave-vector orientation (doubled amplitude), the grey dashed lines reflect the amplitudes for orthogonal ($\sqrt{2}$) and antiparallel orientations (cancellation), respectively. (E) Variant of (C) with multiple concatenations, that is, the two wave vectors are applied multiple times, usually in an alternating manner. Note that the individual wave vectors may have any direction. The angle between the two wave vectors of (C)–(E) will be denoted as θ. It should be emphasized that the MWV experiments are defined based on the diffusion-weighting properties and can be used with any RF pulse sequence.

$$b = \int_0^T k^2(t)\mathrm{d}t = \gamma^2 \int_0^T \left(\int_0^t G(t')\mathrm{d}t' \right)^2 \mathrm{d}t \tag{1}$$

that varies with the angle θ between the two wave vectors:

$$b = \gamma^2 \delta^2 \left[\left(\Delta - \frac{\delta}{3} \right) \left(G_1^2 + G_2^2 \right) - \frac{\delta}{3} G_1 G_2 \cos\theta \right]. \tag{2}$$

The first term represents the effect of the two individual diffusion weightings involved, the second the modulation introduced due to their interaction. Considering trapezoidal diffusion gradient pulses with a finite ramp time t_r ($t_r < \delta$, $\Delta - \delta$), it can be calculated to

$$b = \gamma^2 \left[\left(\delta^2 \Delta - \frac{\delta^3}{3} - \frac{\delta}{6} t_r^2 + \frac{1}{30} t_r^3 \right) \left(G_1^2 + G_2^2 \right) - \left(\frac{\delta^3}{3} + \frac{\delta}{6} t_r^2 - \frac{1}{30} t_r^3 \right) G_1 G_2 \cos\theta \right]. \tag{3}$$

Thus, a maximum b value is obtained for the antiparallel wave-vector orientation ($\theta = 180°$), a minimum for parallel orientations ($\theta = 0°$).

This means that freely diffusing spins show a signal modulation with θ with higher signals for parallel and lower signals for antiparallel wave-vector orientations. This modulation is opposite to that expected for restricted diffusion (see Section 2.4.3). Signal contributions from freely diffusing spins could therefore lead to an underestimation of the modulation related to restriction or may mask or even reverse it completely. This should be kept in mind when performing experiments with vanishing mixing times.

2.4. First theoretical approach

In this part, a first theoretical approach is presented for the NMR signal of spins diffusing in isolated pores. It is based on simplifying assumptions about the timing of the experiment: short gradient pulses ($\delta \to 0$), long diffusion times ($\Delta \to \infty$) and either a long ($\tau_m \to \infty$) or a vanishing mixing time ($\tau_m \to 0$). These assumptions are often referred to as ''ideal'' timing parameters because the specific MWV effects are most pronounced for this case.

The results obtained can be expected to represent a good approximation for experiments as long as the gradient pulses, diffusion times and mixing times are small or large, respectively, compared to the time τ_D which is the time a spin typically needs to cross the pore, that is, $\tau_D = a^2/2D$, where a is the pore size and D the bulk diffusivity. However, even these less stringent assumptions are hard to meet in real experiments and an accurate analysis will require a more sophisticated approach like that presented recently by Özarslan et al.[36] But because the ''ideal'' experiment offers a straightforward and easy access to the specific MWV properties and effects, it will be presented here. Although it has been slightly generalized by allowing for n wave vectors the presentation closely follows the original considerations of Mitra.[7]

2.4.1. Short-pulse approximation

In the short-pulse approximation, that is, assuming that the gradient pulse duration δ approaches 0 while the wave vector $\mathbf{q}$ remains constant, the phase difference $\Delta\varphi$ that a particle accumulates when diffusing along the trajectory $\mathbf{r}(t)$, is given by[37]

$$\Delta\varphi(\mathbf{q},\Delta) = \mathbf{q}\cdot[\mathbf{r}(0) - \mathbf{r}(\Delta)] \tag{4}$$

for a single diffusion weighting, a diffusion time Δ and a wave vector $\mathbf{q}=\gamma\delta\,\mathbf{G}$ with the gyromagnetic ratio γ and the gradient amplitude $\mathbf{G}$. The corresponding MR signal then obeys[37]

$$M(\mathbf{q},\Delta) \propto \left\langle \mathrm{e}^{-i\mathbf{q}\cdot[\mathbf{r}(\Delta)-\mathbf{r}(0)]} \right\rangle, \tag{5}$$

where $\langle\rangle$ denotes the average over the spin ensemble within the sample.

For an experiment with n diffusion-weighting periods as shown in Figure 1B, Equation (5) must be extended to

$$M(\mathbf{q}_1,\ldots,\mathbf{q}_n,\Delta,\tau_\mathrm{m}) \propto \left\langle \mathrm{e}^{-\mathrm{i}\mathbf{q}_1\cdot[\mathbf{r}(\Delta)-\mathbf{r}(0)]}\cdot\mathrm{e}^{\mathrm{i}\mathbf{q}_2\cdot[\mathbf{r}(2\Delta+\tau_\mathrm{m})-\mathbf{r}(\Delta+\tau_\mathrm{m})]}\cdot\ldots \right. \\ \left. \cdot\,\mathrm{e}^{(-1)^n\mathrm{i}\mathbf{q}_n\cdot[\mathbf{r}(n\Delta+(n-1)\tau_\mathrm{m})-\mathbf{r}((n-1)\Delta+(n-1)\tau_\mathrm{m})]} \right\rangle . \tag{6}$$

The sign reversal in the exponent is related to the specific RF pulse sequence used in Figure 1B.

2.4.2. Fully restricted diffusion

For spins diffusing in isolated pores within a diffusion time Δ long compared to $\tau_\mathrm{D}=a^2/2D$ ($\Delta\gg\tau_\mathrm{D}$) some simplifications can be achieved. Under these assumptions, the positions at time t and $t+\Delta$, $\mathbf{r}(t)$ and $\mathbf{r}(t+\Delta)$, are independent and, because both are uniformly distributed in the pore, identical:

$$\left\langle \mathrm{e}^{-\mathrm{i}\mathbf{q}_j\cdot[\mathbf{r}(t+\Delta)-\mathbf{r}(t)]} \right\rangle = \left\langle \mathrm{e}^{-\mathrm{i}\mathbf{q}_j\cdot\mathbf{r}(t+\Delta)} \right\rangle\cdot\left\langle \mathrm{e}^{\mathrm{i}\mathbf{q}_j\cdot\mathbf{r}(t)} \right\rangle = \left\langle \mathrm{e}^{-\mathrm{i}\mathbf{q}_j\cdot\mathbf{r}} \right\rangle\cdot\left\langle \mathrm{e}^{\mathrm{i}\mathbf{q}_j\cdot\mathbf{r}} \right\rangle. \tag{7}$$

Thus, Equation (6) can be re-written to

$$M(\mathbf{q}_1,\ldots,\mathbf{q}_n,\Delta\to\infty,\tau_\mathrm{m}) \propto \left\langle \mathrm{e}^{\mathrm{i}\mathbf{q}_1\cdot\mathbf{r}} \right\rangle\cdot\left\langle \mathrm{e}^{(-1)^n\mathrm{i}\mathbf{q}_n\cdot\mathbf{r}} \right\rangle\cdot\prod_{j=1}^{n-1}\left\langle \mathrm{e}^{(-1)^j\mathrm{i}[\mathbf{q}_j\cdot\mathbf{r}(t)+\mathbf{q}_{j+1}\cdot\mathbf{r}(t+\tau_\mathrm{m})]} \right\rangle. \tag{8}$$

Two limiting cases for the mixing time τ_m between the diffusion weightings, a vanishing and a very large τ_m, are now distinguished.

For a very short mixing time ($\tau_\mathrm{m}\to 0$), the positions at t and $t+\tau_\mathrm{m}$ are identical for each spin, that is, $\mathbf{r}(t+\tau_\mathrm{m})=\mathbf{r}(t)$, and Equation (8) yields

$$M(\mathbf{q}_1,\ldots,\mathbf{q}_n,\Delta\to\infty,\tau_\mathrm{m}\to 0) \propto \left\langle \mathrm{e}^{\mathrm{i}\mathbf{q}_1\cdot\mathbf{r}} \right\rangle\cdot\left\langle \mathrm{e}^{(-1)^n\mathrm{i}\mathbf{q}_n\cdot\mathbf{r}} \right\rangle\cdot\prod_{j=1}^{n-1}\left\langle \mathrm{e}^{(-1)^j\mathrm{i}(\mathbf{q}_j+\mathbf{q}_{j+1})\cdot r} \right\rangle. \tag{9}$$

Because the ensemble average $\left\langle \mathrm{e}^{\mathrm{i}\mathbf{q}\cdot\mathbf{r}} \right\rangle$ is equal to $\tilde{\rho}$, the Fourier transform of the spin density distribution ρ

$$\left\langle e^{i\mathbf{q}\cdot\mathbf{r}}\right\rangle = \int_{\text{pore}} \rho(\mathbf{r}) e^{i\mathbf{q}\cdot r} d\mathbf{r} = \widetilde{\rho}(\mathbf{q}), \tag{10}$$

Equation (10) yields

$$M(\mathbf{q}_1,\ldots,\mathbf{q}_n,\Delta\to\infty,\tau_m\to 0) \propto \widetilde{\rho}(\mathbf{q}_1)\cdot\widetilde{\rho}((-1)^n\mathbf{q}_n)\cdot\prod_{j=1}^{n-1}\widetilde{\rho}\left((-1)^j\left(\mathbf{q}_j+\mathbf{q}_{j+1}\right)\right) \tag{11}$$

for a single pore ensemble.

For a long mixing time ($\tau_m \gg \tau_D$), the positions $\mathbf{r}(t)$ and $\mathbf{r}(t+\tau_m)$ are also independent and uniformly distributed within the pore. Thus, Equation (8) can be simplified to

$$M(\mathbf{q}_1,\ldots,\mathbf{q}_n,\Delta\to\infty,\tau_m\to\infty) \propto \prod_{j=1}^{n}\left\langle e^{i\mathbf{q}_j\cdot\mathbf{r}}\right\rangle\cdot\left\langle e^{-i\mathbf{q}_j\cdot\mathbf{r}}\right\rangle = \prod_{j=1}^{n}\left|\widetilde{\rho}\left(\mathbf{q}_j\right)\right|^2 \tag{12}$$

for a single pore ensemble using $\left\langle e^{-i\mathbf{q}\cdot\mathbf{r}}\right\rangle = \widetilde{\rho}^*(\mathbf{q})$.

If multiple pore ensembles are considered, for example, with different sizes or orientations, the signal contributions according to Equation (11) or (12), respectively, must be added.

2.4.3. Restriction and anisotropy effect

For an experiment with two wave vectors, Equation (11) which is valid for vanishing mixing times yields

$$M(\mathbf{q}_1,\mathbf{q}_2) \propto \sum_i \widetilde{\rho}_i(\mathbf{q}_1)\widetilde{\rho}_i(\mathbf{q}_2)\widetilde{\rho}_i(-\mathbf{q}_1-\mathbf{q}_2), \tag{13}$$

where an index i has been introduced for pore ensemble i to account for multiple pore ensembles with different pore orientations or geometries. Considering this result for an isotropic (random) orientation distribution of identical pores and performing a Taylor expansion to second order in q yields

$$M(q,\theta) \propto 1 - \frac{1}{3}q^2\left\langle R^2\right\rangle(2+\cos\theta) \tag{14}$$

for $q_1 = q_2 = q$, with θ being the angle between the two wave vectors, that is, $\cos\theta = \mathbf{q}_1\mathbf{q}_2/q^2$, and the so-called mean-squared radius of gyration

$$\left\langle R^2\right\rangle = \int_{\text{pore}} r^2 d\mathbf{r}. \tag{15}$$

This means that the signal for short mixing times shows a cosine-shaped modulation if the angle θ between the two wave vectors is varied. Thereby, the modulation amplitude is proportional to $\langle R^2\rangle$, a measure reflecting the pore size.

For two wave vectors, Equation (12) derived for long mixing times simplifies to

$$M(\mathbf{q}_1, \mathbf{q}_2) \propto \sum_i |\widetilde{\rho}_i(\mathbf{q}_1)|^2 |\widetilde{\rho}_i(\mathbf{q}_2)|^2. \tag{16}$$

For this case, Mitra considered spherical and ellipsoidal pores with an isotropic orientation distribution up to the fourth-order terms. He argued that no angular modulation will be present for spherical cells while ellipsoidal pores will exhibit a signal difference between parallel and orthogonal wave vectors arising in the fourth-order terms.[7] A calculation of the signal difference performed by Cheng and Cory[8] for randomly oriented spheroidal pores up to fourth-order terms yielded

$$M_{\parallel}(q) - M_{\perp}(q) = \frac{2}{375}\left(a^2 - b^2\right)^2 q^4, \tag{17}$$

where a and b denote the semi-axes. As expected, it vanishes for spherical pores ($a = b$).

Thus, two effects were predicted by Mitra[7] when exploiting the additional degrees of freedom provided by the DWV experiment, the mixing time and the angle θ between the two wave vectors. First, a signal modulation with $\cos\theta$ at short mixing times that appears in the second order of q for any pore shape and whose amplitude increases with the pore size (Figure 2A). It will be referred to as the ''restriction effect''. Such experiments are a straightforward approach to estimate pore or compartment sizes. The modulation reflects non-Gaussian diffusion and can be considered as a fingerprint for the presence of diffusion restrictions. The $\cos\theta$-shape of the restriction effect implies that the signal amplitude for

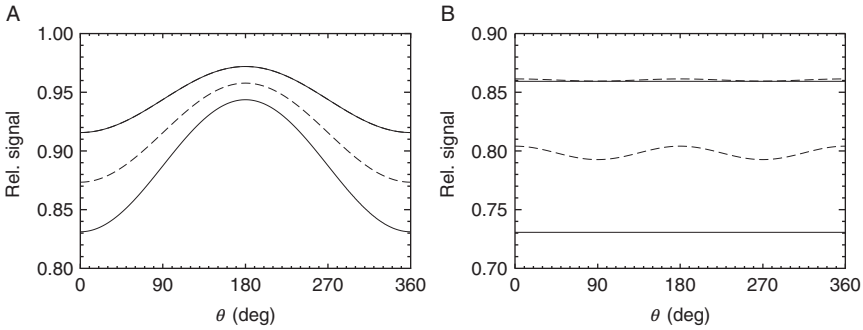

Figure 2 Relative signal amplitude of a DWV experiment versus the angle θ between the two wave vectors with (A) short and (B) long mixing time for ideal timing parameters ($\delta \to 0$, $\Delta \to \infty$, $\tau_m \to 0$ or ∞, respectively). Only terms up to (A) second and (B) fourth order were considered. Solid lines were obtained for spherical pores with two different radii (ratio $1 : \sqrt{2}$), the lower curves correspond to the larger radius. The dashed lines were calculated for spheroidal pores with ratios of 2:1 and 4:1, respectively, for the semi-axes. In (A), the curve with the less eccentric pore is hidden under the upper sphere curve because both pores have an identical mean-squared radius of gyration. The curves demonstrate (A) the cos-shaped signal decay for short mixing times and (B) the $\cos 2\theta$ modulation for eccentric pores at long mixing times.

antiparallel wave-vector orientations ($\theta = 180°$) is larger than that for a parallel orientation ($\theta = 0°$). This change in the signal amplitude upon an inversion of one of the two diffusion weightings seems to be surprising because in single-wave-vector experiments the polarity of a diffusion weighting has no influence on the signal. It is therefore considered from a more intuitive point-of-view in Section 2.5.

Second, at long mixing times, a signal difference between parallel and orthogonal wave-vector orientations is present in the fourth-order terms that is characteristic for microscopically anisotropic diffusion as, for example, in eccentric pores (Figure 2B). This ''anisotropy effect'' can be observed even if the sample macroscopically appears isotropic, for example, because of an isotropic orientation distribution of eccentric pores. Thus, it can reliably detect diffusion anisotropy on a scale beyond the resolution achievable with imaging approaches.

Both effects can provide access to information about the microstructure that is hard or impossible to achieve with single-wave-vector experiments. This can, for instance, be seen in the example of one-dimensional tubes with isotropic orientation distribution.[7] In a single-wave-vector experiment, the signal decay for such a sample is non-exponential but can perfectly be modelled by a two-component diffusion, that is, a mixture of two ensembles with different, isotropic diffusion coefficients (''bi-exponential'' signal decay). For such a system, the signal should be isotropic for the DWV experiment as well, that is, no signal variation should occur if the angle between the two wave vectors is changed. This is in contrast to the tube system where a reduced signal is observed for orthogonal wave vectors compared to parallel or antiparallel wave vectors at long mixing times.[7] Similarly, the DWV experiment with short mixing time could detect the effect of restrictions, even for the isotropic geometry of spheres. Thus, the DWV experiment, for instance, can distinguish whether a non-exponential signal decay is due to different diffusion coefficients or due to local anisotropy or restriction.

It should be noted in this context that the anisotropy effect can also be expected if the diffusion is Gaussian,[38] for example, described by a rank-2 diffusion tensor. This is due to the multiplication of the decay factors in a DWV experiment and can easily be demonstrated for a mixture of two ensembles with anisotropic diffusion and identical number of spins. Each ensemble has diffusion coefficients of D_1 and D_2 in orthogonal axes but their orientations are rotated by 90°. In a single-wave-vector experiment, the diffusion attenuation along any of the two axes is given by $\frac{1}{2}\left(e^{-bD_1} + e^{-bD_2}\right) \approx 1 - \frac{1}{2}\,b(D_1 + D_2) + \frac{1}{4}b^2\left(D_1^2 + D_2^2\right)$. For a DWV experiment with parallel (or antiparallel) wave vectors, the same result is obtained for both axes: $\frac{1}{2}\left(e^{-bD_1}\cdot e^{-bD_1} + e^{-bD_2}\cdot e^{-bD_2}\right) \approx 1 - b(D_1 + D_2) + b^2\left(D_1^2 + D_2^2\right)$. It differs from the single-wave-vector results only due to the effectively doubled b value. But for orthogonal wave vectors, the signal attenuation is given by $e^{-bD_1}\cdot e^{-bD_2} = e^{-b(D_1+D_2)} \approx 1 - b(D_1 + D_2) + \frac{1}{2}b^2(D_1 + D_2)^2$, that is, a difference of $\frac{1}{2}b^2(D_1 - D_2)^2$ compared to parallel orientations. The difference vanishes for $D_1 = D_2$ and is positive for $D_1 \neq D_2$ corresponding to a higher signal amplitude for parallel wave vectors. This means that the anisotropy effect can be expected to be also detectable in samples or under experimental conditions where the diffusion is not (fully) restricted, for example, as in Ref. 38. This may be of particular importance for applications in biological tissue, like white matter in the brain and

spine, where restrictions may be absent in certain directions or, due to finite diffusion times, diffusion is not fully restricted on the time scale of the experiment.

2.4.4. Negative diffraction

Aside from the angular modulation of the signal at short mixing times, the underlying Equation (11) also reflects an unusual and interesting diffraction effect which recently has been discovered by Özarslan and Basser.[9] The basic principles of this ''negative diffraction'' will be summarized in this section similar to the presentation in Ref. 9. Thereby, only a single pore population is considered for simplicity.

For a single-wave-vector experiment, that is, $\mathbf{q}_1 = \mathbf{q}$, $\mathbf{q}_j = \mathbf{0}$, Equation (12), derived for ideal timing parameters, δ, $\tau_m \to 0$ and $\Delta \to \infty$, simplifies to

$$M(\mathbf{q}) \propto |\widetilde{\rho}(\mathbf{q})|^2. \tag{18}$$

For the zero crossings of $\widetilde{\rho}(\mathbf{q})$, the signal vanishes which represents the diffraction minima or ''dips''[39,40] (see Section 2.6). But the signal is always positive, that is, M can be considered to have only zeros of even order.

Özarslan and Basser investigated the corresponding equations for an experiment with n wave vectors[9] as shown in Figure 1B. In the short-pulse approximation and for a long mixing time, the signal decay for parallel or antiparallel wave vectors ($\mathbf{q}_i = \pm\mathbf{q}$) is given by

$$M_n(\pm\mathbf{q}, \ldots, \pm\mathbf{q}) \propto \prod_{j=1}^{n} |\widetilde{\rho}(\mathbf{q})|^2 = |\widetilde{\rho}(\mathbf{q})|^{2n}, \tag{19}$$

where $\widetilde{\rho}(\mathbf{q}) = \widetilde{\rho}^*(-\mathbf{q})$ was used. Thus, aside from a stronger diffusion weighting, no basic difference regarding the diffraction pattern is present: the zeros' positions are untouched, their order changes but remains even.

This is different at short mixing times. For identical wave vectors ($\mathbf{q}_j = \mathbf{q}$), Equation (11) yields[9]

$$\begin{aligned} M_n(\mathbf{q}, \ldots, \mathbf{q}) &\propto \widetilde{\rho}(\mathbf{q}) \cdot \widetilde{\rho}((-1)^n \mathbf{q}) \cdot \prod_{j=1}^{n-1} \widetilde{\rho}\left((-1)^j (2\mathbf{q})\right) \\ &= \begin{cases} |\widetilde{\rho}(\mathbf{q})|^2 |\widetilde{\rho}(2\mathbf{q})|^{n-1} & \text{for } n \text{ odd} \\ \widetilde{\rho}^2(\mathbf{q}) \widetilde{\rho}^*(2\mathbf{q}) |\widetilde{\rho}(2\mathbf{q})|^{n-2} & \text{for } n \text{ even} \end{cases}, \end{aligned} \tag{20}$$

which shows that the signal is always positive for any odd n. The two important findings are that (i) additional zero crossings (diffraction dips) appear for $n > 1$, the first of these at half the q value, and (ii) a sign reversal of the signal occurs at the additional zero crossings for even n (Figure 3A).

The occurrence of the first zero crossing at half the q value is promising as it would relax the gradient hardware demands. So far, ideal timing parameters ($\tau_m = 0$) were considered where the intermediate gradient pulses overlap which means that there is no benefit in the gradient amplitude. However, it has been

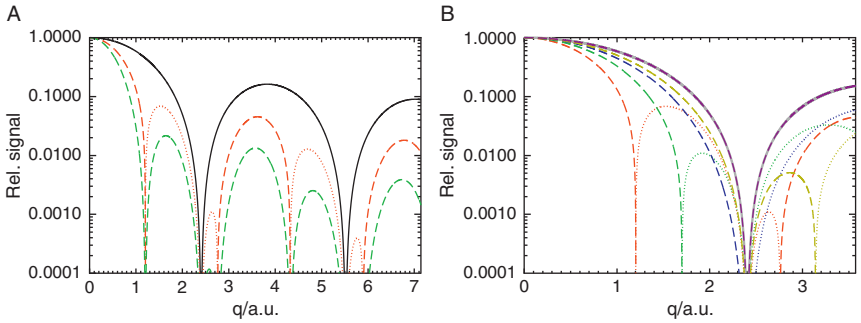

Figure 3 Relative signal amplitude versus the amplitude of the wave vector q for a spherical pore demonstrating the negative diffraction effect. Note that negative signal amplitudes were inverted (dotted) in both plots. (A) Experiment with one (black, solid), two (red) and three (green) wave vectors in parallel orientation. (B) DWV experiment (dashed) with different angles between the two wave vectors: 0° (parallel, red), 90° (orthogonal, green), 120° (blue), 135° (yellow) and 180° (anti-parallel, purple). The reference single-wave-vector experiment is shown in grey (solid). The first zero crossing which has the sign reversal, moves from half the q value of the single-wave-vector experiment to larger q values. Also note that the curve for antiparallel wave vectors (purple) coincides with the single-wave-vector curve. The exact solution for ideal timing parameters, that is, $\delta \to 0$, $\Delta \to \infty$, $\tau_m \to 0$, were used for all simulations.

shown, theoretically[9] and experimentally,[41] that the negative diffraction effect can also be observed for $\tau_m > \delta$, that is, without overlapping gradient pulses. In this case, one half of the gradient amplitude necessary in single-wave-vector experiments is sufficient to observe diffraction effects in DWV experiments which would considerably reduce hardware demands.

Even more interesting is the sign reversal due to the zeros of odd order which also is the reason for using the term ''negative diffraction''. Unlike the zeros of even order, it is very insensitive to wave-vector orientations and size and orientation distributions as will be outlined in detail in Section 5.

For a slightly more general experiment with $\mathbf{q}_{2j+1} = \mathbf{q}_1$ and $\mathbf{q}_{2j} = \mathbf{q}_2$,

$$M_n(\mathbf{q}_1, \mathbf{q}_2) \propto \begin{cases} |\widetilde{\rho}(\mathbf{q}_1)|^2 |\widetilde{\rho}(\mathbf{q}_1 + \mathbf{q}_2)|^{n-1} & \text{for } n \text{ odd} \\ \widetilde{\rho}(\mathbf{q}_1)\widetilde{\rho}(\mathbf{q}_2)\widetilde{\rho}^*(\mathbf{q}_1 + \mathbf{q}_2)|\widetilde{\rho}(\mathbf{q}_1 + \mathbf{q}_2)|^{n-2} & \text{for } n \text{ even} \end{cases} \quad (21)$$

is obtained for the DWV experiment at short mixing times. This implies that the additional zero crossings depend on the angle between the two wave vectors. For a spherical geometry where $\widetilde{\rho}(\mathbf{q}) = \widetilde{\rho}(q)$, they will only depend on $|\mathbf{q}_1 + \mathbf{q}_2|$, that is, the relative orientation of $\mathbf{q}_1$ and $\mathbf{q}_2$. Assuming furthermore $q_1 = q_2 = q$, $|\mathbf{q}_1 + \mathbf{q}_2|$ yields $q\sqrt{2 + 2\cos\theta}$. For $\theta = 0°$, the first additional zero crossing appears at half the q value as mentioned above. With increasing $\theta < 120°$ it moves towards the single-wave-vector zero crossings and coincides with it for $\theta = 120°$ (Figure 3B). Thus, the same dips as in the single-wave-vector experiment are observed in the DWV experiment, however, they still show the sign reversal for even n. For $\theta > 120°$,

the additional dips appear at larger q values, that is, beyond the single-wave-vector dips, and disappear to infinity for $\theta = 180^\circ$ (Figure 3B).

2.5. Phase evolution

The signal difference between parallel and antiparallel wave-vector orientations at short mixing times according to Equation (14) is not very intuitive. Compared to parallel wave vectors the signal decay is reduced by a factor of $1/3$ if the polarity of one of the wave vectors in inverted. This seems to be quite unusual because in single-wave-vector experiments the polarity of the diffusion weighting does not have an influence on the signal amplitude. However, this behaviour can be understood when considering the phase evolution of spins in a simple geometry as will be summarized here.[41a]

Consider spins diffusing between two parallel planes that are perpendicular to the direction of the diffusion weighting. The phase evolution at three different positions is shown in detail in Figure 4. Assuming that this ''pore'' is located in the isocentre, a diffusion-weighting gradient pulse does not affect spins in the middle between the two planes (yellow) but those at the outer positions. They experience a phase shift of the same magnitude (α) but with opposite polarities (red and green; see, e.g. Figure 4C). Note that in this example no refocusing RF pulses are used and the simplified pulse sequence of Figure 4A is considered.

Prior to the first diffusion-weighting gradient pulse, the spins are in phase (Figure 4B). The first (positive) dephasing gradient pulse changes the phase of the spins at the outer positions by α (Figure 4C). During the diffusion time which is assumed to be long, the spins from all positions diffuse anywhere between the two planes and are distributed uniformly. This means that at the three positions the same (uniform) mixture of spin phases with an angular coverage of 2α is present prior to the first rephasing gradient (Figure 4D). The (negative) rephasing gradient then tilts these distributions by α in a direction opposite to that of the dephasing gradient pulse (Figure 4E). The averaged phase distribution then spans an angle of 4α with a triangular-shaped population (Figure 4F): from the maximum at the centre phase (yellow) it linearly decreases to the minimum values at -2α (red) and $+2\alpha$ (green). This distribution represents, as expected,[39] the autocorrelation function of the pore. It is obvious that this phase dispersion yields a lower overall signal than the initial magnetization which reflects the diffusion-induced signal attenuation of single-wave-vector experiments.

Due to the short mixing time assumed, the phase distribution present after the first rephasing gradient (Figure 4E) is identical to that prior to the second dephasing gradient (Figure 4G). The two cases of a parallel and antiparallel orientation must now be distinguished. For the antiparallel orientation, the dephasing gradient of the second wave vector has an inverted polarity compared to the rephasing of the first wave vector, that is, the phase tilt introduced by the latter gradient is removed completely (Figure 4H). This also means that the phase distribution after the dephasing is identical to the uniform distribution obtained after the first diffusion time covering the range between $-\alpha$ and $+\alpha$ at any position. Thus, the second diffusion time has no additional effect as it uniformly mixes uniform

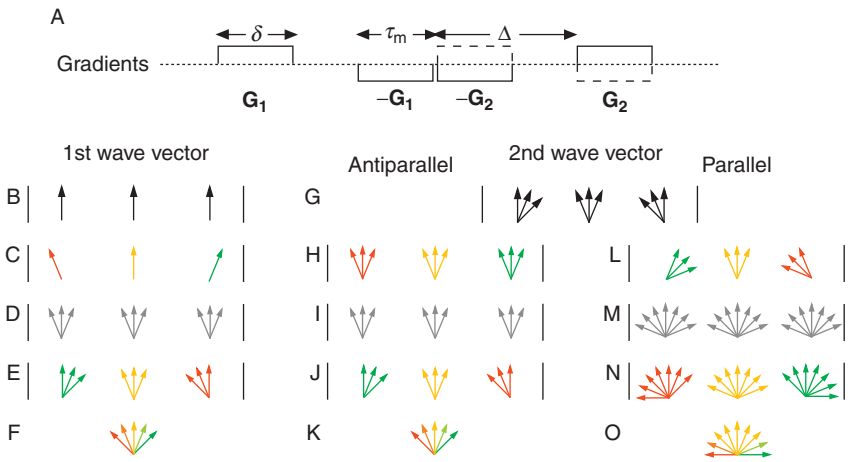

Figure 4 (A) Simplified pulse sequence for a DWV experiment without RF pulses. For a proper rephasing the two gradients of a diffusion weighting need to be applied with opposite polarities. For the second diffusion weighting ($\mathbf{G}_2$), the solid lines correspond to the parallel, the dashed to the antiparallel orientations. (B–O) Phase evolution for spins diffusing between parallel planes during a DWV experiment as sketched in (A) with a short mixing time. Three different positions are considered: in the middle between the two planes, assumed to be in the isocentre, and left and right at the two planes. Note that the gradient pulse duration (δ) is assumed to be short, that is, diffusion during the pulses is neglected, and the diffusion time (Δ) is considered to be long. (B, G) Phase distribution before the first and the second diffusion weighting, respectively. The phase evolutions during (C–E) the first and (H–J, L–N) the second diffusion weighting for (H–J) antiparallel and (L–N) parallel wave-vector orientations. (C, H, L) reflect the effect of the dephasing gradient pulses, (D, I, M) that of the subsequent diffusion time and (E, J, N) the effect of the rephasing gradient pulse. (F, K, O) represent the phase distribution averaged over all three positions considered. Note the identical distributions in (F) and (K) because for the antiparallel orientation the effects of the two middle gradient pulses cancel, the broader distribution for the parallel orientations (O) reflects the lower signal amplitude. For details see text and Ref. 41a.

distributions (Figure 4I). The final rephasing gradient then tilts the phases again by α (Figure 4J) and reproduces the phase distribution (Figure 4K) observed after the first rephasing gradient (Figure 4F) and described above.

The lack of an additional effect for the second diffusion weighting is obvious if the assumptions, a long diffusion time and a vanishing mixing time, are recalled. Effectively, the second and third gradient cancel each other which means that the two-wave-vector experiment with antiparallel orientations is identical to a single-wave-vector experiment with the doubled diffusion time (Figure 4A). However, as the diffusion was assumed to be long, a further prolongation has no additional effect.

The phase evolution is different for the parallel wave-vector orientation where the dephasing gradient pulse of the second wave vector amplifies the phase tilt introduced by the previous rephasing gradient (Figure 4L). This yields locally a

still narrow phase distribution (spanning 2α) but the centre phase varies considerably, by $\pm 2\alpha$, across the pore. During the second diffusion time, the spins mix up again completely and at the end of the diffusion time they are again uniformly distributed with a broad phase distribution that spans 6α at any position (Figure 4M). The final rephasing gradient adds another tilt by α (Figure 4N). Thus the phases in the pore are distributed over a range of 8α (Figure 4O).

Thus, compared to the antiparallel orientation, this distribution covers a doubled phase range. A detailed calculation taking the more flattened population distribution for the parallel orientation into account, yields the factor of 3 between the two signal decays for small α which is consistent with Equation (14).[41a]

From these considerations, it is obvious that the signal difference vanishes for long mixing times. Then, the phase distribution is mixed up after the first rephasing, yielding a uniform and position-independent distribution. It behaves mirror-symmetrically for parallel and antiparallel orientations and, thus, shows no magnitude effect anymore.

In other words, the short mixing time is required to achieve a sensitivity to short-time correlations specific for restrictions: if a spin's displacement is large during the first diffusion-weighting period, it will end up close to the restricting walls which means that the displacement during the second period must be very small or, most likely, in the opposite direction. For a long mixing time, this correlation is lost as the spin in the mean time may have moved to anywhere within the pore, that is, its displacement during the second periods is independent of its position after the first period.

This is in contrast to the anisotropy effect where a long mixing time is desired. In this case, not the interference of the spins with the restrictions is of interest. It would reflect the local boundary properties rather than the geometry on the pore level. More important is the spatial distance the spins can travel in the different directions. Thus, a long time to explore the full, restricted geometry may be beneficial because it does not limit the spins' ''experience'' to their direct neighbourhood. This not only holds for the mixing time but also for the encoding time, that is, the diffusion time, such that ideally all spins are exposed to the pore's eccentricity and exhibit a diffusion anisotropy. In addition, a shorter mixing time would interfere with the restriction effect. It implies an increased signal for orthogonal compared to parallel wave-vector orientations which could mask the anisotropy effect.

2.6. Diffusion propagator

An alternative approach to describe the signal of diffusion-weighted acquisitions is based on the diffusion propagator $P(\mathbf{r}_0|\mathbf{r}_1,t)$ which gives the probability that a particle with an initial position of $\mathbf{r}(0)=\mathbf{r}_0$ is at time t found at $\mathbf{r}(t)=\mathbf{r}_1$.[42] The propagator obeys the diffusion equation, that is,

$$D\nabla^2 P(\mathbf{r}_0|\mathbf{r},t) = \frac{\partial}{\partial t} P(\mathbf{r}_0|\mathbf{r},t) \tag{22}$$

with $P(\mathbf{r}_0|\mathbf{r},0)=\delta(\mathbf{r}_0-\mathbf{r})$. In the short-pulse approximation, the signal amplitude then can be written as

$$M(\mathbf{q}) = \int \rho(\mathbf{r}_0) \int P(\mathbf{r}_0|\mathbf{r}_1,\Delta) e^{i\cdot\mathbf{q}\cdot(\mathbf{r}_1-\mathbf{r}_0)} d\mathbf{r}_1 d\mathbf{r}_0. \quad (23)$$

For restricted geometries it is helpful to use the so-called averaged propagator (e.g. Ref. 43) given by

$$\bar{P}(\mathbf{R},t) = \int \rho(\mathbf{r}) P(\mathbf{r}|\mathbf{r}+\mathbf{R},t) d\mathbf{r}, \quad (24)$$

which describes the average probability for any particle to be displaced by $\mathbf{R}$.

The Fourier transformation of Equation (23) which was derived under the short-pulse approximation yields

$$\widetilde{M}(\mathbf{r}) = \int \rho(\mathbf{r}_0) P(\mathbf{r}_0|\mathbf{r}_0+\mathbf{r},\Delta) d\mathbf{r}_0 = \bar{P}(\mathbf{r},t), \quad (25)$$

which means that the diffusion-weighted signal $M(\mathbf{q})$ is proportional to the Fourier transform of the averaged propagator.[43]

In case of fully restricted diffusion and long diffusion times, the probability is uniformly distributed within the pore, that is, $P(\mathbf{r}_0|\mathbf{r}_0+\mathbf{r},\Delta)=\rho(\mathbf{r}_0+\mathbf{r})$. Thus, Equation (24) can be written as

$$\widetilde{M}(\mathbf{r}) = \int \rho(\mathbf{r}_0)\rho(\mathbf{r}_0+\mathbf{r}) d\mathbf{r}_0. \quad (26)$$

This means that, the Fourier transform of the signal, and thus the averaged propagator, is given by the autocorrelation of the pore geometry.[39] Taking the Wiener–Khintchine theorem into account,

$$M(\mathbf{q}) = |\widetilde{\rho}(\mathbf{q})|^2 \quad (27)$$

can be obtained, that is, the signal amplitude, as a function of $\mathbf{q}$, is proportional to the squared magnitude of the Fourier transform of the pore geometry function.[39] This reproduces Equation (18), that is, Equation (12) with $n=1$.

As pointed out by Cory and Garroway,[39] this result for the NMR signal is equivalent to the power diffraction pattern of a single slit in classical optics whose transmission is described by the pore geometry. This so-called ''diffusion–diffraction'' effect could yield information about the pore geometry with much higher spatial resolution than achievable with conventional imaging approaches. It means that the NMR signal as a function of $\mathbf{q}$ can be expected to exhibit a non-monotonic behaviour with zeros (''dips'') of order 2 whose positions depend on the pore dimension along the direction of the diffusion-weighting gradient.

Extending the approach to porous structures, that is, connected pores characterized by a so-called lattice correlation function, revealed an additional modulation with the Fourier transform of this lattice correlation function[44] which can be considered to reflect the interferences observed in a multi-slit experiment or the

powder grating in X-ray diffraction. The first experimental observation of such a diffraction effect was reported in 1990 by Callaghan et al.[40]

2.7. Bloch–Torrey equation

For a more general description of diffusion-weighted experiments, the Bloch–Torrey equations must be considered that add the terms for translational spin motion to the Bloch equations.[45] For the (complex) transverse magnetization $M(\mathbf{r},t)$ of spins diffusing with a diffusion coefficient D in the presence of a time-variable gradient $\mathbf{G}(t)$ it is given by[45]

$$\frac{\partial}{\partial t}M(\mathbf{r},t) = D\nabla^2 M(\mathbf{r},t) - \mathrm{i}\gamma\mathbf{G}(t)\cdot\mathbf{r}M(\mathbf{r},t), \tag{28}$$

where relaxation, Larmor precession, and bulk motion were ignored in order to focus on the effect of diffusion. For free diffusing spins the solution is straightforward. But the description of spins diffusing in a confined geometry beyond the short-pulse approximation has been a topic for a long time.

One of the first approaches was reported by Robertson[46] as early as in 1966 for spins diffusing between parallel plates in the presence of a constant gradient. He could derive an approximative expression for the signal, however, locally assumed Gaussian diffusion and ended up with the cumulant expansion. His important idea was to express the magnetization in the orthonormal basis of eigenfunctions of the Laplace operator which is present in the Bloch–Torrey equation, for the chosen geometry. Thus, he reduced the problem in the first steps he made to the calculation of the geometry's Laplace eigenfunctions that appear in many fields and have been considered for a variety of geometries.

Later, Sheltraw and Kenkre[47] applied the memory function technique, well known from other physical applications, to the problem. It yields an equation where the partial time derivative of the magnetization depends on the time convolution of the magnetization with a memory function. Furthermore, they could show that their approach reduces to the cumulant expansion if the memory time is considered to be short. This approach can model some features, like diffraction effects, better than the cumulant expansion but accurate results are still limited to small q values.

Caprihan et al.[48] used a different approach which involves an expansion of the diffusion propagator in its eigenfunctions for the geometry considered. Furthermore, they approximated an arbitrary gradient shape by a series of impulses, each fulfilling the narrow-pulse limit, interleaved with periods of spin diffusion. This is why the method often is referred to as the multiple propagator approach. For practical calculations it must be considered that the number of eigenvalues and eigenfunctions is infinite. However, the infinite series converges quite quickly when successively including eigenfunctions with larger eigenvalues. Thus, the approach is able to model diffraction patterns much better than previous approaches.

Callaghan[49] has shown that this approach can be written in a matrix product formalism which improves the efficiency of numerical calculations considerably even for complex gradient waveforms and short raster times. This significantly facilitated the application of the approach.

A different method was presented by Barzykin[50,51] who considered, unlike Robertson, the full problem in the eigenfunctions of the Laplace operator. The infinite number of eigenfunctions is written in a matrix form which yields an analytical solution for a constant gradient field. Considering arbitrary gradient time courses as piecewise constant gradients, the approach can easily be extended to any waveforms. In the limit of infinitely short raster times, it has been shown to be identical to the matrix product formalism.[51] This approach has recently been extended by Grebenkov[52,53] to general diffusion problems, that is, without focusing to the Bloch–Torrey equation, yielding the so-called multiple correlation function (MCF) description. This approach has been extended by Özarslan et al.[36] to DWV experiments (Section 3.3.2).

3. EXTENDED AND GENERALIZED THEORY

The theoretical considerations presented in Section 2.4 are based on the assumption of isolated pores and ''ideal'' timing parameters, that is, short gradient pulses, long diffusion times and either a short or long mixing time. Furthermore, the expression for the angular signal modulation at short mixing times, Equation (14), was derived for small q values and an isotropic orientation distribution of the pores; a corresponding expression for long mixing times has not been reported. Thus, the applicability of these results, although valid for any pore shape, is quite limited.

However, several theoretical extensions and generalizations were introduced in the past few years that will be presented in this section. Two basic branches can be distinguished. In the first, the assumption of ideal timing parameters was retained but the validity for any pore shape as well. The equations for short and long mixing times were generalized to arbitrary orientation distributions and wave-vector orientations using a Taylor expansion to second and fourth order, respectively.[54,55] Furthermore, rotationally invariant measures of the pore size and anisotropy were identified to obtain reliable results independent of the sample's orientation.[54,55] These results were extended to experiments with multiple concatenations of the two wave vectors[56,57] which may improve the detectability of the signal modulations.[56–58] The results for the two limiting cases of a short and long mixing time will be presented in Sections 3.1 and 3.2. This approach was chosen (i) to derive reliable pore measures in the presence of macroscopic anisotropy and (ii) to avoid assumptions on the specific pore shape that may be complex or unknown as, for example, in biological tissue. However, this is, at the expense of the assumption of ideal timing parameters.

In the second branch, summarized in Section 3.3, the timing assumptions were dropped which, however, requires to consider specific pore shapes and orientation distributions to yield usable solutions. The presented approaches are based

on the matrix product formalism of the multiple propagator approach[33] (Section 3.3.1) and the MCF formalism[36] (Section 3.3.2). Both yield accurate results for the finite timing parameters present in real experiments if the eigenfunctions of the Laplace operator are known for the underlying geometry. However, the MCF formalism also holds for arbitrary q values which makes it the most general approach. It involves infinite matrices but converges for a reasonable number of elements to a solution sufficiently accurate in practice. It is required for an accurate modelling of experimental results and a precise determination of pore sizes in known and solvable geometries.

3.1. Ideal timing parameters: Short mixing times

Equation (14) that describes the angular modulation of the signal in a DWV experiment at short mixing times holds only for an isotropic orientation distribution of the pores, an assumption that may be violated, for example, in biological tissue. It cannot be used for macroscopically anisotropic samples.

In this section, the Taylor expansion of Equation (13) is re-investigated to derive signal expressions for arbitrary pore orientation distributions and wave-vector orientation combinations. While the results obtained are valid for any pore shape, ideal timing parameters, including a vanishing mixing time underlying Equation (13), are still assumed. For terms up to second order in q, a rank-2 tensor model has been developed which also allows to identify how the pore size measure can be determined in the more general case[54] (Section 3.1.1). This model has been extended to experiments with multiple concatenations of the two wave vectors (as shown in Figure 1E) which show an improved signal modulation amplitude[56,58] (Section 3.1.2). Considering the fourth-order terms reveals that a $\cos 2\theta$ modulation appears which does not vanish for spherical cells[35] (Section 3.1.3). Thus, the access to microscopic anisotropy seems to be limited to DWV experiments with long mixing times.

3.1.1. Tensor model

3.1.1.1. General signal expression To describe the signal of a short-mixing-time DWV experiment for an arbitrary sample, a rank-2 tensor model has been developed[54] which will be summarized here. In its derivation, a single pore ensemble, that is, a single pore orientation, is considered first. The sum of Equation (13) then is proportional to that of an individual pore, that is,

$$M(\mathbf{q}_1, \mathbf{q}_2) \propto \widetilde{\rho}(\mathbf{q}_1)\widetilde{\rho}(\mathbf{q}_2)\widetilde{\rho}(-\mathbf{q}_1 - \mathbf{q}_2), \tag{29}$$

where the pore index i has been dropped for clarity.

Because in general $\mathbf{q}_1$ and $\mathbf{q}_2$ are independent variables, $M(\mathbf{q}_1, \mathbf{q}_2)$ can be considered as a function of the six-element vector $\mathbf{Q} = \left(\mathbf{q}_1^{\mathrm{T}}, \mathbf{q}_2^{\mathrm{T}}\right)^{\mathrm{T}}$. Equation (29) then can be written as

$$M(\mathbf{Q}) \propto \widetilde{\rho}_1(\mathbf{Q})\widetilde{\rho}_2(\mathbf{Q})\widetilde{\rho}_3(\mathbf{Q}), \tag{30}$$

where the individual factors are also described as functions of $\mathbf{Q}$ according to

$$\begin{aligned} \widetilde{\rho}_1(\mathbf{Q}) &= \widetilde{\rho}(Q_1, Q_2, Q_3) = \widetilde{\rho}(\mathbf{q}_1), \\ \widetilde{\rho}_2(\mathbf{Q}) &= \widetilde{\rho}(Q_4, Q_5, Q_6) = \widetilde{\rho}(\mathbf{q}_2), \\ \widetilde{\rho}_3(\mathbf{Q}) &= \widetilde{\rho}(-Q_1 - Q_4, -Q_2 - Q_5, -Q_3 - Q_6) = \widetilde{\rho}(-\mathbf{q}_1 - \mathbf{q}_2). \end{aligned} \tag{31}$$

For an expansion of Equation (30), $\widetilde{\rho}$ according to Equation (10) must be considered which yields

$$\widetilde{\rho}(\mathbf{q}) = 1 - \frac{1}{2}\mathbf{q}^{\mathrm{T}}\,\underline{\underline{\mathbf{R}}}\,\mathbf{q} + O(q^3), \tag{32}$$

where the pore volume was set to 1, the pore's centre of gravity was chosen as the origin of the coordinate system, and $\underline{\underline{\mathbf{R}}}$ is a 3×3 tensor whose elements are given by

$$R_{ij} = \int_{\text{pore}} \rho(\mathbf{r}) r_i r_j \mathrm{d}\mathbf{r}. \tag{33}$$

Thus,

$$\begin{aligned} \widetilde{\rho}_1(\mathbf{Q}) &= 1 - \frac{1}{2}\mathbf{Q}^{\mathrm{T}}\begin{pmatrix} \underline{\underline{\mathbf{R}}} & 0 \\ 0 & 0 \end{pmatrix}\mathbf{Q} + O(Q^3), \\ \widetilde{\rho}_2(\mathbf{Q}) &= 1 - \frac{1}{2}\mathbf{Q}^{\mathrm{T}}\begin{pmatrix} 0 & 0 \\ 0 & \underline{\underline{\mathbf{R}}} \end{pmatrix}\mathbf{Q} + O(Q^3), \\ \widetilde{\rho}_3(\mathbf{Q}) &= 1 - \frac{1}{2}\mathbf{Q}^{\mathrm{T}}\begin{pmatrix} \underline{\underline{\mathbf{R}}} & \underline{\underline{\mathbf{R}}} \\ \underline{\underline{\mathbf{R}}} & \underline{\underline{\mathbf{R}}} \end{pmatrix}\mathbf{Q} + O(Q^3) \end{aligned} \tag{34}$$

is obtained for the expansion of the individual $\widetilde{\rho}_j(\mathbf{Q})$. The expansion of Equation (30) to second order then can be re-written as

$$M(\mathbf{Q}) \propto 1 - \frac{1}{2}\mathbf{Q}^{\mathrm{T}}\,\underline{\underline{\mathbf{T}}}\,\mathbf{Q} \tag{35}$$

with

$$\underline{\underline{\mathbf{T}}} = \begin{pmatrix} 2\underline{\underline{\mathbf{R}}} & \underline{\underline{\mathbf{R}}} \\ \underline{\underline{\mathbf{R}}} & 2\underline{\underline{\mathbf{R}}} \end{pmatrix}. \tag{36}$$

Equation (35) describes the signal for arbitrary wave vectors $\mathbf{q}_1$ and $\mathbf{q}_2$ that appear as the elements of $\mathbf{Q}$. The ''diagonal'' matrices ($2\underline{\underline{\mathbf{R}}}$) represent the effect of the individual diffusion weightings while the ''off-diagonal'' matrices ($\underline{\underline{\mathbf{R}}}$) reflect the interaction between the two wave vectors in the DWV experiments. Because $\underline{\underline{\mathbf{R}}}$ is symmetric, $\underline{\underline{\mathbf{T}}}$ has only six independent elements that are sufficient to describe the general experiment. They can, in principle, be determined from six measurements with non-collinear $\mathbf{Q}_k$ if the signal without diffusion weighting is known, for example, from a separate acquisition.

In general, Equation (35) does not describe a cos-shaped signal modulation because, in non-spherical pores, the signal decay depends on the wave vectors'

orientation with respect to the pore which changes when varying θ. The corresponding modulation superimposes onto the restriction effect and usually yields a more complex curve as is demonstrated in Figure 5. However, for the special case of an isotropic orientation distribution of identical pores, the tensor description simplifies to Equation (13).[54]

Numerical simulations performed for wave-vector combinations covering the full range of absolute and relative angles showed a good agreement of the fitted tensor equation described by only six elements with the data[54] as can also be seen in Figure 5.

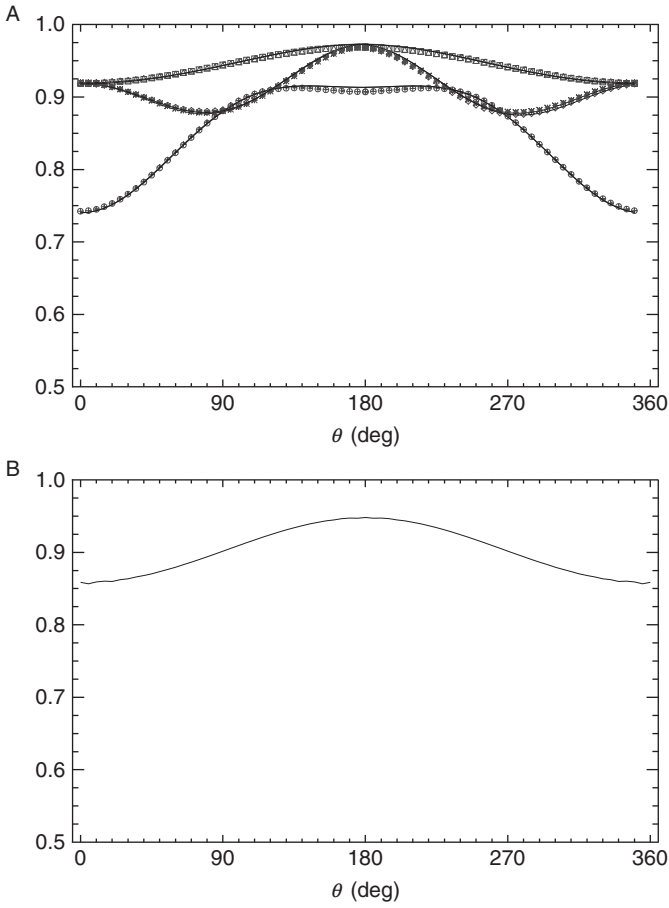

Figure 5 Examples for the signal modulation in short-mixing-time DWV experiments of spheroidal pores versus the angle θ between the two wave vectors. (A) While the first wave vector was fixed, the second sampled different circles starting with a parallel orientation. The symbols represent the results of numerical simulations based on a random walk model; the solid lines depict the fit to the tensor model sketched in Section 3.1.1. (B) shows the simulation result for an isotropic orientations distribution of the pores. For details see Ref. 54. Reprinted from Ref. 54 with permission from Elsevier.

For a mixture of different pore ensembles, for example, with different orientations, pore shapes or pore sizes, the contributions of the individual populations must be summed up according to

$$\underline{\underline{\mathbf{R}}} = \sum_i p_i \underline{\underline{\mathbf{R}}}_i, \tag{37}$$

where i denotes the population and the p_i represent their volume fractions. Thereby, the symmetry of $\underline{\underline{\mathbf{R}}}$ and, thus, $\underline{\underline{\mathbf{T}}}$ is retained because the individual $\underline{\underline{\mathbf{R}}}_i$ are symmetric.

3.1.1.2. Pore size estimate The trace of $\underline{\underline{\mathbf{T}}}$ which is proportional to the trace of $\underline{\underline{\mathbf{R}}}$ is rotationally invariant, that is, its value does not depend on the sample's orientation or the pore orientation distributions. It is proportional to the mean-squared radius of gyration averaged over the pore ensembles and, thus, represents a measure of the effective pore size within the sample:

$$R_{\text{eff}}^2 = \frac{1}{4}\text{Tr}\left(\underline{\underline{\mathbf{T}}}\right) = \text{Tr}\left(\underline{\underline{\mathbf{R}}}\right) = \sum_i p_i \int_{\text{pore}_i} \rho(\mathbf{r}) r^2 \text{d}\mathbf{r} = \sum_i p_i \langle R^2 \rangle_i \tag{38}$$

with $\langle R^2 \rangle_i$ being the mean-squared radius of gyration for the ith pore ensemble according to Equation (15). R_{eff} can be determined, for example, from three acquisitions with appropriate $\mathbf{Q}_k$ if the signal without diffusion weighting is known.

As outlined in Ref. 54, the pore size estimation, as considered so far, can also be performed with a single-wave-vector experiment, that is, with $q_2 = 0$. Mathematically, this reflects the fact that the interaction terms, that is, the ''off-diagonal'' sub-matrices of $\underline{\underline{\mathbf{T}}}$ ($2\underline{\underline{\mathbf{R}}}$), are multiples of the terms describing the effects of the single-wave vectors, the diagonal sub-matrices ($\underline{\underline{\mathbf{R}}}$). For an isotropic orientation distribution, this is equivalent to the observation that $\langle R^2 \rangle$ of Equation (14) can be determined from two acquisitions with different q values but without changing θ. This observation will be met again later on (Section 4.1). But, for instance, in the presence of an additional compartment with freely diffusing spins, there are ambiguities in the single-wave-vector experiments that can be resolved with DWV experiments as will be seen now.

3.1.1.3. Contributions of Gaussian diffusion Such signal contributions may arise not only from freely diffusing spins but also from spins subject to hindered or not fully restricted diffusion. They are, in general, described by the diffusion tensor which in the tensor formalism, as a function of $\mathbf{Q}$ and expanded to the second order, yields

$$M_{\underline{\underline{\mathbf{D}}}}(\mathbf{Q}) \propto 1 - \Delta_{\text{eff}} \mathbf{Q}^{\text{T}} \begin{pmatrix} \underline{\underline{\mathbf{D}}} & 0 \\ 0 & \underline{\underline{\mathbf{D}}} \end{pmatrix} \mathbf{Q} \tag{39}$$

or for isotropic diffusion

$$M_{\mathrm{D}}(\mathbf{Q}) \propto 1 - \Delta_{\mathrm{eff}} D \mathbf{Q}^{\mathrm{T}} \begin{pmatrix} \underline{\underline{\mathbf{1}}} & 0 \\ 0 & \underline{\underline{\mathbf{1}}} \end{pmatrix} \mathbf{Q}. \tag{40}$$

Thus, the diagonal sub-matrices are extended by the contributions of the compartment with Gaussian diffusion which hampers the pore size estimation in a single-wave-vector experiment. But the off-diagonal sub-matrices that reflect the interaction of the two wave vectors, do not change, that is, the signal modulation observed upon varying θ is unaffected by signal contributions from free diffusion and, thus, represents a straightforward access to the restricted compartment.

3.1.1.4. Signal difference for parallel and antiparallel wave-vector orientations The easiest and most reliable approach to determine the diagonal elements of $\underline{\underline{\mathbf{R}}}$ which are required to estimate the pore size, involves acquisitions with parallel and antiparallel orientations of the two wave vectors. Thus, additional signal modulations due to non-spherical cells and non-isotropic orientation distributions are avoided and anisotropy effects due to hardware inadequacies like differing eddy-current behaviour or gradient scaling mismatches between the different physical gradient axes are minimized.

In this case, Equation (35) can be simplified. For $\mathbf{q} = \mathbf{q}_1 = \pm \mathbf{q}_2$, only the off-diagonal matrices of $\underline{\underline{\mathbf{T}}}$ contribute to the signal difference yielding the reduced tensor equation[54]

$$\Delta M(\mathbf{q}) = \mathbf{q}^{\mathrm{T}} 2 \underline{\underline{\mathbf{R}}}\, \mathbf{q}. \tag{41}$$

This means that the rank-2 tensor $\underline{\underline{\mathbf{R}}}$ with its six independent elements is sufficient to describe the signal difference of parallel and antiparallel wave-vector orientations for any orientation of $\mathbf{q}$. In particular, this result is independent of contributions from Gaussian diffusion, which represents the advantage of the double-wave-vector experiment.

3.1.2. Multiple concatenations

Recently, the tensor model has been extended to a double-wave-vector experiment where the two wave vectors are ''concatenated'', that is, applied several times in an alternating manner[56] (see Figure 1E). Because the transition from one wave vector to the other causes the signal difference of the restriction effect, this approach yields a larger accumulated signal difference which may help to improve its detectability. Although such an experiment involves the successive application of more than two diffusion-weighting periods, it will still be considered as a two-wave-vector experiment because the full flexibility of a general multiple-wave-experiment is not exploited.

However, Equation (11) derived for MWVs can be used to describe the signal if $\mathbf{q}_{2j-1} = \mathbf{q}_1$ and $\mathbf{q}_{2j} = \mathbf{q}_2$ are used yielding

$$\begin{aligned} M(\mathbf{q}_1, \mathbf{q}_2, n) &\propto \widetilde{\rho}(\mathbf{q}_1)\widetilde{\rho}(\mathbf{q}_2)\widetilde{\rho}^n(-\mathbf{q}_1 - \mathbf{q}_2)\widetilde{\rho}^{n-1}(\mathbf{q}_1 + q_2) \\ &= \widetilde{\rho}(\mathbf{q}_1)\widetilde{\rho}(\mathbf{q}_2)\widetilde{\rho}^n(-\mathbf{q}_1 - \mathbf{q}_2)\widetilde{\rho}^{*n-1}(-\mathbf{q}_1 - \mathbf{q}_2), \end{aligned} \tag{42}$$

where n is the number of concatenations (see Figure 1E) and the pore index has been dropped for clarity. The derivation of the generalized tensor equation is straightforward and yields[56]

$$M_n(\mathbf{Q}) \propto 1 - \frac{1}{2}\mathbf{Q}^{\mathrm{T}}\underline{\underline{\mathbf{T}}}_n\mathbf{Q}, \tag{43}$$

with a modified tensor definition

$$\underline{\underline{\mathbf{T}}}_n = \begin{pmatrix} 2n\,\underline{\underline{\mathbf{R}}} & (2n-1)\,\underline{\underline{\mathbf{R}}} \\ (2n-1)\,\underline{\underline{\mathbf{R}}} & 2n\,\underline{\underline{\mathbf{R}}} \end{pmatrix}. \tag{44}$$

The corresponding adaptation of the pore size measure derived from the tensor's trace yields

$$R^2_{\mathrm{eff}} = \mathrm{Tr}\left(\underline{\underline{\mathbf{R}}}\right) = \frac{1}{4n}\mathrm{Tr}\left(\underline{\underline{\mathbf{T}}}_n\right). \tag{45}$$

For the reduced tensor equation describing the signal difference between parallel and antiparallel wave vectors

$$\Delta M(\mathbf{q}) = \mathbf{q}^{\mathrm{T}}2(2n-1)\,\underline{\underline{\mathbf{R}}}\,\mathbf{q} \tag{46}$$

can also easily be obtained. For an isotropic orientation distribution of the pores with $|\mathbf{q}_1| = |\mathbf{q}_2| = q$, the signal can be calculated to

$$M_{\mathrm{iso}}(q, \theta) \propto 1 - \frac{1}{3}q^2\langle R^2\rangle(2n + (2n-1)\cos\theta), \tag{47}$$

which extends Equation (14) to multiple concatenations.

For a half-integral number of concatenations, that is, an experiment that terminates with a diffusion weighting of the first wave vector, the signal equation is given by

$$M'(\mathbf{q}_1, \mathbf{q}_2) \propto \widetilde{\rho}_i(\mathbf{q}_1)^2\widetilde{\rho}_i(-\mathbf{q}_1 - \mathbf{q}_2)^{n+1}\widetilde{\rho}_i(\mathbf{q}_1 + \mathbf{q}_2)^n, \tag{48}$$

where n now represents the number of full cycles, yielding[56]

$$\underline{\underline{\mathbf{T}}}_n = \begin{pmatrix} (2n'+1)\,\underline{\underline{\mathbf{R}}} & (2n'-1)\,\underline{\underline{\mathbf{R}}} \\ (2n'-1)\,\underline{\underline{\mathbf{R}}} & (2n'-1)\,\underline{\underline{\mathbf{R}}} \end{pmatrix} \tag{49}$$

with $n' = n + \frac{1}{2}$. Equations (45)–(47) remain valid if n is replaced by n'.

These equations imply that the usage of multiple concatenations increases the signal modulation by a factor of $2n-1$ which is easiest to see in Equation (47). Because the mean signal decay is proportional to $2n$, the relative signal modulation is given by $(2n-1)/2n = 1 - 1/2n$, that is, the relative signal modulation can

be doubled. This optimum gain is achieved in the limit of large n, which is not very feasible for experiments. However, using only two concatenations already yields half of the gain, that is, a relative signal modulation improved by 50%.

Furthermore, numerical simulations reveal that if the higher diffusion-weighting efficiency of multiple concatenations is used to shorten finite pulse durations, an even higher gain of the signal modulation can be obtained. The additional improvement represents a re-gain of some of the signal modulation that is lost for longer gradient pulses (see Section 4.1). This is of particular interest for whole-body MR systems with their weak gradient systems.[58] In the example considered, the modulation for five concatenations was more than five times higher than that for a standard DWV experiment[58] which is well beyond the theoretically expected factor of 1.8. Thus, multiple concatenations may be able to improve the detectability of the signal modulation, in particular on whole-body MR systems with their limited gradient amplitudes.

3.1.3. Fourth-order expansion

While the preceding considerations were limited to second-order terms in q, Özarslan[35] calculated the signal expression for an isotropic orientation distribution of a rotationally and point symmetric pore up to fourth order in q. For such pores and a constant spin density $\rho(\mathbf{r})=\rho$, the expansion of $\widetilde{\rho}(\mathbf{q})$ to fourth order can be written as[35]

$$\widetilde{\rho}(\mathbf{q}) = 1 - \frac{1}{2}q^2\rho\int_{\text{pore}}\left(\hat{\mathbf{q}}\cdot\mathbf{r}\right)^2 d\mathbf{r} + \frac{1}{24}q^4\rho\int_{\text{pore}}\left(\hat{\mathbf{q}}\cdot\mathbf{r}\right)^4 d\mathbf{r} + O\left(q^6\right), \tag{50}$$

where $\hat{q}$ is the unit vector along $\mathbf{q}$. The signal for an isotropic orientation distribution and $q_1=q_2=q$ is then given by[35]

$$\begin{aligned} M_{\text{iso}}\left(\mathbf{q},\mathbf{q}_\perp\right) = 1 &- q^2\textstyle\int_{\text{pore}}(2+\cos\theta)\int_S\left(\hat{\mathbf{q}}\cdot\mathbf{r}\right)^2 d\hat{\mathbf{q}}d\mathbf{r} \\ &+ \frac{1}{12}q^4(4+4\cos\theta+4\cos2\theta)\int_{\text{pore}}\int_S\left(\hat{\mathbf{q}}\cdot\mathbf{r}\right)^4 d\hat{\mathbf{q}}d\mathbf{r} \\ &+ \frac{1}{8}q^4(7+8\cos\theta+3\cos2\theta)\int_{\text{pore}}\int_{\text{pore}}\int_S\left(\hat{\mathbf{q}}\cdot\mathbf{r}_1\right)^2\left(\hat{\mathbf{q}}\cdot\mathbf{r}_2\right)^2 d\hat{\mathbf{q}}d\mathbf{r}_1d\mathbf{r}_2 \\ &+ \frac{3}{8}q^4(1-2\cos2\theta)\int_{\text{pore}}\int_{\text{pore}}\int_S\left(\hat{\mathbf{q}}\cdot\mathbf{r}_1\right)^2\left(\hat{\mathbf{q}}_\perp\cdot\mathbf{r}_2\right)^2 d\hat{\mathbf{q}}d\mathbf{r}_1d\mathbf{r}_2. \end{aligned} \tag{51}$$

Thereby, the $\hat{\mathbf{q}}$ integration is performed over the surface of the unit sphere, that is, all possible orientations of $\hat{\mathbf{q}}$, and $\hat{\mathbf{q}}_\perp$ is a unit vector in a direction perpendicular to $\hat{\mathbf{q}}$ that is obtained if $\hat{\mathbf{q}}_2$ is decomposed into components parallel and perpendicular to $\hat{\mathbf{q}}_1$, that is, it obeys $\hat{\mathbf{q}}_2 = \hat{\mathbf{q}}_1\cos\theta + \hat{\mathbf{q}}_\perp\sin\theta$.

In Equation (51), cos θ and cos 2θ terms are present in the fourth order. While the first modulation is known from the second-order term where it reflects the

restriction effect and is proportional to the pore size, it may, at a first glance, be possible that the cos 2θ modulation contains information about the local anisotropy as it does for the long mixing time regime. However, for spheres with a radius of r_0, Equation (51) yields[35]

$$M_{\mathrm{iso}}(q,\theta) = 1 - \frac{1}{5}q^2 r_0^2(2 + \cos\theta) + \frac{1}{700}q^4 r_0^4(55 + 48\cos\theta + 5\cos 2\theta), \tag{52}$$

which means that the cos 2θ modulation does not disappear for isotropic pores. Thus, short mixing times seem to be unable to identify local anisotropy even if the fourth-order contributions are considered. This is different from the long mixing time regime as mentioned above and will be shown in the next section.

3.2. Ideal timing parameters: Long mixing times

So far, only signal expressions for ellipsoidal pores with isotropic orientation distributions were reported for DWV experiments with long mixing times, that is, investigating the anisotropy effect. Similar to the derivation in the preceding section, Taylor expansions of Equation (16) up to fourth order which have been reported recently will be considered in order to derive equations valid for arbitrary orientation distributions and wave-vector orientations under the assumption of ideal timing parameters. This will include expressions for the signal modulation with the angle θ between the two wave vectors for an isotropic orientation distribution.

First equations were reported by Özarslan[35] for pores exhibiting rotational and point symmetry and yielded a cos 2θ modulation for the anisotropy effect (Section 3.2.1). More recently, a tensor approach for arbitrary pore shapes was presented (Section 3.2.2) from which a rotationally invariant measure of the microscopic anisotropy can be derived[55] (Section 3.2.3). It has also been extended to multiple concatenations[57] (Section 3.2.1).

3.2.1. Rotationally symmetric pores

First expressions for the angular dependency of the DWV signal at long mixing times were derived by Özarslan.[35] Under the assumption of a rotationally symmetric pore that is also point symmetric about its centre of gravity, and a constant spin density $\rho(\mathbf{r}) = \rho$ he obtained

$$\begin{aligned} M_{\mathrm{iso}}(\mathbf{q}_1,\mathbf{q}_2) = 1 &- 2q^2\textstyle\int_{\mathrm{pore}}\int_S (\hat{\mathbf{q}}\cdot\mathbf{r})^2 \mathrm{d}\hat{\mathbf{q}}\mathrm{d}\mathbf{r} + \frac{1}{6}q^4\int_{\mathrm{pore}}\int_S (\hat{\mathbf{q}}\cdot\mathbf{r})^4 \mathrm{d}\hat{\mathbf{q}}\mathrm{d}\mathbf{r} \\ &+ \frac{1}{2}q^4(2+\cos 2\theta)\int_{\mathrm{pore}}\int_{\mathrm{pore}}\int_S (\hat{\mathbf{q}}\cdot\mathbf{r}_1)^2(\hat{\mathbf{q}}\cdot\mathbf{r}_2)^2 \mathrm{d}\hat{\mathbf{q}}\,\mathrm{d}\mathbf{r}_1\mathrm{d}\mathbf{r}_2 \\ &+ \frac{1}{2}q^4(1-\cos 2\theta)\int_{\mathrm{pore}}\int_{\mathrm{pore}}\int_S (\hat{\mathbf{q}}\cdot\mathbf{r}_1)^2(\hat{\mathbf{q}}_\perp\cdot\mathbf{r}_2)^2 \mathrm{d}\hat{\mathbf{q}}\,\mathrm{d}\mathbf{r}_1\mathrm{d}\mathbf{r}_2 \end{aligned} \tag{53}$$

for an isotropic orientation distribution where the expansion of $\widetilde{\rho}(\mathbf{q})$ according to Equation (50) has been used. Furthermore, as in Equation (51), the $\hat{\mathbf{q}}$ integration is

performed over the surface of the unit sphere, that is, all possible orientation of $\hat{\mathbf{q}}$, and $\hat{\mathbf{q}}_\perp$ is a unit vector in a direction perpendicular to $\hat{\mathbf{q}}$ that is obtained if $\hat{\mathbf{q}}_2$ is decomposed into a component parallel and perpendicular to $\mathbf{q}_1$, that is, it obeys $\hat{\mathbf{q}}_2 = \hat{\mathbf{q}}_1 \cos\theta + \hat{\mathbf{q}}_\perp \sin\theta$.

These results demonstrate that the angular modulation shows a $\cos 2\theta$ dependency. As examples for specific pore shapes, ellipsoids of revolution (semi-axes a and b) and cylinders (radius r_0, length l) were considered, the latter being a model for the studies performed on microcapillaries. The calculations yielded

$$\begin{aligned} M_{\mathrm{iso,elli}}(q,\theta) = 1 &- \frac{2}{15}q^2\left(2a^2+b^2\right) \\ &+ \frac{1}{2625}q^4\left(97a^4+32b^4+66a^2b^2+7\left(a^2-b^2\right)^2\cos 2\theta\right) \end{aligned} \tag{54}$$

and

$$\begin{aligned} M_{\mathrm{iso,cyl}}(q,\theta) = 1 &- \frac{1}{18}q^2\left(6r_0^2+l^2\right) \\ &+ \frac{1}{10,800}q^4\left(615r_0^4+22l^4+150r_0^2l^2+5\left(3r_0^2-l^2\right)^2\cos 2\theta\right), \end{aligned} \tag{55}$$

respectively, the first being consistent with the signal difference between parallel and orthogonal wave vectors obtained by Cheng and Cory.[8]

3.2.2. Tensor model

A different approach that is able to handle arbitrary orientation distributions, was presented in Ref. 55 and will be sketched in this section. It is also based on a Taylor expansion of Equation (16) for ideal timing parameters but uses a formulation involving tensor expressions like the one in Equation (35).

3.2.2.1. Taylor expansion Terms up to fourth order are required to be able to model the anisotropy effect that for a single pore ensemble yields an expansion of $\widetilde{\rho}$ given by

$$\begin{aligned} \widetilde{\rho}(\mathbf{q}) = 1 &- \frac{1}{2}\sum_{j,k=1}^{3} q_j q_k \int_{\mathrm{pore}} \rho(r) r_j r_k \mathrm{d}\mathbf{r} - \frac{\mathrm{i}}{6}\sum_{j,k,l=1}^{3} q_j q_k q_l \int_{\mathrm{pore}} \rho(\mathbf{r}) r_j r_k r_l \mathrm{d}\mathbf{r} \\ &+ \frac{1}{24}\sum_{j,k,l,m=1}^{3} q_j q_k q_l q_m \int_{\mathrm{pore}} \rho(\mathbf{r}) r_j r_k r_l r_m \mathrm{d}\mathbf{r} + \mathcal{O}\left(q^5\right), \end{aligned} \tag{56}$$

where the pore volume has again been set to 1 and the pore's centre of gravity was chosen as the origin.

With the rank-2 (3×3) tensor $\underline{\underline{\mathbf{R}}}$ and defining a rank-4 $(3\times 3\times 3\times 3)$ tensor $\underline{\underline{\underline{\underline{\mathbf{S}}}}}$ with elements

$$\begin{aligned} R_{jk} &= \int_{\text{pore}} \rho(\mathbf{r}) r_j r_k \mathrm{d}\mathbf{r}, \\ S_{jklm} &= \int_{\text{pore}} \rho(\mathbf{r}) r_j r_k r_l r_m \mathrm{d}\mathbf{r}, \end{aligned} \tag{57}$$

Equation (56) can be re-written to

$$\begin{aligned} \widetilde{\rho}(\mathbf{q}) = 1 - \frac{1}{2}\mathbf{q}^{\mathrm{T}} \underline{\underline{\mathbf{R}}}\, \mathbf{q} - \frac{\mathrm{i}}{6} \sum_{j,k,l=1}^{3} q_j q_k q_l \int_{\text{pore}} \rho(\mathbf{r}) r_j r_k r_l \mathrm{d}\mathbf{r} \\ + \frac{1}{24} \sum_{j,k,l,m=1}^{3} q_j q_k q_l q_m S_{jklm} + O\left(q^5\right), \end{aligned} \tag{58}$$

from which the Taylor expansion of $|\widetilde{\rho}(\mathbf{q})|^2$ can be calculated to

$$|\widetilde{\rho}(\mathbf{q})|^2 = \widetilde{\rho}(\mathbf{q})\widetilde{\rho}^*(\mathbf{q}) = 1 - \mathbf{q}^{\mathrm{T}} \underline{\underline{\mathbf{R}}}\, \mathbf{q} + \frac{1}{4}\left(\mathbf{q}^{\mathrm{T}} \underline{\underline{\mathbf{R}}}\, \mathbf{q}\right)^2 + \frac{1}{12} \sum_{j,k,l,m=1}^{3} q_j q_k q_l q_m S_{jklm} + O\left(q^5\right). \tag{59}$$

The expansion of Equation (16) up to fourth order then yields

$$\begin{aligned} M(\mathbf{q}_1, \mathbf{q}_2) \propto 1 - \sum_{v=1}^{2} \mathbf{q}_v^{\mathrm{T}} \underline{\underline{\mathbf{R}}}\, \mathbf{q}_v + \frac{1}{4} \sum_{v=1}^{2} \left(\mathbf{q}_v^{\mathrm{T}} \underline{\underline{\mathbf{R}}}\, \mathbf{q}_v\right)^2 + \left(\mathbf{q}_1^{\mathrm{T}} \underline{\underline{\mathbf{R}}}\, \mathbf{q}_1\right)\left(\mathbf{q}_2^{\mathrm{T}} \underline{\underline{\mathbf{R}}}\, \mathbf{q}_2\right) \\ + \frac{1}{12} \sum_{v=1}^{2} \sum_{j,k,l,m=1}^{3} q_{v,j} q_{v,k} q_{v,l} q_{v,m} S_{jklm} + O\left(q^6\right), \end{aligned} \tag{60}$$

where Greek and Latin indexes refer to the wave-vector number and Cartesian coordinates, respectively, and $q_{v,j}$ denotes the jth component of wave vector $\mathbf{q}_v$. After the leading constant, the terms in Equation (60) represent (in the order of appearance) (i) the second-order term of $\widetilde{\rho}$ and (ii) its square (fourth order) for each wave vector, (iii) a mixed product of the second-order terms of $\widetilde{\rho}$ between the two wave vectors (fourth order) that reflects the interaction between the two wave vectors and causes the anisotropy effect and (iv) the fourth-order term of $\widetilde{\rho}$ for each wave vector.

3.2.2.2. Modified Voigt notation A handier notation of Equation (60) could be obtained using the modified Voigt notation which effectively allows to reduce the dimension of symmetric rank-4 tensors. Defining a six-element vector $\widetilde{\mathbf{q}} = \left(q_1^2, q_2^2, q_3^2, q_1 q_2, q_1 q_3, q_2 q_3\right)^{\mathrm{T}}$ yields

$$\frac{1}{12} \sum_{j,k,l,m=1}^{3} q_j q_k q_l q_m S_{jklm} = \frac{1}{12} \widetilde{\mathbf{q}}^{\mathrm{T}} \underline{\underline{\mathbf{S}}}\, \widetilde{\mathbf{q}} \tag{61}$$

for the last sums in Equation (60) with

$$\widetilde{\underline{\underline{\mathbf{S}}}} = \begin{pmatrix} S_{1111} & S_{1122} & S_{1133} & 2S_{1112} & 2S_{1113} & 2S_{1123} \\ S_{1122} & S_{2222} & S_{2233} & 2S_{1222} & 2S_{1223} & 2S_{2223} \\ S_{1133} & S_{2233} & S_{3333} & 2S_{1233} & 2S_{1333} & 2S_{2333} \\ 2S_{1112} & 2S_{1222} & 2S_{1233} & 4S_{1122} & 4S_{1123} & 4S_{1223} \\ 2S_{1113} & 2S_{1223} & 2S_{1333} & 4S_{1123} & 4S_{1133} & 4S_{1233} \\ 2S_{1123} & 2S_{2223} & 2S_{2333} & 4S_{1223} & 4S_{1233} & 4S_{2233} \end{pmatrix}. \tag{62}$$

Note that only the positions of the elements S_{iiii} are uniquely defined while those of the other elements are ambiguous and were chosen to obtain a symmetric tensor. The factors reflect the multiplicity of the index combinations.

Similarly, the squares and the mixed product of the second-order terms can be written as

$$\frac{1}{4}\left(\mathbf{q}^{\mathrm{T}}\,\underline{\underline{\mathbf{R}}}\,\mathbf{q}\right)^2 = \frac{1}{4}\widetilde{\mathbf{q}}^{\mathrm{T}}\,\widetilde{\underline{\underline{\mathbf{R}}}}\,\widetilde{\mathbf{q}} \tag{63}$$

and

$$\left(\mathbf{q}_1^{\mathrm{T}}\,\underline{\underline{\mathbf{R}}}\,\mathbf{q}_1\right)\left(\mathbf{q}_2^{\mathrm{T}}\,\underline{\underline{\mathbf{R}}}\,\mathbf{q}_2\right) = \widetilde{\mathbf{q}}_1^{\mathrm{T}}\,\widetilde{\underline{\underline{\mathbf{R}}}}\,\widetilde{\mathbf{q}}_2, \tag{64}$$

respectively, with

$$\widetilde{\underline{\underline{\mathbf{R}}}} = \begin{pmatrix} R_{11}^2 & R_{11}R_{22} & R_{11}R_{33} & 2R_{11}R_{12} & 2R_{11}R_{13} & 2R_{11}R_{23} \\ R_{11}R_{22} & R_{22}^2 & R_{22}R_{33} & 2R_{12}R_{22} & 2R_{13}R_{22} & 2R_{22}R_{23} \\ R_{11}R_{33} & R_{22}R_{33} & R_{33}^2 & 2R_{12}R_{33} & 2R_{13}R_{33} & 2R_{23}R_{33} \\ 2R_{11}R_{12} & 2R_{12}R_{22} & 2R_{12}R_{33} & 4R_{12}^2 & 4R_{12}R_{13} & 4R_{12}R_{23} \\ 2R_{11}R_{13} & 2R_{13}R_{22} & 2R_{13}R_{33} & 4R_{12}R_{13} & 4R_{13}^2 & 4R_{13}R_{23} \\ 2R_{11}R_{23} & 2R_{22}R_{23} & 2R_{23}R_{33} & 4R_{12}R_{23} & 4R_{13}R_{23} & 4R_{23}^2 \end{pmatrix}. \tag{65}$$

Just as $\widetilde{\underline{\underline{\mathbf{S}}}}$, $\widetilde{\underline{\underline{\mathbf{R}}}}$ was set up symmetrically. It has 21 different elements that are products of the six independent elements of $\underline{\underline{\mathbf{R}}}$. But it must be emphasized that this only holds for a single pore orientation. Accordingly, Equation (60) can be re-written to

$$M(\mathbf{q}_1, \mathbf{q}_2) \propto 1 - \sum_{v=1}^{2} \mathbf{q}_v^{\mathrm{T}}\,\underline{\underline{\mathbf{R}}}\,\mathbf{q}_v + \frac{1}{4}\sum_{v=1}^{2} \widetilde{\mathbf{q}}_v^{\mathrm{T}}\,\widetilde{\underline{\underline{\mathbf{R}}}}\,\widetilde{\mathbf{q}}_v + \widetilde{\mathbf{q}}_1^{\mathrm{T}}\,\widetilde{\underline{\underline{\mathbf{R}}}}\,\widetilde{\mathbf{q}}_2 + \frac{1}{12}\sum_{v=1}^{2} \widetilde{\mathbf{q}}_v^{\mathrm{T}}\,\widetilde{\underline{\underline{\mathbf{S}}}}\,\widetilde{\mathbf{q}}_v \tag{66}$$

without rank-4 tensors.

A combination of the vectors $\mathbf{q}_v$ and $\widetilde{\mathbf{q}}_v$ to single vectors $\mathbf{Q} = \left(\mathbf{q}_1^{\mathrm{T}}, \mathbf{q}_2^{\mathrm{T}}\right)^{\mathrm{T}}$ and $\widetilde{\mathbf{Q}} = \left(\widetilde{\mathbf{q}}_1^{\mathrm{T}}, \widetilde{\mathbf{q}}_2^{\mathrm{T}}\right)^{\mathrm{T}}$, respectively, yields the final tensor equation

$$M(\mathbf{Q}) \propto 1 - \frac{1}{2}\mathbf{Q}^{\mathrm{T}}\,\underline{\underline{\mathbf{T}}}_a\,\mathbf{Q} + \frac{1}{12}\widetilde{\mathbf{Q}}^{\mathrm{T}}\,\widetilde{\underline{\underline{\mathbf{U}}}}\,\widetilde{\mathbf{Q}} \tag{67}$$

with the second-order (6×6) tensor

$$\underline{\underline{\mathbf{T}}}_a = \begin{pmatrix} 2\underline{\underline{\mathbf{R}}} & 0 \\ 0 & 2\underline{\underline{\mathbf{R}}} \end{pmatrix} \tag{68}$$

and the fourth-order (12×12) tensor

$$\underline{\underline{\widetilde{\mathbf{U}}}} = \begin{pmatrix} \underline{\underline{\widetilde{\mathbf{S}}}} + 3\underline{\underline{\widetilde{\mathbf{R}}}} & 6\underline{\underline{\widetilde{\mathbf{R}}}} \\ 6\underline{\underline{\widetilde{\mathbf{R}}}} & \underline{\underline{\widetilde{\mathbf{S}}}} + 3\underline{\underline{\widetilde{\mathbf{R}}}} \end{pmatrix}, \tag{69}$$

respectively, which both are symmetric.

Equation (67) holds for any pore shape, orientation distribution and arbitrary wave-vector orientations. It yields, in general, complex modulations with the angle θ between the two wave vectors and reproduces the results of numerical simulations very well (Figure 6).

3.2.2.3. Multiple pore ensembles For a mixture of pore ensembles, each with a volume fraction of p_i ($\sum_i p_i = 1$), the signal is the weighted average of the individual contributions, that is, the tensor equation (67) remains valid if

$$\underline{\underline{\widetilde{\mathbf{T}}}}_a = \sum_i p_i \underline{\underline{\widetilde{\mathbf{T}}}}_{\mathrm{a},i}, \quad \underline{\underline{\widetilde{\mathbf{U}}}} = \sum_i p_i \underline{\underline{\widetilde{\mathbf{U}}}}_i \tag{70}$$

and

$$\underline{\underline{\mathbf{R}}} = \sum_i p_i \underline{\underline{\mathbf{S}}}_i, \quad \underline{\underline{\widetilde{\mathbf{R}}}} = \sum_i p_i \underline{\underline{\widetilde{\mathbf{R}}}}_i, \quad \underline{\underline{\widetilde{\mathbf{S}}}} = \sum_i p_i \underline{\underline{\widetilde{\mathbf{S}}}}_i \tag{71}$$

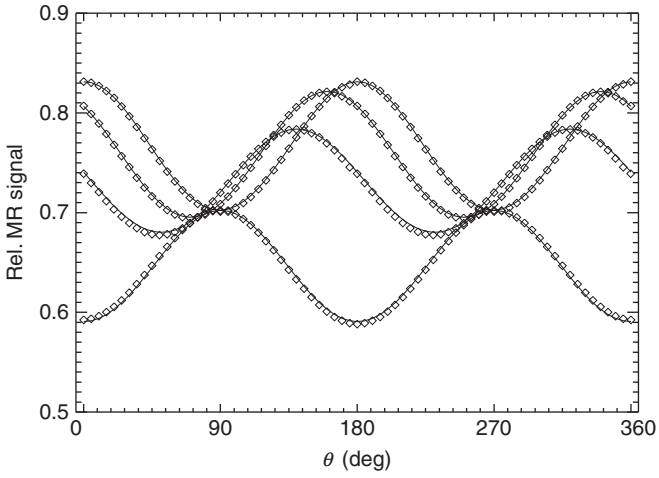

Figure 6 Examples for the signal modulation in long-mixing-time DWV experiments of spheroidal pores versus the angle θ between the two wave vectors. While the first wave vector was fixed, the second sampled different circles starting with a parallel orientation. The symbols represent the results of numerical simulations based on a random walk model; the solid lines depict the fit to the tensor models sketched in Section 3.2.2. Courtesy of M. Lawrenz. Reprinted from Ref. 55 with permission from Elsevier.

are used where $= \underline{\underline{\widetilde{\mathbf{T}}}}_{a,i}$, $\underline{\underline{\widetilde{\mathbf{U}}}}_i$, $\underline{\underline{\mathbf{R}}}_i$, $\underline{\underline{\widetilde{\mathbf{R}}}}_i$ and $\underline{\underline{\widetilde{\mathbf{U}}}}_i$ are the tensors for the individual ensembles. In this general case, Equation (67) contains 42 independent elements, 6 in the second-order ($\underline{\underline{\mathbf{R}}}$) and 36 in the fourth-order terms ($\underline{\underline{\widetilde{\mathbf{U}}}}$). For the special case of an isotropic orientation distribution of identical cells, Equation (67) simplifies to

$$M_{\mathrm{iso}}(q,\theta) \propto 1 - \frac{2}{3}\langle R^2\rangle q^2 + \left[\frac{1}{30}\left(3\langle R^4\rangle + 3\langle R_{kk}R_{ll}\rangle + 4\langle R_{kl}^2\rangle\right) + \frac{1}{15}\langle R_{kl}^2\rangle \cos 2\theta\right] q^4 \tag{72}$$

for $q_1 = q_2 = q$ where $\langle R^2\rangle = \sum_k R_{kk} = \int_{\mathrm{pore}} \rho(\mathbf{r}) r^2 \mathrm{d}\mathbf{r}$ is the mean-squared radius of gyration, $\langle R^4\rangle = \int_{\mathrm{pore}} \rho(\mathbf{r}) r^4 \mathrm{d}\mathbf{r}$, and

$$\begin{aligned} \langle R_{kk}^2\rangle &= 2\sum_k R_{kk}^2 + \sum_{k,l} R_{kk}R_{ll}, \\ \langle R_{kl}^2\rangle &= \frac{3}{2}\sum_k R_{kk}^2 - \frac{1}{2}\sum_{k,l} R_{kk}R_{ll}. \end{aligned} \tag{73}$$

Thus, Equation (72) reproduces the $\cos 2\theta$ dependency of Equation (53). It is caused by the interaction term, that is, the off-diagonal matrices $\underline{\underline{\widetilde{\mathbf{R}}}}$ in $\underline{\underline{\widetilde{\mathbf{U}}}}$. For ellipsoidal pores with semi-axes of a, a and b $\left(R_{aa} = \frac{1}{5}a^2,\ R_{bb} = \frac{1}{5}b^2\right)$, the modulation amplitude yields $\frac{1}{15}\langle R_{kl}^2\rangle = \frac{1}{375}\left(a^2 - b^2\right)^2$ which is consistent with Equation (17) derived by Cheng and Cory.[8]

3.2.3. Measures of microscopic anisotropy

It is obvious that the pre-factor of the angular modulation in Equation (72), $\langle {R_{kl}}^2\rangle$, reflects the pore eccentricity, that is, microscopic anisotropy, because the modulation is known to vanish for spherical cells. However, it is not clear how a rotationally invariant measure of the microscopic anisotropy can be determined in the general case of an arbitrary orientation distribution, that is, from Equation (67). This problem will be addressed in this section.

A measure of the microscopic anisotropy must be based on the fourth-order terms of Equation (67), ideally a linear combination, it must be rotationally invariant, that is, independent of the pore orientation distribution, and depend on the pore eccentricity. Furthermore, it should be accessible with a limited number of measurements, that is, wave-vector combinations, and should be independent of the pore size. It has been shown[55] that such measures can be derived from the tensor model presented. They may help to characterize the microscopic anisotropy in samples with complex or unknown pore geometry and, therefore, will be presented here and compared to a measure of macroscopic anisotropy derived from the diffusion tensor.

3.2.3.1. I_{MA} A first approach towards a microscopic anisotropy measure is the I_{MA} according to[55]

$$I_{\mathrm{MA}} = \sum_{k=1}^{3} \widetilde{R}_{kk} - \sum_{\substack{k,l=1 \\ k<l}}^{3} \widetilde{R}_{kl} + \frac{3}{4} \sum_{m=4}^{6} \widetilde{R}_{mm} \tag{74}$$

which involves nine different elements of $\underline{\underline{\widetilde{\mathbf{R}}}}$. For an ensemble of identical pores with a single orientation, it is given by

$$\begin{aligned} I_{\mathrm{MA}} &= \sum_{k=1}^{3} R_{kk}^2 - \sum_{\substack{k,l=1 \\ k<l}}^{3} R_{kk} R_{ll} + 3 \sum_{\substack{k,l=1 \\ k<l}}^{3} R_{kl}^2 \\ &= \left(\mathrm{Tr}\left(\underline{\underline{\mathbf{R}}} \right) \right)^2 - 3 \sum_{\substack{k,l=1 \\ k<l}}^{3} \left(R_{kk} R_{ll} - R_{kl}^2 \right). \end{aligned} \tag{75}$$

Thus, it is obtained from two invariants of the tensor $\underline{\underline{\widetilde{\mathbf{R}}}}$, the squared trace (invariant I_1) and the surface element (invariant I_2),[59,60] and as such it is also rotationally invariant. Because I_{MA} is a linear combination of elements of $\underline{\underline{\widetilde{\mathbf{R}}}}$, it is for a mixture of pore ensembles given by

$$I_{\mathrm{MA}} = \sum_i p_i I_{\mathrm{MA},i}, \tag{76}$$

that is, also rotationally invariant.

The I_{MA} can be determined from 15 diffusion-weighted measurements with different orientation combinations of the two wave vectors, for example, according to[55]

$$I_{\mathrm{MA}} = \sum_{k=1}^{3} M_{k,k} - \sum_{\substack{k,l=1 \\ k<l}}^{3} M_{k,l} + \frac{3}{2} \sum_{\substack{k,l=1 \\ k<l}}^{3} \left(\frac{1}{2} M_{kl,kl} + \frac{1}{2} M_{k\bar{l},k\bar{l}} - M_{kl,k\bar{l}} \right). \tag{77}$$

Here, $M_{k,l}$ represents the signal obtained with the two wave vectors along the axes $\mathbf{e}_k$ and $\mathbf{e}_l$, and $M_{ij,kl}$ that obtained with the two wave vectors along the diagonals defined by $\mathbf{e}_i + \mathbf{e}_j$ and $\mathbf{e}_k + \mathbf{e}_l$. Note that the number of measurements required is lower than the number of different elements of $\underline{\underline{\widetilde{\mathbf{U}}}}$, that is, not the full tensor needs to be determined to calculate I_{MA}.

For an isotropic orientation distribution, I_{MA} is sensitive to the anisotropy of the pores. This is obvious if the results of Mitra, Cheng, Callaghan and their coworkers presented in Section 2.4.3 are recalled that predict a signal difference between orthogonal and parallel wave-vector orientations for eccentric pores. In Equation (77), all acquisitions with parallel wave-vector combinations contribute with a positive sign while those with orthogonal combinations have a negative sign. The sensitivity for a single pore ensemble with a fixed orientation can also be realized if I_{MA} is considered in the eigenvector coordinate system

where $R_{kl}=0$ for $k\neq l$ and $R_{kk}=R_k$ with the eigenvalues R_k. Then, Equation (75) yields

$$I_{\mathrm{MA}} = \sum_{k=1}^{3} R_k^2 - \sum_{\substack{k,l=1\\k<l}}^{3} R_k R_l = \frac{1}{2}\sum_{\substack{k,l=1\\k<l}}^{3} (R_k - R_l)^2, \tag{78}$$

that is, I_{MA} vanishes for isotropic cells ($R_k=R_l$) and is positive if $R_k\neq R_l$ for any $k\neq l$ (anisotropic cells). Because in mixtures the I_{MA} of the individual pore ensembles are averaged, this also holds for any orientation distribution.

3.2.3.2. MA index For a one-dimensional pore with length $2r$ that can be regarded as an ellipsoid with semi-axes of 0, 0 and r and represents the ''most anisotropic'' case, an I_{MA} value of $(1/9)r^4$ is obtained according to Equation (78). This means that I_{MA} increases with the pore size which may not be an optimal choice for an anisotropy measure. To eliminate this dependency, the second-order term based on $\underline{\underline{\mathbf{R}}}$ can be involved. A simple approach is to use the trace of $\underline{\underline{\mathbf{R}}}$, that is, $\sum_k R_{kk}$, which is rotationally invariant and increases with the square of the pore's dimensions. Correspondingly, a dimensionless, rotationally invariant measure of the anisotropy that does not depend on the pore size, can be defined as[55]

$$\mathrm{MA} := \frac{\sqrt{I_{\mathrm{MA}}}}{\sum_{k=1}^{3} R_{kk}} = \frac{\sqrt{\frac{3}{2}\sum_{k=1}^{3}\widetilde{R}_{kk} - \frac{1}{2}\sum_{k,l=1}^{3}\widetilde{R}_{kl} + \frac{3}{4}\sum_{m=4}^{6}\widetilde{R}_{mm}}}{\sum_{k=1}^{3} R_{kk}}. \tag{79}$$

For an isotropic orientation distribution, the MA is proportional to $\sqrt{\langle R_{kl}^2\rangle}$, that is, the amplitude of the $\cos 2\theta$ modulation ($(1/15)\langle {R_{kl}}^2\rangle$, see Equation (72)) is proportional to the square of MA.[55] If an ensemble of identical pores with a single orientation is considered, Equations (75) and (78) are valid and MA is equivalent to

$$\mathrm{MA}_{\mathrm{single}} = \frac{\sqrt{\frac{1}{2}\sum_{\substack{k,l=1\\k<l}}^{3} (R_k - R_l)^2}}{\sum_{k=1}^{3} R_k}, \tag{80}$$

where the R_k are the eigenvalues of $\underline{\underline{\mathbf{R}}}$. For ellipsoidal pores with semi-axes a, b and c and a single orientation, Equation (80) provides

$$\mathrm{MA}_{\mathrm{elli}} = \frac{\sqrt{(a^2-b^2)^2 + (a^2-c^2)^2 + (b^2-c^2)^2}}{\sqrt{2}(a^2+b^2+c^2)}, \tag{81}$$

which for semi-axes of 0, 0 and r is 1, that is, independent of r.

Equation (80) seems to suggest that the MA can also be determined from the second-order tensor $\underline{\underline{\mathbf{R}}}$. As mentioned, this is only true for a simple pore ensemble where the elements of $\underline{\underline{\widetilde{\mathbf{R}}}}$ are directly related to those of $\underline{\underline{\mathbf{R}}}$ but not for mixtures of pore ensembles as can easily be seen. Modelling the measured signal according to Equation (67) then yields the averaged tensor elements

$$R_{kl} = \sum_i p_i R_{j,kl} \tag{82}$$

with $R_{j,kl}$ being the kl-element of $= \underline{\underline{\mathbf{R}}}_j$ and, for $k, l < 4$,

$$\widetilde{R}_{kl} = \sum_i p_i \widetilde{R}_{i,kl} = \sum_i p_i R_{i,kk} R_{i,ll} \tag{83}$$

which yields the important difference:

$$\widetilde{R}_{kl} = \sum_i p_i R_{i,kk} R_{i,ll} \neq \sum_i p_i R_{i,kk} \cdot \sum_i p_i R_{i,kk} = R_{kk} R_{ll}. \tag{84}$$

Hence, the elements $\widetilde{R}_{kl}$ cannot be obtained from the (averaged) R_{kk} but rather represent in general independent variables.

This crucial difference can be demonstrated for a one-dimensional pore, that is, an ellipsoidal pore with semi-axes of 0, 0 and r. For a single ensemble with pores oriented along x, the only non-vanishing element of $\underline{\underline{\mathbf{R}}}$ is $R_{11} = (1/3)r^2$ which yields a MA value of $\sqrt{\frac{1}{9}r^4}/\left(\frac{1}{3}r^2\right) = 1$. It is identical to the value according to Equation (80). For two ensembles oriented along x and y with equal weighting factors $p_j = 1/2$ the same MA value is obtained: $\sqrt{2 \times \frac{1}{9}\frac{1}{9}r^4}/\left(\frac{1}{3}r^2\right) = 1$. But since $R_{11} = R_{22} = (1/6)r^2$, the value according to Equation (80) yields $\sqrt{2 \times \frac{1}{36}\, r^4 - \frac{1}{36}r^4}/\left(\frac{1}{3}\, r^2\right) = \frac{1}{2}$, that is, only half of the value. Adding a third ensemble along z ($p_j = 1/3$) also does not alter MA because $\sqrt{3 \times \frac{1}{3}\frac{1}{9}r^4}/\left(\frac{1}{3}r^2\right) = 1$. However, now $R_{11} = R_{22} = R_{33} = (1/9)r^2$ and Equation (80) would yield $\sqrt{3 \times \frac{1}{81}\, r^4 - 3 \times \frac{1}{81}r^4}/\left(\frac{1}{3}r^2\right) = 0$.

3.2.3.3. Comparison with measures of macroscopic diffusion anisotropy For a single pore orientation the defined MA shows parallels to anisotropy measures derived from the standard (single-wave-vector) diffusion tensor. For instance, Equation (80) which was derived for a single pore orientation is equivalent to

$$\mathrm{MA}_{\mathrm{single}} = \frac{\sqrt{\sum_k (R_k - \langle R \rangle)^2}}{\sqrt{6}\langle R \rangle}, \tag{85}$$

with $\langle R \rangle = \frac{1}{3}\,\mathrm{Tr}\left(\underline{\underline{\mathbf{R}}}\right) = \frac{1}{3}\sum_k R_k$. This formulation demonstrates the similarity to the (macroscopic) anisotropy measure RA,[61] the relative anisotropy, that is derived from the diffusion tensor according to

$$\mathrm{RA} = \frac{\sqrt{\sum_k (D_k - \langle D \rangle)^2}}{\sqrt{6}\langle D \rangle}, \tag{86}$$

where D_k are the eigenvalues of the diffusion tensor and $\langle D \rangle = \frac{1}{3}\sum_k D_k$. Note that the diffusion coefficients D_k are proportional to the mean-squared displacement,

that is, the elements of Equation (86) can be re-written to be quadratic in r like those of Equation (85).

This comparison underlines the feasibility of the MA to describe diffusion anisotropy. But two things should be emphasized. First, the RA refers to the diffusion tensor, that is, it is effectively based on the *displacement* ellipsoid while MA aims to describe the *pore geometry* directly. Second, the RA vanishes for pores with an isotropic orientation distribution ($D_k = D$) while the MA defined in Equation (79) retains the value that is observed for a single pore orientation as has been shown above.

Thus, the macroscopic and microscopic anisotropy yield complementary information. The macroscopic anisotropy detects the orientation coherence of eccentric pores on a sample or imaging voxel level, however, it cannot distinguish between a reduced coherence and a lower fraction of eccentric pores. This is different for the microscopic anisotropy that reflects only pore eccentricity, independent of their orientation distributions.

3.2.4. Multiple concatenations

For experiments with multiple concatenations of the two diffusion-weighting periods (see Figure 1E), the signal of Equation (12) must be considered. The corresponding adaptations for the presented tensor model and the measures of the microscopic anisotropy have been reported in Ref. 57.

Assuming that the two wave vectors $\mathbf{q}_1$ and $\mathbf{q}_2$ are applied n_1 and n_2 times, respectively, Equation (12) simplifies to

$$M(\mathbf{q}_1, \mathbf{q}_2) \propto |\widetilde{\rho}(\mathbf{q}_1)|^{2n_1} |\widetilde{\rho}(\mathbf{q}_2)|^{2n_2}, \tag{87}$$

where only a single pore ensemble is considered. Furthermore, due to the long mixing times assumed, Equation (87) holds for an arbitrary order of the wave vectors, that is, not only for alternating wave vectors. The tensor equation obtained is given by

$$M(\mathbf{Q}, n_1, n_2) \propto 1 - \frac{1}{2}\mathbf{Q}^{\mathrm{T}} \underline{\underline{\mathbf{T}}}_a(n_1, n_2)\mathbf{Q} + \frac{1}{12}\widetilde{\mathbf{Q}}^{\mathrm{T}} \underline{\underline{\widetilde{\mathbf{U}}}}(n_1, n_2)\widetilde{\mathbf{Q}} \tag{88}$$

with the symmetric second-order (6×6) tensor

$$\underline{\underline{\mathbf{T}}}_a(n_1, n_2) = \begin{pmatrix} 2n_1 \underline{\underline{\mathbf{R}}} & 0 \\ 0 & 2n_2 \underline{\underline{\mathbf{R}}} \end{pmatrix} \tag{89}$$

and the symmetric fourth-order (12×12) tensor

$$\underline{\underline{\widetilde{\mathbf{U}}}}(n_1,n_2)=\begin{pmatrix} n_1+\underline{\underline{\widetilde{\mathbf{S}}}}(3n_1(2n_1-1))\,\underline{\underline{\widetilde{\mathbf{R}}}} & 6n_1n_2\,\underline{\underline{\widetilde{\mathbf{R}}}} \\ 6n_1n_2\,\underline{\underline{\widetilde{\mathbf{R}}}} & n_2\,\underline{\underline{\widetilde{\mathbf{S}}}}+(3n_2(2n_2-1))\,\underline{\underline{\widetilde{\mathbf{R}}}} \end{pmatrix}. \quad (90)$$

Correspondingly, the calculation of I_{MA} must be performed according to

$$I_{\mathrm{MA}}=\frac{1}{n_1n_2}\left(\sum_{k=1}^{3}M_{k,k}-\sum_{\substack{k,l=1\\k<l}}^{3}M_{k,l}+\frac{3}{2}\sum_{\substack{k,l=1\\k<l}}^{3}\left(\frac{1}{2}M_{kl,kl}+\frac{1}{2}M_{k\bar{l},k\bar{l}}-M_{kl,k\bar{l}}\right)\right). \quad (91)$$

The signal expression for an isotropic orientation distribution with $n_1=n_2=n$ then is given by

$$\begin{aligned} M_{\mathrm{iso}}(n,q,\theta)\propto 1-\frac{2}{3}n\langle R^2\rangle q^2+\left[\frac{1}{10}n\langle R^4\rangle+\frac{n^2}{10}\langle R_{kk}^2\rangle-\frac{n}{30}\langle R_{kk}^2\rangle\right]q^4 \\ +\left[\frac{n^2}{30}\langle R_{kk}^2\rangle+\frac{n^2}{15}\langle R_{kl}^2\rangle\cos 2\theta\right]q^4. \end{aligned} \quad (92)$$

Numerical simulations demonstrated the validity of these equations.[57]

These results imply that there is no inherent advantage of multiple concatenations at long mixing times. Instead of applying n concatenations, the gradient amplitude could be increased by a factor n. However, it has been shown in numerical simulations that for experiments involving long gradient pulses that are required due to limited gradient amplitudes, for example, on whole-body MR systems, the signal modulation is increased if the higher diffusion-weighting efficiency of multiple concatenations is used to shorten the pulse length accordingly.[57] Thus, the usage of multiple concatenations may help to improve the detectability of the anisotropy effect on amplitude-limited MR systems.

3.3. Arbitrary timing parameters

While the approaches presented in Sections 3.1 and 3.2 can handle any (unknown) pore shape and orientation distribution, they are based on the assumption of ideal timing parameters that are difficult or impossible to fulfil in real experiments: short gradient pulses ($\delta\to 0$), short or long mixing times ($\tau_{\mathrm{m}}\to 0$ or $\tau_{\mathrm{m}}\to\infty$, respectively) and a long diffusion time ($\Delta\to\infty$). Furthermore, they are limited to small or moderate q values as higher-order terms were neglected in the Taylor expansion. Thus, efforts were made to develop theoretical approaches that are valid for DWV experiments with arbitrary timing parameters.

The first approach to model DWV experiments with arbitrary timing parameters was presented by Özarslan and Basser[33] It is based on the matrix product formalism[49] of the multiple propagator method[48] (see Section 2.7) and considered

terms up to second order in q (Section 3.3.1). More recently, Özarslan and Basser[36] developed an extension of the MCF formalism[50–53] (see Section 2.7) suitable for experiments with gradient pulses applied in different directions, that is, compatible with DWV experiments (Section 3.3.2). It is valid for arbitrary q and, thus, represents the most general approach reported. Both approaches provide general solutions but yield usable results only if specific pore shapes are considered and the corresponding eigenfunctions and eigenvalues are known.

3.3.1. Matrix product formalism

Using the matrix product formalism[49] of the multiple propagator method[48] (see Section 2.7), Özarslan and Basser[33] presented a first model for DWV experiments with arbitrary timing parameters which will be shortly summarized here. They considered d-dimensionally isotropic pores, that is, parallel plates ($d=1$), cylinders ($d=2$) and spheres ($d=3$), for which analytical solutions can be obtained, and applied a modified discretization scheme to improve the accuracy for a reasonable raster time.

3.3.1.1. Isotropic pores For small $qa=\gamma\delta\, Ga$ and an arbitrary gradient pulse shape $\mathbf{G}(t)$ applied for a time T in the direction of restriction, that is, perpendicular to the plates or the cylinder's long axis, the signal obeys

$$\mathbf{M}(\mathbf{G}(t)) \propto 1 - 2\gamma^2 a^2 \sum_{n=1}^{\infty} s_{d,n} \int_0^T \mathrm{e}^{\omega_{d,n} t} \mathbf{G}(t) \cdot \mathbf{F}_{d,n}(t) \mathrm{d}t \tag{93}$$

with

$$\begin{aligned} \mathbf{F}_{d,n}(t) &= \textstyle\int_t^T \mathbf{G}(t') \mathrm{e}^{-\omega_{d,n} t'} \mathrm{d}t', \\ \omega_{d,n} &= \frac{\alpha_{d,n}^2 D}{a^2}, \\ s_{d,n} &= \frac{1}{\alpha_{d,n}^2 \left(\alpha_{d,n}^2 - d + 1\right)}, \end{aligned} \tag{94}$$

where the $s_{d,n}$ satisfy $\sum_{n=1}^{\infty} s_{d,n} = 1/2(2+d)$. D is the bulk diffusivity, $\alpha_{1,n} = \pi(n-(1/2))$, and $\alpha_{2,n}$ and $\alpha_{3,n}$ are, respectively, the roots of the derivatives of the first-order Bessel and spherical Bessel functions, that is, they satisfy the expressions $J'_1(\alpha_{2,n})=0$ and $j'_1(\alpha_{3,n})=0$. For clarity the dimensionality subscript d will be dropped in the following paragraphs.

For a DWV experiment with the pulse sequence of Figure 1C, that is, $\tau_{\mathrm{m}} \geq \delta$, Equation (93) yields

$$\mathbf{M}(\mathbf{G}_1, \mathbf{G}_2) \propto 1 - \left(A\left(G_1^2 + G_2^2\right) + BG_1G_2\cos\theta\right) \tag{95}$$

with

$$A = 2\gamma^2 a^2 \sum_{n=1}^{\infty} s_n \left[\frac{2\delta}{\omega_n} - \frac{1}{\omega_n^2} \left(2 - 2e^{-\omega_n \delta} + e^{-\omega_n(\Delta-\delta)} - 2e^{-\omega_n \Delta} + e^{-\omega_n(\Delta+\delta)} \right) \right],$$

$$B = 2\gamma^2 a^2 \sum_{n=1}^{\infty} \frac{s_n}{\omega_n^2} \left(e^{-\omega_n(\tau_m-\delta)} - 2e^{-\omega_n \tau_m} + e^{-\omega_n(\tau_m+\delta)} - 2e^{-\omega_n(\Delta+\tau_m-\delta)} \right.$$
$$\left. + 4e^{-\omega_n(\Delta+\tau_m)} - 2e^{-\omega_n(\Delta+\tau_m+\delta)} + e^{-\omega_n(2\Delta+\tau_m-\delta)} - 2e^{-\omega_n(2\Delta+\tau_m)} + e^{-\omega_n(2\Delta+\tau_m+\delta)} \right). \quad (96)$$

A similar expression, not reproduced here, is obtained for $\tau_m = 0$. These results represent a generalization of the equations presented earlier, for example, Refs. 62,63, and for ideal timing parameters ($\Delta \to \infty$, $\delta \to 0$, $\tau_m \to 0$ or $\tau_m \to \infty$) simplify to the equations of Mitra[7] (Section 2.4.3) for the geometries considered. It should be noted that these equations contain the bulk diffusion coefficient D in the ω_n terms defined in Equation (94) which means that it needs to be known for an accurate size determination.

With these solutions, the effect of finite timing parameters was analyzed for short mixing times $\tau_m \geq \delta$ which revealed a reduction of the modulation amplitude with increasing δ and τ_m and decreasing Δ, however, without a significant distortion of the cos-shaped curve.[33]

Experiments performed by Shemesh et al.[64] on microcapillaries with diameters in the μm-range (5–19 μm) demonstrated the very good performance of the equations presented above. Thereby, a clever modification was introduced to account for potential higher-order effects. Signals were acquired for several q values and their q dependency was fitted with an expression containing second and fourth-order terms. The second-order contribution identified then was analyzed with the equations described above. Thus, the observed signal curves could be well reproduced with the theoretical model for a variety of wave-vector orientations and finite timing parameters.[64] The estimates of the capillary diameter obtained from the fits were in general in very good agreement with the nominal values, only for very short diffusion times some deviations were observed. These deviations appear due to the very small restriction effect present at short diffusion times which makes the analysis very sensitive to signal distortions caused by noise. The results obtained with the theoretical approach described by Mitra[7] (see Equation (14)) were less accurate and revealed, in particular for finite pulse durations, significant underestimations, for example, about 8 μm were calculated for a 10 ± 1-μm capillary for an experiment with 7.5-ms gradient pulses. This underlines the need for models compatible with arbitrary timing parameters for accurate size estimations.

3.3.1.2. Arbitrary orientation of cylinders So far, gradient pulses perpendicular to a restricting surface were considered which is not a constraint for spheres but, for example, for cylinders. However, Özarslan and Basser[33] could also generalize the

equations to cover arbitrary gradient orientations and presented the results obtained for the example of cylinders.

This is straightforward by decomposing an arbitrary gradient $\mathbf{G}$ into a component $G' = \mathbf{G} \cdot \mathbf{n}$ along the cylinder axis ($\mathbf{n}$) yielding a free diffusion term and a component $\mathbf{G} - (\mathbf{G} \cdot \mathbf{n})\mathbf{n} = \mathbf{G} - G'\mathbf{n}$ perpendicular to it where the signal is described by two-dimensional diffusion in isotropic pores as calculated above. Thus, the signal for $\tau_m \geq \delta$ is given by

$$\begin{aligned} \mathbf{M}_{\tau_m \geq \delta}(\mathbf{G}_1, \mathbf{G}_2, \mathbf{n}) \propto 1 - \mathrm{e}^{-\gamma^2 D \delta^2 (\Delta - \delta/3)\left(G'^2_1 + G'^2_2\right)} \\ \cdot \left(A\left(G'^2_1 + G'^2_2\right) + B_{\tau_m \geq \delta} G'_1 G'_2 \cos\theta + C\right) \end{aligned} \tag{97}$$

with

$$C = 1 - A\left(G_1^2 + G_2^2\right) - B_{\tau_m \geq \delta} G_1 G_2 \cos\theta. \tag{98}$$

As shown in Ref. 33, this approach can be applied to an arbitrary (known) orientation distribution of cylinders; however, the corresponding calculations may be quite tedious. Thus, it is noted that numerical calculations may be more feasible than analytical ones for complex orientation distributions.[33] Corresponding calculations for an isotropic orientation distribution yielded a signal difference between parallel and orthogonal wave-vector orientations although infinitely long cylinders were considered.[33]

This seems to reflect that the anisotropy effect, as pointed out above (Section 2.4.3), is not limited to fully restricted diffusion but also appears for anisotropic Gaussian diffusion.[38] In the current calculations, the Gaussian contributions were included with higher-order terms which seems to introduce the anisotropy effect. As outlined in Ref. 33, the anisotropy effect can also be understood when considering a diffusion weighting that is strong enough to effectively null the signal decay of a cylinder if it has a component along the cylinders axis. Then only those cylinders that are oriented perpendicular to the wave vectors, will contribute significantly to the signal. Clearly, more cylinders, those with an orientation in a full plane, will contribute if the wave vectors are parallel or antiparallel than for an orthogonal orientation where only one orientation fits.

The equations for specific geometries reported in this section were derived for arbitrary timing parameters and, thus, extend the approaches presented in the previous sections and have been applied for the analysis of *in vivo* acquisitions (see Section 4.1.2). However, as already mentioned, they were obtained by considering terms up to second order in the wave vector q. This does not only mean that their validity is limited if wave vectors are large and the signal decay is very pronounced. But also that they are unable to describe the anisotropy effect in fully restricted geometries because there the relevant signal modulation appears in the fourth-order terms. Thus, more general calculations would be desirable that, aside from being valid for arbitrary timing parameters, covers higher-order terms. Such an approach, based on the MCF formalism, was recently presented by Özarslan et al.[36] and will be sketched in the following section.

3.3.2. MCF formalism

For the theoretical consideration of DWV experiments with arbitrary timing parameters, that is, $\delta > 0$, $\Delta < \infty$ and/or $0 < \tau_m < \infty$, the MCF formalism[50–53] (see Section 2.7) is a promising tool. It accurately describes the diffusion-weighted signal for a piecewise constant gradient shape which is fulfilled for rectangular pulse shapes usually considered and provides an approach to approximate the signal for arbitrary gradient waveforms. Recently, it has been extended by Özarslan et al.[36] to experiments with variable gradient directions as required for the general DWV experiment and will be summarized here shortly following the presentation given in Ref. 36.

The Bloch–Torrey equation for the (complex) transverse magnetization $M(\mathbf{r},t)$ for spins diffusing with a diffusion coefficient D in the presence of a time-dependent gradient $\mathbf{G}(t)$ is given by[45]

$$\frac{\partial}{\partial t}M(\mathbf{r},t) = D\nabla^2 M(\mathbf{r},t) - \mathrm{i}\gamma\mathbf{G}(t)\cdot\mathbf{r}M(\mathbf{r},t), \tag{99}$$

where relaxation, Larmor precession and bulk motion were ignored in order to focus on the effect of diffusion.

Using the bra-ket notation,[65,66] the transverse magnetization can be written as

$$M(\mathbf{r},t) = \langle\mathbf{r}|M(t)|\rangle. \tag{100}$$

First, a one-dimensional problem will be considered. With a complete orthonormal basis $|k\rangle$, that is,

$$\begin{aligned} \int \langle k \,|\, \mathbf{r}\rangle\langle \mathbf{r} \,|\, k'\rangle \mathrm{d}\mathbf{r} &= \langle k \,|\, k'\rangle = \delta_{kk'}, \\ \sum_k |\, k\rangle\langle k \,|\, &= I, \end{aligned} \tag{101}$$

where I is the identity operator and M can be written as

$$\langle\mathbf{r}|M(t)\rangle = \sum_k \langle\mathbf{r}|k\rangle\langle k|M(t)\rangle. \tag{102}$$

As the basis system $|k\rangle$, the eigenfunctions of the Laplace operator ∇^2, denoted $u_k(\mathbf{r})$, are chosen with

$$\nabla^2 u_k(\mathbf{r}) = -\lambda_k u_k(\mathbf{r}) \tag{103}$$

for the kth eigenfunction with eigenvalue λ_k where it is assumed that the $u_k(\mathbf{r})$ obey the reflective Neumann boundary condition, that is, surface relaxation or pore leakage is neglected. Thus, and considering the nth time interval with a piecewise constant gradient ($\mathbf{G}_n$), Equation (99) can be written as

$$\begin{aligned} \textstyle\sum_k \langle\mathbf{r}|k\rangle \dfrac{\partial}{\partial t_n}\langle k|M(t_n)\rangle = &-D\sum_k \langle k|M(t_n)\rangle\lambda_k\langle\mathbf{r}|k\rangle \\ &-\mathrm{i}\gamma\mathbf{G}_n\cdot\mathbf{r}\textstyle\sum_k \langle\mathbf{r}|k\rangle\langle k|M(t_n)\rangle. \end{aligned} \tag{104}$$

Integration over $\mathbf{r}$ after multiplication with $\langle k'|\mathbf{r}\rangle$ yields

$$\begin{aligned}\frac{\partial}{\partial t_n}\langle k'|M(t_n)\rangle = &-D\sum_k \langle k|M(t_n)\rangle\lambda_k\delta_{kk'} \\ &-\mathrm{i}\gamma\textstyle\sum_k \langle k|M(t_n)\rangle\mathbf{G}_n\cdot\mathbf{r}\int\langle k'|\mathbf{r}\rangle\mathbf{r}\langle\mathbf{r}|k\rangle\mathrm{d}\mathbf{r}.\end{aligned} \tag{105}$$

By introducing the operators Λ and $\mathbf{A}$ with

$$\langle k'|\Lambda|k\rangle = D\lambda_k\delta_{kk'} \tag{106}$$

and

$$\langle k'|\mathbf{A}|k\rangle = \int\langle k'|\mathbf{r}\rangle\mathbf{r}\langle\mathbf{r}|k\rangle\mathrm{d}\mathbf{r}, \tag{107}$$

Equation (105) can be simplified to

$$\frac{\partial}{\partial t_n}|M(t_n)\rangle = -(\Lambda + \mathrm{i}\gamma\mathbf{G}_n\cdot\mathbf{A})|M(t_n)\rangle. \tag{108}$$

For the temporal evolution of the transverse magnetization in the nth interval, the solution

$$|M(t_n)\rangle = \mathrm{e}^{-(\Lambda+\mathrm{i}\gamma\mathbf{G}_n\cdot\mathbf{A})(t_n-T_{n-1})}|M(T_{n-1})\rangle \tag{109}$$

is obtained where T_{n-1} is the end time of the $(n-1)$th interval. In the bra notation, it yields

$$\langle M(t_n)| = \langle M(T_{n-1})|\mathrm{e}^{-\left(\Lambda-\mathrm{i}\gamma\mathbf{G}_n\cdot\mathbf{A}^\dagger\right)(t_n-T_{n-1})}, \tag{110}$$

where † denotes the Hermitian conjugate. Defining the duration $\delta_n = T_n - T_{n-1}$ for each of the intervals, the magnetization after all N intervals is given by

$$\begin{aligned}\langle M(T_N)| &= \langle M(0)|\prod_{n=1}^{N}\mathrm{e}^{-\left(\Lambda-\mathrm{i}\gamma\mathbf{G}_n\cdot\mathbf{A}^\dagger\right)\delta_n} \\ &= \langle M(0)|\prod_{n=1}^{N}\mathrm{e}^{-\left(\Lambda\delta_n-\mathrm{i}\mathbf{q}_n\cdot\mathbf{A}^\dagger\right)}\end{aligned} \tag{111}$$

with $\mathbf{q} = \gamma\delta\,\mathbf{G}$.

If $M(0)$ is assumed to be constant across the pore, $\langle M(0)| \propto \langle 0|$ and

$$\langle M(T_N)| = \langle 0|\prod_{n=1}^{N}\mathrm{e}^{-\left(\Lambda\delta_n-\mathrm{i}\mathbf{q}_n\cdot\mathbf{A}^\dagger\right)}. \tag{112}$$

Thus, the diffusion-weighted signal is given by

$$M(T_N) = \left\langle 0\left|\prod_{n=1}^{N}\mathrm{e}^{-\left(\Lambda\delta_n-\mathrm{i}\mathbf{q}_n\cdot\mathbf{A}^\dagger\right)}\right|0\right\rangle^*. \tag{113}$$

For arbitrary geometries or a variable gradient direction, the one-dimensional basis $|k\rangle$ considered to far must be extended to $|kmn\rangle$ with

$$\nabla^2 u_{kmn}(\mathbf{r}) = -\lambda_{kmn} u_{kmn}(\mathbf{r}). \tag{114}$$

This also affects, accordingly, the operators Λ

$$\langle k'm'n'|\Lambda|kmn\rangle = D\lambda_{kmn}\delta_{kk'}\delta_{mm'}\delta_{nn'} \tag{115}$$

and $\mathbf{A}$

$$\langle k'm'n'|\mathbf{A}|kmn\rangle = \int \langle k'm'n'|\mathbf{r}\rangle \mathbf{r} \langle \mathbf{r}|kmn\rangle \mathrm{d}\mathbf{r}, \tag{116}$$

that is, $\mathbf{A}$ in general has three components, and the signal equation equals

$$M(T_N) = \left\langle 000 \left| \prod_{n=1}^{N} \mathrm{e}^{-\left(\Lambda\delta_n - \mathrm{i}\mathbf{q}_n \cdot \mathbf{A}^{\dagger}\right)} \right| 000 \right\rangle^{*}. \tag{117}$$

However, for specific geometries the variables may be separable. Thus, the three-dimensional problem is reduced to one- and two-dimensional ones and the signal expression can be written as a product of the individual results. For instance, for a cylindrical pore of radius r_0 and length l, the eigenvalues λ_{kmn} are given by

$$\lambda_{kmn} = \left(\frac{\pi^2 k^2}{l^2} + \frac{\alpha_{mn}^2}{r_0^2} \right) \tag{118}$$

where α_{mn} is the nth zero crossing of the derivative of the mth-order Bessel function, and the variable along the cylinder axis (z) can be separated from those perpendicular to it (r, ϕ).

Example calculations of the MR signal for spherical, ellipsoidal and cylindrical pores were performed[35,36] and will not be given here. For ideal timing parameters, the results obtained reproduce the well-known features for short and long mixing time and show that the basic signal modulations, although distorted at higher q values, are present over a large range of q values. The deviations of the cos 2θ-modulated signal for finite timing parameters from the ideal curve observed at lower q values emphasize the need to apply a framework that takes finite timing parameters into account, for an accurate interpretation of experimental results. This is demonstrated in experiments on cylindrical microcapillaries with typical timing parameters and q values yielding a pronounced signal decay for which the extended framework delivers very good size estimates.[36] A direct comparison of the theoretical curves point up the deviations for approaches focusing on the lower-order terms: for large q, even for the ideal timing parameters, considerable deviations are present.[35]

It should be noted that this approach not only can handle finite pulse duration for the pulse sequences shown in Figure 1 but also can be applied to other diffusion-weighting preparations. For instance, to compensate cross-terms with background gradient fields, additional gradient pulses may be required that can easily be considered in the MCF approach.

The analytical solutions provided involve matrices of infinite dimension ($\Lambda, \mathbf{A}$) which is due to the fact that an infinite number of eigenfunctions and eigenvalues exist. This means that infinite calculations are required for an exact solution. However, only a finite number of these will deliver significant contributions and the equations converge sufficiently fast to be feasible in practice. Özarslan et al.[36] report that considering the eigenfunctions corresponding to the first 20 eigenvalues was sufficient to obtain a very accurate result in their examples.

Thus, solutions based on the MCF framework are expected to be very valuable tools to evaluate experiments with arbitrary timing parameters and for any wave-vector orientations and magnitudes. However, the underlying geometry and the corresponding eigenfunctions and eigenvalues for the Laplace operator need to be known for an accurate estimation. Although the eigenfunction problem is relevant in many fields and has been solved for standard geometries, it may be tedious to derive new solutions for a complex geometry if it is known at all. Thus, relaxing this constraint and deriving general signal expressions or properties for complex or arbitrary (unknown) pore shapes would be very promising but seems to be challenging.

The bulk diffusivity D is contained in the equations within Λ, that is, it either must be known, for example, in model systems from some reference experiment, or has to be included as a fit parameter. Regarding the latter approach, it must be kept in mind that the product of the bulk diffusivity and the geometry eigenvalues appears within the terms. To obtain a result for the size estimate, they have to be distinguished, that is, the eigenvalues must be ''decoupled'' from the bulk diffusivity. This could be achieved with acquisitions at different q values that ensure sufficiently large contributions from different eigenfunctions to reliably discriminate λ_k and D.

As noted in Ref. 35, the MCF framework can also be used to consider the effect of imaging gradients on the acquired MR signal. This does not only cover imaging gradients, like slice-selection and spoiler gradient pulses, applied within the diffusion or mixing time but, for restricted diffusion, may also be relevant for gradient pulses switched *after* the diffusion weightings. In this case, the spins' movement during the imaging gradients may be correlated to their displacement during the diffusion weighting. This also means that the phase dispersion introduced by the imaging gradients may not be independent from that caused by the diffusion weighting and the signal amplitude may change with the imaging gradients.

In a very crude example, this can be seen if the gradient pulses of the second diffusion weighting of a DWV experiment are considered as imaging gradients, for example, for frequency predephasing and encoding. If the predephasing is applied immediately after the diffusion weighting which corresponds to a short-mixing-time DWV experiment, the signal depends on the polarity and direction of the imaging gradients. Only if the temporal gap between the diffusion weighting and the imaging gradients, that is, the ''mixing time'', is long enough to ensure that spin paths and related phase dispersions are uncorrelated, such dependencies will vanish. Note that this differs from free diffusion where avoiding an overlap of diffusion weighting and imaging gradients is sufficient as free diffusion is uncorrelated on any finite time scale.

3.4. Ideal timing parameters versus exact solutions

Regarding the theoretical approaches presented, two basic branches can be distinguished. In the first, the general equations of Mitra[7] which are valid for any pore shape but were derived under the assumption of ideal timing parameters were used as starting point. Their Taylor expansion, to second or fourth order in q, could be performed in a more general context dropping the assumption of randomly oriented pores which may not be realistic in samples like biological tissue. Thus, general signal expressions for arbitrary pore shapes, pore orientation distribution and wave-vector orientations were obtained in terms of tensor models in the limit of short and long mixing times that are applicable to macroscopically anisotropic samples.[54,55] From these expressions, rotationally invariant measures of the pore size and the microscopic anisotropy, that is, the pore eccentricity, were identified that are independent of the macroscopic properties of the sample and can be determined with a few measurements.[54,55] Thus, the tensor models provide a reasonable and practical approach to characterize samples with a complex or unknown inner structure or macroscopic anisotropy like biological tissue.

Multiple concatenations of the two wave vectors have been shown to allow a shortening of the pulse duration[58] (e.g. Sections 3.1.2 and 3.2.4) getting closer to the assumption of short gradient pulses while simultaneously increasing the signal modulation which may help to improve the detectability. Nevertheless, deviations from the equations will be present in experiments with finite timing parameters yielding a reduced modulation amplitude as has been shown with the more elaborated theoretical models yielding exact solutions for specific geometries[33,36] (see Section 3.3) and in numerical simulations[67,68] (see Section 4.1.1). Some strategies to minimize these deviations in experiments or to consider them in the analysis will be discussed in Section 4.

In this context, the concept of the centre-of-mass propagator which was introduced to account for finite gradient pulse durations[69] seems also to be interesting. It allows to consider deviations from the short-pulse approximation, as assumed in the tensor models presented, by replacing the particle propagator by a propagator describing the displacement of the centre-of-mass of the particle's trajectory during the finite pulse. Thus, the basic equation of the short-pulse approximation remains valid.[69] While it is difficult to obtain exact results without considering specific pore shapes and timing parameters, the qualitative impact of finite timing parameters is easy to estimate.

It seems to be straightforward to apply this concept to the tensor models derived. This means that it can be expected that the basic equations and properties of the tensor models and the measures derived from them can be retained for experiments with finite timing parameters but will reflect a slightly distorted rather than the exact pore geometry. Thus, the values determined will depend on the experimental parameters used, pulse duration, diffusion and mixing time, and q value. But it can be expected that the derived results are reproducible and, in particular, that pore size or anisotropy *differences* can be detected reliably. These properties are crucial but also sufficient for many applications in biomedical or clinical research.

Regarding these aspects, the tensor models can be seen in line with the usage of the (single-wave-vector) diffusion tensor[3] *in vivo*. It is obvious, that the diffusion

in tissue is not Gaussian and the tensor elements or measures derived from it like the fractional or relative anisotropy will depend on the b value, the diffusion time and the pulse duration.

In the second branch of theoretical models[33,36] (Section 3.3), solutions for finite timing parameters and larger q values were investigated with the Bloch–Torrey equation as the starting point. The most general model is based on the MCF formalism and provides an exact solution for arbitrary timing parameters and q values in terms of the eigenfunctions of the pore geometry under the Laplace operator[36] (Section 3.3.2). Although infinite sums are involved, the expression can be determined with a high accuracy for a feasible number of eigenfunctions if these are known as for most simple geometries. This approach very successfully, and compared to the models based on ideal timing parameters more accurately, describes the experiments performed on microcapillaries with finite timing parameters, including diffraction effects that usually are difficult to model appropriately (e.g. Sections 4.1.3 and 5.2). Even at large q values, the size estimates derived are in an excellent agreement with the nominal values or the results from light microscopy. As pointed out in Ref. 36, effect like surface relaxation can easily be added to the formalism. Thus, for an accurate determination of pore sizes as may be required, for example, in material sciences, this approach is indispensable.

For samples with complex or unknown pore structure, the approach seems to face some limitations. While a calculation of the eigenfunctions for complex geometries may only be tedious, it may be difficult to obtain expressions for unknown geometries or describe signal properties that are valid in general. Furthermore, for an accurate parameter estimation the bulk diffusivity may be required which may not always be available or easily determinable.

Another problem are samples with an non-isotropic orientation distribution, that is, macroscopic anisotropy. This concerns not only the modelling of the signal for an unknown orientation distribution but also the question which wave-vector combinations need to be chosen to characterize the sample reliably. Although it can be argued that averaging measurements covering the full range of wave-vector orientation yields a result equivalent to an isotropic orientation distribution that can be analyzed,[33] such acquisition schemes are time consuming and may be inappropriate for *in vivo* measurements. This holds in particular for the anisotropy effect where for each orientation of the first wave vector, the equator must be sampled with the second wave vector to ensure a sufficient isotropic measurement.

Thus, both branches provide specific advantages and drawbacks. But an extension towards a model combining the benefits of both approaches would be an ideal solution.

4. ANGULAR SIGNAL MODULATION

Studies investigating the signal modulation with the angle between the wave vectors will be summarized in this section. All of them deal with DWV experiments which is the simplest experiment showing the specific MWV effects. In the first part, the restriction effect will be covered which can be used to estimate pore

or compartment sizes (Section 4.1), in the second, the anisotropy effect is considered which is able to detect diffusion anisotropy on a microscopic level even in macroscopically isotropic samples (Section 4.2).

4.1. Restriction effect

In this section, experimental results and numerical simulations of the restriction effect observed at short mixing times (see Section 2.4.3) are presented that aim to detect and analyze the cos θ-shaped signal modulation with its signal difference between parallel and antiparallel wave vectors. Because of this difference, that is, the modulation amplitude, scales with the pore size, it offers access to an estimation of pore or compartment sizes. The studies cover the range from first experiments in phantoms and extracted spinal cord tissue (Section 4.1.1) to *in vivo* acquisitions in the human brain (Section 4.1.2) and experiments on well-defined model systems validating the size estimation in microcapillaries and fixed yeast cells using light microscopy (Section 4.1.3).

4.1.1. First experiments

First experiments that demonstrate the detectability of the restriction effect according to Equation (14)[7] and estimate the size of diffusion compartments, were performed on a whole-body MR system at 3 T (maximum gradient amplitude 40 mT m^{-1}).[70] In this study, various phantoms, water between polymer beads (diameter 42 μm), plant tissue (radish root) and fixed pig spinal cord as well as bulk water as a control without restrictions were investigated at various mixing times. Thereby, DWV experiments were performed with one static wave vector and the other sampling eight directions uniformly distributed on a circle, that is, all of the diffusion weightings were applied in a plane.

The pulse sequence was set up to minimize systematic variations with the direction of the diffusion weightings. To reduce effects of magnetic field inhomogeneities, diffusion-weighting preparations insensitive to (static) background gradient fields were employed for each wave vector. Slice-selection and spoiler gradients were applied perpendicular to the plane of the diffusion weightings to avoid variable cross-terms. Different spoiler amplitudes around the refocusing RF pulses were used to ensure dephasing of unwanted coherence pathways. Furthermore, the variant with $\tau_m > \delta$ was chosen (Figure 1C) to abandon a modulation of the b value with θ according to Equations (2) and (3). The imaging acquisition was performed with an echo-planar[71] readout.

In all samples, except for the bulk water, a cos-shaped signal modulation was observed when varying θ with a clear signal difference between parallel and antiparallel orientations[70] (see Figure 7). This modulation decreased when the mixing time τ_m was prolonged, most rapidly for the spinal cord, most slowly for the radish. For water between beads and the spinal cord, the increase of the modulation amplitude with q could be shown. These observations are consistent with the theoretical expectations.

The modulation and the parallel-antiparallel difference persisted and only minor variations of the signal curve were observed in additional experiments

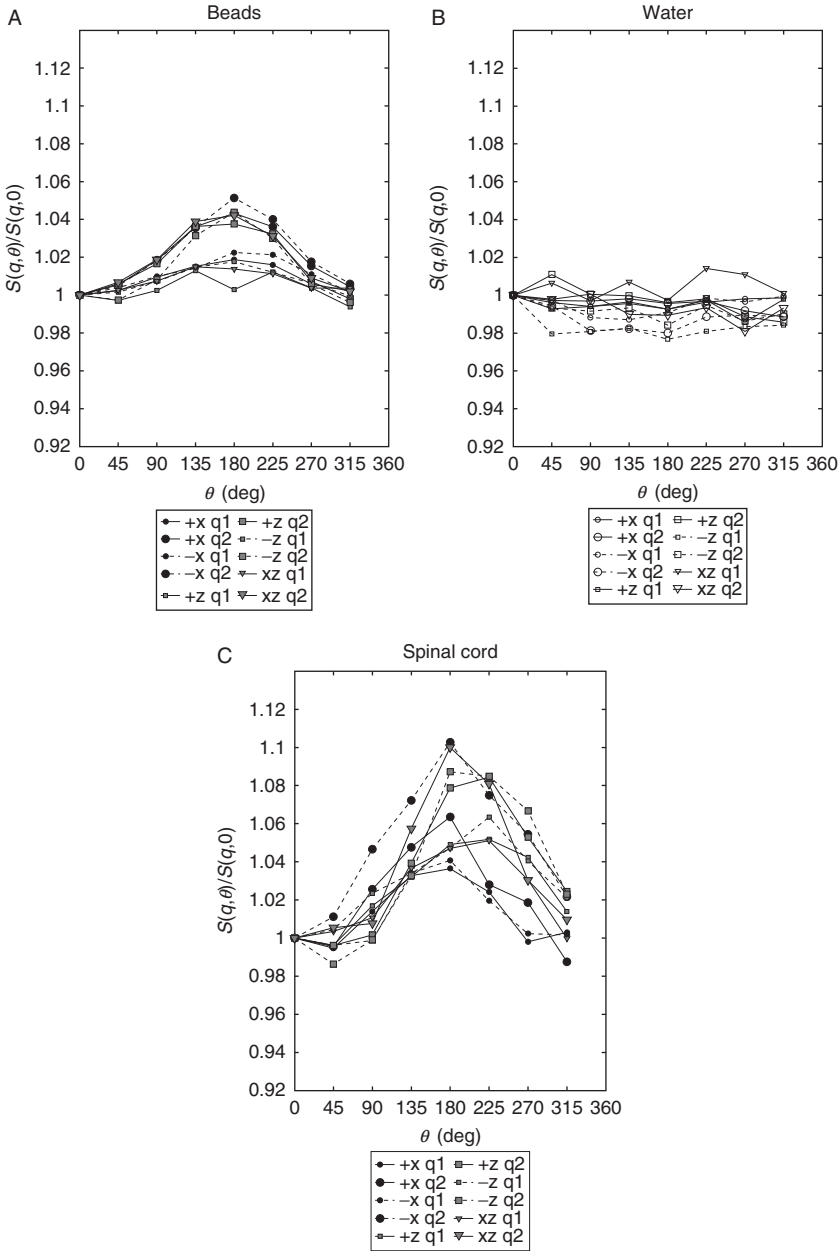

Figure 7 Signal amplitude versus θ acquired on a whole-body MR system with a short-mixing-time DWV experiment on (A) a bead phantom, (B) a bulk water reference and (C) extracted pig spinal cord. For details see text and Ref. 70. Courtesy of M. Koch. Reprinted from Ref. 70 with permission from John Wiley & Sons.

where different parameters were varied like the direction and polarity of the static wave vector, the slice- and phase-encoding directions, the slice thickness, the rise times of the diffusion-weighting gradient pulses, the diffusion times and the direction of the static wave vector.[70] Thus, other causes for the modulation, like cross-terms, gradient scaling errors or eddy currents, could be ruled out and the angular modulation could be assigned to represent the expected restriction effect.

The modulation amplitudes observed were quite low, typically about 5–10%, which was the reason for the careful design of the pulse sequence and the various cross-check experiments. In particular, the signal decay ratio for parallel and anti-parallel wave-vector orientations was far from a value of 3 which is expected from Equation (14). This deviation can, to some extent, be related to the finite pulse durations and mixing times employed. But calculations of the signal amplitudes also revealed that already a 5% volume fraction of freely diffusing spins would reduce the decay ratio from 3 to about 1.03.[70] Such spins may, for instance, be present in the extracellular space of the tissue or, in case of the beads, represent those that leave ''their'' interstitial space via the connections existing.

Thus, the experiments, performed at two different q values, were analyzed with a model that apart from the second-order term of Equation (14) considered a free diffusion term (up to second order) with a variable volume fraction. Involving acquisitions at two different q values, the cell size $\sqrt{\langle R^2 \rangle}$, that is, the square root of the mean-squared radius of gyration, and the relative volume fraction could be determined. The size obtained for the beads (4.1 μm) was in quite good agreement with the mean radius of an interstitial space in a close packing of identical spheres with a radius of 21 μm (about 5 μm). The values obtained in the spinal cord (1.9 μm) were also quite similar to typical axon radii (about 1.5 μm).[72,73] However, it must be kept in mind that the experiment is expected to reveal a volume fraction-weighted average which should be shifted towards larger cells (see also Section 4.1.2). This means that the cell size is underestimated. A more severe underestimation was observed in the radish yielding a size of about 14 μm while it could be estimated to about 100 μm using light microscopy.

As pointed out in Ref. 70, the assumption of ideal timing parameters underlying the derivation of Equation (14) were clearly violated in the experiments which is expected to yield a reduced signal modulation, that is, an underestimation of the pore size. For the radish, the diffusion time achievable at a reasonable SNR value (106 ms) was much below $\tau_D = a^2/2D$ (about 2.5 s) which is the time a spin typically needs to cross a pore of size a with a bulk diffusivity of D. For the spinal cord, the pulse duration (17 ms) exceeded the corresponding τ_D of about 1 ms considerably. And the interstitial spaces in the bead phantom are connected, that is, diffusion is not strictly restricted. While such deviations, to some extent, can be modelled by the free diffusion term, it is obvious that the size estimates obtained do not represent accurate results[70] and may be close to the expected values, for example, in the beads phantom, due to concurrent deviations towards smaller and larger values as pointed out by Weber and Ziener et al.[67]

They simulated the signal for two-dimensional diffusion in a circular geometry (radius r_0) in order to investigate the effect of larger q values and of finite gradient

pulses and diffusion times for, as in their experiments, $\tau_m = 0$ on the apparent cell radius derived from Equation (14).[67] They could show that for qr_0 up to about 1, the deviation from the nominal size is below 10%. For finite δ and Δ, a similar underestimation occurs if $\delta/\tau_D \approx 0.4$ and $\Delta/\tau_D \approx 2.5$. Thus, for the given experimental parameters, there is an ''optimal'' radius with the best size estimation: for smaller cells, the underestimation due to the finite pulse duration dominates while for larger cells it is the insufficient diffusion time that yields systematic errors.[67] This means that cells not ''compatible'' with the experimental parameters will show a signal modulation amplitude that is lower than expected, which may explain the severe underestimation of the radish cell size reported in Ref. 70.

Considering mixtures of pore sizes with distributions determined from tissue samples for short gradient pulses, Weber and Ziener et al.[67] could conclude that an estimate of the mean diameter is quite close to the true value if the relative volume fractions are taken into account.[67] Permeable cell membranes were shown to yield an overestimation of the cell radius which increases with the diffusion time and, thus, can be identified.[67] This is consistent with the idea of Cory et al.[5] to investigate pore leakage with DWV experiments.

But the main target of the study of Weber and Ziener et al.[67] were measurements on excised rat spinal cord tissue on a NMR spectrometer at 17.6 T with a gradient system capable of 1 T m^{-1} which allows considerably shorter gradient pulses (3 ms). In these experiments, the signal difference between the parallel and the antiparallel wave-vector orientations is already visible in the acquired images and a cos-shaped signal modulation with the angle between the two wave vectors is clearly present (Figure 8A and B). With about 25% signal difference at a diffusion time of 50 ms (Figure 8C), its amplitude is much more pronounced than in the earlier experiments on a whole-body MR system (about 5–10%).[70] Regarding the much shorter gradient pulses and the simulations, this difference seems to be caused by the shorter δ achievable on their system.

With increasing diffusion time, the signal modulation and, thus, the estimated radius of the spinal cord cells showed a saturation behaviour which was also found in the simulations. It indicates that in this regime the diffusion time is large enough to observe fully restricted diffusion. This is a clever strategy to reduce the impact of finite timing parameters when using models based on ideal timing parameters, and also is applicable if, for example, the bulk diffusivity appearing in the MCF approach is unknown. The cell size estimated using Equation (14) in the ''saturation'' range was about 3.2 μm which is very good agreement to results obtained from q-space imaging techniques.[74] Thus, despite of the rather simple model used for the data analysis, a very good agreement with the literature is obtained.

The simulation results of Weber and Ziener et al.[67] were reproduced in Ref. 68 and extended by considering three-dimensional diffusion, non-vanishing mixing times and typical whole-body MR gradient amplitudes. An interesting finding was that for amplitude-limited gradients, like on whole-body MR systems, there seems to be an optimum pulse duration where the largest signal modulation is observed. Below it, that is, for shorter pulses, the modulation is reduced due to the lower q values. For longer pulses, the modulation decay with prolonged δ, already reported by Weber and Ziener et al.,[67] dominates. For ellipsoidal cells with

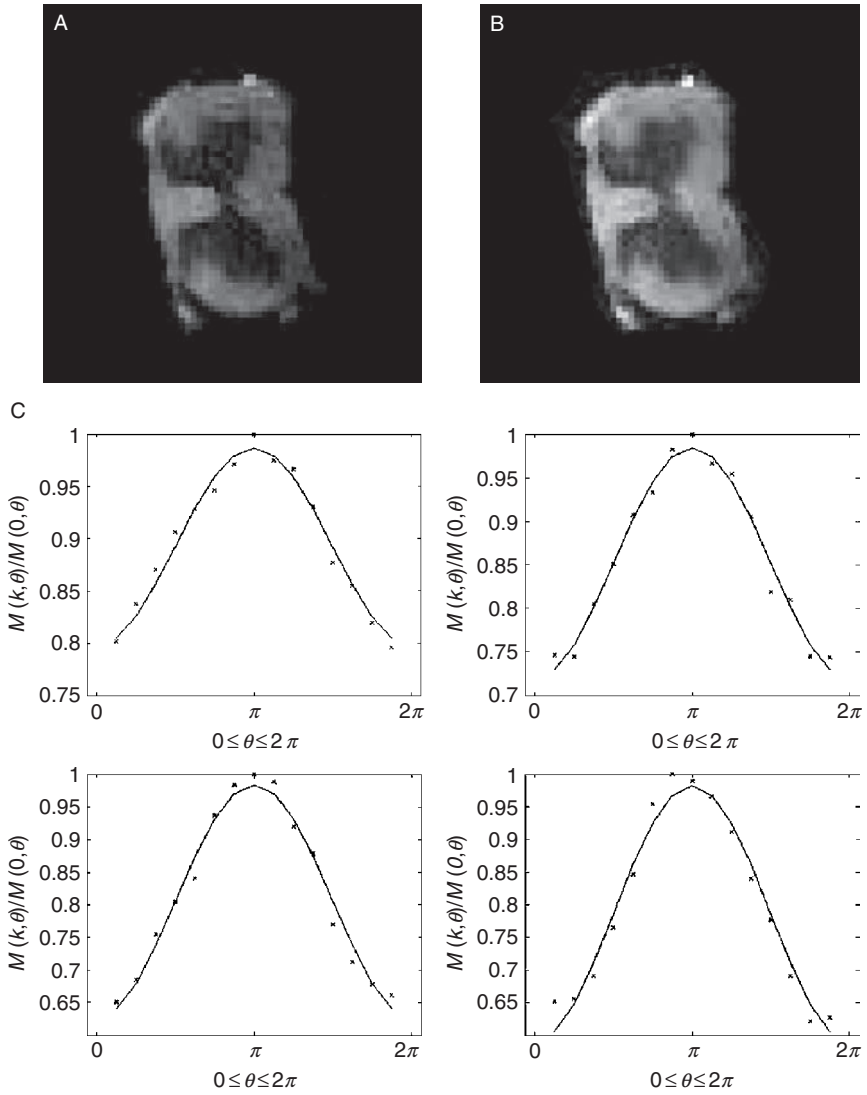

Figure 8 Results of DWV experiments at vanishing mixing times performed in rat spinal cord. (A, B) Spin-echo DWV images of excised rat spinal cord for (A) parallel and (B) antiparallel wave-vector orientations at a diffusion time of 100 ms showing the higher signal intensity for the antiparallel orientation. (C) Signal modulation versus the angle between the two wave vectors for diffusion times of 20, 50, 100 and 200 ms. In contrast to Figure 7, the experiments were performed on a high-field spectrometer (17.6 T) with a gradient system capable of 1 T m^{-1}. For details see text and Ref. 67. Courtesy of C. Ziener. Reprinted from Ref. 67 with permission from John Wiley & Sons.

semi-axes of 2.5, 2.5 and 7.5 μm a modulation of a few percent can be expected for typical whole-body MR parameters, which should be observable on current systems.

4.1.2. *In vivo* experiments

The first *in vivo* demonstrations of the restriction effect were performed in the human corticospinal tract on a standard whole-body MR system (3 T, 40 mT m^{-1}).[75,76] White matter tract fibres are expected to exhibit a pronounced diffusion restriction. The specific target region was chosen because of the dense packing and high orientation coherence of the fibres which maximizes the amount of spins undergoing restricted diffusion if diffusion weighting is applied in a plane (almost) perpendicular to the tract. Furthermore, its location deep in the brain is expected to make it less sensitive to artefacts like ringing effects occurring close to the brain's surface or to the ventricles, or due to magnetic field inhomogeneities and related cross-terms with background gradient fields. This is also the reason why the second study[76] could be performed without the background gradient compensation applied in the phantom[70] and the first *in vivo* study,[75] which yielded considerably shorter echo times and, thus, a significantly improved signal-to-noise ratio (SNR). The diffusion weighting was applied within the transverse image plane which was almost perpendicular to both corticospinal tracts. In the second study,[76] only four diagonal directions were used to apply two physical gradients simultaneously and maximize the diffusion-weighting efficiency. Thus, the gradient pulse durations could be shortened to about 10 ms. In addition, all eight different parallel and antiparallel wave-vector combinations were sampled in order to minimize the influence of absolute wave-vector orientations upon averaging.

The signal difference between parallel and antiparallel wave-vector orientations could be consistently observed in both *in vivo* studies[75,76] with a higher reliability in the second one due to the increase in SNR. Cell diameters were estimated based on the matrix product formalism provided by Özarslan and Basser[33] for cylinders, that is, Equations (97) and (98), which is valid for arbitrary timing parameters. Thus, a mean diameter of about 13 μm[76] was obtained (see Figure 9).

Furthermore, the fit also revealed the angulation of the model cylinders relative to the plane of the diffusion weighting. It showed a correlation with the angulation of the first eigenvector calculated from a standard diffusion-tensor acquisition.[76] Thus, an estimate of the fibre orientation relative to the image plane could be obtained solely based on acquisitions with diffusion weightings applied within the plane.

At a first glance, the mean cell size estimated (13 μm) seems to be too large as typical axon diameters in the corticospinal tract are about 1–3 μm.[72,73] However, taking the axons' volumes and thus their relative signal contributions into account, a volume-weighted mean diameter of about 8 μm can be derived from the spinal cord data of Ref. 73. This is close to the value determined by Weber and Ziener et al.[67] for rat spinal cord (6.4 μm) and not too far away from the value calculated in the corticospinal tract (13 μm) regarding the simplified model of identical cylinders. Deviations may also be related to the appearance of the bulk diffusivity in Equations (95) and (96) via the ω_n defined in Equation (94) and in the additional terms to describe contributions of freely diffusing spins. Its value in the cylinders, that is, within the cells, needs to be known for an accurate estimation but may differ from the self-diffusion coefficient of water at 37° which was used in the study.

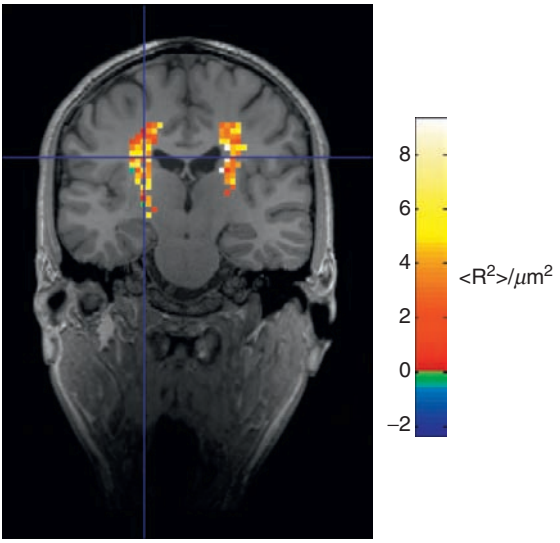

Figure 9 Mean-squared radius of gyration as obtained from a short-mixing-time DWV experiment in the human corticospinal tract *in vivo*. Only voxel exceeding an intensity threshold were considered. For details see text and Ref. 76. Courtesy of M. Koch.

4.1.3. Model systems

First experiments to determine pore sizes in a well-characterized model system were performed by Shemesh et al.[64] on a 8.4-T NMR spectrometer (maximum gradient amplitude 1.9 T m^{-1}). They investigated parallel-oriented microcapillaries with diameters between 5 ± 1 and 19 ± 1 μm for a variety of timing parameters. To minimize the influence of susceptibility-related background gradients, the capillaries were oriented along the static magnetic field.

The experiments revealed, as expected from simulations[67,68] and the theoretical approaches[33] presented, a reduced signal modulation for prolonged gradient pulse durations, mixing times or reduced diffusion times while the basic cos θ dependency was retained (Figure 10). The data were analyzed with the results of the matrix product approach of Özarslan and Basser[33] using Equations (97) and (98). Because these equations only cover second-order terms, multiple q values were sampled and the curve was fitted to an expression $1 - aq^2 + bq^4$ from which only the second-order factor a was used for the analysis. Thus, a very good agreement of the experimentally determined diameters with the nominal ones was obtained.[64] Typical deviations were below 5% of the nominal diameter and well within the variance given by the manufacturer (± 1 μm). Some larger deviations were present for very short diffusion times which are related to the very low modulation amplitude present which causes a high sensitivity to noise or b value-induced distortions.

Using Equation (14) which was derived for ideal timing parameters, the analysis yielded significant underestimations, for example, 8.0 μm were estimated for the 10 ± 1-μm capillaries compared to 10.5 μm for the matrix product

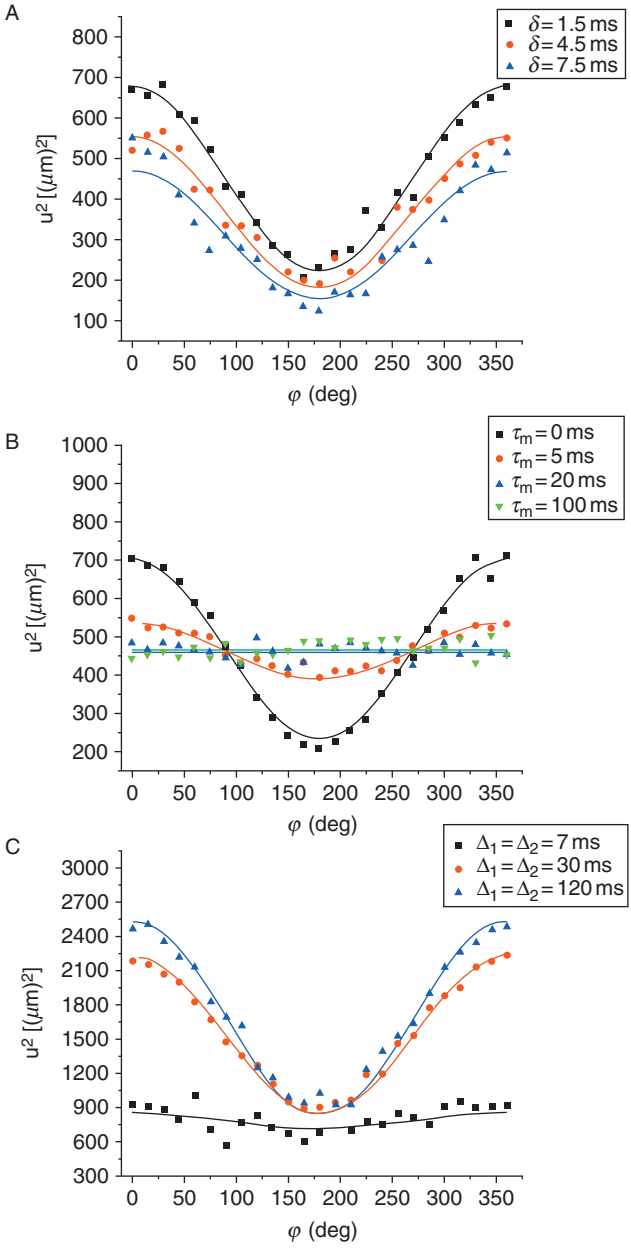

Figure 10 Signal decay versus θ for a short-mixing-time DWV experiment on parallel, water-filled capillaries for different timing parameters varying (A) the gradient pulse duration (δ), (B) the mixing time (τ_m) and (C) the diffusion time (Δ). Both wave vectors were applied in the plane perpendicular to the capillary axis. Note that the signal decay factor (denoted as u^2) is shown, that is, the difference to an experiment without diffusion weighting ($M \propto 1 - u^2q^2$), which reverses the shape shown in Figure 2A. For details see text and Ref. 64. Courtesy of N. Shemesh. Reprinted from Ref. 64 with permission from Elsevier.

formalism if a pulse duration of 7.5 ms was used. This underlines the need to take the finite timing parameters into account if accurate size estimates of known pore geometries are desired.

Another interesting finding of this study was that even in the absence of a signal modulation, for example, at mixing times as long as 100 ms (see Figure 10B), the capillary diameter (10 ± 1 μm) could be well estimated, both with the matrix product formalism (10.4 μm) and Mitra's approach (9.1 μm). At a first glance, this seems to be surprising as the interesting and unique feature of the DWV experiment is the angular modulation that directly reflects restricted diffusion. But both theoretical derivations yielded (second-order) expressions that depend on the cylinder/pore size as the only fit parameter. Thus, these terms do not only describe the modulation amplitude but also the mean signal decay which, for instance, can be seen in Equation (14). In other words, the mean signal decay also reflects the pore size in these models and can be used to estimate the capillary diameter quite reliably. However, the signal decay in more complex systems may not only be defined by the spins in a restricted geometry but may also contain contributions from freely diffusing spins. In this case, size estimates based on the signal decay will fail and only the signal modulation present in DWV experiments is expected to reflect the spins in the restricted compartment only.

Such a model system was investigated in a subsequent study by Shemesh et al.[77] where a compartment with free water has been added to the microcapillaries. In this case, the experiments were analyzed with the recently presented MCF formalism (see Section 3.3.2) provided by Özarslan et al.[36] The angular signal modulation could be reliably observed and the size of the capillaries (19 ± 1 μm) could also be estimated accurately (20.3 ± 0.3 μm) if signal contributions of freely diffusing spins were included in the fit function.

At very low q values the modulation was not detected but this regime ($q < 100\ \mathrm{cm}^{-1}$) was well below that typically used in previous studies of the same authors to investigate the angular modulation (q up to 300–500 cm^{-1}). Thus, the absence of a significant modulation could be related to the low q values involved as is known that the modulation is expected to increase with q^2.

Most recently, two studies[78,79] employed light microscopy to validate pore or cell size estimates based on DWV experiments. Komlosh et al.[78] investigated water-filled glass capillary arrays with a nominal size of 10 μm which by optical microscopy could be determined to have an inner diameter of 9.3 μm. DWV imaging experiments performed on a 7-T NMR spectrometer, using pulsed gradients up to 295 mT m^{-1} and analyzed with the MCF approach of Özarslan et al.[36] (Section 3.3.2) for cylinders, yielded a size of 9.35 ± 0.07 which represents an excellent agreement.

Shemesh et al.[79] performed DWV experiments on fixed yeast cells and, also based on the MCF model[36] (Section 3.3.2) for cylinders, determined the mean size to 5.46 ± 0.45 μm. This value perfectly fits the average size of 5.32 ± 0.83 μm that was determined from light microscopy. These two studies demonstrate the high accuracy achievable with DWV experiments as a tool to investigate pore or cell sizes.

4.1.4. Summary

In summary, the restriction effect characterized by a cos θ modulation and a signal difference between parallel and antiparallel wave-vector orientations, could be detected experimentally, not only on high-field spectrometers but also on standard whole-body MR systems. The accuracy achieved in model systems of known geometry and spherical cells as validated by light microscopy is impressive, in particular if the analysis is performed with the MCF approach that takes the finite timing parameters into account and is valid for arbitrary q values. First experiments in tissue and in the human brain *in vivo* revealed a reasonable to good agreement with values from the literature and demonstrate its feasibility for *in vivo* applications.

4.2. Anisotropy effect

In this section, experiments showing the signal difference between parallel and orthogonal wave-vector orientations as a sign of microscopic diffusion anisotropy are summarized. A pioneering experiment detecting the microscopic anisotropy effect, that is, the signal difference between parallel and orthogonal wave vectors, was performed by Cheng and Cory[8] in 1999 on a 14-T spectrometer capable of 12.5-T m^{-1} pulsed gradients. They investigated macroscopically isotropic samples of yeast cells with different eccentricities as confirmed by light microscopy. Such cells were generated from spherical yeast cells by radiation and controlling their culture time to obtain different eccentricities with a ratio of minor to major axes of about 1:5 and 1:10, respectively.

For q values above 0.15 μm^{-1}, the signal curves of both samples showed a higher signal for parallel than for orthogonal wave vectors[8] which is consistent with the theoretical expectations. By analyzing the results with the signal expression of Equation (17) that they derived for ellipsoidal cells at long mixing times, the cell sizes could be estimated to 2.2 μm along the short axis (ellipsoids of revolution were assumed) and 13.0 and 18.9 μm, respectively, along the long axes. These results were in reasonable agreement with the observations obtained by light microscopy (short axis about 4 μm, long axis about 15 μm and >20 μm). Some deviations were attributed to the finite pulse duration used that, although only 1.0 ms, can be expected to violate the short-pulse approximation which was assumed in their derivation, along the cells' short axes ($\tau_D \approx 1$ ms). However, the finite diffusion time used (20 ms) may also have had an influence towards the slight underestimations because it is shorter than τ_D for the long axis of the prolonged cells (about 33 ms).

Callaghan and Komlosh[38] could observe the anisotropy effect in a polydomain lyotropic liquid crystal system investigated on a 7-T spectrometer. Dispersed in water, lamellar bilayers aggregate that yield randomly oriented domains in which water diffusion effectively is limited to two dimensions. By describing the angular dependency of the diffusion coefficient locally, that is, in a domain, by an ellipsoid of revolution, the signal for parallel and orthogonal wave-vector orientations could be calculated. These calculations yielded a lower signal for the orthogonal orientation as demonstrated for one- and two-dimensional diffusion. The

experiments performed could show such a difference at large q values. The diffusion coefficient obtained from the fit for the short axis of the ellipsoid was an order of magnitude smaller than that of free water.

An extensive study of Komlosh et al.[34] reports the experimental observation of the anisotropy effect in capillaries, cortical grey matter tissue of monkeys and excised pig spinal cord. The capillary phantom consisted of randomly oriented, water-filled tubes (length 0.5 mm, inner diameter 20 μm, outer diameter 90 μm) and was set up to mimic the microstructure of grey matter with a well-characterized model system. The tubes were immersed in a fluid without proton NMR signals and a density lower than that of water which effectively moved residual water out of the sensitive volume of the detection coil. Similarly, the grey and white matter samples were immersed in a fluid which also does not deliver a proton NMR signal and which has a magnetic susceptibility comparable to that of tissue to avoid field gradients caused by susceptibility differences. The experiments were performed on a vertical 7-T system capable of pulsed gradients with an amplitude of 1.5 T m^{-1}.

In the phantom and the grey matter sample, only minor differences in the decay curves for diffusion gradient pulses along three orthogonal axes where observed in a standard single-wave-vector experiment which demonstrates that the samples were macroscopically isotropic. In other words, despite of the diffusion anisotropy present on a microscopic level, the diffusion tensor is (almost) spherical. The spinal cord tissue exhibited a significant macroscopic anisotropy in such experiments, but not within the plane perpendicular to the cord axis.

However, in all three samples, consistently and significantly lower signals were detected in the DWV experiments with orthogonal wave vectors, which reflects the microscopic diffusion anisotropy.[34] In the capillary phantom, the difference increased when prolonging the diffusion time, which is consistent with the expectations. For the pig spinal cord, the signal difference is also observed within the plane perpendicular to the cord axis that appeared isotropic in the single-wave-vector experiment.

In the absence of an alternative model, the signal decay in the capillary phantom was analyzed using the model provided by Callaghan and Komlosh[38] that assumes locally anisotropic but Gaussian diffusion (see above). For a short diffusion time (15 ms) where the anisotropy effect is less pronounced, the fit to the data is quite good, however, at a diffusion time of 70 ms deviations are present, in particular for larger q values. These deviations are expected to be caused by the non-Gaussian character of the diffusion in restricted geometries if the diffusion times are sufficiently long such that most of the spins can ''feel'' the restrictions.

In a subsequent study, the authors extended their experiments to spin-echo MR imaging on the microimaging system used.[80] The results on the phantom and on the spinal cord could be reproduced well which demonstrates that the combination of the DWV diffusion weighting with an imaging readout does not yield significant interferences. Furthermore, different regions-of-interest of the spinal cord sample could be analyzed separately. All regions investigated (left/right lateral and ventral/dorsal white matter and left/right grey matter) revealed a

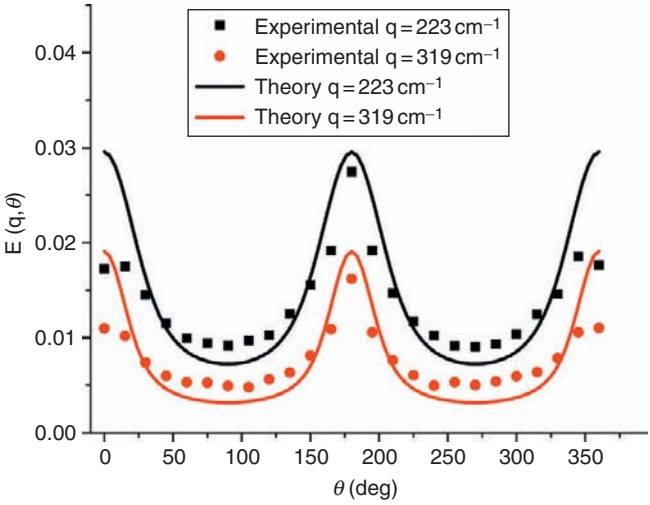

Figure 11 Signal amplitude versus θ for a long-mixing-time DWV experiment on randomly oriented, water-filled capillary fractions at two different q values. The signal difference between parallel and orthogonal wave-vector orientations reflects the microscopic diffusion anisotropy. For details see text and Ref. 81. Courtesy of N. Shemesh. Reprinted from Ref. 81 with permission. Copyright 2010, American Institute of Physics.

very similar difference of about 20% between the parallel and orthogonal wave-vector orientations applied within the plane perpendicular to the cord axis.

In their study investigating randomly oriented fractions of microcapillaries, Shemesh et al.[81] were also able to detect the anisotropy effect and presented results showing the angular dependency of the signal in detail (Figure 11). It basically resembled the cos 2θ-shaped signal curve expected, for example, from Equation (53)[35] but exhibits a slightly higher signal for antiparallel compared to parallel orientations.

The latter deviation cannot be reproduced with the underlying MCF model[36] (Section 3.3.2) which accounts for the finite timing parameters used, that is, it cannot be assigned to residual contributions of the restriction effect. It seems to reflect the influence of uncompensated background gradients that are caused by the susceptibility differences between the water and the capillary material. Although a diffusion weighting insensitive to (constant) background gradients was employed, such effects may not be avoided completely: due to the diffusion movement of the spins the background gradients to which they are exposed to, may vary in time.

In a subsequent study of Shemesh et al.[79] the anisotropy could also be detected in fixed, randomly oriented cells of cyanobacteria. These cells are known to have an elongated shape, as was confirmed with light microscopy, and showed the typical difference between parallel and orthogonal wave-vector orientation.

Recently, experiments detecting the microscopic anisotropy in an echo-planar imaging experiment on a whole-body MR system (3 T, 40 mT m^{-1}) in *ex vivo* pig spinal cord tissue have been reported.[82] In these experiments, diffusion weighting

was performed in a plane perpendicular to the cord axis. Here, all 64 wave-vector combinations obtained from eight directions uniformly distributed on a circle were applied and averaged in order to minimize systematic signal variations depending on the absolute orientations of the wave vectors.

A W-shaped angular modulation with a significant difference between parallel and orthogonal wave-vector orientations could be observed in the tissue that was considerably higher than in a microscopically isotropic reference fluid.[82] This finding is consistent with the studies of Komlosh et al.[34,80] However, it should be noted that the difference could only be reliably detected after averaging all data from the different absolute wave-vector orientations (and polarities) within the diffusion-weighting plane.[82] This reflects the significant influence of the absolute wave-vector orientation on the signal in these experiments which most likely represents eddy currents and related distortions in the echo-planar images but may also be caused by cross-terms with background gradient fields due to the small size of the bottle used, or even slight differences in the gradient scaling along different axes. All these effects are expected to be present for the experiment performed with the reference fluid as well where a systematic signal variation with θ of about 1.0% was observed.[82] Since the modulation in the spinal cord tissue was considerably higher (6–10%),[82] this seems to rule out such systematic effects as the main source for the modulation. Thus, the feasibility of microscopic anisotropy measurements on whole-body MR systems has been demonstrated.

In summary, the anisotropy effect has been detected in a variety of, mostly macroscopically isotropic, samples as a signal difference between parallel and orthogonal wave vectors, even on whole-body MR systems. The effect therefore seems to be feasible for the study of porous media and biological tissue.

5. NEGATIVE DIFFRACTION EFFECT

In this section, the diffraction pattern of diffusion-weighted experiments will be considered. Its properties in standard single-wave-vector experiments are shortly summarized in the following paragraphs before the promising features of the negative diffraction effect of MWV experiments discovered by Özarslan and Basser[9] will be presented covering theoretical considerations (Section 5.1) and the experimental results (Section 5.2) obtained so far.

Following a first experimental observation by Callaghan et al.[40,83] for water diffusing between loosely packed polystyrene spheres, diffusion–diffraction effects were detected in a variety of samples, such as a highly concentrated water/oil emulsion,[84] a stack of rectangular microcapillaries[85] or glass plates,[86] a single cylindrical tube,[87] and erythrocytes.[88–90]

Although very promising for the determination of pore or cell sizes, the method bears some drawbacks. First, short and strong gradient pulses are required which are hard to achieve in human applications. More importantly, the occurrence of the diffraction dips and peaks relies on a proper alignment of the diffusion weighting and a sufficient ''lattice coherence''. For instance, if the diffusion weighting is slightly tilted out of the direction perpendicular to the

restricting geometry, the characteristic dips are rapidly lost as has recently been demonstrated for parallel-oriented microcapillaries.[91] Similarly, a distribution of sizes can reduce or destroy the diffraction effect which has been detected in experiments on erythrocytes[89] and cylinders[92] and was investigated systematically in a recent study on capillaries.[93] Thus, pore or compartment size estimations on the basis of the diffusion–diffraction are often not feasible. However, this may change with DWV experiments as will be shown in the next section.

5.1. Theoretical considerations

Özarslan and Basser[9] could show that in a short-mixing-time MWV experiment additional diffraction ''dips'' appear (see Section 2.4.4). For the parallel orientation of two wave vectors with identical magnitudes, these additional dips occur at half the q values compared to the single-wave-vector experiment. For an even number of diffusion weightings, the additional dips appearing only for $n>1$ share a unique and very interesting feature: they represent zero crossings of the signal of odd order, that is, a sign reversal of the signal is observed at the dips. This is the reason why it is sometimes referred to as a ''negative'' diffraction effect.

One interesting feature of this behaviour is that half the q value is sufficient to observe a diffraction dip, which could reduce gradient hardware demands. The simple theoretical considerations (see also Section 2.4.4) were performed for ideal timing parameters ($\tau_m=0$) where two gradient pulses overlap which would not yield an advantage. But the authors could also show using the matrix product formalism (see Section 3.3.1) that the diffraction pattern is retained for $\tau_m \geq \delta$,[9] that is, for non-overlapping gradients which indeed reduces hardware constraints.

Even more important is the sign reversal of the signals. The authors could show that the corresponding dips are much less sensitive to a distribution of pore sizes.[9] They considered the signal average for parallel planes or spheres with different distributions of the plane distance and the radius, respectively. All dips observed for a single-wave-vector experiment in such systems rapidly level out if the distribution is broadened which is consistent with experimental results.[89,92,93] Thus, a reliable detection of the dips is not possible and the size cannot be estimated. This also holds for the extension to a three-wave-vector experiment. The first dips appear at lower q values for a narrow size distribution but are also lost for broader ones.[9] In contrast, the DWV experiment preserves some of the additional dips, in particular the first one. In the examples investigated theoretically, all dips were retained for parallel planes, in spheres only the first dip while the second faded out for broader size distributions.[9] However, to derive a size estimate, a single dip already is sufficient.

A similar behaviour can be observed for finite timing parameters[9] which were considered using a slightly modified version of the matrix product formalism.[49] The dips with sign reversal remain clearly detectable for finite diffusion times, which also is in contrast to the single- and odd-wave-vector experiments. For finite mixing times, the additional dips are shifted while those also present in the standard experiment are retained and in the limit of very long mixing times the

additional dips coincide with the standard dips (see also Section 2.4.4). For finite pulse durations, all dips are shifted.

In their extension of the MCF formalism (see Section 3.3.2) to DWV experiments,[36] the authors also investigated theoretically the behaviour of the diffraction pattern for spherical pores in a two-wave-vector experiment upon a variation of the angle θ between the two wave vectors which, so far, was assumed to be 0°. They could show that the first negative diffraction dip occurring for the DWV experiment is shifted towards higher q values if the angle is increased. For antiparallel wave vectors ($\theta = 180°$), it vanishes completely. However, it can also appear at q values larger than those for which the first diffraction dip is observed in a single-wave-vector experiment, for example, for $\theta = 135°$. Such an angular shift can also be seen in the signal equation valid for ideal timing parameters, that is, Equation (21) (see Figure 3B and Section 2.4.4).

In a more recent study based on the MCF model (see Section 3.3.2), Özarslan showed that the negative diffraction effect is even present for isotropic orientation distributions of ellipsoids or cylinders.[35] This seems to imply that the effect can be observed for arbitrary orientation distributions and wave-vector orientations. It also represents a major advantage compared to single-wave-vector experiments where the diffraction dips are known to vanish rapidly if the wave-vector orientation is not perpendicular to the restricting geometry.[91]

5.2. Experimental results

The first experimental observation of negative diffraction effects in a two-wave-vector setup was reported by Shemesh and Cohen[41] for arrays of parallel, water-filled microcapillaries (with diameters of 20 and 29 μm) investigated on a 8.4-T spectrometer (maximum gradient amplitude 1.9 T m^{-1}). Thereby, the capillaries were aligned along the static magnetic field to avoid background gradients caused by the different susceptibilities of water and the capillary material. The diffusion weighting was applied perpendicular to the capillaries' axes. The minimum mixing time used (5 ms) was longer than the gradient pulse duration (2 ms), that is, in the DWV experiment the gradient pulses of the two diffusion weightings did not overlap.

In their experiments, they could demonstrate the basic properties of the negative diffraction effect, that is, that (i) the first diffraction dip occurred at half the q value compared to a single-wave-vector experiment and (ii) the signal changed the sign after the first diffraction dip (Figure 12). Estimating the capillaries' diameter based on the first q value at which a dip occurred, yielded correct results within the diameter variance reported by the manufacturer (± 1 μm).

This verifies the theoretical predictions of Özarslan and Basser including the occurrence of the negative diffraction effect without overlapping gradient pulses, that is, at lower amplitudes or shorter gradient pulses.

It was also shown that the additional dips disappear for long mixing times or if one of the diffusion weightings is applied along the cylinder axis which indicates that a correlation of the spins' paths between the two diffusion weightings is necessary for the observation of the negative diffraction effect. Furthermore, it

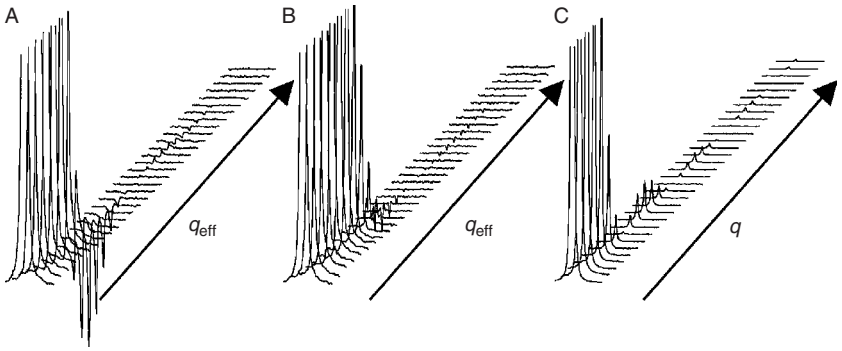

Figure 12 NMR signal versus q for (A, B) DWV experiments with a mixing time of (A) 5 ms and (B) 50 ms and (C) a single-wave-vector experiment acquired on parallel, water-filled capillaries with an inner diameter of 29 μm. Note that $\mathbf{q}_{eff} = \mathbf{q}/2$. For details see text and Ref. 41. Courtesy of N. Shemesh. Reprinted from Ref. 41 with permission from Elsevier.

could be demonstrated that two different diffraction patterns can be observed in a mixture of microcapillaries with two different sizes if the diffusion time is chosen appropriately.

In a second diffraction study,[77] the authors investigated a modified phantom where the tube containing the microcapillaries was surrounded by water, that is, a free compartment had been added. The MCF model used[36] (Section 3.3.2) was extended accordingly by including signal contributions from freely diffusing spins with their volume fraction as a fit parameter. As expected, the signal curve for lower q values was distorted such that the initial decay was quadratic in q which is typical for free diffusion. For larger q values where the signal decay of the free compartment was significant, a bend is observed in the signal curve as a function of q, whose position depends on the relative volume fraction of the free compartment. The signal curve then follows the well-known shape for restricted diffusion including the negative diffraction effects from which the capillary diameter could be estimated accurately.

More recently,[94] their experiments were extended to arrays of microcapillaries of different sizes (between 10 ± 1 and 29 ± 1 μm) (see Figure 13). As expected from the theoretical considerations,[9] the first dip in the DWV experiment remained narrow and deep and could easily be identified for the different size distributions, although it can be shifted towards larger q values for broader size distributions (Figure 13B). In the single-wave-vector experiment, the dips flatten out for broader distributions (Figure 13A). The estimation of the mean capillaries' size is well within the expected range, for example, for the broadest distribution (14.9 ± 4.6 μm) a value of 13.0 μm is obtained. An observation of multiple diffraction patterns is not reported, which may be accounted to the large number of different sizes involved.

Furthermore, an interesting observation is reported[94] that could explain the insensitivity of the first dip over a large range of size distributions. Due to the zero crossing at this dip, pores with sizes smaller or larger than the mean diameter contribute with different signs to the signal. While those being smaller did not

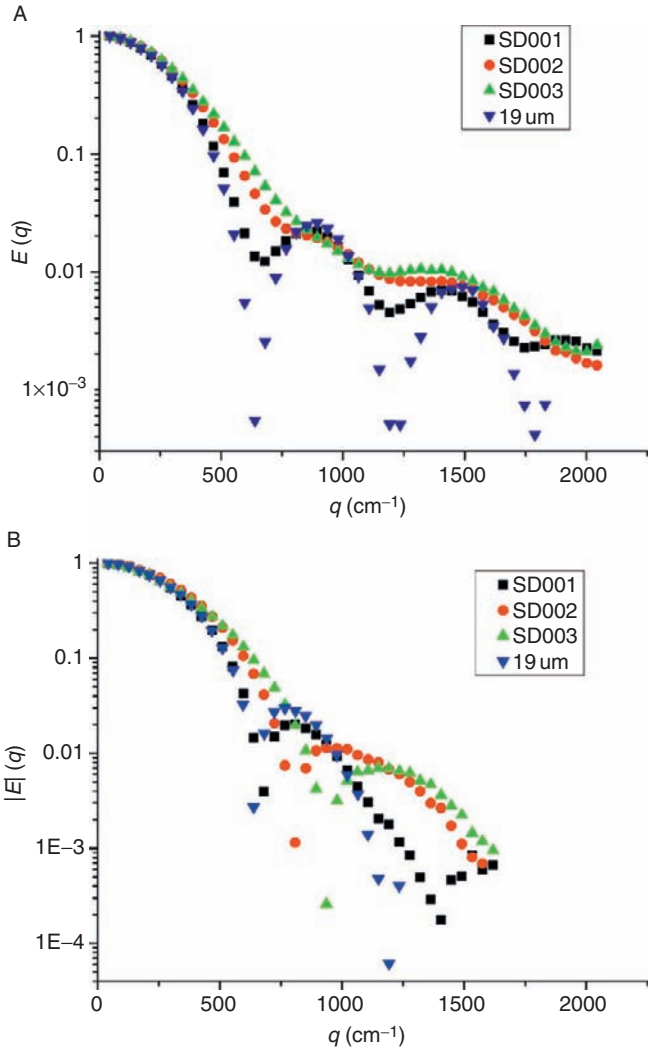

Figure 13 Absolute signal amplitude versus q acquired on samples of parallel-oriented, water-filled microcapillaries with (A) a single-wave-vector and (B) a short-mixing-time DWV experiment. The samples differed by the size distribution of the capillaries they contain, covering 19-μm capillaries only (blue/dark triangles) and mixtures of capillaries between 10 and 29 μm with distributions broadening from SD001 (black/squares) to SD003 (green/light triangles). The diffusion weighting was applied perpendicular to the cylinder axis. Note that, as in Figure 12, the q-axis was adjusted to show dips at the same positions in both plots. For details see text and Ref. 94. Courtesy of N. Shemesh. Reprinted from Ref. 94 with permission. Copyright 2010, American Institute of Physics.

reach their first zero crossing and yield positive signals, the larger ones are already in the negative signal regime. Thus, the zero crossing is quite robust against size distributions. This is different for the single-wave-vector experiment or, more general, odd-wave-vector experiments, where all sizes have a positive signal, that is, all sizes with non-vanishing signal contributions shift the curve towards larger signals and flatten the dip. It should also be noted that the robustness seems to be best for the first dip.[94] At larger q values, not only the signal decays significantly due to the higher diffusion weighting but also the dips for the individual pore sizes diverge more and more.

Investigating a phantom consisting of short fractions of water-filled microcapillaries that were randomly oriented, Shemesh et al.[81] could also demonstrate that the negative diffraction dips persist in samples that exhibit an orientational dispersion (Figure 14). This is another feature unique to the negative diffraction dips of DWV experiments as the single-wave-vector dips were shown to disappear for such orientation distributions[81] (see also Figure 14A). The sizes estimated from the dip again were in very good agreement with the nominal values. As in earlier DWV experiments,[70] diffusion weightings compensating for (static) background gradient effects were applied in this study due to the pronounced magnetic susceptibility differences between the water and the capillary material. Without such a compensation, the diffraction dips were lost completely.[81]

In summary, the negative diffraction dips present in short-mixing-time DWV experiments seem to lack the major drawbacks of the diffusion–diffraction described previously. They are insensitive to an orientation or size distribution of the pores involved which represents a crucial advantage for the application of diffraction experiments in complex samples, for example, like biological tissue. Moreover, DWV diffraction experiments can be realized with lower gradient amplitudes if a mixing time sufficient to avoid gradient overlaps is involved. Thus, the feasibility of such experiments is considerably improved and may even make it possible to observe diffusion–diffraction effects *in vivo*.

6. SUMMARY

MWV diffusion-weighting experiments involve two or more diffusion-weighted periods applied successively, after some mixing time, in a single acquisition. Recent progress in such experiments has been summarized focusing on the angular signal modulation and new aspects of diffusion–diffraction. After presenting the basic principles including prior work (Section 2), extended and generalized theoretical considerations (Section 3) and experimental studies investigating the signal modulation upon a variation of the angle between the wave vectors (Section 4) and diffraction effects (Section 5) were presented.

Interest in MWV experiments has risen due to their ability to provide access to the sample's microstructure beyond the scope of standard, single-wave-vector experiments. This includes the estimation of pore or cell sizes via the ''restriction effect'', that is, the signal difference between parallel and antiparallel wave-vector orientations at short mixing times, which represents a fingerprint of diffusion

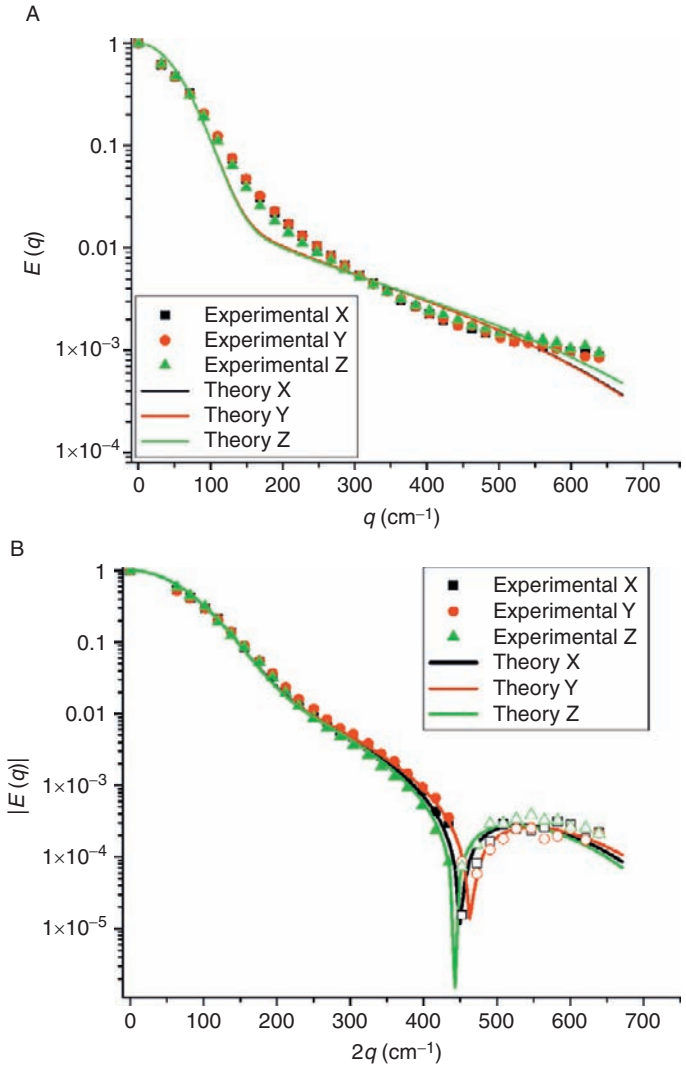

Figure 14 Absolute signal amplitude versus q for different directions of the diffusion weighting acquired on a sample of randomly oriented fractions of water-filled microcapillaries (inner diameter 29 μm) with (A) a single-wave-vector and (B) a short-mixing-time DWV experiment. Note that, as in Figure 12, the q-axis was adjusted to show dips at the same positions in both plots. For details see text and Ref. 81. Courtesy of N. Shemesh. Reprinted from Ref. 81 with permission. Copyright 2010, American Institute of Physics.

restrictions and increases with the pore size. Or the detection of locally anisotropic diffusion via the ''anisotropy effect'', the signal difference between parallel and orthogonal wave-vector orientations at long mixing times, which, for example, reflects pore eccentricity independent of an orientation coherence and, thus, even

can be detected in macroscopically isotropic samples. Another interesting effect is the ''negative diffusion–diffraction'' occurring in experiments with an even number of wave vectors: the presence of zero crossings with a signal reversal of the signal amplitude when increasing the wave vectors' magnitude.

Regarding the theoretical modelling, two basic approaches can be distinguished. The generalized Taylor expansions presented in Sections 3.1 and 3.2 aim to derive signal expressions for arbitrary pore shapes, orientation and size distributions, and wave-vector orientation combinations and could be used to define rotationally invariant measures of the pore size and anisotropy, that is, eccentricity, that can easily be determined experimentally. This is at the expense of (i) ignoring higher-order terms and (ii) retaining the assumptions of ideal timing parameters. Performing acquisitions with several q values and diffusion times and including signal contributions from freely diffusing spins in the equations, improves the modelling of the measured signal modulation and yields better estimates of the pore size (see Section 4.1.1). Similarly, acquisitions focusing on the pore eccentricity, that is, the microscopic anisotropy, can be expected to benefit from such approaches. These approaches aim to characterize samples with unknown or complex microstructure, like biological tissue, in the presence of a macroscopic diffusion anisotropy in order to detect differences and changes without the need to derive exact pore or cell diameters.

Of particular interest could be the MA index defined which characterizes the pore eccentricity, or more general the diffusion anisotropy, on a microscopic level. It reflects solely the pore or cell properties and thus, for instance, could be considered as a good measure for white matter integrity. This is in contrast to the anisotropy measures derived from the standard diffusion tensor which reflect the orientation coherence of eccentric pores or cells on a sample or voxel level, that is, in case of white matter the fibre coherence.

Exact solutions of the Bloch–Torrey equations can be obtained with the MCF formalism (Section 3.3.2), that is, accurate results for arbitrary timing parameters and q values that are even able to model diffraction effect. Thus, it is the method of choice for an accurate signal modelling and the exact determination of pore parameters for experiments with arbitrary timing and diffusion-weighting parameters. Although the exact result involves infinite terms, only a limited number of eigenfunctions will contribute significantly, that is, with a reasonable number of terms practically accurate results can be easily calculated. But the methods relies on *a priori* knowledge of the pores' orientation distribution, and the pore shape's eigenvalues and functions to the Laplace operator which may be difficult to obtain, in particular if the microstructure is complex or unknown.

First experiments detecting the restriction effect were reported in various phantoms including extracted spinal cord tissue (Section 4.1.1). Cell size estimations based on the simplifying assumptions of ideal timing parameters, that is, short gradient pulses and mixing times and long diffusion times, were in a good to reasonable agreement with literature values, depending on the pulse durations involved. This also holds for *in vivo* applications in the human corticospinal tract (Section 4.1.2). Studies of the well-defined model systems of parallel microcapillaries revealed the superior modelling and improved size estimation achievable

with the MCF model (Section 4.1.3) which may also increase the accuracy of *in vivo* applications. The method was validated by light microscopy, in capillaries as well as in samples of yeast cells (Section 4.1.3), which demonstrates its feasibility for accurate estimations of pore and cell sizes.

The experimental observation of the anisotropy effect (Section 4.2) was first reported in elongated yeast cells more than a decade ago. It has been verified in other macroscopically isotropic samples like microcapillaries and monkey grey matter, and in extracted spinal cord tissue, even on a whole-body MR system, demonstrating the accessibility of diffusion anisotropy on a microscopic level. Thus, an information complementary to the macroscopic diffusion anisotropy derived from diffusion-tensor measurements which reflects the combined effect of microscopic anisotropy and pore or cell orientation coherence can be obtained with MWV experiments. It may, for instance, be used to define a measure of white or grey matter integrity that is independent of the macroscopic coherence on a voxel or sample level, and can, for example, help to distinguish a reduced white matter fibre coherence from a lower fibre density. Other potential applications in clinical diagnostics involve the identification of pathologies accompanied by a change of the cell shape or by the absence, appearance or variation of the volume fraction of eccentric cells.

The detectability of both, the restriction and the anisotropy effect, can be improved with multiple concatenations of two wave vectors when applied with limited gradient amplitudes like on whole-body MR systems. While such experiments to investigate the microscopic anisotropy simply benefit from the shorter pulse durations sufficient to achieve the desired diffusion weighting (see Section 3.2.4), experiments aiming to detect the restriction effect in addition show an inherent increase of the modulation amplitude of typically 50% up to a factor of two which is related to the increased number of transitions from one wave vector to the other (Section 3.1.2).

While the restriction effect could not be observed in the 2D variants of MWV experiments, the microscopic diffusion anisotropy has also been investigated with the DDOSY method previously (see Section 2.1). Compared to this approach involving an independent variation of the amplitudes of the two wave vectors, the one-dimensional experiment based on the angular signal modulation considered here in detail bears several advantages. First, considerably less wave-vector combinations need to be sampled to detect the anisotropy effect speeding up the acquisition significantly which could be crucial, in particular for *in vivo* applications. Second, an interpretation of the experiment seems to be easier with a direct assignment to the pore shape or geometry instead of referring to a more abstract distribution of diffusion coefficients that, in addition, may be distorted due to the pearling effect of the inverse Laplace transform (e.g. Ref. 25). Thus, the angular modulation may provide a faster and simpler approach to detect and characterize microscopic diffusion anisotropy.

Of particular interest is also the negative diffraction effect. The feasibility of the diffusion–diffraction dips to determine pore or cell sizes has been known for a long time, however, applications to complex pore geometries or in tissue suffered from its sensitivity to size or orientation distributions which severely hampers the

reliable detection of the dips. However, as demonstrated theoretically (Section 5.1) and experimentally (Section 5.2), the zero crossings with sign reversal appearing in MWV experiments with an even number of wave vectors, are much more robust and can even be observed in isotropically distributed microcapillaries. Furthermore, the dips appear at lower q values which reduce hardware demands and facilitate the observation. Using the MCF model for the analysis, yields very good results for the capillary diameter which demonstrates the feasibility for a robust and reliable estimation of pore sizes. Thus, MWV experiments may be of considerable value to improve the applicability of diffusion–diffraction in practice.

7. CONCLUSION

The extension of standard, single-wave-vector experiments to MWV experiments with multiple diffusion-weighting periods provides additional and complementary information about the sample yielding new insights into its microstructure. The modulation of the signal with the angle between the wave vectors can be used to assess pore or cell size and shape, that is, eccentricity, with a simple experiment that is also applicable on whole-body MR systems. The negative diffraction present in even-wave-vector experiments is expected to represent a crucial advance towards an application of the diffusion–diffraction effect to pore characterization because of its robustness against size and orientation distributions. Thus, MWV experiments can be expected to become a very valuable NMR tool.

ACKNOWLEDGEMENTS

The author would like to thank Martin Busch, Dr. Michal Komlosh, Dr. Martin A. Koch, Dr. Marco Lawrenz, Dr. Evren Özarslan and Dr. Noam Shemesh for helpful discussions. The author is very grateful to Dr. Martin A. Koch, Dr. Marco Lawrenz, Dr. Noam Shemesh and Dr. Christian Ziener for providing figures.

REFERENCES

1. E. O. Stejskal and J. E. Tanner, Spin diffusion measurements: Spin echoes in the presence of a time-dependent field gradient. *J. Chem. Phys.*, 1965, **42,** 288–292.
2. M. E. Moseley, J. Kucharczyk, J. Mintorovitch, Y. Cohen, J. Kurhanewicz, N. Derugin, H. Asgari and D. Norman, Diffusion-weighted MR imaging of acute stroke—Correlation with T2-weighted and magnetic susceptibility-enhanced MR imaging in cats. *Am. J. Neuroradiol.*, 1990, **11,** 423–429.
3. P. J. Basser, J. Mattiello and D. Le Bihan, MR diffusion tensor spectroscopy and imaging. *Biophys. J.*, 1994, **66,** 259–267.
4. S. Mori, B. J. Crain, V. P. Chacko and P. C. M. van Zijl, Three-dimensional tracking of axonal projections in the brain by magnetic resonance imaging. *Ann. Neurol.*, 1999, **45,** 265–269.
5. D. G. Cory, A. N. Garroway and J. B. Miller, Applications of spin transport as a probe of local geometry. *Polym. Preprints*, 1990, **31,** 149–150.
6. P. T. Callaghan and B. Manz, Velocity exchange spectroscopy. *J. Magn. Reson. A*, 1994, **106,** 260–265.
7. P. P. Mitra, Multiple wave-vector extensions of the NMR pulsed-field-gradient spin-echo diffusion measurement. *Phys. Rev. B*, 1995, **51,** 15074–15078.

8. Y. Cheng and D. G. Cory, Multiple scattering by NMR. *J. Am. Chem. Soc.*, 1999, **121,** 7935–7936.
9. E. Özarslan and P. J. Basser, MR diffusion–''diffraction'' phenomenon in multi-pulse-field-gradient experiments. *J. Magn. Reson.*, 2007, **188,** 285–294.
10. P. T. Callaghan, S. L. Codd and J. D. Seymor, Spatial coherence phenomena arising from translational spin motion in gradient spin echo experiments. *Concepts Magn. Reson.*, 1999, **11,** 181–202.
11. P. T. Callaghan and A. A. Khrapitchev, Time-dependent velocities in porous media dispersive flow. *Magn. Reson. Imaging*, 2001, **19,** 301–305.
12. A. A. Khrapitchev and P. T. Callaghan, Double PGSE NMR with stimulated echoes: Phase cycles for the selection of desired encoding. *J. Magn. Reson.*, 2001, **152,** 259–268.
13. S. Stapf, Determination of velocity autocorrelation functions by multiple data acquisitions in NMR pulsed-field gradient experiments. *J. Magn. Reson.*, 2001, **152,** 308–312.
14. A. Jerschow and N. Müller, Suppression of convection artifacts in stimulated-echo diffusion experiments. Double-stimulated-echo experiments. *J. Magn. Reson.*, 1997, **125,** 372–375.
15. B. Manz, J. D. Seymour and P. T. Callaghan, PGSE NMR measurements of convection in a capillary. *J. Magn. Reson.*, 1997, **125,** 153–158.
16. S.-I. Han, S. Stapf and B. Blümich, Two-dimensional PFG NMR for encoding of position, velocity, and acceleration in fluid transport. *J. Magn. Reson.*, 2000, **146,** 169–180.
17. A. A. Khrapitchev, S. Stapf and P. T. Callaghan, NMR visualization of displacement correlations for flow in porous media. *Phys. Rev. E*, 2002, **66,** 051203.
18. A. A. Khrapitchev, S. Han, S. Stapf and B. Blümich, Spectrally resolved velocity exchange spectroscopy of two-phase flow. *J. Magn. Reson.*, 2002, **159,** 36–45.
19. S. Stapf and K. J. Packer, Two-dimensional propagators and spatio-temporal correlations for flow in porous media: A comparative study. *Appl. Magn. Reson.*, 1998, **15,** 303–322.
20. S. Stapf, R. A. Damion and K. J. Packer, Time correlations in fluid transport obtained by sequential rephasing gradient pulse. *J. Magn. Reson.*, 1999, **137,** 316–323.
21. B. Blümich, P. T. Callaghan, R. A. Damion, S. Han, A. A. Khrapitchev, K. J. Packer and S. Stapf, Two-dimensional NMR velocity exchange: VEXSY and SERPENT. *J. Magn. Reson.*, 2001, **152,** 162–167.
22. M. W. Hunter and P. T. Callaghan, NMR measurements of nonlocal dispersion in complex flow. *Phys. Rev. Lett.*, 2007, **99,** 210602.
23. M. W. Hunter, A. N. Jackson and P. T. Callaghan, PGSE NMR measurement of the non-local dispersion tensor for flow in porous media. *J. Magn. Reson.*, 2010, **204,** 11–20.
24. P. T. Callaghan, S. Godefroy and B. N. Ryland, Use of the second dimension on PGSE NMR studies of porous media. *Magn. Reson. Imaging*, 2003, **21,** 243–248.
25. P. T. Callaghan and I. Furó, Diffusion–diffusion correlation and exchange as a signature for local order and dynamics. *J. Chem. Phys.*, 2004, **120,** 4032–4038.
26. S. Godefroy and P. T. Callaghan, 2D relaxation/diffusion correlations in porous media. *Magn. Reson. Imaging*, 2003, **21,** 243–248.
27. P. L. Hubbard, K. M. McGrath and P. T. Callaghan, A study of anisotropic water self-diffusion and defects in lamellar mesophase. *Langmuir*, 2005, **21,** 4340–4346.
28. P. L. Hubbard, K. M. McGrath and P. T. Callaghan, Orientational anisotropy in the polydomain lamellar phase of a lyotropic liquid crystal. *Langmuir*, 2006, **22,** 3999–4003.
29. P. L. Hubbard, K. M. McGrath and P. T. Callaghan, Evolution of lamellar domain structure for an equilibrating lyotropic liquid crystal. *J. Phys. Chem. B*, 2006, **110,** 20781–20788.
30. M. Gratz, M. Wehring, P. Galvosas and F. Stallmach, Multidimensional NMR diffusion studies in microporous materials. *Microporous Mesoporous Mater.*, 2009, **125,** 30–34.
31. Y. Qiao, P. Galvosas and P. T. Callaghan, Diffusion correlation NMR spectroscopic study of anisotropic diffusion of water in plant tissues. *Biophys. J.*, 2005, **89,** 2899–2905.
32. P. T. Callaghan, NMR imaging, NMR diffraction and applications of pulsed gradient spin echoes in porous media. *Magn. Reson. Imaging*, 1996, **14,** 701–709.
33. E. Özarslan and P. J. Basser, Microscopic anisotropy revealed by NMR double pulsed field gradient experiments with arbitrary timing parameters. *J. Chem. Phys.*, 2008, **128,** 154511.
34. M. E. Komlosh, F. Horkay, R. Z. Freidlin, U. Nevo, Y. Assaf and P. J. Basser, Detection of microscopic anisotropy in gray matter and in a novel tissue phantom using double pulsed gradient spin echo MR. *J. Magn. Reson.*, 2007, **189,** 38–45.

35. E. Özarslan, Compartment shape anisotropy (CSA) revealed by double pulsed field gradient MR. *J. Magn. Reson.*, 2009, **199,** 56–67.
36. E. Özarslan, N. Shemesh and P. J. Basser, A general framework to quantify the effect of restricted diffusion on the NMR signal with applications to double pulsed field gradient NMR experiments. *J. Chem. Phys.*, 2009, **130,** 104702.
37. D. C. Douglass and D. W. McCall, Diffusion in paraffin hydrocarbons. *J. Chem. Phys.*, 1958, **62,** 1102–1107.
38. P. T. Callaghan and M. E. Komlosh, Locally anisotropic motion in a macroscopically isotropic system: Displacement correlations measured using double pulsed gradient spin-echo NMR. *Magn. Reson. Chem.*, 2002, **40,** S15–S19.
39. D. G. Cory and N. Garroway, Measurement of translational displacement probabilities by NMR: An indicator of compartmentation. *Magn. Reson. Med.*, 1990, **14,** 435–444.
40. P. T. Callaghan, A. Coy, D. MacGowan, K. J. Packer and F. O. Zelaya, Diffraction-like effects in NMR diffusion studies of fluids in porous solids. *Nature*, 1991, **351,** 467–469.
41. N. Shemesh and Y. Cohen, The effect of experimental parameters on the signal decay in double-PGSE experiments: Negative diffractions and enhancement of structural information. *J. Magn. Reson.*, 2008, **195,** 153–161.

41a. J. Finsterbusch, The parallel-antiparallel signal difference in double-wave-vector diffusion-weighted MR at short mixing times: A phase evolution perspective. *J. Magn. Reson.*, (EPub). doi:10.1016/j.jmr.2010.10.012.

42. J. E. Tanner and E. O. Stejskal, Restricted self-diffusion of protons in colloidal systems by the pulsed-gradient, spin-echo method. *J. Chem. Phys.*, 1968, **49,** 1768–1777.
43. J. Kärger and W. Heink, The propagator representation of molecular transport in microporous crystallites. *J. Magn. Reson.*, 1983, **51,** 1–7.
44. P. T. Callaghan, D. MacGowan, K. J. Packer and F. O. Zelaya, High-resolution q-space imaging in porous structures. *J. Magn. Reson.*, 1990, **90,** 177–182.
45. H. C. Torrey, Bloch equations with diffusion terms. *Phys. Rev.*, 1956, **104,** 563–565.
46. B. Robertson, Spin-echo decay of spins diffusing in a bounded region. *Phys. Rev.*, 1966, **151,** 273–277.
47. D. Sheltraw and V. M. Kenkre, The memory-function technique for the calculation of pulsed-gradient NMR signals in confined geometries. *J. Magn. Reson. A*, 1996, **122,** 126–136.
48. A. Caprihan, L. Z. Wang and E. Fukushima, A multiple-narrow-pulse approximation for restricted diffusion in a time-varying field gradient. *J. Magn. Reson. A*, 1996, **118,** 94–102.
49. P. T. Callaghan, A simple matrix formalism for spin echo analysis of restricted diffusion under generalized gradient waveforms. *J. Magn. Reson.*, 1997, **129,** 74–84.
50. A. V. Barzykin, Exact solution of the Torrey–Bloch equation for a spin echo in restricted geometries. *Phys. Rev. B*, 1998, **58,** 14171–14174.
51. A. V. Barzykin, Theory of spin echo in restricted geometries under a step-wise gradient pulse sequence. *J. Magn. Reson.*, 1999, **139,** 342–353.
52. D. S. Grebenkov, NMR survey of reflected Brownian motion. *Rev. Mod. Phys.*, 2007, **79,** 1077–1137.
53. D. S. Grebenkov, Analytical solution for restricted diffusion in circular and spherical layers under inhomogeneous magnetic fields. *J. Chem. Phys.*, 2008, **128,** 134702.
54. J. Finsterbusch and M. A. Koch, A tensor approach to double wave vector diffusion-weighting experiments on restricted diffusion. *J. Magn. Reson.*, 2008, **195,** 23–32.
55. M. Lawrenz, M. A. Koch and J. Finsterbusch, A tensor model and measures of microscopic anisotropy for double-wave-vector diffusion-weighting experiments with long mixing times. *J. Magn. Reson.*, 2010, **202,** 43–56.
56. J. Finsterbusch, Extension of the double-wave-vector diffusion-weighting experiment to multiple concatenations. *J. Magn. Reson.*, 2009, **198,** 174–182.
57. M. Lawrenz and J. Finsterbusch, Double-wave-vector diffusion-weighting experiments with multiple concatenations at long mixing times. *J. Magn. Reson.*, 2010, **206,** 112–119.
58. J. Finsterbusch, Numerical simulations of short-mixing-time double-wave-vector diffusion-weighting experiments with multiple concatenations on whole-body MR systems. *J. Magn. Reson.*, 2010, **207,** 274–282.

59. P. B. Kingsley, Introduction to diffusion tensor imaging mathematics: Part I. Tensors, rotations, and eigenvectors. *Concepts Magn. Reson. A*, 2006, **28,** 101–122.
60. P. B. Kingsley, Introduction to diffusion tensor imaging mathematics: Part III. Tensor calculation, noise, simulations, and optimization. *Concepts Magn. Reson. A*, 2006, **28,** 155–179.
61. P. J. Basser and C. Pierpaoli, Microstructural and physiological features of tissues elucidated by quantitative-diffusion-tensor MRI. *J. Magn. Reson. B*, 1996, **111,** 209–219.
62. J. S. Murday and R. M. Cotts, Self-diffusion of liquid lithium. *J. Chem. Phys.*, 1968, **48,** 4938–4944.
63. C. H. Neuman, Spin echo of spins diffusing in a bounded medium. *J. Chem. Phys.*, 1974, **60,** 4508–4511.
64. N. Shemesh, E. Özarslan, P. J. Basser and Y. Cohen, Measuring small compartmental dimensions with low-*q* angular double-PGSE NMR: The effect of experimental parameters on signal decay. *J. Magn. Reson.*, 2009, **198,** 15–23.
65. S. Axelrod and P. N. Sen, Nuclear magnetic resonance spin echoes for restricted diffusion in an inhomogeneous field: Methods and asymptotic regimes. *J. Chem. Phys.*, 2001, **114,** 6878–6895.
66. S. Ryu, Probing pores using elementary quantum mechanics. *Magn. Reson. Imaging*, 2001, **19,** 411–415.
67. T. Weber, C. H. Ziener, T. Kampf, V. Herold, W. R. Bauer and P. M. Jakob, Measurement of apparent cell radii using a multiple wave vector diffusion experiment. *Magn. Reson. Med.*, 2009, **61,** 1001–1006.
68. M. A. Koch and J. Finsterbusch, Numerical simulations of double-wave vector experiments investigating diffusion in randomly oriented ellipsoidal pores. *Magn. Reson. Med.*, 2009, **62,** 247–254.
69. P. P. Mitra and B. I. Halperin, Effects of finite gradient-pulse width in pulsed-field-gradient diffusion measurements. *J. Magn. Reson. A*, 1995, **113,** 94–101.
70. M. A. Koch and J. Finsterbusch, Compartment size estimation with double wave vector diffusion-weighted imaging. *Magn. Reson. Med.*, 2008, **60,** 90–101.
71. P. Mansfield, Multi-planar image formation using NMR spin echoes. *J. Phys. C*, 1977, **10,** 349–352.
72. G. Sobue, Y. Hashizume, T. Mitsuma and A. Takahashi, Size-dependent myelinated fiber loss in the corticospinal tract in Shy–Drager syndrome and amyotrophic lateral sclerosis. *Neurology*, 1987, **37,** 529–532.
73. S. Terao, G. Sobue, Y. Hashizume, F. Tanaka and T. Mitsuma, The lateral corticospinal tract and spinal ventral horn in X-linked recessive spinal and bulbar muscular atrophy: A quantitative study. *Acta Neuropathol.*, 1997, **93,** 1–6.
74. Y. Assaf, A. Mayk and Y. Cohen, Displacement imaging of spinal cord using q-space diffusion-weighted MRI. *Magn. Reson. Med.*, 2000, **44,** 713–722.
75. M. A. Koch and J. Finsterbusch, Double wave vector diffusion weighting in the human corticospinal tract *in vivo*. Proceedings of the International Society for Magnetic Resonance in Medicine, 16th Annual Meeting, Toronto, Canada, 2006, p. 764.
76. M. A. Koch and J. Finsterbusch, *In vivo* pore size estimation in white matter with double wave vector diffusion weighting. Proceedings of the International Society for Magnetic Resonance in Medicine, 18th Annual Meeting, Stockholm, Sweden, 2010, p. 194.
77. N. Shemesh, E. Özarslan, A. Bar-Shir, P. J. Basser and Y. Cohen, Observation of restricted diffusion in the presence of a free diffusion compartment: Single-and double-PFG experiments. *J. Magn. Reson.*, 2009, **200,** 214–225.
78. M. E. Komlosh, E. Özarslan, M. J. Lizak, F. Horkay, V. Schram, N. Shemesh, Y. Cohen and P. J. Basser, Pore diameter mapping using double pulsed-field gradient MRI and its validation using a novel glass capillary array phantom. *J. Magn. Reson.*, 2010, (EPub). doi:10.1016/j.jmr.2010.10.014.
79. N. Shemesh, E. Özarslan, P. J. Basser and Y. Cohen, First experimental observation of both microscopic (uA) and compartment shape anisotropy (CSA) in randomly oriented biological cells using double-PFG NMR. Proceedings of the International Society for Magnetic Resonance in Medicine, 18th Annual Meeting, Stockholm, Sweden, 2010, p. 193.
80. M. E. Komlosh, M. J. Lizak, F. Horkay, R. Z. Freidlin and P. J. Basser, Observation of microscopic diffusion anisotropy in the spinal cord using double-pulse gradient spin echo MRI. *Magn. Reson. Med.*, 2008, **59,** 803–809.

81. N. Shemesh, E. Özarslan, T. Adiri, P. J. Basser and Y. Cohen, Noninvasive bipolar double-pulsed-field-gradient NMR reveals signatures for pore size and shape in polydisperse, randomly oriented, inhomogeneous porous media. *J. Chem. Phys.*, 2010, **133,** 044705.
82. M. Lawrenz, M. A. Koch and J. Finsterbusch, Evidence for microscopic diffusion anisotropy in spinal cord tissue observed with DWV imaging on a whole-body MR system. Proceedings of the International Society for Magnetic Resonance in Medicine, 18th Annual Meeting, Stockholm, Sweden, 2010, p. 4005.
83. P. T. Callaghan, A. Coy, T. P. J. Halpin, D. MacGowan, K. J. Packer and F. O. Zelaya, Diffusion in porous systems and the influence of pore morphology in pulsed gradient spin-echo nuclear magnetic resonance studies. *J. Chem. Phys.*, 1992, **97,** 651–662.
84. B. Balinov, O. Söderman and J. C. Ravey, Diffraction-like effects observed in the PGSE experiment when applied to a highly concentrated water/oil emulsion. *J. Phys. Chem.*, 1994, **98,** 393–395.
85. A. Coy and P. T. Callaghan, Pulsed gradient spin echo nuclear magnetic resonance for molecules diffusing between partially reflecting rectangular barriers. *J. Chem. Phys.*, 1994, **101,** 4599–4609.
86. M. Appel, G. Fleischer, D. Geschke, J. Kärger and M. Winkler, Pulsed-field-gradient NMR analogue of the single-slit diffraction pattern. *J. Magn. Reson. A*, 1996, **122,** 248–250.
87. S. J. Gibbs, Observations of diffusive diffraction in a cylindrical pore by PFG NMR. *J. Magn. Reson.*, 1997, **124,** 223–226.
88. P. W. Kuchel, A. Coy and P. Stilbs, NMR ''diffusion–diffraction'' of water revealing alignment of erythrocytes in a magnetic field and their dimensions and membrane transport characteristics. *Magn. Reson. Med.*, 1997, **37,** 637–643.
89. A. M. Torres, R. J. Michniewicz, B. E. Chapman, G. A. R. Young and P. W. Kuchel, Characterisation of erythrocyte shapes and sizes by NMR diffusion–diffraction of water: Correlations with electron micrographs. *Magn. Reson. Imaging*, 1998, **16,** 423–434.
90. G. Pages, D. Szekely and P. W. Kuchel, Erythrocyte-shape evolution recorded with fast-measurement NMR diffusion–diffraction. *J. Magn. Reson. Imaging*, 2008, **28,** 1409–1416.
91. L. Avram, Y. Assaf and Y. Cohen, The effect of rotational angle and experimental parameters on the diffraction patterns and microstructural information obtained from *q*-space diffusion NMR: Implications for diffusion in white matter fibers. *J. Magn. Reson.*, 2004, **169,** 30–38.
92. A. Bar-Shir, E. Avram, L. Özarslan, P. J. Basser and Y. Cohen, The effect of the diffusion time and pulse gradient duration ratio on the diffraction pattern and the structural information estimated from *q*-space diffusion MR: Experiments and simulations. *J. Magn. Reson.*, 2008, **194,** 230–236.
93. L. Avram, E. Özarslan, Y. Assaf, A. Bar-Shir, Y. Cohen and P. J. Basser, Three-dimensional water diffusion in impermeable cylindrical tubes: Theory vs. experiment. *NMR Biomed.*, 2008, **21,** 888–898.
94. N. Shemesh, E. Özarslan, P. J. Basser and Y. Cohen, Detecting diffusion–diffraction patterns in size distribution phantoms using double-pulsed field gradient NMR: Theory and experiments. *J. Chem. Phys.*, 2010, **132,** 034703.

This page intentionally left blank

SUBJECT INDEX

N